

# Spatiotemporal variability of the carbonate system in the North Atlantic Ocean

Elisa Fernández Guallart

Tesis doctoral presentada por D<sup>a</sup> Elisa Fernández Guallart para obtener el grado de Doctor por la Universidad de las Palmas de Gran Canaria, Programa de Doctorado en Oceanografía

Directores: Dr. Carles Pelejero Bou y Dr. Fiz Fernández Pérez

Universidad de las Palmas de Gran Canaria  
Institut de Ciències del Mar (ICM - CSIC)  
Instituto de Investigaciones Marinas (IIM - CSIC)

En Barcelona, a de de 2015

La Doctoranda	El Director	El Codirector
Elisa Fernández Guallart	Carles Pelejero Bou	Fiz Fernández Pérez



Institut  
de Ciències  
del Mar





*A la meva germana.*

*A les meves amigues.*

*A mis padres.*



## **CONTENTS**

<b>Resumen/Summary</b>	<b>10</b>
<b>1. Introduction</b>	<b>13</b>
General background: The climate change scenario	15
The ocean carbon sink	20
The subtropical North Atlantic Ocean	30
<b>2. Aims of the Thesis and data collection</b>	<b>51</b>
Objectives and Thesis outline	53
Oceanographic cruises in the (sub)tropical North Atlantic	54
<b>3. Results</b>	<b>63</b>
Trends in anthropogenic CO <sub>2</sub> in water masses of the Subtropical North Atlantic Ocean	63
Anthropogenic CO <sub>2</sub> changes in the Equatorial Atlantic Ocean	99
Ocean acidification along the 24.5°N section in the Subtropical North Atlantic	135
<b>4. Discussion and Conclusions</b>	<b>159</b>
Synthesis of the results and general discussion	161
Main conclusions by chapters	174
Future perspectives and open questions	176
<b>Thesis summary (Spanish version)</b>	<b>179</b>
<b>References</b>	<b>233</b>
<b>Appendices</b>	<b>245</b>
Appendix I. WOCE A05 report	247
Appendix II. Abbreviations and acronyms	271



*Llebrícia i Tortugàlia*

qui camina i va distret  
no pot veure on posa els peus  
i ha d'avançar  
fent lenta passa;  
però també es fa sa saber  
que molt llebre s'ha de ser  
per saltar llamps  
i no enrampar-se

qui camina amb el cap cot  
bo i mirant on posa els peus  
pot avançar  
llençant la passa;  
però també es fa sa saber  
que tortuga s'ha de ser  
per saltar el temps  
i no enganyar-se

qui mira lluny pot caure a prop  
qui mira a prop no cala lluny  
més valdrà, per tant -dic jo-  
no mirar enllloc  
i anar veient què passa  
a cada passa

*Pau Riba*

## **Resumen**

El sumidero oceánico de carbono contribuye a mitigar el calentamiento global. Pero la entrada al océano de este CO<sub>2</sub> de origen antropogénico (C<sub>ant</sub>) tiene consecuencias sobre los balances químicos del sistema del carbónico en agua de mar, que se traducen en una reducción del pH superficial del océano. El Océano NortAtlántico tiene la tasa de acumulación de C<sub>ant</sub> más alta de todos los océanos. El mecanismo clave para explicar este hecho es el transporte de aguas cálidas tropicales y subtropicales enriquecidas en C<sub>ant</sub> hasta las zonas de formación de agua profunda, a través de la circulación de retorno. Estas aguas profundas vuelven hacia el sur dentro de la corriente profunda de frontera oeste, transportando cantidades moderadas pero crecientes de C<sub>ant</sub>. Teniendo en cuenta el papel predominante del Atlántico (sub)tropical en la captación de C<sub>ant</sub> atmosférico, la acidificación oceánica asociada a esta captación y considerando también el papel de la circulación en la distribución del C<sub>ant</sub> absorbido entre distintas cuencas, esta tesis evalúa los cambios decenales y tendencias en algunos parámetros del sistema del carbónico a lo largo de dos secciones oceanográficas situadas a 24.5°N y 7.5°N de latitud, ocurridos desde principios de 1990s a principios de 2010s. Hemos evaluado la interacción entre la circulación oceánica y el sistema del carbónico, en concreto respecto a los mecanismos que controlan y condicionan las tasas de acumulación de C<sub>ant</sub> y la acidificación asociada. Esto se consiguió estudiando las masas de agua presentes en cada una de las dos secciones separadamente en distintas zonas o regiones que se definieron de acuerdo a criterios oceanográficos. Esta metodología mostró que la variabilidad espaciotemporal en la acumulación de C<sub>ant</sub> a lo largo de las dos secciones está fuertemente relacionada con la señal de C<sub>ant</sub> transportada dentro de la corriente principal (la corriente profunda de frontera oeste) que atraviesa las dos secciones. La separación de las diferencias de pH encontradas en los componentes antropogénico y no-antropogénico (natural) mostró que estos tienen una magnitud similar pero muestran diferente distribución en profundidad y en longitud. Nuestros resultados sugieren que todavía es necesario describir de una forma más completa cuál es la variabilidad natural de los parámetros del sistema del carbónico, para definir con más claridad la capacidad de predicción de las tendencias observadas más allá de la escala de tiempo decenal.

## **Summary**

The ocean carbon sink contributes to mitigate global warming. However, the resulting anthropogenic CO<sub>2</sub> (C<sub>ant</sub>) oceanic invasion affects the chemical balances of the CO<sub>2</sub> system in seawater, which translates into a decrease in surface ocean pH. The North Atlantic Ocean presents the largest C<sub>ant</sub> storage rate of all oceans. The key mechanism contributing to this high value is the northward transport of warm tropical and subtropical waters that contain high C<sub>ant</sub> concentrations from low latitudes poleward into the regions of deep water formation, through the upper limb of the Atlantic Meridional Overturning Circulation. These deep waters return southward into the Deep Western Boundary Current (DWBC) containing moderate but increasing C<sub>ant</sub> levels. Given the predominant part of the (sub)tropical North Atlantic region in the uptake of atmospheric C<sub>ant</sub>, the anthropogenically derived acidification and taking into account the role of ocean circulation on the distribution of the absorbed C<sub>ant</sub> between basins, this thesis assesses decadal changes and trends in some parameters of the carbonate system along two oceanographic sections located at 24.5°N and at 7.5°N of latitude, occurred between the early 1990s and the early 2010s. We assessed the interactions between ocean circulation and the carbonate system, in particular regarding the processes that control and modulate the storage rates of C<sub>ant</sub> and the associated acidification. This was accomplished by splitting the water masses present in each of the two sections into separated zonal regions that were defined following oceanographic criteria. This methodological approach showed that the spatiotemporal variability in the storage of C<sub>ant</sub> along the two sections is strongly related with the deep C<sub>ant</sub> signal conveyed by the main circulation current (i.e. DWBC) that spreads across the two sections. The deconvolution of the temporal pH differences into anthropogenic and non-anthropogenic (natural) components revealed that these are of similar magnitudes but have different representations with depth and longitude. Our results emphasize the need to provide more insight into natural variability of the parameters of the carbonate system, with the aim of providing further insight on the predictability of the observed trends for time periods over decadal timescales.



# Introduction



## GENERAL BACKGROUND: THE CLIMATE CHANGE SCENARIO

Multiple lines of evidence from observations of changes in the atmosphere, land, ocean, biosphere and cryosphere have already shown that climate across the Earth is changing due to the perturbation of the Earth's radiation budget (Figure 1.1), largely as a result of human activities. Many of the observed changes are unprecedented over decades to millennia: the amounts of snow and ice have diminished, sea level has risen and the concentrations of greenhouse gases (GHGs) have increased in the atmosphere, but the most relevant evidence of climate change is that the atmosphere and ocean have warmed. Regarding global warming, GHGs are significant drivers of climate change since they produce a positive radiative forcing that has caused global mean air temperature to increase over the last hundred years. Consequently, land and sea surface temperatures have also increased. Warming of the climate is unequivocal, with ocean warming dominating the increase in energy stored in the climate system, accounting for more than 90% of the energy accumulated between 1971 and 2010 (IPCC, 2013).

The atmospheric concentrations of the GHGs carbon dioxide ( $\text{CO}_2$ ), methane ( $\text{CH}_4$ ), and nitrous oxide ( $\text{N}_2\text{O}$ ) have all increased since 1750 due to human activities such as the burning of fossil fuels and changes in land use. In 2011 the concentrations of these GHGs exceeded the pre-industrial levels by about 40%, 150%, and 20%, respectively (IPCC, 2013). Among them,  $\text{CO}_2$  is the primary GHG emitted through human activities and dominates the total radiative forcing caused by well mixed GHGs (Hofmann *et al.*, 2011), being together with  $\text{CH}_4$  the only ones that continue to increase at a regular rate (<http://www.esrl.noaa.gov/>). The Mauna Loa atmospheric  $\text{CO}_2$  record (Figure 1.2a) was started in 1958 by Charles David Keeling. This record which has come to be called 'the Keeling Curve', has become an iconic graph of climate change, being the first in evidencing the clear rise in atmospheric  $\text{CO}_2$  concentrations, whose annual averages have increased from 277 ppm in 1750 (Joos and Spahni, 2008) to 395.31 ppm in 2013 (Dlugokencky and Tans, 2013). On May, 9, 2013, the daily mean of atmospheric  $\text{CO}_2$  measured in Mauna Loa surpassed, for the first time, the 400 ppm level and, in year 2014,  $\text{CO}_2$  monthly averages in the same station remained above this level for a few months (Dr. Pieter Tans, NOAA/ESRL; [www.esrl.noaa.gov/gmd/ccgg/trends/](http://www.esrl.noaa.gov/gmd/ccgg/trends/)). According to recent projections based on the new Representative Concentration Pathway (RCP) scenarios, which represent GHG concentration trajectories, it is clear that continued emissions of GHGs will cause further warming and changes in all components of the climate system (IPCC, 2013) (Figure 1.2b).

Anthropogenic  $\text{CO}_2$  ( $\text{C}_{\text{ant}}$ ) emissions occur on top of an active natural carbon cycle (Figure 1.3) that circulates carbon between the atmosphere, ocean and terrestrial biosphere reservoirs on a broad range of timescales. Two main domains in the global carbon cycle can be differentiated (Zeebe, 2012; Ciais *et al.*, 2013):

- A fast domain, which consists of carbon in the atmosphere, the ocean, surface ocean sediments and land in vegetation, soils and freshwaters. It is characterized by large exchange fluxes and relatively rapid res-

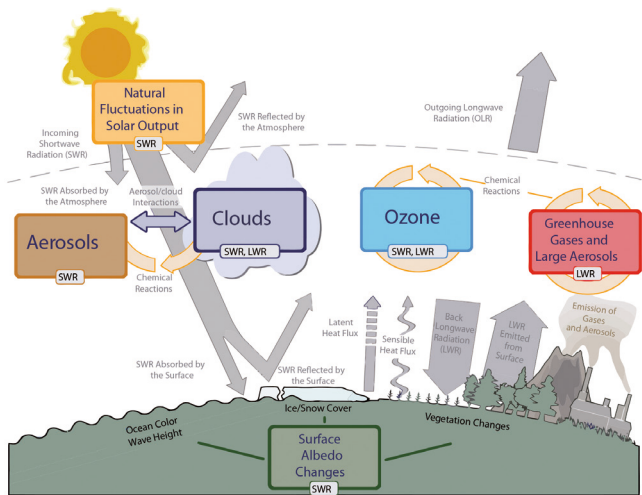


**Figure 1.1.** Main drivers of climate change. The radiative balance between incoming solar shortwave radiation (SWR) and outgoing longwave radiation (LWR) is influenced by different global climate ‘drivers’. Natural fluctuations in solar output (solar cycles) can cause changes in the energy balance through fluctuations in the amount of incoming SWR. Human activity changes the emissions of gases and, in turn, aerosols and ozone amounts, which also influence the energetic balance. Changes in the properties of clouds by means of aerosols also have important implications for the radiative budget. Anthropogenic changes in GHGs and large aerosols modify the amount of outgoing LWR by absorbing outgoing LWR and re-emitting less energy at a lower temperature (for instance,  $\text{CO}_2$ ,  $\text{CH}_4$  and  $\text{N}_2\text{O}$  altogether amount to 80% of the total radiative forcing from well-mixed GHG as  $\text{CO}_2$ ,  $\text{CH}_4$ ,  $\text{N}_2\text{O}$ ,  $\text{O}_3$  and CFCs). Surface albedo is changed by changes in vegetation or land surface properties, snow or ice cover and ocean colour. These changes are driven by natural changes, as well as human influence. Source: IPCC (2013).

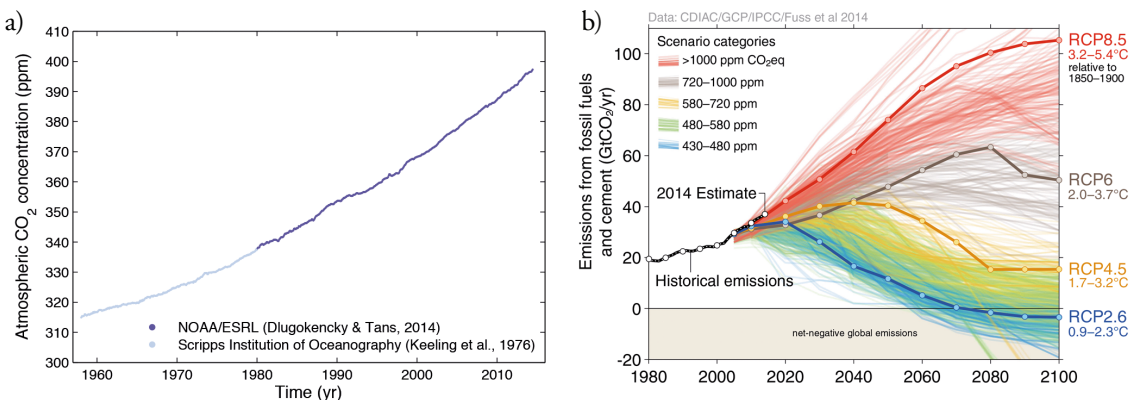


**Figure 1.2.** a) Surface average atmospheric  $\text{CO}_2$  concentration, deseasonalised (ppm). The 1980–2014 monthly data are from NOAA/ESRL and are an average of direct atmospheric  $\text{CO}_2$  measurements from multiple stations in the marine boundary layer. The 1958–1979 monthly data are from the Scripps Institution of Oceanography, based on an average of direct atmospheric  $\text{CO}_2$  measurements from the Mauna Loa and South Pole stations. Source: Le Quéré et al., (2015). b)  $\text{CO}_2$  emissions from fossil fuels and cement associated to the Representative Concentration Pathway (RCP) scenarios used in the Coupled Model Intercomparison Project Phase 5 (CMIP5). Increase of global mean surface temperatures for 2081–2100 relative to 1986–2005 is projected to likely be in the ranges of  $0.3^\circ\text{C}$  to  $1.7^\circ\text{C}$  (RCP2.6),  $1.1^\circ\text{C}$  to  $2.6^\circ\text{C}$  (RCP4.5),  $1.4^\circ\text{C}$  to  $3.1^\circ\text{C}$  (RCP6.0),  $2.6^\circ\text{C}$  to  $4.8^\circ\text{C}$  (RCP8.5). Source: Global Carbon Project (<http://www.globalcarbonproject.org/>).

ervoir turnover times that range between a few years for the atmosphere to decades to millennia for the major carbon reservoirs of vegetation, soil and the ocean.

- A slow domain that consists of the carbon stored in rocks and sediments, with turnover times of 10,000 years or longer.

The two domains exchange carbon through volcanic emissions of CO<sub>2</sub>, chemical weathering, erosion and sediment formation on the sea floor. Prior to the Industrial Era the fast domain was close to a steady state but fossil fuel extraction from geological reservoirs and their combustion since the beginning of the Industrial Era has resulted in the transfer of a significant amount of fossil carbon from the slow domain into the fast domain, thus causing an unprecedented, major human-induced perturbation in the carbon cycle.

The need of an accurate assessment of the C<sub>ant</sub> emissions and their redistribution among the major reservoirs has led to international collaborative efforts to complete and continuously update the global carbon budget (Le Quéré *et al.*, 2013; Le Quéré *et al.*, 2014; Le Quéré *et al.*, 2015). Mainly, the global carbon budget is quantified into five main components (Figure 1.4 and Table 1.1). All components except the land-use-change have grown since 1959, despite showing some decadal variability (Table 1.1; from Le Quéré *et al.*, (2015)). Although the CO<sub>2</sub> sinks have continued to grow with increasing emissions, climate change will affect carbon cycle processes that exchange carbon between the main reservoirs in a way that will aggravate the increase of CO<sub>2</sub> in the atmosphere (IPCC, 2013).

**Table 1.1.** Decadal mean in the five components of the anthropogenic CO<sub>2</sub> budget for the periods 1960–1969, 1970–1979, 1980–1989, 1990–1999, 2000–2009 and last decade (2004–2013). All values are in GtC yr<sup>-1</sup>. All uncertainties are reported as  $\pm 1\sigma$ . A data set containing data for each year during 1959–2013 is available at <http://cdiac.ornl.gov/GCP/carbonbudget/2014/>. Source: modified from Le Quéré *et al.*, (2015).

	Mean (GtCyr <sup>-1</sup> )						
	1960–1969	1970–1979	1980–1989	1990–1999	2000–2009	2004–2013	2013
<i>Emissions</i>							
Fossil fuel combustion and cement production	3.1 ± 0.2	4.7 ± 0.2	5.5 ± 0.3	6.4 ± 0.3	7.8 ± 0.4	8.9 ± 0.4	9.9 ± 0.5
Land-use-change emissions	1.5 ± 0.5	1.3 ± 0.5	1.4 ± 0.5	1.6 ± 0.5	1.0 ± 0.5	0.9 ± 0.5	0.9 ± 0.5
<i>Partitioning</i>							
Atmospheric growth rate	1.7 ± 0.1	2.8 ± 0.1	3.4 ± 0.1	3.1 ± 0.1	4.0 ± 0.1	4.3 ± 0.1	5.4 ± 0.2
Ocean sink	1.1 ± 0.5	1.5 ± 0.5	1.9 ± 0.5	2.2 ± 0.5	2.4 ± 0.5	2.6 ± 0.5	2.9 ± 0.5
Residual terrestrial sink	1.8 ± 0.7	1.8 ± 0.8	1.6 ± 0.8	2.7 ± 0.8	2.4 ± 0.8	2.9 ± 0.8	2.5 ± 0.9

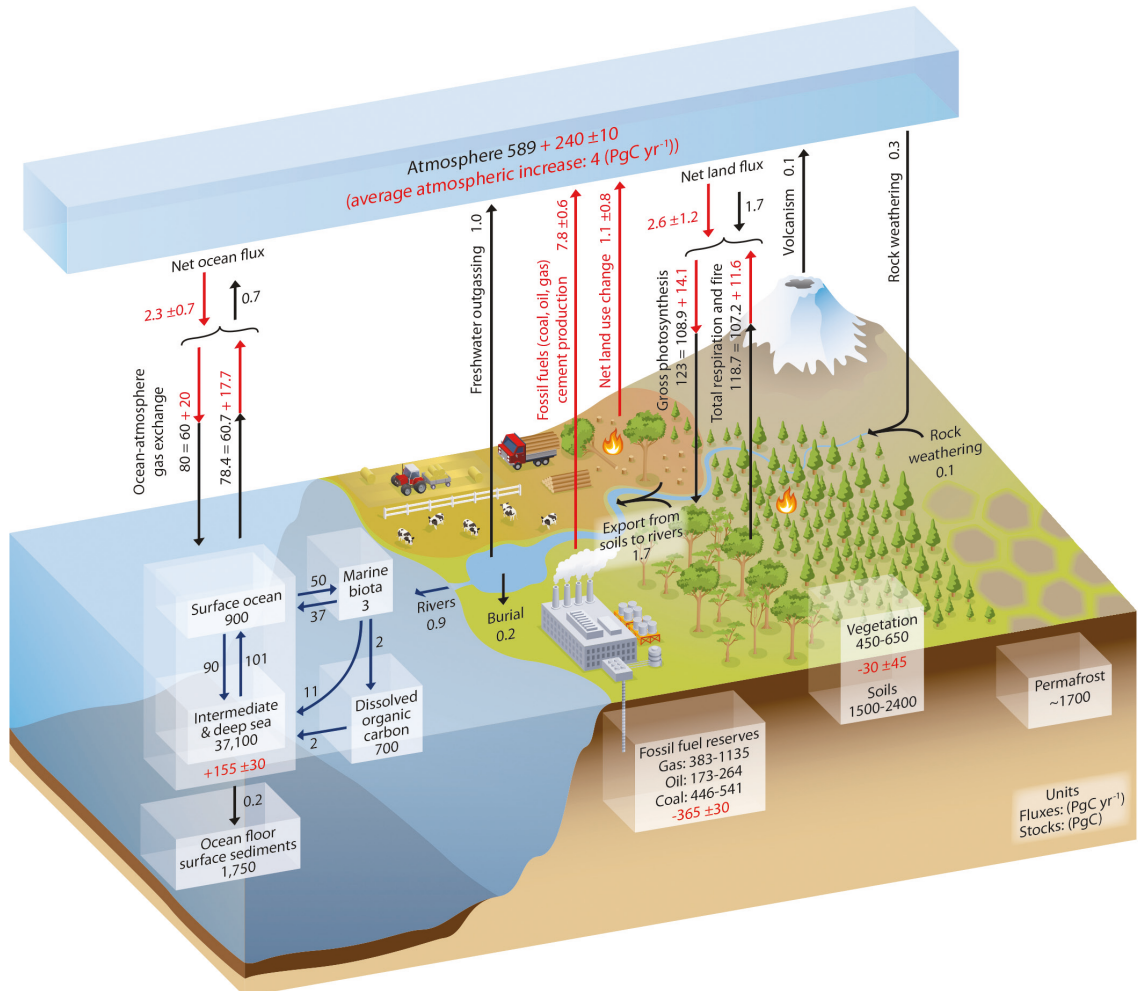


**Figure 1.3.** Scheme of the global carbon cycle. Numbers represent mass reservoirs in PgC ( $1 \text{ PgC} = 10^{15} \text{ gC}$ ) and annual carbon exchange fluxes (in  $\text{PgC yr}^{-1}$ ). Black numbers and arrows indicate mass reservoirs and exchange fluxes estimated for the time prior to the Industrial Era ( $\sim 1750$ ). Red arrows and numbers indicate annual anthropogenic fluxes averaged over the 2000–2009 time period. These fluxes are a perturbation of the carbon cycle during Industrial Era (post 1750). The red arrows parts of the ‘Net land flux’ and the ‘Net ocean flux’ are the uptake of anthropogenic  $\text{CO}_2$  by the ocean and by terrestrial ecosystems, respectively (carbon sinks). Red numbers in the reservoirs denote cumulative changes of anthropogenic carbon over the Industrial Period 1750–2011. By convention, a positive cumulative change means that a reservoir has gained carbon since 1750. Uncertainties are reported as 90% confidence intervals. Source: Ciais et al. (2013).

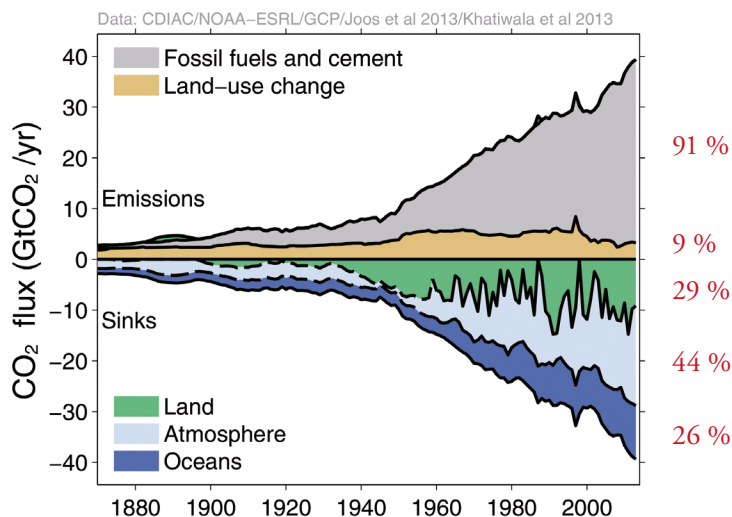


**Figure 1.4.** Combined components of the global carbon budget as a function of time: annual anthropogenic  $\text{CO}_2$  ( $\text{C}_{\text{ant}}$ ) emissions and their partitioning among the main reservoirs ( $\text{GtC yr}^{-1}$ ) from 1750 to 2013. Red values in % show the global average contribution of the five components described over the decade 2004–2013: fossil fuel and cement  $\text{CO}_2$  emissions (grey),  $\text{CO}_2$  emissions from net land use change (brown), the atmospheric  $\text{CO}_2$  growth rate (light blue), ocean  $\text{CO}_2$  sink (dark blue) and land sink (green). The budget does not include the contribution of anthropogenic  $\text{CO}$  and  $\text{CH}_4$  nor carbon fluxes in the land-to-ocean continuum. Source: adapted from the Global Carbon Budget 2014 (<http://www.globalcarbonproject.org/>); average % values from Le Quéré *et al.* (2015).

The ocean sink represents  $\sim 45\%$  of fossil fuel emissions over the industrial period, and  $\sim 30\%$  assuming total  $\text{C}_{\text{ant}}$  emissions since the preindustrial era (Sabine *et al.*, 2004; Khatiwala *et al.*, 2013). The growth rate of this sink has increased from  $1.1 \pm 0.5 \text{ Gt yr}^{-1}$  in the 1960s to  $2.6 \pm 0.5 \text{ Gt yr}^{-1}$  for the period 2004–2013 (Le Quéré *et al.*, 2015), roughly in line with the atmospheric increase when averaged over large regions during the last decades (Ciais *et al.*, 2013). The uptake and storage of  $\text{C}_{\text{ant}}$  by the ocean depends on ventilation, formation and transport of water masses and show substantial regional and temporal variability (Gruber *et al.*, 2009; Sabine and Tanhua, 2010; Khatiwala *et al.*, 2013; DeVries, 2014). The absorption of  $\text{CO}_2$  by the ocean contributes to mitigate global warming but ocean uptake and chemical equilibration of  $\text{C}_{\text{ant}}$  in seawater leads to a progressive reduction in seawater pH and the saturation states of calcium carbonate minerals in a process known as ocean acidification (Doney *et al.*, 2009; Feely *et al.*, 2009). This substantial change in the chemistry of the oceans has led to changes in the physiology of marine organisms (Riebesell *et al.*, 2000; Fabry *et al.*, 2008; Iglesias-Rodriguez *et al.*, 2008; Ries *et al.*, 2009; Sett *et al.*, 2014; Bach, 2015; Meyer and Riebesell, 2015), thus impacting in the ecology of the ocean (Guinotte and Fabry, 2008; Doney *et al.*, 2012; Andersson *et al.*, 2015; Bach *et al.*, 2015). Since it is a phenomenon that affects not only biological but also chemical and biogeochemical processes, ocean acidification has been termed “the other  $\text{CO}_2$  problem” (Doney *et al.*, 2009), to bring it to the attention of the public as another global threat as important as global warming (IPCC, 2013).

There is a need to better understand the anthropogenic perturbation and the intrinsic variability of the natural carbon cycle in the ocean with time, and to establish the rate at which ocean acidification is taking place. This will allow us to unravel the response of the ocean sink and the marine ecosystems to changes in climate, which is crucial information to establish CO<sub>2</sub> emission regulations addressed to achieve CO<sub>2</sub> concentration stabilization targets.

## THE OCEAN CARBON SINK

The ocean plays a key role in the regulation of Earth's climate since it exchanges large quantities of heat, water, gases and particles with the atmosphere. The continuous interaction between the atmosphere and the ocean leads to CO<sub>2</sub> gas exchange between these two major reservoirs which translates, on average, in an uptake of anthropogenic CO<sub>2</sub> into the surface layers of the ocean. Taking into consideration that the global ocean overturning time is of the order of one millennium (Holzer and Primeau, 2006), small changes in the large ocean carbon reservoir can induce significant changes in atmospheric CO<sub>2</sub> concentration and, correspondingly, perturbations in atmospheric CO<sub>2</sub> can be buffered by the ocean, leading, for example, to the typical glacial-interglacial CO<sub>2</sub> cycles (Luthi *et al.*, 2008).

### Overview of the ocean carbon cycle

The oceans regulate atmospheric CO<sub>2</sub> mainly through three mechanisms (Volk and Hoffert, 1985) (Figure 1.5):

- Solubility pump. It involves processes of absorption or release of CO<sub>2</sub> in the atmosphere-ocean interface due to changes in solubility of gaseous CO<sub>2</sub>. The sequestration of atmospheric CO<sub>2</sub> through this mechanism starts with the CO<sub>2</sub> dissolution, its hydration to carbonic acid and the dissociation of carbonic acid that leads to the carbonate system in seawater, and continuous with the transport and mixing of the different forms of dissolved CO<sub>2</sub> through downwelling to the deep ocean (physical pump).
- Organic carbon (soft tissue) pump. It involves the CO<sub>2</sub> uptake and its fixation into organic matter in surface waters by means of photosynthesis, its export into the deep ocean and the gradual remineralization of organic matter back to CO<sub>2</sub> and nutrients.
- Carbonate pump. It consists in the formation of calcium carbonate (CaCO<sub>3</sub>) structures by calcifying organisms in the surface oceans, and their dissolution deeper in the water column. This process represents one component of the ocean's biological carbon pump but operates counter to the organic carbon pump, which tends to reduce atmospheric CO<sub>2</sub>. On the contrary, the precipitation of CaCO<sub>3</sub> involves an increase in CO<sub>2</sub> because this gas is liberated during CaCO<sub>3</sub> precipitation according to the reaction:



However, the increase in CO<sub>2</sub> is not one mole per mole of CaCO<sub>3</sub> precipitated but a bit less (today

it is of about 0.6 mols per mol, (Frankignoulle *et al.*, 1994)) because of buffering, since most of the newly formed  $\text{CO}_2$  will be converted to bicarbonate. The medium does however decrease in pH with  $\text{CaCO}_3$  precipitation. Hence,  $\text{CaCO}_3$  production in the surface ocean tends to increase atmospheric  $\text{CO}_2$ .

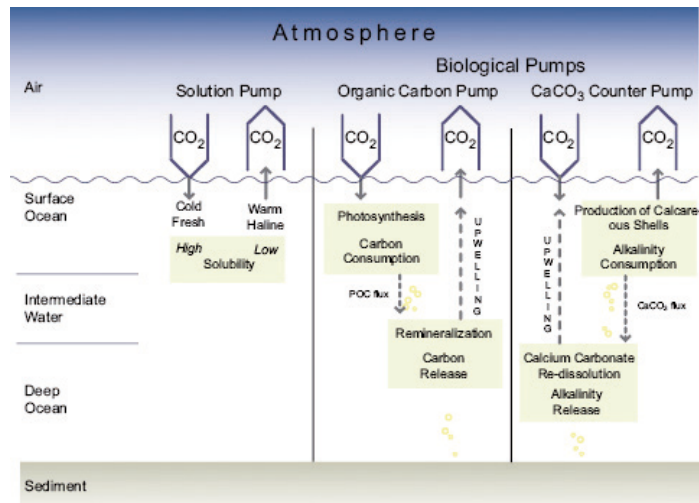
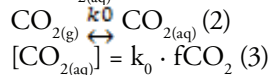


**Figure 1.5.** Three main ocean carbon pumps which control the regulation of natural atmospheric  $\text{CO}_2$  changes by the ocean: the solubility pump, the organic carbon pump and the  $\text{CaCO}_3$  'counter pump' Source: Heinze *et al.*, (1991).

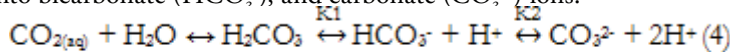
At the scale of decades to a century, and in the context of the oceanic sequestration of anthropogenic  $\text{CO}_2$ , the most important mechanism is the downward transport of surface water into the deep ocean. In this transport, the physical carbon pump stands as the most important, and the two biological pumps modulate, but do not dominate, the net marine uptake of  $\text{CO}_2$  (Heinze *et al.*, 2015). Biological activity helps lowering  $\text{CO}_2$  concentrations in the upper layers of the ocean, while values increase with depth due to remineralization of sinking particles. Once in the deep ocean,  $\text{CO}_2$  concentrations increase horizontally with the age of the water masses along the trajectory of the water flow and the loop closes when the deeper waters upwell bringing  $\text{CO}_2$  and nutrients back to the surface, leading to outgassing and stimulating marine productivity (Figure 1.5). As described above, while the soft tissue pump tends to decrease  $\text{CO}_2$  in the surface ocean, the carbonate pump has the opposite effect. Altogether, the biological pumps still lower surface  $\text{CO}_2$  levels due to the fact that more organic carbon than carbonate is exported from the surface layer. The measure of the relative strengths of the two pumps is termed 'rain ratio' (inorganic / organic export) and can play an important role in the efficiency of  $\text{CO}_2$  sequestration by the ocean (Archer *et al.*, 2000). In particular, changes in the rain ratio have been invoked as a possible mechanism in controlling the glacial interglacial changes in atmospheric  $\text{CO}_2$  (Archer *et al.*, 2000), and paleoceanographic reconstructions using molecular biomarkers in deep sea sediment cores have attempted to evaluate its importance in different areas (Calvo *et al.*, 2004; Calvo *et al.*, 2011).

## The seawater carbonate system

The atmosphere and the surface ocean exchange gaseous CO<sub>2</sub>. The equilibrium between the atmospheric CO<sub>2</sub> (CO<sub>2(g)</sub>) and in its content in seawater (CO<sub>2(aq)</sub>) is set by Henry's Law:



where [CO<sub>2(aq)</sub>] is the concentration of aqueous CO<sub>2</sub>, fCO<sub>2</sub> is the fugacity of CO<sub>2</sub> in the air and k<sub>0</sub> is the solubility coefficient, which depends on temperature and salinity. fCO<sub>2</sub> can be considered as the partial pressure of CO<sub>2</sub> by assuming ideal gas behaviour. The quantity that determines this physical process is the difference in partial pressure of CO<sub>2</sub> (pCO<sub>2</sub>) between surface seawater and the atmosphere. The pCO<sub>2</sub> assigned to a seawater sample refers to the partial pressure of CO<sub>2</sub> in the gas phase that is in equilibrium with that seawater. It is strongly influenced by temperature, decreasing with increasing temperature because of the decrease in CO<sub>2</sub> solubility. Equilibration of surface ocean and atmosphere occurs on a time scale of roughly one year (Caias *et al.*, 2013). Changes in pCO<sub>2</sub> in the atmosphere are thus paralleled in the ocean. However, the consequences in both compartments are very different since CO<sub>2</sub> has no atmospheric chemistry and is simply mixed there, while increasing CO<sub>2</sub> in sea water induces changes in seawater carbonate chemistry (Zeebe and Wolf-Gladrow, 2001). Dissolved CO<sub>2</sub> (CO<sub>2(aq)</sub>) reacts with seawater to form carbonic acid (H<sub>2</sub>CO<sub>3</sub>) that rapidly dissociates into bicarbonate (HCO<sub>3</sub><sup>-</sup>), and carbonate (CO<sub>3</sub><sup>2-</sup>) ions:



where K<sub>1</sub> and K<sub>2</sub> are stoichiometric equilibrium constants dependent on temperature, pressure and salinity, which are often referred to as the first and second dissociation constants of carbonic acid. These reactions produce protons that lower the pH of seawater. However, CO<sub>2</sub> that dissolves in seawater does not fully dissociate into carbonate since it is also effectively neutralized by reaction with CO<sub>3</sub><sup>2-</sup> to produce HCO<sub>3</sub><sup>-</sup> due to the natural buffering capacity of seawater. The HCO<sub>3</sub><sup>-</sup> produced then partly dissociates, releasing protons and hence lowering the pH. The resulting pH decrease is, however, much smaller than for an un-buffered system. The sum of all dissolved CO<sub>2</sub> species is called total dissolved inorganic carbon (C<sub>T</sub>):

$$C_T = [\text{CO}_2] + [\text{HCO}_3^-] + [\text{CO}_3^{2-}] \quad (5)$$

This quantity can also be found referred to in the literature as DIC, TIC, TCO<sub>2</sub> or ΣCO<sub>2</sub>. The distribution of C<sub>T</sub> between the different species varies with seawater pH (Figure 1.6). Most of the dissolved CO<sub>2</sub> is in the form of HCO<sub>3</sub><sup>-</sup> and not in the form of CO<sub>2</sub>. With all remaining properties being equal, as more CO<sub>2</sub> is added to seawater, the proportion between the three carbonate species will change, with [CO<sub>2(aq)</sub>] and [HCO<sub>3</sub><sup>-</sup>] increasing and [CO<sub>3</sub><sup>2-</sup>] decreasing, making the pH decrease. This is the fingerprint of anthropogenic ocean acidification.

The next essential parameter for the description of the carbonate system is the total alkalinity (A<sub>T</sub>). This quantity is related to the charge balance in seawater. It can be defined as the excess of bases (proton acceptors) over acids (proton donors) in seawater, which reflects the ability of seawater to neutralize acids or to accept protons. For this reason, not only the carbonate system but every similar acid-base system in solution will

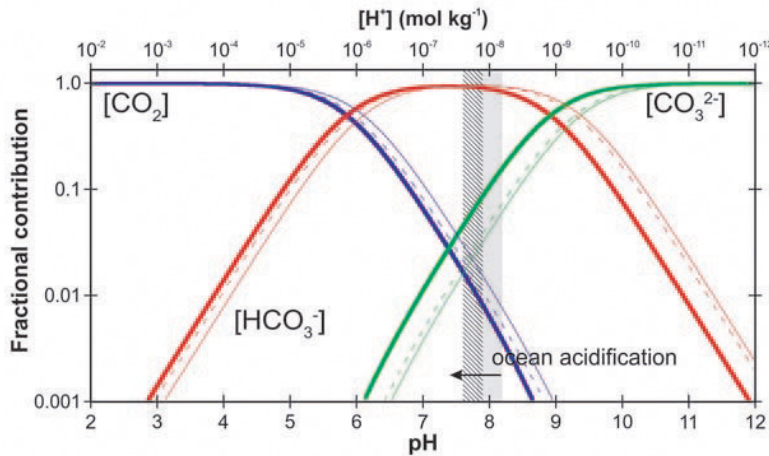


**Figure 1.6.** Bjerrum plot showing the relative proportions of  $[HCO_3^-]$ ,  $[CO_3^{2-}]$  and  $[CO_2]$  to the total dissolved inorganic carbon in seawater at different salinities ( $S$ ), temperatures ( $T$ ), and pressures ( $P$ ) (heavy curves are for  $S = 35, T = 25^\circ C, P = 0$  dbar; narrow curves are  $S = 35, T = 0^\circ C, P = 0$  dbar; dashed curves are  $S = 35, T = 0^\circ C, P = 3000$  dbar). The shaded region reflects the range of modern ocean surface (annual average), with the hashed region reflecting the corresponding projected year 2100 range taken from the global ocean geochemistry model projections of Turley *et al.*, (2010). Adapted from Barker and Ridgwell (2012).

contribute to alkalinity. According to Dickson (1981), alkalinity is “the number of moles of hydrogen ( $H^+$ ) ions equivalent to the excess of proton acceptors (bases formed from weak acids with a dissociation constant  $K \leq 10^{-4.5}$ , at  $25^\circ C$  and zero ionic strength) over proton donors (acids with  $K > 10^{-4.5}$ ) in one kilogram of sample”. The expression for  $A_T$  derived from this definition is:

$$A_T = [HCO_3^-] + 2[CO_3^{2-}] + [B(OH)_4^-] + [OH^-] + [HPO_4^{2-}] + 2[PO_4^{3-}] + [SiO(OH)_3^-] + [HS^-] + 2[S_2^-] + [NH_3] - [H^+]F - [HSO_4^-] - [HF] - [H_3PO_4] \quad (6)$$

where the carbonate species contribute 96% to  $A_T$ . In addition to carbonic acid, the most important acid-base systems that contribute to  $A_T$  are boric acid and water itself, with the remaining contributors being micro-compounds.  $C_T$  and  $A_T$  are conservative quantities i.e., their concentrations, measured in  $\mu\text{mol}\cdot\text{kg}^{-1}$  are unaffected by changes in pressure or temperature, and they obey the linear mixing law. Finally, the carbonate system includes water and its dissociation products  $H^+$  and  $OH^-$ . pH is determined by the concentration of  $H^+$  ( $-\log_{10}[H^+]$ ) in solution and is dependent on temperature and pressure.

The two equilibrium conditions (Eq. 4), the mass balance for  $C_T$  (Eq. 5) and the charge balance (Eq. 6) constitute four equations with six unknowns, which are fundamental variables in thermodynamic equilibrium:  $[CO_2]$ ,  $[HCO_3^-]$ ,  $[CO_3^{2-}]$ ,  $[H^+]$ ,  $C_T$  and  $A_T$ . The entire system can be constrained if any two parameters and total dissolved boron are known (Zeebe and Wolf-Gladrow, 2001), because we are left with four equations and four unknowns. For this purpose, the most used parameters are pH,  $pCO_2$ ,  $C_T$  and  $A_T$ , because these can be determined analytically with high precision (Dickson *et al.*, 2007).

The carbonate system is the main natural buffer of seawater pH. The buffering capacity of seawater depends on the amount of  $\text{CO}_3^{2-}$  present to accept protons and its conversion to  $\text{HCO}_3^-$ . As more  $\text{CO}_2$  is added and thus more  $\text{CO}_3^{2-}$  is progressively consumed, the buffering capacity of seawater will decrease, leading to an increase in the proportion of  $\text{CO}_2$  that remains as  $\text{CO}_2(\text{aq})$ . This effect is quantified by the Revelle factor (Revelle and Suess, 1957) that relates the ratio of the relative change of  $[\text{CO}_2]$  to the relative change of  $\text{C}_T$ :

$$\text{Revelle factor (or buffer factor)} = (\Delta[\text{CO}_2] / [\text{CO}_2]) / (\Delta[\text{C}_T] / [\text{C}_T])$$

It is an indicator of the buffering capacity of the ocean to uptake  $\text{CO}_2$ . The lower the Revelle factor the larger the buffering capacity of seawater. Increasing atmospheric  $\text{pCO}_2$  increases the Revelle factor, making the ocean less efficient at absorbing more  $\text{CO}_2$ . The current Revelle factors are already about one unit higher than they were in the preindustrial ocean (Sabine *et al.*, 2004).

### Oceanic carbonate chemistry, controls and ocean acidification

The ocean carbon sink contributes to mitigate global warming. However, the resulting anthropogenic  $\text{CO}_2$  oceanic invasion affects the chemical balances of the  $\text{CO}_2$  system in seawater, raising the amount of  $\text{C}_T$  in the upper layers, which translates into a decrease in surface ocean pH. On average, the ocean surface waters have already acidified by 0.1 pH-units from their pre-industrial levels (Raven *et al.*, 2005). Surface ocean pH, on average, has probably not been below 8.1 during the past 20 million years (Pelejero *et al.*, (2010) and references therein) and, if  $\text{C}_{\text{ant}}$  emissions continue, surface ocean pH could decline by approximately 0.7 units by the year 2300 (Zeebe *et al.*, 2008) (Figure 1.7). Given the potential impacts of ocean acidification on a number of important chemical and biogeochemical properties and processes, it has been termed “the other  $\text{CO}_2$  problem” (Doney *et al.*, 2009). A well-documented implication is the lowering of  $\text{CaCO}_3$  saturation states, which has adverse effects for marine organisms, with calcifiers amongst the most clearly affected (Chan and Connolly, 2013; Bach, 2015; Bach *et al.*, 2015). Contemporaneous temporal and spatial variability exists in seawater pH and reconstructions of seawater pH have also shown some degree of inter-decadal variability that provides insight into the natural pH ranges within which marine calcifiers live (Pelejero *et al.*, 2010). Nevertheless, establishing the rate at which ocean acidification is taking place is important to study the fate of most marine biota in the face of this global change but also to understand the future diminishing capacity of the oceans to take up atmospheric  $\text{CO}_2$  (Sabine and Tanhua, 2010).

The shift in carbonate system equilibria associated with the atmospheric  $\text{CO}_2$  dissolution in the oceans leads to a reduction of carbonate ions (Eq. 4) and, in turn, to a decline in the  $\text{CaCO}_3$  saturation states. The saturation state of  $\text{CaCO}_3$  minerals ( $\Omega$ ) is defined as:

$$\Omega = [\text{Ca}^{2+}] [\text{CO}_3^{2-}] / K_{\text{sp}}$$

the ion product of calcium and carbonate ion concentrations, divided by the stoichiometric solubility product ( $K_{\text{sp}}$ ) for a given  $\text{CaCO}_3$  mineral phase. Mainly,  $\text{CaCO}_3$  occurs either as aragonite or as calcite, with aragonite being more soluble at given conditions due to its crystal structure being less stable than that of calcite. The solubility of both compounds increases slightly at lower temperature and strongly with increasing pressure.

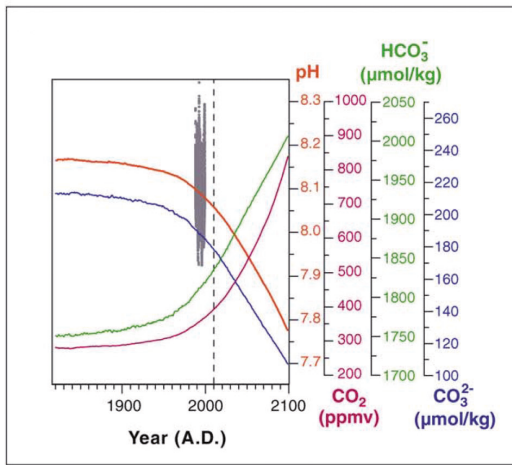


**Figure 1.7.** Near past (1800) and near future (2100) evolution of surface pH (orange, on total scale) and atmospheric  $\text{CO}_2$  (magenta) from (Steinacher *et al.*, 2009) based on prescribed fossil-fuel and land-use  $\text{CO}_2$  emissions from historical data for the period 1820 to 2000 and considering the A2 IPCC SRES emissions scenario afterwards. Evolution of bicarbonate (green) and carbonate ion (blue) concentrations, computed from dissolved inorganic carbon and pH data from (Steinacher *et al.*, 2009). The grey cloud of points shows all  $1 \times 1$  degree mixed surface layer (upper 50 m) pH values in the oceans, computed from total carbon and alkalinity data. Source: Pelejero *et al.* (2010).

Since  $[\text{Ca}^{2+}]$  is closely proportional to salinity,  $\Omega$  is largely determined by variations in  $[\text{CO}_3^{2-}]$ :

$$\Omega = [\text{CO}_3^{2-}]_{\text{in situ}} / [\text{CO}_3^{2-}]_{\text{saturation}}$$

Hence,  $\Omega$  reflects the equilibrium point between the tendency of dissolved  $[\text{CO}_3^{2-}]$  to attach to the given crystal surface (precipitation) or to detach from the crystal to enter solution (dissolution). According to this,  $\text{CaCO}_3$  precipitation occurs under supersaturated conditions ( $\Omega > 1$ ) and dissolution under undersaturated conditions ( $\Omega < 1$ ). The water depth at which  $\Omega = 1$  represents the saturation level or saturation horizon. Saturation states of calcite and aragonite are higher in shallow, warm tropical waters and lower in cold high-latitude regions and at depth, which reflects the increase in  $\text{CaCO}_3$  solubility with decreasing temperature and increasing pressure (Feely *et al.*, 2004; Zeebe, 2012).

The pH and the whole ocean carbonate chemistry are determined by the inventories of  $C_T$  and  $A_T$  (Zeebe and Wolf-Gladrow, 2001). Many changes in the carbonate system in the ocean are best described when considering the change in  $C_T$  and  $A_T$  that is associated to them (Figure 1.8). For example, the invasion (release) of  $\text{C}_{\text{ant}}$  into (from) the ocean changes only  $C_T$ , leading to an increase (decrease) of  $C_T$  and a decrease (increase) of pH, while  $A_T$  remains constant, because the charge balance is not affected. Photosynthesis (respiration) reduces (increases)  $C_T$  and slightly increases (decreases)  $A_T$  because of nitrate uptake (release). The formation of calcium carbonate ( $\text{CaCO}_3$ ) decreases both  $C_T$  and  $A_T$  in a ratio of 1:2, and increases  $[\text{CO}_2]$  even though the decrease in  $C_T$ , resulting in a shift of the carbonate system to higher  $\text{CO}_2$  levels and lower pH.  $\text{CaCO}_3$  dissolution has the reverse effect. Temperature, salinity and pressure also affect the seawater carbonate system

since they influence the solubility coefficients and the dissociation constants that characterize the thermodynamic equilibrium. For instance,  $\text{CO}_2$  is less soluble at higher temperatures, leading to outgassing to the atmosphere and hence to a local decrease of  $C_T$ . On the contrary, in colder waters  $C_T$  is higher because  $\text{CO}_2$  uptake is more favorable in these conditions. For this reason, warm regions show higher  $[\text{CO}_3^{2-}]$  and are more saturated with respect to carbonate minerals than colder regions (Feely *et al.*, 2009). Evaporation (precipitation), in addition to increased (decreased) salinity due to a concentration (dilution) effect, also increase (reduce) the concentration of  $C_T$  and  $A_T$  in a 1:1 ratio.

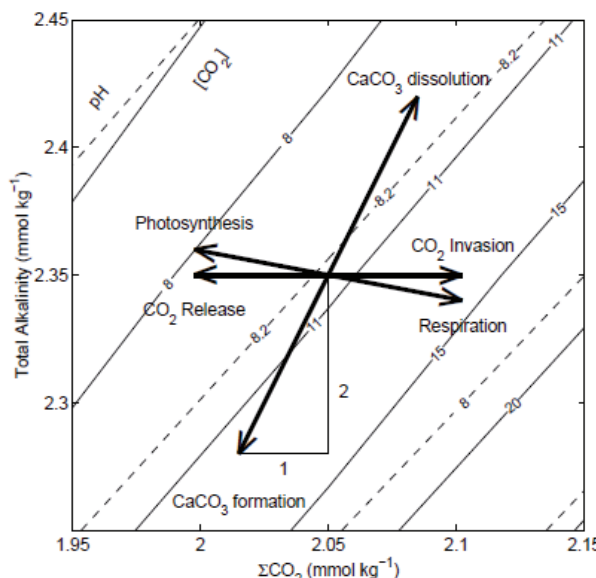


**Figure 1.8.** Effect of various processes on total dissolved inorganic carbon ( $C_T$ ) and total alkalinity ( $A_T$ ) (arrows). Solid and dashed lines indicate levels of constant dissolved  $\text{CO}_2$  (in  $\mu\text{mol kg}^{-1}$ ) and pH, respectively, as a function of  $C_T$  and  $A_T$ . Modified from Zeebe and Wolf-Gladrow (2001).

Therefore, changes in the  $C_T$  and  $A_T$  inventories with time constrain the evolution of the carbonate system in seawater and, eventually, the ability of the ocean to continue removing atmospheric  $\text{CO}_2$  at different timescales. Although the ocean and the terrestrial biosphere sinks have performed comparably until present (Table 1.1), the global ocean has a much larger carbon reservoir (~38000 PgC) than the biosphere (~450-650 PgC) (Figure 1.3) and thus, a greater capacity to store  $\text{CO}_2$  on larger timescales as emissions continue, by means of seawater buffering and  $\text{CaCO}_3$  neutralization (Archer, 2005; Zeebe, 2012): On timescales of a few hundred years, atmospheric  $\text{CO}_2$  will be redistributed between the atmospheric, the terrestrial and the upper oceanic sinks. However, all combined, these sinks will not be able to keep the estimated existing fossil fuel reserves in case they are burned completely, so their storage capacity may be overwhelmed (Zeebe, 2012). Most of the emitted  $\text{CO}_2$  will eventually be absorbed into the deep ocean and neutralized by reaction with carbon-

ate sediments as ocean has time to mix, on timescales on the order of millennia. On longer timescales, the burial of  $\text{CaCO}_3$  in marine sediments through calcite compensation represents one major pathway to remove carbon from the ocean-atmosphere system (Sigman *et al.*, 1998).

On the timescales of millennia, the ocean carbonate pump leads only to shifts in the vertical  $C_T$  and  $A_T$  distributions in the ocean rather than changes in their inventories. Exceptions to this are rapid  $\text{CO}_2$  inputs from long-term storage reservoirs such as the case of the fossil fuels currently combusted by human activity. The closest analog to the current carbon cycle anthropogenic perturbation event is probably the Paleocene-Eocene Thermal Maximum (PETM), marked by a global increase in temperatures and a substantial carbon release that led to ocean acidification and dissolution of deep-sea carbonates (Zachos *et al.*, 2005; Zeebe *et al.*, 2009). The geologic record hence may provide important information regarding the future changes of ocean chemistry and their effects on marine life through the study of such past changes in ocean chemistry. When studying the geologic record, it would be ideal to identify appropriate analogues for the future. To this end, it is important to differentiate the changes in ocean chemistry that occur during long-term steady states with respect to transient events occurring in the order of centuries, since it is well known that the carbonate chemistry parameters do not vary with the same relationship in both cases, with a clear dependence on the rate of change and the initial chemical conditions (Zeebe, 2012). In the case of transient events, knowledge of the magnitude and timescale of the acidification event is necessary. With this regard, although some events in the geological record show similarities with the current ocean acidification perturbation, there is not a true analogue that perfectly parallels the future alterations of the carbonate system chemistry due to the rapid  $\text{CO}_2$  release currently taking place (Haywood *et al.*, 2011). However, past rapid events in Earth history provide a unique opportunity to investigate the crucial operating processes, not only in association to acidification events but also to warming and deoxygenation, which are also important global stressors impacting the oceans today (Hönisch *et al.*, 2012).

### Oceanic anthropogenic $\text{CO}_2$ . Methodology for its estimation

$C_{\text{ant}}$  in the ocean is defined as the excess of  $\text{CO}_2$  in relation to the preindustrial (or natural) levels of  $\text{CO}_2$ . Assessing the uptake and storage of  $C_{\text{ant}}$  in the ocean requires a differentiation between the natural and anthropogenic contributions to changes in  $C_T$  over time. However, achieving such estimation is not simple because the oceanic  $C_{\text{ant}}$  is a small perturbation (~ 3%) on top of the natural  $\text{CO}_2$  levels that shows a heterogeneous distribution and is also involved in biogeochemical processes (Sabine and Tanhua, 2010; Khatiwala *et al.*, 2013). Since it is not directly measurable because it is not easily distinguishable from natural  $\text{CO}_2$  (Dassie *et al.*, 2013), several methods have been developed for its estimation. In essence,  $C_{\text{ant}}$  concentrations can be approached by two main kinds of methodologies: the so-called ‘back-calculation’ methods and the tracer based methods. Back-calculation (also called carbon-based) methods attempt to separate the anthropogenic perturbation from the large background distribution of  $C_T$  assuming that  $C_{\text{ant}}$  can be isolated by correcting the measured  $C_T$  ( $C_m$ ) for changes due to biological activity ( $C_{\text{bio}}$ ) and by removing an estimate of the prein-

dustrial preformed properties and the effects of the solubility pump ( $C_{\text{phys}}$ ):

$$C_{\text{ant}} = C_m - C_{\text{bio}} - C_{\text{phys}}$$

Overall, they rely on the assumption that ocean circulation and the biological pump have operated in steady state since the preindustrial era. Brewer (1978) and Chen and Millero (1979) presented the first  $C_{\text{ant}}$  calculations in the late 1970s. Several authors have tried to improve those first back-calculation methods, leading to a number of methodologies. The classical  $\Delta C^*$  approach (Gruber *et al.*, 1996) is a widely applied technique based on the estimation of the quasi-conservative  $\Delta C^*$  tracer. The fundamental improvement that this method first introduced was to split  $C_{\text{phys}}$  into two terms: a zero- $C_{\text{ant}}$  reference term related to  $C_T$  that waters would have in equilibrium with a preindustrial atmosphere ( $C_{\text{eq}}$ ) and a term that takes into consideration that surface waters are actually not in complete equilibrium with the atmosphere ( $C_{\text{dis}}$ ):

$$\begin{aligned} C_{\text{ant}} &= C_m - C_{\text{bio}} - C_{\text{eq}} - C_{\text{dis}} \\ \Delta C_{\text{ant}} &= \Delta C^* - \Delta C_{\text{dis}} \end{aligned}$$

by considering  $\Delta C^* = C_m - C_{\text{bio}} - C_{\text{eq}}$ . The equilibrium term is the largest part of the preformed concentration and is calculated from thermodynamic equations as a function of potential temperature and salinity, preformed alkalinity ( $A_T^0$ ) and the corresponding preindustrial atmospheric  $\text{CO}_2$  concentration (i.e. 280 ppm).

The  $\Delta C^*$  method first introduced the  $\Delta C_{\text{dis}}$  concept to the back-calculation techniques, under the assumption that it has remained steady since the preindustrial era. The  $\varphi C_T^0$  method (Vázquez-Rodríguez *et al.*, 2009a) shares principles with  $\Delta C^*$  yet it proposes some upgrades to the  $\Delta C_{\text{dis}}$  and  $A_T^0$  determinations. While in the  $\Delta C^*$  method the water column is divided into isopycnal intervals and properties of the subsurface waters are referenced back to the outcrop region of each interval, the  $\varphi C_T^0$  method uses the subsurface layer (100–200m) as a reference for characterising water mass properties at their wintertime formation conditions, thus avoiding the short-term variability of the uppermost layers (Vázquez-Rodríguez *et al.*, 2012). One important point in this approach is that the  $A_T^0$  or  $\Delta C_{\text{dis}}$  parameterizations rely on conservative parameters from the subsurface layer exclusively. Further, the variability of both terms is taken into account, in order to address the assumption of invariable  $\Delta C_{\text{dis}}$  (Matsumoto and Gruber, 2005).

The TrOCA method (Touratier and Goyet, 2004; Touratier *et al.*, 2007) is an easy-to-apply technique based on the universal quasi-conservative TrOCA tracer (Tracer combining Oxygen,  $C_T$  and  $A_T$ ), which is based on a Redfield ratio similarly to classical conservative tracers such as NO and PO (Broecker, 1974; Ríos *et al.*, 1989). It shares with the above methods its consideration of the biological pumps contribution to  $C_T$  but does not take into account the  $C_{\text{phys}}$  estimation in its parameterization.  $C_{\text{ant}}$  concentrations are estimated from the difference between TrOCA and the preformed TrOCA tracer ( $\text{TrOCA}^0$ ), defined from the “natural” concentrations of  $\text{O}_2$ ,  $C_T$  and  $A_T$ .  $\text{TrOCA}^0$  is a zero- $C_{\text{ant}}$  term defined as a function of  $\Theta$  and  $A_T$ , obtained after the study of  $\Delta^{14}\text{C}$  and CFC-11 tracer distributions in the Pacific and Indian Oceans in order to derive it in water parcels can be assumed to be free of  $C_{\text{ant}}$ . The method assumes that  $A_T$  and  $\text{O}_2$  are not affected by the increase of atmospheric  $\text{CO}_2$  (Goyet *et al.*, 1999) and uses a constant oxygen to carbon Redfield ratio (Rc) value of 1.35 (after Körtzinger *et al.*, (1998)) to calculate the biological contribution to  $C_T$ , while both  $\varphi C_T^0$  and  $\Delta C^*$

methods use the  $R_c$  ratio of 1.45 proposed by Anderson and Sarmiento (1994). Despite being an universal equation (Yool *et al.*, 2010), it provides comparable  $C_{\text{ant}}$  inventories to those obtained by other approaches in the Atlantic (Vázquez-Rodríguez *et al.*, 2009b).

In addition to back-calculation techniques, other conceptual approaches (Broecker and Peng, 1974; Thomas and Ittekkot, 2001; Haine and Hall, 2002) do not use  $C_T$  measurements and treat  $C_{\text{ant}}$  as a conservative tracer (i.e. a tracer that is not influenced by biological processes in the ocean) that responds to an evolving history in surface waters, thus avoiding the uncertainties related to the biological correction. Tracer-based methods rely on the assumption that  $C_{\text{ant}}$  at any point in the ocean interior should be related to the history of  $C_{\text{ant}}$  at the surface and the spectrum of times it took the water to reach the interior ocean locations. Hence, these methods consist of a mathematical description of how the ocean's circulation connects surface boundary conditions with interior ocean concentrations of tracers as a proxy of how ocean's circulation connects and transports  $C_{\text{ant}}$  from the surface to the ocean interior. Tracer observations are used to calibrate the transport from the surface into the ocean interior in order to estimate the age of the water masses and, therefore, their  $C_{\text{ant}}$  content at the time they were formed. However, it is difficult to find a tracer that behaves like  $\text{CO}_2$  because most tracers (e.g.  $^{39}\text{Ar}$ ,  $^{14}\text{C}$ , tritium, CFCs,  $\text{SF}_6$  or  $\text{CCl}_4$ ) are non-reactive, unlike  $\text{CO}_2$ . Moreover, many of them started to be emitted after  $C_{\text{ant}}$  and their penetration and transports into the ocean interior do not fully mimic that of  $C_{\text{ant}}$ .

One simplification in order to apply this principle consists in assuming that a single surface region dominates the  $C_{\text{ant}}$  concentration at interior locations. The resulting approximation depends only on the time elapsed since a water parcel was last in contact with the surface and tracer distributions can be established by using the so-called TTD functions (Transit Time Distributions) (Hall *et al.*, 2002; Waugh *et al.*, 2004; Waugh *et al.*, 2006; Steinfeldt *et al.*, 2009). TTDs are probability functions that describe a distribution of ventilation times approximated as inverse Gaussian functions. In order to estimate the ocean interior  $C_{\text{ant}}$  concentration, the only necessary information is the knowledge about the temporal evolution of  $C_{\text{ant}}$  in the surface mixed layer and the rate at which this surface boundary condition is transported and mixed into the ocean interior. The assumption of the transport is steady. Constant air-sea disequilibrium in time is also assumed. Thus,  $C_{\text{ant}}$  is the difference between  $C_T$  at the time when the measurements were carried out, and  $C_T$  just in the beginning of the preindustrial era.

The Green's function (GF) technique (Khatiwala *et al.*, 2001; Khatiwala *et al.*, 2009) applies a more general parametrization of the transport of tracers in the ocean and recognizes that, in the presence of mixing, there is no single ventilation time (Khatiwala *et al.*, 2013). Air-sea disequilibrium is allowed to evolve in space and time, and the mixing of waters of different ages and different source regions is taken into account. The transport of any tracer is described as a continuous joint distribution, known as the boundary propagator, of the time and surface location at which a water parcel was last in contact with the atmosphere. The GF is the solution to the advection-diffusion equation for the ocean with an impulse boundary condition at the surface.

Additionally, there exists a third kind of approach which, instead of providing the concentration of  $C_{\text{ant}}$ , is used for assessing  $C_{\text{ant}}$  changes between two cruises separated in time. The eMLR (extended multiple linear regression) depends on the linear approximation of  $C_T$  from a suite of physical and biochemical ocean parameters and is commonly used to derive the change in  $C_T$  between two temporally-separated hydrographic cruises (with the difference inferred as the  $C_{\text{ant}}$  build-up). The multiple linear regression approach was introduced by Wallace (1995) and extended by Friis *et al.* (2005). Moreover, taking advantage of the exponential nature of atmospheric  $C_{\text{ant}}$  increase and assuming a steady state of  $C_{\text{ant}}$  distributions in the ocean (Gammon *et al.*, 1982; Tanhua *et al.*, 2006),  $C_{\text{ant}}$  inventories to any given year can be scaled to the  $C_{\text{ant}}$  storage derived from the use of this method (Tanhua *et al.*, 2007). This method assumes that baseline correlations and the resulting residual fields will remain constant with time even under the influence of secular climate changes. However, this method is supposed to not fully represent subdecadal variability (Levine *et al.*, 2008), in comparison with other techniques, nor to describe  $C_{\text{ant}}$  uptake for time intervals greater than 30 years for many regions in the Southern Ocean, Atlantic and western Pacific. This method is more suitable to accurately predict the uptake of  $C_{\text{ant}}$  at decadal timescales (Goodkin *et al.*, 2011).

There is no clear consensus about the most appropriate method to estimate  $C_{\text{ant}}$  (Sabine and Tanhua, 2010). All data-based estimates of  $C_{\text{ant}}$  assume constant climate, biological pumps and ocean circulation, which may introduce significant errors in studies of future  $C_{\text{ant}}$  uptake, although the error in global inventories due to neglecting the impact of changing climate on both the natural carbon system and uptake of  $C_{\text{ant}}$  is currently much smaller than the intrinsic uncertainty of the various methods (typically 20%) (Khatiwala *et al.*, 2013). While some authors have reported  $C_{\text{ant}}$  estimates by using only one method (Macdonald *et al.*, 2003; Rosón *et al.*, 2003; Tanhua *et al.*, 2008; Ríos *et al.*, 2012), it may be more appropriated using two or more methods for comparative purposes, for example TrOCA and  $\phi C_T^0$  ((Castaño-Carrera *et al.*, 2012; Fajardo *et al.*, 2012), TrOCA,  $\phi C_T^0$  and  $\Delta C^*$  (Flecha *et al.*, 2012),  $\Delta C^*$ ,  $\Delta C_T^0$  and TrOCA (Lo Monaco *et al.*, 2005) or  $\Delta C^*$ , TrOCA,  $\Delta C_T^0$ , TTD and  $\phi C_T^0$  (Vázquez-Rodríguez *et al.*, 2009b)). Moreover, some authors suggest that a combination of approaches is necessary to achieve a robust quantification of the ocean sink of  $C_{\text{ant}}$  (Khatiwala *et al.*, 2013).

## THE SUBTROPICAL NORTH ATLANTIC OCEAN

### Physical perspective: circulation features

The North Atlantic region (Figure 1.9) has an important role in climate regulation mainly due to heat and freshwater exchanges with the atmosphere that takes place during the flow of warm waters from lower latitudes northward. The North Atlantic is also a key climatic region due to the process of deep water formation, when warm surface waters reach subpolar latitudes and cool and sink originating what is considered the main starting point of the Meridional Overturning Circulation (MOC).

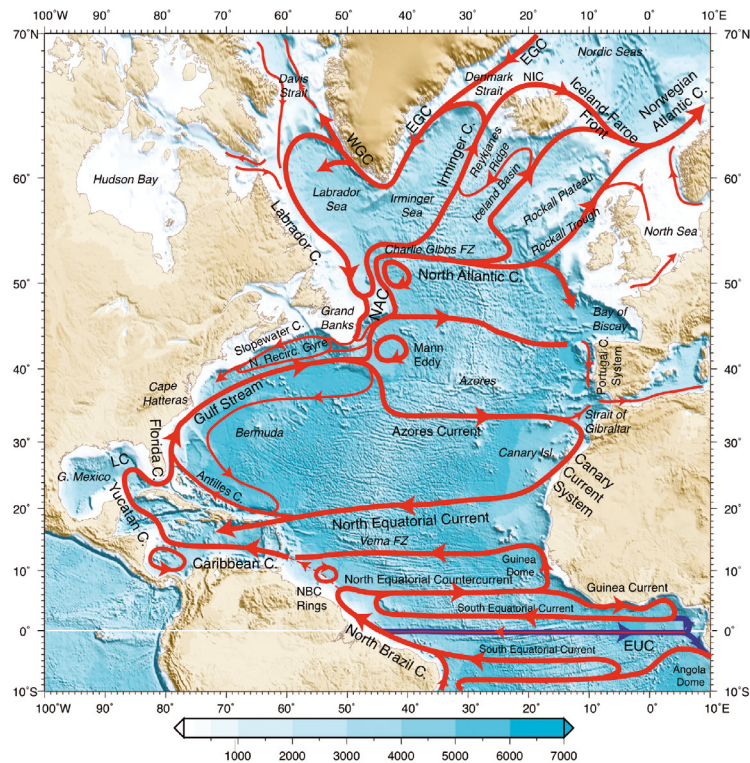


**Figure 1.9.** North Atlantic Ocean region. Surface circulation (red) and Equatorial Undercurrent just below the surface layer (blue). Source: Talley et al., (2011).

### Surface circulation along the (sub)tropical North Atlantic

The upper ocean circulation is driven by the friction of wind on the atmosphere-ocean interface. The combination of wind stress and the Coriolis effect cause the surface currents to form large circular movements called gyres. The surface circulation of the subtropical North Atlantic includes an anticyclonic subtropical gyre (NASTG), while the tropical circulation is strongly zonal.

The NASTG is embedded between the European and American continents in the range of 15–45°N of latitude (Figure 1.9). Like all subtropical gyres, it is asymmetric, with strong, narrow western boundary currents and a broad southward flow throughout the central and eastern subtropical regions. The subtropical western boundary system is composed of two connected portions (Talley et al., 2011): the Gulf Stream System south of about 40 °N, and part of the North Atlantic Current system east of Newfoundland and north of 40°N. The western boundary system of the NASTG, mainly the Gulf Stream (GS), is the main path for warm surface waters from low latitudes to reach high latitudes at the Northern Hemisphere. The GS consists of a series of currents that start where the North Equatorial Current enters the Caribbean Sea through the Antilles is-

lands and emerge through the Florida Straits escaping into the North Atlantic as a merged current that flows northward along the coast of Florida to Cape Hatteras (about 35°N), where the stream no longer follows the shelf break and continues to the northeast into deep waters (Talley *et al.*, 2011). East of the separation at Cape Hatteras, the GS is one of the most powerful currents in the world oceans in terms of volume transport (up to 140 Sv;  $1\text{Sv} = 10^6 \text{ m}^3 \cdot \text{s}^{-1}$ ), maximum velocity (up to 250 cm/s), average velocity (about 150 cm/s) and eddy variability (Talley *et al.*, 2011). It carries a warm and saline core of surface water eastward into the North Atlantic that feeds the North Atlantic Current, which connects the subtropical and subpolar surface circulations with a net northward transfer of upper waters into the Subpolar Gyre (Talley *et al.*, 2011). The GS also continues eastward and southward into the Azores Current that recirculates waters into the NASTG in the central and eastern North Atlantic and has an associated westward flow called the Azores countercurrent. These flows turn westward and feed the North Equatorial Current, closing the circulation of the gyre (Talley *et al.*, 2011).

For clarification, the Florida Current refers to the western boundary current through the constriction between Florida and the Bahamas, and GS refers to the continuation of this boundary current north of the Florida Straits and also after it separates from the western boundary flowing eastward out to sea (Talley *et al.*, 2011). The Florida Current is well constrained in the enclosed strait between Florida and the Bahamas. The mean transport at 27°N is 32 Sv (Baringer and Larsen, 2001).

The eastern boundary upwelling system of the NASTG is the Canary and Portugal Current System (Figure 1.9). The classical eastern boundary Canary Current flows equatorward (southward) along the north African coast, and shows a seasonally dependent termination in the south: it flows near the African coast in spring, through the entire Canary archipelago in summer, only through the western islands in fall and is almost negligible in winter (Machín *et al.*, 2006). Between 20°N and 23°N the Canary Current turns offshore to join the North Equatorial Current.

The tropical circulation is characterized by currents flowing in the zonal direction (Figure 1.9) (Talley *et al.*, 2011): the North Equatorial Countercurrent and the South Equatorial Current, which are separated by the eastward Equatorial Undercurrent (EUC). There exists a low-latitude western boundary current (North Brazil Current). The structure and variability of circulation is driven by the wind field over the Tropical Atlantic, in particular by the variability of the Intertropical Convergence Zone (ITCZ) (Talley *et al.*, 2011).

### *The Atlantic Meridional Overturning Circulation*

Surface currents play a significant role in transporting heat from equatorial to polar latitudes. Hence, they are exposed to changes in temperature through heat exchange with the atmosphere. They also experience changes in salinity through evaporation, precipitation and sea-ice formation. The resulting exchange of mass and energy leads to density changes in these waters that eventually become denser than waters below and sink into

the ocean interior. The sinking of waters at high latitudes, a process known as deep water mass formation, is balanced by the upwelling and return of water from depth to the surface (Talley *et al.*, 2011). Deep-ocean circulation is thus driven by density changes and deep-currents on a flow that is known as Thermohaline Circulation or Meridional Overturning Circulation (MOC), where the word “overturning” implies a vertical transformation of the water mass. The MOC connects the different world oceans, distributing a number of oceanic properties between basins. Because of this, it was termed “the great ocean conveyor” by Broecker (1987), which described in a very simplified way the actual global overturn but clearly exemplified the global deep ocean interdependence (Figure 1.10).

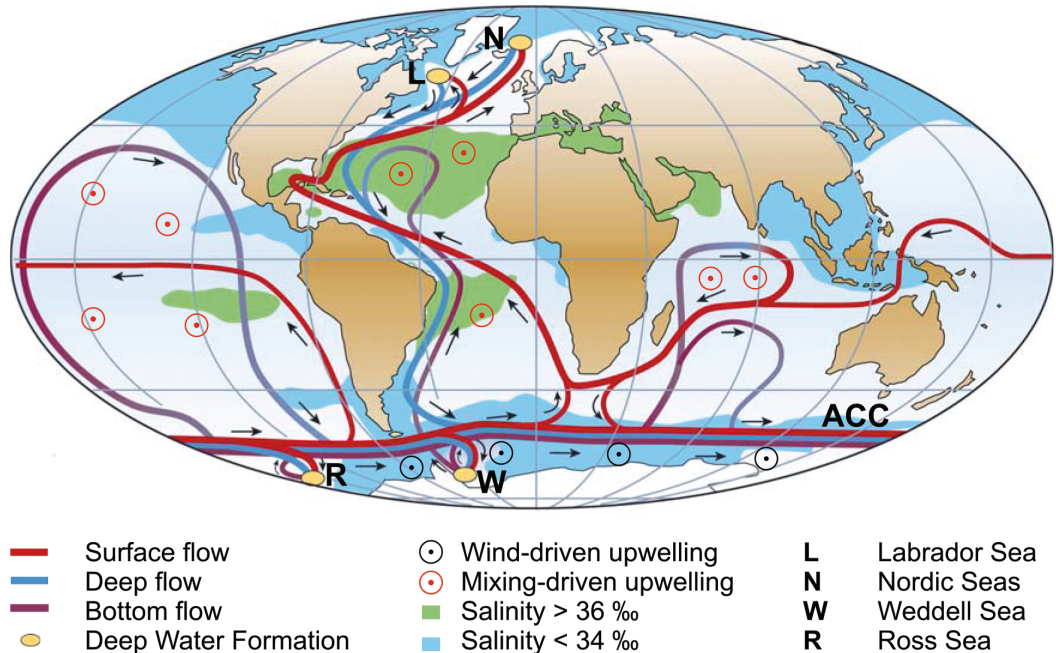


**Figure 1.10.** Simplified sketch of the global overturning circulation system. In the Atlantic, warm and saline waters flow northward all the way from the Southern Ocean into the Labrador and Nordic Seas. By contrast, there is no deepwater formation in the North Pacific, and its surface waters are fresher. Deep waters formed in the Southern Ocean become denser and thus spread in deeper levels than those from the North Atlantic. Note the small, localized deepwater formation areas in comparison with the widespread zones of mixing-driven upwelling. Wind-driven upwelling occurs along the Antarctic Circumpolar Current (ACC). Source: Kuhlbrodt *et al.*, (2007).

The North Atlantic Ocean is amongst the most important regions in the world where formation of deep water masses occurs, in addition to the Ross and Weddell Seas, in the Southern Ocean (Figure 1.10). Most of the conversion of upper waters to denser intermediate and deep waters occurs within the Labrador Sea and Nordic Seas. The newly formed cold intermediate and deep waters are carried into the Deep Western Boundary Current that emerges below 1500m from the subpolar North Atlantic and moves southward towards the equator. This new cold and deep water mass is called North Atlantic Deep Water (NADW). It comes out of the Atlantic basin joining the Antarctic Circumpolar Current finally contributing to the Circumpolar Deep Water. Bottom waters formed in the Southern Ocean are transported northward. The Atlantic MOC (AMOC) thus consists of a double cell of (1) northward flow of upper ocean waters that become denser in the northern North Atlantic and flow out southward at depth after becoming NADW and (2) northward flow of dense Antarctic Bottom Water (AABW) that upwells into the lower part of the NADW, disappearing in the midlatitudes of the North Atlantic. This overturning circulation results in a net northward transport through all latitudes of the Atlantic, since upper waters from the South Atlantic flow across the equator to feed the overturn in the North Atlantic.

Regarding its role as a conveyor, the MOC is responsible for part of the redistribution of heat on Earth that is enough to generate a climate shift (Weaver *et al.*, 2012). The AMOC plays an important part on this, since the Atlantic it is the only ocean where heat is transported northward across the equator, causing it to be the only ocean that contributes with positive (northward) heat transport throughout its entire basin. Maximum northward heat transport in the Atlantic occurs at 24° to 26° N, of about 1.3 PW, corresponding to ~ 25% of total (atmosphere and ocean) poleward heat transport at these latitudes (Bryden *et al.*, 2014). Future changes in the AMOC due to global warming could have substantial feedbacks on climate through the subtle balance of temperature and salinity that controls this overturning. The process by which warm and salty water of the GS reaches further north and becomes colder NADW that returns south is considered one of the ‘engines’ that drive the AMOC (Kuhlbrodt *et al.*, 2007). In fact, today this is the only loop of the global conveyor in the Northern Hemisphere because there is no area in the Pacific where salty subtropical water can travel far enough north and cool down sufficiently to sink, though this situation may have been different in specific glacial periods in the past, when deep water formation in the North Pacific may have formed (Rae *et al.*, 2014).

Given all the characteristics mentioned above, the AMOC has an important role in regulating the European climate. If North Atlantic surface water were to become less salty because of climate change (i.e. due to increased melting of ice sheets and/or increased rain-fall at mid to high latitudes), it may no longer become dense enough to sink, no matter how much it cools down, and the formation of NADW would stop (Figure 1.11) or, at least, slow down. So would the entire global conveyor. The poleward heat transport and the flow of mild air across Western Europe, would thus be reduced, causing a rapid drop in winter temperature.

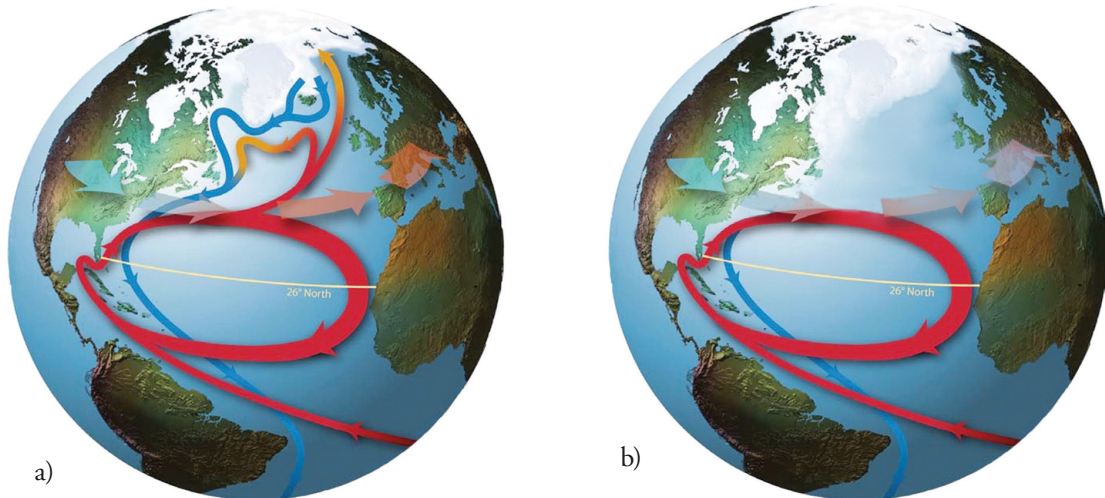


**Figure 1.11.** Possible changes to the AMOC. a) Atlantic circulation at present. b) Possible Atlantic circulation in the future, If deep water formation in the North Atlantic were to stop. Source: Project Science Education through Earth Observation for High Schools (SEOS; <http://www.seos-project.eu/home.html>) of the 6th Framework Programme of the European Commission.

Understanding the AMOC variability is an important challenge for the scientific community. Multiple lines of evidence suggest that a slowdown of the AMOC has been occurring over the last decades, which is leading to a cooling in the northern Atlantic (Robson *et al.*, 2014; Rahmstorf *et al.*, 2015). Whilst the main impact of an AMOC slowdown would be a reduction of the poleward heat transport, there is also another indirect effect related to the North Atlantic ability to take up and store  $C_{\text{ant}}$ , since the process of deep water masses formation associated to this overturning in the North Atlantic is one of the greatest  $C_{\text{ant}}$  sinks of the global ocean (Sabine *et al.*, 2004; Steinfeldt *et al.*, 2009; Pérez *et al.*, 2010). (Watson *et al.*, 2009) reported sea-atmosphere  $\text{CO}_2$  fluxes into the North Atlantic on the order of 20% lower in the early 2000s than five to ten years earlier that were mainly explained by changes in circulation driven by natural climate variability. Their findings are consistent with climate model results that suggest that natural interdecadal variation of the AMOC may range from 20% to 30% of its long term value (Häkkinen, 1999). None of the climate models contributing to the IPCC 5th model intercomparison (CMIP-5) show a shut-down of the AMOC, but most show a slow-down, which is greater with a faster rate of global warming (Weaver *et al.*, 2012). However, the question whether observed changes of the AMOC result from natural variability or they are due to external forcing is still under research.

## Monitoring temporal changes in the ocean: hydrographic and mooring lines across the Subtropical North Atlantic

The oceans are a key element in the climate system because they transport heat and fresh water and exchange these with the atmosphere. The oceans also have a huge impact on the global carbon cycle since they also transport large amounts of CO<sub>2</sub>, and big efforts have been made over the past several decades in order to constrain, from in-situ observations, the ocean's role as a sink for anthropogenic CO<sub>2</sub>.

While the study of the oceanic uptake of CO<sub>2</sub> in surface waters takes advantage of the combination of measurements from research oceanographic vessels, moorings, drifters and remote sensing, measurements of carbon in the ocean interior can only be obtained through costly and demanding oceanographic cruises to collect the needed data. Because of the complexity of this goal on the global scale, worldwide hydrographic surveys require an international coordination through collaborative programs in order to achieve the necessary amount of data to keep track of decadal-scale changes in the ocean interior. In this regard, the first global efforts involving well-documented methodology for inorganic carbon data acquisition were The Geochemical Sections (GEOSECS) program of the 1970s and regional studies like the Transient Tracers in the Ocean (TTO) and South Atlantic Ventilation Experiment (SAVE) in the Atlantic during the 1980s. In the years following, measurement techniques were significantly improved and it was not until the 1990s that the next global survey of carbon distributions in the ocean was addressed. This was done through collaboration of several international programs which completed nearly a hundred cruises that included inorganic carbon measurements, such as the World Ocean Circulation Experiment (WOCE), the Joint Global Ocean Flux Study (JGOFS) and the NOAA Ocean-Atmosphere Carbon Exchange Study (OACES). In particular, WOCE was a part of the World Climate Research Program (WCRP) and meant the first attempt to study physical processes that affect oceanic circulation and are responsible for climate variability globally, from in-situ and satellite observations of the global ocean between 1990 and 1998.

The GLobal Ocean Data Analysis Project (GLODAP) synthesized the hydrographic data obtained within the context of WOCE, JGOFS and OACES with the aim of generating a unique oceanographic database of unprecedented data quantity and quality. This ocean carbon unified data set benefited from the development of many new techniques for evaluating the carbonate system in seawater and other anthropogenic tracers with proper accuracy. For these data to be useful they had to be evaluated and sometimes recommended to be adjusted, in order to be unified into internally consistent data sets at basin scale (i.e. Indian, Pacific and Atlantic). The results of the carbonate system data compilation and evaluation for the Atlantic were presented in (Wanninkhof *et al.*, 2003). At the same time, the methodologies for estimating C<sub>ant</sub> were also significantly improved during the 1990s, thus permitting the first descriptions of oceanic C<sub>ant</sub> distributions that were accepted by the carbon cycle community. These historical observations and estimates provided an important benchmark that helped determine the global distributions of both natural and anthropogenic CO<sub>2</sub>, against which subsequent observational studies have been compared.

The WCRP stimulated subsequent programs for assessing ocean variability and change and evaluating and attributing significant trends in the global oceanic carbon budget. During the first decade of the 2000s, the effort to continue collecting full water column hydrographic and geochemical data has been mainly achieved through the CLIVAR/CO<sub>2</sub> Repeat Hydrography Program, which has facilitated observations along a subset of the cruises that were initially run as part of the WOCE/JGOFS global survey in the 1990s. Similarly to GLODAP, more recent synthesis projects have been undergone for evaluation and compilation of oceanic carbon data collected after the 1990s. CARbon IN the Atlantic Ocean (CARINA) emerged as the reference collaborative project concerning CO<sub>2</sub> data acquisition, compilation, evaluation and related research, in the Atlantic. Similarly to CARINA, the PACIFICA database encompasses all cruises in the Pacific Ocean that were not included in the GLODAP database.

#### *The WOCE A05 section*

The WOCE A05 section crosses the North Atlantic subtropical gyre along 24.5°N (Figure 1.11). It has been occupied several times since 1957, some of them to characterize the carbonate system, in 1992, 1998, 2004, 2010 and 2011. This has provided a great opportunity to analyze natural and anthropogenic CO<sub>2</sub> meridional transports and quantify changes in the carbon budget in the subtropical North Atlantic. The hydrographic parameters relative to this section have also been used to evaluate the Atlantic MOC in a number of studies (Bryden *et al.*, 2005; Atkinson *et al.*, 2012).

Research interest on the major influence that it plays on global climate and the need to clarify whether a slowdown of AMOC was taking place (Bryden *et al.*, 2005), encouraged more continuous observations of the AMOC at this latitude. This led to the extensive joint U.K/U.S. RAPID-MOCHA program <http://www.rapid.ac.uk/rapidmoc/>) for monitoring the variability of the AMOC strength, across 26.5°N (Figure 1.12) in the subtropical North Atlantic (Cunningham *et al.*, 2007; McCarthy *et al.*, 2015).

Since 2004, a decade of RAPID observations has shed light on some important questions about the mechanisms controlling the AMOC natural variability on interannual (McCarthy *et al.*, 2012; Smeed *et al.*, 2014) to seasonal (Atkinson *et al.*, 2010; Kanzow *et al.*, 2010) and decadal (Srokosz and Bryden, 2015) timescales. Some of the findings of this monitoring program include an AMOC variability of significantly higher amplitude in only one year than in the 50 years studied previously, an amplitude of the seasonal cycle (minimum in spring and maximum in autumn) larger than anticipated, a totally unexpected 30% AMOC decline in 2009-2010, and a progressive decrease in the AMOC of 0.5 Sv per year, 10 times faster than that predicted by climate models (Srokosz and Bryden, 2015). All these observations might be used with other observing systems to improve our ability to predict AMOC variations (Srokosz *et al.*, 2012) and their impact on climate and the ocean carbon sink at seasonal to decadal and longer time scales.

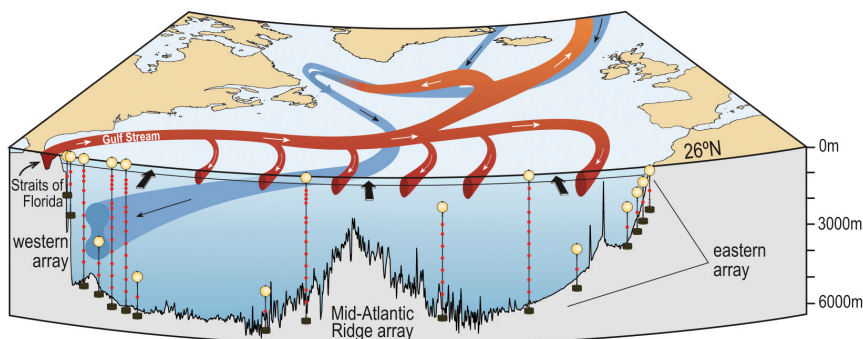


**Figure 1.12.** Section of the RAPID-MOCHA mooring array distribution along 26.5°N. Source: <http://www.rapid.ac.uk/rapidmoc/>.

### Chemical perspective: Spatiotemporal variability in the carbonate system

A major motivation on ocean biogeochemical research over the past several decades has been to better understand the ocean's role as a sink for anthropogenic CO<sub>2</sub>. In turn, assessing the associated acidification of seawater has also raised strong interest with time. Carbon cycle and ocean acidification data obtained in this context provide crucial information for assessing the different ocean sinks and the pH changes that determine the response of marine ecosystems to ocean acidification. In addition, these data is also used to test global coupled ocean-atmosphere models which, ultimately, allow the attribution of changes to both anthropogenic and natural causes.

### Time-series stations in the NASTG

The direct determination of long-term trends in the carbonate system in seawater of a duration in the order of decades is limited to a few oceanic observational studies. Apart from repeat hydrographic sections that allow the study of changes in the carbonate chemistry on decadal time scales, there exist several ocean time-series of seawater chemistry of higher frequency that have allowed the assessment of intra and inter-annual trends of surface seawater carbonate chemistry. Some of them are the BATS (Bermuda Atlantic Time series Study) and the Hydrostation S stations near Bermuda, located in the NW Atlantic Ocean (Bates *et al.*, 1996; Bates, 2001; 2007; Bates *et al.*, 2012), the ESTOC (European Station for Time series in the Ocean, the Canary Islands), located near the Canary Islands in the NE Atlantic Ocean (González-Dávila *et al.*, 2003; Santana-Casiano *et al.*, 2007; González-Dávila *et al.*, 2010), the IS-ts (Iceland Sea time series), in the North of Iceland (Olafsson *et al.*, 2009; Olafsson *et al.*, 2010); the station M, located in the Norwegian Sea (Skjelvan *et al.*, 2008), the CARIACO (CARbon Retention In A Colored Ocean), in the Cariaco Basin (Astor *et al.*, 2005; Taylor *et al.*, 2012; Astor *et al.*, 2013), the Munida time series (Currie *et al.*, 2011) in the South Pacific, the HOT site (Hawaii Ocean Time series), located within the 6 mile radius station ALOHA (A Long-term Oligotrophic Habitat Assessment) near Hawaii in the North Pacific Ocean (Dore *et al.*, 2009) and the KNOT

(Kyodo North Pacific Ocean Time series) in the Northwest Pacific (Tsurushima *et al.*, 2002; Wakita *et al.*, 2005; Wakita *et al.*, 2010).

Two of these time-series lay within the NASTG, covering both zonal extremes:

- In the western end of this gyre, a time-series combines carbonate system data collected from two sites, near Bermuda: BATS ( $31^{\circ} 40'N$ ,  $64^{\circ} 10'W$ ) and Hydrostation S ( $32^{\circ} 10'$ ,  $64^{\circ} 30'$ ) (Steinberg *et al.*, 2001; Bates *et al.*, 2012). It provides  $C_T$  and  $A_T$  with depth measured fourteen to sixteen times a year from 1983 until present (Bates *et al.*, 2014).
- In the eastern end of the NASTG, the other time-series provides carbonate system data collected since 1994 until present near the Canary Islands, in the transition zone between the coastal upwelling region and open ocean waters: ESTOC ( $29^{\circ} 10'N$ ,  $15^{\circ} 30'W$ ). In this site, measurements of pH (total scale),  $A_T$ ,  $C_T$  and  $fCO_2$  (in some instances only  $C_T$  and  $A_T$ ) are taken from four to six times a year and sometimes monthly (González-Dávila *et al.*, 2010; Bates *et al.*, 2014).

Interannual to seasonal to long-term variations in the carbonate system parameters at these two locations (Figure 1.13 and Figure 1.14) have been evaluated and discussed in a number of studies (Bates *et al.*, 1996; Bates, 2001; González-Dávila *et al.*, 2003; Bates, 2007; Santana-Casiano *et al.*, 2007; González-Dávila *et al.*, 2010; Bates *et al.*, 2012; Bates *et al.*, 2014) that have allowed describing processes that influence the  $CO_2$  budget variability over the entire North Atlantic (Gruber *et al.*, 2002; Bates, 2012). Although the seasonal variability of the carbonate chemistry and the physical variables shows the same fluctuations at the western and eastern sides of the gyre, the amplitude of the signals is normally higher for BATS than for ESTOC.

In the following we describe, for each of the four most important carbonate system parameters, the long-term trends (summarized in Table 1.2) and the average seasonal variability at the two sites:

#### *a) Dissolved Inorganic Carbon*

The variability exhibited by  $C_T$  reflects seasonal changes in primary production and gas exchange in the upper ocean that are reinforced or counteracted by mixing processes (Bates, 2001). The seasonal changes in  $C_T$  show a variability opposite to temperature at the two sites: the higher values are found at the end of spring due to vertical mixing with cold deep water during winter, and lower values are found at the end of autumn because primary production accounts for the decrease in  $C_T$  as upper waters get warmer and stratify during summer, without turnover (Fig. 1.13). The amplitude in seasonal variability of  $C_T$  at ESTOC is of 20-30  $\mu\text{mol kg}^{-1}$  (Santana-Casiano *et al.*, 2007), while it is slightly higher at BATS, showing a range of 30-40  $\mu\text{mol kg}^{-1}$  along an annual cycle (Bates, 2001). The long-term changes in surface salinity-normalized  $C_T$  ( $nC_T$ ) at the two sides of the NASTG (Table 1.2) show an increasing trend with time, as expected due to the ocean uptake of anthropogenic  $CO_2$  (Bates *et al.*, 2014).

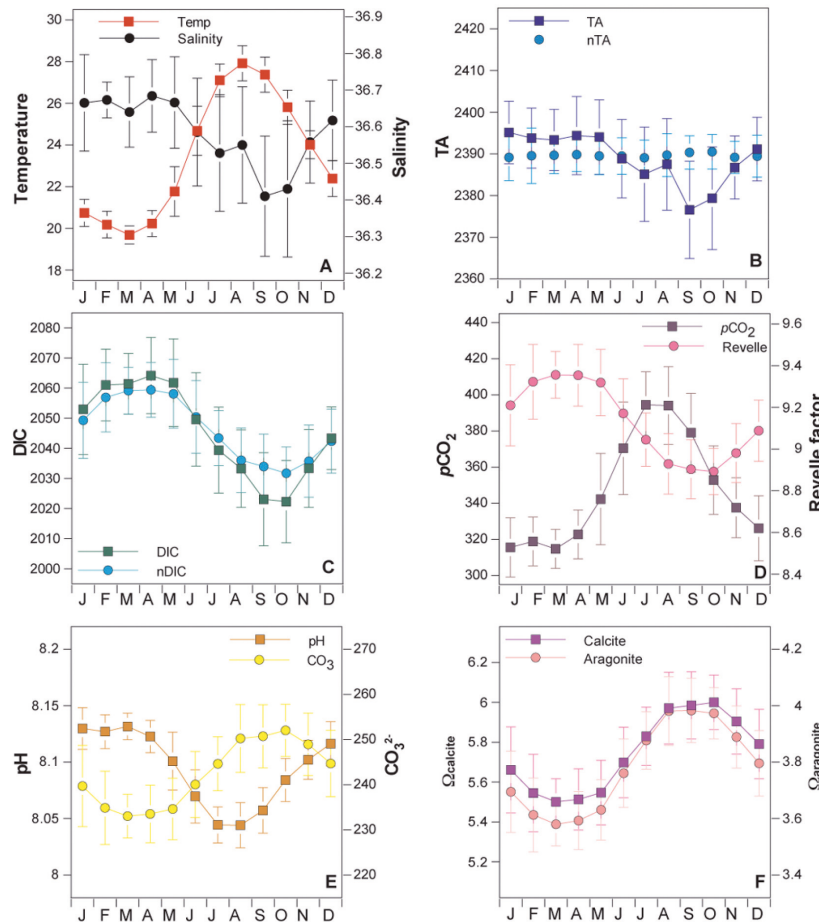


**Figure I.13.** Seasonal variability at BATS/Hydrostation S for the period 1983-2011: mean monthly values for surface temperature and salinity (A), total alkalinity (B,  $\mu\text{mol kg}^{-1}$ ),  $C_T$  ( $\mu\text{mol kg}^{-1}$ ), seawater  $\text{pCO}_2$  and Revelle factor (D,  $\mu\text{atm}$ ), pH and  $[\text{CO}_3^{2-}]$  (E,  $\mu\text{mol kg}^{-1}$  for  $[\text{CO}_3^{2-}]$ ), and  $\Omega_{\text{calcite}}$  and  $\Omega_{\text{aragonite}}$  (F). The standard deviation is shown by y error bars. Source: Bates *et al.*, (2012).

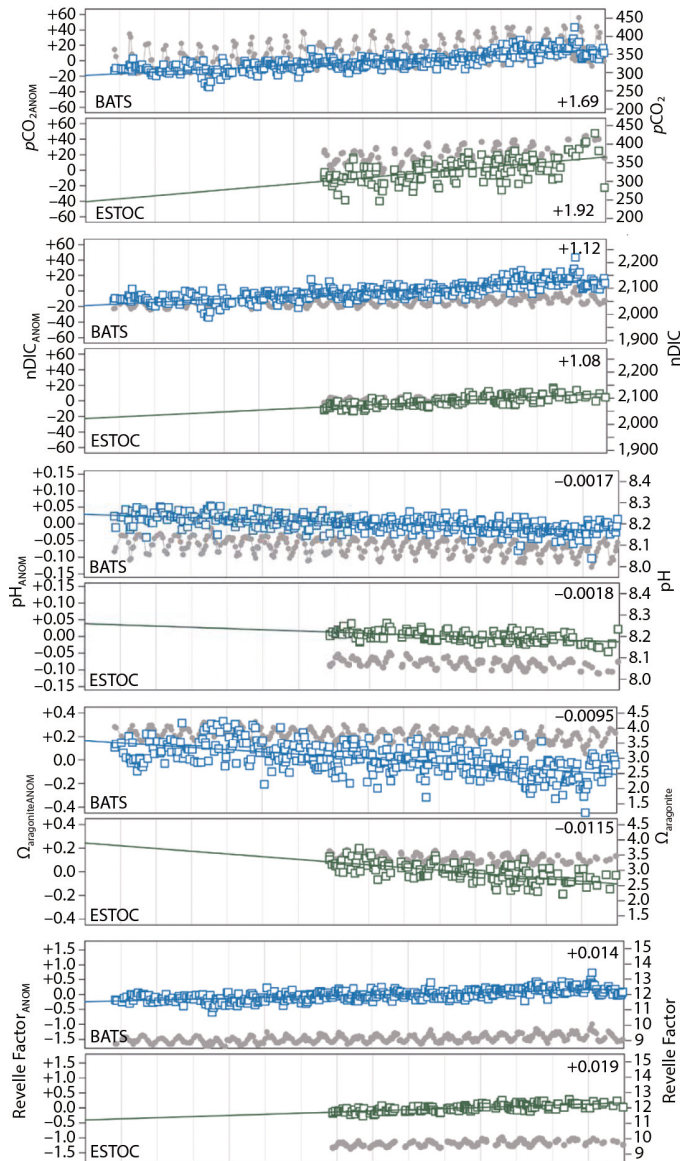


**Figure 1.14.** Time Series of surface seawater anomalies (colored symbols) and observations (gray symbols), with trends (solid lines) reported in Table 1.2 shown in the top right corner of each panel, of different parameters of the carbonate system: (a) surface ocean  $p\text{CO}_2$ ; b) salinity-normalized DIC (nDIC, in  $\mu\text{mol kg}^{-1}$ ); c) pH; d) aragonite saturation state ( $\Omega_{\text{aragonite}}$ ) and e) Revelle factor. Note that BATS is located at higher latitude than ESTOC. Adapted from Bates et al. (2014).

### b) Alkalinity

Surface total alkalinity ( $A_T$ ) shows an annual variability of around  $30 \mu\text{mol}\cdot\text{kg}^{-1}$  and  $25 \mu\text{mol}\cdot\text{kg}^{-1}$  at BATS and ESTOC, respectively (Bates, 2001; Santana-Casiano *et al.*, 2007). This parameter is well correlated with salinity. At BATS, it has been increasing at a rate of  $0.48 \pm 0.27 \mu\text{mol}\cdot\text{kg}^{-1} \text{ yr}^{-1}$  due to a progressive increase in the salinity of surface subtropical gyre waters (Bates *et al.*, 2012). However, alkalinity trends normalized at the average salinity of each site show a relative constant value over time (González-Dávila *et al.*, 2010) or a slightly increase that cannot be considered statistically significant (Bates *et al.*, 2012) (Table 1.2).

### c) pH

pH in situ also shows seasonal variability coupled to temperature. Maximum values are found during winter and minimum values are found when the water column warms and stratifies (Figure 1.13). The difference between the two time series is, again, the amplitude of the seasonal variability of this parameter, where BATS shows higher amplitude in pH values during the year, compared to ESTOC (Pelejero *et al.*, 2010). The pH records from the two time-series show a clear acidifying trend over time with close values at each side of the gyre (Table 1.2). Since  $nA_T$  remains constant with time, pH changes are explained due to the long-term increasing levels in  $C_T$ . Other indicators of ocean acidification such as  $[\text{CO}_3^{2-}]$ ,  $\Omega_{\text{calcite}}$  and  $\Omega_{\text{aragonite}}$  also exhibit a progressive decrease in both time series (Table 1.2).

### d) Partial pressure of $\text{CO}_2$ ( $p\text{CO}_2$ )

The seasonal seawater  $p\text{CO}_2$  cycle is also strongly influenced by temperature: seawater  $p\text{CO}_2$  levels are low during winter and spring and high at the end of summer and during autumn. Surface seawater  $p\text{CO}_2$  exhibits an increasing trend at the two sites (Table 1.2). The difference between partial pressure of  $\text{CO}_2$  in seawater and the atmosphere ( $\Delta p\text{CO}_2 = [(p\text{CO}_2)_{\text{ocean}} - (p\text{CO}_2)_{\text{air}}]$ ) determines the direction of the gas transference (i.e. the  $\text{CO}_2$  flux) between the two sinks, when wind velocity and  $\text{CO}_2$  solubility are also taken into account. On a general basis, the NASTG acts as a source of  $\text{CO}_2$  into the atmosphere during the stratification period, from June to November, and as a sink when vertical mixing takes place, from December to May (González-Dávila *et al.*, 2003). The annual budget is negative indicating that the gyre acts as a net  $\text{CO}_2$  sink for atmospheric  $\text{CO}_2$  that ranges between 0 and 1 mol  $\text{CO}_2 \text{ m}^{-2} \text{ yr}^{-1}$  (Takahashi *et al.*, 2002; Santana-Casiano *et al.*, 2007; Takahashi *et al.*, 2009). However, the Subtropical Gyre seems to act as a more intense sink for atmospheric  $\text{CO}_2$  at its western side, showing values for  $\text{CO}_2$  flux of  $-810 \pm 249$  to  $-1184 \pm 298 \text{ mmol CO}_2 \text{ m}^{-2} \text{ yr}^{-1}$  for the period 1983-2005 at BATS (Bates, 2007). On the contrary,  $\text{CO}_2$  fluxes for the period 1995-2004 at the ESTOC site were lower, of  $-51 \pm 36$  to  $-54 \pm 28 \text{ mmol CO}_2 \text{ m}^{-2} \text{ yr}^{-1}$  (Santana-Casiano *et al.*, 2007) and the site acted as a minor source of  $\text{CO}_2$  during the period 1995-2000 (González-Dávila *et al.*, 2003).

**Table 1.2.** Long-term trends of surface hydrography and carbonate chemistry at BATS (5m) and ESTOC (10m). The trends are reported for the period 1983–2014 (BATS) and 1995–2014 (ESTOC) following Bates *et al.*, (2014). (\*) indicates trends reported for shorter periods, according to available literature: between 1995 and 2004 at ESTOC ((Santana-Casiano *et al.*, 2007; González-Dávila *et al.*, 2010) and between 1983 and 2011 at BATS (Bates *et al.*, 2012)).

	BATS	ESTOC
Temperature*	$0.011 \pm 0.006 \text{ }^{\circ}\text{C yr}^{-1}$	$0.002 \pm 0.019 \text{ }^{\circ}\text{C yr}^{-1}$
Salinity*	$0.0054 \pm 0.0001$	$0.0088 \pm 0.0025$
$\text{C}_T$	$1.37 \pm 0.07 \mu\text{mol kg}^{-1} \text{yr}^{-1}$	$1.09 \pm 0.10 \mu\text{mol kg}^{-1} \text{yr}^{-1}$
$n\text{C}_T$	$1.12 \pm 0.04 \mu\text{mol kg}^{-1} \text{yr}^{-1}$	$1.08 \pm 0.08 \mu\text{mol kg}^{-1} \text{yr}^{-1}$
$\text{A}_T^*$	$0.48 \pm 0.27 \mu\text{mol kg}^{-1} \text{yr}^{-1}$	$-0.79 \pm 0.14 \mu\text{mol kg}^{-1} \text{yr}^{-1}$
$n\text{A}_T^*$	$0.10 \pm 0.03 \mu\text{mol kg}^{-1} \text{yr}^{-1}$	$-0.08 \pm 0.06 \mu\text{mol kg}^{-1} \text{yr}^{-1}$
$\text{pCO}_2$	$1.69 \pm 0.11 \mu\text{atm yr}^{-1}$	$1.92 \pm 0.24 \mu\text{atm yr}^{-1}$
pH	$-0.0017 \pm 0.0001$	$-0.0018 \pm 0.0002$
carbonate ion*	$-0.58 \pm 0.041 \mu\text{mol kg}^{-1} \text{yr}^{-1}$	$-0.90 \pm 0.08 \mu\text{mol kg}^{-1} \text{yr}^{-1}$
$\Omega_{\text{calcite}}^*$	$-0.0141 \pm 0.0009 \text{yr}^{-1}$	$-0.0209 \pm 0.0023 \text{yr}^{-1}$
$\Omega_{\text{aragonite}}$	$-0.0095 \pm 0.0007 \text{yr}^{-1}$	$0.0115 \pm 0.0023 \text{yr}^{-1}$
Revelle factor	$0.014 \pm 0.001 \text{yr}^{-1}$	$0.019 \pm 0.002 \text{yr}^{-1}$

### *Changes in the uptake and transport of $\text{C}_{\text{ant}}$ in the North Atlantic*

The North Atlantic Ocean presents the largest  $\text{C}_{\text{ant}}$  storage rate of all oceans ( $0.386 \pm 0.012 \text{ Pg y}^{-1}$ ) (Mikaloff Fletcher *et al.*, 2007). More than 23% of the global oceanic  $\text{C}_{\text{ant}}$  inventory is found in the North Atlantic even though the region only covers approximately 15% of the global ocean (Figure 1.15a) (Sabine *et al.*, 2004; Sabine and Tanhua, 2010). The key mechanism contributing to this high value is the northward transport of warm subtropical waters that contain high  $\text{C}_{\text{ant}}$  concentrations from the NASTG into the regions of deep water formation, through the upper limb of the MOC, which sustains up to 65±13% of the  $\text{C}_{\text{ant}}$  storage in the North Atlantic (Figure 1.15b) (Álvarez *et al.*, 2003; Macdonald *et al.*, 2003; Rosón *et al.*, 2003; Sabine *et al.*, 2004; Pérez *et al.*, 2013). Despite its large  $\text{C}_{\text{ant}}$  storage rate, air-sea uptake in the northern North Atlantic is not predominantly anthropogenic because, as these warm waters move northward, they cool, favoring the natural  $\text{CO}_2$  uptake over the anthropogenic perturbation (Watson *et al.*, 1995; Pérez *et al.*, 2013). So, in the North Atlantic subpolar Gyre (NASPG), the wintertime vertical deep convection contributes to both the  $\text{C}_{\text{ant}}$  and natural  $\text{CO}_2$  storage in depth, significantly contributing to the efficiency of the North Atlantic sink. These deep waters return southward into the Deep Western Boundary Current (DWBC) containing moderate but increasing  $\text{C}_{\text{ant}}$  levels (Pérez *et al.*, 2008; Steinfeldt *et al.*, 2009; Pérez *et al.*, 2010). The advection of the physic-chemical signals of the newly formed North Atlantic Deep Water (NADW) within de DWBC explains why the western North Atlantic is the major contributor to the whole basin inventories of  $\text{C}_{\text{ant}}$  (Kortzinger *et al.*, 1998; Brown *et al.*, 2010) and CFCs (Kieke *et al.*, 2007; Kieke *et al.*, 2006; Steinfeldt *et al.*, 2007). Hence, the decadal storage variability of the whole basin inventories of  $\text{C}_{\text{ant}}$  (Pérez *et al.*, 2013)

and CFC depends on and is modulated by the formation rate of this deep water mass and, more particularly, of the Labrador Sea Water (LSW) component.

Inverse estimates of the atmospheric CO<sub>2</sub> absorption by the global ocean found considerable C<sub>ant</sub> uptake in the equator and the tropics (Mikaloff Fletcher *et al.*, 2006), favored by the low Revelle factors found in tropical and subtropical warm waters that facilitate the absorption of atmospheric C<sub>ant</sub>. The advection to the north of the absorbed C<sub>ant</sub> and its weak deeper penetration at lower latitudes explains why Lee *et al.* (2003) reported relative small total and specific inventories for the (sub)tropical North Atlantic relative to the sub-polar North Atlantic. On timescales of decades, the rate at which C<sub>ant</sub> is moved into the ocean interior limits the rate of ocean uptake (Sarmiento *et al.*, 1992). Given the predominant part of the Tropical North Atlantic region (Zunino *et al.*, 2015) and the NASTG (Pérez *et al.*, 2013) in the uptake of C<sub>ant</sub> from the atmosphere, the WOCE A05 (24.5°N) and WOCE A06 (7.5°N) sections are suitable and, indeed, fundamental, for the evaluation and quantification of the North Atlantic C<sub>ant</sub> sink. Taking into account the role of ocean circulation on the distribution of the absorbed C<sub>ant</sub> between basins and the derived temporal change in its storage at regional scales (Gruber *et al.*, 1996), a reassessment of the C<sub>ant</sub> distributions along different sections that characterize different oceanic regions is necessary to constrain how the ocean carbon sink operates. The A05 and A06 sections are representative for the entire (sub)tropical North Atlantic, with the former having a strategic location for the evaluation of the MOC and also for assessing changes in the C<sub>ant</sub> (upper) entry to and (deeper) exit from the great northern North Atlantic reservoir (Figure 1.15).

When comparing hydrographic “snapshots” of the ocean, by means of the comparison of the same hydrographic section through time, a classic problem associated with the interpretation of decadal changes is the possible aliasing of changes in the ocean state at shorter timescales (Atkinson *et al.*, 2012) because processes affecting climate can exhibit considerable natural variability on a broad range of spatial and temporal scales. In the Tropical Atlantic, Zunino *et al.*, (2015) reported an increase in the C<sub>ant</sub> transport across 7.5°N and 24.5°N between 1993-2010 and 1992-2011, respectively, which resulted from changes in the intermediate and deep circulation across these sections, as well as from the notorious C<sub>ant</sub> increase with time within the thermocline waters. The authors also described substantial C<sub>ant</sub> storage within deep waters of the tropical Atlantic enclosed between the two sections due to the injection of C<sub>ant</sub> across 24.5°N by the DWBC and the northward recirculation of NADW along 7.5°N.

C<sub>ant</sub>-enriched NADW has been explained due to the strong renewal of LSW during the mid-1990s coinciding with a positive phase of the North Atlantic Oscillation period (Pérez *et al.*, 2008). Indeed, much of the variability in the North Atlantic is associated with the quasi-decadal NAO climate mode (Walker and Bliss, 1932; Barnston and Livezey, 1987). Low frequency modes such as NAO cannot themselves exert influence on air-sea CO<sub>2</sub> fluxes, but rather on physical parameters such as sea surface temperature and wind speed that can, in turn, influence seawater pCO<sub>2</sub> and, thus, air-sea fluxes (Bates, 2007). Positive (negative) values of the

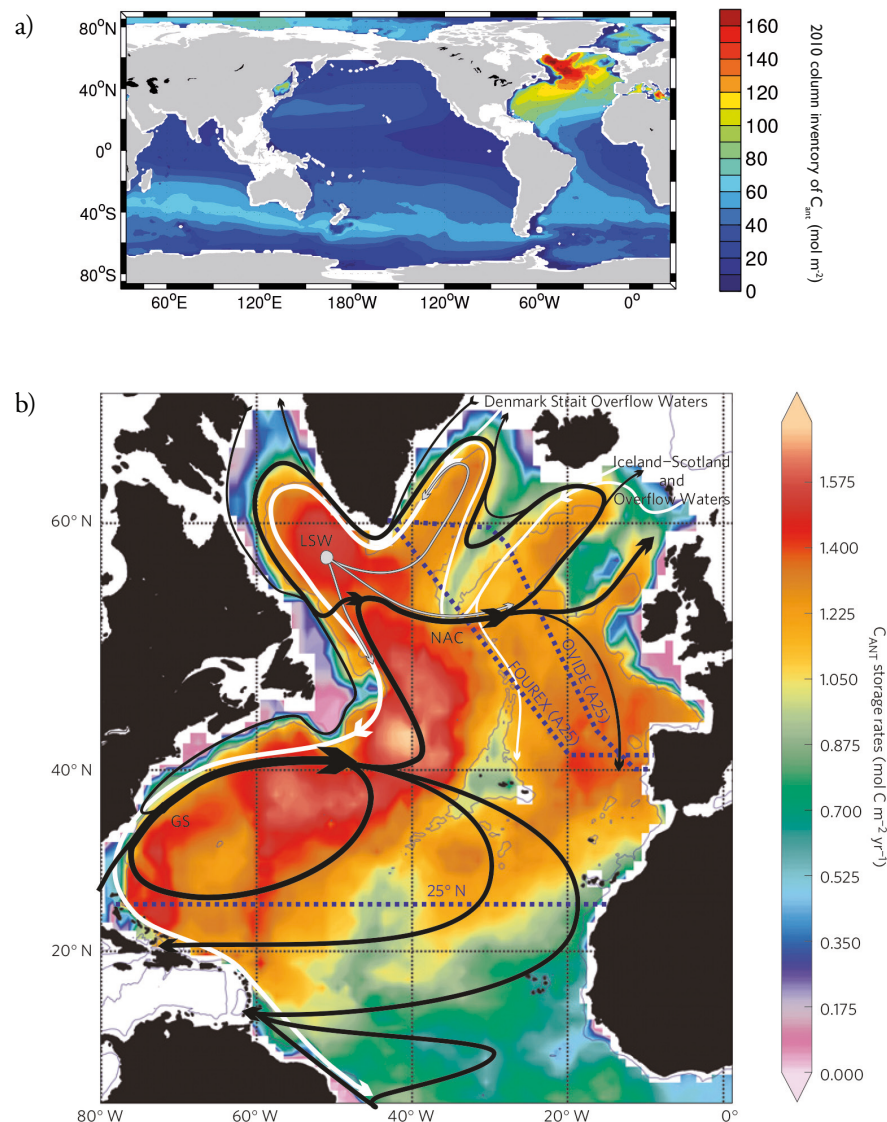


**Figure 1.15.** a) Global 2010 column inventory of  $C_{ant}$  ( $\text{mol m}^{-2}$ ) excluding the marginal seas (Source: modified from Khatiwala et al. (2013)). b) Circulation and  $C_{ant}$  in the North Atlantic;  $C_{ant}$  storage rates ( $\text{mol C}_{ant} \text{m}^{-2} \text{yr}^{-1}$ ) and the main currents and water masses involved in the AMOC (black line: North Atlantic Current (NAC) and Gulf Stream (GS); grey line: Labrador Sea Water (LSW); white lines: Denmark Strait and Iceland-Scotland Overflow Waters (DSOW and ISOW)). The A05 (25°N), FOUREX and OVIDE hydrographic sections are indicated (blue dotted lines). Source: Pérez et al. (2013).

winter NAO index are associated with strong (weak) zonal flow between Azores and Iceland (Rogers, 1984). Since the phase of the NAO index affects the wind field, large-scale changes in the atmospheric forcing related to changes in the NAO maintained during several years affect the ocean circulation in the NASTG and the NASPG, which have contrasting responses to different NAO periods. The intensification of the winter convection in the NASPG during periods of high NAO index increases the CO<sub>2</sub> uptake and storage of this region (Pérez *et al.*, 2010). In contrast, in the NASTG, CO<sub>2</sub> uptake increases during the years of low NAO index (Gruber *et al.*, 2002; Bates, 2007). The shift between climatic states can occur as a result of natural variability, or due to external forcing. It is thus necessary to understand the relationship among natural climate variability, the potential existence of anthropogenic forcing and the derived responses to decipher how marine carbon cycle will evolve in the North Atlantic in the future due to climate change.

#### *Impacts of C<sub>ant</sub> penetration on the CaCO<sub>3</sub> system in the Subtropical North Atlantic*

The level at which CaCO<sub>3</sub> minerals, aragonite and calcite, are in thermodynamic equilibrium is known as the saturation depth or saturation horizon ( $\Omega = 1$ ). This depth is significantly shallower for aragonite than for calcite, because aragonite is more soluble in seawater than calcite. In addition, there is pronounced shoaling of both minerals saturation horizons from the Atlantic through the Indian to the Pacific oceans because of the higher C<sub>T</sub>/A<sub>T</sub> ratios in the intermediate and deep waters of these two oceans relative to the Atlantic. This is due to the enrichment in C<sub>T</sub> of the water masses because of respiration processes. Most of the upper Atlantic, in particular north of 30°S and at depths above 2000m, is supersaturated with respect to aragonite, while much of the deep Atlantic is undersaturated (Chung *et al.*, 2004).

Dissolution of CaCO<sub>3</sub> minerals occurs when seawater is undersaturated ( $\Omega < 1$ ) with respect to these minerals. Classically, and when the solubility of CaCO<sub>3</sub> in seawater is controlled more by kinetic constraints than by thermodynamic equilibrium, an important part of the dissolution of CaCO<sub>3</sub> particles occurs at greater depths than the saturation horizons (Millero, 2006). In the North Atlantic, the highest CaCO<sub>3</sub> dissolution rates take place near or below the average aragonite saturation horizon around 3500m (Feely *et al.*, 2004), being higher north of 40°N than the rates to the south (Chung *et al.*, 2003). However, it has also been shown that as much as 60% or more of the exported CaCO<sub>3</sub> out of the surface ocean dissolves in the upper 1000–2000m (Milliman and Droxler, 1996; Milliman *et al.*, 1999; Chung *et al.*, 2003; Feely *et al.*, 2004). Recent analyses may also suggest that considerable CaCO<sub>3</sub> dissolution may occur in the top 1000 m of the eastern North Atlantic (Barrett *et al.*, 2014).

Processes that increase the A<sub>T</sub> in the upper ocean such as CaCO<sub>3</sub> dissolution facilitate the uptake of C<sub>ant</sub> from the atmosphere (Zeebe and Wolf-Gladrow, 2001). As the oceans become enriched in C<sub>ant</sub>, the location and extent of regions where dissolution occurs is expected to increase linked to the decrease in  $\Omega$  of CaCO<sub>3</sub> minerals. Comparison of preindustrial and current saturation horizons in the North Atlantic reveals that, in regions between 20°N and 50°N, the preindustrial aragonite saturation horizon laid nearly at the same depth

as today, while in the eastern South and North Atlantic, the aragonite horizon has shoaled by approximately 80 to 150m (Feely *et al.*, 2004) (Figure 1.16). Related to this, (Chung *et al.*, 2004) reported that, although the (sub)tropical Atlantic between 30°N and 30°S is supersaturated by as much as 300-400% with respect to aragonite above 2500m, layers of undersaturated water can be observed in its upper eastern region at depths of 600-1100 from 14°N to 16°S and at depths of 500-1000m from the equator to 20°S. The authors related much of the reduction in  $\Omega_{\text{aragonite}}$  to oxidation of organic matter, since these layers encompass regions of relatively high apparent oxygen utilization and  $C_T$ . However, they also assigned the lateral expansion of such layers (that joined the two regions into a large area of understauration) to the accumulation of  $C_{\text{ant}}$  with time.

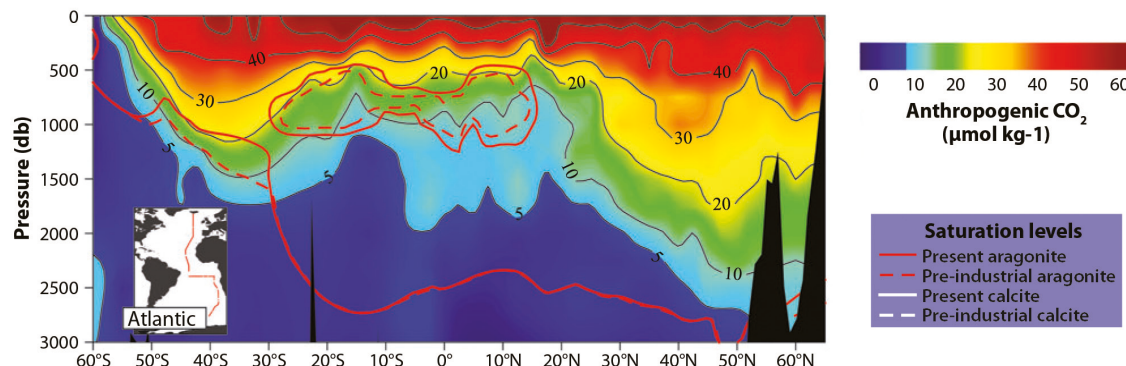


**Figure 1.16.** Vertical distributions of anthropogenic CO<sub>2</sub> concentrations in  $\mu\text{mol kg}^{-1}$  and the saturation horizons for aragonite and calcite along a north-south transect in the Atlantic Ocean. Adapted from Feely *et al.*, (2004).

The ongoing expansion of the undersaturated area as more C<sub>ant</sub> is absorbed into this region will increase the in situ dissolution of CaCO<sub>3</sub>, which will eventually result in a greater supply of A<sub>T</sub> to the upper waters but a smaller supply of CaCO<sub>3</sub> to the sediments (Ilyina and Zeebe, 2012). Recent model results allow discerning significant trends in A<sub>T</sub> due to reduced calcification as waters become more acidified which will start being detectable by the middle of this century, with the largest increases predicted for tropical and subtropical regions (Ilyina *et al.*, 2009). This A<sub>T</sub> increase is ascribed to decreased CaCO<sub>3</sub> export in surface waters. Indeed, the decrease in the exportation of CaCO<sub>3</sub> particles can also be caused by increased dissolution in upper waters. Although higher CaCO<sub>3</sub> dissolution would increase the ocean capacity to take up C<sub>ant</sub> it could, in turn, affect the rain ratio (organic:inorganic carbon) to the deep sea trough the affection of the process of CaCO<sub>3</sub> ballasting of organic carbon, which could result in a shallower remineralization of organic carbon. Model results report a compensation of the increase in buffering capacity of upper waters due to increased alkalinity by the shoaling of the remineralization horizon (Heinze, 2004). Moreover, model results also project that the reduction of CaCO<sub>3</sub> ballast in an acidifying upper ocean could result in reduced oxygen concentrations

in intermediate waters, in addition to decreased organic export (Hofmann and Schellnhuber, 2009). Such findings have led some authors (Barrett *et al.*, 2014) link the reported expanding oxygen minimum zone in the eastern tropical North Atlantic (Stramma *et al.*, 2008) with changes in upper water  $\text{CaCO}_3$  dissolution in this region.

Nonetheless, Ilyna and Zeebe (2012) show that the different assumptions regarding dissolution and calcification rates have little impact on future projections on the degree of perturbation of seawater chemistry and conclude that  $\text{CaCO}_3$  dissolution has insignificant potential in mitigating  $\text{C}_{\text{ant}}$  and ocean acidification in the next millennia. Hence, by assuming steady  $\text{C}_{\text{ant}}$  storage rates, the intermediate water of the entire (sub)tropical Atlantic between 20°N and 20°S (in the range 500 -1100m depth) is projected to become undersaturated with respect to aragonite by about the middle of this century (Chung *et al.*, 2004).





# **Aims of the thesis and data collection**



## OBJECTIVES AND THESIS OUTLINE

The main objective of this thesis was to improve our knowledge of the spatiotemporal variability of the carbonate system in the (sub)tropical North Atlantic. This broad aim can be split into the following major questions, already raised in the general introduction, that correspond to the chapters of the thesis:

**What is the spatial and temporal distribution of anthropogenic CO<sub>2</sub> in the (sub)tropical North Atlantic region?**

**Chapter 3.1.** Trends in anthropogenic CO<sub>2</sub> in water masses of the Subtropical North Atlantic Ocean

**Chapter 3.2.** Anthropogenic CO<sub>2</sub> changes in the Equatorial Atlantic Ocean

The continuous collection of field data on the carbonate system in seawater through several repeat cruises conducted along two hydrographic sections in the (sub)tropical North Atlantic region between the early 1990s and the early 2010s prompted us to assess the changes in the distribution of C<sub>ant</sub> in this region during this period. To this aim, we used historical and new data, with application of different C<sub>ant</sub> estimation techniques for comparative purposes. The reference historical data had to be revised and updated in order to perform the temporal comparisons. Once revised, and to facilitate the instrumental use of these data to explore changes in the carbonate system variables, we reported these data to CDIAC (Carbon Dioxide Information and Analysis Center) (Appendix I) to make it available to the scientific community.

**How have these changes in anthropogenic CO<sub>2</sub> distribution affected the water masses pH over the subtropical North Atlantic and what are the relative anthropogenic and natural contributions?**

**Chapter 3.3.** Ocean acidification along the 24.5°N section in the Subtropical North Atlantic.

The study of the changes in C<sub>ant</sub> distributions prompted us to investigate the derived pH changes that have occurred in the subtropical North Atlantic between 1992 and 2011. We used direct pH measurements to investigate such changes. Furthermore, we also assessed to what extent these pH changes were explained due to the accumulation of C<sub>ant</sub> and what was the contribution of the natural variability. For this purpose, the variability of natural pH changes was estimated from changes in the concentration of dissolved oxygen.

**Appendix I.** High spatial resolution alkalinity and pH measurements by IIM-CSIC group along 24.5°N during the R/V Hespérides WOCE Section A05 cruise (July 14 - August 15, 1992).

## OCEANOGRAPHIC CRUISES IN THE (SUB)TROPICAL ATLANTIC

The WOCE A05 (also called 24N or 25N) and A06 repeat hydrography have allowed the study of the decadal fluctuations of the water masses flowing across the two sections and how they influence the AMOC (Hernández-Guerra *et al.*, 2014) which, in turn, modulates the meridional transport of C<sub>ant</sub> and makes the North Atlantic one of the main CO<sub>2</sub> sinks of the global ocean. For our purposes in this thesis, the A05 and A06 data records allowed us assessing the spatial and the decadal variability of the carbonate system in the (sub)tropical North Atlantic from observational data, and demonstrated their suitability as key zonal sections for the evaluation of the North Atlantic C<sub>ant</sub> sink.

### WOCE sections studied

#### WOCE A05 section

The A05 section is located at 24.5°N of latitude, spanning across the subtropical North Atlantic gyre. It has been occupied several times since 1957, but it was in 1992 when observations of the properties of the carbonate system along the section were made for the first time, within the frame of the WOCE program. Four more occupations of interest have been made since then, in 1998, 2004, 2010 and 2011 (Figure 2.1. and Table 2.1.), in terms of reassessing those first observations. Data from the 1992 and 1998 cruises is hosted in the GLODAP database (<http://cdiac.ornl.gov/oceans/glodap/>) which compiles historical data from the 1990s. The 2004, 2010 and 2011 cruises are modern repeats of the 1998 transect whose data sets can be found in the CARINA database (<http://cdiac.ornl.gov/oceans/CARINA/>). Several studies have focused on the carbonate system and C<sub>ant</sub> distributions and fluxes along this section by using the measurements performed in 1992 (Rosón *et al.*, 2003), 1998 (Macdonald *et al.*, 2003) and 2004 (Brown *et al.*, 2010). In this thesis dissertation, the two more recent occupations, in 2010 and 2011, are added to the A05 data record in order to address a number of questions regarding the spatiotemporal variability of the carbonate system between 1992-2011 in the subtropical North Atlantic.

#### WOCE A06 section

The A06 section is located at 7.5°N of latitude, in the tropical North Atlantic. Likewise for the A05 section, it was occupied for the first time in 1957 during the International Geophysical Year and it was included within the net of selected sections surveyed during the 1990s within the WOCE program (Figure 2.1 and Table 2.2.). It was in 1993 when the first assessment of the carbonate system was performed along this section. These data were not included in the GLODAP database (Wanninkhof *et al.*, 2003) but are available in other data repositories (e.g. Clivar & Carbon Hydrographic Data Office, CCHDO). The section was reoccupied in 2010 following the same track as in 1993. In this thesis dissertation, data on the last A06 occupation are used to assess the changes of the carbonate system between 1993-2010 in the tropical North Atlantic.

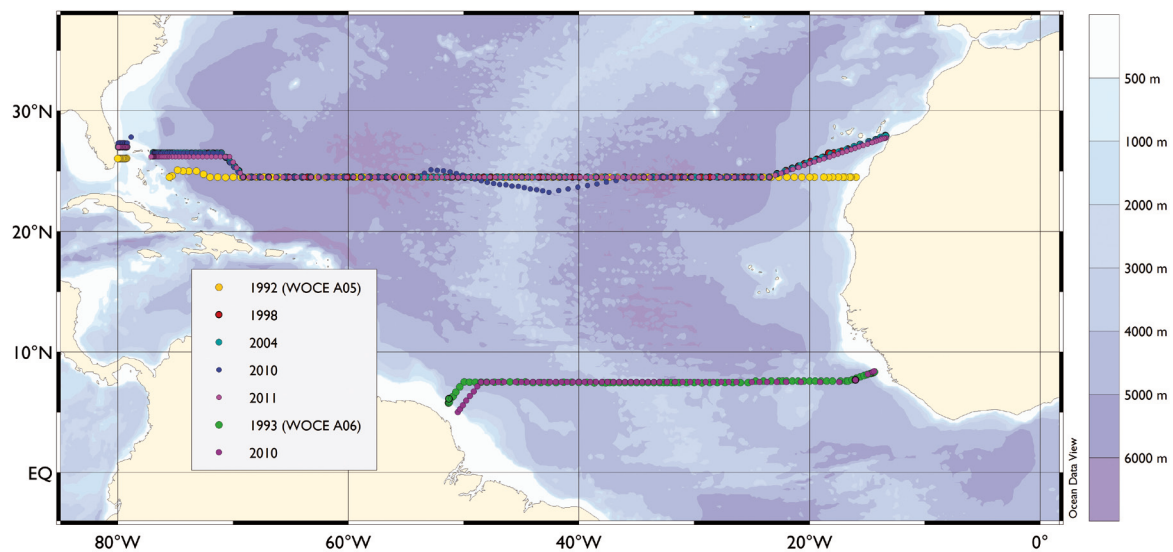


**Figure 2.1.** a) Tracks and station locations for the 1992, 1998, 2004, 2010 and 2011 A05 repeat section, along 24.5°N in the subtropical North Atlantic and for the 1993 and 2010 A06 repeat section, along 7.5°N in the tropical North Atlantic. The 1992 occupation was carried out along 24.5°N, lying south of the following cruises at the boundary regions and sampling the Florida Strait at 26°N. Subsequent occupations were set starting from 28°N next to the African shelf, joining the 24.5°N line at 24°W and angling northward near the opposite shelf to complete the line at 26.5°N, sampling the Florida Strait at 27°N. The 2010 cruise crossed the Mid Atlantic Ridge following the Kane Fracture Zone, thus slightly deviating from the common track.

### Analytical measurements

In 2010, the latest occupation of the A06 section was carried out on board the Spanish R/V *Hespérides* as part of the MOC<sup>2</sup> project (Ocean Climate Memory: fluxes of intermediate waters in the Southern Atlantic and their transformation into surface waters in the Equatorial Atlantic). The cruise occupied 110 hydrographic stations, from 5<sup>th</sup> April to 16<sup>th</sup> May 2010. In 2011, the most recent occupation of the A05 section was carried out on board the Spanish R/V *Sarmiento de Gamboa* as part of the Circumnavigation Expedition MALASPINA 2010 (<http://www.expedicionmalaspina.es/>). From 27th January to 15th March 2011, the cruise occupied 167 full-depth stations. Continuous profiles of temperature, salinity (S) and dissolved oxygen were obtained in each station of the two cruises, by using a Conductivity-Temperature-Depth (CTD) instrument. The CTD was incorporated to a rosette equipped with 24 Niskin bottles that was used for collecting water samples. The sequence for seawater chemistry sampling was: O<sub>2</sub>, pH, total dissolved inorganic carbon (C<sub>T</sub>), total alkalinity (A<sub>T</sub>), nutrients and S, in the two cruises (Table 2.3).

**Table 2.1** Cruises information on the repeat section A05. Datasets regarding the respective occupations of the section are available at the Carbon Dioxide Information Analysis Center (CDIAC) website: <http://cdiac.ornl.gov/oceans/RepeatSections/>.<sup>a</sup> (m) = measured parameter, (calc) = calculated parameter.

Cruise name (Exocode)	Dataset	Year	Period	Research Vessel	Sampled stations	CO <sub>2</sub> parameters	Carbon related data PI(s)
29HE06_1-3	GLODAP	1992	7/14 - 8/15	R/V <i>Bio Hespérides</i>	112	A <sub>T</sub> (m), pH(m), C <sub>T</sub> (calc)	F. Millero /A.F. Ríos
33RO19980123	CARINA	1998	1/23-2/24	R/V <i>Ronald H. Brown</i>	130	A <sub>T</sub> (m), pH(m), C <sub>T</sub> (m)	R. Wanninkhof/ R.Feely
74DI20040404	CARINA	2004	4/4-5/10	R/V <i>Discovery</i>	125	A <sub>T</sub> (m), C <sub>T</sub> (m)	U. Schuster
74DI20100106	CARINA	2010	1/6-2/18	R/V <i>Discovery</i>	135	A <sub>T</sub> (m), C <sub>T</sub> (m)	U. Schuster
29AH20110128	CARINA	2011	1/28-3/14	R/V <i>Sarmiento de Gamboa</i>	167	A <sub>T</sub> (m), pH(m), C <sub>T</sub> (calc)	A.F. Ríos/F.F. Pérez

**Table 2.2.** Cruises information on the repeat section A06. Datasets regarding the respective occupations of the section are available at the Carbon Dioxide Information Analysis Center (CDIAC) website: <http://cdiac.ornl.gov/oceans/RepeatSections/> and the Clivar & Carbon Hydrographic Data Office (CCHDO) <http://cchdo.ucsd.edu/>.<sup>a</sup> (m) = measured parameter, (calc) = calculated parameter.

Cruise name (Exocode)	Dataset	Year	Period	Research Vessel	Sampled stations	CO <sub>2</sub> parameters	Carbon related data PI(s)
WOCE A06	CCHDO	1993	4/5- 5/16	R/V <i>L'Atalante</i>	82	A <sub>T</sub> (m), pH(m), C <sub>T</sub> (m)	Claude Oudot
29HE20100405	CARINA	2010	2/13- 3/19	R/V <i>Bio Hespérides</i>	57	A <sub>T</sub> (m), pH(m), C <sub>T</sub> (calc)	A.F. Ríos/F.F. Pérez

**Table 2.3.** Number of sampled stations for different chemical parameters during the 2011 A05 and 2010 A06 cruises.

	O <sub>2</sub>	C <sub>T</sub>	pH	A <sub>T</sub>	nutrients	salinity
A05	167	11	167	67	167	167
A06	72	16	70	43	104	85

## pH

Seawater samples for pH were collected at every depth level, directly into optical glass spectrophotometric cells of 28 ml that were filled to overflowing and immediately closed, preventing the entry of air bubbles. The cells were stored in a thermostatic bath in order to bring them to stabilization at 25°C before analysis. Seawater pH was measured following the spectrophotometric method described in Clayton and Byrne (1993). This method consists on adding a volume of indicator solution to the seawater sample, so that measuring the absorbance of the sample at different wavelengths and obtaining the ratio between two absorbances at two different wavelengths is proportional to the sample pH. The indicator was an m-cresol purple solution prepared in seawater, 2mM in concentration. The reaction of interest is the dissociation  $\text{HI}^-(\text{aq}) = \text{H}^+(\text{aq}) + \text{I}^{2-}(\text{aq})$ . pH, on the total hydrogen ion concentration scale ( $\text{pH}_T$ ) can be determined by  $\text{pH} = \text{pK}_2 + \log_{10} [\text{I}^{2-}] / [\text{HI}^-]$ , following the formula of Clayton and Byrne (1993):

$\text{pH}_T = 1245.69/T + 3.8275 + 2.11 \cdot 10^{-3}(35 - S) + \log((R - 0.0069)/(2.222 - R \cdot 0.133))$  where R is the ratio of the absorbances of the acidic and basic forms of the indicator,  $[\text{I}^{2-}] / [\text{HI}^-]$ , at their maximum absorption wavelength (i.e  $R = A578/A434$ ), corrected for baseline absorbance at 730 nm, T is temperature in Kelvin scale and S is salinity. R is calculated following equations described in Dickson *et al.*, (2007). Hence, the absorbance was measured at three different fixed wavelengths (434, 578 and the non-absorbing wavelength of 730 nm) before and after the addition of 75 µL of the dye. All the absorbance measurements were obtained with a Perkin Elmer Lambda 800 UV-VIS (A05) and a Shimadzu UV-2041 PC (A06) spectrophotometer. The 2010 pH data were corrected following del Valls and Dickson (1998). A correction for dye impurities was applied to the 2011 pH data (Yao *et al.*, 2007).

## Alkalinity

$A_T$  samples were usually taken every two stations. Water samples were taken directly from the Niskin bottles into 600 mL borosilicate glass bottles, avoiding the formation of air bubbles during filling, by doing so from the bottle bottom, regulating the flow and ensuring overflowing before closing them. The samples were not filtered, following Chanson and Millero (2007) and they were stored for at least 24 hours before their analysis. Measurements of  $A_T$  were performed by using an automatic potentiometric titrator (Titrand Metrohm) with a combined glass electrode and a probe to check the temperature (Perez and Fraga, 1987). A calibrated Knudsen pipette (~195 mL) was used to transfer the samples into an open Erlenmeyer flask in which the potentiometric titration was carried out with hydrochloric acid ( $[\text{HCl}] = 0.1 \text{ M}$ ). The final volume of titration was determined by means of two pH endpoints very close to one another (i.e. 4.45 and 4.42) (Mintrop *et al.*, 2000). Each sample was analysed twice for quality control purposes. Certified Reference Material (CRM batch #100 distributed by A.G. Dickson from the Scripps Institution of Oceanography) was analyzed prior to each analysis session for calibration of the measurements and, in addition, an extra calibration was conducted by analyzing seawater substandard at the beginning and at the end of each samples batch belonging to a given analysis session. This seawater substandard consisted of deep and very stable seawater stored in the dark into a large container (50-75L) during some days before use, that served as reference water in order to monitor the drift of the  $A_T$  determinations with time during the analysis session.

### Dissolved inorganic carbon

The  $C_T$  data were calculated from  $A_T$  and pH by using the dissociation constants of Mehrbach *et al.*, (1973) refitted by Dickson and Millero (1987) using the CO2SYS program (Pierrot *et al.*, 2006). However, discrete  $C_T$  samples were taken at selected depths on 11 stations and analysed for quality control. The internal consistency between calculated and measured  $C_T$  was estimated to be of  $0.9 \pm 3.5 \mu\text{mol}\cdot\text{kg}^{-1}$  ( $n=22$ ) for the A05 data and of  $2.8 \pm 3.9 \mu\text{mol}\cdot\text{kg}^{-1}$  ( $n=43$ ) for the A06 data. Seawater samples for  $C_T$  analysis were taken directly from the Niskin bottles into 600 mL borosilicate glass bottles. Sampling bottles were filled avoiding the formation of air bubbles. Samples were prepared for their storage by discarding part of the sample, leaving a headspace of 1% of the bottle volume and adding 0.3 mL of saturated aqueous solution of mercuric chloride in order to prevent biological alteration of the sample. The bottles were sealed with glass stoppers covered with Apiezon-L grease and stored in the dark at room temperature until their analysis on land.  $C_T$  measurements were performed at the IIM-CSIC laboratory through a coulometric determination using a Single-Operator Multiparameter Metabolic Analyzer SOMMA system (Johnson *et al.*, 1998) coupled with a CM101\_093 coulometer. Each sample was analyzed twice for quality control purposes.

### Oxygen ( $O_2$ )

In order to allow the performance of  $C_{\text{ant}}$  back-estimations,  $O_2$  concentration was determined in water samples at each depth level in each station. The samples were taken into calibrated (~ 120 mL) glass bottles. The sampling was performed carefully avoiding the entry of air bubbles. The sample temperature was measured during the filling of the bottles with an electronic thermometer probe, while waiting for the sample overflow to equal at least three times the equivalent volume of the bottle. Afterwards, the samples were fixed bringing  $O_2$  to precipitation with 0.6 mL of manganese chloride ( $\text{MnCl}_2 \cdot 4\text{H}_2\text{O}$ ) and 0.6 mL of alkali-iodide solution ( $\text{NaOH} + \text{NaI}$ ) and stored in the dark for at least 24 hours before analysis to allow them to stabilize at room temperature. The  $O_2$  concentration was determined by potentiometric titration with the Winkler method following the WOCE standards (Culberson, 1991). The samples were acidified prior to titration with 0.8 ml of sulphuric acid (5M). The titration was performed with a 0.02 N sodium thiosulphate solution. The concentration of this thiosulfate solution was determined daily by comparison with a solution of potassium iodate with a normality of 0.020013 N. Blank measurements were determined at the beginning of each analyses session to account for the introduction of  $O_2$  with the reagents and for impurities in the  $\text{MnCl}_2$ .

### Nutrients

Seawater samples for nutrients, nitrate ( $\text{NO}_3^-$ ), phosphate ( $\text{PO}_4^{3-}$ ) and silicate ( $\text{SiO}_4^{4-}$ ), were collected at every depth level. Samples for nutrients were taken directly from the Niskin bottles into 125 mL polypropylene tubes and immediately frozen until analysis on land (A05) or on board (A06). In the two cruises, nutrient concentrations were determined with a Technicon segmented-flow autoanalyzer (Treguer and LeCorre, 1975; Oudot and Montel, 1988; Alvarez-Salgado *et al.*, 1992).

### Salinity

Seawater samples were taken in order to calibrate the conductivity sensor. The measurement of salinity at the different sampling depths is also important for  $A_T$  determinations. The samples were taken directly from the Niskin bottles into glass bottles closed by a rubber seal. The samples stored in the analysis laboratory at a controlled temperature for more than 24 hours to enable them to reach thermal stabilization. Seawater samples were analysed with an AUTOSAL salinometer in the two cruises, following the WOCE standards (Culberson, 1991).

### Recovery of historical A05 data

As reported above, in 1992 the section A05 was included in the net of selected hydrographic cruises to be studied within the frame of the WOCE program. The cruise was carried out between 14 July and 15 August 1992 along 24°N on board the R/V Hespérides from Cadiz (Spain) to Miami (Florida, U.S.A.). Full-depth CTD profiles were performed at 112 hydrographic stations. At each station, water samples were taken at different depths for different chemical analyses. A detailed description of the cruise and analysis performed can be found in Millero *et al.*, (2000): [http://cdiac.ornl.gov/oceans/ndp\\_074/](http://cdiac.ornl.gov/oceans/ndp_074/). Regarding the characterization of the carbonate system in seawater, two different datasets were obtained:

- A shorter one, consisting of  $C_T$ ,  $A_T$  and pH measurements obtained on 33 stations by the group of the Rosenstiel School of Marine and Atmospheric Science (RSMAS) University of Miami, Florida. This dataset was reported in CLIVAR & Carbon Hydrographic Data Office (CCHDO) and CDIAC.
- A larger dataset, consisting in pH and  $A_T$  measurements, obtained on 107 stations by the  $CO_2$  group of the Instituto de Investigación Mariñas (CSIC) of Vigo. Spain.

The second dataset was never reported in global hydrographic data repositories despite having been quality controlled in the GLODAP Atlantic synthesis on carbon measurements from 1990 to 1998 (Wanninkhof *et al.*, 2003). However, this was the dataset chosen in all studies on carbonate system distributions along, and meridional transports across, the A05 section (Macdonald *et al.*, 2003; Rosón *et al.*, 2003; Brown *et al.*, 2010). The main reason for choosing this dataset was because it included four times more data than the dataset available in CCHDO or CDIAC and, more important, because it included also the sampling of the Florida Strait, which is crucial to correctly assess meridional fluxes across this section. Thus, the better spatial coverage of the section achieved in the IIM dataset, which allows a better description of the carbon system variables over time along the A05 section, prompted its report to CDIAC (<http://cdiac.ornl.gov/oceans/>) in order to make the data available for further studies. The revision and report of this dataset has been one of the main contributions of this thesis, thus becoming the benchmark for all the studies on the A05 section presented in this dissertation. It has also recently been used in the latter study on the  $C_{ant}$  transport across this section (Zunino *et al.*, 2015).

Appendix I includes the report on the evaluation of this dataset:

Guallart, E. F., F. F. Pérez, G. Roson, and A. F. Ríos. 2013. High spatial resolution alkalinity and pH measurements by IIM-CSIC group along 24.5°N during the R/V Hesperides WOCE Section A05 cruise. (July 14 - August 15, 1992). [http://cdiac.ornl.gov/ftp/ndp074/IIM\\_CSIC\\_data](http://cdiac.ornl.gov/ftp/ndp074/IIM_CSIC_data). Carbon Dioxide Information Analysis Center, Oak Ridge National Laboratory, US Department of Energy, Oak Ridge, Tennessee. doi: 10.3334/CDIAC/OTG.IIM\_CSIC\_WOCE\_A05.

Briefly, the IIM dataset was subjected to a secondary quality control (2ndQC) following CARINA (CARbon IN the Atlantic) procedures (Tanhua *et al.*, 2010), which basically consisted in the comparison of the data of interest with the respective data from other cruises at cross-over locations in the deep ocean, in order to quantify possible systematic biases. The 2ndQC was performed on measured pH and  $A_T$  and calculated  $C_T$  from these two parameters. The cruise to cruise comparison was performed on data below 1500 dbar in order to obtain a series of offsets that were then used to calculate a final mean correction for each parameter. The pH data were corrected by -0.009 units, since the offset found almost doubled the recommended threshold (0.005 units) for a minimum adjustment.  $A_T$  data were also adjusted by -4  $\mu\text{mol}\cdot\text{kg}^{-1}$  despite not surpassing the threshold (6  $\mu\text{mol}\cdot\text{kg}^{-1}$ ), in order to avoid a new bias in the calculated  $C_T$  due to a reduction of pH values without changing  $A_T$ . By doing this, original  $C_T$  data, which had shown a very low offset after 2ndQC (of only 1  $\mu\text{mol}\cdot\text{kg}^{-1}$ ), were kept invariable. It is important to remark that the performed 2ndQC is the best indicator of the consistency of pH,  $A_T$  and  $C_T$  data with other datasets, and thus of their accuracy.  $C_T$  data had shown a very low offset and these data did not change due to the adjustment of the other two parameters, thus not compromising the studies undertaken before this reevaluation of the dataset. It should be taken into consideration that, over the last years, ocean  $\text{CO}_2$  research has evolved from classical studies centered only on  $\text{CO}_2$  and  $C_{\text{ant}}$  inventories and transports, in which the most critical consideration was to obtain the amount of  $C_T$ , to a wider range of research topics that focused in the remaining carbonate system variables, such as pH or carbonate saturation states. In this sense, and following the CARINA advice, measured pH and  $A_T$  from 1992 were adjusted to allow their profitable use in these newly oriented studies.





# Chapter 3.I.

Trends in anthropogenic CO<sub>2</sub>  
in water masses of the  
Subtropical North Atlantic Ocean

Guallart E.F., Shuster U., Fajar NM., Legge O., Brown P., A., Pelejero, Messias MJ., Calvo E., Watson A., Ríos A.F., Pérez. F.F. 2015. Trends in anthropogenic CO<sub>2</sub> in water masses of the Subtropical North Atlantic Ocean. Progress in Oceanography, 131: 21-32.



**CHAPTER 3.1.****Trends in anthropogenic CO<sub>2</sub> in water masses of the Subtropical North Atlantic Ocean**

*Elisa F. Guallart, Ute Schuster, Noelia M. Fajar, Oliver Legge, Peter Brown, Carles Pelejero, Marie-Jose Messias, Eva Calvo, Andrew Watson, Aida F. Ríos and Fiz F. Pérez.*

**Abstract**

The variability in the storage of the oceanic anthropogenic CO<sub>2</sub> (C<sub>ant</sub>) on decadal timescales is evaluated within the main water masses of the Subtropical North Atlantic along 24.5°N. Inorganic carbon measurements on five cruises of the A05 section are used to assess the changes in C<sub>ant</sub> between 1992 and 2011, using four methods ( $\Delta C^*$ , TrOCA,  $\phi C_T^0$ , TTD). We find good agreement between the C<sub>ant</sub> distribution and storage obtained using chlorofluorocarbons and CO<sub>2</sub> measurements in both the vertical and horizontal scales. C<sub>ant</sub> distribution shows higher concentrations and greater decadal storage rates in the upper layers with both values decreasing with depth. The greatest enrichment is observed in the central water masses, with their upper limb showing a mean annual accumulation of about 1  $\mu\text{mol}\cdot\text{kg}^{-1}\cdot\text{yr}^{-1}$  and the lower limb showing, on average, half that value. We detect zonal gradients in the accumulation of C<sub>ant</sub>. This finding is less clear in the upper waters, where greater variability exists between methods. In accordance with data from time series stations, greater accumulation of C<sub>ant</sub> is observed in the upper waters of the western basin of the North Atlantic Subtropical Gyre. In intermediate and deep layers, the zonal gradient in the storage of C<sub>ant</sub> is more robust between methods. The much lower mean storage rates found along the section (< 0.25  $\mu\text{mol}\cdot\text{kg}^{-1}\cdot\text{yr}^{-1}$ ) become more obvious when longitudinal differences in the C<sub>ant</sub> accumulation are considered. In particular, west of 70°W the ventilation by the Labrador Sea Water creates a noticeable accumulation rate up to ~0.5  $\mu\text{mol}\cdot\text{kg}^{-1}\cdot\text{yr}^{-1}$  between 1000 and 2500 dbar. If a transient stationary state of the C<sub>ant</sub> distributions is considered, significant bi-decadal trends in the C<sub>ant</sub> storage rates in the deepest North Atlantic waters are detected, in agreement with recent estimations.

## Introduction

The ocean plays a major role as a sink for carbon dioxide (CO<sub>2</sub>) released by humankind to the atmosphere, annually removing about a quarter of the total anthropogenic CO<sub>2</sub> (C<sub>ant</sub>) emissions (Khatiwala *et al.*, 2013). The North Atlantic Ocean plays an important part in absorbing and, especially, storing C<sub>ant</sub> (Watson *et al.*, 1995; Vázquez-Rodríguez *et al.*, 2009a; Pérez *et al.*, 2010a). It contains up to 25% of the oceanic C<sub>ant</sub>, although its surface represents only 13% of the global ocean (Sabine *et al.*, 2004). Despite its large C<sub>ant</sub> storage rate, air-sea uptake in the North Atlantic is not predominantly anthropogenic, since natural CO<sub>2</sub> uptake largely prevails over the anthropogenic perturbation in the North Atlantic Subpolar Gyre (NASPG) (Pérez *et al.*, 2013). The entrance of C<sub>ant</sub> into the ocean interior takes place in the NASPG through deep convection, significantly contributing to the efficiency of the North Atlantic sink. This C<sub>ant</sub> entrance is sustained up to 65±13% due to lateral transports that carry C<sub>ant</sub>-loaded subtropical waters to these northern latitudes through the upper limb of the Meridional Overturning Circulation (MOC) (Álvarez *et al.*, 2003; Macdonald *et al.*, 2003; Rosón *et al.*, 2003; Pérez *et al.*, 2013). At 24.5°N, the MOC is responsible for almost 90% of the meridional heat flux (Johns *et al.*, 2011) and it also transports up to 0.17-0.20 PgC·y<sup>-1</sup> of C<sub>ant</sub> (Macdonald *et al.*, 2003; Rosón *et al.*, 2003). Due to the importance of the North Atlantic Subtropical Gyre (NASTG) in the uptake of C<sub>ant</sub> from the atmosphere, the WOCE A05 hydrographic line, situated at 24.5°N, is suitable for the evaluation and quantification of the North Atlantic C<sub>ant</sub> sink. The A05 line has been studied several times using high spatial resolution in situ CO<sub>2</sub> system measurements performed in 1992 (Rosón *et al.*, 2003), 1998 (Macdonald *et al.*, 2003) and 2004 (Brown *et al.*, 2010). Two recent occupations, in 2010 and 2011, add to this historical record.

Estimating C<sub>ant</sub> storage in the ocean is not simple because C<sub>ant</sub> is a small perturbation (3% at most) on top of natural, oceanic inorganic carbon (C<sub>T</sub>). As C<sub>ant</sub> is not directly measurable it has to be estimated from indirect techniques using in-situ observations. Brewer (1978) and Chen and Millero (1979) presented the first C<sub>ant</sub> calculations in the late 1970s, which attempted to separate the C<sub>ant</sub> signal from the background CO<sub>2</sub> distribution by correcting the measured C<sub>T</sub> for changes due to biological activity and by removing an estimate of the preindustrial preformed C<sub>T</sub>. Several authors have tried to improve those first back-calculation (also called carbon-based) methods, leading to a number of methodologies: ΔC\* (Gruber *et al.*, 1996), ΔC<sub>T</sub><sup>0</sup> (Körtzinger *et al.*, 1998), TrOCA (Touratier and Goyet, 2004; Touratier *et al.*, 2007) and φC<sub>T</sub><sup>0</sup> (Vázquez-Rodríguez *et al.*, 2009b). Overall, they rely on the assumption that ocean circulation and the biological pump have operated in steady state since the preindustrial era. In addition, other conceptual approaches (Broecker and Peng, 1974; Thomas and Ittekkot, 2001; Haine and Hall, 2002) do not use C<sub>T</sub> measurements and treat C<sub>ant</sub> as a conservative tracer (i.e. a tracer that is not influenced by biological processes in the ocean), avoiding the uncertainties related to the biological correction of the back-calculation methodologies. Tracer distributions can be established by using the so-called TTD functions (Transit Time Distributions). TTDs are mathematical expressions which serve to constrain the time elapsed since a water parcel was last in contact with the surface (Waugh *et al.*, 2004; Waugh *et al.*, 2006; Steinfeldt *et al.*, 2009), to describe how the ocean's circulation

connects and transports C<sub>ant</sub> from the surface to the ocean interior. Nevertheless, there is no clear consensus about the most appropriate method to estimate C<sub>ant</sub> (Sabine and Tanhua, 2010). While some authors have reported C<sub>ant</sub> estimates using only one method, ΔC\* (Macdonald *et al.*, 2003; Rosón *et al.*, 2003), TTD (Tanhua *et al.*, 2008) or φC<sub>T</sub><sup>0</sup> (Pérez *et al.*, 2010a; Ríos *et al.*, 2012), other authors have used two or more methods for comparative purposes: TrOCA and φC<sub>T</sub><sup>0</sup> (Pérez *et al.*, 2010b; Castaño-Carrera *et al.*, 2012; Fajar *et al.*, 2012), TrOCA, φC<sub>T</sub><sup>0</sup> and ΔC\*, (Flecha *et al.*, 2012), ΔC\*, ΔC<sub>T</sub><sup>0</sup> and TrOCA (Lo Monaco *et al.*, 2005) or ΔC\*, TrOCA, ΔC<sub>T</sub><sup>0</sup>, TTD and φC<sub>T</sub><sup>0</sup> (Vázquez-Rodríguez *et al.*, 2009b). Moreover, some authors suggest that a combination of approaches is necessary to achieve a robust quantification of the ocean sink of C<sub>ant</sub> (Khatiwala *et al.*, 2013).

The A05 repeat section cruises provide a valuable time series to better constrain the decadal variability of the North Atlantic C<sub>ant</sub> storage from observational data. To this end, the present work studies the C<sub>ant</sub> changes between 1992 and 2011 along 24.5°N using four methods. Three back calculation methods (ΔC\* (Gruber *et al.*, 1996), TrOCA (Touratier *et al.*, 2007) and φC<sub>T</sub><sup>0</sup> (Vázquez-Rodríguez *et al.*, 2009b)) and a tracer based technique (TTD (Waugh *et al.*, 2006)) are used to quantify the temporal changes in C<sub>ant</sub> concentrations within six different water masses of the Subtropical North Atlantic. This study also addresses possible longitudinal differences in the decadal C<sub>ant</sub> storage rates and provides a comparison of the results to a transient stationary state of oceanic C<sub>ant</sub> accumulation.

## Data

Five repeats of the A05 hydrographic section are used to study the temporal evolution of C<sub>ant</sub> storage in the Subtropical North Atlantic Ocean (Table 3.1.1). The cruises in 1992, 1998 and 2004 are referred to as earlier cruises, compared to the two more recent occupations in 2010 and 2011. All the cruise tracks are shown in figure 3.1.1a: the 1992 occupation was carried out along 24.5°N, lying south of the later cruises at either end of the section and sampling the Florida Strait at 26°N. Subsequent occupations crossed the African shelf at approximately 28°N and the continental shelf off the Bahamas at 26.5°N, sampling the Florida Strait at 27°N. The 2010 cruise followed the Kane fracture Zone, thus slightly deviating from the other cruise tracks across the Mid Atlantic Ridge (MAR).

### Earlier cruises

Datasets from the earlier cruises are available on the CDIAC website (<http://cdiac.ornl.gov/>). The 1992 cruise was conducted under the framework of the WOCE Project. Procedures for CO<sub>2</sub> system parameters analyses and their adjustments are described in Rosón *et al.* (2003) and Guallart *et al.* (2013). The 1998 measurements are reported in Peltola *et al.* (2001) and Macdonald *et al.* (2003). Gaps in nutrient data in positions where C<sub>T</sub> and A<sub>T</sub> were available were filled using a multiparameter linear regression (MLR) technique (Velo *et al.*, 2010). In 2004, the section was reoccupied within the framework of the CLIVAR Program. The analysis methodologies are described in Cunningham (2005) and Brown *et al.* (2010). The 2004 dataset used in this

work is a combination between the data available at CDIAC and the Florida Strait measurements available at the British Oceanographic Data Center (<http://www.bodc.ac.uk/>). Where C<sub>T</sub> was available and A<sub>T</sub> was not, interpolated normalized A<sub>T</sub> ( $nA_T = A_T \cdot 35 / \text{salinity}$ ) was used in order to fill the gaps. The interpolation was performed on nA<sub>T</sub> data because they are less variable than A<sub>T</sub> (Millero *et al.*, 1998).

### Recent cruises

In 2010, the C<sub>T</sub> was measured by coulometry (Dickson *et al.*, 2007) and A<sub>T</sub> was determined by potentiometric titration (Dickson *et al.*, 2007) using a VINDTA system (Marianda, Kiel, Germany). Certified reference material (CRM, batch 97) supplied by the Scripps Institution of Oceanography was analysed twice every day. Accuracy was calculated as  $\pm 2.9 \mu\text{mol}\cdot\text{kg}^{-1}$  ( $n = 399$ ) for C<sub>T</sub> and  $\pm 1.9 \mu\text{mol}\cdot\text{kg}^{-1}$  ( $n = 397$ ) for A<sub>T</sub>. After Secondary Quality Control (2ndQC) (Tanhua *et al.*, 2010b) on C<sub>T</sub>, A<sub>T</sub>, nutrients and oxygen (O<sub>2</sub>) data, O<sub>2</sub> and silicate were bias-adjusted (Table 3.1.1). The C<sub>T</sub> and A<sub>T</sub> data are further described in Schuster *et al.* (2013). The CFCs were measured at the LGMAC lab following Smethie *et al.* (2000) and Law *et al.* (1994). Nutrient gaps were filled as described above. In 2011, the most recent occupation of the A05 section was carried out as part of the Circumnavigation Expedition MALASPINA 2010 (<http://www.expedicionmalaspina.es/>). The pH was measured spectrophotometrically (Clayton and Byrne, 1993) and A<sub>T</sub> was determined potentiometrically by titration at endpoint detection (Mintrop *et al.*, 2000). A<sub>T</sub> gaps were filled as reported above. The C<sub>T</sub> was calculated from A<sub>T</sub> and pH using the dissociation constants of Mehrbach *et al.* (1973) refitted by Dickson and Millero (1987) using the CO2SYS program (Pierrot *et al.*, 2006). Discrete C<sub>T</sub> samples were taken at 11 stations and analysed for quality control at the IIM-CSIC laboratory by coulometric determination using a SOMMA system (Johnson *et al.*, 1998). The internal consistency between calculated and measured C<sub>T</sub> was estimated to be of  $0.9 \pm 3.5 \mu\text{mol}\cdot\text{kg}^{-1}$  ( $n=22$ ). No adjustments were necessary after 2ndQC.

**Table 3.1.1.** Cruises information on the repeat section A05.

Cruise name (Exocode)	Dataset	Year	Period	Research Vessel	Sampled stations	CO <sub>2</sub> parameters <sup>a</sup>	Carbon related data PI(s)	Data adjustments in this study ( $\mu\text{mol}\cdot\text{kg}^{-1}$ )
29HE06_1-3	GLODAP	1992	7/14-8/15	R/V <i>Bio Hespérides</i>	112	A <sub>T</sub> (m), pH(m), C <sub>T</sub> (calc)	F. Millero / A. Ríos	A <sub>T</sub> (+4) <sup>b</sup> pH(-0.009 units) <sup>b</sup>
33RO19980123	CARINA	1998	1/23-2/24	R/V <i>Ronald H. Brown</i>	130	A <sub>T</sub> (m), pH(m), C <sub>T</sub> (m)	R. Wanninkhof/ R. Feely	O <sub>2</sub> (*0.99) <sup>c</sup>
74DI20040404	CARINA own data	2004	4/4-5/10	R/V <i>Discovery</i>	125	A <sub>T</sub> (m), C <sub>T</sub> (m)	U. Schuster	SiO <sub>4</sub> (*0.98) <sup>d</sup> NO <sub>3</sub> (*0.97) <sup>d</sup>
74DI20100106	New data <sup>e</sup>	2010	1/6-2/18	R/V <i>Discovery</i>	135	A <sub>T</sub> (m), C <sub>T</sub> (m)	U. Schuster	O <sub>2</sub> (*1.03) <sup>f</sup> SiO <sub>4</sub> (*0.94) <sup>f</sup>
29AH20110128	New data	2011	1/28-3/14	R/V <i>Sarmiento de Gamboa</i>	167	A <sub>T</sub> (m), pH(m), C <sub>T</sub> (calc)	A. Ríos/F.F. Pérez	--

<sup>a</sup>(m) = measured parameter, (calc) = calculated parameter.

<sup>b</sup>(Guallart *et al.*, 2013)

<sup>c</sup>(Stendardo *et al.*, 2009)

<sup>d</sup>(Tanhua *et al.*, 2010a)

<sup>e</sup>(Schuster *et al.*, 2013)

<sup>f</sup> this study

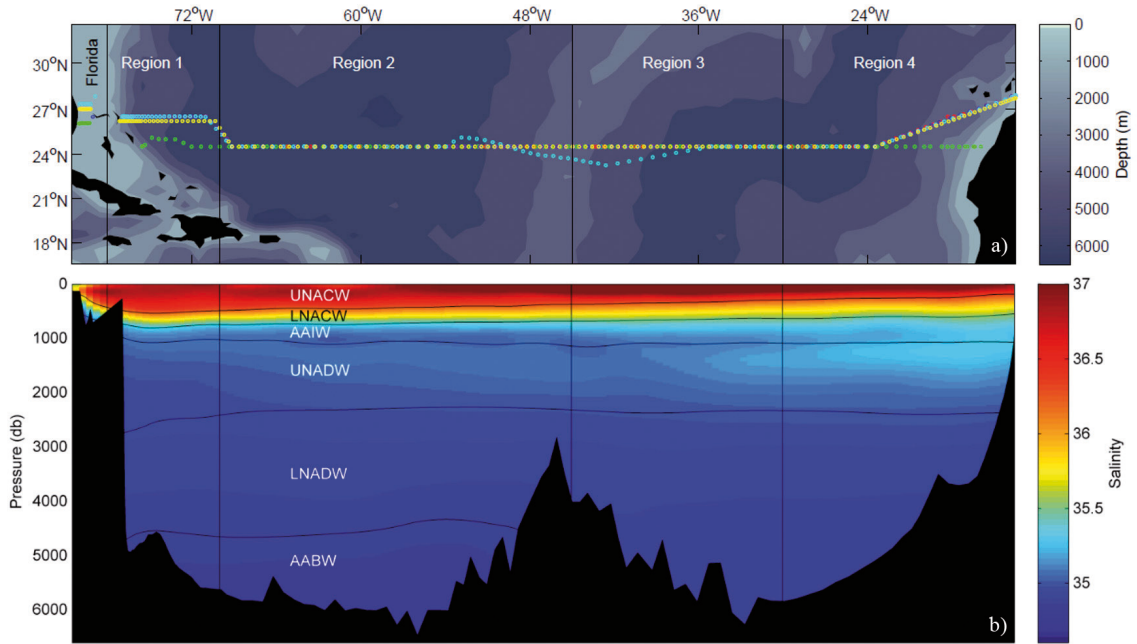


**Figure 3.1.1.** a) A05 section tracks for the 1992 (green), 1998 (red), 2004 (dark blue), 2010 (light blue) and 2011 (yellow) cruises. b) Regions, layers and defined boxes over the salinity distribution of the 2011 cruise. The sections were zonally divided into five regions: Region 0 (Florida Strait, 80°W to 78°W), region 1 (78°W to 70°W), region 2 (70°W to 45°W), region 3 (45°W to 30°W) and region 4 (30°W to 10°W). Six density layers were defined identifying the main water masses of the Subtropical North Atlantic: uNACW ( $\sigma_0 < 26.7 \text{ kg m}^{-3}$ ), INACW ( $26.7 \text{ kg m}^{-3} < \sigma_0 < 27.2 \text{ kg m}^{-3}$ ), AAIW ( $27.2 \text{ kg m}^{-3} < \sigma_0 < 27.6 \text{ kg m}^{-3}$ ), uNADW ( $\sigma_0 > 27.6 \text{ kg m}^{-3}$  and  $\sigma_2 < 37 \text{ kg m}^{-3}$ ), INADW ( $\sigma_2 > 37 \text{ kg m}^{-3}$  and  $\sigma_4 < 45.9 \text{ kg m}^{-3}$ ) and AABW ( $\sigma_4 > 45.9 \text{ kg m}^{-3}$ ).

## Methods

### C<sub>ant</sub> determinations

Three back-calculation methods ( $\Delta C^*$ (Gruber *et al.*, 1996),  $\phi C_T^0$  (Vázquez-Rodríguez *et al.*, 2009b) and TrOCA (Touratier and Goyet, 2004; Touratier *et al.*, 2007)) and one tracer-based method (TTD (Waugh *et al.*, 2006)) were used to determine the C<sub>ant</sub> distributions. The overall uncertainties in C<sub>ant</sub> are  $\pm 9 \mu\text{mol}\cdot\text{kg}^{-1}$ ,  $\pm 5.2 \mu\text{mol}\cdot\text{kg}^{-1}$ ,  $\pm 6.25 \mu\text{mol}\cdot\text{kg}^{-1}$  and  $\pm 6 \mu\text{mol}\cdot\text{kg}^{-1}$  for  $\Delta C^*$ ,  $\phi C_T^0$ , TrOCA and TTD estimates, respectively. Further details on the specific assumptions of each of the four methodologies are provided in Appendix A.

### Averaging by regions and layers

The five A05 datasets were divided vertically into six density layers and longitudinally into five regions (figure 3.1.1b). The water column was divided by identifying the main water masses representative of the Subtropical North Atlantic Ocean following Talley *et al.* (2011): North Atlantic Central Waters (NACW), Antarctic Intermediate Water (AAIW), North Atlantic Deep Waters (NADW) and Antarctic Bottom Water (AABW). The subducted thermocline (NACW) was further split into two main cores: the upper (uNACW), including

a warm and saline component related to SubTropical Mode Water and the lower (INACW), which is denser and fresher and related to SubPolar Mode Waters (McCartney and Talley, 1982). The boundary between AAIW and uNADW was also constrained according to the TS properties. Thus, the three uppermost layers were delimited using  $\sigma_0$  along the isopycnals  $\sigma_0 = 26.7 \text{ kg}\cdot\text{m}^{-3}$ ,  $\sigma_0 = 27.2$  and  $\sigma_0 = 27.6 \text{ kg}\cdot\text{m}^{-3}$ , respectively (Fig.1b). The uNACW layer includes depths between ~150 - 450 dbar. Since the delimiting isopycnal is tilted up towards the east, this layer is far shallower on the eastern side of the section, where it reaches ~250 dbar. This layer shows the highest salinity in the water column, with an average of 36.6. The INACW layer is located between ~250 and ~850 dbar. The top of the AAIW layer (from ~600 to ~1100 dbar) encompasses the oxygen minimum zone. The slight eastward salinization at these depths results from the influence of Mediterranean Water (MW), as it spreads through the layer below. The two NADW components were delimited according to a reference level of 2000 dbar ( $\sigma_2$ ), along  $\sigma_2 = 37 \text{ kg}\cdot\text{m}^{-3}$  (Fig.1b). The uNADW layer extends from ~1100 to ~2500 dbar. Its freshening close to the western margin is related to Labrador Sea Water (LSW) spreading. INADW layer fills the eastern basin from ~2100 dbar to the ocean floor but extends to ~4500 dbar in the western basin. AABW was delimited in the western basin along the isopycnal  $\sigma_4 = 45.9 \text{ kg}\cdot\text{m}^{-3}$ . In addition to this classification of water masses, the section was zonally divided, separating the eastern and western basins at the Mid-Atlantic Ridge, at 45°W. The division of the western basin was refined in order to better constrain, in terms of its circulation features, the temporal variability of C<sub>ant</sub> distributions. The Florida Strait was identified as an independent region ranging from 80°W to 78°W. It was isolated from the main section due to its independent behaviour in terms of transports (Schmitz and Richardson, 1991; Macdonald *et al.*, 2003; Rosón *et al.*, 2003). The zone of deep ventilation by the Deep Western Boundary Current (DWBC), Region 1 (R1), was separated from the ocean interior at 70°W, isolating it from Region 2 (R2), where AABW fills a considerable volume of the deep ocean. Despite not showing, *a priori*, distinct oceanographic features, the eastern basin was also halved at 30°W, separating Region 3 (R3) from Region 4 (R4) to isolate the relative salinity maximum of MW that enters the section from the African Coast.

These divisions result in a total of 25 boxes (Fig. 3.1.1b), within which the temporal variability of the mean C<sub>ant</sub> estimates was studied. Data above 150 dbar were removed to avoid seasonal biological effects, since conservative tracers do not vary seasonally in the subsurface (100-200m) (Vázquez-Rodríguez *et al.*, 2012). Mean C<sub>ant</sub> values ( $[C_{\text{ant}}^X]$ , where X =  $\phi C_T^0$ , TrOCA,  $\Delta C^*$  or TTD, in  $\mu\text{mol}\cdot\text{kg}^{-1}$ ) within each box were computed as the mean and standard deviation of ensembles of 100 averages obtained through random perturbations of the  $\phi C_T^0$ , TrOCA,  $\Delta C^*$  and TTD estimates. Random perturbation of the data was performed using each method's uncertainty in order to propagate the uncertainty of the C<sub>ant</sub> estimates into the uncertainty of the box averages and the trends, independently of the number of data within each box. This led us to obtain means that were more robust but that did not change from the means obtained without perturbation calculations. This also permitted not using the error of the mean (of the raw data) as the uncertainty, which would have been lower in boxes with a large number of data. The values obtained are shown, for each cruise, in Appendix B of the Supplementary Information. Mean values  $\pm$  standard error of the mean ( $x \pm \sigma/\sqrt{N}$ ) of pressure (dbar),

salinity, O<sub>2</sub> (μmol·kg<sup>-1</sup>), potential temperature (Θ, °C) and Apparent Oxygen Utilization (AOU, μmol·kg<sup>-1</sup>) within each box are also shown as Supporting Information of the C<sub>ant</sub> data.

### Decadal trend and rate of change in C<sub>ant</sub> storage

#### Decadal trend in C<sub>ant</sub> storage

In order to study the temporal changes in the mean C<sub>ant</sub> concentrations ([C<sub>ant</sub>]) of φC<sub>T</sub><sup>0</sup>, TrOCA and ΔC\* within each box for the period 1992–2011, an ensemble of 100 linear regressions between the five years and the 100 random-perturbed averages was obtained. Linear regressions for TTD were performed from 1992 to 2010. The mean and the standard deviation of the 100 linear regressions were considered as the Decadal Trend (DT) and the uncertainty (in μmol·kg<sup>-1</sup> yr<sup>-1</sup>) for [C<sub>ant</sub>] inside each box. As each C<sub>ant</sub> method yields a specific DT, hereafter they will be denoted as DT (method), e.g. DT(φC<sub>T</sub><sup>0</sup>), DT(TrOCA), DT(ΔC\*) and DT(TTD). Table 3.1\_C1 in the Appendix C shows the DT values in each box for each method.

### Transient Steady State rate in C<sub>ant</sub> storage

Tanhua *et al.* (2006) found that C<sub>ant</sub> is in transient steady state (TSS) in the North Atlantic, from comparison of the observed changes in C<sub>T</sub> and CFC fields with those predicted from an eddy-permitting ocean circulation model. This means that C<sub>ant</sub> increases over time through the whole water column in a manner that is proportional to the time-dependent surface concentration. Hence, C<sub>ant</sub> changes for a given time period can be determined from [C<sub>ant</sub>] (Tanhua *et al.*, 2007; Steinfeldt *et al.*, 2009; Khatiwala *et al.*, 2013; Pérez *et al.*, 2013) considering the exponential fit  $C_{(t)}^0 = Ae^{\lambda t}$ , that describes the history of atmospheric CO<sub>2</sub> and C<sub>ant</sub><sup>0</sup> in the ocean surface mixed layer since the Industrial Revolution. Steinfeldt *et al.* (2009) reported an annual rate increase of 1.69% for the factor λ(yr<sup>-1</sup>), for characteristic NADW properties. The uncertainty associated to λ was found to be 0.10%, based on the variability between 1992 and 2012 in the estimated rates of C<sub>ant</sub><sup>0</sup> increase in the surface mixed layer. The C<sub>ant</sub> storage rate (μmol·kg<sup>-1</sup>·yr<sup>-1</sup>) under a transient steady state can be calculated within each box as the product of λ (yr<sup>-1</sup>) and [C<sub>ant</sub>] (μmol·kg<sup>-1</sup>), the [C<sub>ant</sub>] term varying depending on the method used to estimate it:

$$\frac{dC_{ant}}{dt} = \lambda \cdot [C_{ant}] \quad (1)$$

To obtain robust  $\frac{dC_{ant}}{dt}$  within each box, an ensemble of 100  $\frac{dC_{ant}}{dt}$  were obtained for each cruise using equation (1), from the 100 random-perturbed averages ( $[C_{ant}^{\phi C_T^0}]$ ,  $[C_{ant}^{\text{TrOCA}}]$ ,  $[C_{ant}^{\Delta C^*}]$ ,  $[C_{ant}^{\text{TTD}}]$ ) obtained as reported above and also considering the random perturbation of λ. Since all of the cruises were grouped to increase the amount of  $\frac{dC_{ant}}{dt}$  estimations, the 100 random-perturbed averages relative to each cruise were time-normalized (Khatiwala *et al.*, 2013) to the year 2000, using equation 2:

$$C_{(t2)} = C_{(t1)} e^{\lambda(t2-t1)} \quad (2)$$

where t1 corresponds to each A05 cruise occupation year and t2 is the reference year 2000. C<sub>(t1)</sub> corresponds

to [C<sub>ant</sub>] for each cruise, and C<sub>(2)</sub> to the one normalized to year 2000. The temporal rescaling was performed to reduce the variability in the obtained storages due to the difference in [C<sub>ant</sub>] between years, obtaining Transient steady state rates (TSSR) storages that were set in the middle of the studied period. The TSSR and its uncertainty were considered as the mean and standard deviation of the 500  $\frac{dC_{ant}}{dt}$  (100 per cruise). Hereafter, the C<sub>ant</sub> storage rates ( $\mu\text{mol}\cdot\text{kg}^{-1}\text{yr}^{-1}$ ) computed following the Transient Stationary State approximation will be denoted as TSSR (method), e.g. TSSR( $\phi C_T^0$ ), TSSR(TrOCA), TSSR( $\Delta C^*$ ) and TSSR(TTD). Table 3.1\_C1, in the Supplementary Information, shows the TSSR values in each box, for each method.

Taking into account that sometimes the C<sub>ant</sub> estimates from different methods extend over a broad range of values, Khatiwala *et al.*, (2013) suggested that a combination of C<sub>ant</sub> estimation methods, each with its own strengths and weaknesses, should be necessary to achieve a robust quantification of the ocean sink of C<sub>ant</sub>. By applying their consideration to the C<sub>ant</sub> storage, table 3.1\_C1 shows the mean DT and TSSR within each box, where the four methods used to compute C<sub>ant</sub> are combined. Since DT uncertainties show a large variability between them, averaging was performed by weighting the mean from the three back-calculations, and then averaging this with the tracer method. The mean of the TSSR results was obtained by averaging the four methods without weighting them, because all of them showed much closer uncertainties. The time-normalized [C<sub>ant</sub>] (to year 2000) obtained by averaging the four methods' estimates is also shown in table 3.1\_C1. The main objective of calculating the accumulation of C<sub>ant</sub> by these two different approaches was to compare the consistency between their results.

## Results

### Modern C<sub>ant</sub> distribution

Figure 3.1.2 shows the average vertical distributions of C<sub>ant</sub><sup>VCT</sup> in 1992 and 2011, for the eastern and western basins separately. All profiles show higher C<sub>ant</sub><sup>VCT</sup> values near the surface that decrease with depth. The vertical gradient is particularly strong in the upper ocean, from 150 to 1000 dbar, whilst concentrations remain low and almost constant below this. Below 1000 dbar, only the DWBC contributes to the deep ocean ventilation, mostly through the LSW spreading pathway. Its role can be identified as the relative maximum in C<sub>ant</sub><sup>VCT</sup> between 1100 and 1800 dbar, in the western basin. Temporal differences in the profiles reveal a substantial enrichment in C<sub>ant</sub><sup>VCT</sup> in both basins in the first 1000 dbar. This pressure range encompass the three uppermost density layers. Two of these water masses, uNACW and lNACW, show the largest accumulation detected in the water column and this accumulation is of a similar magnitude in each basin. In the deep ocean, C<sub>ant</sub><sup>VCT</sup> penetration occurs faster in the western basin than the eastern basin due to the DWBC spreading. It is difficult to discern changes in C<sub>ant</sub><sup>VCT</sup> below 2000 dbar as the uncertainty estimates overlap (Fig.3.1.2).

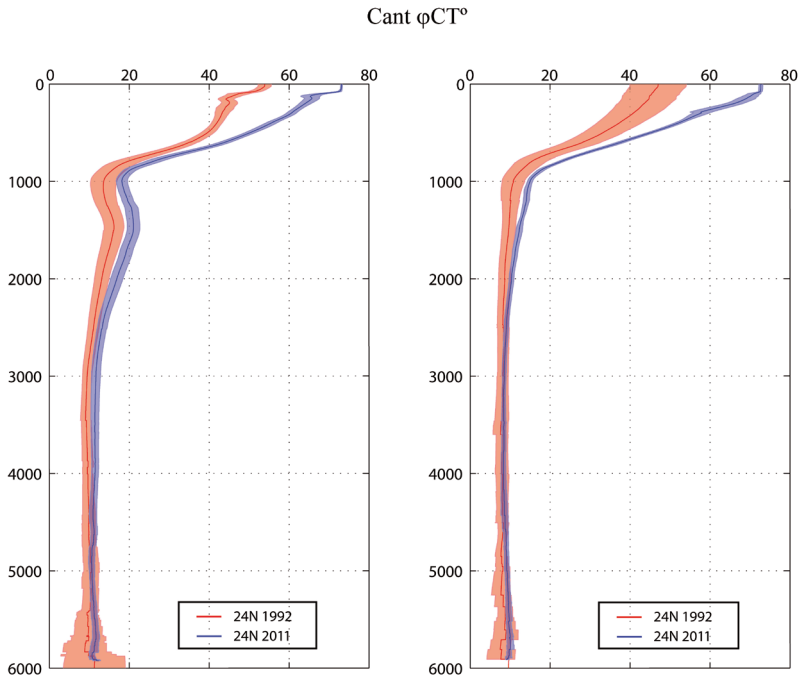


**Figure 3.1.2.** Mean distributions of  $C_{\text{ant}} \varphi C_T^0$  ( $\mu\text{mol kg}^{-1}$ ) along the A05 section for the eastern (right panel) and western (left panel) subtropical North Atlantic basins, in 1992 (red line) and 2011 (blue line). The respective shaded areas correspond to the standard deviation of the mean  $C_{\text{ant}} \varphi C_T^0$  estimates.

### Decadal Trends in $C_{\text{ant}}$ storage by layer

$u\text{NACW}$  ( $\sigma_0 < 26.5 \text{ kg m}^{-3}$ )

All four  $C_{\text{ant}}$  methods show the highest  $[C_{\text{ant}}]$  in  $u\text{NACW}$ , as it is the most ventilated layer (Fig. 3.1.3). The range in  $[C_{\text{ant}}]$  between 1992 and 2011 is wide and depends on the method used, suggesting a rise of about  $\sim 10 - 22 \mu\text{mol kg}^{-1}$ . The four methods show similar DT values in the eastern basin (R3 and R4, Fig. 3.1.4) but different DT in the  $C_{\text{ant}}$  accumulation of the western basin (R1 and R2). There, DT (TTD) indicates much lower decadal increases in  $[C_{\text{ant}}^{\text{TTD}}]$  than the DT obtained using back-calculation methods. Thus, while  $[C_{\text{ant}}^{\varphi CT}]$ ,  $[C_{\text{ant}}^{\text{TrOCA}}]$  and  $[C_{\text{ant}}^{\Delta C^*}]$  are estimated to have been increasing up to  $\sim 1 \mu\text{mol kg}^{-1} \text{ yr}^{-1}$ ,  $[C_{\text{ant}}^{\text{TTD}}]$  shows a smaller decadal increase (DT and TSSR values are reported in table 3.1\_C1). The TTD method typically produces the highest estimates in the upper layers (Vázquez-Rodríguez *et al.*, 2009a; Khatiwala *et al.*, 2013). However,  $[C_{\text{ant}}^{\text{TTD}}]$  gives similar values to the other three estimates in 1992, and progressively lower values in later years. The difference between  $[C_{\text{ant}}^{\text{TTD}}]$  and the back-calculation results remains approximately constant between cruises in the layers below (Fig. 3.1.3). This can presumably be attributed to the decline in the atmospheric CFC concentrations since their peak during the past decade (Tanhua *et al.*, 2008), which would lead to increasing underestimation of  $[C_{\text{ant}}^{\text{TTD}}]$  in this layer (the most recently ventilated) with time during the study period.

**INACW ( $26.5 < \sigma_0 < 27.1 \text{ kg m}^{-3}$ )**

In each year,  $[C_{\text{ant}}^{\psi C_T^0}]$ ,  $[C_{\text{ant}}^{\text{TrOCA}}]$ ,  $[C_{\text{ant}}^{\Delta C^*}]$  and  $[C_{\text{ant}}^{\text{TTD}}]$  in INACW generally increase eastwards, coinciding with a higher ventilation due to tilting isopycnals (Fig. 3.1.3). This layer shows an increase in  $[C_{\text{ant}}]$ , of about  $\sim 6$  to  $11 \mu\text{mol}\cdot\text{kg}^{-1}$  when considering the four methods. All methods agree that R4 has the highest storage at this depth range (Fig. 3.1.4). Close to the western margin (R1), DT(TTD) suggests lower storage than back-calculations estimates. This can be explained by the decline in the atmospheric CFC concentrations (as in uNACW) and intense mixing with the layer above due to the winter outcrop (Bates, 2012).

**AAIW ( $27.1 < \sigma_0 < 27.5 \text{ kg m}^{-3}$ )**

The four methods agree on greater storage in R1 than in the other regions (Fig. 3.1.4). DT( $\phi C_T^0$ ), DT(TrOCA) and DT(TTD) results show a similar longitudinal pattern: their high DT in R1 is reduced in the ocean interior (R2-R4) with quite similar DT values in R2 and R4 and a near absence of significant accumulation in R3. The stabilization of  $[C_{\text{ant}}^{\psi C_T^0}]$  and  $[C_{\text{ant}}^{\text{TrOCA}}]$  in R3 (Fig. 3.1.3), seems to be a real feature and not an artefact of the methodologies used, since  $[C_{\text{ant}}^{\text{TTD}}]$  does not show changes over time either. However, the values of DT(TTD) are low in general compared to back-calculations (Fig. 3.1.4). DT( $\Delta C^*$ ) results mostly agree with this zonal pattern but suggest a larger increase in  $[C_{\text{ant}}^{\Delta C^*}]$  in R3 and R4. It is important to note that determining  $C_{\text{ant}}$  in this layer is particularly difficult for a number of reasons. The AAIW layer includes biogeochemical features such as the O<sub>2</sub> minimum layer and it is strongly influenced by the dynamic water mass front between AAIW and MW and the coastal upwelling (Brown *et al.*, 2010). The different behaviour in  $[C_{\text{ant}}^{\Delta C^*}]$  could be related to the fact that this method appears to be more sensitive than the other methods to shifts in Θ and O<sub>2</sub> horizons that occur in R3 and R4, in AAIW and uNADW (tables 3.1\_B3 and 3.1\_B4 in Appendix B), which could have an effect on the computation of the disequilibrium term in these regions. It is therefore difficult to correctly compute  $[C_{\text{ant}}]$  or interpret its decadal trend at these depth ranges. The fact that the temporal evolution of the  $C_{\text{ant}}$  averages along the AAIW layer practically parallels that of uNADW (Fig. 3.1.3) suggests that it might also be somewhat influenced by LSW C<sub>ant</sub> ventilation. Steinfeldt *et al.*, (2007) also found a noticeable increase in CFC-12 concentration with time close to the western boundary, at depth ranges directly above the layer where the LSW spreads.

**uNADW ( $\sigma_0 > 27.5 \text{ and } \sigma_2 < 37 \text{ kg m}^{-3}$ )**

The DT results from the four methods show significantly higher accumulation in R1 (up to  $\sim 8$  to  $11 \mu\text{mol}\cdot\text{kg}^{-1}$ ) than in other regions (Fig. 3.1.4). The DT values in R1 are similar to, or greater than in the layer above, with an increase of  $\sim 0.5 \mu\text{mol}\cdot\text{kg}^{-1} \text{ yr}^{-1}$ . This value, which is comparable to the yearly C<sub>ant</sub> accumulation in INACW and half of that in uNACW, indicates significant C<sub>ant</sub> advection at depth due to the LSW spreading. As reported above, the DT( $\Delta C^*$ ) results are somewhat higher than the other three methods in the eastern basin (Fig. 3.1.4), doubling  $[C_{\text{ant}}^{\psi C_T^0}]$ ,  $[C_{\text{ant}}^{\text{TrOCA}}]$  and  $[C_{\text{ant}}^{\text{TTD}}]$  in R4. These three methods suggest storage rates slightly above zero in R3.

**INADW ( $\sigma_2 > 37$  and  $\sigma_4 < 45.9 \text{ kg m}^{-3}$ )**

The magnitude of  $[C_{\text{ant}}^{\Delta C}]$ ,  $[C_{\text{ant}}^{\varphi C_T}]$ ,  $[C_{\text{ant}}^{\text{TrOCA}}]$  and  $[C_{\text{ant}}^{\text{TTD}}]$  are different in some regions (Fig. 3.1.3) but, nonetheless, their temporal trends are relatively consistent (Fig. 3.1.4). DT values from the four methods agree on a significant, albeit low, decadal increase in  $[C_{\text{ant}}]$  in R1, that amounts to about half of the annual increase in the layer above.  $\Delta C^*$  and TTD methods agree on a significant  $C_{\text{ant}}$  accumulation in the entire western basin, while  $\varphi C_T^0$  and TrOCA do not indicate any increase in R2 (Fig. 3.1.4). In the eastern basin, the four methods indicate that mean concentrations are significant (Fig. 3.1.3), but only the  $\Delta C^*$  results reveal significant accumulation of  $C_{\text{ant}}$  in the basin during the last two decades (the TTD method supports this only in R4) (Fig. 3.1.4).

**AABW ( $\sigma_4 > 45.9 \text{ kg m}^{-3}$ )**

In this layer, changes in  $[C_{\text{ant}}]$  over time are negligible (Fig. 3.1.3). Although all four methods identify significantly non-zero  $C_{\text{ant}}$  concentrations (mostly from 2004 onwards), the error bars are too large to confirm a significant rise in their concentrations. In R1, of the back-calculation methods, DT( $\varphi C_T^0$ ) and DT(TrOCA) results suggest a small accumulation (Fig. 3.1.4) while  $[C_{\text{ant}}^{\text{TTD}}]$  remains almost constant in time (Fig. 3.1.3). In R2, DT results show no change over the last two decades. This could be representative of insignificant loadings of  $C_{\text{ant}}$  in AABW at these latitudes. Alternatively, it could be related to the quantification limits of the methods applied, whereby the 19 year period investigated is currently insufficient to identify the small increases of  $C_{\text{ant}}$  in these waters.

**Florida Strait**

As shown in Figure 3.1.3,  $[C_{\text{ant}}]$  increases are observed in all three layers that move through the FS. Although larger differences are found in the  $[C_{\text{ant}}]$  estimates within the FS, DT results for uNACW and INACW in this region show higher accumulations than the same water masses in R1. However, for the AAIW layer a much lower accumulation is identified for FS than in R1, particularly when using the TTD method. This can be explained by the respective origins of the three layers entering the FS compared to those on the main section, according to Schmitz and Richardson (1991). Both uNACW and INACW originate from the recirculation of the North Equatorial Current. The AAIW layer in the FS however, originates directly from the South Eastern Atlantic. While the two uppermost layers show similar Θ/S and oxygen values within R1, AAIW shows lower Θ/S and higher AOU values than AAIW on the main section (tables in Appendix B of the Supplementary Information). Thus, DT(TTD) suggests lower decadal increases than back-calculation methods (Fig. 3.1.4), as there is no increase in  $[C_{\text{ant}}^{\text{TTD}}]$  during the last two decades. Back-calculation DT results show consistent values throughout the water column in the FS, with the exception of DT( $\varphi C_T^0$ ) that exhibits slightly lower values in the upper layers.

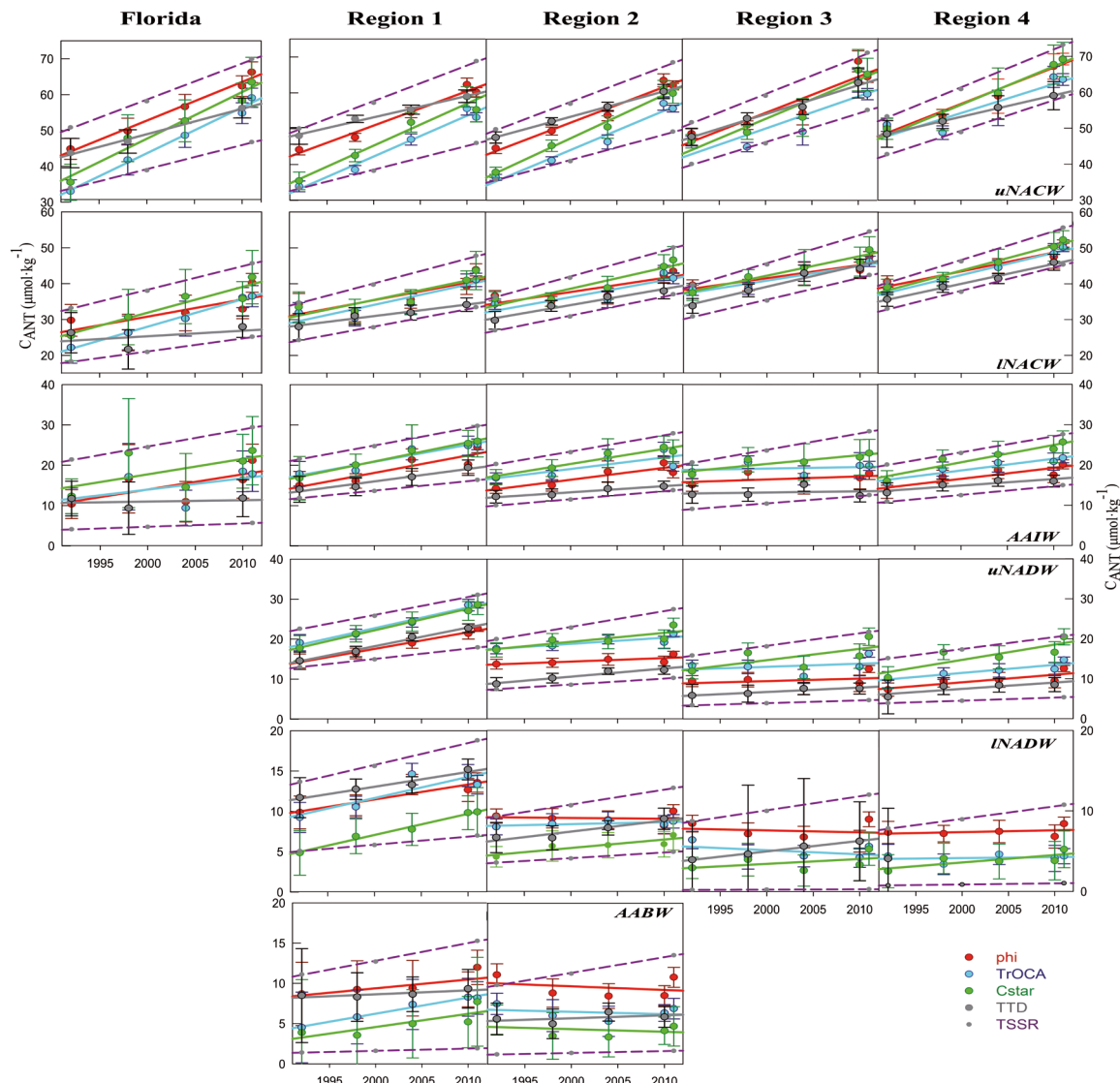


**Figure 3.I.3.** Averaged  $\text{C}_{\text{ant}}$  concentrations ( $\mu\text{mol kg}^{-1}$ ) within each box and its uncertainty indicated by the coloured dots and the corresponding error bars (double of std):  $\phi \text{C}_T^0$  (red), TrOCA (blue),  $\Delta \text{C}^*$  (green), TTD (grey). The associated coloured lines are the respective DT ( $\mu\text{mol kg}^{-1} \text{yr}^{-1}$ ). Each horizontal panel corresponds to each layer, which are divided in subpanels identifying the regions. Mean TSSR  $\pm$  standard deviation is indicated in each box as the area between purple dotted lines. Note that the scale in the y-axes is different depending on the layer, in order to help distinguishing the change in  $\text{C}_{\text{ant}}$  between cruises; the total range of the y-axes spans  $45 \mu\text{mol kg}^{-1}$  for uNACW and INACW,  $40 \mu\text{mol kg}^{-1}$  for AAIW and uNADW, and  $20 \mu\text{mol kg}^{-1}$  for INADW and AABW.

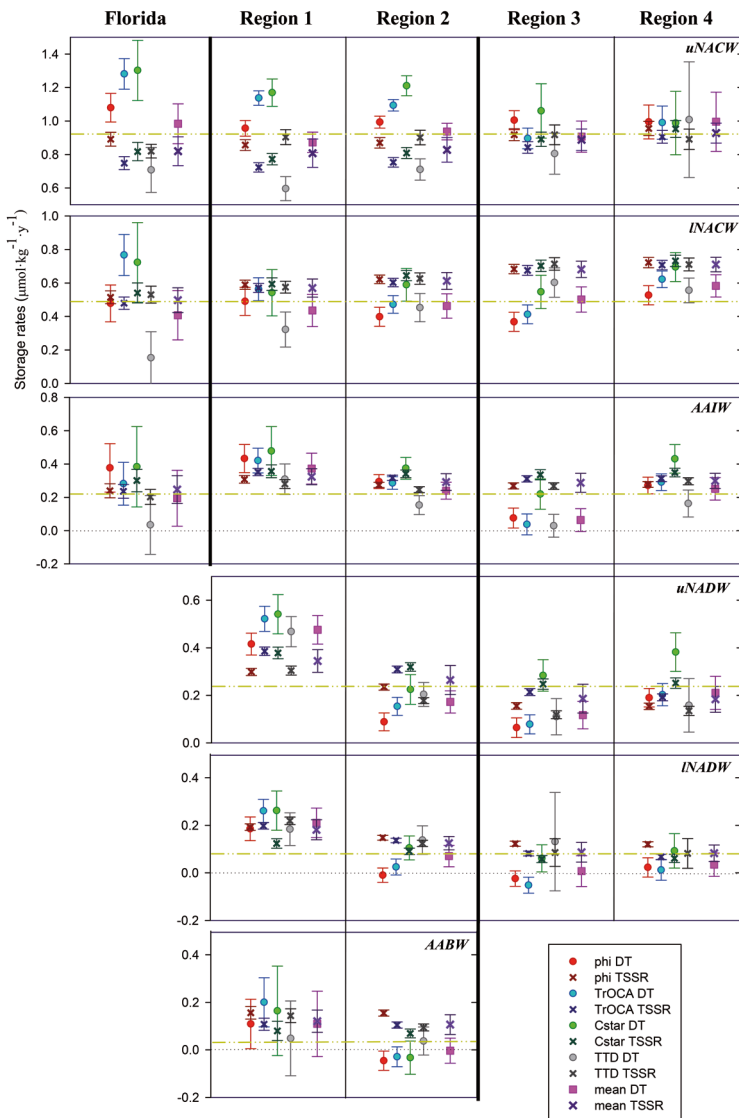


**Figure 3.1.4.**  $\text{C}_{\text{ant}}$  storage rates ( $\mu\text{mol kg}^{-1} \text{yr}^{-1}$ ), with their uncertainty. The storage rates calculated through the DT (coloured circles) or the TSSR (coloured crosses) approaches, by using each method:  $\Delta\text{C}^*$  (green),  $\phi\text{C}_T^0$  (red), TrOCA (blue) and TTD (grey). Mean values, considering the four methods, through the DT (pink) and the TSSR (purple) approaches are also shown. Each horizontal panel corresponds to each layer, which are divided in subpanels identifying the regions. The yellow dashed-dotted line indicates the average DT along each whole layer, summing up the regions. Vertical thicker lines highlight the boundary between the Florida Strait and the main section and that between the western and the eastern basins along the Mid-Atlantic Ridge. The corresponding values are reported in Table 3.1\_C1, in Appendix C. Note that the scale in the y-axis is different depending on the layer, in order to help distinguishing the values of the storage rates between methods. The total range of the y-axis spans 1  $\mu\text{mol kg}^{-1} \text{yr}^{-1}$  for uNACW, INACW and AAIW panels, and in 0.7  $\mu\text{mol kg}^{-1} \text{yr}^{-1}$  for uNADW, INADW and AABW.

### Comparison between Decadal Trends and Transient Stationary State rates in C<sub>ant</sub> storage by layers

Purple dashed lines in Figure 3.1.3 correspond to the mean TSSR ± its confidence interval, as reported in Table 3.1\_C1 of Appendix C. TSSR results represent the expected storage of C<sub>ant</sub> in each box, assuming that concentrations increase in agreement with the exponential increase of C<sub>ant</sub> in the surface ocean. TSSR values thus follow the [C<sub>ant</sub>] distribution (i.e. boxes containing higher concentrations are expected to also exhibit the highest storages, and accumulation rates decrease with depth or according to the progressively lower concentrations found in different layers). TSSR results generally show greater consistency between methods than they do for the DT approach, indicating that [C<sub>ant</sub><sup>WT</sup>], [C<sub>ant</sub><sup>TrOCA</sup>], [C<sub>ant</sub><sup>ΔC</sup>] and [C<sub>ant</sub><sup>TTD</sup>] estimations are similar between them. Although TSSR results do not always correspond well with those obtained from the DT approach (Fig. 3.1.4), they show much lower uncertainties (particularly in the deep ocean), due to the time-normalization of the data. This is the main benefit of using the TSSR approach. By referencing the mean [C<sub>ant</sub>] of the five cruises to the year 2000 (values in table 3.1\_C1 in the Supplementary Information), possible biases in any single dataset are smoothed by averaging with the other years. The uncertainties of the obtained storages are therefore reduced, making them more robust. Although the DT approach is much more sensitive to the data quality of individual cruises (exemplified by the low number of data inputs (n=5) used to perform the linear regressions) it does allow the detection of a more realistic C<sub>ant</sub> storage rate for the 19 year study period. This is since changes are only computed using data from this time frame. Conversely, TSSR results need to be interpreted in terms of the total previous accumulative history of [C<sub>ant</sub>], as storage is computed based on the exponential fit of the C<sub>ant</sub> increase at the surface since the preindustrial era. Thus possible real variations in the storage of C<sub>ant</sub> which deviate from a steady-state accumulation could become masked in the TSSR results due to its integration into the past accumulative history of C<sub>ant</sub>.

The main objective of including the TSSR approach is to check whether C<sub>ant</sub> has been increasing at all depths along the section in accordance with the accumulation expected assuming a steady-state ocean. It is hoped that the inclusion of four C<sub>ant</sub> estimation methods in this comparison should make any inferences more robust. As TSSR results are interpreted as the expected theoretical steady accumulation of C<sub>ant</sub>, any observed deviation from this using DT could be evidence that the accumulation of C<sub>ant</sub> has been impacted by recent changes in circulation or ventilation. Alternatively, when DT and TSSR outputs coincide, it could be taken as an indication that the short-term (here bi-decadal) C<sub>ant</sub> storage (DT) is following a steady-state C<sub>ant</sub> storage (TSSR).

### The upper ocean: uNACW, INACW and AAIW

Central Waters (uNACW and INACW) show progressively higher TSSR values from R1 to R4 (Fig. 3.1.4), suggesting a higher expected storage in the eastern than in the western basin. This pattern is in accordance with the [C<sub>ant</sub>] distributions observed along the layers. For uNACW, TSSR and DT results from all methods compare well in R4, but start to progressively differ on moving westwards: while back-calculation TSSR outputs decrease slightly on moving from R3 to R1 (similar to [C<sub>ant</sub>]), the corresponding DT results remain more

or less equal ( $\phi C_T^0$ ) or even increase (TrOCA or  $\Delta C^*$ ) (Fig. 3.1.4). For TTD, observed DT values suggest a lower  $[C_{ant}^{TTD}]$  accumulation towards the west while TSSR results indicate that similar accumulation should be expected along the layer. A significant difference between the DT and TSSR approaches is apparent for the four methods in the western basin: TTD outputs suggest that  $[C_{ant}^{TTD}]$  has been accumulating slower than expected, at least during the last two decades, while DT( $\phi C_T^0$ ), DT(TrOCA) and DT( $\Delta C^*$ ) results suggest  $C_{ant}$  concentrations have exceeded the expected steady-state increase. In contrast to this, the eastern basin shows decadal trends closer to a more stationary build-up. The most noticeable feature in INACW is the stronger longitudinal gradient in storage rates between the eastern (higher) and the western (lower) basins for TSSR results than for DT results. This is due to the strong gradient in  $[C_{ant}]$  associated with the shallowing of isopycnals towards the east. However, only DT(TTD) shows the same pattern, as DT from back-calculation methods generally show greater coherence along the layer. In AAIW, TSSR values from the four methods match closely and indicate similar storages throughout the section (Fig. 3.1.4). This is in contrast to the DT results, that suggest greater accumulation in region R1. The expected TSSR storages in the ocean interior (R2 to R4) are mostly similar between the TTD and the back-calculated results. However, DT(TTD) outputs are generally lower than back-calculated DT results. The TSSR storages found from R2 to R4 are consistent to the observed DT values for  $\phi C_T^0$  and TrOCA. The only mismatch occurs in R3, where a TSSR storage similar to the surrounding regions is expected, as the  $C_{ant}$  concentrations are significant, but neither  $[C_{ant}^{DT}]$ ,  $[C_{ant}^{TrOCA}]$  nor  $[C_{ant}^{TTD}]$  actually appear to have increased over the 19 year time period.

### The deep ocean: uNADW, INADW and AABW

In the deep layers (uNADW and INADW) both approaches show R1 to be the region with the greatest build-up in  $C_{ant}$ , with TSSR results then exhibiting a smoother zonal gradient along the section than their respective DT values (Fig. 3.1.4) (primarily in uNADW). This result highlights the significant role of the DWBC in carrying high levels of  $C_{ant}$  in the deeper western basin, especially in LSW (see below). The boxes of the ocean interior where  $[C_{ant}]$  are close to the detection limits show low but significant TSSR storages (Fig. 3.1.4), whereas the DT values are not always significant. This might be due to the inherent difficulty in accurately estimating  $C_{ant}$  levels in deep waters and also identifying its temporal increase. It is thus difficult to ascertain if the absence of rising  $[C_{ant}]$  observed in the deep interior ocean (mainly in INADW) is a real signal or a consequence of the time series simply not being long enough in duration. This issue is also relevant for AABW, where TSSR results show consistent storage rates in R1. For DT outputs, although significant levels of  $C_{ant}$  are identified for all methods (Fig. 3.1.3), only  $\phi C_T^0$  and TrOCA show significant, non-zero rates (Fig. 3.1.4). TSSR results also suggest that significant  $C_{ant}$  build-up could additionally be considered to be occurring in R2.

## Discussion

The mean TSSR storage rate for the whole uNACW layer using all four methods gives an expected accumulation of  $0.84 \pm 0.07 \text{ } \mu\text{mol}\cdot\text{kg}^{-1}\cdot\text{yr}^{-1}$ . The equivalent mean DT suggests a slightly higher observed value of  $0.93 \pm 0.09 \text{ } \mu\text{mol}\cdot\text{kg}^{-1}\cdot\text{yr}^{-1}$  (Fig. 3.1.4) that is mostly influenced by the significant dissimilarity between the two approaches in the western basin compared to the eastern basin, where DT values are closer to a steady-state accumulation. DT results from the back-calculation methods stand out; if only  $\phi C_T$ , TrOCA and  $\Delta C^*$  DT values were considered, these would suggest an even higher storage in the uppermost layer ( $1.07 \pm 0.08 \text{ } \mu\text{mol}\cdot\text{kg}^{-1}\cdot\text{yr}^{-1}$  on average), mainly due to the higher storage found in FS, R1 and R2 compared to those in R3 and R4.

Our findings are in accordance with those reported at time series stations in the Subtropical North Atlantic. Observations at BATS (Bermuda Atlantic Time-series Study), situated in the Western Subtropical North Atlantic, suggest a three-decade trend (1983–2011) of  $1.08 \pm 0.06 \text{ } \mu\text{mol}\cdot\text{kg}^{-1}\cdot\text{yr}^{-1}$  for surface salinity-normalized  $C_T$  ( $nC_T$ ) (Bates *et al.*, 2012). Conversely, at ESTOC (European Times Series Canary Islands), situated in the Eastern basin, a surface  $nC_T$  storage rate of  $0.99 \pm 0.20 \text{ } \mu\text{mol}\cdot\text{kg}^{-1}\cdot\text{yr}^{-1}$  was reported (1995–2004) (Santana-Casiano *et al.*, 2007). Although both values indicate an equivalent  $nC_T$  storage when taking into account error estimates, a slightly increased  $nC_T$  accumulation could be suggested for the western basin. In addition, based on  $C_T$  and  $A_T$  observations for Subtropical Mode Water (STMW, the main component of the uNACW layer in the western basin), Bates (2012) estimated a  $C_{\text{ant}}$  storage rate of  $1.06 \text{ } \mu\text{mol}\cdot\text{kg}^{-1}\cdot\text{yr}^{-1}$  between 1988 and 2011 at BATS. At ESTOC, the observed increase in  $nC_T$  for the seasonal thermocline (around 120 m) amounted to  $0.85 \pm 0.16 \text{ } \mu\text{mol}\cdot\text{kg}^{-1}\cdot\text{yr}^{-1}$ . This value matched the estimated  $C_{\text{ant}}$  storage rate for the first 200 m obtained using the TrOCA method (González-Dávila *et al.*, 2010). Furthermore, net CO<sub>2</sub> air-sea fluxes of  $-0.81 \pm 0.25$  to  $-1.3 \pm 0.3 \text{ mol}\cdot\text{m}^{-2}\cdot\text{yr}^{-1}$  (1983 – 2005) and  $-0.051 \pm 0.036$  to  $-0.054 \pm 0.03 \text{ mol}\cdot\text{m}^{-2}\cdot\text{yr}^{-1}$  (1995 – 2004), reported respectively for BATS (Bates, 2007) and ESTOC (Santana-Casiano *et al.*, 2007), indicate that the eastern side of the NASTG has been acting as a much weaker sink for atmospheric CO<sub>2</sub> than the western side. These findings are consistent with previous results, where BATS was found to be in a region of strong spatial gradients in air-sea CO<sub>2</sub> flux (Nelson *et al.*, 2001). In this context, our data suggest that during these two decades  $C_{\text{ant}}$  may have been absorbed more intensely in the western side of the NASTG.

Circulation patterns additionally support these findings; STMW that forms near the Sargasso Sea both recirculates near its formation site and travels to the eastern NASTG through the Azores Current (Schmitz and Richardson, 1991; Follows *et al.*, 1996). The larger amounts of CO<sub>2</sub> entering into the ocean near Bermuda (Bates, 2007) would be thus advected to the eastern part of the section below the surface. The transport of  $C_{\text{ant}}$  enriched waters towards the east could explain the existence of higher  $[C_{\text{ant}}]$  at this side of the section (tables in appendix A), despite the lower CO<sub>2</sub> uptake rates reported there (Santana-Casiano *et al.*, 2007). It is important to note that there is no complete consensus among the four different methods used to evaluate the storage in  $C_{\text{ant}}$  for uNACW in the western basin (Fig. 3.1.4). The TrOCA and  $\Delta C^*$  methods suggest a faster

DT in C<sub>ant</sub> moving closer to the west, while the φC<sub>T</sub><sup>0</sup> method shows the same storage values throughout the layer. As highlighted above, the TTD method (that tends towards lower values in recent years) likely underestimates concentrations in this basin. Future updated trends for the CO<sub>2</sub> system parameters at ESTOC will help confirm whether different accumulation rates have been occurring at each side of the NASTG. The annual mixing of INACW with uNACW due to the winter outcrop in the west (Bates, 2012) could also favour the observed opposite TSSR and DT zonal gradients. This outcrop might favour lower [C<sub>ant</sub>] closer to R1 due to mixing with less saturated underlying waters, maintaining a higher C<sub>ant</sub> uptake by uNACW at the western side of the section.

In contrast to central waters that show a general sustained long-term increase in [C<sub>ant</sub>] values over their whole extent throughout the 19 year time period, the layers below (AAIW, NADW, AABW) show a generally divergent behaviour between the DT results in R1 and those in the ocean interior (R2-R4). The influence of the DWBC extends to R2 in most layers, resulting in contrasting DT between the western and eastern basins as a whole. In the AAIW layer, the greater rise in concentrations appears to occur in the western basin. Brown *et al.* (2010) pointed out that the variability in [C<sub>ant</sub>] at these intermediate depths most likely results from changing mixing characteristics of waters of southern and Mediterranean origin, mainly due to a lateral movement of the water mass front that occurs between the AAIW and the MW. Regardless of the modulation of the C<sub>ant</sub> budget from the spreading of MW (Álvarez *et al.*, 2005), the eastern basin shows almost no (R3) or only slight (R4) [C<sub>ant</sub>] changes in time, which indicates that the observed DT storage rate for the whole AAIW ( $0.22 \pm 0.08 \mu\text{mol}\cdot\text{kg}^{-1}\cdot\text{yr}^{-1}$ ) might have been mainly driven by R1. Although the higher weighted DT in R1 represents a relative minimum compared to those in INACW and uNADW in the same region, it might have been mainly influenced by the C<sub>ant</sub> signal of the LSW spreading underneath (Steinfeldt *et al.*, 2007).

The prevailing role of R1 in the full section storage variability on decadal timescales becomes much more evident in deep waters below 1000 dbar (Macdonald *et al.*, 2003; Brown *et al.*, 2010). In the uNADW and INADW layers, DT and TSSR results show storage rates that are higher in R1 than those further east (Fig. 3.1.4), due to the influence of recently ventilated waters moving southwards as part of the DWBC. These waters are enriched in C<sub>ant</sub> with respect to the less-ventilated layers that recirculate in the ocean interior (Steinfeldt *et al.*, 2009; Pérez *et al.*, 2010a), which themselves show small (uNADW) or not significant (INADW) DT values. As reported above, the zonal gradient in the storage rates along the section is stronger for DT outputs than the TSSR approach due to their differing responses for LSW. The significantly higher storages observed (DT) for the period of study (Fig. 3.1.4) with respect to the expected steady-state increase are confirmed by all four methods and can be explained by changes (increase) in deep-water ventilation owing to the strong renewal of LSW during the mid-1990s (Pérez *et al.*, 2008). It is likely that we are detecting the arrival, at 24.5°N, of the greater amounts of C<sub>ant</sub> that entered into the subpolar gyre more than a decade ago, and have been transported southward by the DWBC.

With regards to AABW, weighted DT results in R1 show a non significant trend of about  $0.11 \pm 0.14 \mu\text{mol}\cdot\text{kg}^{-1}\cdot\text{yr}^{-1}$  (Fig. 3.1.4), while those in R2 suggest no increase in  $[\text{C}_{\text{ant}}]$ . However, the corresponding TSSR values ( $0.12 \pm 0.05 \mu\text{mol}\cdot\text{kg}^{-1}\cdot\text{yr}^{-1}$  in R1 and  $0.11 \pm 0.04 \mu\text{mol}\cdot\text{kg}^{-1}\cdot\text{yr}^{-1}$  in R2) suggest similar storages for the whole layer that are, in turn, equivalent to the observed DT results in R1. Ríos *et al.* (2012) reported a significant  $\text{C}_{\text{ant}}$  storage rate of  $0.15 \pm 0.04 \mu\text{mol}\cdot\text{kg}^{-1}\cdot\text{yr}^{-1}$  (1971 - 2003) in AABW in the Western South Atlantic ( $55^{\circ}\text{S}$ - $10^{\circ}\text{N}$ ). For this same basin, Wanninkhof *et al.* (2013) were able to detect, from pCO<sub>2</sub> measurements, small C<sub>T</sub> changes in deep waters from  $44^{\circ}\text{S}$  to the Equator, obtaining a storage rate of  $0.47 \text{ mol}\cdot\text{m}^{-2}\cdot\text{yr}^{-1}$  for depths under 2000 m. Considering an average thickness of the water column of about ~3000 m (from -2000 m to the ocean bottom) it can be deduced that they found storage rates equivalent to  $\sim 0.15 \mu\text{mol}\cdot\text{kg}^{-1}\cdot\text{yr}^{-1}$ , that are applicable to deep and bottom water masses at these latitudes in the North Atlantic, in agreement with Ríos *et al.* (2012). Both results are consistent with the mean TSSR values obtained in the AABW (table 3.1\_C1, in Appendix C), which indicate the expected storage according to the estimated  $[\text{C}_{\text{ant}}]$  in this layer. Only the weighted DT in R1 appears to confirm this. In addition, a mean TSSR of  $0.12 \pm 0.05 \mu\text{mol}\cdot\text{kg}^{-1}\cdot\text{yr}^{-1}$  is also obtained for the whole LNADW layer, which is also consistent with Ríos *et al.* (2012) and Wanninkhof *et al.* (2013). Only DT(TTD) and DT( $\Delta\text{C}^*$ ) suggest similar results for the LNADW layer in R2 (table 3.1\_C1). Brown *et al.* (2010) described a significantly non-zero  $\text{C}_{\text{ant}}$  signal at  $24.5^{\circ}\text{N}$  for depth ranges between 4000 - 6000 dbar in the deep eastern basin (Fig 7 in Brown *et al.* (2010)), that was confirmed from CCl<sub>4</sub> measurements. These authors suggested that these  $[\text{C}_{\text{ant}}]$  levels might be related to the arrival of ventilated waters from the North along the eastern flank of the Mid-Atlantic Ridge, which Paillet and Mercier (1997) described as Iceland-Scotland Overflow Water. Roughly, it would correspond to an approximate storage of about  $\sim 0.2 - 0.3 \mu\text{mol}\cdot\text{kg}^{-1}\cdot\text{yr}^{-1}$ , which is consistent with our results, given the fact that our storage is referred to a layer with almost double the thickness (between 2500- 5500 dbar).

Differences in the storage rates found between methods were more evident where the  $\text{C}_{\text{ant}}$  detection limits became more important. In deep homogeneous waters with very low  $\text{C}_{\text{ant}}$ , absolute uncertainties were of the same order of magnitude as the  $\text{C}_{\text{ant}}$  concentrations, making significant trends difficult to separate from the background noise on a timescale of two decades. This is the case for LNADW and AABW, where there was no obvious accumulation of  $\text{C}_{\text{ant}}$  (considering the uncertainties) despite the fact that the estimated  $\text{C}_{\text{ant}}$  content could be considered to be significant. Here, we found significant bi-decadal trends in the  $\text{C}_{\text{ant}}$  storage rates of the deepest Subtropical North Atlantic waters by using all five A05 datasets and the assumption of a transient steady state of the  $\text{C}_{\text{ant}}$  distributions, in order to reduce the uncertainties related to deep waters measurements. Our results are consistent with Ríos *et al.* (2012), who used the same methodology as in our study (C<sub>T</sub> and A<sub>T</sub> measurements), but a larger timescale (three decades), to compute the  $\text{C}_{\text{ant}}$  storage in the Western South Atlantic basin. Our findings also match those obtained by Wanninkhof *et al.* (2013), who studied the  $\text{C}_{\text{ant}}$  change along the entire Atlantic Ocean during a period of time similar to ours, almost two decades, but with more precise pCO<sub>2</sub> measurements.

## Conclusions

The CO<sub>2</sub> system measurements from the most recent occupations of the A05 section across 24.5°N in the Subtropical North Atlantic in 2010 and 2011 were compared with data from the three previous cruises. These five sections permitted the estimation of the C<sub>ant</sub> storage on decadal timescales within the main water masses present at the section. To better constrain the accumulation of C<sub>ant</sub>, this was estimated by using four different methods that include back-calculation ( $\Delta C^*$ , TrOCA and  $\phi C_T^0$ ) and tracer (TTD) principles. Regardless of the method used to estimate [C<sub>ant</sub>], the overall distribution showed higher C<sub>ant</sub> concentrations near the surface that decreased towards the bottom. By investigating the accumulation of C<sub>ant</sub> in different water masses along the section, we found that the greatest decadal storage rates were observed in the central water masses. uNACW showed a mean storage rate close to ~1 μmol·kg<sup>-1</sup>·yr<sup>-1</sup> and lNACW displayed ~0.5 μmol·kg<sup>-1</sup>·yr<sup>-1</sup>, on average. Our results for uNACW are in accordance with the reported storage rates of C<sub>ant</sub> and nC<sub>T</sub> at BATS (Bates, 2012) and ESTOC (González-Dávila *et al.*, 2010) time series stations. Below the central layers, neither intermediate nor deep water masses showed average storage rates greater than ~0.25 μmol·kg<sup>-1</sup>·yr<sup>-1</sup>. Zonal gradients in the accumulation of C<sub>ant</sub> were detected throughout the water column, with robust results identified for intermediate and deep water masses. The four methods gave evidence of higher storages of C<sub>ant</sub> occurring close to the western continental slope due to the conveyer role of the DWBC, in comparison with the low storage rates of the ocean interior. In particular, the storage rate of the uNADW layer within the DWBC region amounted to ~0.5 μmol·kg<sup>-1</sup>·yr<sup>-1</sup> due to the contribution of recently ventilated LSW. In the upper layers (mode waters), the zonal gradient was less clear due to the greater variability that existed between the different methods of C<sub>ant</sub> estimaton. Results suggest that, at least for the period of study, C<sub>ant</sub> might have been absorbed more intensely in the western side of the NASTG, although more evidence is needed to confirm this.

For the vast majority, the four methods gave consistent storage rates indicating a good agreement between tracer and CO<sub>2</sub>-based results. However, some differences in the obtained storage rates were observed: the TTD method may have underestimated storages in the two uppermost layers (mode waters). The  $\Delta C^*$  method gave **decadal storage values slightly higher than the other three methods in the eastern basin** in intermediate and deep layers, which likely results from the estimation of its disequilibria. The C<sub>ant</sub> accumulation calculated by using TrOCA method usually lied between the  $\Delta C^*$  and  $\phi C_T^0$  results, with the latter method indicating storage rates closer to the TTD method. There was generally better agreement between the storage rates of the four methods in the layers where the estimation of C<sub>ant</sub> is more robust. Agreement between the four methods was found in regions where the recent evolution of C<sub>ant</sub> for the period 1992- 2011 (DT results) appeared similar to the expected steady behaviour of the C<sub>ant</sub> distributions (TSSR results), suggesting that the accumulation of C<sub>ant</sub> was not impacted by recent changes in circulation. However, the four methods exhibited greater variability in regions where DT results suggested a departure from a transient steady state behaviour of the ocean. Due to the steady-state assumption inherent in each different C<sub>ant</sub> estimation

technique, this observed variability will make it more difficult in the coming years to consistently track and constrain the oceanic C<sub>ant</sub> increase.

The A05 repeat hydrography thus permits the robust estimation of the storage of C<sub>ant</sub> on decadal timescales and allows a better constraint of the interactions between the ocean circulation and the carbon cycle, in particular regarding the mechanisms governing the accumulation of C<sub>ant</sub> in the Subtropical North Atlantic.

### **Acknowledgements**

We would like to thank captains, officers and crews of RRS Discovery and R/V Sarmiento de Gamboa and the scientific and technical teams for their support and indispensable help during the cruises in 2010 and 2011. We acknowledge funding from the Spanish Ministry of Economy and Competitiveness through grants CSD2008-00077 (Circumnavigation Expedition MALASPINA 2010 Project), CTM2009-08849 (ACDC Project) and CTM2012-32017 (MANIFEST Project). We also acknowledge funding from the EU FP7 project CARBOCHANGE under grant agreement no. 264879 and by the Marine Biogeochemistry and Global Change research group (Generalitat de Catalunya, 2014SGR1029). E.F. Guallart was funded through a JAE-Pre grant that was financed by the Spanish National Research Council Agency (Consejo Superior de Investigaciones Científicas, CSIC) and by the European Social Fund.

## Appendix A. Methods

### Anthropogenic CO<sub>2</sub> computations

We used three back-calculation methods to estimate anthropogenic CO<sub>2</sub> (C<sub>ant</sub>) from in situ measurements. The principles of the carbon-based methods were established by Brewer (1978) and Chen and Millero (1979) and rely on separating the contributions to dissolved inorganic carbon (C<sub>T</sub>) of organic matter remineralization and CaCO<sub>3</sub> dissolution, according to Redfield equations. In addition, the preindustrial preformed C<sub>T</sub> (C<sub>T</sub><sup>0</sup>, i.e. the C<sub>T</sub> that the water mass had at the moment of its formation in the preindustrial atmosphere) is also removed, taking the remaining C<sub>T</sub> amount as the C<sub>ant</sub> perturbation. The classical ΔC\* approach (Gruber *et al.*, 1996) is a widely applied technique based on the estimation of the quasi-conservative ΔC\* tracer. This method first introduced the time-independent ΔC<sub>dis</sub> term to the back-calculation techniques, under the assumption that it has remained steady since the preindustrial era. The authors proposed the ΔC<sub>dis</sub> as one of the two terms in which they separated the C<sub>T</sub><sup>0</sup>, together with a zero-C<sub>ant</sub> reference term that can be estimated according to the CO<sub>2</sub> system chemistry. The authors proposed a formal way to estimate the ΔC<sub>dis</sub> through the use of age tracers, according to which old water masses are assumed to be void of C<sub>ant</sub> and ΔC<sub>dis</sub> is assigned the value of ΔC\*. For younger water masses ΔC<sub>dis</sub> is calculated according to water age information. The uncertainties of the ΔC\* method were evaluated at ±9 μmol·kg<sup>-1</sup> (Gruber *et al.*, 1996). This error was evaluated assuming a lower precision for both C<sub>T</sub> and total alkalinity data than the obtained using modern and standardized methods of analysis. For modern measurements the C<sub>ant</sub><sup>ΔC\*</sup> error would thus be lower (Gruber, 1998) and closer to the uncertainty reported for other methods of estimation (around ±6 μmol·kg<sup>-1</sup>).

The φC<sub>T</sub><sup>0</sup> method (Vázquez-Rodríguez *et al.*, 2009a) shares similar principles with ΔC\*. It proposes some upgrades to the ΔC<sub>dis</sub> and the preformed A<sub>T</sub> (A<sub>T</sub><sup>0</sup>) determinations by using the subsurface layer (100–200m) as a reference for characterising water mass properties at their wintertime formation conditions. It thus avoids the short-term variability of the uppermost layers (Vázquez-Rodríguez *et al.*, 2012). One important point in this approach is that none of the A<sub>T</sub><sup>0</sup> or ΔC<sub>dis</sub> parametrizations rely on CFC data but on conservative parameters exclusively. Both terms are further assumed not to be in steady state. To address the assumption of invariable ΔC<sub>dis</sub> (Matsumoto and Gruber, 2005), the φC<sub>T</sub><sup>0</sup> method proposes an approximation to the spatial and temporal variability of ΔC<sub>dis</sub> (ΔΔC<sub>dis</sub>) (Vázquez-Rodríguez *et al.*, 2009a). It also accounts for the small increase of A<sub>T</sub><sup>0</sup> since the Industrial era due to CaCO<sub>3</sub> dissolution changes projected from models (Heinze, 2004) and the effect of rising sea surface temperatures on A<sub>T</sub><sup>0</sup>. The C<sub>ant</sub> concentrations are directly estimated in waters above the 5°C isotherm while they are estimated by using an extended Optimum MultiParameter (eOMP) analysis in waters with Θ<5°C, improving the estimations in cold deep waters. An uncertainty of ±5.2 μmol·kg<sup>-1</sup> is obtained for C<sub>ant</sub><sup>φCT0</sup> estimations (Vázquez-Rodríguez *et al.*, 2009a).

The TrOCA method (Touratier and Goyet, 2004; Touratier *et al.*, 2007) is an easy-to-apply technique based on the universal quasi-conservative TrOCA tracer (Tracer combining Oxygen, C<sub>T</sub> and A<sub>T</sub>). It shares with the above methods its consideration of the biological contribution to C<sub>T</sub> but does not take into account the C<sub>T</sub><sup>0</sup> estimation in its parameterization. The C<sub>ant</sub><sup>TrOCA</sup> concentration is estimated from the difference between

TrOCA and the preindustrial zero-C<sub>ant</sub> term TrOCA<sup>0</sup>, defined from the “natural” concentrations of O<sub>2</sub>, C<sub>T</sub> and A<sub>T</sub>. The universal TrOCA<sup>0</sup> equation is a function of Θ and A<sub>T</sub>, and was derived from Δ<sup>14</sup>C and CFC-11 tracer data in the global ocean, to establish which water parcels can be assumed to be free of C<sub>ant</sub>. The method assumes that A<sub>T</sub> is not affected by the increase of atmospheric CO<sub>2</sub> (Goyet *et al.*, 1999) and uses a constant oxygen to carbon Redfield ratio (Rc) value of 1.35 (after Körtzinger *et al.*, 1998) to calculate the biological contribution to C<sub>T</sub> while both φC<sub>T</sub><sup>0</sup> and ΔC\* methods use the Rc ratio of 1.45 proposed by Anderson and Sarmiento (1994). Despite being a simple universal equation (Yool *et al.*, 2010), it provides comparable C<sub>ant</sub> inventories to those obtained by other approaches in the Atlantic (Vázquez-Rodríguez *et al.*, 2009b). The reported uncertainty for C<sub>ant</sub><sup>TrOCA</sup> estimations is ±6.25 μmol·kg<sup>-1</sup> (Touratier *et al.*, 2007).

Given the availability of CFC measurements on four cruises (1992, 1998, 2004 and 2010), C<sub>ant</sub> concentrations were also estimated using the TTD method (Waugh *et al.*, 2006), without using CO<sub>2</sub> measurements. Similar to all tracer-based methods, it aims to mathematically describe the Transit Time Distributions (TTD) of the CFC observations to “calibrate” how the ocean’s circulation connects surface boundary conditions with interior ocean concentrations. To estimate the ocean interior C<sub>ant</sub> at any given point of space and time, the only necessary information is the knowledge about the temporal evolution of C<sub>ant</sub> in the surface mixed layer and the rate at which this surface boundary condition is transported and mixed into the ocean interior. The assumption of the transport is steady and TTDs are modelled as Inverse Gaussian functions (Waugh *et al.*, 2004). A constant air–sea disequilibrium in time is also assumed. Thus, C<sub>ant</sub><sup>TTD</sup> is the difference between C<sub>T</sub> at the time when the measurements were done, and C<sub>T</sub> just in the beginning of the preindustrial era (Waugh *et al.*, 2004). The reported uncertainties of the TTD approach are ±6 μmol·kg<sup>-1</sup> (Waugh *et al.*, 2006). CFC-12 was used as a proxy for C<sub>ant</sub> to constrain the TTD functions in each cruise (with a ratio of 1 for the mean and width of the TTD). The atmospheric histories for CFC-12 in the northern hemisphere are from John Bullister at CDIAC ([http://cdiac.ornl.gov/oceans/new\\_atmCFC.html](http://cdiac.ornl.gov/oceans/new_atmCFC.html)) and the CO<sub>2</sub> are from <ftp://ftp.cmdl.noaa.gov>. CFC-12 partial pressures at interior locations were calculated from its dissolved measured concentration using the solubility functions determined by Warner and Weiss (1985) with a time-invariant initial saturation at 100% for mode waters, at 85% for intermediate waters and at 65% for deep and bottom waters. We only used CFC-12 for consistency between cruises as this tracer was available for the 4 cruises (SF6 was only measured during the 2010 cruise) but this is problematic for the recently ventilated waters (uppermost water layers here) surveyed after the mid-1990’s because of the decrease of atmospheric CFC-12 since then. The exclusion of data above 150 dbar from our estimates should help with this issue, and no correction was done by using any other tracer (such as SF<sub>6</sub>) to adjust results for younger waters or for change of saturation of the CFC-12 overtime (Tanhua *et al.*, 2008). However, we took these issues into account in the interpretation section.

## Appendix B. Data tables

### Box-averaged physico-chemical properties and C<sub>ant</sub> estimations

The tables in this appendix summarize mean values  $\pm$  standard error of the mean ( $x \pm \sigma/\sqrt{N}$ ) for pressure (dbar), salinity, O<sub>2</sub> ( $\mu\text{mol}\cdot\text{kg}^{-1}$ ), potential temperature Θ (°C) Apparent Oxygen Utilization (AOU,  $\mu\text{mol}\cdot\text{kg}^{-1}$ ) within each given layer and region box. Regarding the C<sub>ant</sub> estimations, tables summarize mean C<sub>ant</sub>  $\pm$  standard deviation of an ensemble of 100 C<sub>ant</sub> averages computed by random perturbations of the C<sub>ant</sub> estimates within each given box according to each method uncertainty. Tables are found following the description of Appendix C.

## Appendix C. Data tables

### C<sub>ant</sub> storage rates along the A05 section

The temporal changes in the mean C<sub>ant</sub> concentrations ([C<sub>ant</sub>]) of φC<sub>T</sub><sup>0</sup>, TrOCA and ΔC\* ([C<sub>ant</sub><sup>φC<sub>T</sub><sup>0</sup>], [C<sub>ant</sub><sup>TrOCA</sup>], [C<sub>ant</sub><sup>ΔC\*</sup>], [C<sub>ant</sub><sup>TTD</sup>]) within each box of the A05 section, for the period 1992-2011, were studied by two different approximations. The first one consisted in performing linear regressions between the five years in which the different datasets were obtained and their corresponding [C<sub>ant</sub>] to estimate the respective decadal trend (DT, in  $\mu\text{mol}\cdot\text{kg}^{-1}\cdot\text{yr}^{-1}$ ). The second approach consisted in the estimation of the respective C<sub>ant</sub> storage rates ( $\mu\text{mol}\cdot\text{kg}^{-1}\cdot\text{yr}^{-1}$ ) assuming a steady state of the oceanic C<sub>ant</sub> distribution, considering a specific annual percentage rate of [C<sub>ant</sub>] according to the literature. The table following tables of appendix B summarizes the obtained results.</sup>

**Table 3.1\_B1.** Physico-chemical properties and C<sub>ant</sub> estimations in Region I (78°W to 70°W).

	Press (dbar)	salinity	Θ (°C)	AOU (µmol/kg)	$\varphi C_T^0$ (µmol/kg)	TrOCA (µmol/kg)	$\Delta C^*$ (µmol/kg)	TTD (µmol/kg)
<b>I REGION</b>								
<b>uNACW</b>								
1992	268.3±14.0	36.627±0.021	19.49±0.24	29.7±1.9	44.1±0.7	33.9±0.7	35.5±1.2	48.0±1.2
1998	310.7±6.4	36.578±0.010	18.60±0.08	33.1±0.7	47.6±0.6	38.6±0.6	42.5±0.9	52.8±0.5
2004	355.8±10.9	36.556±0.017	18.61±0.15	37.9±1.5	54.5±0.7	47.0±0.8	51.8±1.4	55.3±0.6
2010	321.7±11.5	36.552±0.017	18.51±0.14	36.1±1.2	62.3±0.9	55.6±0.9	58.9±1.4	59.1±0.9
2011	279.7±9.7	36.611±0.014	18.89±0.14	30.8±1.3	60.2±0.6	53.2±0.6	55.3±1.7	
<b>INACW</b>								
1992	630.0±22.5	35.768±0.061	13.19±0.42	89.7±5.4	34.3±1.5	31.9±1.4	33.5±2.1	28.0±1.8
1998	666.4±8.5	35.748±0.025	13.08±0.17	92.6±1.9	31.3±1.0	30.4±1.1	32.3±1.7	31.0±1.2
2004	714.1±10.4	35.632±0.031	12.32±0.23	103.5±3.5	35.5±1.2	34.4±1.4	34.9±1.8	31.9±1.0
2010	678.1±10.1	35.664±0.030	12.57±0.21	101.0±2.6	39.2±1.1	40.9±0.9	41.0±1.3	34.1±0.9
2011	642.7±12.2	35.718±0.032	12.98±0.23	100.8±2.4	43.9±0.8	41.1±0.9	43.7±2.7	
<b>AAIW</b>								
1992	887.9±27.0	35.158±0.021	7.99±0.30	124.8±2.3	15.0±1.7	17.9±1.5	16.8±2.7	14.1±1.6
1998	926.2±9.5	35.160±0.010	8.07±0.13	126.5±0.9	16.1±0.9	18.7±0.8	20.1±1.3	14.7±1.1
2004	923.8±12.8	35.149±0.012	7.98±0.16	125.7±1.9	21.4±1.4	24.1±1.4	23.7±3.2	17.1±1.0
2010	921.5±10.7	35.150±0.009	7.89±0.14	121.9±1.5	20.2±1.1	24.9±1.2	25.4±1.6	19.4±1.0
2011	899.3±8.6	35.137±0.007	7.76±0.11	124.8±1.3	24.4±0.6	25.2±0.7	26.0±2.0	
<b>uNADW</b>								
1992	1,741.5±67.5	35.003±0.005	3.98±0.12	62.0±1.7	14.5±0.9	19.1±1.0	17.7±1.6	14.6±1.1
1998	1,787.1±29.1	35.000±0.003	4.00±0.05	60.9±0.8	16.4±0.7	21.2±0.6	21.4±1.0	16.9±0.7
2004	1,735.8±37.0	34.997±0.004	4.06±0.07	63.3±1.1	19.0±0.6	24.2±0.6	24.4±1.2	20.5±0.5
2010	1,821.3±34.9	34.985±0.003	3.84±0.06	56.0±0.7	21.4±0.7	28.5±0.7	27.0±1.2	22.7±0.5
2011	1,596.3±29.3	35.005±0.003	4.27±0.06	65.3±0.8	22.7±0.4	28.5±0.4	28.6±1.2	
<b>INADW</b>								
1992	3,779.6±111.3	34.913±0.003	2.19±0.05	62.3±0.5	9.9±1.0	9.2±0.9	4.9±1.4	11.7±1.2
1998	3,533.1±43.3	34.916±0.001	2.27±0.02	59.4±0.2	10.8±0.6	10.5±0.7	6.9±1.1	12.7±0.6
2004	3,626.7±46.9	34.910±0.001	2.19±0.02	63.2±0.3	13.3±0.6	14.6±0.7	7.8±1.0	13.3±0.5
2010	3,540.3±60.0	34.910±0.002	2.23±0.03	58.1±0.3	12.7±0.7	14.4±0.7	9.8±1.1	15.2±0.6
2011	3,726.8±56.8	34.908±0.002	2.17±0.03	63.2±0.3	13.6±0.6	13.3±0.6	9.9±1.5	
<b>AABW</b>								
1992	5,406.6±107.9	34.865±0.004	1.67±0.03	78.8±1.7	8.7±2.0	4.5±2.2	3.9±3.3	8.5±2.9
1998	5,042.7±58.8	34.871±0.002	1.71±0.02	75.0±0.8	9.2±1.8	5.8±1.7	3.5±2.5	8.3±1.5
2004	5,007.9±50.1	34.870±0.002	1.71±0.01	78.2±0.8	9.4±1.7	7.4±1.6	5.0±2.1	8.6±1.1
2010	4,939.6±60.9	34.961±0.049	1.72±0.01	72.5±5.8	9.3±1.1	8.3±1.2	5.2±1.6	9.3±1.2
2011	5,031.8±60.0	34.871±0.002	1.71±0.01	77.0±0.9	12.0±1.1	8.2±1.0	7.7±2.8	

**Table 3.1\_B2.** Physico-chemical properties and C<sub>ant</sub> estimations in Region 2 (70°W to 45°W).

	<b>Press (dbar)</b>	<b>salinity</b>	<b>Θ (°C)</b>	<b>AOU (µmol/kg)</b>	<b>gC<sub>T</sub><sup>0</sup> (µmol/kg)</b>	<b>TrOCA (µmol/kg)</b>	<b>ΔC* (µmol/kg)</b>	<b>TTD (µmol/kg)</b>
<b>2 REGION</b>								
<b>uNACW</b>								
1992	252.9±6.5	36.618±0.017	18.71±0.12	33.4±0.9	44.5±0.5	36.4±0.4	37.8±0.7	47.5±0.8
1998	277.9±4.7	36.569±0.011	18.26±0.07	35.0±0.6	49.3±0.5	41.1±0.5	45.3±0.8	52.0±0.5
2004	299.3±10.2	36.514±0.020	18.05±0.14	38.9±1.4	53.7±1.1	46.3±1.0	50.5±1.6	56.1±0.6
2010	271.5±8.2	36.574±0.022	18.37±0.13	39.3±1.2	63.5±0.9	57.1±0.9	61.1±1.2	60.4±1.0
2011	272.7±8.5	36.580±0.019	18.41±0.14	38.0±1.0	62.1±0.5	55.6±0.5	59.9±1.4	
<b>INACW</b>								
1992	562.3±9.9	35.823±0.024	13.37±0.17	79.0±2.0	36.6±0.7	34.2±0.7	35.8±1.0	29.7±1.2
1998	562.1±7.7	35.822±0.019	13.46±0.13	84.4±1.5	35.0±0.7	33.8±0.8	35.6±0.9	33.7±0.8
2004	600.8±12.7	35.739±0.035	12.89±0.25	91.9±3.1	36.5±1.1	35.5±1.1	38.8±1.6	36.3±0.8
2010	563.1±10.1	35.776±0.027	13.25±0.18	92.7±2.3	42.4±1.0	43.0±1.1	44.8±1.6	37.9±1.1
2011	574.9±10.4	35.752±0.025	13.06±0.17	94.7±2.1	43.5±0.8	41.5±0.8	46.6±1.9	
<b>AAIW</b>								
1992	899.1±11.9	35.165±0.014	7.87±0.15	129.6±0.9	14.2±0.6	16.8±0.6	17.0±0.9	12.1±0.8
1998	899.9±8.6	35.149±0.010	7.91±0.10	130.4±0.7	15.0±0.7	17.3±0.7	19.2±1.0	12.6±0.7
2004	897.6±14.3	35.152±0.018	7.82±0.17	127.1±1.7	18.4±1.3	21.7±1.1	22.9±1.8	14.1±0.9
2010	882.9±9.9	35.149±0.013	8.05±0.13	134.1±1.1	20.5±0.9	23.9±0.9	24.4±1.4	14.7±0.6
2011	914.2±9.4	35.110±0.008	7.49±0.11	131.4±0.9	18.1±0.6	19.7±0.6	23.3±1.4	
<b>uNADW</b>								
1992	1,672.1±27.5	35.046±0.003	4.26±0.06	72.9±1.0	13.7±0.6	17.5±0.6	17.3±0.9	8.7±0.8
1998	1,690.8±22.0	35.035±0.002	4.25±0.05	72.4±0.9	14.0±0.6	18.3±0.6	19.7±0.8	10.2±0.6
2004	1,652.7±25.9	35.034±0.002	4.29±0.06	73.6±1.1	14.9±0.7	19.9±0.6	19.4±0.9	11.9±0.4
2010	1,767.1±26.5	35.028±0.005	4.14±0.06	72.3±1.0	14.2±0.8	19.1±0.8	20.0±1.1	12.2±0.5
2011	1,536.7±19.5	35.044±0.002	4.53±0.05	76.7±0.9	16.2±0.4	21.3±0.4	23.4±0.9	
<b>INADW</b>								
1992	3,421.9±51.6	34.922±0.002	2.32±0.03	70.6±0.4	9.4±0.4	8.0±0.5	4.3±0.6	6.7±0.9
1998	3,314.0±38.6	34.925±0.002	2.38±0.02	69.0±0.3	9.1±0.6	8.4±0.6	5.6±0.9	6.6±0.8
2004	3,398.9±41.2	34.921±0.002	2.32±0.02	69.4±0.3	8.9±0.6	8.8±0.6	5.7±0.8	7.9±0.4
2010	3,436.7±50.4	34.921±0.002	2.33±0.03	69.8±0.4	8.2±0.5	8.3±0.6	5.9±0.8	9.0±0.7
2011	3,403.2±46.9	34.921±0.002	2.32±0.03	71.5±0.3	10.0±0.4	8.7±0.4	7.0±0.9	
<b>AABW</b>								
1992	5,279.1±65.3	34.858±0.002	1.59±0.02	82.1±0.5	11.1±0.7	7.5±0.7	5.5±0.9	5.6±1.0
1998	5,302.8±47.2	34.856±0.001	1.60±0.01	79.9±0.4	8.8±0.9	6.0±1.0	3.5±1.4	5.0±0.9
2004	5,313.0±37.6	34.857±0.001	1.60±0.01	80.9±0.5	8.4±0.8	5.3±0.9	3.4±1.2	6.5±0.6
2010	5,473.9±69.5	34.886±0.016	1.66±0.04	81.5±0.6	8.5±0.6	6.4±0.5	4.1±0.8	5.9±0.6
2011	5,300.6±44.0	34.858±0.001	1.61±0.01	83.2±0.4	10.8±0.6	6.9±0.6	4.7±1.2	

**Table 3.1\_B3.** Physico-chemical properties and C<sub>ant</sub> estimations in Region 3 (45°W to 30°W).

	Press (dbar)	salinity	Θ (°C)	AOU (µmol/kg)	$\varphi C_T^0$ (µmol/kg)	TroCA (µmol/kg)	$\Delta C^*$ (µmol/kg)	TTD (µmol/kg)
<b>3 REGION</b>								
<b>uNACW</b>								
1992	220.0±6.5	36.656±0.033	18.30±0.17	32.9±1.5	48.6±0.7	46.6±0.7	46.5±0.9	47.8±1.2
1998	248.3±4.9	36.588±0.020	18.02±0.11	34.3±0.9	51.0±0.6	44.9±0.6	48.9±1.0	52.8±0.8
2004	259.2±13.5	36.497±0.040	17.76±0.24	38.7±1.6	54.4±1.7	49.2±1.9	53.1±2.6	56.0±1.0
2010	220.1±7.4	36.724±0.039	18.67±0.19	35.2±1.5	68.8±1.5	63.4±1.6	66.3±2.9	62.8±2.1
2011	219.9±8.7	36.676±0.036	18.63±0.21	34.8±1.6	64.4±0.8	59.6±0.8	65.2±2.2	
<b>INACW</b>								
1992	489.0±11.6	35.807±0.023	13.20±0.17	74.8±2.1	39.5±0.7	38.3±0.8	37.4±1.1	33.7±1.0
1998	501.8±9.4	35.865±0.022	13.53±0.15	73.6±1.8	39.6±0.8	38.6±0.8	41.9±1.0	38.1±0.9
2004	474.0±15.9	35.879±0.031	13.77±0.23	77.4±2.9	42.8±1.6	42.8±1.7	44.4±2.5	42.9±1.1
2010	489.9±13.5	35.840±0.033	13.42±0.23	84.1±2.9	43.7±1.2	44.2±1.3	46.1±2.0	44.2±1.3
2011	488.7±13.4	35.850±0.030	13.47±0.21	81.6±2.6	47.5±0.7	46.2±0.7	49.4±1.8	
<b>AAIW</b>								
1992	875.4±15.7	35.250±0.016	8.22±0.17	132.2±1.2	15.1±0.8	18.3±0.8	17.7±1.1	12.7±1.1
1998	877.9±13.3	35.259±0.015	8.39±0.15	128.7±1.2	18.2±0.9	20.7±0.8	21.3±1.5	12.7±0.8
2004	877.6±22.4	35.245±0.023	8.32±0.24	129.3±1.5	15.4±1.3	17.4±1.2	20.8±2.3	15.2±0.8
2010	877.1±13.1	35.195±0.013	7.95±0.14	138.4±1.0	16.8±1.4	19.9±1.6	21.9±2.2	12.4±0.8
2011	922.3±10.8	35.172±0.009	7.64±0.10	135.2±0.6	17.9±0.7	19.8±0.6	23.0±1.7	
<b>uNADW</b>								
1992	1,725.5±40.5	35.070±0.006	4.44±0.10	87.6±1.6	9.4±0.7	13.4±0.7	11.9±1.0	5.8±1.4
1998	1,717.4±30.1	35.063±0.004	4.47±0.07	87.0±1.2	9.8±0.9	13.0±0.9	16.5±1.2	6.3±1.1
2004	1,725.3±37.1	35.067±0.005	4.47±0.09	88.4±1.5	7.6±0.8	10.6±0.9	12.9±1.4	7.6±0.8
2010	1,733.1±34.7	35.061±0.006	4.42±0.08	89.1±1.4	8.9±1.0	13.0±1.1	15.7±1.5	7.6±0.7
2011	1,539.3±23.7	35.081±0.004	4.90±0.06	95.3±1.2	12.5±0.4	16.3±0.4	20.6±1.1	
<b>INADW</b>								
1992	3,788.6±87.6	34.921±0.003	2.32±0.03	81.6±0.2	8.5±0.5	6.4±0.5	3.0±0.7	4.0±2.4
1998	3,706.8±66.8	34.922±0.002	2.33±0.02	81.5±0.2	7.2±0.7	4.3±0.8	4.0±1.0	4.7±4.3
2004	3,891.3±70.9	34.916±0.002	2.26±0.02	81.6±0.3	6.8±0.7	4.4±0.7	2.6±1.0	5.6±4.2
2010	4,064.4±84.2	34.912±0.003	2.23±0.03	81.5±0.2	6.3±0.7	4.2±0.6	3.3±1.0	6.3±2.5
2011	3,919.6±71.0	34.916±0.002	2.26±0.03	83.9±0.2	9.0±0.5	5.6±0.4	5.3±1.0	

**Table 3.1\_B4.** Physico-chemical properties and C<sub>ant</sub> estimations in Region 4 (30°W to 10°W).

	Press (dbar)	salinity	Θ (°C)	AOU (µmol/kg)	$\phi C_T^0$ (µmol/kg)	TrOCA (µmol/kg)	$\Delta C^*$ (µmol/kg)	TTD (µmol/kg)
<b>4 REGION</b>								
<b>uNACW</b>								
1992	182.7±5.0	36.630±0.033	17.78±0.15	33.1±2.4	50.3±0.9	51.0±0.9	49.8±1.5	48.4±1.9
1998	204.8±4.7	36.493±0.021	17.45±0.11	44.1±2.2	53.3±1.0	48.8±0.9	52.3±1.5	51.9±1.0
2004	213.7±5.6	36.420±0.037	17.18±0.19	46.0±3.1	58.9±2.4	55.7±2.5	59.7±3.5	55.8±1.6
2010	202.5±6.0	36.557±0.030	17.56±0.15	49.7±3.6	67.2±1.8	64.3±1.5	67.7±2.7	59.1±2.0
2011	165.4±4.0	36.522±0.020	17.77±0.13	43.5±2.4	69.3±0.8	63.6±0.8	69.2±2.4	
<b>INACW</b>								
1992	379.7±13.0	35.889±0.031	13.67±0.20	84.4±3.1	40.7±0.8	38.6±0.7	39.1±1.1	35.7±1.0
1998	396.9±8.3	35.869±0.016	13.45±0.11	84.5±1.7	40.8±0.6	39.8±0.7	41.3±1.0	39.1±0.7
2004	385.1±11.5	35.786±0.020	13.08±0.15	90.2±2.6	45.0±1.0	44.5±1.1	46.0±1.8	41.5±0.7
2010	413.3±13.8	35.865±0.029	13.45±0.19	87.2±3.2	47.5±1.6	48.4±1.4	50.3±2.0	46.0±1.1
2011	391.8±12.0	35.907±0.023	13.72±0.16	79.9±2.5	51.3±0.5	50.2±0.6	52.3±1.3	
<b>AAIW</b>								
1992	812.0±19.1	35.235±0.015	8.38±0.16	155.0±1.9	13.3±0.8	15.4±0.9	16.0±1.3	13.1±1.2
1998	829.5±11.8	35.297±0.008	8.59±0.09	143.9±1.1	17.1±0.8	19.0±0.9	21.5±1.1	15.0±0.7
2004	820.1±17.5	35.276±0.013	8.51±0.14	147.0±1.5	18.7±1.1	20.5±1.2	22.6±1.6	16.1±0.7
2010	839.3±13.9	35.272±0.010	8.48±0.12	148.1±1.1	17.5±1.0	20.8±1.1	23.9±1.7	16.0±0.7
2011	874.6±11.8	35.279±0.008	8.29±0.09	144.2±0.9	20.1±0.6	21.7±0.6	25.7±1.4	
<b>uNADW</b>								
1992	1,703.6±45.1	35.104±0.010	4.65±0.13	102.5±2.1	7.3±0.8	9.8±1.0	10.2±1.4	5.4±2.1
1998	1,678.4±28.2	35.151±0.007	5.00±0.09	102.5±1.0	9.4±0.7	11.3±0.7	16.6±0.9	8.1±1.1
2004	1,695.6±38.7	35.133±0.008	4.90±0.12	101.5±1.7	9.7±0.9	12.1±0.8	15.3±1.4	8.3±0.9
2010	1,764.6±31.5	35.130±0.008	4.70±0.10	98.6±1.0	9.4±0.9	12.4±0.8	16.6±1.3	8.5±0.9
2011	1,503.6±22.2	35.190±0.006	5.54±0.08	109.8±1.0	12.5±0.4	14.7±0.4	20.5±1.0	
<b>INADW</b>								
1992	3,701.4±103.5	34.923±0.004	2.33±0.04	84.7±0.5	7.3±0.7	4.4±0.7	2.5±1.0	4.1±3.1
1998	3,565.0±57.5	34.927±0.002	2.37±0.03	86.4±0.4	7.2±0.5	3.4±0.6	4.1±0.9	
2004	3,734.6±70.0	34.921±0.002	2.31±0.03	85.3±0.5	7.4±0.7	4.6±0.6	3.7±1.1	
2010	3,708.2±83.0	34.925±0.003	2.35±0.03	86.6±0.5	6.8±0.7	4.1±0.8	3.8±1.2	
2011	3,698.2±75.0	34.923±0.003	2.35±0.03	88.7±0.5	8.4±0.4	4.4±0.5	5.2±1.1	

**Table 3.I\_B5.** Physico-chemical properties in Region 0 (Florida Strait, 80°W to 78°W).

	<b>Press (dbar)</b>	<b>salinity</b>	<b>Θ (°C)</b>	<b>AOU (µmol/kg)</b>	<b>φ CT0 (µmol/kg)</b>	<b>TrOCA (µmol/kg)</b>	<b>ΔC* (µmol/kg)</b>	<b>TTD (µmol/kg)</b>
<b>Florida</b>								
<b>uNACW</b>								
1992	229.1±15.7	36.552±0.066	19.08±0.60	58.9±5.9	44.9±1.5	33.0±1.6	35.6±2.5	43.7±2.0
1998	250.7±10.8	36.514±0.037	18.78±0.32	69.6±2.6	49.8±1.8	41.8±2.1	47.8±3.3	46.9±1.6
2004	241.8±28.8	36.569±0.073	19.71±0.72	51.9±5.5	56.6±1.7	48.6±1.7	52.7±2.9	
2010	261.1±18.6	36.520±0.040	18.67±0.34	53.6±5.1	62.4±1.4	54.8±1.4	58.4±2.4	56.3±1.4
2011	228.1±14.5	36.543±0.042	18.89±0.37	63.9±3.1	66.3±1.4	59.1±1.3	63.5±3.5	
<b>INACW</b>								
1992	363.5±50.3	35.654±0.120	12.86±0.75	118.8±10.1	29.8±2.2	22.2±2.2	25.5±3.5	26.3±2.8
1998	380.3±22.9	35.508±0.051	12.02±0.34	135.3±3.0	26.4±2.6	26.3±2.4	30.7±3.9	21.7±2.7
2004	396.6±38.0	35.652±0.104	12.78±0.66	117.8±11.0	31.8±2.5	30.2±2.4	36.4±3.8	
2010	472.9±29.3	35.484±0.062	11.80±0.41	126.8±5.7	32.9±1.3	36.1±1.4	35.8±2.4	28.0±1.5
2011	399.6±34.3	35.435±0.065	11.47±0.44	135.4±4.4	40.2±1.3	36.5±1.5	41.8±3.7	
<b>AAIW</b>								
1992	398.6±39.7	34.989±0.020	7.58±0.25	155.8±1.1	10.4±1.8	11.2±1.6	12.3±2.1	11.8±2.2
1998	561.8±31.7	34.951±0.017	7.24±0.27	157.9±1.4	16.7±4.2	17.2±4.1	23.0±6.8	9.4±3.3
2004	611.3±47.1	35.061±0.077	8.04±0.58	155.1±6.3	11.0±2.5	9.4±2.2	14.5±4.2	
2010	665.7±44.8	34.988±0.028	7.38±0.21	164.0±16.8	16.4±2.3	18.5±2.5	21.0±3.3	11.9±2.3
2011	545.0±49.7	34.940±0.012	7.10±0.20	158.9±0.7	21.2±2.0	17.9±2.2	23.6±4.2	

**Table 3.1\_C1.** Decadal Trend (DT) ( $\mu\text{mol kg}^{-1} \text{yr}^{-1}$ ) and Transient Stationary State Rate (TSSR) ( $\mu\text{mol kg}^{-1} \text{yr}^{-1}$ ) by using each  $C_{\text{ant}}$  method ( $\varphi C_T^0$ , TrOCA,  $\Delta C^*$  and TTD), for each box of the A05 section. The weighted DT and the mean TSSR of the four methods are shown in bold. The averaged time-normalized estimates of  $[C_{\text{ant}}]$  ( $C_{\text{ant}} 2000$ ,  $\mu\text{mol kg}^{-1}$ ) are also shown in bold.

Layer Region	Decadal Trend (DT)				Weighted	Transient Stationary State Rate (TSSR)				$C_{\text{ant}}^{2000}$
	$\varphi C_T^0$	TrOCA	$\Delta C^*$	TTD		$\varphi C_T^0$	TrOCA	$\Delta C^*$	TTD	
<b>uNACW</b>										
Florida	1.08±0.09	1.28±0.09	1.30±0.18	0.71±0.13	<b>0.98±0.12</b>	0.89±0.04	0.75±0.04	0.82±0.05	0.82±0.04	<b>0.82±0.09</b>
R1	0.96±0.05	1.14±0.04	1.17±0.08	0.60±0.07	<b>0.87±0.06</b>	0.86±0.03	0.72±0.03	0.77±0.03	0.90±0.04	<b>0.81±0.08</b>
R2	0.99±0.04	1.09±0.03	1.21±0.06	0.71±0.06	<b>0.94±0.05</b>	0.87±0.03	0.75±0.03	0.81±0.03	0.90±0.04	<b>0.83±0.07</b>
R3	1.00±0.06	0.90±0.06	1.06±0.16	0.80±0.12	<b>0.91±0.09</b>	0.92±0.04	0.84±0.03	0.89±0.04	0.92±0.06	<b>0.89±0.06</b>
R4	0.99±0.10	0.99±0.10	0.99±0.19	1.01±0.35	<b>1.00±0.18</b>	0.96±0.04	0.91±0.04	0.95±0.05	0.89±0.06	<b>0.93±0.06</b>
<b>INACW</b>										
Florida	0.48±0.11	0.77±0.12	0.72±0.24	0.15±0.16	<b>0.41±0.15</b>	0.51±0.04	0.48±0.04	0.54±0.06	0.53±0.05	<b>0.50±0.07</b>
R1	0.49±0.08	0.56±0.07	0.54±0.14	0.32±0.10	<b>0.44±0.10</b>	0.59±0.03	0.57±0.03	0.59±0.04	0.58±0.04	<b>0.57±0.05</b>
R2	0.40±0.06	0.47±0.05	0.59±0.10	0.45±0.08	<b>0.46±0.07</b>	0.62±0.03	0.60±0.03	0.64±0.03	0.63±0.03	<b>0.61±0.05</b>
R3	0.37±0.06	0.41±0.06	0.55±0.10	0.60±0.09	<b>0.50±0.08</b>	0.68±0.03	0.68±0.03	0.70±0.03	0.71±0.04	<b>0.68±0.05</b>
R4	0.53±0.06	0.62±0.05	0.70±0.09	0.56±0.07	<b>0.58±0.07</b>	0.72±0.03	0.71±0.03	0.73±0.03	0.71±0.04	<b>0.71±0.04</b>
<b>AAIW</b>										
Florida	0.38±0.15	0.28±0.13	0.38±0.24	0.03±0.18	<b>0.19±0.17</b>	0.24±0.04	0.24±0.04	0.30±0.07	0.20±0.04	<b>0.25±0.08</b>
R1	0.43±0.08	0.42±0.07	0.48±0.15	0.31±0.09	<b>0.37±0.09</b>	0.31±0.02	0.35±0.02	0.36±0.04	0.28±0.03	<b>0.32±0.05</b>
R2	0.29±0.04	0.29±0.04	0.37±0.07	0.15±0.06	<b>0.24±0.05</b>	0.27±0.02	0.32±0.02	0.34±0.02	0.25±0.02	<b>0.29±0.05</b>
R3	0.08±0.06	0.04±0.06	0.22±0.09	0.03±0.07	<b>0.06±0.07</b>	0.27±0.02	0.31±0.02	0.34±0.03	0.27±0.02	<b>0.29±0.06</b>
R4	0.27±0.05	0.29±0.05	0.43±0.09	0.16±0.08	<b>0.25±0.07</b>	0.28±0.02	0.31±0.02	0.35±0.03	0.30±0.02	<b>0.30±0.05</b>
<b>uNADW</b>										
R1	0.42±0.05	0.52±0.05	0.54±0.08	0.47±0.06	<b>0.48±0.06</b>	0.30±0.01	0.39±0.02	0.38±0.02	0.30±0.02	<b>0.34±0.05</b>
R2	0.09±0.04	0.15±0.04	0.22±0.06	0.20±0.05	<b>0.17±0.05</b>	0.23±0.01	0.31±0.01	0.32±0.02	0.18±0.01	<b>0.26±0.06</b>
R3	0.06±0.04	0.08±0.04	0.28±0.07	0.11±0.08	<b>0.12±0.06</b>	0.16±0.01	0.21±0.01	0.25±0.02	0.12±0.02	<b>0.19±0.06</b>
R4	0.19±0.04	0.20±0.05	0.38±0.08	0.16±0.11	<b>0.21±0.07</b>	0.15±0.01	0.19±0.01	0.25±0.02	0.13±0.02	<b>0.18±0.05</b>
<b>INADW</b>										
R1	0.19±0.05	0.26±0.05	0.26±0.08	0.18±0.07	<b>0.21±0.06</b>	0.19±0.01	0.20±0.01	0.12±0.02	0.22±0.02	<b>0.18±0.04</b>
R2	-0.01±0.03	0.02±0.03	0.10±0.05	0.14±0.06	<b>0.07±0.05</b>	0.15±0.01	0.14±0.01	0.09±0.01	0.12±0.01	<b>0.12±0.03</b>
R3	-0.02±0.03	-0.05±0.03	0.06±0.06	0.13±0.21	<b>0.01±0.06</b>	0.12±0.01	0.08±0.01	0.06±0.01	0.09±0.06	<b>0.09±0.04</b>
R4	0.02±0.04	0.01±0.04	0.09±0.07	--	<b>0.03±0.05</b>	0.12±0.01	0.07±0.01	0.06±0.02	0.08±0.06	<b>0.08±0.03</b>
<b>AABW</b>										
R1	0.11±0.10	0.20±0.10	0.16±0.19	0.05±0.16	<b>0.11±0.14</b>	0.16±0.03	0.11±0.03	0.08±0.04	0.14±0.03	<b>0.12±0.05</b>
R2	-0.05±0.04	-0.03±0.04	-0.03±0.07	0.04±0.06	<b>0.00±0.05</b>	0.15±0.01	0.10±0.01	0.07±0.02	0.09±0.01	<b>0.11±0.04</b>

## References

- Álvarez, M., Pérez, F.F., Shoosmith, D.R., Bryden, H.L., 2005. Unaccounted role of Mediterranean Water in the draw-down of anthropogenic carbon. *Journal of Geophysical Research: Oceans* (1978–2012), 110.
- Álvarez, M., Ríos, A.F., Pérez, F.F., Bryden, H.L., Rosón, G., 2003. Transports and budgets of total inorganic carbon in the subpolar and temperate North Atlantic. *Global Biogeochemical Cycles*, 17, 1002.
- Anderson, L.A., Sarmiento, J.L., 1994. Redfield ratios of remineralization determined by nutrient data analysis. *Global Biogeochemical Cycles*, 8, 65-80.
- Bates, N.R., 2007. Interannual variability of the oceanic CO<sub>2</sub> sink in the subtropical gyre of the North Atlantic Ocean over the last 2 decades. *Journal of Geophysical Research: Oceans*, 112, C09013.
- Bates, N.R., 2012. Multi-decadal uptake of carbon dioxide into subtropical mode water of the North Atlantic Ocean. *Biogeosciences*, 9, 2649-2659.
- Bates, N.R., Best, M.H.P., Neely, K., Garley, R., Dickson, A.G., Johnson, R.J., 2012. Detecting anthropogenic carbon dioxide uptake and ocean acidification in the North Atlantic Ocean. *Biogeosciences* 9, 2509-2522.
- Brewer, P.G., 1978. Direct observation of the oceanic CO<sub>2</sub> increase. *Geophysical Research Letters*, 5, 997-1000.
- Broecker, W.S., Peng, T.H., 1974. Gas exchange rates between air and sea. *Tellus*, 26, 21-35.
- Brown, P.J., Bakker, D.C.E., Schuster, U., Watson, A.J., 2010. Anthropogenic carbon accumulation in the subtropical North Atlantic. *Journal of Geophysical Research-Oceans*, 115, 4016.
- Castaño-Carrera, M., Pardo, P.C., Álvarez, M., Lavín, A., Rodríguez, C., Carballo, R., Ríos, A.F., Pérez, F.F., 2012. Anthropogenic carbon and water masses in the bay of Biscay. *Scientia Marina*, 38, 191-207.
- Chen, G.T., Millero, F.J., 1979. Gradual increase of oceanic CO<sub>2</sub>. *Nature*, 277, 205-206.
- Clayton, T.D., Byrne, R.H., 1993. Spectrophotometric seawater pH measurements: total hydrogen ion concentration scale calibration of m-cresol purple and at-sea results. *Deep Sea Research Part I: Oceanographic Research Papers*, 40, 2115-2129.
- Cunningham, S.A., 2005. Cruise Report No. 54. RRS Discovery Cruise D279, 04 Apr - 10 May 2004. A Transatlantic hydrographic section at 24.5°N. . Southampton Oceanography Centre.
- Dickson, A.G., Millero, F.J., 1987. A comparison of the equilibrium constants for the dissociation of carbonic acid in seawater media. *Deep Sea Research Part A. Oceanographic Research Papers* 34, 1733-1743.
- Dickson, A.G., Sabine, C.L., Christian, J.R., 2007. Guide to best practices for ocean CO<sub>2</sub> measurements.
- Fajar, N.M., Pardo, P.C., Carracedo, L., Vázquez-Rodríguez, M., Ríos, A.F., Pérez, F.F., 2012. Trends of anthropogenic CO<sub>2</sub> along 20°W in the Iberian Basin. *Scientia Marina*, 38, 287-306.
- Flecha, S., Pérez, F.F., Navarro, G., Ruiz, J., Olivé, I., Rodríguez-Gálvez, S., Costas, E., Huertas, I.E., 2012. Anthropogenic carbon inventory in the Gulf of Cádiz. *Journal of Marine Systems*, 92, 67-75.
- Follows, M.J., Williams, R.G., Marshall, J.C., 1996. The solubility pump of carbon in the subtropical gyre of the North Atlantic. *Journal of Marine Research*, 54, 605-630.
- González-Dávila, M., Santana-Casiano, J.M., Rueda, M.J., Llinás, O., 2010. The water column distribution of carbonate system variables at the ESTOC site from 1995 to 2004. *Biogeosciences* 7, 3067-3081.
- Goyet, C., Coatanoan, C., Eischeid, G., Amaoka, T., Okuda, K., Healy, R., Tsunogai, S., 1999. Spatial variation of total CO<sub>2</sub> and total alkalinity in the northern Indian Ocean: A novel approach for the quantification of anthropogenic CO<sub>2</sub> in seawater. *Journal of Marine Research*, 57, 135-163.

- Gruber, N., 1998. Anthropogenic CO<sub>2</sub> in the Atlantic Ocean. *Global Biogeochemical Cycles*, 12, 165-191.
- Gruber, N., Sarmiento, J.L., Stocker, T.F., 1996. An improved method for detecting anthropogenic CO<sub>2</sub> in the oceans. *Global Biogeochemical Cycles*, 10, 809-837.
- Guallart, E.F., Pérez, F.F., Rosón, G., Ríos, A.F., 2013. High spatial resolution alkalinity and pH measurements by IIM-CSIC group along 24.5°N during the R/V Hespérides WOCE Section A05 cruise. (July 14 - August 15, 1992). Oak Ridge, Tennessee: Carbon Dioxide Information Analysis Center, Oak Ridge National Laboratory, US Department of Energy.
- Haine, T.W.N., Hall, T.M., 2002. A Generalized Transport Theory: Water-Mass Composition and Age. *Journal of Physical Oceanography*, 32, 1932.
- Johns, W.E., Baringer, M.O., Beal, L.M., Cunningham, S.A., Kanzow, T., Bryden, H.L., Hirschi, J.J.M., Marotzke, J., Meinen, C.S., Shaw, B., Curry, R., 2011. Continuous, Array-Based Estimates of Atlantic Ocean Heat Transport at 26.5°N. *Journal of Climate*, 24, 2429-2449.
- Johnson, K.M., Dickson, A.G., Eischeid, G., Goyet, C., Guenther, P., Key, R.M., Millero, F.J., Purkerson, D., Sabine, C.L., Schottle, R.G., Wallace, D.W.R., Wilke, R.J., Winn, C.D., 1998. Coulometric total carbon dioxide analysis for marine studies: Assessment of the quality of total inorganic carbon measurements made during the US Indian Ocean CO<sub>2</sub> survey 1994-1996. *Marine Chemistry*, 63, 21-37.
- Khatiwala, S., Tanhua, T., Mikaloff Fletcher, S., Gerber, M., Doney, S.C., Graven, H.D., Gruber, N., McKinley, G.A., Murata, A., Ríos, A.F., Sabine, C.L., Sarmiento, J.L., 2013. Global ocean storage of anthropogenic carbon. *Biogeosciences*, 10, 2169-2191.
- Körtzinger, A., Mintrop, L., Duinker, J.C., 1998. On the penetration of anthropogenic CO<sub>2</sub> into the North Atlantic Ocean. *Journal of Geophysical Research: Oceans*, 103, 18681-18689.
- Law, C.S., Watson, A.J., Liddicoat, M.I., 1994. Automated vacuum analysis of sulphur hexafluoride in seawater: derivation of the atmospheric trend (1970–1993) and potential as a transient tracer. *Marine Chemistry*, 48, 57-69.
- Lo Monaco, C., Goyet, C., Metzl, N., Poisson, A., Touratier, F., 2005. Distribution and inventory of anthropogenic CO<sub>2</sub> in the Southern Ocean: Comparison of three data-based methods. *Journal of Geophysical Research C: Oceans*, 110, 1-12.
- Macdonald, A.M., Baringer, M.O., Wanninkhof, R., Lee, K., Wallace, D.W.R., 2003. A 1998–1992 comparison of inorganic carbon and its transport across 24.5°N in the Atlantic. *Deep Sea Research Part II: Topical Studies in Oceanography*, 50, 3041-3064.
- McCartney, M.S., Talley, L.D., 1982. The Subpolar Mode Water of the North Atlantic Ocean. *Journal of Physical Oceanography*, 12, 1169-1188.
- Mehrbach, C., Culberson, C.H., Hawley, J.E., Pytkowicz, R.M., 1973. Measurement of the Apparent Dissociation Constants of Carbonic Acid in Seawater at Atmospheric Pressure. *Limnology and Oceanography*, 18, 897-907.
- Millero, F.J., Lee, K., Roche, M., 1998. Distribution of alkalinity in the surface waters of the major oceans. *Marine Chemistry*, 60, 111-130.
- Mintrop, L., Pérez, F.F., Gonzalez-Dávila, M., Santana-Casiano, J.M., Körtzinger, A., 2000. Alkalinity determination by potentiometry: intercalibration using three different methods. *Ciencias Marinas*, 26(1), 23-27.
- Nelson, N.B., Bates, N.R., Siegel, D.A., Michaels, A.F., 2001. Spatial variability of the CO<sub>2</sub> sink in the Sargasso Sea. *Deep Sea Research Part II: Topical Studies in Oceanography*, 48, 1801-1821.
- Paillet, J., Mercier, H., 1997. An inverse model of the eastern North Atlantic general circulation and thermocline ventilation. *Deep Sea Research Part I: Oceanographic Research Papers*, 44, 1293-1328.
- Peltola, E., Lee, K., Wanninkhof, R., Feely, R., Roberts, M., Greeley, D., Baringer, M., Johnson, G., Bullister, J., Mordy,

- C., Zhang, J.-Z., P. Quay, F., Millero, F., Hansell, D., Minnett, P., 2001. Chemical and Hydrographic measurements on a climate and global change cruise along 24°N in the Atlantic Ocean Woce Section A5R(repeat) during JAnuary-February 1998. Miami, Florida: Atlantic Oceanographic and Meteorological Laboratory. .
- Pérez, F.F., Vázquez-Rodríguez, M., Mercier, H., Velo, A., Lherminier, P., Ríos, A.F., 2010a. Trends of anthropogenic CO<sub>2</sub> storage in North Atlantic water masses. *Biogeosciences*, 7, 1789-1807.
- Pérez, F.F., Aristegui, J., Vázquez-Rodríguez, M., Ríos, A.F., 2010b. Anthropogenic CO<sub>2</sub> in the Azores region. *Scientia Marina*, 74, 11-19.
- Pérez, F.F., Vázquez-Rodríguez, M., Louarn, E., Padín, X.A., Mercier, H., Ríos, A.F., 2008. Temporal variability of the anthropogenic CO<sub>2</sub> storage in the Irminger Sea. *Biogeosciences* 5 (6), 1669-1679.
- Pérez, F.F., Mercier, H., Vázquez-Rodríguez, M., Lherminier, P., Velo, A., Pardo, P.C., Rosón, G., Ríos, A.F., 2013. Atlantic Ocean CO<sub>2</sub> uptake reduced by weakening of the meridional overturning circulation. *Nature Geoscience*, 6, 146-152.
- Pierrot, D., Lewis, E., Wallace, D., 2006. MS Excel Program Developed for CO<sub>2</sub> System Calculations, ORNL/CDIAC-105a. Carbon Dioxide Information Analysis Center, Oak Ridge National Laboratory, US Department of Energy, Oak Ridge, Tennessee.
- Ríos, A.F., Velo, A., Pardo, P.C., Hoppema, M., Pérez, F.F., 2012. An update of anthropogenic CO<sub>2</sub> storage rates in the western South Atlantic basin and the role of Antarctic Bottom Water. *Journal of Marine Systems*, 94, 197-203.
- Rosón, G., Ríos, A.F., Pérez, F.F., Lavín, A., Bryden, H.L., 2003. Carbon distribution, fluxes, and budgets in the subtropical North Atlantic Ocean (24.5°N). *Journal of Geophysical Research: Oceans*, 108, n/a-n/a.
- Sabine, C.L., Feely, R.A., Gruber, N., Key, R.M., Lee, K., Bullister, J.L., Wanninkhof, R., Wong, C.S., Wallace, D.W.R., Tilbrook, B., Millero, F.J., Peng, T.-H., Kozyr, A., Ono, T., Ríos, A.F., 2004. The oceanic sink for anthropogenic CO<sub>2</sub>. *Science*, 305, 367-371.
- Sabine, C.L., Tanhua, T., 2010. Estimation of Anthropogenic CO<sub>2</sub> Inventories in the Ocean. *Annual Review of Marine Science*, 2, 175-198.
- Santana-Casiano, J.M., González-Dávila, M., Rueda, M.-J., Llinás, O., González-Dávila, E.-F., 2007. The interannual variability of oceanic CO<sub>2</sub> parameters in the northeast Atlantic subtropical gyre at the ESTOC site. *Global Biogeochemical Cycles*, 21, GB1015.
- Schmitz Jr.W.J., Richardson, P.L., 1991. On the sources of the Florida Current. *Deep Sea Research Part A. Oceanographic Research Papers*, 38, Supplement 1, S379-S409.
- Schuster, U., Watson, A.J., Bakker, D.C.E., de Boer, A.M., Jones, E.M., Lee, G.A., Legge, O., Louwerse, A., Riley, J., Scally, S., 2013. Measurements of total alkalinity and inorganic dissolved carbon in the Atlantic Ocean and adjacent Southern Ocean between 2008 and 2010. *Earth Syst. Sci. Data Discuss.*, 6, 621-639.
- Smethie, W.M., Schlosser, P., Bönisch, G., Hopkins, T.S., 2000. Renewal and circulation of intermediate waters in the Canadian Basin observed on the SCICEX 96 cruise. *Journal of Geophysical Research: Oceans*, 105, 1105-1121.
- Steinfeldt, R., Rhein, M., Bullister, J.L., Tanhua, T., 2009. Inventory changes in anthropogenic carbon from 1997–2003 in the Atlantic Ocean between 20°S and 65°N. *Global Biogeochemical Cycles*, 23, GB3010.
- Steinfeldt, R., Rhein, M., Walter, M., 2007. NADW transformation at the western boundary between and. *Deep Sea Research Part I: Oceanographic Research Papers*, 54, 835-855.
- Stendardo, I., Gruber, N., Körtzinger, A., 2009. CARINA oxygen data in the Atlantic Ocean. *Earth system science data*, 1, 87-100.
- Talley, L.D., Pickard, G.L., Emery, W.J., Swift, J.H., 2011. Chapter 9 - Atlantic Ocean. *Descriptive Physical Oceanography* (Sixth Edition) (pp. 245-301). Boston: Academic Press.

- Tanhua, T., Biastoch, A., Körtzinger, A., Lüger, H., Böning, C., Wallace, D.W.R., 2006. Changes of anthropogenic CO<sub>2</sub> and CFCs in the North Atlantic between 1981 and 2004. *Global Biogeochemical Cycles*, 20, GB4017.
- Tanhua, T., Körtzinger, A., Friis, K., Waugh, D.W., Wallace, D.W.R., 2007. An estimate of anthropogenic CO<sub>2</sub> inventory from decadal changes in oceanic carbon content. *Proceedings of the National Academy of Sciences*, 104, 3037-3042.
- Tanhua, T., Steinfeldt, R., Key, R.M., Brown, P., Gruber, N., Wanninkhof, R., Pérez, F., Körtzinger, A., Velo, A., Schuster, U., van Heuven, S., Bullister, J.L., Stendardo, I., Hoppema, M., Olsen, A., Kozyr, A., Pierrot, D., Schirnick, C., Wallace, D.W.R., 2010a. Atlantic Ocean CARINA data: overview and salinity adjustments. *Earth system science data*, 2, 17-34.
- Tanhua, T., van Heuven, S., Key, R.M., Velo, A., Olsen, A., Schirnick, C., 2010b. Quality control procedures and methods of the CARINA database. *Earth system science data*, 2, 35-49.
- Tanhua, T., Waugh, D.W., Wallace, D.W.R., 2008. Use of SF6 to estimate anthropogenic CO<sub>2</sub> in the upper ocean. *Journal of Geophysical Research C: Oceans*, 113.
- Thomas, H., Ittekkot, V., 2001. Determination of anthropogenic CO<sub>2</sub> in the North Atlantic Ocean using water mass ages and CO<sub>2</sub> equilibrium chemistry. *Journal of Marine Systems*, 27, 325-336.
- Touratier, F., Azouzi, L., Goyet, C., 2007. CFC-11, Δ14C and 3H tracers as a means to assess anthropogenic CO<sub>2</sub> concentrations in the ocean. *Tellus, Series B: Chemical and Physical Meteorology*, 59, 318-325.
- Touratier, F., Goyet, C., 2004. Definition, properties, and Atlantic Ocean distribution of the new tracer TrOCA. *Journal of Marine Systems*, 46, 169-179.
- Vázquez-Rodríguez, M., Padín, X.A., Pardo, P.C., Ríos, A.F., Pérez, F.F., 2012. The subsurface layer reference to calculate preformed alkalinity and air-sea CO<sub>2</sub> disequilibrium in the Atlantic Ocean. *Journal of Marine Systems*, 94, 52-63.
- Vázquez-Rodríguez, M., Touratier, F., Lo Monaco, C., Waugh, D.W., Padín, X.A., Bellerby, R.G.J., Goyet, C., Metzl, N., Ríos, A.F., Pérez, F.F., 2009a. Anthropogenic carbon distributions in the Atlantic Ocean: data-based estimates from the Arctic to the Antarctic. *Biogeosciences*, 6, 439-451.
- Vázquez-Rodríguez, M., Padín, X.A., Ríos, A.F., Bellerby, R.G.J., Pérez, F.F., 2009b. An upgraded carbon-based method to estimate the anthropogenic fraction of dissolved CO<sub>2</sub> in the Atlantic Ocean. *Biogeosciences Discuss.*, 6, 4527.
- Velo, A., Vázquez-Rodríguez, M., Padín, X.A., Gilcoto, M., Ríos, A.F., Pérez, F.F., 2010. A multiparametric method of interpolation using WOA05 applied to anthropogenic CO<sub>2</sub> in the atlantic. *Scientia Marina*, 74, 21-32.
- Wanninkhof, R., Park, G.-H., Takahashi, T., Feely, R.A., Bullister, J.L., Doney, S.C., 2013. Changes in deep-water CO<sub>2</sub> concentrations over the last several decades determined from discrete pCO<sub>2</sub> measurements. *Deep Sea Research Part I: Oceanographic Research Papers*, 74, 48-63.
- Watson, A.J., Nightingale, P.D., Cooper, D.J., 1995. Modelling atmosphere-ocean CO<sub>2</sub> transfer. *Philosophical Transactions - Royal Society of London*, B, 348, 125-132.
- Warner, M.J., Weiss, R.F., 1985. Solubilities of chlorofluorocarbons 11 and 12 in water and seawater. *Deep Sea Research Part A: Oceanographic Research Papers*, 32, 1485-1497.
- Waugh, D.W., Haine, T.W.N., Hall, T.M., 2004. Transport times and anthropogenic carbon in the subpolar North Atlantic Ocean. *Deep-Sea Research Part I: Oceanographic Research Papers*, 51, 1475-1491.
- Waugh, D.W., Hall, T.M., McNeil, B.I., Key, R., Matear, R.J., 2006. Anthropogenic CO<sub>2</sub> in the oceans estimated using transit time distributions. *Tellus, Series B: Chemical and Physical Meteorology*, 58, 376-389.
- Yool, A., Oschlies, A., Nurser, A.J.G., Gruber, N., 2010. A model-based assessment of the TrOCA approach for estimating anthropogenic carbon in the ocean. *Biogeosciences*, 7, 723-751.



## Chapter 3.2.

Anthropogenic CO<sub>2</sub> changes  
in the Equatorial Atlantic Ocean

Fajar NM., Guallart E.F., Steinfeldt R., Ríos A.F., Pelegrí JL., Pelejero C., Calvo E., Pérez. F.F. Anthropogenic CO<sub>2</sub> changes in the Equatorial Atlantic Ocean. Progress in Oceanography. 134: 256-270.



## **CHAPTER 3.2.**

### **Anthropogenic CO<sub>2</sub> changes in the Equatorial Atlantic Ocean**

*Fajar N. M., Guallart E. F., Steinfeldt R., Ríos A. F.,<sup>1</sup> Pelegrí J. L., Pelejero C., Calvo E., Pérez F. F.*

#### **Abstract**

Methods based on CO<sub>2</sub> and chlorofluorocarbon (CFC) data are used to describe and evaluate the anthropogenic CO<sub>2</sub> (C<sub>ant</sub>) concentrations, C<sub>ant</sub> specific inventories, and C<sub>ant</sub> storage rates in the Equatorial Atlantic Ocean. The C<sub>ant</sub> variability in the water masses is evaluated from the comparison of two hydrographic sections along 7.5° N carried out in 1993 and 2010. During both cruises, high C<sub>ant</sub> concentrations are detected in the upper layers, with values decreasing progressively towards the deep layers. Overall, the C<sub>ant</sub> concentrations increase from 1993 to 2010, with a large increment in the upper North Atlantic Deep Water layer of about  $0.18 \pm 0.03 \text{ } \mu\text{mol}\cdot\text{kg}^{-1}\cdot\text{y}^{-1}$ . In 2010, the C<sub>ant</sub> inventory along the whole section amounts to  $58.9 \pm 2.2$  and  $45.1 \pm 2.0 \text{ mol}\cdot\text{m}^{-2}$  using CO<sub>2</sub> and CFC based methods, respectively, with most C<sub>ant</sub> accumulating in the western basin. Considering the time elapsed between the two cruises, C<sub>ant</sub> storage rates of  $1.01 \pm 0.18$  and  $0.75 \pm 0.17 \text{ mol}\cdot\text{m}^{-2}\cdot\text{y}^{-1}$  (CO<sub>2</sub> and CFC based methods, respectively) are obtained. Below ~1000 m, these rates follow the pace expected from a progressive increase of C<sub>ant</sub> at steady state; above ~1000 m, C<sub>ant</sub> increases faster, mainly due to the retreat of the Antarctic Intermediate Waters.

## Introduction

Since the beginning of the industrial revolution, humankind has emitted large quantities of CO<sub>2</sub> into the atmosphere (Le Quéré *et al.*, 2009), raising global atmospheric CO<sub>2</sub> concentrations from 280 ppm at the start of industrial revolution to nearly ~ 400 ppm by the end of 2013 (Tans and Keeling, 2014). This increase has been mainly caused by the anthropogenic release of CO<sub>2</sub> to the atmosphere from fossil fuel combustion, deforestation, and other land-use change activities. Fuel combustion has become the dominant source of anthropogenic emissions to the atmosphere since around 1920 (Le Quéré *et al.*, 2013). Only a portion of the CO<sub>2</sub> emitted to the atmosphere is accumulated there, as nearly 55% of the anthropogenic CO<sub>2</sub> (C<sub>ant</sub>) is taken up by the ocean and the terrestrial biosphere (Le Quéré *et al.*, 2009; Ballantyne *et al.*, 2012). Ongoing efforts are being made to quantify the magnitude of these two sinks with high accuracy. Model results, for example, constrain the mean CO<sub>2</sub> uptake rates of the land and the ocean to  $2.9 \pm 0.8$  and  $2.6 \pm 0.5$  PgC·yr<sup>-1</sup>, respectively, for the period 2004–2013 (Le Quéré *et al.*, 2014). Over the last 200 years, the ocean has acted as a growing net CO<sub>2</sub> sink (Gruber *et al.*, 2009). There is evidence suggesting that the oceanic uptake fraction, the net CO<sub>2</sub> emissions taken up by the ocean, was possibly lower during 1980–2005 ( $37 \pm 7\%$ ) as compared to 1750–1994 ( $42 \pm 7\%$ ) (Sabine *et al.*, 2004), even though the uncertainty in the estimates is larger than the difference between them. This decrease in the ocean uptake fraction may be related to the increase in the terrestrial sink (Ciais *et al.*, 2013). Also this decrease in the oceanic uptake fraction is consistent with the current understanding that the ocean CO<sub>2</sub> sink is limited by the transport rate of CO<sub>2</sub> from the surface to the deep ocean (Zeebe, 2012). It is also in agreement with the known nonlinearity of the carbonate chemistry, according to which the CO<sub>2</sub> uptake capacity of seawater is reduced as its CO<sub>2</sub> concentration increases (Zeebe and Wolf-Gladrow, 2001).

In order to better constrain the oceanic CO<sub>2</sub> budget, oceanographers have focused on separating the C<sub>ant</sub> signal from the natural CO<sub>2</sub>. However, estimating the anthropogenic component of the total inorganic carbon (C<sub>T</sub>) is a difficult task because C<sub>ant</sub> cannot be directly measured and its signal in the ocean is only a small perturbation (of the order of a few percentage points at most) on the natural background distribution of CO<sub>2</sub>. In the late 1970s, several studies used different calculations based on total alkalinity (A<sub>T</sub>), C<sub>T</sub>, and dissolved oxygen measurements to estimate the C<sub>ant</sub> concentration ([C<sub>ant</sub>]), the so-called back-calculation techniques. Since the first approaches by Brewer (1978) and Chen and Millero (1979), several authors have tried to improve the methods of estimating C<sub>ant</sub> [ $\Delta C^*$  (Gruber *et al.*, 1996), LM05 (Lo Monaco *et al.*, 2005), TrOCA (Touratier *et al.*, 2007), or  $\phi C_T^0$  (Vázquez-Rodríguez *et al.*, 2009a)], all of them with strengths and weaknesses (van Heuven *et al.*, 2011). In addition, other C<sub>ant</sub> estimation techniques use tracers such as chlorofluorocarbons (CFCs), for example the Transit Time Distribution (TTD) (Waugh *et al.*, 2004, 2006) or the “short-cut method” (Thomas and Ittekkot, 2001), and other authors estimate C<sub>ant</sub> using multiple linear regression approaches (MLR and eMLR) based on independent chemical and hydrographic parameters (Friis *et al.*, 2005; Tanhua *et al.*, 2007; Wanninkhof *et al.*, 2010). Khatiwala *et al.* (2013) suggested that a combination of C<sub>ant</sub> estimation methods is necessary to achieve a robust quantification of the C<sub>ant</sub> ocean sink. In the

present study, two methods are used to estimate the [C<sub>ant</sub>] in the Equatorial Atlantic Ocean: the  $\phi C_T^0$  method based on CO<sub>2</sub> data and the TTD method based on CFC data.

The interplay of air-sea exchange processes and ocean circulation in the winter mixed layer (WML) determines the properties of a water mass, such as salinity, temperature, preformed components of nutrient salts, and tracers of atmospheric origin. These properties are subsequently transported into the ocean interior, where they mix with other water parcels from different winter mixing layers. Hence, the local water mass properties at any point in the interior are determined considering the different transit times since the different water parcels last contacted the surface. The back-calculation techniques assume a steady state (SS) of the ocean properties, which makes it possible to calculate the biological impact on the carbon cycle from the oxygen and nutrient observations, with the empirical relationship of the preformed C<sub>T</sub> and A<sub>T</sub> in the WML. Also, a steady state of the ocean properties is an underlying assumption of the MLR methods when using a single parametrization that fits the natural C<sub>T</sub> between cruises (Plancherel *et al.* 2014). The TTD method (Waugh *et al.* 2004) and Green's function method (Khatiwala *et al.* 2009) also assume a steady state in the ocean transport that permits each point of the ocean to be linked with the surface. Moreover, based on earlier studies of transient tracers (Keeling and Bolin, 1967; Broecker *et al.*, 1979), Holfort *et al.* (1998), Alvarez *et al.* (2003), and Rosón *et al.* (2003) determined the volumetrically integrated C<sub>ant</sub> storage rate proportionally to the temporal increase of [C<sub>ant</sub>] in the WML. Tanhua *et al.* (2007) infer the C<sub>ant</sub> inventories in the subtropical North Atlantic from the decadal C<sub>ant</sub> storage rate computed using eMLR and assuming a steady state. Previously, Tanhua *et al.* (2006), from a comparison of the observed changes in C<sub>T</sub> and CFC fields with those predicted from an eddy-permitting ocean circulation model, found that C<sub>ant</sub> is in transient steady state in the North Atlantic. This means that C<sub>ant</sub> increases over time through the whole water column in a manner that is proportional to the time-dependent of [C<sub>ant</sub>] in the WML. Hence, changes in [C<sub>ant</sub>] for a given time period can be determined from [C<sub>ant</sub>] considering the exponential fit  $[C_{ant}] = Ae^{\lambda t}$ , which describes the history of atmospheric CO<sub>2</sub> and [C<sub>ant</sub>] in the ocean surface WML since the Industrial Revolution (Tanhua *et al.*, 2007; Steinfeldt *et al.*, 2009; Khatiwala *et al.*, 2013; Pérez *et al.*, 2013). Under a steady-state approximation, the time derivative of [C<sub>ant</sub>] (C<sub>ant</sub> storage rate) can be calculated by multiplying the inventory of [C<sub>ant</sub>] by the annual growth rate ( $\lambda$ ), that is, SS\_ΔC<sub>ant</sub> rate =  $\lambda[C_{ant}]$ . Steinfeldt *et al.* (2009) reported an annual rate of increase of 1.69% for the factor  $\lambda$ . Based on the estimated variability in the increase in [C<sub>ant</sub>] in the surface, the uncertainty associated with  $\lambda$  was found to be 0.10 %.

Historically, and because of its important role in deep water formation, the northern North Atlantic region has been sampled far more than the tropics. Nonetheless, it is of crucial importance to expand our knowledge from subpolar to tropical regions to better understand the dynamics and biogeochemical characteristics of the whole North Atlantic Ocean. In terms of C<sub>ant</sub>, there are several works on the Atlantic Ocean that include C<sub>ant</sub> estimations in the Equatorial Atlantic (Lee *et al.*, 2003; Steinfeldt *et al.*, 2009; Vázquez-Rodríguez *et al.*, 2009b; Ríos *et al.*, 2010; Wanninkhof *et al.*, 2010), although none of them described the variability of

the C<sub>ant</sub> storage rate along this equatorial region. Inverse estimates of the atmospheric CO<sub>2</sub> absorption by the global ocean found considerable C<sub>ant</sub> uptake at the equator and in the tropics (Mikaloff Fletcher *et al.*, 2006), favoured by the low Revelle factors of tropical and subtropical warm waters that facilitate the absorption of atmospheric C<sub>ant</sub>. However, Lee *et al.* (2003) reported relatively small total and specific inventories in the tropical Atlantic. The absorbed C<sub>ant</sub> at these low latitudes appears to be mostly advected northward along the surface with low depth penetration. In fact, the tropical Atlantic is the main contributor to North Atlantic C<sub>ant</sub> storage associated with the upper limb of the overturning circulation (Álvarez *et al.*, 2003). Taking into account the role of the oceanic circulation in the distribution of C<sub>ant</sub> between basins and the potential temporal change of the C<sub>ant</sub> storage at regional scales (Gruber *et al.*, 1996), a reassessment of the C<sub>ant</sub> storage rates and the specific inventories in different oceanic regions is necessary to better constrain how the ocean carbon cycle evolves on decadal scales in the face of climate change.

The 7.5°N section is situated in a dynamically complex area (Figure 3.2.1) characterized by currents flowing mainly in the zonal direction: the North Equatorial (NEC) and the South Equatorial (SEC) currents (branches of the subtropical gyres), which are separated by the Eastward Equatorial Undercurrent (EUC), the North Equatorial Countercurrent (NECC), and the North Equatorial Undercurrent (NEUC). The structure and variability of all of them are largely driven by the wind field over the tropical Atlantic, in particular by the variability and/or movement of the Intertropical Convergence Zone (ITCZ) (Stramma and Schott, 1999; Urbano *et al.*, 2008; Rosell-Fieschi *et al.*, 2015). In the western basin the section is situated two to three degrees to the north of the NEUC (Arhan *et al.*, 1998), while in the eastern basin, it lies in the southern margin of the Guinea Dome (Brandt *et al.*, 2010).

The vertical thermohaline structure of the 7.5° N section is characterized by six main water masses (Figure 3.2.2), which are used here to divide the section into density layers. The surface is dominated by the South Atlantic Central Water (SACW) (Stramma and England, 1999; Stramma and Schott, 1999), which is formed in the confluence zone of the Brazil and Falkland currents. The SACW is transported within the South Atlantic Current (SAC) until it flows into the SEC. The Sub-Antarctic Mode Water (SAMW) extends from near the surface to more than 600 m depth (Herraiz-Borreguero and Rintoul, 2011). The SAMW is formed in the South Atlantic, at about 40° S, and is transported by the anti-cyclonic circulation in the South Atlantic subtropical gyre (Tsuchiya *et al.*, 1994). The Antarctic Intermediate Water (AAIW) spans around 1000 m of depth (Murata *et al.*, 2008), originating from subduction of surface waters in the northern Drake Passage and the Falkland Current loop (Stramma and England, 1999; Stramma and Schott, 1999). The North Atlantic Deep Water (NADW), located between 1200 and 4500 m, is formed by the confluence of deep waters formed in the Nordic and Labrador Seas and is then transported towards the equator by the Deep Western Boundary Current (DWBC) (Steinfeldt *et al.*, 2007). Finally, the bottom waters are characterized by the Antarctic Bottom Water (AABW) (Rhein *et al.*, 1998), formed by the confluence of water masses originating in different locations around Antarctica (Johnson, 2008), which are exported northward and ventilate the ocean's bottom layer.

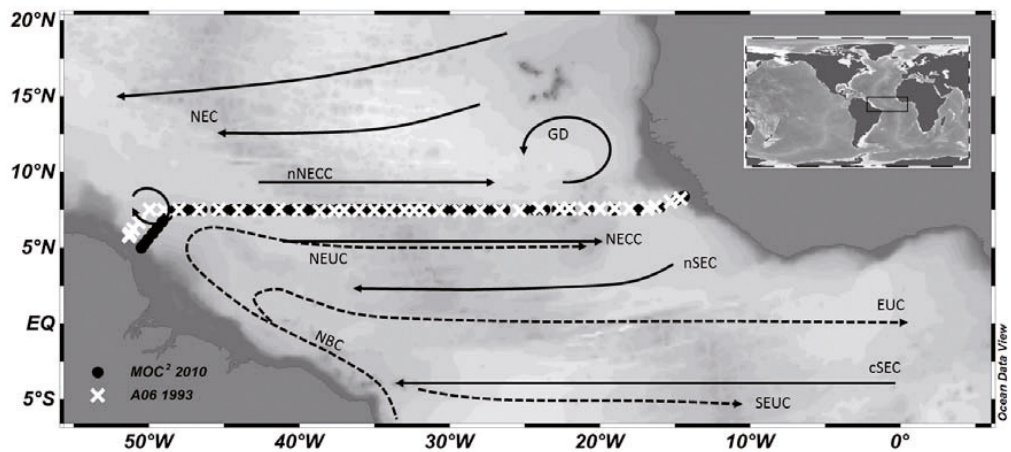


**Figure 3.2.1.** Stations of the A06 cruise of 1993 (black dots) and MOC2 cruise of 2010 (white crosses) along 7.5° N, together with a schematic diagram of the shallow circulation in the Subtropical and Tropical Atlantic. Surface (black solid arrows) and thermocline (black dashed arrows). Currents shown are the North Equatorial Current (NEC), the north and central South Equatorial Current (nSEC, cSEC), the North Equatorial Counter-current (NECC), the North Brazil Current (NBC), the North and South Equatorial Under Current (NEUC, SEUC), the Equatorial Under Current (EUC), and the cyclonic circulation around the Guinea Dome (GD). Adapted from Brandt et al. (2012, 2010).

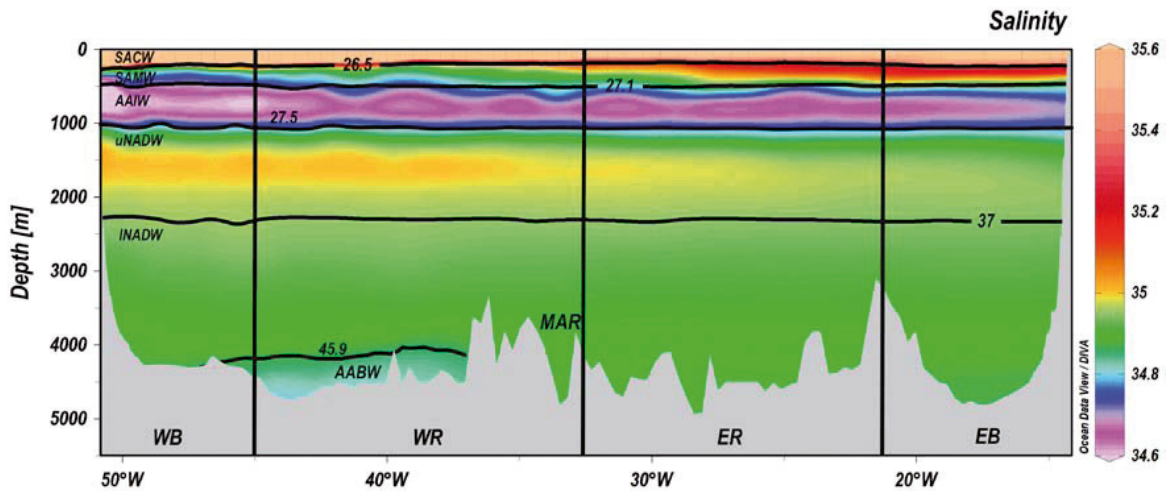


**Figure 3.2.2.** Vertical distribution of salinity along the 7.5° N section in 2010 (MOC2). Vertical black lines mark the division into regions: The Western Boundary (WB) and Western Ridge (WR) regions are located westward of the Mid-Atlantic Ridge (MAR) while the Eastern Ridge (ER) and Eastern Boundary (EB) regions are located eastward. Black horizontal lines correspond to the isopycnals used to separate the section into different layers, according to the water mass properties. From the sea surface toward deep-waters, the reference density levels are  $\sigma_0 = 26.5$ ,  $\sigma_2 = 27.1$ ,  $\sigma_4 = 27.5$ ,  $\sigma_6 = 37$ , and  $\sigma_8 = 45.9$ ; subscripts 0, 2, and 4 refer to the reference pressures of 0, 2000, and 4000 dbar, respectively.

Recent studies have demonstrated the existence of substantial changes in the Atlantic Meridional Overturning Circulation (AMOC) at the equatorial Atlantic Ocean (San Antolín Plaza *et al.*, 2012; Hernández-Guerra *et al.*, 2014), mostly affecting the AAIW and uNADW. These changes in circulation, together with the high increase of C<sub>ant</sub> between 1989 and 2005 in the South Atlantic as compared with the North Atlantic (Wanninkhof *et al.*, 2010), suggest the existence of major processes that affect C<sub>ant</sub> in the equatorial Atlantic Ocean. Our objective is to use the two occupations of the 7.5° N section in order to assess the changes in C<sub>ant</sub> in the Equatorial North Atlantic between 1993 and 2010. The section is divided into different layers according to the main water masses present in the section and the layers are further split them into different zonal regions according to the hydrographic features and bathymetry. The C<sub>ant</sub> specific inventories are computed and the C<sub>ant</sub> storage rates are evaluated and compared to the expected rates under the assumption of a steady state.

## Data and methodology

### Cruises

In 2010, the MOC2-Equatorial cruise (hereinafter MOC2) sailed the 7.5° N section eastward, following the same route as the first WOCE A06 cruise (hereinafter A06) in 1993. The section extends from the north-eastern coast of South America, at ~ 51.3° W, to the western coast of Central Africa, at ~14.4° W (Figure 3.2.1).

### MOC2 in 2010

The MOC2 2010 cruise was carried out on board the Spanish R/V Hespérides from April to May 2010 (Ríos *et al.*, 2012a), completing 59 full depth CTD casts (Figure 3.2.1). The distance between stations was 30 nautical miles from the coast of South America to the Mid-Atlantic Ridge (MAR) and ~60 nautical miles from the MAR to the African coast. An SBE911plus CTD probe was used for the station-based profiling of the water column. The CTD unit was equipped with temperature and conductivity sensors and a SBE-43 oxygen probe. The rosette was equipped with 24 Niskin bottles of 12 L. At each station, samples were taken for dissolved oxygen (O<sub>2</sub>), inorganic nutrients, A<sub>T</sub>, and pH at 24 depths throughout the whole water column, and samples for C<sub>T</sub> were taken at four depth levels. Water samples in glass ampoules for the analysis of CFCs were drawn at least at every second station.

Samples were analysed on board for inorganic nutrients, O<sub>2</sub>, A<sub>T</sub>, and pH, while C<sub>T</sub> samples were poisoned with 300 µL of saturated HgCl<sub>2</sub> and stored in darkness until their analysis in the CO<sub>2</sub> lab of the Marine Research Institute (IIM-CSIC) in Vigo (Spain). The O<sub>2</sub> measurements were performed following the modified Winkler method (Culberson, 1991) with a potentiometric titration, where the O<sub>2</sub> content of the sample transforms iodide into iodine that is titrated with thiosulfate afterwards. The samples of A<sub>T</sub> were analysed by an endpoint method using an automatic potentiometric titrator with a combined glass electrode (Mintrop *et al.*, 2000), in which the titration was carried out using two pH endpoints (Pérez and Fraga, 1987). The seawater pH measurements were obtained on the total scale using the spectrophotometric method described

by Clayton and Byrne (1993), adding m-Cresol Purple as an indicator, controlling the temperature at 25 °C with a thermostatic bath, and introducing a correction of +0.0047 pH units (DelValls and Dickson, 1998). The C<sub>T</sub> samples were measured using a SOMMA (Single-Operator Multiparameter Metabolic Analyzer) system, where an aliquot of 20 mL is acidified with H<sub>3</sub>PO<sub>4</sub> in a glass stripping chamber and the CO<sub>2</sub> gas formed is carried into a coulometric cell by a CO<sub>2</sub>-free gas (N<sub>2</sub>), where the titration is performed (Johnson *et al.*, 1993). Both A<sub>T</sub> and C<sub>T</sub> measurements were calibrated with CO<sub>2</sub> certified reference material provided by Dr Andrew Dickson (Scripps Institute of Oceanography). Since C<sub>T</sub> was not measured at all levels of the water column, it was calculated from A<sub>T</sub> and pH data using the thermodynamic equations of the carbonate system and the CO<sub>2</sub> dissociation constants from Mehrbach *et al.* (1973), refitted by Dickson and Millero (1987).

The good agreement between the measured and calculated C<sub>T</sub> values is evidenced by their linear fit, yielding a correlation coefficient ( $r^2$ ) of 0.998 (Ríos *et al.*, 2012a) with a slope of  $1.003 \pm 0.006$  and a mean difference of  $2.8 \pm 3.9 \mu\text{mol}\cdot\text{kg}^{-1}$  ( $n = 43$ ). The secondary quality control (2ndQC), that is, the crossover analysis method (Key *et al.*, 2010; Tanhua *et al.*, 2010) was applied to MOC2 data [O<sub>2</sub>, pH, A<sub>T</sub> and C<sub>T</sub>, phosphate (PO<sub>4</sub><sup>3-</sup>) and nitrate (NO<sub>3</sub><sup>-</sup>)] for waters deeper than 3500 m, where the long-term changes are minimal or within the analytical method uncertainties. Only PO<sub>4</sub><sup>3-</sup> and NO<sub>3</sub><sup>-</sup> needed to be bias-adjusted by multiplicative factors of 1.03 and 1.01, respectively, while the remaining parameters showed offsets indistinguishable from zero within the CARINA and GLODAP uncertainties (Tanhua *et al.*, 2010), further attesting the good quality of the data. The CFC ampoules were flame sealed on board and then sent to the tracer lab at the University of Bremen, where they were measured with a gas chromatographic system as described in Bulsiewicz *et al.* (1998). The detection limit is 0.003 pmol·kg<sup>-1</sup> for both CFC-11 and CFC-12, and the accuracy is 2% or 0.008 pmol·kg<sup>-1</sup>, whichever is greater. All data were compiled and are available at the CLIVAR and Carbon Hydrographic Data Office (CCHDO) (<http://cchdo.ucsd.edu/cruise/29HE20100405>).

#### A06 in 1993

February–March 1993, the Cither-I cruise (WOCE A06 line) was carried out along the parallel 7.5° N on board the French R/V L'Atalante (Oudot, 1993). CTD profiles of potential temperature ( $\Theta$ ), salinity (S), and O<sub>2</sub> (Arhan *et al.*, 1998) were obtained at each station, separated by ~30 nautical miles except over the continental slopes, where spacing was reduced to 10–20 nautical miles (Oudot *et al.*, 1998). The rosette was equipped with 32 Niskin bottles of 8 L. Samples for O<sub>2</sub>, nutrients, CFC-11, and CFC-12 were also taken at each station along the cruise (Andrié *et al.*, 1998). In addition, pH and C<sub>T</sub> samples were taken every two stations and analysed on board (Oudot and Ternon, 1994; Oudot *et al.*, 1995; Ternon *et al.*, 2001). pH was measured at 25 °C and based on the total hydrogen ion concentration scale (pH<sub>T25</sub>), using a Ross combination electrode calibrated with Tris buffer, and C<sub>T</sub> samples were analysed by gas chromatography (Oudot and Ternon, 1994; Oudot *et al.*, 1995; Ternon *et al.*, 2001). The poor quality and noise of the C<sub>T</sub> data prevented their inclusion in the GLODAP global compilation (Wanninkhof *et al.*, 2003). The original pH data of the A06 1993 cruise used by Ternon *et al.* (2001), together with the remaining hydrographic and biogeochemical data, including CFC-11 and CFC-12, are available at the CCHDO.

The θ, S, nutrients and O<sub>2</sub> data were corrected following the recommendations of Gouretski and Jancke (2000) and their confidence was confirmed by application of the crossover analysis (Key *et al.*, 2010; Tanhua *et al.*, 2010). The pH data set was reported to CCHDO at seawater scale and in situ temperature ( $\text{pH}_{\text{SWSin situ}}$ ) (Oudot and Ternon, 1994; Ternon *et al.*, 2001). Hence, as described in Oudot and Ternon (1994), we reverted the equations to transform the reported  $\text{pH}_{\text{SWSin situ}}$  into the initially measured  $\text{pH}_{T25}$  (Gieskes, 1969; Millero, 1979) and finally rescaled them to  $\text{pH}_{\text{SWS}25}$  (van Heuven *et al.*, 2009). A 2ndQC was applied, finding only a positive bias of 0.007 pH units east of the MAR, which was corrected in the present work by adding -0.007 units. In order to estimate [C<sub>ant</sub>], A<sub>T</sub> and C<sub>T</sub> are needed. Thus, a 3D moving window multilinear regression algorithm (Velo *et al.*, 2013) was used to estimate the A<sub>T</sub> data. This algorithm was developed to fill gaps in the A<sub>T</sub> of the CARINA and GLODAP data collections for the Atlantic Ocean, generating values with estimated uncertainties of about 6  $\mu\text{mol}\cdot\text{kg}^{-1}$ . Afterwards, C<sub>T</sub> was computed using  $\text{pH}_{\text{SWS}25}$  and A<sub>T</sub> and the dissociation constants of Mehrbach *et al.* (1973) refitted by Dickson and Millero (1987). Finally, a last 2ndQC was used to verify the confidence of A<sub>T</sub> and C<sub>T</sub> data (Tanhua *et al.* 2010), obtaining a mean offset of  $0.8 \pm 1.6$  and  $1.1 \pm 3.3 \mu\text{mol}\cdot\text{kg}^{-1}$ , respectively (see Appendix A for details).

### Regions and water mass layers of the 7.5° N section

The 7.5° N section was divided into two basins and two regions each, and six vertical density layers (Figure 3.2.2). The western and eastern basins are divided by the MAR, located at about 32.5° W. Westward of the MAR, the Western Boundary (WB) region extends from the coast of Guiana (~ 50° W) to 45° W, enclosing the region of most AAIW and NADW influence, while the Western Ridge (WR) region extends from 45° W to 32.5° W, where the AABW signal is most evident. Eastward of the MAR, we differentiated the Eastern Ridge (ER) region, from 32.5° W to 21° W (Sierra Leone ridge), and the Eastern Boundary (EB) region, from 21° W to the African coast (~ 15° W), in order to distinguish between the Gambia abyssal plain and the Sierra Leone basin (Arhan *et al.*, 1998). The density layers were selected according to the main water masses present in the Equatorial Atlantic Ocean (Tsuchiya *et al.*, 1994; Arhan *et al.*, 1998; Stramma and England, 1999; Stramma and Schott, 1999; Mémery *et al.*, 2000; Brea *et al.*, 2004; Sarafanov *et al.*, 2007; Murata *et al.*, 2008; Herraiz-Borreguero and Rintoul, 2011).

The upper layer is dominated by the SACW, from the sea surface to the isopycnal  $\sigma_0 = 26.5 \text{ kg}\cdot\text{m}^{-3}$  (Stramma and Schott, 1999). The SACW in this region is characterized by  $\theta > 14^\circ\text{C}$  and salinities of 34.8–36.8. The SAMW layer is enclosed between  $\sigma_0 = 26.5$  and  $\sigma_0 = 27.1 \text{ kg}\cdot\text{m}^{-3}$  (Mémery *et al.*, 2000) and contains all waters with  $\theta$  between 7 and 15 °C and salinities between 34.7 and 35.9. The SACW and SAMW are the components of the permanent thermocline, which includes waters warmer than 8 °C. The third layer corresponds to the AAIW, which includes waters in the density range of  $27.1 \leq \sigma_0 \leq 27.5 \text{ kg}\cdot\text{m}^{-3}$  (Murata *et al.*, 2008). The potential temperature varies between 4 and 9 °C and the salinity shows the minimum values of the water column at 7.5 °N, between 34.5 and 34.9. In the deep waters, NADW is split into upper NADW (uNADW) and lower NADW (lNADW). The uNADW layer incorporates waters with densities between  $\sigma_0 = 27.5 \text{ kg}\cdot\text{m}^{-3}$

and  $\sigma_2 = 37 \text{ kg}\cdot\text{m}^{-3}$  (Murata *et al.*, 2008), mainly including Labrador Sea Water (LSW), which is easily identified by a relatively deep maximum signal in salinity of about 34.7–35.0 and  $\theta$  between ~3 and 5 °C in this region. The INADW layer is delimited by  $\sigma_2 = 37.0 \text{ kg}\cdot\text{m}^{-3}$  and  $\sigma_4 = 45.9 \text{ kg}\cdot\text{m}^{-3}$  (Johnson, 2008) and is characterized by waters that are progressively colder (~2–3 °C) than uNADW. The AABW layer encloses waters below  $\sigma_4 = 45.9 \text{ kg}\cdot\text{m}^{-3}$  (Rhein *et al.*, 1998; Sarafanov *et al.*, 2007). AABW is characterized by low salinity values of 34.8–34.9, coincident with the coldest waters (< 2 °C) at 7.5° N. The mean  $\theta$  and S values for each layer and region are detailed in Appendix B for 1993 and Appendix C for 2010 (see Table 3.2.1).

The salinity distribution for 2010 (Figure 3.2.2) shows its highest values along the SACW layer and progressively decreases with depth along the SAMW layer until it reaches a minimum at about 800 m that represents the core of AAIW. In deeper waters (~1700 m), the relative maximum in salinity identifies the uNADW layer. The S values decrease again with depth in the INADW until they reach the characteristic relative minimum of the AABW.

**Table 3.2.1.** Minimum and maximum potential temperature ( $\theta$ ) and salinity (S) values for the characteristic water masses at 7.5° N in 1993 and 2010: South Atlantic Central Water (SACW), SubAntarctic Mode Water (SAMW), Antarctic Intermediate Water (AAIW), upper North Atlantic Deep Water (uNADW), lower North Atlantic Deep Water (INADW), and Antarctic Bottom Water (AABW). The last column shows the isopycnals used to define the layers corresponding to those water masses.

Water mass layer	S		$\theta$ (°C)		$\sigma$ (kg m <sup>-3</sup> )
	1993	2010	1993	2010	
SACW	35.1–36.8	34.8–36.6	14.2–27.6	14.1–30.1	$\sigma_0 < 26.5$
SAMW	34.7–35.9	34.7–35.9	7.3–15.2	7.7–15.5	$26.5 < \sigma_0 < 27.1$
AAIW	34.5–34.8	34.5–34.9	4.6–7.9	4.7–8.6	$27.1 < \sigma_0 < 27.5$
uNADW	34.7–35.0	34.8–35.0	2.8–5.1	2.9–5.0	$\sigma_0 > 27.5$ and $\sigma_2 < 37$
INADW	34.9–35.0	34.9–35.0	1.8–3.0	1.8–2.9	$\sigma_2 > 37$ and $\sigma_4 < 45.9$
AABW	34.8–34.9	34.8–34.9	1.1–1.9	1.1–1.8	$\sigma_4 > 45.9$

### C<sub>ant</sub> estimations

The [C<sub>ant</sub>] estimations were obtained for the A06 (1993) and MOC2 (2010) data sets by applying both the  $\phi C_T^0$  (Vázquez-Rodríguez *et al.*, 2009a, 2012) and the TTD method (Waugh *et al.*, 2006; Steinfeldt *et al.*, 2009). Hereinafter, we differentiate between C<sub>ant</sub>- $\phi C_T^0$  and C<sub>ant</sub>-TTD according to the method used to estimate [C<sub>ant</sub>].

The  $\phi C_T^0$  method (Vázquez-Rodríguez *et al.*, 2009a, 2012) is a back-calculation approach oriented to estimate C<sub>ant</sub> from the comparison of modern C<sub>T</sub> concentrations with estimates of their preindustrial reference concentrations, under the assumption that biogeochemical processes that modulate oceanic C<sub>T</sub> have operated invariably with time. It shares principles with the classical  $\Delta C^*$  method, but proposes different parameterizations to calculate the air-sea disequilibrium ( $\Delta C_{dis}$ ) and the preformed alkalinity (A<sub>T</sub><sup>0</sup>) to assess the contribution of CaCO<sub>3</sub> dissolution to C<sub>T</sub>. A relevant aspect of these parameterizations is that they rely on conservative

properties of the subsurface layer (100–200 m), which is taken as a record for characterizing WML properties (Vázquez-Rodríguez *et al.*, 2012). These parameters are obtained from subsurface data and applied directly to calculate [C<sub>ant</sub>] in waters above the 5 °C isotherm or estimated by means of an extended Optimum MultiParameter (eOMP) analysis for cold deep waters (< 5 °C). This procedure especially improves the C<sub>ant</sub> estimations in cold deep waters involved in complex mixing processes between northern and southern hemispheric water masses. An uncertainty of ±5.2 µmol·kg<sup>-1</sup> was calculated from the random propagation of the errors for the φC<sub>T</sub><sup>0</sup> method (Vázquez-Rodríguez *et al.*, 2009a). The φC<sub>T</sub><sup>0</sup> C<sub>ant</sub> estimations at 7.5° N for 1993 and 2010 are shown in Figure 3.2.3 (a,b).

The TTD method is an indirect method that uses measurements of transient tracers (e.g., CFCs) to estimate C<sub>ant</sub> without using carbon data. The basis of the TTD method, developed by Waugh *et al.* (2004), is that the only information necessary to estimate C<sub>ant</sub> is the knowledge about the time-dependent evolution of C<sub>ant</sub> in the surface ocean and the rate at which this surface boundary condition is transported and mixed into the ocean's interior. This is done by means of particular transfer functions (here called TTDs) that try to represent the water mass age distribution within the ocean interior, according to the measured tracer data. It is assumed that the transport is steady and that TTDs can be modelled as Inverse Gaussian functions (Waugh *et al.*, 2004). Thus, C<sub>ant</sub> is determined from the difference between C<sub>T</sub> at the time the water masses were formed, as deduced from the age distribution, and C<sub>T</sub> in the preindustrial period, assuming a preindustrial atmospheric CO<sub>2</sub> concentration of 280 ppm (Waugh *et al.*, 2004). To calculate the water masses' age distribution, it is necessary to know their atmospheric time histories (Walker *et al.*, 2000) and their solubility functions (Warner and Weiss, 1985). As in Steinfeldt *et al.* (2009), it is assumed that the surface waters are in equilibrium, for example, that their CFC saturation is 100%, whereas this saturation is smaller for the formation of deep water masses (e.g., 85% for uNADW and 65% for lNADW and AABW). For the A06 cruise, both CFC-11 and CFC-12 data were used, and C<sub>ant</sub> is inferred from the TTD resulting from the mean age of both tracers. For the MOC2 cruise, only CFC-12 data have been used to infer the TTDs for two reasons: First, the CFC-11 peak in the chromatogram of flame-sealed samples that have been stored for a longer time is overlaid by a negative signal, which makes the determination of the peak area more difficult. Second, CFC-11 increased in the atmosphere only until 1994, in contrast to CFC-12, whose concentrations grew until 2003. It is not possible to derive a unique mean age for very young waters from CFC-11 data in 2010, as waters formed at the end of the 1980s and after 2000 have the same CFC-11 concentration. The uncertainty of the TTD approach evaluated by Waugh *et al.* (2006) is ± 6 µmol·kg<sup>-1</sup> for individual C<sub>ant</sub> estimations. The TTD C<sub>ant</sub> estimations at 7.5° N for 1993 and 2010 are shown in Figure 3.2.3 (c, d).

### C<sub>ant</sub> changes, C<sub>ant</sub> specific inventories, and C<sub>ant</sub> storage rates

Considering the selected regions and layers along 7.5° N, the mean values of S, θ, A<sub>T</sub>, C<sub>T</sub>, C<sub>ant</sub>-φC<sub>T</sub><sup>0</sup>, and C<sub>ant</sub>-TTD, together with the standard error of their means ( $x \pm \epsilon$ ), were calculated for 22 regional layers (boxes) from the 1993 and 2010 datasets (Appendices B and C, respectively). The uncertainty of the mean ( $\epsilon$ )

$= \sigma/\sqrt{n}$ ) was determined from the standard deviation ( $\sigma$ ) of the samples (n) in each box, including a randomly propagated error in each sample due to the C<sub>ant</sub> method uncertainty. The thickness of each layer (within each region) was computed as the average vertical distance between layers weighted by the separation between stations and normalized to obtain the identical water column depth in the four regions of both cruises, taking the 2010 MOC2 cruise water column depth as reference (see Appendix B).

Considering these mean values, the C<sub>ant</sub> changes ( $\Delta C_{\text{ant}} - \varphi C_T^0$  and  $\Delta C_{\text{ant}} - \text{TTD}$ ) between 1993 and 2010 were calculated as the difference between the values of [C<sub>ant</sub>] in 2010 minus those in 1993 (Table 3.2.2), together with the differences in S and θ ( $\Delta S$  and  $\Delta \theta$ , respectively – Figure 3.2.4). The annual C<sub>ant</sub> changes and the associated uncertainties and  $\Delta C_{\text{ant}} - \varphi C_T^0$  and  $\Delta C_{\text{ant}} - \text{TTD}$  rates ( $\mu\text{mol}\cdot\text{kg}^{-1}\cdot\text{y}^{-1}$ ) were calculated as  $\Delta X = 1/17 * [(X_{2010} - X_{1993}) \pm \sqrt{(\varepsilon_{2010})^2 + (\varepsilon_{1993})^2}]$  (Table 3.2.2), where X and ε are given in Appendices B and C. In order to visualize the spatial distribution of the changes at 7.5° N, additional calculations were necessary because the 1993 and 2010 datasets do not have the same stations grid. More specifically, the 2010 bottle grid was used as the reference grid into which the bottle data in 1993 were interpolated using a Delaunay triangulation. In this way, a C<sub>ant</sub> profile for 1993 was obtained at the 2010 positions. The differences between the 2010 and the 1993 profiles represent the  $\Delta C_{\text{ant}} - \varphi C_T^0$  and  $\Delta C_{\text{ant}} - \text{TTD}$ , respectively (Figure 3.2.5).

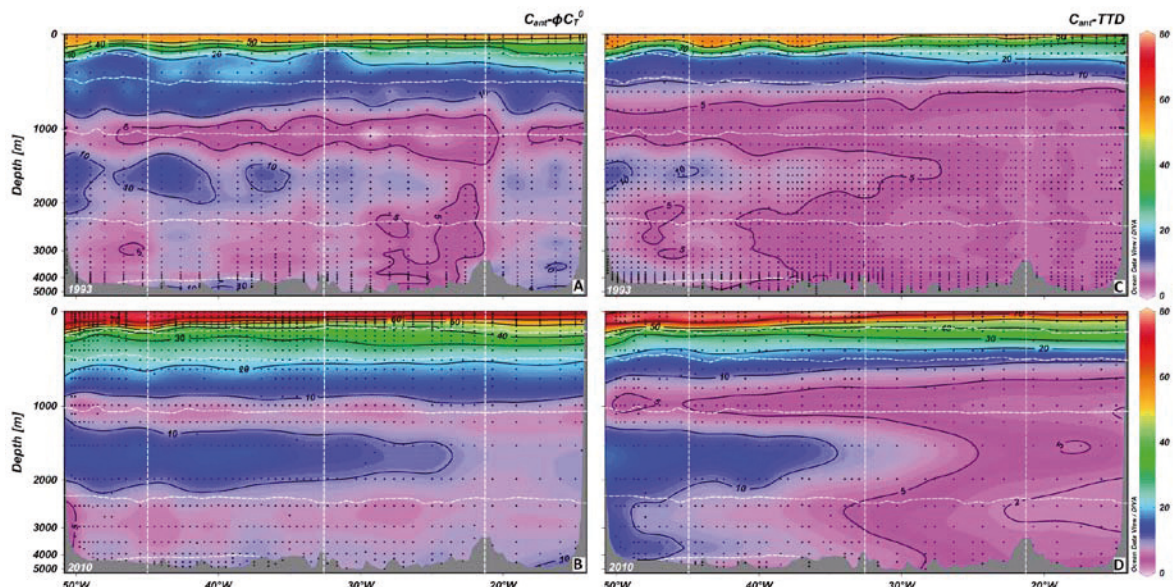


**Figure 3.2.3.** Distribution of  $C_{\text{ant}} - \varphi C_T^0$  and  $C_{\text{ant}} - \text{TTD}$  ( $\mu\text{mol}\cdot\text{kg}^{-1}$ ) along the 7.5°N section in 1993 (A, C) and 2010 (B, D). (A) and (B) panels show the profiles of  $C_{\text{ant}} - \varphi C_T^0$  while panels (C) and (D) show the profiles of  $\text{TTD} - C_{\text{ant}}$ . The horizontal white dashed lines mark the layers and the vertical white dashed lines mark the regions.

In each region, the C<sub>ant</sub> specific inventory ( $iC_{ant}$ , mol·m<sup>-2</sup>) was calculated for either method as the sum of the mean [C<sub>ant</sub>] of each layer multiplied by its thickness. The  $iC_{ant}$  was also calculated for the western basin (WB + WR), the eastern basin (ER + EB), and the whole 7.5° N basin (50° W – 15° W). In order to calculate the  $iC_{ant}$  errors, an uncertainty between 0 and the maximum standard error of the mean value of [C<sub>ant</sub>] was assigned to the [C<sub>ant</sub>] values, and the  $iC_{ant}$  was recalculated 100 times. Hence, the  $iC_{ant}$  errors are the standard deviation of these 100 calculations. Both the  $iC_{ant}$ - $\phi C_T^0$  and  $iC_{ant}$ -TTD values together with their errors are shown in Table 3.2.3.

The annual C<sub>ant</sub> storage rates in mol·m<sup>-2</sup>·y<sup>-1</sup> were calculated from the difference between  $iC_{ant1993}$  and  $iC_{ant2010}$  (Table 3.2.4). Both sets of C<sub>ant</sub> storage rates were calculated for the section and they were also obtained for the western and eastern basins and upper (including SACW, SAMW, and AAIW) and lower (including uNADW, INADW, and AABW) layers (Table 3.2.4). Furthermore, the observed C<sub>ant</sub> storage rates were compared to the expected rates assuming a steady state (SS) of the C<sub>ant</sub> distributions (SS- $C_{ant}$ - $\phi C_T^0$  and SS- $C_{ant}$ -TTD rates). The SS- $\Delta C_{ant}$  rates (μmol·kg<sup>-1</sup>·y<sup>-1</sup>) were calculated (Table 3.2.2) as the product between  $\lambda = 0.0169 \pm 0.001$  y<sup>-1</sup> and the averaged [C<sub>ant</sub>] between 1993 and 2010 (Appendices B and C) for each of the 22 boxes. Subsequently, the expected SS- $C_{ant}$  storage rate (mol·m<sup>-2</sup>·y<sup>-1</sup>) was calculated for the whole section and the upper and lower layers in the western and eastern basins (Table 3.2.4).

## Results

### Distribution of $C_{ant}$ - $\phi C_T^0$ and $C_{ant}$ -TTD

The vertical distributions of [C<sub>ant</sub>- $\phi C_T^0$ ] and [C<sub>ant</sub>-TTD] show similar patterns along the 7.5° N section in 1993 (Figure 3.2.3a, c) and 2010 (Figure 3.2.3b, d). High [C<sub>ant</sub>] values are found in the upper layers, from where the signal decreases to a minimum within the AAIW layer at about 1000 m depth. A relatively high C<sub>ant</sub> signal is observed in the uNADW. A second [C<sub>ant</sub>] minimum is present at the upper boundary of the INADW, where levels are close to the uncertainty of both methods and similar to the minimum within the AAIW. Towards the bottom, in the lower part of the INADW layer, [C<sub>ant</sub>] increases slightly. Below 1000 m, there is a general horizontal gradient of [C<sub>ant</sub>] with the western basin presenting higher values of [C<sub>ant</sub>] than the eastern one, likely due to the transport of more recently ventilated water masses by the DWBC, close to the western margin of the Atlantic Ocean (Steinfeldt *et al.*, 2007). The main difference in the vertical structure between [C<sub>ant</sub>- $\phi C_T^0$ ] and [C<sub>ant</sub>-TTD] is the vertical gradient in the upper 1000 m, which is sharper for the TTD method, which results in a smaller [C<sub>ant</sub>-TTD] for AAIW. Another difference for both the 1993 and the 2010 distributions is the westward increase of [C<sub>ant</sub>] in the uNADW, which is more pronounced with the TTD method, with a distinct maximum in the WB region in 2010. The mean and standard deviation of the differences found by the  $\phi C_T^0$  and TTD methods ( $C_{ant}$ - $\phi C_T^0$  –  $C_{ant}$ -TTD) are  $1.7 \pm 2.4$  μmol·kg<sup>-1</sup> in 1993 and  $2.7 \pm 4.2$  μmol·kg<sup>-1</sup> in 2010, which indicates that there is a good agreement between the two methods, illustrated by a very high correlation ( $r^2 = 0.98$  for 1993 and  $r^2 = 0.97$  for 2010; Appendices B and C).

The SACW layer presents the maximum  $[C_{ant} - \phi C_T^0]$  for the whole section (Figure 3a, c), with mean values in the WR region increasing from  $53.4 \pm 0.7 \mu\text{mol}\cdot\text{kg}^{-1}$  in 1993 to  $69.8 \pm 0.7 \mu\text{mol}\cdot\text{kg}^{-1}$  in 2010 (Appendices B and C, respectively). The  $[C_{ant}\text{-TTD}]$  in the WR region is almost identical, with values changing from  $54.2 \pm 0.6 \mu\text{mol}\cdot\text{kg}^{-1}$  (1993) to  $72.0 \pm 1.7 \mu\text{mol}\cdot\text{kg}^{-1}$  (2010). Regarding the SAMW layer, there is a noticeable penetration of the  $C_{ant} - \phi C_T^0$  from 1993 to 2010 (Figure 3.2.3a, c). Regardless of the method used, the isolines 30 and 40  $\mu\text{mol}\cdot\text{kg}^{-1}$  moved down from SACW to SAMW layers. The mean values of  $[C_{ant} - \phi C_T^0]$  range between  $18.8 \pm 0.9 \mu\text{mol}\cdot\text{kg}^{-1}$  (WR) and  $22.1 \pm 1.3 \mu\text{mol}\cdot\text{kg}^{-1}$  (EB) in 1993 and between  $31.0 \pm 0.9 \mu\text{mol}\cdot\text{kg}^{-1}$  (WB) and  $35.0 \pm 1.9 \mu\text{mol}\cdot\text{kg}^{-1}$  (EB) in 2010. The mean values of  $[C_{ant}\text{-TTD}]$  and  $[C_{ant} - \phi C_T^0]$  are very similar in the SAMW layer, with values varying between  $18.0 \pm 0.7 \mu\text{mol}\cdot\text{kg}^{-1}$  (WR) and  $21.2 \pm 0.9 \mu\text{mol}\cdot\text{kg}^{-1}$  (WB) in 1993 and between  $26.7 \pm 1.1 \mu\text{mol}\cdot\text{kg}^{-1}$  (WB) and  $33.7 \pm 1.5 \mu\text{mol}\cdot\text{kg}^{-1}$  (EB) in 2010 (Appendices B and C). In the AAIW layer, both methods exhibit a clear minimum horizon during both cruises, which is more extreme and wider in 1993 than in 2010. This thinning of the  $C_{ant}$  signal in 2010 is due to the mixing/dilution of the AAIW with  $C_{ant}$ -loaded surrounding waters, which generate an increase of  $C_{ant}$ . This finding agrees with the fact that the northward flow of AAIW was less intense in 2010 than in 1993 (San Antolín Plaza *et al.*, 2012; Hernández-Guerra *et al.*, 2014). The AAIW layer displays lower values for  $[C_{ant}\text{-TTD}]$  than for  $[C_{ant} - \phi C_T^0]$ , especially in 2010. The  $[C_{ant} - \phi C_T^0]$  reveals a homogenous longitudinal distribution with mean values around  $6 \mu\text{mol}\cdot\text{kg}^{-1}$  in 1993 and around  $15 \mu\text{mol}\cdot\text{kg}^{-1}$  in 2010 (Figure 3.2.3a, b), with the exception of the WB region in 1993, which shows a mean  $[C_{ant} - \phi C_T^0]$  of  $9.8 \pm 0.7 \mu\text{mol}\cdot\text{kg}^{-1}$ . The  $[C_{ant}\text{-TTD}]$  shows a higher gradient toward the western basin, varying from  $7.2 \pm 0.4 \mu\text{mol}\cdot\text{kg}^{-1}$  (WB) to  $3.6 \pm 0.2 \mu\text{mol}\cdot\text{kg}^{-1}$  (EB) in 1993 and from  $8.3 \pm 0.6 \mu\text{mol}\cdot\text{kg}^{-1}$  (WB) to  $5.6 \pm 0.6 \mu\text{mol}\cdot\text{kg}^{-1}$  (EB) in 2010 (Figure 3.2.3c, d).

The important difference in  $C_{ant}$  between the two cruises within the AAIW stratum has also been recently noticed by Guallart *et al.* (2015) along 24.5°N. In that study, the authors suggested that, regarding the  $C_{ant}$  computation in the AAIW layer, it is important to consider that methods based on CO<sub>2</sub> measurements are particularly sensitive to changes in that water mass. The  $\phi C_T^0$  method is strongly linked to natural processes through the Redfield ratios (Vázquez-Rodríguez *et al.*, 2009a), which in these regions are influenced by the presence of the oxygen minimum zone (OMZ) (Stramma *et al.*, 2008). Additionally, the large increase found for the South Atlantic Ocean (Wanninkhof *et al.*, 2010) could explain the relatively high  $[C_{ant} - \phi C_T^0]$  in waters with southern origin. It should also be noticed that the TTD method does not always detect the same  $C_{ant}$  as  $\phi C_T^0$  (Tanhua *et al.*, 2007). In old water masses that have been in equilibrium with an atmosphere previous to 1960,  $C_{ant} - \phi C_T^0$  could exhibit values higher than  $C_{ant}\text{-TTD}$ , because at that time the atmospheric concentration of CFCs was very low.

In the deep layers, the most remarkable structure is the signal of the LSW (the main component of the uNADW), which is associated to a tongue of relatively high values of  $[C_{ant}]$  during both cruises (Figure 3.2.3). According to Lazier *et al.* (2002), the early 1990s were a period of exceptionally intense convection, which created a fresher deep pool of LSW. Significant decreases in salinity are detected in the WB and WR

regions, where LSW spreads. Further, the eastward recirculation of the NADW (Arhan *et al.*, 1998; Mémery *et al.*, 2000) would have promoted the extension of the LSW signal into the eastern regions in 2010, as the results using either the  $\phi C_T^0$  or TTD methods suggest (Figure 3.2.3b, d) for the uNADW layer. In 1993, the LSW signal is mainly restricted to the western regions (WB and WR), where there are some bowls of uNADW with  $[C_{ant}-\phi C_T^0]$  and  $[C_{ant}-TTD]$  slightly higher than  $10 \mu\text{mol}\cdot\text{kg}^{-1}$ , with mean  $[C_{ant}-\phi C_T^0]$  and  $[C_{ant}-TTD]$  values of  $8.9\pm0.3$  and  $8.5\pm0.2 \mu\text{mol}\cdot\text{kg}^{-1}$  in the WB region, respectively. In 2010, not only the western basin but also the ER region exhibit  $[C_{ant}-\phi C_T^0] > 10 \mu\text{mol}\cdot\text{kg}^{-1}$ , with a mean  $[C_{ant}-\phi C_T^0]$  of  $9.2\pm0.3 \mu\text{mol}\cdot\text{kg}^{-1}$ . However, the  $[C_{ant}-TTD]$  values are significantly lower than  $[C_{ant}-\phi C_T^0]$  in the ER and EB regions during both cruises.

The LNADW layer shows the lowest values of  $C_{ant}$  of the whole section in both cruises, rarely reaching values above  $10 \mu\text{mol}\cdot\text{kg}^{-1}$  (Figure 3.2.3b, d). In this layer, the TTD approach detects lower (higher) concentrations in the eastern (western) regions than the  $\phi C_T^0$  method, with estimates more homogenous throughout the section (Figure 3.2.3). The average  $[C_{ant}-\phi C_T^0]$  in the LNADW ranges from  $5.4\pm0.2 \mu\text{mol}\cdot\text{kg}^{-1}$  in the WB in 1993 to  $8.2\pm0.3 \mu\text{mol}\cdot\text{kg}^{-1}$  in the EB in 2010, and the mean  $[C_{ant}-TTD]$  values are between  $2.9\pm0.1 \mu\text{mol}\cdot\text{kg}^{-1}$  in the EB in 1993 and  $10.7\pm0.3 \mu\text{mol}\cdot\text{kg}^{-1}$  in the WB in 2010. Once again, the pulse of LSW in the early 1990's (Lazier *et al.*, 2002), together with the eastward branching of the DWBC (Mémery *et al.*, 2000) and the northward cyclonic flow of the NADW into the south-eastern part of the Gambia Basin reported by Sarafanov *et al.* (2007), could be the processes responsible for the  $C_{ant}$  redistribution in the ER region observed during 2010. Nevertheless, no pattern could be easily described there because our estimates of  $[C_{ant}]$  were within the methodology uncertainty. The AABW layer is located at the bottom of the WB and WR (Figure 3.2.3). In 1993, the mean  $[C_{ant}-\phi C_T^0]$  ranged between  $4.8\pm0.4 \mu\text{mol}\cdot\text{kg}^{-1}$  (WB) and  $7.7\pm0.2 \mu\text{mol}\cdot\text{kg}^{-1}$  (WR), while in 2010 the concentrations are slightly higher:  $7.2\pm0.3 \mu\text{mol}\cdot\text{kg}^{-1}$  in the WB and  $8.8\pm0.2 \mu\text{mol}\cdot\text{kg}^{-1}$  in the WR. The TTD approach leads to similar estimates of mean  $[C_{ant}-TTD]$ , between  $5.0\pm0.1 \mu\text{mol}\cdot\text{kg}^{-1}$  (WR) and  $7.3\pm0.1 \mu\text{mol}\cdot\text{kg}^{-1}$  (WB) in 1993 and between  $6.7\pm0.1 \mu\text{mol}\cdot\text{kg}^{-1}$  (WR) and  $9.0\pm0.4 \mu\text{mol}\cdot\text{kg}^{-1}$  (WB) in 2010.

### Thermohaline changes

The A06 and MOC2 cruises were carried out in different seasons, with A06 being a boreal winter cruise while MOC2 was a boreal spring cruise. The seasonality in the position of the ITCZ leads to changes in the tropical North Atlantic circulation (Rosell-Fieschi *et al.*, 2015). One major change is the formation of the NECC, which begins in May in the EB and advances west until it joins with the North Brazil Current (NBC) by July. Hence, the greatest changes in the thermohaline properties took place in the uppermost layers (SACW, SAMW) (Table 3.2.2, Figure 3.2.4). In general, S diminishes from 1993 to 2010 within the SACW layer of all regions, associated with a decrease in temperature in the regions close to the MAR, probably related to the different seasons when the cruises were carried out. However, in the WB, the SACW layer shows higher temperatures and lower salinities in 2010 than in 1993, likely due to the closer proximity of the stations to the Amazon River in 2010 (Figure 3.2.1). In the SAMW layer, it is worth highlighting the influence of the

strong NBC seasonality in the WB, driving less saline and relatively colder waters in 2010 than in 1993. In the remaining regions, both the salinity and temperature show a slight increment (Figure 3.2.4). In the case of the AAIW layer,  $\Delta\theta$  and  $\Delta S$  are positive (properties were higher in 2010 than in 1993), with a slight trend toward increasing  $\Delta\theta$  eastwards (Figure 3.2.4) in agreement with the lower northward advection of AAIW in 2010 (San Antolín Plaza *et al.*, 2012; Hernández-Guerra *et al.*, 2014). In 2010, the uNADW layer was slightly fresher and warmer and the INADW layer showed small changes, being saltier and warmer (Figure 3.2.4 and Table 3.2.2). Finally, AABW showed a slight decrease in  $\theta$  and  $S$  in 2010 (together with an increment in SiO<sub>2</sub> from [SiO<sub>2</sub>]<sub>1993</sub> = 43.1 ± 0.8 to [SiO<sub>2</sub>]<sub>2010</sub> = 47.5 ± 2.6 μmol·kg<sup>-1</sup> in the WB and from [SiO<sub>2</sub>]<sub>1993</sub> = 62.4 ± 1.3 to [SiO<sub>2</sub>]<sub>2010</sub> = 66.1 ± 1.4 μmol·kg<sup>-1</sup> in the WR). These findings suggest an increase of AABW and a decrease of INADW that would agree with the weakening of the southward advection of INADW in 2010 (Hernández-Guerra *et al* (2014)).

**Table 3.2.2.** Changes ( $\pm$  standard deviation) in potential temperature ( $\theta$ , °C), salinity ( $S$ ),  $C_{ant} - \phi C_T^0$  ( $\mu\text{mol}\cdot\text{kg}^{-1}$ ), and  $C_{ant}$ -TTD ( $\mu\text{mol}\cdot\text{kg}^{-1}$ ) for each region and layer.  $\Delta C_{ant} = C_{ant,2010} - C_{ant,1993}$ . The  $\Delta C_{ant}$  annual rates ( $\pm$  standard error of mean) and SS\_ΔC<sub>ant</sub> rates (calculated as the averaged  $C_{ant}$  in 1993 and 2010 multiplied by 0.0169  $\text{yr}^{-1}$ ) ( $\mu\text{mol}\cdot\text{kg}^{-1}\text{ yr}^{-1}$ ) were calculated using the  $\phi C_T^0$  and TTD methods. Italic typeface indicates values not significantly different from zero (p-level > 0.05).

Region	Layer	$\Delta S$	$\Delta\theta$	$\Delta C_{ant}$ $\phi C_T^0$	$\Delta C_{ant}$ TTD	$\Delta C_{ant}$ $\phi C_T^0$ rate <sup>a</sup>	SS_ΔC <sub>ant</sub> $\phi C_T^0$ rate <sup>a</sup>	$\Delta C_{ant}$ rate <sup>b</sup>	TTD rate <sup>b</sup>	SS_ΔC <sub>ant</sub> TTD rate <sup>a</sup>
WB	SACW	-0.227±0.286	0.30±3.5	16.4±6.6	17.8±6.5	0.96±0.06	1.04 (0.2)	1.05±0.11	1.07 (0.8)	
	SAMW	-0.136±0.346	-0.75±2.5	10.2±6.4	6.7±6.6	0.60±0.09	0.44 (0.10)	0.39±0.11	0.42 (0.8)	
	AAIW	0.014±0.093	0.21±1.28	5.6±6.2	1.4±5.3	0.33±0.06	0.21 (0.05)	<b>0.08±0.04</b>	0.13 (0.2)	
	uNADW	-0.028±0.100	0.23±1.02	2.0±4.6	2.6±5.3	0.11±0.03	0.17 (0.08)	0.15±0.04	0.16 (0.8)	
	INADW	0.003±0.027	0.09±0.45	1.9±3.5	3.4±3.6	0.11±0.02	0.11 (0.9)	<b>0.20±0.02</b>	<b>0.15 (0.01)</b>	
	AABW	-0.010±0.012	-0.05±0.08	2.4±1.9	1.7±1.5	0.14±0.03	0.10 (0.2)	0.10±0.02	0.14 (0.15)	
WR	SACW	-0.100±0.213	0.47±4.1	13.4±10.4	19.0±7.8	0.79±0.11	0.98 (0.08)	<b>1.12±0.11</b>	1.06 (0.6)	
	SAMW	0.040±0.240	0.49±1.75	13.1±9.0	8.7±6.3	0.77±0.06	0.43 (<0.001)	<b>0.51±0.08</b>	0.38 (0.10)	
	AAIW	0.012±0.061	0.33±1.14	8.5±6.7	2.6±5.1	0.50±0.06	<b>0.18 (&lt;0.001)</b>	<b>0.15±0.03</b>	0.11 (0.2)	
	uNADW	-0.016±0.061	0.30±0.74	3.0±5.3	2.9±4.6	0.18±0.03	0.15 (0.2)	0.17±0.03	0.13 (0.10)	
	INADW	0.006±0.022	0.11±0.45	1.8±3.2	2.2±4.6	0.11±0.01	0.11 (0.6)	0.13±0.01	<b>0.10 (0.02)</b>	
	AABW	-0.008±0.025	-0.05±0.29	1.2±2.7	1.7±2.4	0.07±0.02	<b>0.14 (&lt;0.001)</b>	0.10±0.01	0.10 (1.0)	
ER	SACW	-0.198±0.248	-1.0±5.2	11.0±8.5	12.9±8.1	0.65±0.09	<b>0.98 (0.001)</b>	0.76±0.19	0.92 (0.4)	
	SAMW	-0.011±0.201	0.01±1.8	13.6±7.9	6.9±6.7	0.80±0.09	<b>0.47 (&lt;0.001)</b>	<b>0.41±0.15</b>	0.41 (1.0)	
	AAIW	0.023±0.080	0.42±1.28	8.7±5.6	2.5±3.8	0.51±0.06	<b>0.18 (&lt;0.001)</b>	<b>0.15±0.04</b>	0.09 (0.12)	
	uNADW	-0.007±0.067	0.23±0.69	2.4±5.0	1.5±4.4	0.14±0.02	0.13 (0.5)	0.09±0.02	0.07 (0.4)	
	INADW	0.006±0.021	0.09±0.39	1.2±3.1	0.6±1.1	0.07±0.01	<b>0.12 (&lt;0.001)</b>	<b>0.04±0.01</b>	0.06 (0.10)	
EB	SACW	0.000±0.184	-0.03±4.9	12.7±7.3	17.2±9.6	0.75±0.11	0.93 (0.11)	1.01±0.25	0.86 (0.6)	
	SAMW	0.027±0.165	0.22±1.72	12.9±5.9	15.3±6.0	0.76±0.13	0.48 (0.05)	0.90±0.11	<b>0.44 (&lt;0.001)</b>	
	AAIW	0.015±0.063	0.45±1.19	8.8±4.6	2.0±3.3	0.52±0.07	<b>0.18 (&lt;0.001)</b>	<b>0.12±0.04</b>	0.08 (0.3)	
	uNADW	-0.010±0.047	0.17±0.60	0.6±4.0	0.6±3.2	0.03±0.03	<b>0.13 (&lt;0.001)</b>	0.04±0.04	0.05 (0.8)	
	INADW	0.000±0.028	0.02±0.36	-0.4±3.2	-0.5±3.7	-0.03±0.02	<b>0.14 (&lt;0.001)</b>	-0.03±0.01	<b>0.04 (&lt;0.001)</b>	

a)Bold typefaces indicate values significantly different from the values of  $\Delta C_{ant}$  located on the left (p-level < 0.05 at 95%, given in parentheses)

b)Bold typefaces indicate values of  $\Delta C_{ant} - \phi C_T^0$  and  $\Delta C_{ant}$ -TTD rates that are different (p-level < 0.05 at 95%)

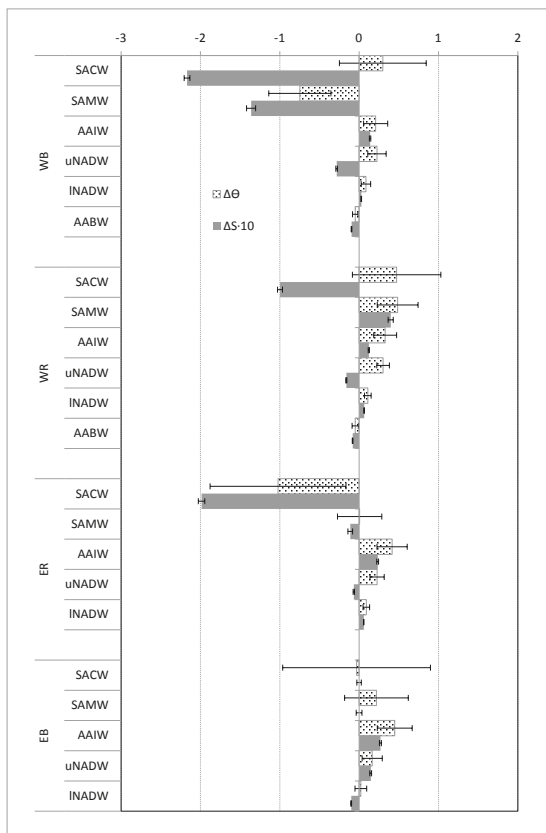


**Figure 3.2.4.** Changes in potential temperature ( $\Delta\theta$ , °C, dotted bars) and salinity ( $\Delta S$ , 0.1, grey bars) from 1993 to 2010 for each region and layer. Note that  $\Delta S$  is multiplied by 10 in order to have comparable scales. Error bars represent the standard error of the mean.

### Changes in $C_{ant}$ distribution

The distribution of  $\Delta C_{ant} - \varphi C_T^0$  and  $\Delta C_{ant} - TTD$  indicates a clear increase in  $C_{ant}$  from 1993 to 2010 in the upper and eastward parts of the section (Figure 3.2.5). The SACW layer presents the largest increase in  $[C_{ant} - \varphi C_T^0]$ , around  $14 \mu\text{mol}\cdot\text{kg}^{-1}$  on average, with the highest  $\Delta C_{ant} - \varphi C_T^0$  ( $16.4 \pm 6.6 \mu\text{mol}\cdot\text{kg}^{-1}$ ) in WB (Table 3.2.2). These values are even slightly higher in the case of  $\Delta C_{ant} - TTD$ , with an average increase of about  $17 \mu\text{mol}\cdot\text{kg}^{-1}$  along the whole layer, and the highest  $\Delta C_{ant} - TTD$  ( $19.0 \pm 6.5 \mu\text{mol}\cdot\text{kg}^{-1}$ ) found in the WR region. Regarding the SAMW layer, there is a homogenous high increase in  $C_{ant}$  with  $\Delta C_{ant} - \varphi C_T^0$  between  $10.2 \pm 6.4 \mu\text{mol}\cdot\text{kg}^{-1}$  (WR) and  $13.6 \pm 7.9 \mu\text{mol}\cdot\text{kg}^{-1}$  (ER). The  $\Delta C_{ant} - TTD$  ranges between  $6.7 \pm 6.6 \mu\text{mol}\cdot\text{kg}^{-1}$  (WR) and  $15.3 \pm 6.0 \mu\text{mol}\cdot\text{kg}^{-1}$  (EB). Throughout the AAIW layer,  $\Delta C_{ant} - \varphi C_T^0$  values of around  $5-10 \mu\text{mol}\cdot\text{kg}^{-1}$  are observed, while  $\Delta C_{ant} - TTD$  is significantly lower (close to  $2 \mu\text{mol}\cdot\text{kg}^{-1}$ ; Figure 3.2.5). The difference in the  $\Delta C_{ant}$  magnitude restates the different sensitivities of the  $\varphi C_T^0$  and TTD methods, as reported previously.

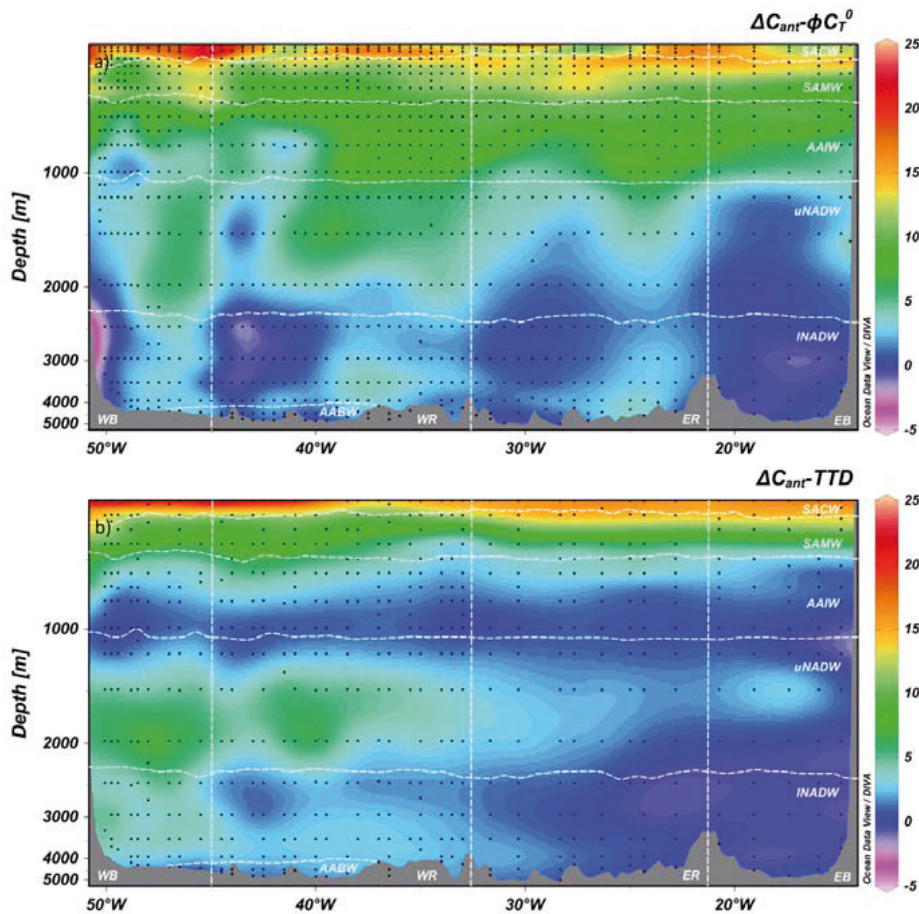


**Figure 3.2.5.** Distribution of  $\Delta C_{ant} - \phi C_T^0$  (a) and  $\Delta C_{ant} - TTD$  (b) along the 7.5° N section, where  $\Delta C_{ant} = C_{ant, 2010} - C_{ant, 1993}$ . The dots represent the sampling locations during the 2010 cruise. A Delaunay triangulation was used to calculate these  $C_{ant}$  differences. The position and depth of the MOC2 stations (2010) were used as the reference grid and the data of A06 (1993) were interpolated into that grid.

In deep waters, there is a good agreement between the  $\phi C_T^0$  and TTD methods, which show  $C_{ant}$  changes lower than 4  $\mu\text{mol}\cdot\text{kg}^{-1}$  (Table 3.2.2) and a higher  $\Delta C_{ant}$  in the western section and closer to MAR regions (Figure 3.2.5). According to the eastward spread of the high  $[C_{ant}]$  tongue and its mixing with less  $C_{ant}$ -loaded waters (i.e., less ventilated waters) (Steinfeldt *et al.*, 2007) (Figure 3.2.3), the greater changes are located in the uNADW layer, with the highest  $\Delta C_{ant} - \phi C_T^0$  of 3.0  $\mu\text{mol}\cdot\text{kg}^{-1}$  (WR). Regarding the  $\Delta C_{ant} - TTD$ , the largest change is found in the WB region of the INADW. It is worth remarking that in deep and bottom waters, with  $[C_{ant}]$  values close to the uncertainty of the methodology, the differences in the concentrations could only be detected above the methodological noise when studying time periods of more than three decades (Ríos *et al.*, 2012b).

In order to evaluate the annual changes,  $\Delta C_{\text{ant}}$  rates are calculated for each of the 22 boxes (Table 3.2.2). According to the  $C_{\text{ant}}$  changes previously described, both the  $\Delta C_{\text{ant}} - \phi C_T^0$  and  $\Delta C_{\text{ant}} - \text{TTD}$  rates are higher in the surface layer and they progressively decrease with depth, with similarities and differences always within uncertainties. In the SACW, the  $\Delta C_{\text{ant}} - \phi C_T^0$  and  $\Delta C_{\text{ant}} - \text{TTD}$  rates show a very similar increase of  $C_{\text{ant}}$  in the WB and ER regions, while in WR and EB the  $\Delta C_{\text{ant}} - \text{TTD}$  rates are larger than those detected with the  $\phi C_T^0$  method. The  $\Delta C_{\text{ant}} - \phi C_T^0$  rates are generally higher than the  $\Delta C_{\text{ant}} - \text{TTD}$  rates in the SAMW, with the exception of EB, which displays a lower rate. The  $\Delta C_{\text{ant}} - \phi C_T^0$  rates of the AAIW layer show a  $C_{\text{ant}}$  increase that is clearly higher than the  $\Delta C_{\text{ant}} - \text{TTD}$  rates in the whole section. However those differences seem to disappear in deep waters, particularly in the uNADW layer, where the  $\Delta C_{\text{ant}}$  rates estimated with the  $\phi C_T^0$  and TTD methods agree in their values. The  $\Delta C_{\text{ant}} - \text{TTD}$  rates are in general a bit higher in the INADW than the rates from the  $\Delta C_{\text{ant}} - \phi C_T^0$ , with the only exception being the ER, where the  $\Delta C_{\text{ant}} - \phi C_T^0$  rate is slightly higher. Regarding the AABW, both  $\Delta C_{\text{ant}} - \phi C_T^0$  and  $\Delta C_{\text{ant}} - \text{TTD}$  display similar rates.

The absolute values of the differences between  $\Delta C_{\text{ant}} - \phi C_T^0$  and  $\Delta C_{\text{ant}} - \text{TTD}$  are usually less than 2  $\mu\text{mol}\cdot\text{kg}^{-1}$ , meaning that there should be a good agreement between  $\phi C_T^0$  and TTD estimations of  $C_{\text{ant}}$  storages rates. The largest differences are found in the SAMW layer and, mostly, in the AAIW layer. The SAMW in the EB ( $\Delta C_{\text{ant}} - \phi C_T^0$  rate <  $\Delta C_{\text{ant}} - \text{TTD}$  rate), where the OMZ is located, shows a decrease in  $O_2$  concentration in 2010 (~3  $\mu\text{mol}\cdot\text{kg}^{-1}$ ). However, the AAIW layer displays a decrease in the  $O_2$  concentration in 2010 (~8  $\mu\text{mol}\cdot\text{kg}^{-1}$ ) at the east of MAR, which parallels a slight increase in salinity (Brandt *et al.*, 2010), which has also been detected in our results (Table 3.2.2). The eastward increase of salinity suggests a dilution of AAIW with surrounding water masses, Mediterranean Water and, mainly, SACW, both of them with higher  $[C_{\text{ant}}]$  than AAIW. It is also noticeable in our results that this AAIW layer at the eastern basin presents a clear warming. This, together with the fact that Hernández-Guerra *et al.* (2014) found a very strong decline in the AAIW northward transport, could be the reason why  $\Delta C_{\text{ant}} - \phi C_T^0$  is higher than  $\Delta C_{\text{ant}} - \text{TTD}$  in these layers. This will also have a large influence on the  $C_{\text{ant}}$  storage rates.

The objective of including the  $SS - \Delta C_{\text{ant}}$  rates is to check whether  $C_{\text{ant}}$  has been increasing at all depths along the section in accordance with what is expected from a steady state accumulation of  $C_{\text{ant}}$ . The  $SS - \Delta C_{\text{ant}}$  rates do not always match those obtained from the bi-decadal  $\Delta C_{\text{ant}}$  rates (Table 3.2.2). Since  $SS - \Delta C_{\text{ant}}$  rates have to be interpreted as the expected steady state accumulation of  $C_{\text{ant}}$ , any observed ( $\Delta C_{\text{ant}}$  rates) deviation from this could be evidencing that the  $C_{\text{ant}}$  accumulation has been impacted by recent changes in circulation or ventilation. Equally, when the  $\Delta C_{\text{ant}}$  rates coincide with the  $SS - \Delta C_{\text{ant}}$  rates, it is an indication that the bi-decadal changes in  $C_{\text{ant}}$  follow a growing steady state. When comparing the  $\Delta C_{\text{ant}} - \phi C_T^0$  rates with the  $SS - \Delta C_{\text{ant}} - \phi C_T^0$  rates, there is no general pattern throughout the water column. In the upper layers, the SACW  $\Delta C_{\text{ant}} - \phi C_T^0$  rates are lower than the  $SS - \Delta C_{\text{ant}} - \phi C_T^0$  rates, while in the SAMW and AAIW the observed  $\Delta C_{\text{ant}} - \phi C_T^0$  rates are higher than the expected  $SS - \Delta C_{\text{ant}} - \phi C_T^0$  rates. In the deeper layers, most bi-decadal rates agree in their steady-state values, but there are some regions where the  $\Delta C_{\text{ant}} - \phi C_T^0$  rates show slightly lower values

than the SS\_ΔC<sub>ant</sub>-φC<sub>T</sub><sup>0</sup> rates, such as for example the uNADW in the EB region. When a comparison is made between the observed ΔC<sub>ant</sub>-TTD and the expected SS\_ΔC<sub>ant</sub>-TTD rates, we find that most of the rates are comparable, with the exception of the SAMW in the EB region, which displays much higher ΔC<sub>ant</sub>-TTD rates than SS\_ΔC<sub>ant</sub>-TTD rates. The reason why the ΔC<sub>ant</sub>-TTD rates are so close to SS\_ΔC<sub>ant</sub>-TTD rates could be methodological, as the TTD method uses inverse Gaussian functions (Waugh *et al.*, 2004) that are based in the solution of an advection–diffusion equation with constant velocity and diffusivity, and a steady-state circulation.

### C<sub>ant</sub> inventories

Considering the complete 7.5° N section, we observe an increase of iC<sub>ant</sub>-φC<sub>T</sub><sup>0</sup> from 41.7 ± 2.3 mol·m<sup>-2</sup> in 1993 to 58.9 ± 2.2 mol·m<sup>-2</sup> in 2010 and an increase in iC<sub>ant</sub>-TTD from 32.3 ± 2.3 mol·m<sup>-2</sup> in 1993 to 45.1 ± 2.0 mol·m<sup>-2</sup> in 2010. The section averaged iC<sub>ant</sub>-φC<sub>T</sub><sup>0</sup> values are higher than the iC<sub>ant</sub>-TTD (Table 3.2.3), but both methods detect a similar increase in C<sub>ant</sub> accumulation during the elapsed 17 years for the whole section: ~17 and ~13 mol·m<sup>-2</sup> for iC<sub>ant</sub>-φC<sub>T</sub><sup>0</sup> and iC<sub>ant</sub>-TTD, respectively. The differences are likely related to the assumptions behind each method and the different values in the waters below the 5 °C isotherm, where, in general, the TTD method returns lower values (Vázquez-Rodríguez *et al.*, 2009b). The TTD method is not expected to perfectly mimic C<sub>ant</sub>-φC<sub>T</sub><sup>0</sup> because of the relatively recent introduction of CFCs (Tanhua *et al.*, 2007).

**Table 3.2.3.** Specific inventories of C<sub>ant</sub>-φC<sub>T</sub><sup>0</sup> (iC<sub>ant</sub>-φC<sub>T</sub><sup>0</sup>) and C<sub>ant</sub>-TTD (iC<sub>ant</sub>-TTD), in mol·m<sup>-2</sup>, for each cruise and each region along 7.5° N. The shaded lines correspond to the 2010 inventories and the empty lines to the 1993 ones.

Year	iC <sub>ant</sub> -φC <sub>T</sub> <sup>0</sup> (mol·m <sup>-2</sup> )				iC <sub>ant</sub> -TTD (mol·m <sup>-2</sup> )							
	WEST		EAST		WEST		EAST					
	RI	R2	R3	R4	RI	R2	R3	R4				
1993	40.1±3.4	42.8±4.4	40.0±4.7	44.1±3.7	41.3±3.7	37.3±4.0	27.3±4.3	23.6±4.2				
2010	56.1±3.5	62.2±4.0	58.2±4.5	56.7±4.0	57.4±3.7	53.3±4.2	37.0±4.3	32.9±4.1				
1993	41.9±3.2		41.5±3.3		38.6±2.9		26.0±3.2					
2010	60.2±3.0		57.7±3.2		54.7±3.2		35.5±3.0					
1993	41.7±2.3				32.3±2.3							
2010	58.9±2.2				45.1±2.0							

Comparing the western and eastern basins, iC<sub>ant</sub>-TTD values suggest a higher C<sub>ant</sub> accumulation in the western than in the eastern basin on both cruises, while iC<sub>ant</sub>-φC<sub>T</sub><sup>0</sup> shows similar values for both basins. To be precise, the WB is the region that displayed the highest iC<sub>ant</sub>-TTD, and there was a progressive decrease towards the EB region (Table 3.2.3). In 1993, the iC<sub>ant</sub>-TTD was 38.6 ± 2.9 mol·m<sup>-2</sup> for the western basin and 26.0 ± 3.2 mol·m<sup>-2</sup> for the eastern basin. These results may be compared with the few related studies focused on the Equatorial Atlantic Ocean (Lee *et al.*, 2003; Steinfeldt *et al.*, 2009; Vázquez-Rodríguez *et al.*, 2009b;

Ríos *et al.*, 2010). Our inventories ( $iC_{ant}$ -TTD) qualitatively agree with other studies that also support the idea of a greater accumulation of  $C_{ant}$  in the western basin compared to the eastern basin (Vázquez-Rodríguez *et al.*, 2009b; Ríos *et al.*, 2010). In the western basin, Ríos *et al.* (2010) reported a  $C_{ant}$  specific inventory of  $\sim 38 \text{ mol}\cdot\text{m}^{-2}$  for the  $7.5^\circ \text{ N}$  latitude, based on a study using the TTD method in the WOCE A17N (1994) meridional transect. Their values are similar to our  $iC_{ant}$ -TTD (Table 3.2.3). In the eastern basin, an inventory of  $\sim 21 \text{ mol}\cdot\text{m}^{-2}$  was reported for the  $7.5^\circ \text{ N}$  latitude from the CLIVAR A16N (2003) meridional transect (Vázquez-Rodríguez *et al.*, 2009b), where the estimation of the  $C_{ant}$  inventory was obtained using the TTD method referred to the year 1994. Additionally, we may compare our  $iC_{ant}$ -TTD with the results from Steinfeldt *et al.* (2009) for the year 1997. These authors obtained values of  $40\text{--}50 \text{ mol}\cdot\text{m}^{-2}$  in the western basin and  $30\text{--}40 \text{ mol}\cdot\text{m}^{-2}$  in the eastern one, which are higher than our  $iC_{ant}$ -TTD, mostly because of the selected year of reference (1997 instead of 1993), but they reinforce our result of a higher  $C_{ant}$ -TTD accumulation in the western basin. Lee *et al.* (2003) reported contrasting results with respect to the east–west gradient in the  $C_{ant}$  inventories, between the Equator and  $10^\circ \text{ N}$ , using the  $\Delta C^*$  method. They described a lower  $C_{ant}$  inventory in the west ( $-26.7 \text{ mol}\cdot\text{m}^{-2}$ ) than in the east ( $-31.4 \text{ mol}\cdot\text{m}^{-2}$ ) at these latitudes, taking as a reference the year 1994. The inventory reported by Lee *et al.* (2003) for the eastern basin is consistent with that reported by Vazquez-Rodríguez *et al.* (2009b). However, the underestimation of the western inventory by Lee *et al.* (2003) may be due to an unaccounted-for offset in the  $A_T$  data of the WOCE dataset, which was amended in the more recent work of Ríos *et al.* (2010).

### $C_{ant}$ storage rates

In order to provide an overall view of the  $C_{ant}$  accumulation for the  $7.5^\circ \text{ N}$  transect, the  $iC_{ant}\text{-}\phi C_T^0$  storage rate was calculated for the whole section, obtaining a value of  $1.01 \pm 0.18 \text{ mol}\cdot\text{m}^{-2}\cdot\text{y}^{-1}$ , which is higher than the  $C_{ant}$ -TTD storage rate ( $0.75 \pm 0.17 \text{ mol}\cdot\text{m}^{-2}\cdot\text{y}^{-1}$ ) (Table 3.2.4). The east and west components of the  $C_{ant}$  storage rates reveal that both basins have been accumulating  $C_{ant}\text{-}\phi C_T^0$  at approximately the same rate ( $1.07 \pm 0.23$  and  $0.95 \pm 0.27 \text{ mol}\cdot\text{m}^{-2}\cdot\text{y}^{-1}$  in the western and eastern basins, respectively). However, the  $C_{ant}$ -TTD storage rates suggest a relatively faster rate of accumulation in the WB ( $0.95 \pm 0.24 \text{ mol}\cdot\text{m}^{-2}\cdot\text{y}^{-1}$ ) than in the EB ( $0.56 \pm 0.25 \text{ mol}\cdot\text{m}^{-2}\cdot\text{y}^{-1}$ ).

In addition, by dividing the water column into two layers, we considered separately the rates of increase occurring in the upper and the deeper water masses of the section: an upper layer enclosing the SACW, SAMW, and AAIW layers, and a lower layer enclosing the uNADW, INADW, and AABW layers. These two partitions were also divided into their respective western and eastern basins. Within the uncertainties, both the  $C_{ant}\text{-}\phi C_T^0$  and  $C_{ant}$ -TTD storage rates show similar values in the upper layer at the western and eastern basins together, slightly larger than those found in the lower layer (Table 4). The important role of the NADW in the  $C_{ant}$  storage suggested by Steinfeldt *et al.* (2009) is emphasized by both methods, showing a faster  $C_{ant}$  increase in the western lower layer than in the eastern one (Table 3.2.4).

**Table 3.2.4.** C<sub>ant</sub> and SS\_C<sub>ant</sub> rates (mol m<sup>-2</sup> y<sup>-1</sup>) for the western and eastern basins and for the whole 7.5° N section, as obtained using the φC<sub>T</sub><sup>0</sup> and TTD methods. The C<sub>ant</sub> and SS\_C<sub>ant</sub> storage rates are also shown for the upper (regular font) and lower layers (grey italics) defined in the western and eastern basins.

C <sub>ant</sub> storage rate (mol m <sup>-2</sup> y <sup>-1</sup> )	Western basin		Eastern basin		7.5°N
	All	Upper/Lower	All	Upper/Lower	All
C <sub>ant</sub> -φC <sub>T</sub> <sup>0</sup>	1.07±0.23	0.67±0.07 0.40±0.21	0.95±0.27	0.76±0.08 0.19±0.26	1.01±0.18
SS_C <sub>ant</sub> -φC <sub>T</sub> <sup>0</sup>	0.86±0.04	0.41±0.01 0.45±0.04	0.84±0.04	0.41±0.01 0.43±0.04	0.85±0.03
C <sub>ant</sub> -TTD	0.95±0.24	0.44±0.09 0.50±0.22	0.56±0.25	0.46±0.08 0.10±0.24	0.75±0.17
SS_C <sub>ant</sub> -TTD	0.79±0.04	0.36±0.01 0.42±0.04	0.52±0.04	0.33±0.01 0.19±0.04	0.65±0.03

The observed C<sub>ant</sub> storage rates (Table 3.2.4) are slightly higher than the expected SS\_C<sub>ant</sub>-φC<sub>T</sub><sup>0</sup> (0.85 ± 0.03 mol·m<sup>-2</sup>·y<sup>-1</sup>) and SS\_C<sub>ant</sub>-TTD (0.65 ± 0.03 mol·m<sup>-2</sup>·y<sup>-1</sup>) rates found in the 7.5° N section, but both are consistent if the uncertainties are considered. These results suggest that the mean [C<sub>ant</sub>] over the whole section has been increasing at a pace similar to that expected assuming a steady state. Regarding the SS\_C<sub>ant</sub>-φC<sub>T</sub><sup>0</sup> rates, these suggest that the growth in both basins has been quite similar (Table 3.2.4), while the SS\_C<sub>ant</sub>-TTD rates indicate a slower growth in the eastern basin, which agrees with the C<sub>ant</sub>-TTD storage rate value found for that basin. Overall, the SS\_C<sub>ant</sub>-φC<sub>T</sub><sup>0</sup> rates suggest an increase in C<sub>ant</sub> with time of around 0.4 mol·m<sup>-2</sup>·y<sup>-1</sup> for each layer and basin. The SS\_C<sub>ant</sub>-TTD rates suggest a similar rate in the upper layer of both basins (~0.3 mol·m<sup>-2</sup>·y<sup>-1</sup>), while in the lower layer, these rates exhibit a slower growth in the eastern basin (Table 3.2.4). We find that the upper layer in the western basin shows C<sub>ant</sub>-TTD rates that are very close to but higher than the SS\_C<sub>ant</sub>-TTD storage rate. This could be mostly influenced by the SAMW layer, which displays a ΔC<sub>ant</sub>-TTD rate much higher than the SS\_ΔC<sub>ant</sub>-TTD rates (Table 3.2.2). The C<sub>ant</sub>-φC<sub>T</sub><sup>0</sup> storage rate is higher than the SS\_C<sub>ant</sub>-φC<sub>T</sub><sup>0</sup> rate (Table 3.2.4). For this method, the most prevailing layers are the SAMW and AAIW, which show larger ΔC<sub>ant</sub>-φC<sub>T</sub><sup>0</sup> rates than SS\_ΔC<sub>ant</sub>-φC<sub>T</sub><sup>0</sup> rates (Table 3.2.2). In the western lower layer, both the observed C<sub>ant</sub>-φC<sub>T</sub><sup>0</sup> and C<sub>ant</sub>-TTD storage rates agree with their expected SS\_C<sub>ant</sub>-φC<sub>T</sub><sup>0</sup> and SS\_C<sub>ant</sub>-TTD rates (Table 3.2.4), indicating that the western lower layer is accumulating C<sub>ant</sub> at a steady state pace, independently of the method used, in agreement with the previous description of SS\_ΔC<sub>ant</sub>-TTD and ΔC<sub>ant</sub>-TTD rates (Table 3.2.2).

Regarding the eastern basin, the upper layer experienced C<sub>ant</sub> storage rates higher than the SS\_C<sub>ant</sub> rates. As we previously detected in the changes of C<sub>ant</sub> distribution (Table 3.2.2), the SAMW and AAIW again show the largest mismatch in the upper layer, showing a higher C<sub>ant</sub>-φC<sub>T</sub><sup>0</sup> storage rate than SS\_C<sub>ant</sub>-φC<sub>T</sub><sup>0</sup> rate (Table 3.2.4). This could be directly related to the decrease in the AMOC between 1993 and 2010 induced by

the retreat of the AAIW (San Antolín Plaza *et al.*, 2012; Hernández-Guerra *et al.*, 2014), as suggested by the changes in salinity (Table 3.2.2). On the other hand, the observed C<sub>ant</sub>-TTD storage rates are slightly higher but agree with the expected steady-state rates. In the eastern lower layer, the observed C<sub>ant</sub>-TTD storage rate reflects the expected SS\_C<sub>ant</sub>-TTD rates, which also match the C<sub>ant</sub>- $\phi C_T^0$  storage rate. Hence, we suggest that the C<sub>ant</sub> in the eastern lower layer is growing at steady state pace. However, the SS\_C<sub>ant</sub>- $\phi C_T^0$  rate is higher than the C<sub>ant</sub>- $\phi C_T^0$  rate, which could be due to the larger SS\_ΔC<sub>ant</sub>- $\phi C_T^0$  rates found in the EB for the uNADW and INADW (Table 3.2.2). As suggested before, the decrease in the AMOC affecting the uNADW (Hernández-Guerra *et al.*, 2014) and the dilution of the C<sub>ant</sub> signal with the less C<sub>ant</sub>-loaded surrounding waters could influence these results.

To sum up, when comparing the observed C<sub>ant</sub> storage rates with the expected SS\_C<sub>ant</sub> rates (for both the  $\phi C_T^0$  and TTD methods), our results suggest that C<sub>ant</sub> has been accumulating at a steady state rate in the lower layer while the rates in the upper layer exhibit a faster growth, mostly influenced by the weakening of the northward flow of AAIW. Despite the faster rates in the upper layer, the lower layer presents higher uncertainty in its values. This relatively large error of the C<sub>ant</sub> storage rates in the lower layer makes it impossible to detect a [C<sub>ant</sub>] increase that is significantly different from the steady state assumption.

## Conclusions

The distribution of anthropogenic CO<sub>2</sub> (C<sub>ant</sub>) along the 7.5° N section in 2010, as estimated by the  $\phi C_T^0$  and TTD methods, reveals higher values and a deeper penetration of the anthropogenic signal in the South Atlantic Central Water layer with respect to the distribution found in 1993, while the C<sub>ant</sub> core in the Antarctic Intermediate Water layer is narrower in 2010 than in 1993. In the deep layers, the signal of the Labrador Sea Water within the upper North Atlantic Deep Water layer (uNADW) is clear, having a stronger presence in the eastern basins of the section in 2010. The difference in the C<sub>ant</sub> signal of the uNADW between 1993 and 2010 in the region adjacent to the West of the Mid-Atlantic Ridge leads to a ΔC<sub>ant</sub>- $\phi C_T^0$  rate as high as 0.18 ± 0.03 μmol·kg<sup>-1</sup>·y<sup>-1</sup>, in agreement with the ΔC<sub>ant</sub>-TTD rate of 0.17 ± 0.03 μmol·kg<sup>-1</sup>·y<sup>-1</sup>.

The C<sub>ant</sub>- $\phi C_T^0$  specific inventories (iC<sub>T</sub><sup>0</sup>-C<sub>ant</sub>) found for the whole section are 41.7 ± 2.3 mol·m<sup>-2</sup> in 1993 and 58.9 ± 2.2 mol·m<sup>-2</sup> in 2010, while the C<sub>ant</sub>-TTD specific inventories (iC<sub>ant</sub>-TTD) are lower: 32.3 ± 2.3 mol·m<sup>-2</sup> in 1993 and 45.1 ± 2.0 mol·m<sup>-2</sup> in 2010. For both cruises, the iC<sub>ant</sub>-TTD is higher in the western basin than in the eastern basin. The C<sub>ant</sub>- $\phi C_T^0$  storage rate for the whole section over the studied period is 1.01 ± 0.18 mol·m<sup>-2</sup>·y<sup>-1</sup>, slightly higher than but in agreement, within the uncertainties, with the C<sub>ant</sub>-TTD storage rate of 0.75 ± 0.17 mol·m<sup>-2</sup>·y<sup>-1</sup>. When compared with the expected SS\_C<sub>ant</sub> rates, these observed C<sub>ant</sub> storage rates suggest that C<sub>ant</sub> was accumulating at close to a steady-state rate. When dividing the water column at a depth of ~1000 m, the C<sub>ant</sub> of the lower layer generally grows at steady-state pace, while the upper layer increases faster. This is mainly due to a weakening of the northward advection of the Antarctic Intermediate Water, with the influence of the more C<sub>ant</sub>-loaded surrounding waters favouring the C<sub>ant</sub> increase.

## Acknowledgements

Thanks are due to the cruise participants of the MOC2 cruise, the BIO Hespérides crew and the scientific and technical team, for their indispensable help. We also wish to thank A. Velo for his support with the 3DwMLR method, Paula C. Pardo for her very useful comments and advices and two anonymous reviewers for their careful reading and their many insightful and constructive comments. This work was funded by the 7th Framework Programme (EU FP7 CARBOCHANGE, under grant agreement no. 264879) and by the Spanish Ministry of Economy and Competitiveness through Projects GHGMOC (CTM2009-07574-E), MOC2 (CTM2008-06438-C02-01/MAR) and ESCLAT (CTM2009-07405-E/MAR) and by the Deutsche Forschungsgemeinschaft (DFG) (M. Rhein, grant Rh25/36-1). FFP and AFR were supported by the Spanish Government and co-founded by the European Regional Development Fund (CTM2013-41048-P).

## Appendix A

**Table 3.2** CI. 2010 mean data. Mean values and standard errors of the mean ( $x \pm \varepsilon$ ) salinity, potential temperature ( $\theta, ^\circ\text{C}$ ),  $A_T$  ( $\mu\text{mol}\cdot\text{kg}^{-1}$ ),  $C_T$  ( $\mu\text{mol}\cdot\text{kg}^{-1}$ ),  $C_{\text{ant}} - \phi C_T^0$  ( $\mu\text{mol}\cdot\text{kg}^{-1}$ ) and  $C_{\text{ant}}\text{-TTD}$  ( $\mu\text{mol}\cdot\text{kg}^{-1}$ ) for 2010. The thickness (m) of each layer was computed as the averaged vertical distance between layers weighted by the distance between stations.

Cruise (Exocode)	year	$A_T$	$C_T$
TTO/TAS Leg 3	1981	-0.2±3.9	-4.7±5.0
32OC133 A20) 1983	1983	0.8±1.8	
32OC202_1-2_(A16Nad-1988)	1988	0.2±2.1	
3230CITHER2 (WOCE A17-1994)	1994	-3.0±2.3	-3.2±2.7
06MT19940219 (WOCE AR04e)	1994	1.5±1.4	
316N142_3 (A15/1994)	1994	1.7±1.3	
35LU19950909 (WOCE AR04g)	1995	-0.4±2.8	0.2±4.5
33LK19960415 (WOCE AR04h/AR15)	1996	0.4±3.1	0.3±1.6
35TH19990712 (Equalant 99)	1999	-0.6±1.7	-5.0±4.1
06MT20020607	2002	2.0±1.1	
06MT20021013	2002	3.2±1.2	
33RO20030604 (A16N/2003)	2003	0.9±2.4	0.3±1.6
29HE20100405 (MOC2/2010)	2010	0.6±2.7	1.5±3.5
29HE20130320 (A17-2013)	2013	0.0±1.2	
weighted average		<b>0.8±1.8</b>	<b>-1.1±3.3</b>

## Appendix B

**Table 3.2** BI. 1993 mean data. Mean values and standard errors of the mean ( $x \pm \varepsilon$ ) salinity, potential temperature ( $\Theta$ , °C),  $A_T$  ( $\mu\text{mol}\cdot\text{kg}^{-1}$ ),  $C_T$  ( $\mu\text{mol}\cdot\text{kg}^{-1}$ ),  $C_{\text{ant}}-\varphi C_T^0$  ( $\mu\text{mol}\cdot\text{kg}^{-1}$ ) and  $C_{\text{ant}}-\text{TTD}$  ( $\mu\text{mol}\cdot\text{kg}^{-1}$ ) for 1993. The thickness (m) of each layer was computed as the averaged vertical distance between layers weighted by the distance between stations. An additional factor, shown in the first column, was applied so that each region had the same total depth as in the 2010 MOC2 cruise..

Region	Layer	Thickness	Salinity	$\Theta$	$A_T$	$C_T$	$C_{\text{ant}}-\varphi C_T^0$	$C_{\text{ant}}-\text{TTD}$
WB 1.012	SACW	143±12	36.315±0.022	25.18±0.32	2379±1	2050±6	53.4±0.7 (n=40)	54.2±0.6 (n=68)
	SAMW	269±19	35.114±0.046	10.75±0.31	2315±2	2182±3	20.8±1.3 (n=28)	21.2±0.9 (n=53)
	AAIW	658±21	34.642±0.012	5.81±0.12	2303±1	2213±1	9.8±0.7 (n=40)	7.2±0.4 (n=78)
	uNADW	1167±59	34.980±0.009	4.06±0.07	2315±0	2166±1	8.9±0.3 (n=78)	8.5±0.2 (n=151)
	INADW	1532±129	34.913±0.002	2.22±0.03	2326±0	2170±0	5.4±0.2 (n=69)	7.4±0.1 (n=133)
WR 0.988	AABW	156±18	34.877±0.002	1.75±0.01	2334±1	2183±2	4.8±0.4 (n=11)	7.3±0.1 (n=24)
	SACW	146±9	36.164±0.027	24.48±0.42	2369±2	2046±9	51.3±1.4 (n=27)	53.3±1.0 (n=60)
	SAMW	347±10	34.973±0.027	9.89±0.21	2308±1	2193±3	18.8±0.9 (n=26)	18.0±0.7 (n=55)
	AAIW	579±12	34.688±0.006	5.83±0.10	2302±0	2218±1	6.2±0.9 (n=31)	5.0±0.3 (n=71)
	uNADW	1306±28	34.962±0.003	3.86±0.04	2318±0	2172±1	7.5±0.3 (n=107)	6.1±0.1 (n=217)
ER 0.988	INADW	1709±63	34.908±0.001	2.24±0.02	2333±0	2179±1	5.9±0.1 (n=109)	5.1±0.1 (n=235)
	AABW	552±59	34.835±0.003	1.42±0.03	2348±1	2208±2	7.7±0.2 (n=38)	5.0±0.1 (n=70)
	SACW	103±6	36.014±0.035	22.67±0.62	2361±2	2058±13	52.5±1.0 (n=25)	48.2±1.5 (n=45)
	SAMW	383±6	35.149±0.024	11.47±0.22	2314±1	2198±4	20.7±1.3 (n=28)	20.7±0.8 (n=56)
	AAIW	573±7	34.694±0.007	5.83±0.12	2304±1	2225±1	6.1±0.7 (n=28)	4.1±0.2 (n=60)
EB 1.023	uNADW	1424±16	34.932±0.004	3.84±0.04	2321±0	2180±1	6.7±0.3 (n=102)	3.6±0.1 (n=206)
	INADW	1927±103	34.900±0.001	2.18±0.02	2340±0	2189±1	6.5±0.1 (n=114)	3.3±0.0 (n=212)
	SACW	148±7	35.609±0.024	20.53±0.46	2335±2	2108±13	48.5±1.0 (n=48)	42.4±1.4 (n=70)
	SAMW	338±9	35.182±0.021	11.61±0.23	2314±1	2215±4	22.1±1.3 (n=26)	18.4±1.0 (n=40)
	AAIW	588±7	34.718±0.005	5.88±0.11	2306±1	2234±2	6.4±0.7 (n=27)	3.6±0.2 (n=49)
EB 1.023	uNADW	1251±54	34.922±0.003	3.78±0.04	2322±0	2192±1	7.2±0.3 (n=64)	2.6±0.1 (n=104)
	INADW	1791±152	34.905±0.002	2.26±0.02	2345±1	2198±1	8.7±0.2 (n=60)	2.9±0.1 (n=109)

## Appendix C

**Table 3.2** CI. 2010 mean data. Mean values and standard errors of the mean ( $x \pm \varepsilon$ ) salinity, potential temperature ( $\theta$ , °C),  $A_T$  ( $\mu\text{mol}\cdot\text{kg}^{-1}$ ),  $C_T$  ( $\mu\text{mol}\cdot\text{kg}^{-1}$ ),  $C_{\text{ant}}\cdot\varphi C_T^0$  ( $\mu\text{mol}\cdot\text{kg}^{-1}$ ) and  $C_{\text{ant}}\text{-TTD}$  ( $\mu\text{mol}\cdot\text{kg}^{-1}$ ) for 1993. The thickness (m) of each layer was computed as the averaged vertical distance between layers weighted by the distance between stations.

Region	Layer	Thickness	Salinity	$\theta$	$A_T$	$C_T$	$C_{\text{ant}}\cdot\varphi C_T^0$	$C_{\text{ant}}\text{-TTD}$
WB	SACW	168±8	36.098±0.029	25.48±0.45	2365±2	2040±7	69.8±0.7 (n=74)	72.0±1.7 (n=26)
	SAMW	290±17	34.974±0.036	10.02±0.25	2308±2	2192±2	31.0±0.9 (n=49)	27.9±1.6 (n=18)
	AAIW	564±21	34.645±0.007	5.96±0.12	2300±1	2219±1	15.5±0.8 (n=56)	8.3±0.6 (n=32)
	uNADW	1162±62	34.944±0.009	4.23±0.11	2314±0	2179±3	10.9±0.4 (n=44)	11.0±0.6 (n=31)
	INADW	1581±83	34.916±0.003	2.30±0.05	2324±1	2172±1	7.3±0.2 (n=45)	10.7±0.3 (n=33)
	AABW	161±14	34.867±0.004	1.70±0.03	2338±1	2191±2	7.2±0.3 (n=6)	9.0±0.4 (n=5)
WR	SACW	148±4	36.064±0.015	24.95±0.36	2363±1	2052±6	64.7±1.2 (n=105)	72.3±1.5 (n=42)
	SAMW	349±10	35.013±0.018	10.37±0.14	2309±1	2195±2	31.9±0.7 (n=132)	26.7±1.1 (n=39)
	AAIW	600±10	34.700±0.005	6.15±0.10	2302±0	2225±1	14.8±0.5 (n=101)	7.6±0.5 (n=61)
	uNADW	1160±20	34.946±0.006	4.16±0.07	2316±0	2180±2	10.6±0.3 (n=76)	8.9±0.4 (n=48)
	INADW	1881±63	34.915±0.002	2.35±0.04	2329±0	2177±1	7.7±0.1 (n=98)	7.3±0.2 (n=61)
	AABW	502±33	34.827±0.003	1.38±0.03	2348±1	2210±1	8.8±0.2 (n=33)	6.7±0.1 (n=19)
ER	SACW	127±5	35.815±0.021	21.65±0.60	2349±1	2106±10	63.5±1.2 (n=74)	61.1±2.9 (n=21)
	SAMW	363±15	35.138±0.017	11.47±0.17	2314±1	2204±3	34.4±0.8 (n=89)	27.6±2.4 (n=18)
	AAIW	610±13	34.718±0.009	6.24±0.15	2304±0	2234±1	14.8±0.6 (n=62)	6.6±0.6 (n=33)
	uNADW	1179±33	34.926±0.008	4.06±0.08	2317±0	2187±2	9.2±0.3 (n=46)	5.2±0.4 (n=25)
	INADW	2131±115	34.906±0.002	2.27±0.04	2337±1	2188±1	7.7±0.1 (n=73)	3.9±0.2 (n=38)
EB	SACW	192±7	35.609±0.014	20.50±0.81	2338±2	2124±18	61.2±1.6 (n=38)	59.6±4.1 (n=15)
	SAMW	268±9	35.209±0.030	11.82±0.33	2316±1	2229±4	35.0±1.9 (n=19)	33.7±1.5 (n=8)
	AAIW	644±5	34.733±0.011	6.33±0.19	2305±1	2242±2	15.2±0.9 (n=26)	5.6±0.6 (n=22)
	uNADW	1035±111	34.912±0.010	3.95±0.12	2320±1	2196±3	7.8±0.3 (n=17)	3.2±0.6 (n=15)
	INADW	1978±230	34.905±0.005	2.28±0.07	2343±2	2197±2	8.2±0.3 (n=21)	2.4±0.2 (n=20)

## References

- Álvarez, M., Ríos, A.F., Pérez, F.F., Bryden, H.L., Rosón, G., 2003. Transports and budgets of total inorganic carbon in the subpolar and temperate North Atlantic. *Glob. Biogeochem Cycles* 17, 1002. doi:10.1029/2002GB001881
- Andrié, C., Ternon, J.-F., Messias, M.-J., Memery, L., Bourlès, B., 1998. Chlorofluoromethane distributions in the deep equatorial Atlantic during January–March 1993. *Deep Sea Res. Part Oceanogr. Res. Pap.* 45, 903–930. doi:10.1016/S0967-0637(98)00003-X
- Arhan, M., Mercier, H., Bourles, B., Gouriou, Y., 1998. Hydrographic sections across the Atlantic at 7°30N and 4°30S. *Deep Sea Res. Part Oceanogr. Res. Pap.* 45, 829–872.
- Ballantyne, A.P., Alden, C.B., Miller, J.B., Tans, P.P., White, J.W.C., 2012. Increase in observed net carbon dioxide uptake by land and oceans during the past 50 years. *Nature* 488, 70–72.
- Brandt, P., Greatbatch, R.J., Claus, M., Didwischus, S.-H., Hormann, V., Funk, A., Hahn, J., Krahmann, G., Fischer, J., Kötzinger, A., 2012. Ventilation of the equatorial Atlantic by the equatorial deep jets. *J. Geophys. Res. Oceans* 117, C12015. doi:10.1029/2012JC008118
- Brandt, P., Hormann, V., Kötzinger, A., Visbeck, M., Krahmann, G., Stramma, L., Lumpkin, R., Schmid, C., 2010. Changes in the ventilation of the oxygen minimum zone of the tropical North Atlantic. *J. Phys. Oceanogr.* 40, 1784–1801. doi:10.1175/2010JPO4301.1
- Brea, S., Álvarez-Salgado, X.A., Álvarez, M., Pérez, F.F., Mémery, L., Mercier, H., Messias, M.J., 2004. Nutrient mineralization rates and ratios in the eastern South Atlantic. *J. Geophys. Res.* 109. doi:10.1029/2003JC002051
- Brewer, P.G., 1978. Direct observation of the oceanic CO<sub>2</sub> increase. *Geophys. Res. Lett.* 5, 997–1000. doi:10.1029/GL005i012p00997
- Bulsiewicz, K., Rose, H., Klatt, O., Putzka, A., Roether, W., 1998. A capillary-column chromatographic system for efficient chlorofluorocarbon measurement in ocean waters. *J. Geophys. Res. Oceans* 1978–2012 103, 15959–15970.
- Ciais, P., Sabine, C., Bala, G., Bopp, L., Brovkin, V., Canadell, J., Chhabra, A., DeFries, R., Galloway, J., Heimann, M., Jones, C., Le Quéré, C., Myneni, R.B., Piao, S., Thornton, P., 2013: Carbon and Other Biogeochemical Cycles. In: Climate Change 2013: The Physical Science Basis. Contribution of Working Group I to the Fifth Assessment Report of the Intergovernmental Panel on Climate Change [Stocker, T.F., D. Qin, G.-K. Plattner, M. Tignor, S.K. Allen, J. Boschung, A. Nauels, Y. Xia, V. Bex and P.M. Midgley (eds.)]. Cambridge University Press, Cambridge, United Kingdom and New York, NY, USA.
- Chen, G.-T., Millero, F.J., 1979. Gradual increase of oceanic CO<sub>2</sub>. *Nature* 277, 205–206. doi:10.1038/277205a0
- Clayton, T.D., Byrne, R.H., 1993. Spectrophotometric seawater pH measurements: total hydrogen ion concentration scale calibration of m-cresol purple and at-sea results. *Deep-Sea Res.* 40, 2115–2129.
- Culberson, C.H., 1991. WOCE operations manual (WHP operations and methods), WHPO 91/1. Woods Hole Oceanogr. Inst., Woods Hole, Mass.
- DelValls, T., Dickson, A., 1998. The pH of buffers based on 2-amino-2-hydroxymethyl-1, 3-propanediol (“tris”) in synthetic sea water. *Deep-Sea Res. Part I* 45, 1541–1554.
- Dickson, A., Millero, F., 1987. A comparison of the equilibrium constants for the dissociation of carbonic acid in seawater media. *Deep-Sea Res.* 34, 1733–1743. doi:10.1016/0198-0149(87)90021-5
- Friis, K., Kötzinger, A., Pätsch, J., Wallace, D.W.R., 2005. On the temporal increase of anthropogenic CO<sub>2</sub> in the subpolar North Atlantic. *Deep Sea Res. Part Oceanogr. Res. Pap.* 52, 681–698. doi:10.1016/j.dsr.2004.11.017

- Gammon, R.H., Cline, J., Wisegarver, D., 1982. Chlorofluoromethanes in the northeast Pacific Ocean: Measured vertical distributions and application as transient tracers of upper ocean mixing. *J. Geophys. Res. Oceans* 1978–2012 87, 9441–9454.
- Gieskes, J.M., 1969. Effect of temperature on the pH of seawater. *Limnol. Oceanogr.* 14, 679–685. doi:10.4319/lo.1969.14.5.0679
- Gouretski, V.V., Jancke, K., 2000. Systematic errors as the cause for an apparent deep water property variability: global analysis of the WOCE and historical hydrographic data. *Prog. Oceanogr.* 48, 337–402. doi:[http://dx.doi.org/10.1016/S0079-6611\(00\)00049-5](http://dx.doi.org/10.1016/S0079-6611(00)00049-5)
- Gruber, N., Gloor, M., Mikaloff Fletcher, S.E., Doney, S.C., Dutkiewicz, S., Follows, M.J., Gerber, M., Jacobson, A.R., Joos, F., Lindsay, K., Menemenlis, D., Mouchet, A., Müller, S.A., Sarmiento, J.L., Takahashi, T., 2009. Oceanic sources, sinks, and transport of atmospheric CO<sub>2</sub>. *Glob. Biogeochem. Cycles* 23. doi:10.1029/2008GB003349
- Gruber, N., Sarmiento, J.L., Stocker, T.F., 1996. An improved method for detecting anthropogenic CO<sub>2</sub> in the oceans. *Glob. Biogeochem. Cycles* 10, 809–837.
- Guallart, E.F., Schuster, U., Fajar, N.M., Legge, O., Brown, P., Pelejero, C., Messias, M.-J., Calvo, E., Watson, A., Ríos, A.F., Pérez, F.F., 2015. Trends in anthropogenic CO<sub>2</sub> in water masses of the Subtropical North Atlantic Ocean. *Prog. Oceanogr.* 131, 21–32.
- Hernández-Guerra, A., Pelegrí, J.L., Fraile-Nuez, E., Benítez-Barrios, V., Emelianov, M., Pérez-Hernández, M.D., Vélez-Belchí, P., 2014. Meridional overturning transports at 7.5N and 24.5N in the Atlantic Ocean during 1992–93 and 2010–11. *Prog. Oceanogr.* 128, 98–114. doi:10.1016/j.pocean.2014.08.016
- Herraiz-Borreguero, L., Rintoul, S.R., 2011. Subantarctic mode water: distribution and circulation. *Ocean Dyn.* 61, 103–126. doi:10.1007/s10236-010-0352-9
- Holfort, J., Johnson, K.M., Schneider, B., Siedler, G., Wallace, D.W., 1998. Meridional transport of dissolved inorganic carbon in the South Atlantic Ocean. *Glob. Biogeochem. Cycles* 12, 479–499.
- Johnson, G.C., 2008. Quantifying Antarctic bottom water and North Atlantic deep water volumes. *J Geophys Res* 113, C05027. doi:10.1029/2007JC004477
- Johnson, K.M., Wills, K.D., Butler, D.B., Johnson, W.K., Wong, C.S., 1993. Coulometric total carbon dioxide analysis for marine studies: maximizing the performance of an automated gas extraction system and coulometric detector. *Mar. Chem.* 44, 167–187.
- Keeling, C.D., Bolin, B., 1967. The simultaneous use of chemical tracers in oceanic studies I. General theory of reservoir models. *Tellus* 19, 566–581. doi:10.1111/j.2153-3490.1967.tb01509.x
- Key, R.M., Tanhua, T., Olsen, A., Hoppema, M., Jutterström, S., Schirnick, C., van Heuven, S., Kozyr, A., Lin, X., Velo, A., Wallace, D.W.R., Mintrop, L., 2010. The CARINA data synthesis project: Introduction and overview. *Earth Syst Sci Data* 2, 105–121. doi:10.5194/essd-2-105-2010
- Khatiwala, S., Primeau, F., Hall, T., 2009. Reconstruction of the history of anthropogenic CO<sub>2</sub> concentrations in the ocean. *Nature*, 462, 346–349, doi:10.1038/nature08526.
- Khatiwala, S., Tanhua, T., Mikaloff Fletcher, S., Gerber, M., Doney, S.C., Graven, H.D., Gruber, N., McKinley, G.A., Murata, A., Ríos, A.F., Sabine, C.L., 2013. Global ocean storage of anthropogenic carbon. *Biogeosciences* 10, 2169–2191. doi:10.5194/bg-10-2169-2013
- Lazier, J., Hendry, R., Clarke, A., Yashayaev, I., Rhines, P., 2002. Convection and restratification in the Labrador Sea, 1990–2000. *Deep Sea Res. Part Oceanogr. Res. Pap.* 49, 1819–1835. doi:10.1016/S0967-0637(02)00064-X
- Lee, K., Choi, S.D., Park, G.H., Wanninkhof, R., Peng, T.H., Key, R.M., Sabine, C.L., Feely, R.A., Bullister, J.L., Millero, F.J., 2003. An updated anthropogenic CO<sub>2</sub> inventory in the Atlantic Ocean. *Glob. Biogeochem. Cycles* 17, 1116. doi:10.1029/2003GB002067

- Le Quéré, C., Andres, R.J., Boden, T., Conway, T., Houghton, R.A., House, J.I., Marland, G., Peters, G.P., van der Werf, G.R., Ahlström, A., Andrew, R. M., Bopp, L., Canadell, J. G., Ciais, P., Doney, S. C., Enright, C., Friedlingstein, P., Huntingford, C., Jain, A. K., Jourdain, C., Kato, E., Keeling, R. F., Klein Goldewijk, K., Levis, S., Levy, P., Lomas, M., Poulter, B., Raupach, M. R., Schwinger, J., Sitch, S., Stocker, B. D., Viovy, N., Zaehle, S., and Zeng, N., 2013. The global carbon budget 1959–2011. *Earth Syst. Sci. Data* 5, 165–185. doi:10.5194/essd-5-165-2013
- Le Quéré, C., Moriarty, R., Andrew, R.M., Peters, G.P., Ciais, P., Friedlingstein, P., Jones, S.D., Sitch, S., Tans, P., Arneth, A., Boden, T.A., Bopp, L., Bozec, Y., Canadell, J.G., Chevallier, F., Cosca, C.E., Harris, I., Hoppema, M., Houghton, R.A., House, J.I., Jain, A., Johannessen, T., Kato, E., Keeling, R.F., Kitidis, V., Klein Goldewijk, K., Koven, C., Landa, C.S., Landschützer, P., Lenton, A., Lima, I.D., Marland, G., Mathis, J.T., Metzl, N., Nojiri, Y., Olsen, A., Ono, T., Peters, W., Pfeil, B., Poulter, B., Raupach, M.R., Regnier, P., Rödenbeck, C., Saito, S., Salisbury, J.E., Schuster, U., Schwinger, J., Séférian, R., Segschneider, J., Steinhoff, T., Stocker, B.D., Sutton, A.J., Takahashi, T., Tilbrook, B., van der Werf, G.R., Viovy, N., Wang, Y.-P., Wanninkhof, R., Wiltshire, A., Zeng, N., 2014. Global carbon budget 2014. *Earth Syst. Sci. Data Discuss.* 7, 521–610. doi:10.5194/essd-7-521-2014
- Le Quéré, C., Raupach, M.R., Canadell, J.G., Marland, G., Bopp, L., Conway, T.J., Doney, S.C., Feely, R.A., Foster, P., Friedlingstein, P., Gurney, K., Houghton, R.A., House, J.I., Huntingford, C., Levy, P.E., Lomas, M.R., Majkut, J., Metzl, N., Ometto, J.P., Peters, G., Prentice, I.C., Randerson, J.T., Running, S.W., Sarmiento, J.L., Schuster, U., Sitch, S., Takahashi, T., Viovy, N., van der Werf, G.R., Woodward, F.I., 2009. Trends in the sources and sinks of carbon dioxide. *Nat. Geosci.* 2, 831–836. doi:10.1038/ngeo689
- Lo Monaco, C., Goyet, C., Metzl, N., Poisson, A., Touratier, F., 2005. Distribution and inventory of anthropogenic CO<sub>2</sub> in the Southern Ocean: Comparison of three data-based methods. *J. Geophys. Res.* 110, 9. doi:10.1029/2004JC002571
- Mehrbach, C., Culberson, C., Hawley, J., Pytkowicz, R., 1973. Measurement of the apparent dissociation constants of carbonic acid in seawater at atmospheric pressure. *Limnol. Oceanogr.* 897–907.
- Mémery, L., Arhan, M., Álvarez-Salgado, X.A., Messias, M.J., Mercier, H., Castro, C.G., Ríos, A.F., 2000. The water masses along the western boundary of the south and equatorial Atlantic. *Prog. Oceanogr.* 47, 69–98. doi:10.1016/S0079-6611(00)00032-X
- Mikaloff Fletcher, S.E., Gruber, N., Jacobson, A.R., Doney, S.C., Dutkiewicz, S., Gerber, M., Follows, M., Joos, F., Lindsay, K., Menemenlis, D., others, 2006. Inverse estimates of anthropogenic CO<sub>2</sub> uptake, transport, and storage by the ocean. *Glob. Biogeochem. Cycles* 20. doi:10.1029/2005GB002530
- Millero, F.J., 1979. The thermodynamics of the carbonate system in seawater. *Geochim. Cosmochim. Acta* 43, 1651–1661. doi:10.1016/0016-7037(79)90184-4
- Mintrop, L., Pérez, F., González-Dávila, M., Santana-Casiano, J., Kötzinger, A., 2000. Alkalinity determination by potentiometry: Intercalibration using three different methods. *Cienc. Mar.* 26, 23–37.
- Murata, A., Kumamoto, Y., Sasaki, K., Watanabe, S., Fukasawa, M., 2008. Decadal increases of anthropogenic CO<sub>2</sub> in the subtropical South Atlantic Ocean along 30°S. *J. Geophys. Res.* 113, C06007. doi:10.1029/2007JC004424
- Oudot, C., 1993. Total CO<sub>2</sub> and Total Alkalinity Data Obtained during the R/V L'Atalante cruise in the Atlantic Ocean (WOCE Section A06, 02 Jan. - 10 Feb., 1993). Carbon Dioxide Information Analysis Center, Oak Ridge National Laboratory, US Department of Energy, Oak Ridge, Tennessee. doi:10.3334/CDIAC/otg.WOCE\_A06\_1993
- Oudot, C., Morin, P., Baurand, F., Wafar, M., Corre, P.L., 1998. Northern and southern water masses in the equatorial Atlantic distribution of nutrients on the WOCE A6 and A7 lines. *Deep-Sea Res. Part I* 45, 873–902. doi:10.1016/S0967-0637(98)00002-8
- Oudot, C., Ternon, J.F., 1994. Mesures des paramètres du système CO<sub>2</sub>. Recueil de Données, Campagne CITHER 1, (Traceurs géochimiques/2). Doc Sci 0ORSTOM Cayenne 4, 9–48.

- Oudot, C., Ternon, J.F., Lecomte, J., 1995. Measurements of atmospheric and oceanic CO<sub>2</sub> in the tropical Atlantic: 10 years after the 1982-1984 FOCAL cruises. *Tellus B* 47, 70–85. doi:10.1034/j.1600-0889.47.issue1.8.x
- Pérez, F.F., Fraga, F., 1987. A precise and rapid analytical procedure for alkalinity determination. *Mar. Chem.* 21, 169–182. doi:10.1016/0304-4203(87)90037-5
- Pérez, F.F., Mercier, H., Vázquez-Rodríguez, M., Lherminier, P., Velo, A., Pardo, P.C., Rosón, G., Ríos, A.F., 2013. Atlantic Ocean CO<sub>2</sub> uptake reduced by weakening of the meridional overturning circulation. *Nat. Geosci.* 6, 146–152. doi:10.1038/ngeo1680.
- Plancherel, Y., Rodgers, K. B., Key, R.M., Jacobson, A. R., Sarmiento, J.L., 2013. Role of regression model selection and station distribution on the estimation of oceanic anthropogenic carbon change by eMLR. *Biogeosciences*, 10, 4801–4831, doi:10.5194/bg-10-4801-2013
- Rhein, M., Stramma, L., Krahmann, G., 1998. The spreading of Antarctic Bottom Water in the tropical Atlantic. *Deep Sea Res.-Part -Oceanogr. Res. Pap.* 45, 507–528. doi:10.1016/S0967-0637(97)00030-7
- Ríos, A.F., Pérez, F.F., Pelegrí, J.L., Fajardo, N.M., 2012a. Carbon Data Obtained During the R/V Hesperides Cruise in the Atlantic Ocean on CLIVAR Repeat Hydrography Section A06 (5 April - 16 May, 2010). Carbon Dioxide Information Analysis Center, Oak Ridge National Laboratory, US Department of Energy, Oak Ridge, Tennessee. doi:10.3334/CDIAC/OTG.CLIVAR\_A06\_2010
- Ríos, A.F., Vázquez-Rodríguez, M., Padín, X.A., Pérez, F.F., 2010. Anthropogenic carbon dioxide in the South Atlantic western basin. *J. Mar. Syst.* 83, 38–44. doi:<http://dx.doi.org/10.1016/j.jmarsys.2010.06.010>
- Ríos, A.F., Velo, A., Pardo, P.C., Hoppema, M., Pérez, F.F., 2012b. An update of anthropogenic CO<sub>2</sub> storage rates in the western South Atlantic basin and the role of Antarctic Bottom Water. *J. Mar. Syst.* 94, 197–203. doi:10.1016/j.jmarsys.2011.11.023
- Rosell-Fieschi, M., Pelegrí, J.L., Gourrion, J., 2014. Zonal jets in the equatorial Atlantic Ocean. *Prog. Oceanogr.* 130, 1–18. doi:10.1016/j.pocean.2014.08.008
- Roson, G., Rios, A.F., Perez, F. F., Lavin, A., Bryden, H. L., 2003. Carbon distribution, fluxes, and budgets in the subtropical North Atlantic Ocean (24.5°N). *J. Geophys. Res.*, 108(C5), 3144, doi:10.1029/1999JC000047.
- Sabine, C.L., Feely, R.A., Gruber, N., Key, R.M., Lee, K., Bullister, J.L., Wanninkhof, R., Wong, C.S., Wallace, D.W.R., Tilbrook, B., Millero, F.J., Peng, T.-H., Kozyr, A., Ono, T., Rios, A.F., 2004. The Oceanic Sink for Anthropogenic CO<sub>2</sub>. *Science* 305, 367–371. doi:10.1126/science.1097403
- San Antolín Plaza, M.Á., Pelegrí, J.L., Machín, F.J., Benítez Barrios, V., 2012. Inter-decadal changes in stratification and double diffusion in a transatlantic section along 7.5 N. *Sci. Mar.* 76, 189–207. doi:10.3989/scimar.03616.19G
- Sarafanov, A., Sokov, A., Demidov, A., 2007. Water mass characteristics in the equatorial North Atlantic: A section nominally along 6.5°N, July 2000. *J. Geophys. Res. Oceans* 112, C12023. doi:10.1029/2007JC004222
- Steinfeldt, R., Rhein, M., Bullister, J.L., Tanhua, T., 2009. Inventory changes in anthropogenic carbon from 1997–2003 in the Atlantic Ocean between 20°S and 65°N. *Glob. Biogeochem. Cycles* 23, GB3010. doi:10.1029/2008GB003311
- Steinfeldt, R., Rhein, M., Walter, M., 2007. NADW transformation at the western boundary between 66W/20N and 60W/10N. *Deep Sea Res. Part Oceanogr. Res. Pap.* 54, 835–855. doi:10.1016/j.dsr.2007.03.004
- Stramma, L., Brandt, P., Schafstall, J., Schott, F., Fischer, J., Körtzinger, A., 2008. Oxygen minimum zone in the North Atlantic south and east of the Cape Verde Islands. *J. Geophys. Res.* 113,
- Stramma, L., England, M., 1999. On the water masses and mean circulation of the South Atlantic Ocean. *J. Geophys. Res.* 104, 20863–20. doi:10.1029/1999JC900139

- Stramma, L., Schott, F., 1999. The mean flow field of the tropical Atlantic Ocean. Deep Sea Res.-Part II-Top. Stud. Oceanogr. 46, 279–304. doi:10.1016/S0967-0645(98)00109-X
- Tanhua, T., Biastoch, A., Körtzinger, A., Lüger, H., Böning, C., Wallace, D.W.R., 2006. Changes of anthropogenic CO<sub>2</sub> and CFCs in the North Atlantic between 1981 and 2004. Glob. Biogeochem. Cycles 20, GB4017. doi:10.1029/2006GB002695
- Tanhua, T., Körtzinger, A., Friis, K., Waugh, D.W., Wallace, D.W., 2007. An estimate of anthropogenic CO<sub>2</sub> inventory from decadal changes in oceanic carbon content. Proc. Natl. Acad. Sci. 104, 3037. doi:10.1073/pnas.0606574104
- Tanhua, T., van Heuven, S., Key, R.M., Velo, A., Olsen, A., Schirnick, C., 2010. Quality control procedures and methods of the CARINA database. Earth Syst Sci Data 2, 35–49. doi:10.5194/essd-2-35-2010, 2010
- Tans, P., Keeling, R., 2014. Trends in Atmospheric Carbon Dioxide [WWW Document]. URL <http://www.esrl.noaa.gov/gmd/ccgg/trends/>
- Ternon, J.F., Oudot, C., Gourlaouen, V., Diverres, D., 2001. The determination of pH in the equatorial Atlantic Ocean and its role in the sound absorption modeling in seawater. J. Mar. Syst. 30, 67–87. doi:10.1016/S0924-7963(01)00038-0
- Thomas, H., Ittekkot, V., 2001. Determination of anthropogenic CO<sub>2</sub> in the North Atlantic Ocean using water mass ages and CO<sub>2</sub> equilibrium chemistry. J. Mar. Syst. 27, 325–336. doi:10.1016/S0924-7963(00)00077-4
- Touratier, F., Azouzi, L., Goyet, C., 2007. CFC-11, D14C and 3H tracers as a means to assess anthropogenic CO<sub>2</sub> concentrations in the ocean. Tellus B 59, 318–325. doi:10.1111/j.1600-0889.2006.00247.x
- Tsuchiya, M., Talley, L.D., McCartney, M.S., 1994. Water-mass distributions in the western South Atlantic; A section from South Georgia Island (54S) northward across the equator. J. Mar. Res. 52, 55–81. doi:<http://dx.doi.org/10.1357/0022240943076759>
- Urbano, D.F., De Almeida, R.A.F., Nobre, P., Hay, A.E., Williams, G.D., Bindoff, N.L., Marsland, S.J., Rintoul, S.R., Anderson, C.R., Siegel, D.A., 2008. Equatorial Undercurrent and North Equatorial Counter-current at 38°W: A new perspective from direct velocity data. J Geophys Res 113, C04041.
- Van Heuven, S.M.A.C., Hoppema, M., Huhn, O., Slagter, H.A., de Baar, H.J.W., 2011. Direct observation of increasing CO<sub>2</sub> in the Weddell Gyre along the Prime Meridian during 1973–2008. Deep Sea Res. Part II Top. Stud. Oceanogr., Physics, Carbon Dioxide, Trace Elements and Isotopes in the Southern Ocean: The Polarstern Expeditions ANT XXIV-3 (2008) and ANT XXIII/3 (2006) 58, 2613–2635. doi:10.1016/j.dsr2.2011.08.007
- Van Heuven, S., Pierrot, D., Lewis, E., Wallace, D., 2009. MATLAB Program developed for CO<sub>2</sub> system calculations. ORNL/CDIAC-105b, Carbon Dioxide Information Analysis Center, Oak Ridge National Laboratory, U.S. Department of Energy, Oak Ridge, Tennessee.
- Vázquez-Rodríguez, M., Padín, X.A., Pardo, P.C., Ríos, A.F., Pérez, F.F., 2012. The subsurface layer reference to calculate preformed alkalinity and air-sea CO<sub>2</sub> disequilibrium in the Atlantic Ocean. J. Mar. Syst. 94, 52–63. doi:10.1016/j.jmarsys.2011.10.008
- Vázquez-Rodríguez, M., Padín, X.A., Ríos, A.F., Bellerby, R.G.J., Pérez, F.F., 2009a. An upgraded carbon-based method to estimate the anthropogenic fraction of dissolved CO<sub>2</sub> in the Atlantic Ocean. Biogeosciences Discuss 6, 4527–4571. doi:10.1016/j.jmarsys.2011.11.023
- Vázquez-Rodríguez, M., Touratier, F., Lo Monaco, C., Waugh, D.W., Padín, X.A., Bellerby, R.G.J., Goyet, C., Metzl, N., Ríos, A.F., Pérez, F.F., 2009b. Anthropogenic carbon distributions in the Atlantic Ocean: data-based estimates from the Arctic to the Antarctic. Biogeosciences 6, 439–451. doi:10.5194/bg-6-439-2009

- Velo, A., Pérez, F.F., Tanhua, T., Gilcoto, M., Ríos, A.F., Key, R.M., 2013. Total alkalinity estimation using MLR and neural network techniques. *J. Mar. Syst.* 111–112, 11–18. doi:10.1016/j.jmarsys.2012.09.002
- Walker, S.J., Weiss, R.F., Salameh, P.K., 2000. Reconstructed histories of the annual mean atmospheric mole fractions for the halocarbons CFC-11 CFC-12, CFC-113, and carbon tetrachloride. *J. Geophys. Res. Oceans* 1978–2012 105, 14285–14296.
- Wanninkhof, R., Doney, S.C., Bullister, J.L., Levine, N.M., Warner, M., Gruber, N., 2010. Detecting anthropogenic CO<sub>2</sub> changes in the interior Atlantic Ocean between 1989 and 2005. *J. Geophys. Res. Oceans* 115, C11028. doi:10.1029/2010JC006251
- Wanninkhof, R., Tsung-Hung, P., Huss, B., Sabine, C.L., Lee, K., 2003. Comparison of inorganic carbon system parameters measured in the Atlantic Ocean from 1990 to 1998 and recommended adjustments. Carbon Dioxide Information Analysis Center, Oak Ridge National Laboratory, ORNL/CDIAC-140. doi:10.2172/814517
- Warner, M.J., Weiss, R.F., 1985. Solubilities of chlorofluorocarbons 11 and 12 in water and seawater. *Deep Sea Res. Part Oceanogr. Res. Pap.* 32, 1485–1497.
- Waugh, D.W., Haine, T.W.N., Hall, T.M., 2004. Transport times and anthropogenic carbon in the subpolar North Atlantic Ocean. *Deep Sea Res. Part Oceanogr. Res. Pap.* 51, 1475–1491. doi:10.1016/j.dsr.2004.06.011
- Waugh, D.W., Hall, T.M., McNeil, B.I., Key, R., Matear, R.J., 2006. Anthropogenic CO<sub>2</sub> in the oceans estimated using transit time distributions. *Tellus B* 58, 376–389. doi:10.1111/j.1600-0889.2006.00222.x
- Zeebe, R.E., 2012. History of Seawater Carbonate Chemistry, Atmospheric CO<sub>2</sub>, and Ocean Acidification. *Annu. Rev. Earth Planet. Sci.* 40, 141–165. doi:10.1146/annurev-earth-042711-105521
- Zeebe, R., Wolf-Gladrow, D., 2001. CO<sub>2</sub> in seawater: equilibrium, kinetics, isotopes. Elsevier Science.





## Chapter 3.3.

Ocean acidification  
along the 24.5°N section  
in the  
subtropical North Atlantic

Guallart E.F., Fajar NM., Padín XA., Vázquez-Rodríguez M., Calvo E., Ríos A.F., Hernández-Guerra A., Pelejero C., Pérez. F.F. 2015. Ocean Acidification along the 24.5°N section in the subtropical North Atlantic. *Geophysical Research Letters*. 42: 450-458.



## **CHAPTER 3.3.**

### **Ocean acidification along the 24.5°N section in the subtropical North Atlantic**

*Elisa F. Guallart<sup>1</sup>, Noelia M Fajardo<sup>2</sup>, Xose Antonio Padín<sup>2</sup>, Marcos Vázquez-Rodríguez<sup>2</sup>, Eva Calvo<sup>1</sup>, Aida F. Ríos<sup>2</sup>, Alonso Hernández-Guerra<sup>3</sup>, Carles Pelejero<sup>1,4</sup>, Fiz F. Pérez<sup>2</sup>.*

#### **Abstract**

Ocean acidification is directly related to increasing atmospheric CO<sub>2</sub> levels due to human activities and the active role of the global ocean in absorbing part of this anthropogenic CO<sub>2</sub>. Here we present an assessment of the pH changes that have occurred along 24.5°N in the subtropical North Atlantic through comparison of pH observations conducted in 1992 and 2011. It reveals an overall decline in pH values in the first 1000 dbar of the water column. The deconvolution of the temporal pH differences into anthropogenic and non-anthropogenic components reveals that natural variability, mostly owed to a decrease in oxygen levels in particular regions of the section, explains the vertical distribution of the larger pH decreases (up to -0.05 pH-units), which are found within the permanent thermocline. The detection of long-term trends in dissolved oxygen in the studied region gains importance for future pH projections, as these changes modulate the anthropogenically-derived acidification. The anthropogenic forcing explains significant acidification deeper than 1000 dbar in the western basin, within the Deep Western Boundary Current.

## Introduction

Oceans have already absorbed 20–35% of the anthropogenic CO<sub>2</sub> (C<sub>ant</sub>) emissions (Khatiwala *et al.*, 2009), contributing to mitigate global warming. However, the resulting C<sub>ant</sub> oceanic invasion affects the chemical balances of the CO<sub>2</sub> system in seawater, raising the amount of total dissolved inorganic carbon in the upper layers, which translates into a decrease in surface ocean pH. On average, the ocean surface waters have already acidified by 0.1 pH units from their pre-industrial levels (Raven *et al.*, 2005). The oxidation of organic matter also lowers seawater pH by adding CO<sub>2</sub> into the water column. A decrease in seawater acidity can thus also be driven by a larger accumulation of respired CO<sub>2</sub> as water masses get older, or by a slowdown in the ventilation of these water masses (Gruber, 2011). Ocean acidification has been termed “the other CO<sub>2</sub> problem” (Doney *et al.*, 2009), a phenomenon that affects a number of chemical and biogeochemical properties and processes. The most well-documented implication is the lowering of calcium carbonate (CaCO<sub>3</sub>) saturation states, which has adverse effects for calcifying organisms, with corals among the most clearly affected marine organisms (Chan and Connolly, 2013). Establishing the rate at which ocean acidification is taking place is important not only to study the fate of marine biota in the face of this global change, but also to understand the future diminishing capacity of the oceans to take up atmospheric CO<sub>2</sub> (Sabine and Tanhua, 2010).

In addition to constraining the past variability of seawater pH through the geological record (Pelejero *et al.*, 2010; Hönisch *et al.*, 2012) and forecasting the future from modeling studies (Resplandy *et al.*, 2013), there is still a lot of work to do regarding modern instrumental measurements to document the most recent evolution of ocean pH. A number of studies (Dore *et al.*, 2009; Byrne *et al.*, 2010; González-Dávila *et al.*, 2010; Vázquez-Rodríguez *et al.*, 2012b) have already reported pH changes at decadal scale by means of monitoring at fixed stations and repeating oceanographic sections. The present work assesses the pH changes that have occurred in the Subtropical North Atlantic between 1992 and 2011 from direct observations along a trans-oceanic line at 24.5°N. These changes, which are studied separately for different water masses, are discussed in the context of the basin-wide circulation.

## Data and Methods

In July and August 1992, high spatial resolution in situ pH measurements were made along the World Ocean Circulation Experiment line A05 at 24.5°N (Figure 3.3.1a), between Las Palmas de Gran Canaria, Spain, and Miami, U.S.A. The pH was measured potentiometrically on 107 stations, with a combined glass electrode associated to a temperature probe (Perez and Fraga, 1987), on the National Bureau of Standards scale. The shipboard precision was ± 0.005 pH units (Ríos and Rosón, 1996). The hydrographic section A05 was reoccupied in January–March 2011, within the frame of the Malaspina 2010 expedition (García-Corral *et al.*, 2014). The pH measurements were obtained on 167 stations using spectrophotometry (Clayton and Byrne, 1993), on the total hydrogen ion scale. A correction for dye impurities was applied to the 2011 pH data (Yao *et al.*, 2007). Measured precision was ± 0.0006. The two pH data sets were converted to the seawater scale

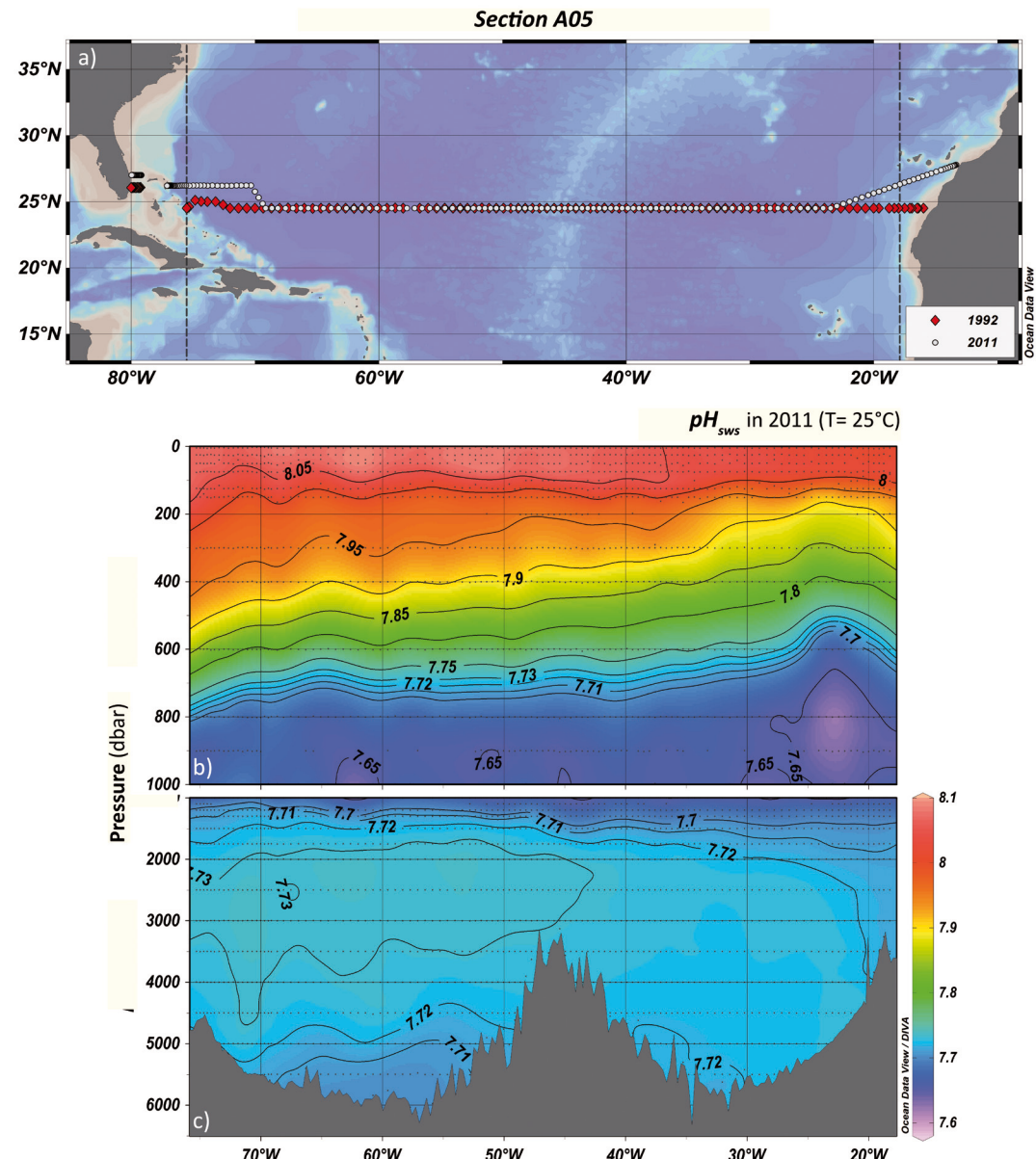


Figure 3.3.1. a) Sampling stations for pH measurements along the hydrographic section A05 in the subtropical North Atlantic, in 1992 (red) and in 2011 (white). (b and c) The distributions of reference pH ( $25^{\circ}\text{C}$ ) on the seawater scale ( $\text{pH}_{\text{sws}}$ ) in 2011 for the upper (first 1000 dbar) and the deep ocean, respectively. The reported pH values correspond to longitude coordinates within the vertical dashed lines in Figure 3.3.1a.

and referenced to 25°C, for comparison, using the CO<sub>2</sub>sys program (Pierrot *et al.*, 2006) with dissociation constants of Mehrbach *et al.* (1973) and refitted by Dickson and Millero (1987). Total alkalinity (A<sub>T</sub>) measurements were obtained in the two cruises by titration of seawater with potentiometric endpoint detection (Mintrop *et al.*, 2000), and the pH–A<sub>T</sub> pair was used to derive the complete CO<sub>2</sub> system in each cruise, using the thermodynamic equations reported above. The accuracy of calculated total dissolved inorganic carbon (C<sub>T</sub>) was assessed through an analysis of internal consistency, by means of a comparison with calibrated C<sub>T</sub> measurements that were also obtained in some of the sampled bottles, in each cruise, in addition to the pH and A<sub>T</sub> measurements. The accuracy for calculated C<sub>T</sub> data was of ± 2–4 µmol kg<sup>-1</sup> (n = 12) in 1992 (Rosón *et al.*, 2003) and ± 3.5 µmol kg<sup>-1</sup> (n = 22) in 2011.

The consistency between the two datasets was investigated by performing a secondary quality control (QC) analysis, following CARbon dioxide IN the Atlantic Ocean (CARINA) procedures (Tanhua *et al.*, 2010). Measured pH and A<sub>T</sub>, calculated C<sub>T</sub>, and measured dissolved oxygen (O<sub>2</sub>) data were compared in the deep ocean with the respective data from other cruises at cross-over locations, in order to look for systematic biases. After the analysis, the 1992 pH data were bias adjusted by adding -0.009 pH units and, in order to avoid a new bias in the calculated C<sub>T</sub> due to the reduction of pH values without changing A<sub>T</sub>, the obtained 1992 A<sub>T</sub> correction (- 4 µmol kg<sup>-1</sup>) was also taken into account (further details in Guallart *et al.* (2013)). By doing this, the original 1992 C<sub>T</sub> data, which had shown good consistency with the discrete measured C<sub>T</sub> values and a very low offset after QC, were kept almost invariable. No further data adjustments were needed.

Comparison between the 1992 and 2011 data sets was done using bottle data from the stations located within the vertical dashed lines in Fig.3.3.1a. For a better comparison, the 1992 and 2011 tracks were made equivalent on latitude first and then the 1992 bottle data grid was interpolated by triangulation into the corresponding depth positions of the 2011 bottle grid using a potential density criterion. The difference in measured pH between 1992 and 2011, ΔpH<sub>m</sub>, was calculated as ΔpH<sub>m</sub> = pH<sub>m,2011</sub> – pH<sub>m,1992</sub>. In order to separate ΔpH<sub>m</sub> in its anthropogenic (ΔpH<sub>ant</sub>) and non-anthropogenic (ΔpH<sub>var</sub>, i.e., attributed to natural variability) components, we performed calculations analogous to those reported by Byrne *et al.*, (2010) for a hydrographic line in the North Pacific, maintaining the same nomenclature. We estimated ΔpH<sub>ant</sub> and ΔpH<sub>var</sub> from the observed changes in C<sub>ant</sub> and natural C<sub>T</sub> during the studied period, by means of the thermodynamic equations of the carbonate system. In order to differentiate between the C<sub>ant</sub> temporal change (ΔC<sub>ant</sub> = C<sub>ant,2011</sub> – C<sub>ant,1992</sub>) and the temporal variability of the natural background of oceanic C<sub>T</sub> (ΔC<sub>var</sub> = C<sub>Var,2011</sub> – C<sub>Var,1992</sub>), the C<sub>ant</sub> fraction of the C<sub>T</sub> estimates in both datasets was isolated using the φC<sub>T</sub><sup>0</sup> method (Pérez *et al.*, 2008; Vázquez-Rodríguez *et al.*, 2009). This method follows the principles of the ΔC\* method (Gruber *et al.*, 1996) given that C<sub>ant</sub> is calculated from the measured C<sub>T</sub> by removing the contribution of organic matter remineralization, calcium carbonate (CaCO<sub>3</sub>) dissolution and an estimate of the C<sub>T</sub> in the preindustrial atmosphere:

$$\begin{aligned} C_{\text{ant}} &= C_T - C_{\text{var}} \\ &= C_T - C_{\text{bio}} - \Delta \text{CaCO}_3 - C_{T,280} - C_{\text{dis}}, \end{aligned}$$

$$= C_T - AOU/Rc - 0.5 (PA_T - PA_T^\circ) - C_{T,280} - C_{dis},$$

yet it uses different parameterizations to calculate the air-sea disequilibrium ( $C_{dis}$ ) and the preformed alkalinity to assess the contribution of  $\text{CaCO}_3$  dissolution ( $\Delta\text{CaCO}_3$ ) on  $C_T$  (Vázquez-Rodríguez *et al.*, 2012a). During the period of study,  $C_{dis}$  is assumed not to change significantly.  $C_{T,280}$  is the  $C_T$  in equilibrium with the preindustrial atmosphere. It is calculated from thermodynamic equations as a function of potential temperature and salinity, preformed alkalinity ( $A_T^\circ$ ), and the corresponding  $\text{pCO}_2$  level of 280 ppm. The  $A_T^\circ$  correction for  $\text{CaCO}_3$  dissolution is parameterized from potential  $A_T$  ( $PA_T$ ). Organic matter remineralization has no effect on  $PA_T$ , because it already considers the contribution from nitrate and phosphate remineralization, according to Redfield ratios proposed by Broecker (1974), but the parameter is subject to alkalinity shifts through the relationship between the dissolution of opal and calcium carbonate (Vázquez-Rodríguez *et al.*, 2012a). The changes in  $\text{CaCO}_3$  dissolution can be considered to be negligible over the period of study (Ilyina *et al.*, 2009). Hence, only the contribution from organic matter remineralization ( $C_{bio}$ ), which is calculated from apparent oxygen utilization (AOU) according to the oxygen to carbon Redfield ratio (Rc) is a major source of changes in  $C_{var}$  at decadal scale, due to changes in the amount of  $O_2$ . This method, following the  $\Delta C^*$  method, uses the Rc ratio from Anderson and Sarmiento (1994).

The  $C_T$  that these water masses would have had at the end of the 19 years period without the presence of the anthropogenic perturbation ( $C_{Var,2011}$ ) over this timeframe was estimated from the subtraction of  $\Delta C_{ant}$  from the  $C_T$  values in 2011 ( $C_{Var,2011} = C_{T,2011} - \Delta C_{ant}$ ). The associated pH ( $pH_{Var,2011}$ ) was then calculated using the carbonate system equations with the dissociation constants reported above.  $pH_{Var,2011}$  was used to compute the anthropogenic component of the pH change ( $\Delta pH_{ant}$ ) as:  $\Delta pH_{ant} = pH_{m,2011} - pH_{Var,2011}$ . The natural background component of the pH change was thus computed as  $\Delta pH_{Var} = \Delta pH_m - \Delta pH_{ant}$ . The uncertainty for  $\Delta pH_m$  amounts to  $\pm 0.0071$  and results from error propagation of the uncertainty that can be assigned to each pH data set (i.e., 0.005 pH units) after secondary quality control. The uncertainties for  $\Delta pH_{ant}$  and  $\Delta pH_{Var}$  were calculated as the standard deviation of the results found for the respective changes in abyssal waters east of 70°W, as these waters are expected to show  $C_{ant}$  levels that fall within the uncertainty of the methodology to estimate  $C_{ant}$  (Brown *et al.*, 2010). These amounted to  $\pm 0.006$  and  $\pm 0.005$  pH-units, respectively. Following Sabine *et al.*, (1999), who found that the error of single  $C_{ant}$  estimations (i.e. the method uncertainty) may be a maximum estimate of the random variability in their results because it was larger than the standard deviation of the  $C_{ant}$  values below the deepest  $C_{ant}$  penetration depth, we also found that the value of  $\pm 0.0071$  may be the maximum error for  $\Delta pH_m$ ,  $\Delta pH_{ant}$  and  $\Delta pH_{Var}$ .

In addition to these calculations, the water column was split into different particular regions following hydrographic criteria: water mass categories and circulation features along the section (see Appendix A). The observed changes in pH within these different regions were studied in terms of the observed changes in other chemical properties (Table 3.3\_B1 in Appendix B) to better assess the anthropogenic and non-anthropogenic processes that contribute to them.

## Results

Figures 3.3.1b and 3.3.1c show the pH distribution along section A05 in 2011, which depict the same basin-wide features as in 1992. The overall pattern consists of high-surface values, higher than 8.05, that decrease rapidly with depth until a pH minimum zone at ~1000 dbar. The prominent pH decrease in the first 1000 dbar is largely associated with remineralization of sinking organic matter by microorganisms (Millero, 2007). The pH minimum (values < 7.65) is found close to the oxygen minimum zone (OMZ) although it is also associated with the influence of aged Antarctic Intermediate Water (AAIW) at depths 800–1100 m depth (Talley, 1996). In the upper ocean, the tilting up of the isolines generates a horizontal gradient in pH in the upper ocean, with pH values becoming lower to the East, with differences of about 0.05 to 0.10 between West and East (Fig. 3.3.1b). Below 1200 dbar, the whole section shows relatively homogeneous low pH values of about 7.70–7.73 pH units (Fig. 3.3.1c). In the deep ocean, the western basin (>45°W) shows slightly higher pH values between 1500 and 3000 dbar due to the influence of the more recently ventilated Labrador Sea Water (LSW). Closer to the bottom, between 5000 and 6000 dbar, a relative pH minimum identifies the Antarctic Bottom Water.

Figure 3.3.2 shows the change in measured pH ( $\Delta\text{pH}_m$ ) along the section over the 19 year period (a negative  $\Delta\text{pH}_m$  indicates a lower pH in 2011). Below the seasonal thermocline (red line in the figure (González-Dávila *et al.*, 2010; Bates *et al.*, 2012), the first 1000 dbar of the water column evidence a general decline in pH along the section that ranges between 0 and -0.06 pH units. The larger changes occur mainly in two depth horizons: the subsurface, between ~150 and ~300 dbar ( $\Delta\text{pH}_m = -0.03$  to -0.06 pH units) and along the whole western basin above the pH minimum zone, between ~400 and ~800 dbar ( $\Delta\text{pH}_m = -0.02$  to -0.04 pH units). Significant positive differences are observed East of 30°W at intermediate depths. As we discuss below, most of the processes that explain this vertical profile have sub-annual variability. The mean overall pH difference from 150 to 1000 dbar is  $-0.023 \pm 0.021$  pH units. In the deeper ocean,  $\Delta\text{pH}_m$  is greater than -0.01 pH units in the Deep Western Boundary Current (DWBC), West of 70°W, reaching noticeable changes up to -0.02 down to 2000 dbar. The remaining deep ocean does not show pH changes with time distinguishable from zero.

The corresponding  $\Delta\text{pH}_{ant}$  field (Figure 3.3.3) indicates the component of  $\Delta\text{pH}_m$  attributed to the atmospheric  $C_{ant}$  penetration into the ocean. The  $\Delta\text{pH}_{ant}$  distribution matches the general profile of changes in  $C_{ant}$ , which are larger at the surface and progressively lower toward the bottom (Brown *et al.*, 2010). The greater differences ( $\Delta\text{pH}_{ant}$  of -0.02 to -0.04) extend from the surface until ~600 dbar, corresponding to  $\Delta C_{ant}$  between +10 and 15  $\mu\text{mol kg}^{-1}$  (calculated from our data). When these changes are studied by splitting the section into different density layers, the observed  $\Delta\text{pH}_{ant}$  for the uppermost central layer show mean differences between -0.025 and -0.034 pH-units (Table S2). These values lead to acidification trends for the 1992 – 2011 period, of  $-0.0014 \pm 0.0004$  and  $-0.0018 \pm 0.0004$  pH units  $\text{yr}^{-1}$  in the regions next to the western and eastern margins, respectively, which are consistent with those reported for surface waters at BATS (Bermuda

Atlantic time-series Study) and ESTOC (European Station for Time series in the Ocean, Canary Islands Time Series in the Subtropical North Atlantic Gyre (González-Dávila *et al.*, 2010; Bates *et al.*, 2012). Below 1000 dbar, significant negative  $\Delta p\text{H}_{\text{ant}}$  are observed at the edges of the section. The deep acidification in the eastern margin ( $\Delta p\text{H}_{\text{ant}} \sim -0.02$ ) suggests a confined  $C_{\text{ant}}$  enrichment (+5 to +10  $\mu\text{mol kg}^{-1}$ ) that is presumably due to the influence of the  $C_{\text{ant}}$ -enriched Mediterranean Water (MW) (Álvarez *et al.*, 2005). The resulting pH trends in the eastern side, in the two layers where MW spreads, are  $-0.0008 \pm 0.0005$  and  $-0.0006 \pm 0.0005$  pH-units  $\text{yr}^{-1}$ , which are in agreement with previous results reported in ESTOC (González-Dávila *et al.*, 2010) and in a transect north of 40°N in the eastern North Atlantic Basin (Vázquez-Rodríguez *et al.*, 2012b). West of 70°W,  $\Delta p\text{H}_{\text{ant}}$  exhibits a vertically homogeneous structure, from below 1000 dbar to the bottom, of more than  $-0.011$  pH units on average that fully explains the observed  $\Delta p\text{H}_{\text{m}}$  (Figure 3.2.2). These changes result from the  $C_{\text{ant}}$  advected by the DWBC along the deep western margin (Steinfeldt *et al.*, 2009; Pérez *et al.*, 2010). The acidification signal due to the  $C_{\text{ant}}$  uptake is even higher from  $\sim 1000$  to  $\sim 2500$  dbar ( $\Delta p\text{H}_{\text{ant}} = -0.02$ ) due to the spreading of the more recently ventilated core of LSW (Steinfeldt *et al.*, 2009) that moves at these pressure ranges. This upper core shows an acidification trend of  $-0.0008 \pm 0.0005$  pH units  $\text{yr}^{-1}$ , which amounts to half the observed trend for this water mass near the formation region, in the Iceland Basin ( $-0.0016 \pm 0.0002$  pH units  $\text{yr}^{-1}$ ) (Vázquez-Rodríguez *et al.*, 2012b). This can be explained by the dilution of the  $C_{\text{ant}}$  signal of the water masses within the DWBC while they move southward, owing to mixing with waters from the ocean interior, as already observed in the tropical Atlantic (Steinfeldt *et al.*, 2007). The extent to which the  $C_{\text{ant}}$  signal dilutes (denoted by the lower decreasing trend at 24.5°N) is also consistent with the findings of Van Sebille *et al.* (2011), who described a reduction by half of the salinity anomaly signal that was advected through the DWBC, from the source region in the Labrador Sea until 26°N, due to the existence of interior pathways for its transport. The observed full-depth distribution of  $\Delta p\text{H}_{\text{ant}}$  along 24.5°N shows a high correlation ( $r^2 = 0.85$ ) with the independent estimation of this parameter from  $C_{\text{ant}}$  estimations based in chlorofluorocarbons observations (more details in Appendix C).

The  $\Delta p\text{H}_{\text{Var}}$  field (Figure 3.3.4) is obtained from the difference between  $\Delta p\text{H}_{\text{m}}$  and  $\Delta p\text{H}_{\text{ant}}$  fields and indicates changes in  $C_{\text{T}}$  due to natural variability in ocean ventilation and respiration processes. In the first 150 dbar, seasonal changes in  $C_{\text{T}}$  are driven by biological processes such as primary production and respiration, which encompass seasonal mixing or stratification events. Below this seasonal thermocline three main structures can be identified as follows:

1. East of 35°W, two cores with values greater than  $-0.03$  pH-units merge through a gradient in  $\Delta p\text{H}_{\text{Var}}$  that decreases until  $\sim 600$  dbar, evidencing a coherent structure near the continental margin. These may correspond to the Canary Eddy Corridor, which is a permanent structure in the north-eastern subtropical Atlantic that extends latitudinally from 29°N to 22°N and reaches at least 30°W of longitude (Sangrà *et al.*, 2009). This corridor recurrently contains long-lived ( $>3$  months) westward propagating mesoscale eddies generated by the Canary Islands whose maximum depths range between 300 and 700 dbar.
2. At deeper depths, a structure with values of  $-0.01$  to  $-0.03$  extends along most of the section with its core

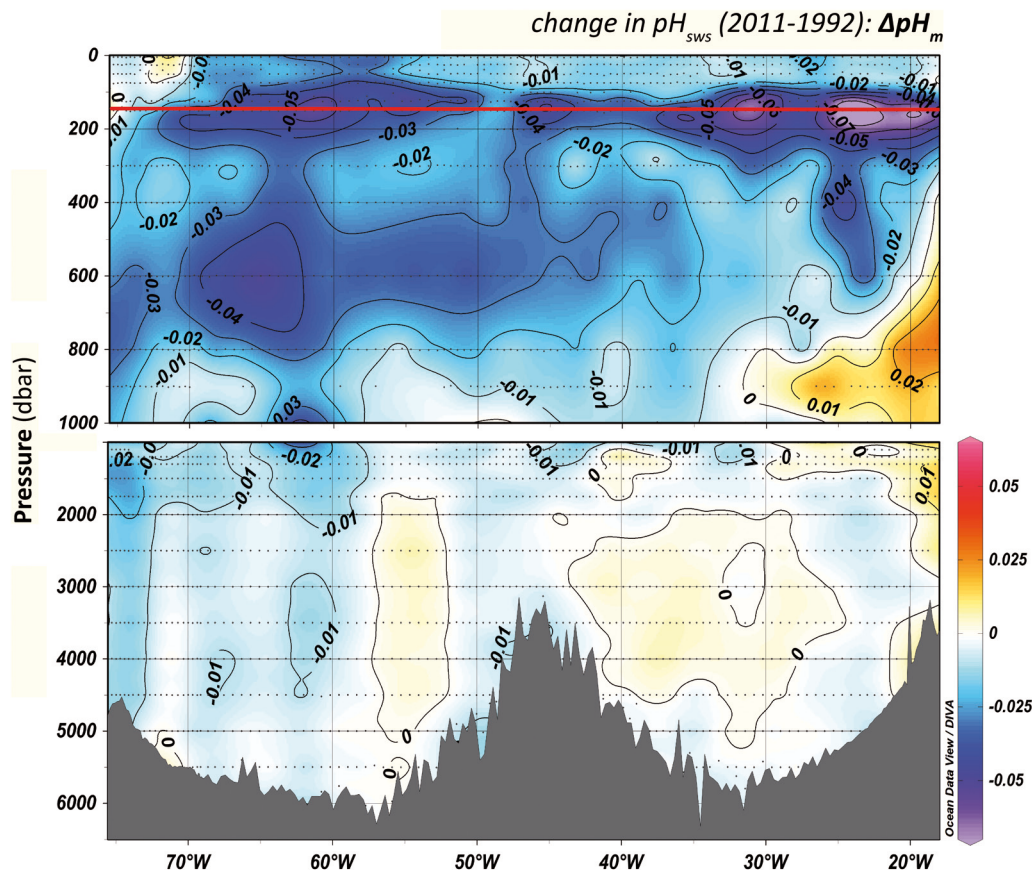


**Figure 3.3.2.** Change in seawater pH,  $\Delta p\text{H}_m$ , along the section A05 between 1992 and 2011. The red line shows the location of the seasonal thermocline at these latitudes (González-Dávila *et al.*, 2010; Bates *et al.*, 2012).

between 50°W and 70°W and at ~ 500 to ~ 800 dbar. These changes are located above and partially overlapping the OMZ. They coincide with a region of considerable decrease in  $O_2$  that explain the rise in AOU values by an average of +14  $\mu\text{mol kg}^{-1}$ . These changes may be the cause of the thickening of the OMZ ( $O_2$  below 155  $\mu\text{mol kg}^{-1}$ ), since 1992, toward shallower depths.

3. East of 30°W, below 700 dbar, positive  $\Delta p\text{H}_{\text{Var}}$  originate from an increase of +10  $\mu\text{mol kg}^{-1}$  in  $O_2$  within the OMZ, without changes in its thickness. The ventilation of the OMZ in the eastern basin is attributable to an enhanced MW presence in 2011. This water mass presents a seasonal intrusion in the section with a greater contribution in late winter and spring (Hernández-Guerra *et al.*, 2014). Hence, this increase in  $O_2$  might be due to latitudinal displacements of waters of southern and Mediterranean origin. On the contrary, the OMZ thickening likely originated from the slow-down in the ventilation of

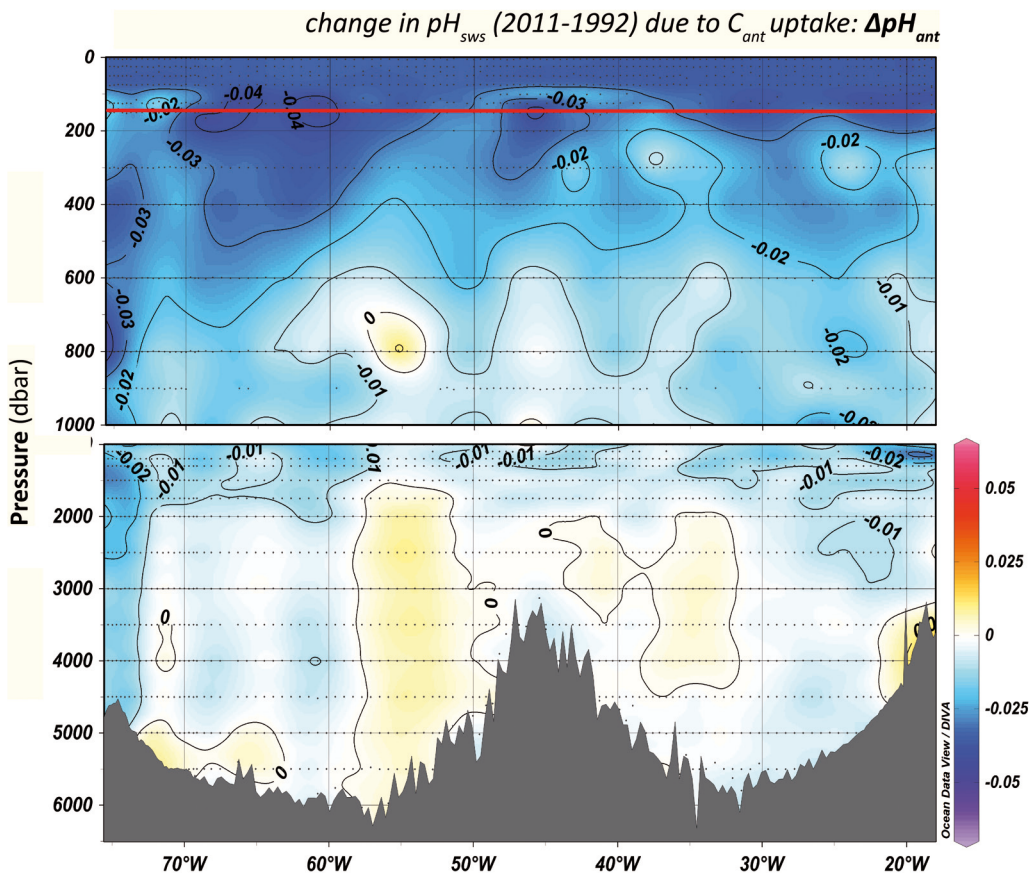


**Figure 3.3.3.** Change in seawater pH attributed to the  $C_{ant}$  uptake by the surface ocean between 1992 and 2011,  $\Delta pH_{ant}$ , along the A05 section. Red line as in Figure 3.3.2.

Subpolar Mode Waters (McCartney and Talley, 1982) that flow above AAIW, modulated by shifts in the winds associated to the North Atlantic Oscillation (NAO) (Bates, 2012; Stendardo and Gruber, 2012). According to Johnson and Gruber (2007), the NAO shift to neutral/negative phase after the mid 1990s (i.e. after the 1992 cruise) caused a lightening of the Subpolar Mode Waters formed afterwards and a reduction of the ventilation of the denser horizons where they spread. This is consistent with our finding of large increases of AOU at the base of the subpolar mode water layer (Fig. 3.3.4 and Table 3.3\_B1, in Appendix B).

When comparing absolute values of  $\Delta pH_{ant}$  and  $\Delta pH_{var}$  (Figures 3.3.3 and 3.3.4, respectively), the most relevant feature is that  $\Delta pH_{var}$  arises as an important contributor to the observed  $\Delta pH_m$  (Figure 3.3.2) in par-

ticular regions of the upper ocean. In the deep ocean, the observed decline in seawater pH within the DWBC is explained only due to changes in  $C_{\text{ant}}$ . Natural variability of  $C_T$  is therefore very likely responsible of the larger decrease in measured pH found below the subsurface within central waters, due to decreases in  $O_2$  (Table 3.3\_B1) that have encompassed the accumulation of  $C_{\text{ant}}$ . This vertical distribution in negative  $\Delta pH_m$  matches model simulations of the future evolution of seawater pH over centennial timescales (Resplandy *et al.*, 2013), which project highest-acidification rates in subsurface (mode and intermediate) waters.

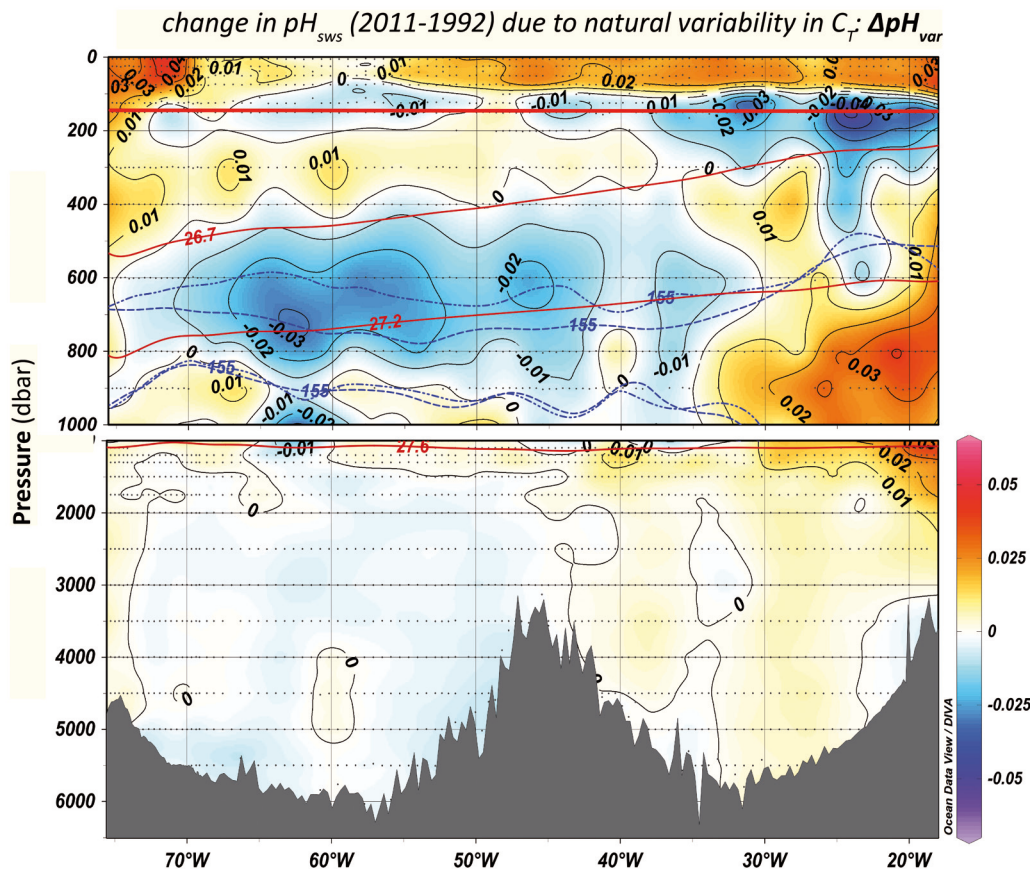


**Figure 3.3.4.** Change in seawater pH attributed to changes in the natural  $C_T$  background between 1992 and 2011,  $\Delta pH_{\text{var}}$ , along the A05 section. Thick red line as in Figure 3.3.2. The three thin dark red lines below depict the bottom isopycnal boundaries ( $\sigma_0 = 26.7$ ;  $\sigma_0 = 27.2$ ;  $\sigma_0 = 27.6$ ) chosen to delimit, respectively, the upper (subtropical origin) and lower (subpolar origin) limbs of Central Water: uNACW and INACW and Antarctic Intermediate Water (AAIW) (see supporting information). The blue lines depict the OMZ (i.e., oxygen levels under  $155 \mu\text{mol kg}^{-1}$ ) horizon in 1992 (dashed line) and in 2011 (dashed-dotted line).

The magnitude of the anthropogenic component of the observed pH decrease is expected to increase as atmospheric  $C_{\text{ant}}$  is gradually absorbed by the ocean (Byrne *et al.*, 2010; Resplandy *et al.*, 2013). Since  $C_{\text{ant}}$  changes will always lead to a decreasing  $\Delta pH_m$ , the anthropogenic forcing becomes more significant for deep and bottom waters because of the higher sensitivity of the more stable deep waters to  $\text{CO}_2$  increases, due to their lower alkalinity, temperature, and higher  $C_T$  compared with intermediate and mode waters (Resplandy *et al.*, 2013). In this context, our results suggest that, in the upper ocean, natural  $C_T$  variability is large enough to regionally modulate the seawater pH in two different ways, reinforcing or counteracting the anthropogenically-derived acidification. The reinforcement of  $\Delta pH_{\text{ant}}$  due to negative  $\Delta pH_{\text{Var}}$  is observable close to the OMZ in the western basin, between 400 and 800 dbar and east of 40°W from the subsurface until 600 dbar, causing an even larger reduction of pH. However, in other regions and depths,  $\Delta pH_{\text{Var}}$  counteracts the  $C_{\text{ant}}$  enrichment, resulting in a net dampening of the acidification signal or even in a pH increase, as observed at intermediate levels of the eastern basin. In addition, the more spatially confined distribution of  $\Delta pH_{\text{Var}}$  results from its modulation by particular changes in  $\text{O}_2$  levels.

Similar to the North Pacific, where ventilation was shown to exert a strong control over changes in  $\text{O}_2$  (Byrne *et al.*, 2010), in the Subtropical North Atlantic the slow-down in ventilation appears to be the main explanation for the large negative  $\Delta pH_m$  observed close to the OMZ. These  $\text{O}_2$  anomalies operate on decadal timescales, from its relationship to the NAO. Our results also suggest that other important players that modulate  $\text{O}_2$  in the studied section include oceanic mesoscale dynamic structures with monthly to seasonal variability such as the Canary Eddy Corridor (Sangrà *et al.*, 2009) and the Frontal Zone between MW and Antarctic Intermediate Water (Zenk *et al.*, 1991; Hernández-Guerra *et al.*, 2003). It is difficult to figure out whether the observed changes in  $\text{O}_2$  over longer time frames results from natural variability or from anthropogenic forcing. However, this could be important for long-term pH trends in the studied region given the large interannual to decadal variability in  $\text{O}_2$  in the North Atlantic (Frölicher *et al.*, 2009). In this sense, isolating the human-induced  $\text{O}_2$  changes from the mechanisms of ocean  $\text{O}_2$  variability that operate on timescales from months to centuries is necessary to better constrain in which regions larger decreases in pH will take place in the future, in the context of anthropogenic climate change.

## Conclusions

The comparison of seawater pH measurements for the whole water column at 24.5°N in the North Atlantic, between years 1992 and 2011, points to a general decrease in pH values in the first 1000 dbar. Interestingly, highest-acidification rates are exhibited at the subsurface, particularly below the seasonal thermocline. This is caused by a combination of anthropogenic and non-anthropogenic components of similar magnitudes but different representations with depth and longitude along the section. The anthropogenic component is, as expected, more important toward the surface. The nonanthropogenic component, however, displays a much more heterogeneous pattern, with highest decreasing pH rates in specific regions such as that confined below the seasonal thermocline, east of 35°W, and further to the west between 500 and 800 dbar, above the OMZ.

This non-anthropogenic component also leads to basification in specific regions along the section. Finally, in the deep western basin there is clear evidence of significant acidification from anthropogenic forcing much deeper than 1000 dbar, virtually extending to the ocean interior, on water masses that move south within the DWBC.

### **Acknowledgements**

The 1992 dataset for this paper is available at CDIAC (<http://cdiac.ornl.gov>); dataset name: 10.3334/CDIAC/OTG.IIM\_CSIC\_WOCE\_A05. The 2011 dataset consists of new data obtained within the frame of the Expedition Malaspina 2010 (<http://www.expedicionmalaspina.es>) shown here for the first time, which is also available at CDIAC. We acknowledge funding by the Spanish Ministry of Economy and Competitiveness through grants CSD2008-00077 (Circumnavigation Expedition MALASPINA 2010 Project), CTM2009-08849 (ACDC Project) and CTM2012-32017 (MANIFEST Project), and from the Seventh Framework Programme FP7 CARBOCHANGE (grant agreement 264879). E.F. Guallart was funded by CSIC through a JAE-Pre grant. We thank the editor and two anonymous reviewers for their critical reading and constructive comments.

## Appendix A.

### Division of the datasets in density layers and zonal regions

In order to better assess the processes behind the observed changes in the chemical properties between 1992 and 2011, the water column was divided in six density categories following Talley *et al.*, (2011). The main water masses present in the Subtropical North Atlantic were identified as: upper North Atlantic Central Water (uNACW), lower North Atlantic Central Water (INACW), Antarctic Intermediate Water (AAIW), upper North Atlantic Deep Water (uNADW), lower North Atlantic Deep Water (INADW) and Antarctic Bottom Water (AABW). The dataset was further divided longitudinally taking into account the separation into the two main basins (western/eastern) and a more refined subdivision of these to isolate the spreading regions of the Deep Western Boundary Current and the Mediterranean Water, which are situated at the western and eastern margins, respectively. Table 3.3\_A1 sums up the corresponding isopycnals and geographic coordinates taken into account to split the section A05 in different regions. A number of 22 subdivisions of the section were obtained (Figure 3.3\_A1).

**Table 3.3\_A1.** Isopycnal boundaries and geographic coordinates considered to split the section A05 in different subdivisions following hydrographic criteria.

WATER MASS	Density layer ( $\text{kgm}^{-3}$ )	REGION	Longitude ( $^{\circ}$ )
uNACW	$\sigma_0 < 26.7$	Region 1	80 $^{\circ}$ W to 70 $^{\circ}$ W
INACW	26.7 $< \sigma_0 < 27.2$	Region 2	70 $^{\circ}$ W to 45 $^{\circ}$ W
AAIW	27.2 $< \sigma_0 < 27.6$	Region 3	45 $^{\circ}$ W to 30 $^{\circ}$ W
uNADW	$\sigma_0 > 27.6$ and $\sigma_2 < 37$	Region 4	30 $^{\circ}$ W to 10 $^{\circ}$ W
INADW	$\sigma_2 > 37$ and $\sigma_4 < 45.9$		
AABW	$\sigma_4 < 45.9$		

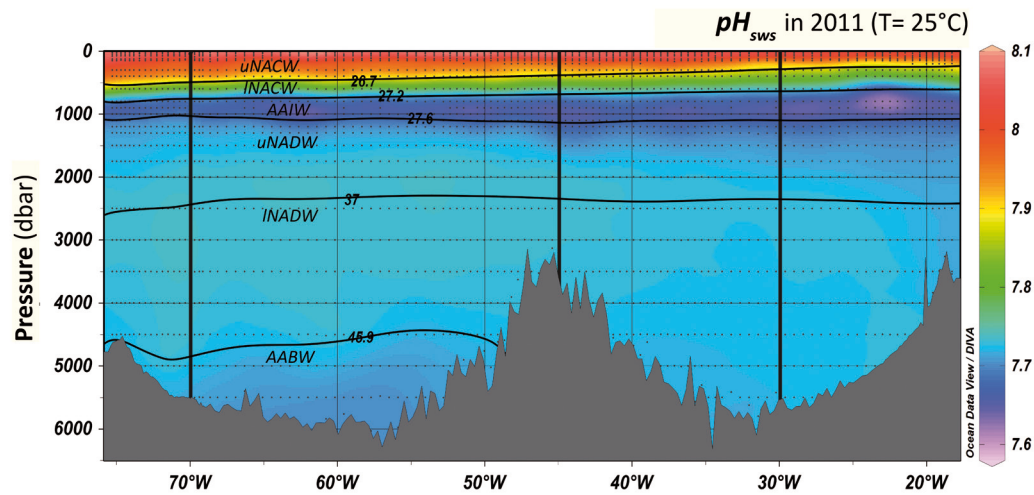


**Figure 3.3\_A1.** Hydrographic regions in which the section A05 was divided, over the pH distribution of the 2011 cruise. The boundaries of the different subdivisions follow details given in Table 3.3\_A1.

## Appendix B.

### Average parameters per layer and region

The average and standard deviation (SD) of the mean of the following parameters was computed with data within each of the 22 subdivisions: Measured pH in the seawater scale and referred to 25°C ( $\text{pH}_{\text{sws}25}$ ) in 2011 and 1992; Change in measured pH (2011-1992,  $\Delta\text{pH}_m$ ), further decomposed into the respective anthropogenic ( $\Delta\text{pH}_{\text{ant}}$ ) and non-anthropogenic ( $\Delta\text{pH}_{\text{var}}$ ) contributions; Change in Apparent Oxygen Utilization, AOU ( $\Delta\text{AOU}$ ); Change in  $C_{\text{ant}}$  using the  $\phi C_T^0$  method ( $\Delta\phi C_T^0$ ) and change in  $C_{\text{ant}}$  using the TTD method ( $\Delta\text{TTD}$ , further details in Appendix C).

Only bottle data between 75.27°W and 18.27°W were considered for the computations, in order to calculate the changes between the two datasets with data closer than 2 degrees of latitude. Data of the first 150 dbar were also rejected to avoid seasonal variability in the above parameters. Mean values  $\pm$  uncertainty (SD) are shown in Table 3.3\_B1.

**Table 3.3\_B1.** Mean values  $\pm$  standard deviation ( $x \pm SD$ ) for measured pH (pHsws25) in 2011 and 1992, change in measured pH ( $\Delta pH_m$ ), anthropogenic ( $\Delta pH_{ant}$ ) and non-anthropogenic ( $\Delta pH_{var}$ ) contributions to  $\Delta pH_m$ , change in Apparent Oxygen Utilization ( $\Delta AOU$ ) in  $\mu\text{mol kg}^{-1}$  change in  $C_{ant}$  using the  $\phi C_T^0$  ( $\Delta \phi C_T^0$ ) and TTD (TTTD) methods in  $\mu\text{mols kg}^{-1}$ , within each given subdivision. By dividing mean  $\Delta pH_{ant}$  in regions 1 and 4 in uNACW, region 4 in AAIW and uNADW and region 1 in uNADW, the following pH decreasing trends (pH-units yr $^{-1}$ ) due to  $C_{ant}$  uptake are obtained, respectively:  $-0.0014 \pm 0.0004$ ,  $-0.0018 \pm 0.0004$ ,  $-0.0008 \pm 0.0004$ ,  $-0.0006 \pm 0.0005$  and  $-0.0008 \pm 0.0005$ . Bold numbers indicate statistical significance ( $t$  test  $< 0.05$ ). Column N indicates the number of values within each subdivision.

		pHsws25 2011	pHsws25 1992	N	$\Delta pH_m$ (2011-1992)	p- value	$\Delta pH_{ant}$ (2011-1992)	p- value	$\Delta pH_{var}$ (2011-1992)	p- value	$\Delta AOU$ (2011-1992)	$\Delta \phi C_T^0$ (2011-1992)	$\Delta TTD$ (2011-1992)
uNACW	<b>1</b>	7.972 $\pm$ 0.036	7.992 $\pm$ 0.033	48	<b>-0.020<math>\pm</math>0.015</b>	0.000	<b>-0.028<math>\pm</math>0.008</b>	0.000	<b>0.008<math>\pm</math>0.012</b>	0.000	<b>-3.4<math>\pm</math>9.8</b>	<b>16.2<math>\pm</math>4.8</b>	20.9 $\pm$ 1.6
	<b>2</b>	7.950 $\pm$ 0.034	7.980 $\pm$ 0.040	139	<b>-0.030<math>\pm</math>0.014</b>	0.000	<b>-0.032<math>\pm</math>0.008</b>	0.000	<b>0.002<math>\pm</math>0.009</b>	0.048	<b>2.5<math>\pm</math>8.2</b>	<b>18.4<math>\pm</math>5.4</b>	21.3 $\pm$ 1.7
	<b>3</b>	7.953 $\pm$ 0.038	7.984 $\pm$ 0.046	67	<b>-0.031<math>\pm</math>0.023</b>	0.000	<b>-0.025<math>\pm</math>0.015</b>	0.000	<b>-0.006<math>\pm</math>0.012</b>	0.000	<b>8.6<math>\pm</math>10.4</b>	<b>14.5<math>\pm</math>9.0</b>	21.7 $\pm$ 1.7
	<b>4</b>	7.922 $\pm$ 0.030	7.984 $\pm$ 0.025	29	<b>-0.062<math>\pm</math>0.028</b>	0.000	<b>-0.034<math>\pm</math>0.008</b>	0.000	<b>-0.028<math>\pm</math>0.027</b>	0.000	<b>28.1<math>\pm</math>18.7</b>	<b>19.3<math>\pm</math>4.6</b>	21.9 $\pm$ 0.8
INACW	<b>1</b>	7.794 $\pm$ 0.050	7.824 $\pm$ 0.051	21	<b>-0.029<math>\pm</math>0.007</b>	0.000	<b>-0.027<math>\pm</math>0.010</b>	0.000	<b>-0.003<math>\pm</math>0.007</b>	0.080	<b>3.7<math>\pm</math>4.7</b>	<b>12.4<math>\pm</math>4.2</b>	13.3 $\pm$ 2.4
	<b>2</b>	7.792 $\pm$ 0.039	7.830 $\pm$ 0.038	56	<b>-0.038<math>\pm</math>0.010</b>	0.000	<b>-0.018<math>\pm</math>0.009</b>	0.000	<b>-0.019<math>\pm</math>0.010</b>	0.000	<b>14.2<math>\pm</math>6.0</b>	<b>8.5<math>\pm</math>4.3</b>	14.3 $\pm$ 2.0
	<b>3</b>	7.812 $\pm$ 0.055	7.837 $\pm$ 0.057	67	<b>-0.025<math>\pm</math>0.011</b>	0.000	<b>-0.018<math>\pm</math>0.008</b>	0.000	<b>-0.006<math>\pm</math>0.011</b>	0.000	<b>8.0<math>\pm</math>7.6</b>	<b>8.9<math>\pm</math>4.1</b>	15.4 $\pm$ 2.7
	<b>4</b>	7.797 $\pm$ 0.065	7.816 $\pm$ 0.068	63	<b>-0.019<math>\pm</math>0.024</b>	0.000	<b>-0.020<math>\pm</math>0.012</b>	0.000	<b>0.001<math>\pm</math>0.026</b>	0.764	<b>2.8<math>\pm</math>18.1</b>	<b>9.5<math>\pm</math>5.7</b>	15.9 $\pm$ 2.5
AAIW	<b>1</b>	7.674 $\pm$ 0.011	7.691 $\pm$ 0.013	42	<b>-0.017<math>\pm</math>0.009</b>	0.000	<b>-0.018<math>\pm</math>0.007</b>	0.000	<b>0.000<math>\pm</math>0.008</b>	0.201	<b>0.7<math>\pm</math>4.8</b>	<b>7.1<math>\pm</math>3.0</b>	6.8 $\pm$ 0.9
	<b>2</b>	7.666 $\pm$ 0.017	7.681 $\pm$ 0.017	118	<b>-0.015<math>\pm</math>0.015</b>	0.000	<b>-0.008<math>\pm</math>0.011</b>	0.000	<b>-0.006<math>\pm</math>0.015</b>	0.000	<b>2.4<math>\pm</math>6.9</b>	<b>3.4<math>\pm</math>4.4</b>	5.3 $\pm$ 1.2
	<b>3</b>	7.664 $\pm$ 0.012	7.676 $\pm$ 0.013	93	<b>-0.012<math>\pm</math>0.009</b>	0.000	<b>-0.010<math>\pm</math>0.006</b>	0.000	<b>0.002<math>\pm</math>0.011</b>	0.187	<b>1.4<math>\pm</math>5.2</b>	<b>4.1<math>\pm</math>2.3</b>	4.5 $\pm$ 1.3
	<b>4</b>	7.646 $\pm$ 0.019	7.638 $\pm$ 0.019	66	<b>0.008<math>\pm</math>0.021</b>	0.000	<b>-0.014<math>\pm</math>0.008</b>	0.000	<b>0.025<math>\pm</math>0.018</b>	0.000	<b>-8.7<math>\pm</math>8.5</b>	<b>5.7<math>\pm</math>3.2</b>	4.8 $\pm$ 1.9
uNADW	<b>1</b>	7.718 $\pm$ 0.011	7.732 $\pm$ 0.013	99	<b>-0.015<math>\pm</math>0.008</b>	0.000	<b>-0.016<math>\pm</math>0.009</b>	0.000	<b>0.001<math>\pm</math>0.003</b>	0.000	<b>-0.5<math>\pm</math>1.6</b>	<b>6.6<math>\pm</math>3.6</b>	7.8 $\pm$ 1.4
	<b>2</b>	7.716 $\pm$ 0.015	7.725 $\pm$ 0.015	238	<b>-0.008<math>\pm</math>0.007</b>	0.000	<b>-0.008<math>\pm</math>0.007</b>	0.000	<b>-0.001<math>\pm</math>0.005</b>	0.089	<b>-1.1<math>\pm</math>2.9</b>	<b>3.2<math>\pm</math>3.0</b>	4.8 $\pm$ 1.6
	<b>3</b>	7.704 $\pm$ 0.019	7.706 $\pm$ 0.019	160	<b>-0.003<math>\pm</math>0.007</b>	0.000	<b>-0.007<math>\pm</math>0.007</b>	0.000	<b>0.004<math>\pm</math>0.006</b>	0.000	<b>-0.3<math>\pm</math>2.9</b>	<b>2.9<math>\pm</math>2.7</b>	2.7 $\pm$ 0.4
	<b>4</b>	7.698 $\pm$ 0.016	7.697 $\pm$ 0.018	121	0.001 $\pm$ 0.008	0.143	<b>-0.012<math>\pm</math>0.009</b>	0.000	<b>0.013<math>\pm</math>0.011</b>	0.000	<b>-2.8<math>\pm</math>3.7</b>	<b>5.1<math>\pm</math>3.7</b>	2.8 $\pm$ 1.0
INADW	<b>1</b>	7.750 $\pm$ 0.004	7.738 $\pm$ 0.006	74	<b>-0.008<math>\pm</math>0.007</b>	0.000	<b>-0.008<math>\pm</math>0.009</b>	0.000	<b>0.000<math>\pm</math>0.004</b>	0.605	<b>1.0<math>\pm</math>2.2</b>	<b>3.2<math>\pm</math>3.9</b>	4.8 $\pm$ 0.6
	<b>2</b>	7.729 $\pm$ 0.004	7.735 $\pm$ 0.006	209	<b>-0.005<math>\pm</math>0.006</b>	0.000	<b>-0.002<math>\pm</math>0.006</b>	0.000	<b>-0.003<math>\pm</math>0.003</b>	0.000	<b>1.1<math>\pm</math>2.4</b>	<b>0.7<math>\pm</math>2.7</b>	2.6 $\pm$ 0.8
	<b>3</b>	7.724 $\pm$ 0.004	7.724 $\pm$ 0.006	203	0.000 $\pm$ 0.006	0.542	<b>-0.001<math>\pm</math>0.006</b>	0.032	<b>0.001<math>\pm</math>0.003</b>	0.011	<b>2.1<math>\pm</math>1.9</b>	<b>0.4<math>\pm</math>2.4</b>	1.6 $\pm$ 0.3
	<b>4</b>	7.723 $\pm$ 0.005	7.726 $\pm$ 0.006	117	<b>-0.002<math>\pm</math>0.006</b>	0.000	<b>-0.006<math>\pm</math>0.006</b>	0.000	<b>0.003<math>\pm</math>0.003</b>	0.000	<b>-0.5<math>\pm</math>3.0</b>	<b>2.4<math>\pm</math>2.7</b>	1.5 $\pm$ 0.2
AABW	<b>1</b>	7.719 $\pm$ 0.006	7.725 $\pm$ 0.010	18	-0.004 $\pm$ 0.008	0.061	-0.001 $\pm$ 0.012	0.614	-0.003 $\pm$ 0.006	0.082	1.0 $\pm$ 2.8	0.7 $\pm$ 5.0	3.0 $\pm$ 0.8
	<b>2</b>	7.711 $\pm$ 0.007	7.715 $\pm$ 0.008	112	<b>-0.004<math>\pm</math>0.007</b>	0.000	0.000 $\pm$ 0.006	0.506	<b>-0.005<math>\pm</math>0.004</b>	0.000	<b>2.4<math>\pm</math>2.1</b>	-0.2 $\pm$ 2.7	2.6 $\pm$ 1.4

## Appendix C.

### Change in $C_{ant}$ TTD

$C_{ant}$  needs to be derived by indirect techniques from in-situ observations. The  $\phi C_T^0$  method (Pérez *et al.*, 2008; Vázquez-Rodríguez *et al.*, 2009) for  $C_{ant}$  estimation builds on back-calculation principles that try to separate the  $C_{ant}$  signal from the background  $\text{CO}_2$  distribution (Brewer, 1978; Chen and Millero, 1979). It is performed by removing an estimate of the preindustrial preformed  $C_T$  and by correcting the  $C_T$  values for changes due to the biological activity. Together with a number of other close methodologies ( $\Delta C^*$  (Gruber *et al.*, 1996),  $\Delta C_T^0$  (Kortzinger *et al.*, 1998), TrOCA (Touratier and Goyet, 2004; Touratier *et al.*, 2007)), the  $\phi C_T^0$  method relies on observations of the parameters of the  $\text{CO}_2$  system to estimate  $C_{ant}$ . However, there exist other approaches to estimate  $C_{ant}$  without using  $\text{CO}_2$  measurements, which depend on tracer observations. Due to the availability of CFCs measurements in the 1992 occupation (W. Smethie, Principal Investigator, Lamont-Doherty Earth Observatory, <http://cdiac.ornl.gov/>),  $C_{ant}$  concentrations were also estimated using

the TTD method (Waugh *et al.*, 2006). Thus, CFCs observations are used as a proxy of  $C_{\text{ant}}$  since they serve to constrain the time elapsed since a water parcel was last in contact with the surface to describe how the ocean circulation connects the surface with the interior ocean concentrations, by means of particular functions called Transient Time Distributions (TTD) (Waugh *et al.*, 2004; Waugh *et al.*, 2006). CFC-12 data were used to constrain the TTD functions. The CFC-12's partial pressures at interior locations were calculated by using the solubility functions determined by Warner and Weiss (1985) assuming a time-invariant initial saturation at 100% for mode waters, at 85% for intermediate waters and at 65% for deep and bottom waters.

Since the assumption of the TTD transport is steady, the temporal change in the TTD estimates (from 1992 until 2011) can be approximated considering a steadier behavior of the  $C_{\text{ant}}$  concentrations distributions in the region of interest (Tanhua *et al.*, 2006; Tanhua *et al.*, 2007; Steinfeldt *et al.*, 2009). The change in the  $C_{\text{ant}}$  concentrations by the end of the studied period (2011) can be thus computed assuming an annual increment of 1.69% (Steinfeldt *et al.*, 2009) of the  $C_{\text{ant}}$  estimations for a given year (cruise) and considering the lapse in time from then until 2011.

Following the average  $\Delta pH_{\text{ant}}$  values reported in Table 3.3\_B1, the estimation of the anthropogenic component of  $\Delta pH_m$  between 1992 and 2011 was evaluated, through linear regression, in terms of the average  $\Delta pH_{\text{ant}}\text{-TTD}$  that resulted from the change in the obtained  $C_{\text{ant}}\text{-TTD}$  estimates during the same period (Figure 3.3\_C1). The linear regression between the two estimations ( $\Delta pH_{\text{ant}} = 0.745\Delta pH_{\text{ant}}\text{-TTD} - 0.0004$ ) showed a coefficient of determination ( $r^2$ ) of 0.85. This high value attests to the robustness of the  $C_{\text{ant}}$  values used to estimate  $\Delta pH_{\text{ant}}$  through the  $\phi C_T^0$  method, since the estimated  $\Delta pH_{\text{ant}}$  strongly correlates with the corresponding independent estimations of  $\Delta pH_{\text{ant}}\text{-TTD}$  that do not rely on  $\text{CO}_2$  measurements. There are some values, corresponding to the two central layers, that slightly deviate from the  $\Delta pH_{\text{ant}} = \Delta pH_{\text{ant}}\text{-TTD}$  regression line, which may be due to the fact that the  $C_{\text{ant}}\text{-TTD}$  values were somewhat high (Khatiwala *et al.*, 2013) compared to the  $C_{\text{ant}}\text{-}\phi C_T^0$  values in the uppermost layer for the 1992 cruise and also due to the assumption of overall steady accumulation. These two factors may lead to greater  $C_{\text{ant}}\text{-TTD}$  and, thus, to greater  $\Delta pH_{\text{ant}}\text{-TTD}$  changes for these two layers at the end of the studied period. However, the error of the y-intercept ( $b = -0.0004$ ) of the linear fit amounts to  $\pm 0.0016$ , which also suggests that the residuals fall within the uncertainty of the pH changes and that both  $\Delta pH_{\text{ant}}$  and  $\Delta pH_{\text{ant}}\text{-TTD}$  estimates are thus consistent between them. The uncertainty related to the linear fit (i.e. the error related to the calculation of the  $\Delta pH_{\text{ant}}$  term by using this linear equation) equals  $\pm 0.004$ . Taking into account that the two estimations are independent between them, this error can be considered as the uncertainty related to the estimation of the anthropogenic component of  $\Delta pH_m$ , since the linear equation includes variability not only due to the uncertainty of the measurements but to the actual variability, of unknown origin, in this parameter. This value is lower than the uncertainty of  $\pm 0.0071$  considered in the main manuscript, so we have taken this latter value also in a conservative way as the maximum error for  $\Delta pH_m$ ,  $\Delta pH_{\text{ant}}$  and  $\Delta pH_{\text{Var}}$ .

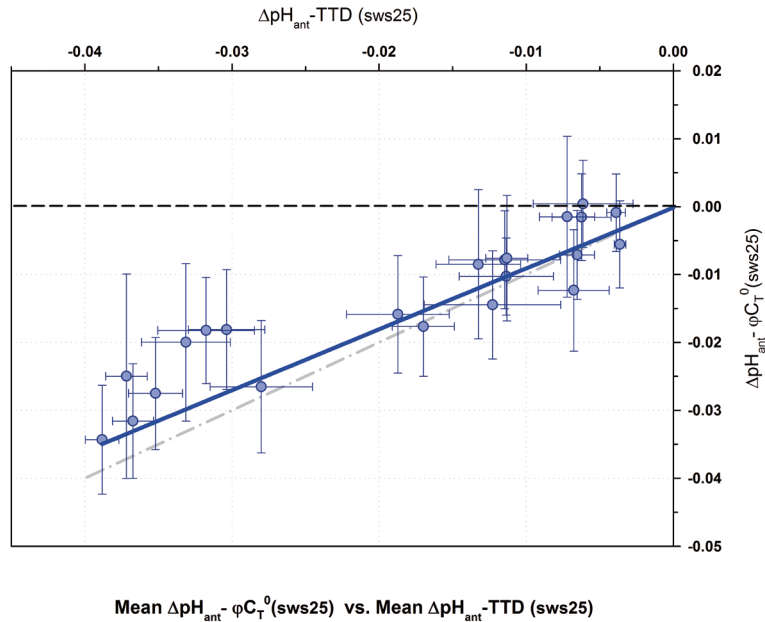


**Figure 3.3\_C1.** Linear correlation (in blue) between the change in measured pH due to the anthropogenic forcing between 1992 and 2011 obtained by using the  $\varphi\text{C}_T^0$  method ( $\Delta\text{pH}_{\text{ant}}$ ), and the same parameter obtained by using CFC measurements and the TTD method ( $\Delta\text{pH}_{\text{ant}} - \text{TTD}$ ). The coefficient of determination ( $r^2$ ) was 0.85. The linear correlation corresponding to  $\Delta\text{pH}_{\text{ant}} = \Delta\text{pH}_{\text{ant}} - \text{TTD}$  is showed with the dashed-dotted grey line.

## References

- Álvarez, M., F. F. Pérez, D. R. Shoosmith, and H. L. Bryden (2005), Unaccounted role of Mediterranean Water in the drawdown of anthropogenic carbon, *J. Geophys. Res.*, 110, C09S03, doi:10.1029/2004JC002633.
- Anderson, L. A., and J. L. Sarmiento (1994), Redfield ratios of remineralization determined by nutrient data analysis, *Global Biogeochem. Cycles*, 8(1), 65–80, doi:10.1029/93GB03318.
- Bates, N. R. (2012), Multi-decadal uptake of carbon dioxide into subtropical mode water of the North Atlantic Ocean, *Biogeosciences*, 9(7), 2649–2659.
- Bates, N. R., M. H. P. Best, K. Neely, R. Garley, A. G. Dickson, and R. J. Johnson (2012), Detecting anthropogenic carbon dioxide uptake and ocean acidification in the North Atlantic Ocean, *Biogeosciences*, 9(1), 2509–2522.
- Broecker, W. S. (1974), “NO” a conservative water mass tracer, *Earth Planet. Sci. Lett.*, 23, 8761–8776.
- Brown, P. J., D. C. E. Bakker, U. Schuster, and A. J. Watson (2010), Anthropogenic carbon accumulation in the subtropical North Atlantic, *J. Geophys. Res.*, 115, C04016, doi:10.1029/2008JC005043.
- Byrne, R. H., S. Mecking, R. A. Feely, and X. Liu (2010), Direct observations of basin-wide acidification of the North Pacific Ocean, *Geophys. Res. Lett.*, 37, L02601, doi:10.1029/2009GL040999.
- Chan, N. C. S., and S. R. Connolly (2013), Sensitivity of coral calcification to ocean acidification: A meta-analysis, *Global Change Biol.*, 19(1), 282–290.
- Clayton, T. D., and R. H. Byrne (1993), Spectrophotometric seawater pH measurements: Total hydrogen ion concentration scale calibration of m-cresol purple and at-sea results, *Deep Sea Res., Part I*, 40(10), 2115–2129.
- Dickson, A. G., and F. J. Millero (1987), A comparison of the equilibrium constants for the dissociation of carbonic acid in seawater media, *Deep Sea Res., Part A*, 34(10), 1733–1743.
- Doney, S. C., V. J. Fabry, R. A. Feely, and J. A. Kleypas (2009), Ocean acidification: The other CO<sub>2</sub> problem, *Annu. Rev. Mar. Sci.*, 1(1), 169–192, doi:10.1146/annurev.marine.010908.163834.
- Dore, J. E., R. Lukas, D. W. Sadler, M. J. Church, and D. M. Karl (2009), Physical and biogeochemical modulation of ocean acidification in the central North Pacific, *Proc. Natl. Acad. Sci. U.S.A.*, 106(30), 12,235–12,240.
- Frölicher, T. L., F. Joos, G. K. Plattner, M. Steinacher, and S. C. Doney (2009), Natural variability and anthropogenic trends in oceanic oxygen in a coupled carbon cycle-climate model ensemble, *Global Biogeochem. Cycles*, 23, GB1003, doi:10.1029/2008GB003316.
- García-Corral, L. S., E. Barber, A. Regaudie-de-Gioux, S. Sal, J. M. Holding, S. Agustí, N. Navarro, P. Serret, P. Mozetič, and C. M. Duarte (2014), Temperature dependence of planktonic metabolism in the subtropical North Atlantic Ocean, *Biogeosciences*, 11(16), 4529–4540.
- González-Dávila, M., J. M. Santana-Casiano, M. J. Rueda, and O. Llinás (2010), The water column distribution of carbonate system variables at the ESTOC site from 1995 to 2004, *Biogeosciences*, 7, 3067–3081.
- Gruber, N. (2011), Warming up, turning sour, losing breath: Ocean biogeochemistry under global change, *Philos. Trans. R. Soc. A*, 369(1943), 1980–1996.
- Gruber, N., J. L. Sarmiento, and T. F. Stocker (1996), An improved method for detecting anthropogenic CO<sub>2</sub> in the oceans, *Global Biogeochem. Cycles*, 10(4), 809–837, doi:10.1029/96GB01608.
- Guallart, E. F., F. F. Pérez, G. Rosón, and A. F. Ríos (2013), High spatial resolution alkalinity and pH measurements by IIM-CSIC group along 24.5°N during the R/V Hespérides WOCE section A05 cruise, Rep., Instituto de Investigaciones Marinas, Consejo Superior de Investigaciones Científicas. (Available at <http://digital.csic.es/handle/10261/93331>).

- Hernández-Guerra, A., E. Fraile-Nuez, R. Borges, F. López-Laatzén, P. Vélez-Belchí , G. Parrilla, and T. J. Müller (2003), Transport variability in the Lanzarote passage (eastern boundary current of the North Atlantic subtropical Gyre), Deep Sea Res., Part I, 50(2), 189–200.
- Hernández-Guerra, A., J. L. Pelegrí, E. Fraile-Nuez, V. Benítez-Barrios, M. Emelianov, M. D. Pérez-Hernández, and P. Vélez-Belchí (2014), Meridional overturning transports at 7.5 N and 24.5 N in the Atlantic Ocean during 1992–93 and 2010–11, Prog. Oceanogr., 128, 98–114.
- Hönisch, B., et al. (2012), The geological record of ocean acidification, Science, 335(6072), 1058–1063.
- Ilyina, T., R. E. Zeebe, E. Maier-Reimer, and C. Heinze (2009), Early detection of ocean acidification effects on marine calcification, Global Biogeochem. Cycles, 23, GB1008, doi:10.1029/2008GB003278.
- Johnson, G. C., and N. Gruber (2007), Decadal water mass variations along 20°W in the Northeastern Atlantic Ocean, Prog. Oceanogr., 73(3–4), 277–295.
- Khatiwala, S., F. Primeau, and T. Hall (2009), Reconstruction of the history of anthropogenic CO<sub>2</sub> concentrations in the ocean, Nature, 462(7271), 346–349.
- McCartney, M. S., and L. D. Talley (1982), The subpolar mode water of the North Atlantic Ocean, J. Phys. Oceanogr., 12(11), 1169–1188.
- Mehrback, C., C. H. Culberson, J. E. Hawley, and R. M. Pytkowicz (1973), Measurement of the apparent dissociation constants of carbonic acid in seawater at atmospheric pressure, Limnol. Oceanogr., 18(6), 897–907.
- Millero, F. J. (2007), The marine inorganic carbon cycle, Chem. Rev., 107(2), 308–341.
- Mintrop, L., F. F. Pérez, M. González-Dávila, J. M. Santana-Casiano, and A. Körtzinger (2000), Alkalinity determination by potentiometry: Intercalibration using three different methods, Cienc. Mar., 26(1), 23–27. (Available at <http://hdl.handle.net/10261/25136>.)
- Pelejero, C., E. Calvo, and O. Hoegh-Guldberg (2010), Paleo-perspectives on ocean acidification, Trends Ecol. Evol., 25(6), 332–344.
- Perez, F. F., and F. Fraga (1987), The pH measurements in seawater on the NBS scale, Mar. Chem., 21(4), 315–327.
- Pérez, F. F., M. Vázquez-Rodríguez, E. Louarn, X. A. Padín, H. Mercier, and A. F. Ríos (2008), Temporal variability of the anthropogenic CO<sub>2</sub> storage in the Irminger Sea, Biogeosciences, 5(6), 1669–1679.
- Pérez, F. F., M. Vázquez-Rodríguez, H. Mercier, A. Velo, P. Lherminier, and A. F. Ríos (2010), Trends of anthropogenic CO<sub>2</sub> storage in North Atlantic water masses, Biogeosciences, 7(5), 1789–1807.
- Pierrot, D., E. Lewis, and D. Wallace (2006), MS Excel Program Developed for CO<sub>2</sub> System Calculations, ORNL/CDIAC-105a, edited, Carbon Dioxide Information Analysis Center, Oak Ridge National Laboratory, US Department of Energy, Oak Ridge, Tenn.
- Raven, J., K. Caldeira, H. Elderfield, O. Hoegh-Guldberg, P. Liss, U. Riebesell, J. Shepherd, C. Turley, and A. Watson (2005), Ocean Acidification Due to Increasing Atmospheric Carbon Dioxide, Royal Society, London.
- Resplandy, L., L. Bopp, J. C. Orr, and J. P. Dunne (2013), Role of mode and intermediate waters in future ocean acidification: Analysis of CMIP5 models, Geophys. Res. Lett., 40, 3091–3095, doi:10.1002/grl.50414.
- Ríos, A. F., and G. Rosón (1996), pH and alkalinity measurements, Rep., pp. 64–73, Lab. de Phys. des Océans, Brest, France.
- Rosón, G., A. F. Ríos, F. F. Pérez, A. Lavín, and H. L. Bryden (2003), Carbon distribution, fluxes, and budgets in the subtropical North Atlantic Ocean (24.5°N), J. Geophys. Res., 108(C5), 3144, doi:10.1029/1999JC000047.
- Sabine, C. L., and T. Tanhua (2010), Estimation of anthropogenic CO<sub>2</sub> inventories in the ocean, Annu. Rev. Mar. Sci., 2(1), 175–198.

- Sabine, C. L., R. M. Key, K. M. Johnson, F. J. Millero, A. Poisson, J. L. Sarmiento, D. W. R. Wallace, and C. D. Winn (1999), Anthropogenic CO<sub>2</sub> inventory of the Indian Ocean, *Global Biogeochem. Cycles*, 13(1), 179–198, doi:10.1029/1998GB900022.
- Sangrà, P., A. Pascual, Á. Rodríguez-Santana, F. Machín, E. Mason, J. C. McWilliams, J. L. Pelegrí, C. Dong, A. Rubio, and J. Aristegui (2009), The Canary Eddy Corridor: A major pathway for long-lived eddies in the subtropical North Atlantic, *Deep Sea Res., Part I*, 56(12), 2100–2114.
- Steinfeldt, R., M. Rhein, and M. Walter (2007), NADW transformation at the western boundary between 66°W/20°N and 60°W/10°N, *Deep Sea Res., Part I*, 54, 835–855.
- Steinfeldt, R., M. Rhein, J. L. Bullister, and T. Tanhua (2009), Inventory changes in anthropogenic carbon from 1997–2003 in the Atlantic Ocean between 20°S and 65°N, *Global Biogeochem. Cycles*, 23, GB3010, doi:10.1029/2008GB003311.
- Stendardo, I., and N. Gruber (2012), Oxygen trends over five decades in the North Atlantic, *J. Geophys. Res.*, 117, C11004, doi:10.1029/2012JC007909.
- Talley, L. D. (1996), Antarctic intermediate water in the South Atlantic, in *The South Atlantic*, edited, pp. 219–238, Springer, Berlin.
- Tanhua, T., S. van Heuven, R. M. Key, A. Velo, A. Olsen, and C. Schirnick (2010), Quality control procedures and methods of the CARINA database, *Earth Syst. Sci. Data*, 2, 35–49.
- van Sebille, E., M. O. Baringer, W. E. Johns, C. S. Meinen, L. M. Beal, M. F. de Jong, and H. M. van Aken (2011), Propagation pathways of classical Labrador Sea water from its source region to 26°N, *J. Geophys. Res.*, 116, C12027, doi:10.1029/2011JC007171.
- Vázquez-Rodríguez, M., F. Touratier, C. Lo Monaco, D. W. Waugh, X. A. Padín, R. G. J. Bellerby, C. Goyet, N. Metzl, A. F. Ríos, and F. F. Pérez (2009), Anthropogenic carbon distributions in the Atlantic Ocean: Data-based estimates from the Arctic to the Antarctic, *Biogeosciences*, 6(3), 439–451.
- Vázquez-Rodríguez, M., X. A. Padín, P. C. Pardo, A. F. Ríos, and F. F. Pérez (2012a), The subsurface layer reference to calculate preformed alkalinity and air-sea CO<sub>2</sub> disequilibrium in the Atlantic Ocean, *J. Mar. Syst.*, 94, 52–63.
- Vázquez-Rodríguez, M., F. F. Pérez, A. Velo, A. F. Ríos, and H. Mercier (2012b), Observed acidification trends in North Atlantic water masses, *Biogeosciences*, 9(12), 5217–5230.
- Yao, W., X. Liu, and R. H. Byrne (2007), Impurities in indicators used for spectrophotometric seawater pH measurements: Assessment and remedies, *Mar. Chem.*, 107(2), 167–172.
- Zenk, W., B. Klein, and M. Schroder (1991), Cape Verde Frontal Zone, *Deep Sea Res., Part A*, 38(Supplement 1), S505–S530.





# **Discussion and Conclusions**



## SYNTHESIS OF RESULTS AND GENERAL DISCUSSION

In the previous three main sections we have detailed some crucial aspects regarding the penetration of  $C_{\text{ant}}$  in the Atlantic Ocean and the associated seawater acidification. Each of these sections, which have already been published as independent scientific research papers, have focused independently on one of the two North Atlantic Ocean studied transects, either the WOCE A05 at 24.5°N or the WOCE A06 at 7.5°N. In this synthesis and discussion section, in addition to summarizing the main results obtained, we discuss all data in an integrated way, by comparing changes occurring at both oceanographic lines and putting them into a wider context. This comparative effort is made first to study more in depth into the magnitudes, paths and main regions of  $C_{\text{ant}}$  accumulation and transport in the North Atlantic and, secondly, to gain insight on the water column acidification and the associated changes in calcium carbonate saturation state in seawater with respect to aragonite. In this regard, trends on the expected decrease of the saturation states of aragonite are evaluated for the two sections and predictions are made on the number of years pending to reach undersaturation in water masses of the upper subtropical and tropical North Atlantic.

### Anthropogenic $\text{CO}_2$

$C_{\text{ant}}$  variability is linked to the circulation of water masses. Since  $C_{\text{ant}}$  is absorbed in surface waters during winter mixing convection events, central water masses along the two studied sections (A05 at 24.5°N and A06 at 7.5°N) show the highest  $C_{\text{ant}}$  values. This is so because these water masses form in the surroundings of both sections and thus they have experienced the most recent contact with the atmosphere, compared with the water masses below. Overall, vertical gradients show high surface concentrations that decrease towards the bottom, along the two sections. This decrease is rapid in the upper ocean whereas, below 1000 dbar  $C_{\text{ant}}$ , concentrations remain low in general, since deep and bottom water masses were formed long time ago, reflecting the concentration of a preceding atmosphere with less  $C_{\text{ant}}$ . The general  $C_{\text{ant}}$  pattern within intermediate and deep layers along the two sections is determined by their advection from their respective formation regions. Each of the intermediate and deeper layers, which roughly correspond to the different intermediate, deep and bottom water masses, show a particular  $C_{\text{ant}}$  content depending on their particular ventilation (i.e. on the specific time elapsed for each layer to reach the 24.5°N and 7.5°N sections from their formation regions, where they were last in contact with the atmosphere). Since these layers originated either in the subpolar North Atlantic or in the Southern Ocean, their vertical organization according to the density they acquire at the time of their formation leads to a sandwiched vertical profile that shows relative  $C_{\text{ant}}$  maxima and minima, depending on their respective northern or southern origin. AAIW and AABW are formed in the more faraway Southern Ocean and thus show lower  $C_{\text{ant}}$  levels than LSW (uNADW) and, to a lesser extent, than INADW, which are formed in the subpolar North Atlantic region. In this sense, intermediate and bottom Antarctic waters at 7.5°N show a lower influence of mixing with the more  $C_{\text{ant}}$ -enriched deep North Atlantic waters with respect to these water masses at 24.5°N.

Of particular interest in the two sections was the noticeable deep  $C_{ant}$  signal located between 1200-1800 dbar that results from the southward spreading of  $C_{ant}$ -enriched LSW (Steinfeldt *et al.*, 2009) as part of the upper core of the DWBC. The LSW is a water mass of particular recent formation compared with the older water masses of the remaining deep ocean at these latitudes, hence the higher  $C_{ant}$  levels in this water mass. It shows a ventilation of around a decade at 24.5°N (van Sebille *et al.*, 2011) and of about three decades into the equator at 7.5°N (Rhein *et al.*, 2015). Over its journey to the south, the LSW also mixes with less  $C_{ant}$ -loaded waters at these densities (Steinfeldt *et al.*, 2007; van Sebille *et al.*, 2011). As shown in chapters 3.1 and 3.2. of this thesis, this fact was easily identified as a pattern of moderate  $C_{ant}$  levels (20 - 25  $\mu\text{mol}\cdot\text{kg}^{-1}$ ) at 24.5°N, entering the section from the west, that influenced concentrations eastward and within the lower limb of the DWBC. The LSW  $C_{ant}$  footprint diluted further south at 7.5°N due to the existence of secondary alternative interior pathways for transport beyond the DWBC (van Sebille *et al.*, 2011), but was still detectable there showing lower  $C_{ant}$  levels (10  $\mu\text{mol}\cdot\text{kg}^{-1}$ ) and reaching the eastern basin due to the eastward recirculation of NADW (Arhan *et al.*, 1998; Mémery *et al.*, 2000).

The overall profile in the distribution of  $C_{ant}$  along the two sections was confirmed by all methods of  $C_{ant}$  estimation used in chapters 3.1. and 3.2 of this thesis. When the two sections are compared in terms of the observed decadal changes in their  $C_{ant}$  distributions (i.e. their respective decadal  $C_{ant}$  storage rates, Figure 4.1), there appear some similarities and disagreements between them. The two sections show greater storage rates along central layers. This observation is in agreement with the fact that these are the most ventilated layers along the vertical profile and thus they accumulate  $C_{ant}$  more rapidly. In turn,  $C_{ant}$  storage rates within central layers are greater at 24.5°N than at 7.5°N. This is an expected result, since the 24.5°N section is closer to the formation region (i.e. the Sargasso Sea) of the different water mass components within NACW than it is the 7.5°N section from the respective SACW formation regions (i.e. the Southern Atlantic). In addition, the relative proximity of each section to the deep waters (i.e. NADW) formation regions explains the higher  $C_{ant}$  storage rates observed within the DWBC at 24.5°N than at 7.5°N (Figure 4.1), which is also an expected result, according to the northernmost location of the former section. However, this is in disagreement with the unexpected higher storage rates observed in the NADW layers at 7.5°N in the two most interior regions, compared to those observed at 24.5°N. A possible explanation for this is that the ventilation of the DWBC at 24.5°N is confined to the west of 70°W and the regions of the ocean interior along this section only receive  $C_{ant}$  loads through mixing processes due to the inexistence of alternative major interior pathways for transport. In contrast, at 7.5°N the NADW spreading pathway moves away from the western continental margin making this water mass to recirculate and penetrate further to the east. Since in 1993 there only existed detectable  $C_{ant}$  levels in NADW in the region closest to the western margin, the highest increments in  $C_{ant}$  observed for this water mass along 7.5°N between 1993-2010 occurred in the two interior regions, which did not show detectable  $C_{ant}$  levels in 1993. As reported in chapter 3.3.2. of this thesis, this accumulation of  $C_{ant}$  occurred at rates that are in accordance with a steady circulation, as  $C_{ant}$ -loaded NADW has been arriving to equatorial latitudes. In this sense, our results also suggest that the recirculation of NADW has still not reached the region closest to the eastern margin.

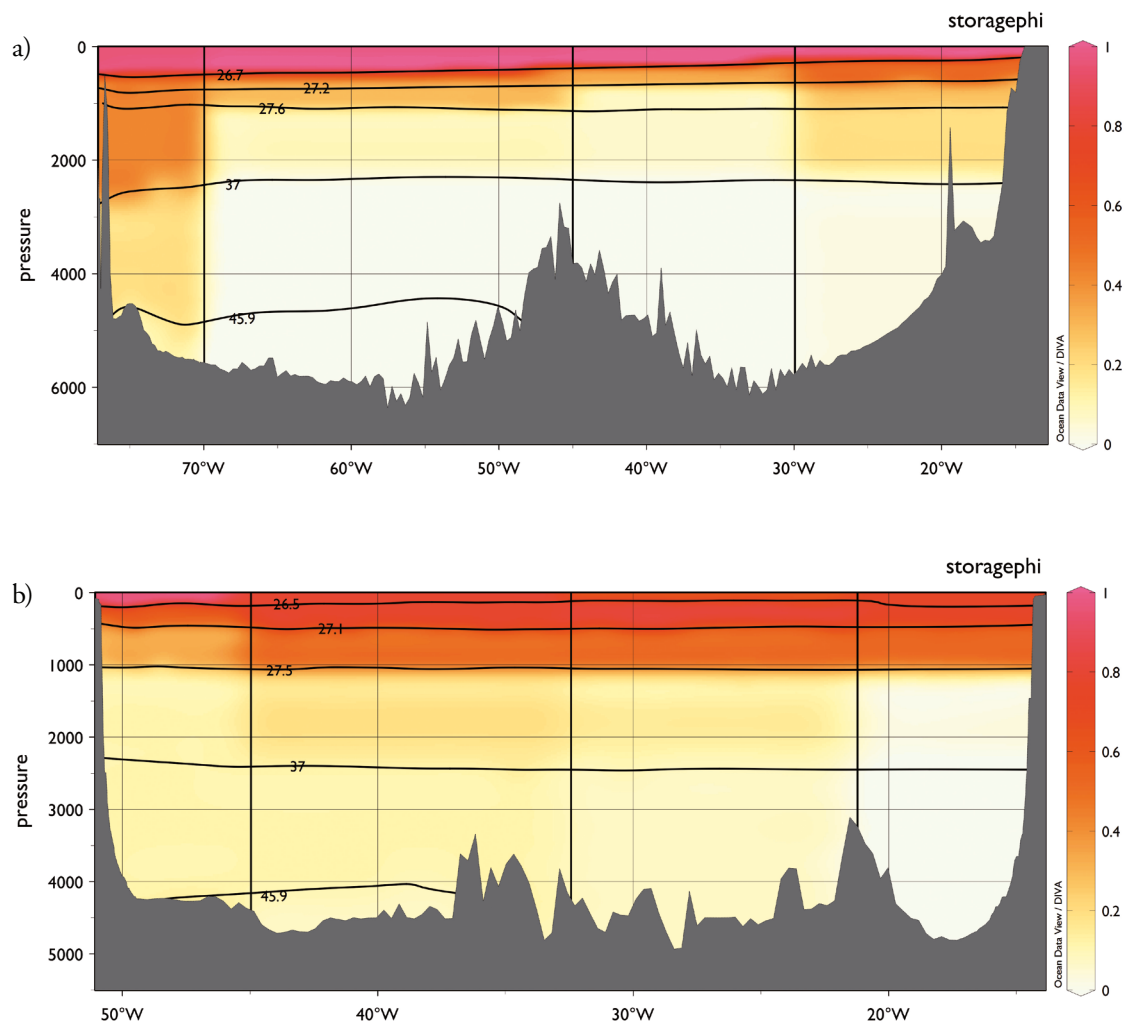


**Figure 4.1.**  $C_{ant}$  storage rates ( $\mu\text{mol kg}^{-1} \text{yr}^{-1}$ ) according to the  $\varphi C_T^0$  method of  $C_{ant}$  estimation, in color scale. a)  $C_{ant}$  storage rates between 1992 and 2011, for each box at  $24.5^\circ\text{N}$ , along the A05 section. b)  $C_{ant}$  storage rates between 1993 and 2010, for each box at  $7.5^\circ\text{N}$ , along the A06 section.

In contrast, at 24.5°N, the two interior ocean regions show storage rates below those that would be expected under a steady circulation, possibly because the spreading pathways of the water masses that carry the  $C_{ant}$  signal within deep layers at this latitude are confined to the eastern (MW) and western (LSW) boundary regions. Since the transference of  $C_{ant}$  into the regions of the interior ocean depends on the mixing of MW and LSW, and given that these two regions are not areas for their direct transit, this may explain why  $C_{ant}$  in these regions has been increasing at a slower rate than what would have been expected according to a steady circulation. Furthermore, in the DWBC, the storage rates of  $C_{ant}$  are greater than those expected according to a steady accumulation, presumably due to the arrival of the important pulse of  $\text{C}_{\text{ant}}$ -enriched LSW formed during the early 1990s. Hence, changes in circulation also explain the deviation from the steady state of the  $C_{ant}$  storage rates in some regions and layers. The decadal changes in circulation may also be the cause for the unexpected increase in  $C_{ant}$  levels above and below a steadier accumulation in the AAIW at 7.5°N and at 24.5°N, respectively. However, it should be taken into account that changes along 7.5°N are calculated by using only two cruises and thus the derived storage rates may reflect more poorly part of the existing decadal variability when compared to the storages at 24.5°N, which are calculated by using five cruises that monitor in a more regular way the changes occurred during the studied period.

In sum, the observed decadal changes in the general  $C_{ant}$  distributions along the two sections (Figure 4.1) point to two main findings:

- 1) The vertical profile in the accumulation of  $C_{ant}$  is mostly parallel with the  $C_{ant}$  concentrations profile, showing greater storage rates along central waters and lower storage rates further deep in the ocean.
- 2) There exist clear zonal gradients in the storage rates of  $C_{ant}$  along intermediate and deep water masses.

Figure 4.1 also shows a third but still not considered factor that has important implications for the study of the integrated storage of  $C_{ant}$  along the two sections, which is the thickness of the different water masses considered. Central waters show the greater storage rates and thus, they accumulate  $C_{ant}$  relatively fast (~ 0.5 to 1  $\mu\text{mol}\cdot\text{kg}^{-1}\cdot\text{yr}^{-1}$ ), but have a relatively small thickness of a few hundred meters. On the contrary, intermediate and deep layers show much lower storage rates (mostly below ~0.20  $\mu\text{mol}\cdot\text{kg}^{-1}\cdot\text{yr}^{-1}$ ), but they encompass huge volumes of water, of thousands of meters in depth that, along these sections, represent around 80% of the water column. Hence, they contribute significantly to the integrated storage of  $C_{ant}$  along the full-depth water column. In addition, the thickness of the different water masses gains importance when the storage is evaluated by splitting the sections into different regions. Even though intermediate, deep and bottom layers show overall low storage rates, small zonal differences in the storage rates in them become meaningful, since they can impact significantly the integrated storage of  $C_{ant}$  throughout the sections.

In Table 3.2.4 in chapter 3.2 of this thesis we reported the integrated  $C_{ant}$  storage rates at 7.5°N for the period 1993-2010, separately for the western and eastern basins, calculated by using the  $\varphi C_T^0$  and the TTD methods. The  $C_{ant}$  storage rates obtained by using the  $\varphi C_T^0$  method indicated that the two whole basins had been

accumulating  $C_{ant}$  during the period of study at approximately the same rate ( $1.07 \pm 0.23 \text{ mol m}^{-2} \text{ yr}^{-1}$  in the west and  $0.95 \pm 0.27 \text{ mol m}^{-2} \text{ yr}^{-1}$  in the east). However, the parallel storage rates obtained by using the TTD method suggested a faster accumulation of  $C_{ant}$  in the western ( $0.95 \pm 0.24 \text{ mol m}^{-2} \text{ yr}^{-1}$ ) than in the eastern basins ( $0.56 \pm 0.25 \text{ mol m}^{-2} \text{ yr}^{-1}$ ). This inconsistency was due to the fact that although the two methods highlighted a greater storage of  $C_{ant}$  in the deep western than in the deep eastern basin (within water masses below ~1000 dbar), the two methods of estimation showed different results regarding the integrated storages between the two basins in the upper ocean (which comprised intermediate and central waters). While the TTD method suggested that  $C_{ant}$  had been accumulating at the same rate in the eastern and western upper tropical ocean, the  $\phi C_T^0$  method suggested a greater  $C_{ant}$  accumulation rate in the eastern upper ocean that resulted in the net balance of the full depth storages between the two basins.

Table 4.1. reports the full-depth  $C_{ant}$  storage rates at  $24.5^\circ\text{N}$  for the period 1992-2011, separated for each of the four typical regions into which we split the whole section, and also for the Florida Strait, calculated by using the  $\phi C_T^0$  and the TTD methods. Initially, the regions of the main section were not merged into the western and eastern basins and were studied separately due to the high heterogeneity found in the zonal gradient in the storage rates of intermediate and deep layers along this section (Figure 4.1). Both the  $\phi C_T^0$  and the TTD methods suggest a greater integrated  $C_{ant}$  storage into region 1, which matches the spreading domain of the DWBC, than in the remaining regions of the ocean interior and the western boundary. The difference between the storage in R1 and those in R2 to R4 displays a noticeable zonal contrast by using the  $\phi C_T^0$  method, while zonal differences are less pronounced according to the TTD method. The reason behind this observation could be that methodological approaches for estimating TTD  $C_{ant}$  are based in the solution of an advection-diffusion equation with constant velocity and diffusivity under the assumption of a steady-state circulation (Waugh *et al.*, 2006) that may lead to a closer behavior between regions. Additionally, another explanation for the different behavior between methods is that, as reported in chapters 3.1. and 3.2. of this thesis, the method of back-calculation  $\phi C_T^0$  seems to be particularly sensitive to changes in water masses relative to natural processes in which dissolved oxygen is involved, through redfield ratios. As an example, this fact appeared to be cause of the low storage rates found for AAIW and uNADW in R3 and, in a more general way, could be an explanation for the lower storages found in the ocean interior by using this method. Anyhow, and regardless of which is the more accurate relationship between the storage of  $C_{ant}$  that occurs in the DWBC and in the remaining regions, the two methods show that this difference is significantly enhanced when deep layers are included in the calculations. This means that the faster  $C_{ant}$  storage described in the DWBC region is mostly explained by NADW layers and thus, mainly due to the advection of  $C_{ant}$ -enriched LSW within the DWBC (chapters 3.1 and 3.2 of this thesis). NADW, including its upper and lower layers, shows a similar thickness along the entire section (about 70% of the water column on average in each defined region) but contributes from about 60% to 70 % to the full-depth  $C_{ant}$  storage described in R1, according to the  $\phi C_T^0$  or the TTD methods results, respectively. NADW layers explain much less of the full-depth  $C_{ant}$  storage observed in the remaining three regions, since they contribute 15% to 40% on

average, to the  $C_{ant}$  storage along the ocean interior and the eastern boundary regions, according to the  $\varphi C_T^0$  or the TTD methods, respectively.

**Table 4.1.**  $C_{ant}$  storage rates ( $\text{mol m}^2 \text{y}^{-1}$ ) over the entire water column, calculated separately for each of the four regions of the main section and the Florida Strait. They were calculated taking into account the decadal  $C_{ant}$  storage rates described in each box and the mean thickness of each layer. The value of storage for R4 through the TTD method is missing due to the absence of TTD  $C_{ant}$  data within NADW.

Storage $\text{mol m}^2 \text{y}^{-1}$	R0 Florida	R1 80°W to 70°W	R2 70°W to 45°W	R3 45°W to 30°W	R4 30°W to 10°W
$\varphi C_T^0$	$0.49 \pm 0.06$	$1.83 \pm 0.31$	$0.66 \pm 0.23$	$0.49 \pm 0.22$	$0.84 \pm 0.23$
TTD	$0.27 \pm 0.09$	$1.62 \pm 0.44$	$1.12 \pm 0.36$	$1.03 \pm 0.86$	-

Overall, the study of the full-depth  $C_{ant}$  storage rates along 7.5°N and 24.5°N into split regions or basins highlights that, on a decadal timescale, the spatial variability in the storage of  $C_{ant}$  along the subtropical and the tropical North Atlantic is strongly related with the deep  $C_{ant}$  signal conveyed by the main circulation current (i.e. DWBC) that spreads across the two sections. As reported in chapters 3.1. and 3.2. of this thesis, it is widely known that this noticeable deep advection of  $C_{ant}$  is related with a period of exceptional intense convection into the NASPG that led to a fresher deep pool of LSW in the early 1990s, during a period of positive phase of the NAO (Lazier *et al.*, 2002). The resulting great pulse of LSW has also been related to the higher  $C_{ant}$  storage rates into the subpolar North Atlantic that occurred during that period (Pérez *et al.*, 2008; Pérez *et al.*, 2010), which, in turn, have been correlated with the AMOC intensity, by means of changes in the  $C_{ant}$  that is transported from low latitudes into the NASPG during different NAO phases (Pérez *et al.*, 2013).

The contrasting storage of  $C_{ant}$  occurring along 24.5°N, between the DWBC west of 70°W and the remaining three regions, is also of strong importance when taking into account that there exists a covariance between this storage gradient and the water mass transport on either side of 70°W. It is known from a number of studies in the literature (Atkinson *et al.*, 2012; Hernández-Guerra *et al.*, 2014) that the cyclonic circulation of deep waters along the A05 section consists of a huge southward transport of water within the DWBC, west of 70°W, and a recirculation of lower intensity to the northeast, through the ocean interior. Zunino *et al.*, (2015) show the value of accumulated southward mass transport of NADW within the DWBC (with a northward transport in the ocean interior) to be of  $\sim 25$  ( $\sim 13$ ) Sv in 1992 and  $\sim 18$  ( $\sim 9$ ) Sv in 2011. Leaving aside the interannual variability in the resulting total transport, it can be assumed from this two snapshots that the recirculation of water through the ocean interior is approximately about half of that into the DWBC. This consideration is consistent with the mass transports described within NADW in the work of Macdonald *et al.* (2003) (Fig 9 in the article, layers 8-17), for the years 1992 and 1998. Regarding the  $C_{ant}$  transport, Macdonald *et al.* (2003) (Fig 10 in the article) showed an enhancement in the  $C_{ant}$  advected by the NADW along the A05 section from 1992 to 1998, from  $-0.05$  to  $-0.11 \text{ Pg.y}^{-1}$ , respectively, despite they showed very

similar water mass transports in the two years (-18.8 vs -18.1 Sv, respectively). Zunino *et al.* (2015) (Fig 6e in the article) report the transport of  $C_{ant}$  within NADW along the section in 2011 to be of  $-362 \pm 55 \text{ kmol s}^{-1}$ , coupled with a mass transport of -17.5 Sv. This value of  $C_{ant}$  transport equals  $-0.14 \text{ Pg.y}^{-1}$  (units of  $\text{Pg.y}^{-1}$  are equal to the value in  $\text{kmol s}^{-1}$  divided by 2640). The increasing values of  $C_{ant}$  transport but close values of mass transport with time, according to these two studies, suggests an increase with time of the  $C_{ant}$  advected within deep waters, which is in accordance with the gradually increasing  $C_{ant}$  concentrations observed at these depth ranges from 1992 until 2011, predominantly in LSW (Chapter 3.1.). Hence,  $C_{ant}$  within the DWBC (R1) is advected southwards more intensively than the  $C_{ant}$  that moves northwards through the ocean interior (R2 to R4).

Since the zonal gradient in  $C_{ant}$  concentrations along the NADW strengthens considerably with time due to the different storage rates occurring west and east of  $70^\circ\text{W}$ , the high covariance between the  $C_{ant}$  concentrations and the flow speed may lead to a reinforcement with time of the southward exit of  $C_{ant}$  from the Subtropical North Atlantic. This fact can be preliminarily approached according to mean interannual values for the MOC strength obtained from the series of observations of the RAPID array reported by McCarthy *et al.* (2012) and considering the average concentrations of  $C_{ant}$  for the period 1992-2011, obtained separately inside and outside the DWBC for both the upper and lower limbs of NADW. With this purpose, the mean  $C_{ant}$  values were multiplied by the mean meridional transports of  $-12 \pm 0.3 \text{ Sv}$  (uNADW) and  $-7.9 \pm 0.7 \text{ Sv}$  (lNADW) following McCarthy *et al.* (2012), assuming a recirculation of water of  $50 \pm 20 \%$  in the ocean interior with respect to the DWBC, as reported above. According to these calculations, the average  $C_{ant}$  advected by the NADW during the studied period would have been of  $-369 \text{ kmol s}^{-1}$  or  $\sim -0.14 \text{ Pg.y}^{-1}$ . This amount, obtained according to mean values of the MOC strength, is in agreement with the value obtained by means of an ocean inverse model by Zunino *et al.* (2015). Taking into account only the DWBC, the deep transport south of  $C_{ant}$  represents  $\sim -466 \text{ kmol s}^{-1}$  or  $\sim -0.18 \text{ Pg.y}^{-1}$ , an amount that represents nearly half (46%) of the  $C_{ant}$  storage reported for the North Atlantic ( $0.386 \pm 0.012 \text{ Pg.y}^{-1}$ ) (Mikaloff Fletcher *et al.*, 2007). Moreover, assuming a steady state of the flow, this last southward advection of  $C_{ant}$  within the DWBC through the A05 section would have been increasing by  $0.03 \text{ Pg.y}^{-1}$  per decade during the studied period.

Superimposed above the deep conveyor, in the surface ocean, the NASTG behaves as a shallower circulation cell that does not attract much attention at first, from a  $\text{CO}_2$  sequestration point of view, because of its restricted scale. However, the subtropical shallow western boundary system, mainly the Gulf Stream, is responsible for most of the upper ocean  $C_{ant}$  redistribution into the NASPG. Despite its shallowness, the Florida Strait plays a key role in terms of  $C_{ant}$  transport across the A05 section (Macdonald *et al.*, 2003; Rosón *et al.*, 2003; Zunino *et al.*, 2015) (Table 4.1.), since the mass flow compensation for NADW that takes place into the upper ocean through the Florida Strait contributes in leading to the net northward meridional  $C_{ant}$  transport across the section.  $C_{ant}$  concentrations and the respective storage rates reported within central and intermediate layers are higher in the Florida Strait than in the regions of the main section (chapter 3.1. of this

thesis). Hence, it would be expected that  $C_{ant}$  transported north into the Florida Current may have also increased significantly during the studied period, in relation to the  $C_{ant}$  that is exported south into the DWBC. Similarly to the procedure described above, the  $C_{ant}$  storage rates within the Florida Current (Table 3.1\_C1 in chapter 3.1.) were used in order to assess the decadal changes in  $C_{ant}$  transport by multiplying them by average current transports (following Schmitz *et al.*, (1996) and (McCarthy *et al.*, 2012)) across each of the three layers present into the Florida Strait. The resulting increase in the transport of  $C_{ant}$  across the Florida Strait amounts to  $601 \pm 40 \text{ kmol}\cdot\text{s}^{-1}$ , between 1992 and 2011. This increase is mainly due to the increase in  $C_{ant}$  concentrations in this current because the mass transport has been reported to be rather stable (McCarthy *et al.*, 2012). Hence, the temporal variability in the relative shallow深深 increases in the advection of  $C_{ant}$  within the paths of the western boundary currents gains importance in order to understand the variability in the net transport and storage of  $C_{ant}$  north of  $24.5^\circ\text{N}$ , into the North Atlantic sink.

### Acidification and $\text{CaCO}_3$ saturation states

The comparison of pH observations conducted in 1992 and 2011, along  $24.5^\circ\text{N}$  in the Subtropical North Atlantic, revealed an overall decline in pH values in the first 1000 dbar of the water column (Chapter 3.3.). The described pH changes translated into noticeable acidification trends along the whole extension of the central waters but also to significant decreasing trends in pH values in particular zones within intermediate and deeper water masses. Ocean acidification is characterized by an increase in the concentration of protons ( $\text{H}^+$ ) that causes a decrease of pH and a concurrent decrease of carbonate ion concentration ( $\text{CO}_3^{2-}$ ). This, in turn, leads to changes in  $\text{CaCO}_3$  saturation states of seawater with respect to calcite and aragonite. In this section we focus on these latter parameters, which constrain calcification and dissolution processes in the water column, and are thus important when assessing the possible effects of the ocean acidification pressure over marine organisms. By comparing data obtained during the different North Atlantic cruises through time, we present a first attempt to assess decadal changes in calcium carbonate saturation states with time. We focus on aragonite, because it is a mineral form of  $\text{CaCO}_3$  more soluble than calcite, for which undersaturation will be reached considerably earlier, as ocean pH keeps lowering (e.g. (Feely *et al.*, 2009; Turley *et al.*, 2010)). When assessing the changes in the distributions of the saturation state of aragonite ( $\Omega_{arg}$ ) along  $24.5^\circ\text{N}$  (A05) and  $7.5^\circ\text{N}$  (A06) sections, we find that the overall distribution patterns in 2011 and 2010 are, respectively, virtually the same as those determined by using data collected in 1992 and 1993 (Figure 4.2.). At  $24.5^\circ\text{N}$ , seawater in the upper ocean is supersaturated ( $\Omega_{arg} > 1$ ) with respect to aragonite along the entire section, and values decrease progressively with increasing pressure until saturation ( $\Omega_{arg} = 1$ ) is reached at about 2500 dbar, coinciding approximately with the isopycnal surface that delimits LNADW along its upper boundary. Below this pressure range seawater is undersaturated ( $\Omega_{arg} < 1$ ) and the extent of undersaturation increases towards the seafloor. At  $7.5^\circ\text{N}$ , the vertical profile shows overall lower  $\Omega_{arg}$  values than those at  $24.5^\circ\text{N}$ . The upper ocean is also supersaturated with respect to aragonite but the decrease in  $\Omega_{arg}$  values with depth is more pronounced, reaching a first saturation level at about 500 dbar, coinciding approximately with the isopycnal that delimits the upper boundary of AAIW. The whole AAIW layer is undersaturated with respect to aragonite.

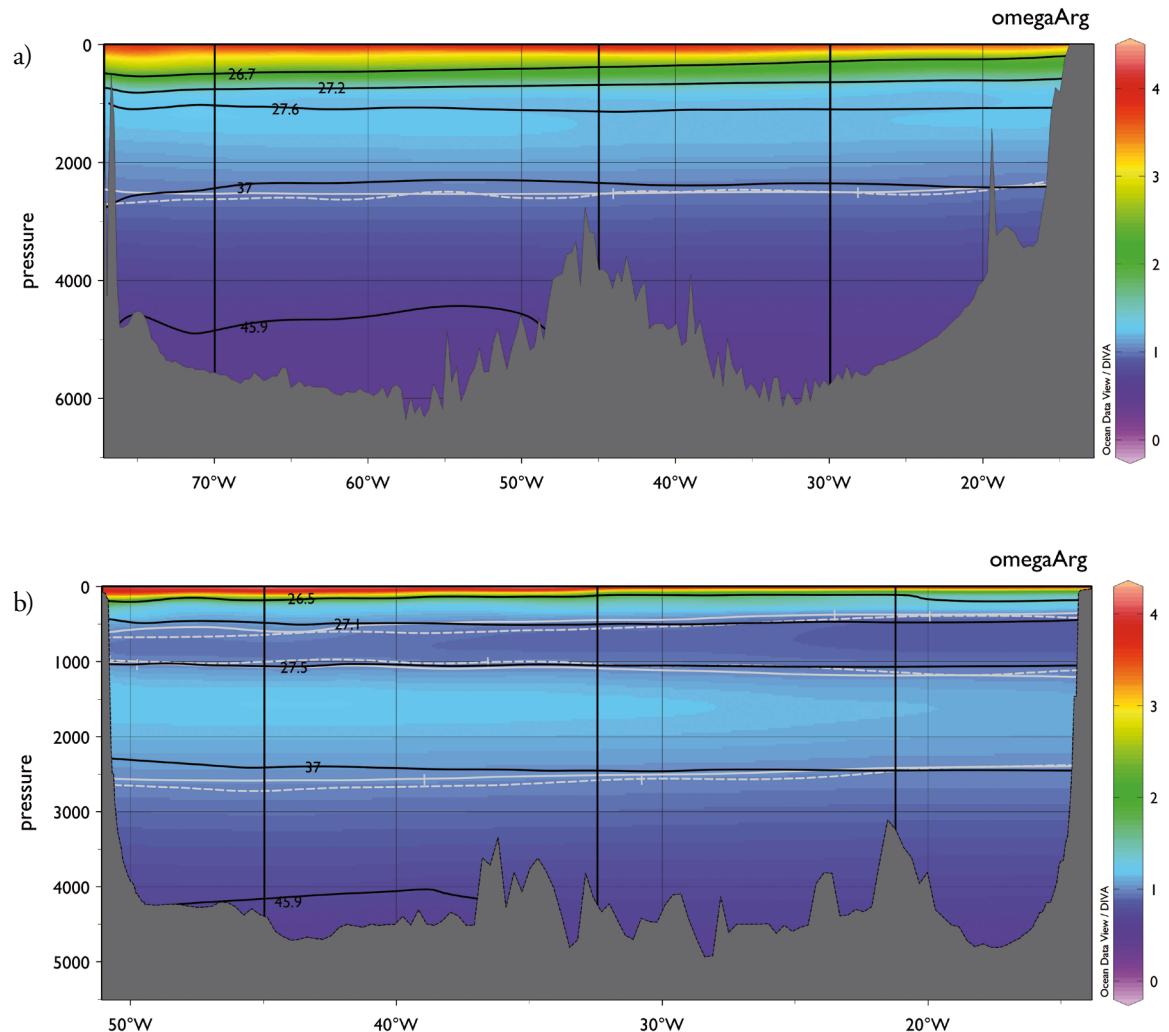


**Figure 4.2.** Distribution of  $\Omega_{\text{arg}}$  at a) 24.5°N in 2011 and at b) 7.5°N in 2010. Saturation horizons ( $\Omega_{\text{arg}} = 1$ ) are depicted as grey dashed lines (years 1992 and 1993 for 24.5°N and 7.5°N, respectively) and grey solid lines (years 2011 and 2010 for 24.5°N and 7.5°N, respectively). Horizontal black solid lines indicate isopycnal surfaces ( $\text{kg m}^{-3}$ ) that delimit the density boundaries considered to split the section into different water masses. Vertical black solid lines indicate zonal boundaries that delimit the different regions along each section.

Below this water mass,  $\Omega_{\text{arg}}$  values increase again with depth with values above saturation, along uNADW, and a second horizon of saturation is reached again at around 2500 dbar, coinciding approximately with the isopycnal of the upper boundary of lNADW, similar to what occurs at 24.5°N. Below this pressure range undersaturation increases towards the seafloor.

Given that the respective deep (~2500 dbar) saturation levels did not change significantly along the two sections, in the following we focus on the changes in aragonite saturation state in the upper ocean (<1200 dbar). At 24.5°N, the changes in the distributions of  $\Omega_{\text{arg}}$  between 1992 and 2011 in the upper ocean exhibited a clear decrease that resulted in the shoaling of the different oversaturation levels above the value of  $\Omega_{\text{arg}} = 1.5$ . At 7.5°N, even though the  $\Omega_{\text{arg}}$  values were generally lower compared to those described at 24.5°N, the respective changes observed between 1993 and 2010 appeared to be smaller in magnitude. At this latitude, the range in pressures with undersaturation in 2010 expanded slightly with respect to 1993. However, most of the two uppermost water masses appeared oversaturated, with  $\Omega_{\text{arg}}$  levels quite close to those observed in 1993.

As described in the introduction,  $\Omega_{\text{arg}}$  is calculated as the product of the concentrations of  $\text{Ca}^{2+}$  and  $\text{CO}_3^{2-}$  divided by the stoichiometric solubility product of this  $\text{CaCO}_3$  mineral phase. Nevertheless, since  $\text{Ca}^{2+}$  is closely proportional to salinity,  $\Omega_{\text{arg}}$  is largely determined by variations in  $\text{CO}_3^{2-}$ :

$$\Omega_{\text{arg}} = [\text{CO}_3^{2-}]_{\text{in situ}} / [\text{CO}_3^{2-}]_{\text{Arg Saturation}}$$

According to this, we calculated the oversaturation of  $\text{CO}_3^{2-}$  ion regarding the saturation concentration of aragonite in the first 1200 dbar of the water column, along the two sections, as:

$$\delta_{\text{Arg}} = [\text{CO}_3^{2-}] - [\text{CO}_3^{2-}]_{\text{SatArg}}$$

where  $[\text{CO}_3^{2-}]$  is the in situ carbonate ion concentration and  $[\text{CO}_3^{2-}]_{\text{SatArg}}$  the saturation concentration for aragonite (i.e. the carbonate concentration at which aragonite precipitates), in  $\mu\text{mol}\cdot\text{kg}^{-1}$ .  $\delta_{\text{Arg}}$  values were obtained for four of the repeat cruises of the A05 section, performed in 1992, 1998, 2004 and 2011 and for the two repeat cruises of the A06, performed in 1993 and 2010. The corresponding calculated  $\delta_{\text{Arg}}$  values for each year were averaged within the different water masses present into the upper 1200 dbar of the water column, separately for the western and eastern basins. Finally, the obtained mean  $\delta_{\text{Arg}}$  were studied in terms of the excess ( $\Delta[\text{CO}_2]$ ) of atmospheric  $\text{CO}_2$  at the time (year) of each cruise with respect to the preindustrial levels of  $\text{CO}_2$  in the atmosphere:

$$\Delta[\text{CO}_2] = [\text{CO}_2]_y - 280$$

where  $[\text{CO}_2]_y$  equals the atmospheric  $\text{CO}_2$  levels occurring at each cruise's year and 280 equals the preindustrial atmospheric  $\text{CO}_2$  levels, in ppm. Following these definitions, Figure 4.3. shows the relationship between the mean oversaturation of  $\text{CO}_3^{2-}$  with respect to the saturation concentration of aragonite ( $\delta_{\text{Arg}}$ ) in relation with the increase in atmospheric  $\text{CO}_2$  since the preindustrial era ( $\Delta[\text{CO}_2]$ ), for the four repeats of the A05 considered. This relationship is shown separately for the western and eastern basins.

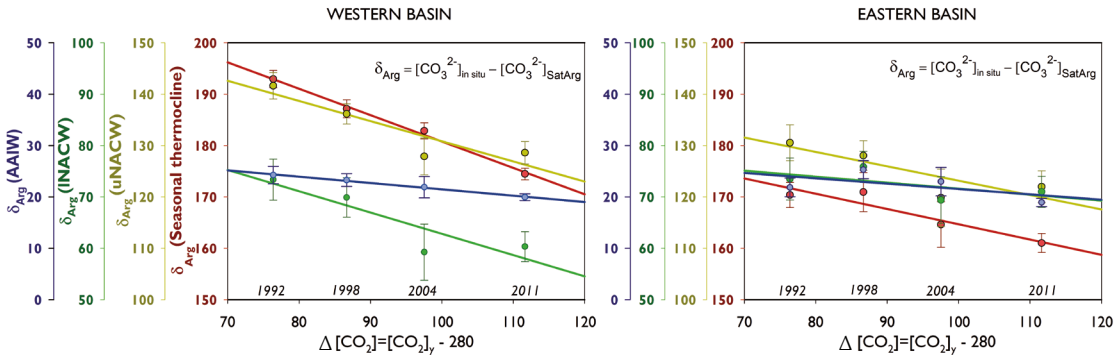


**Figure 4.3.** Mean  $\delta_{\text{Arg}}$  values  $\pm$  standard error of the mean with respect to the increase in  $\text{CO}_2$  in the atmosphere since the preindustrial era, for the 1992, 1998, 2004 and 2011 repeat cruises of the A05 section. The associated colour lines are the respective trends in mean  $\delta_{\text{Arg}}$  between 1992 and 2011. Results within the seasonal thermocline (first 150 dbar, red), uNACW (yellow), INACW (green) and AAIW (blue) are presented, separately for the western (left panel) and eastern (right panel) basins. Note that the scale in the y-axes is different depending on the water mass, yet the total range of the y-axes spans 50  $\mu\text{mol kg}^{-1}$  in all the plots, in order to help distinguishing the change in  $\delta_{\text{Arg}}$  between layers and basins.  $\text{CO}_2$  data used are available at: <http://www.esrl.noaa.gov/gmd/obop/mlo/>

As evidenced in Figure 4.3, the decadal change in mean  $\delta_{\text{Arg}}$  exhibits a pretty linear correspondence with the respective coexisting excess of atmospheric  $\text{CO}_2$  relative to the preindustrial era. This means that the decadal trends in mean  $\delta_{\text{Arg}}$  are in accordance with a relatively steady oceanic uptake of the accumulated  $\text{CO}_2$  into the atmosphere. However, the resulting slopes of these linear trends depend on the water mass considered and also differ between basins. The respective values of these slopes (reported in Table 4.2.) suggest greater rates of undersaturation in the seasonal thermocline and the existence of progressively lower rates with increasing pressure. Moreover, the rates of undersaturation appear to be faster in the western compared to the eastern basins. Taking into account uncertainties, some of the trends in the eastern basin are not significantly different than zero, indicating an absence of change in  $\delta_{\text{Arg}}$ . Regression statistics of the linear fits (Table 4.2.) allow the calculation of some parameters of interest, under the assumption that the relationship found between  $\delta_{\text{Arg}}$  and  $\Delta[\text{CO}_2]$  is representative of its variability beyond decadal timescales. The intercept term ( $b$ ) indicates the value of  $\delta_{\text{Arg}}$  in the preindustrial era (i.e. when  $\Delta[\text{CO}_2] = 0$  or  $[\text{CO}_2]_y = 280$ ). The relationship between the intercept and the slope of each linear fit indicates the  $\Delta[\text{CO}_2]$  value at which the saturation level ( $[\text{CO}_3^{2-}]_{\text{in situ}} = [\text{CO}_3^{2-}]_{\text{SatArg}}$ ) will be reached within each layer and in each studied basin. By considering that the current  $\Delta[\text{CO}_2]$  in 2014 is ~120 ppm (Table 4.2.), about 132 to 154 ppm still have to accumulate in the atmosphere in order to reach saturation within INACW and AAIW, respectively. According to the current  $\text{CO}_2$  annual growth rate of ~2 ppm yr<sup>-1</sup> (Table 4.2.), this would indicate that saturation within these two water masses will be reached in about 66 and 77 years, respectively, in the western basin of the section, despite these water masses do not show the greatest rates of undersaturation along the section. In contrast, it will

**Figure 4.3.** Mean  $\delta_{\text{Arg}}$  values  $\pm$  standard error of the mean with respect to the increase in  $\text{CO}_2$  in the atmosphere since the preindustrial era, for the 1992, 1998, 2004 and 2011 repeat cruises of the A05 section. The associated colour lines are the respective trends in mean  $\delta_{\text{Arg}}$  between 1992 and 2011. Results within the seasonal thermocline (first 150 dbar, red), uNACW (yellow), INACW (green) and AAIW (blue) are presented, separately for the western (left panel) and eastern (right panel) basins. Note that the scale in the y-axes is different depending on the water mass, yet the total range of the y-axes spans 50  $\mu\text{mol}\cdot\text{kg}^{-1}$  in all the plots, in order to help distinguishing the change in  $\delta_{\text{Arg}}$  between layers and basins.  $\text{CO}_2$  data used are available at: <http://www.esrl.noaa.gov/gmd/obop/mlo/>

		$\delta_{\text{Arg}}$ initial $\mu\text{mol}\cdot\text{kg}^{-1}$	$\delta_{\text{Arg}}$ final $\mu\text{mol}\cdot\text{kg}^{-1}$	mean $\delta_{\text{Arg}}$ $\mu\text{mol}\cdot\text{kg}^{-1}$	Slope (m) $\delta_{\text{Arg}} \text{ Trend}$ $\mu\text{mol}\cdot\text{kg}^{-1} \text{ ppm}^{-1}$	intercept (b) $\delta_{\text{Arg}} \text{ Prein}$ $\mu\text{mol}\cdot\text{kg}^{-1}$	$r^2$	years SatArg
<b>A05</b> <b>(24.5°N)</b> 1992- 2011	Western Basin							
	Thermocline	193 $\pm$ 2	174 $\pm$ 1	184 $\pm$ 8	-0.51 $\pm$ 0.03	232 $\pm$ 3	0.99	166
	uNACW	142 $\pm$ 3	129 $\pm$ 2	134 $\pm$ 7	-0.39 $\pm$ 0.13	170 $\pm$ 12	0.82	157
	INACW	73 $\pm$ 4	60 $\pm$ 3	66 $\pm$ 7	-0.41 $\pm$ 0.15	104 $\pm$ 14	0.80	66
	AAIW	24 $\pm$ 2	20 $\pm$ 1	22 $\pm$ 2	-0.12 $\pm$ 0.01	34 $\pm$ 1	0.99	77
	Eastern Basin							
	Thermocline	170 $\pm$ 2	161 $\pm$ 2	167 $\pm$ 5	-0.30 $\pm$ 0.07	194 $\pm$ 7	0.89	267
	uNACW	131 $\pm$ 3	122 $\pm$ 3	125 $\pm$ 5	-0.28 $\pm$ 0.13	151 $\pm$ 12	0.71	210
<b>A06</b> <b>(7.5°N)</b> 1993 - 2010	Western Basin							
	SACW	167 $\pm$ 8	161 $\pm$ 6	164 $\pm$ 4	-0.17	180	-	463
	SAMW	29 $\pm$ 5	24 $\pm$ 3	27 $\pm$ 4	-0.15	41	-	74
	AAIW	0 $\pm$ 1	-4 $\pm$ 1	-2 $\pm$ 3	-0.12	9	-	-21
	Eastern Basin							
	SACW	122 $\pm$ 15	108 $\pm$ 12	115 $\pm$ 10	-0.43	155	-	121
	SAMW	21 $\pm$ 5	20 $\pm$ 3	21 $\pm$ 1	n.s	24	-	278
	AAIW	-6 $\pm$ 1	-9 $\pm$ 1	-7 $\pm$ 2	-0.08	0	-	-59

MLO  $\text{CO}_2$  annual 2014 mean = 399 ppm;  $\Delta[\text{CO}_2] = 398.55-280 = 119$  ppm ;  $\Delta[\text{CO}_2] = \sim 120$  ppm

MLO  $\text{CO}_2$  annual 2014 mean growth rate = 2.13 ppm yr $^{-1}$ ;  $\text{CO}_2$  growth rate =  $\sim 2$  ppm yr $^{-1}$

take more than 150 years to reach saturation along uNACW and into the thermocline although they show greater undersaturation rates. Undersaturation and, in turn, acidification rates within INACW and AAIW are more sensitive to a given increase in CO<sub>2</sub> than the rates within uNACW and into the seasonal thermocline due to their lower temperature, higher C<sub>T</sub> concentration and lower alkalinity. Table 4.2. also reports the analogous calculations along 7.5°N. However, it should be considered that since there exists only two repeats of this section, the regression statistics of the linear fit between two pairs of data loses most of its sense, if we consider that any differences between two different years are not able to inform about trends but only about changes over a given period of time. Taking into account that these results need to be interpreted with more caution, the comparison of the mean  $\delta_{\text{Arg}}$  values between 1993 and 2010 suggests that no significant changes have occurred along the upper tropical Atlantic during the studied period, with the exception of a noticeable decrease in  $\delta_{\text{Arg}}$  within SACW in the eastern basin.

As reported above, the decadal changes in mean  $\delta_{\text{Arg}}$  exhibit a pretty linear trend with time, in accordance with the expected gradual oceanic enrichment in C<sub>ant</sub> as the ocean keeps absorbing atmospheric CO<sub>2</sub>. However, another important finding reported in chapter 3.3. was that acidification occurring along the upper ocean at 24.5°N was also explained by particular changes in oxygen levels and not only due to the accumulation of C<sub>ant</sub>. Despite their more confined spatial distribution compared to C<sub>ant</sub>, changes in oxygen were responsible for a noticeable part of the changes in pH in particular regions of the section. As an example, processes related to the expansion of the oxygen minimum zone in the western subtropical North Atlantic explained almost half of the observed decrease in pH between 1992 and 2011. Thus, in addition to C<sub>ant</sub>, possible changes in oxygen arise as an important factor in the modulation of long-term pH and saturation states trends in the studied region. Regarding the carbonate system and oxygen changes, much of the decadal variability in the North Atlantic is associated with the different states of the NAO, which is manifested at sea surface and ultimately induces changes in circulation and water mass formation rates and properties. However, movement between states can occur as a result of natural variability, or in response to external forcing. Hence, the still unknown relationship between variability, forcing and the derived responses over decadal timeframes reveals the complexity in projecting or figuring out what the dynamics of the climate system will be in the future.

## MAIN CONCLUSIONS by Chapters

**Chapter 3.1.** We used five years of carbonate system data covering a period between 1992 and 2011 to investigate the decadal variability in the storage of  $C_{\text{ant}}$  along the subtropical North Atlantic. We observed that the overall distribution showed higher  $C_{\text{ant}}$  concentrations and greater decadal storage rates near the surface, with both values decreasing towards the bottom. This was confirmed with the four methods of estimation used. We detected zonal gradients in the storage of  $C_{\text{ant}}$  throughout the water column that are explained by circulation features. This result is more robust for intermediate and deep water masses, which showed noticeably higher storage rates close to the western continental margin due to the conveyer role of the Deep Western Boundary Current, with particular contribution from the more recently ventilated Labrador Sea Water. We also found significant trends in the  $C_{\text{ant}}$  storage rates of the deepest water masses, where  $C_{\text{ant}}$  detection limits become important, following the assumption of a transient steady state of the  $C_{\text{ant}}$  distributions (i.e. by assuming that the accumulation of  $C_{\text{ant}}$  was not impacted by recent changes in circulation).

**Chapter 3.2.** We investigated the decadal changes in  $C_{\text{ant}}$  distributions along the tropical North Atlantic through comparison of two years of carbonate system data collected in 1993 and 2010. This comparison showed higher  $C_{\text{ant}}$  concentrations and storage rates in the uppermost layers, with both values decreasing with depth, yet intermediate waters aroused as a layer with relative minimum concentrations with respect to surrounding waters. This was confirmed by using two methods of  $C_{\text{ant}}$  estimation. The western tropical region showed a higher  $C_{\text{ant}}$  inventory. We observed clear zonal gradients in the storage of  $C_{\text{ant}}$  within deep waters, in accordance with the spreading pathway of the Deep Western Boundary Current that branches eastward and recirculates northward redistributing  $C_{\text{ant}}$  into the eastern basin. Changes in the distribution of  $C_{\text{ant}}$  concentrations into layers of the upper ocean appeared to be impacted by seasonal changes in circulation and the retreat of intermediate waters.

**Chapter 3.3.** The comparison of pH observations conducted in 1992 and 2011 revealed an overall decline in pH values in the first 1000 dbar of the water column, in the subtropical North Atlantic. The deconvolution of the temporal pH differences into anthropogenic and non-anthropogenic (natural) components revealed that these are of similar magnitudes but have different representations with depth and longitude along the studied section: anthropogenically-derived pH changes dominated in surface and deep waters, while both anthropogenic and natural components affected mode (central) and intermediate waters. We explained natural variability to be mostly owed to changes in oxygen levels that displayed a quite heterogeneous pattern and could be attributed to different processes that show temporal variability on a broad range of scales. We observed that changes in oxygen levels modulate the anthropogenically-derived acidification. These results emphasize the need to distinguish whether long-term trends in dissolved oxygen obey to different states of the North Atlantic Oscillation climate mode or should be attributed to human-induced forcing of climate, since they impact acidification trends.

## **General Conclusions**

The carbonate system repeat hydrography of the A05 and A06 sections allowed the quantification of the storage of  $C_{ant}$  along the subtropical and tropical North Atlantic on decadal timescales. We also assessed the interactions between ocean circulation and the carbonate system, in particular regarding the processes that control and modulate the storage rates described. This was accomplished by splitting the water masses present in each of the two sections into separated zonal regions that were defined following oceanographic criteria, in order to study the accumulation of  $C_{ant}$  within them. This methodological approach showed that the spatio-temporal variability in the storage of  $C_{ant}$  along the two sections is strongly related with the deep  $C_{ant}$  signal conveyed by the main circulation current (i.e. Deep Western Boundary Current) that spreads across the two sections. In addition, changes in circulation among the Antarctic Intermediate Water appeared to explain the observed storage of  $C_{ant}$  into the upper ocean.

We assessed the decadal changes and trends in some of the parameters of the carbonate system such as  $C_{ant}$  and pH, with some insight into the saturation states of  $\text{CaCO}_3$  with respect to aragonite. The projection of the described rates of change into the future should be made with caution, under the assumption that the variability described is representative of time periods over decadal timescales. In this sense, further insight regarding the variability of the processes behind the observed rates is necessary in order to distinguish between natural variability from anthropogenic forcing of the climate system.

## FUTURE PERSPECTIVES AND OPEN QUESTIONS

The inclusion of systematic physical and chemical measurements within a network of selected repeat hydrographic sections has allowed scientists to describe trends in different seawater parameters worldwide. Despite the challenging enterprise that requires compiling these field observations, this provides tools and valuable knowledge for the direct evaluation of numerical ocean carbon models that are used for identifying processes responsible for climate variability. As a result, the collection and analysis of observations and the development and application of models of the climate system makes possible to monitor, simulate and project global climate with high accuracy. Observational estimates of  $C_{\text{ant}}$  and ocean circulation models have been combined in inverse schemes to estimate  $C_{\text{ant}}$  air-sea fluxes,  $C_{\text{ant}}$  storage rate, and  $C_{\text{ant}}$  transport in the ocean interior (Mikaloff Fletcher *et al.*, 2006; Gruber *et al.*, 2009; DeVries, 2014). However, it is necessary to evaluate the performance of carbon cycle models against observational estimates of the oceanic  $C_{\text{ant}}$  uptake (Khatiwala *et al.*, 2009). Such model tests are needed to gain confidence in model predictions, but are limited by the availability of data that reflect the climate system variability into a broad range of both the spatial and temporal scales.

One of the major challenges for making predictions of the future carbonate system state and the related impacts on climate on timescales of years to decades is the ability to obtain high quality carbonate data observations of enough spatial and temporal resolution, in order to couple them with the huge amount of data already available that has been used to describe the variability in circulation on time scales from subannual to multiannual. Hence, new developments in observational techniques of the carbonate system by means of the use of autonomous platforms and the corresponding data transmission will be crucial. Some efforts have already been made in order to accurately estimate pH and  $\text{CaCO}_3$  saturation states from Argo profiling floats (Juraneck *et al.*, 2011). The development of accurate autonomous sensors of the different parameters of the carbonate system and the resulting combination of measurements from moorings, drifters and even remote sensing will shed light regarding the upper ocean waters. However, obtaining such kind of data in the ocean interior for the whole water column without depending on oceanographic cruises will be extremely difficult. In this sense, the use of neural networks techniques in order to reconstruct the non-linear relationships between biogeochemical parameters will also be a priority (Telszewski *et al.*, 2009; Velo *et al.*, 2013).







# Thesis Summary *(Spanish version)*



## I. INTRODUCCIÓN

### ESCENARIO GENERAL: EL CAMBIO CLIMÁTICO

Múltiples observaciones de los cambios en la atmósfera, la tierra, el océano, la biosfera y la criosfera han demostrado que el clima terrestre está cambiando debido a la perturbación del balance de radiación de la Tierra (Figura 1.1), en gran parte como resultado de la actividad humana. Muchos de los cambios observados no tienen precedentes. La evidencia más relevante del cambio climático es que la atmósfera y el océano se han calentado. En cuanto a calentamiento global, los gases de efecto invernadero son los principales causantes del cambio climático ya que producen un forzamiento radiativo positivo que ha provocado que la temperatura media global del aire aumente en los últimos cien años. En consecuencia, las temperaturas de la tierra y la de la superficie del mar también se han incrementado. El calentamiento del clima es inequívoco, donde el calentamiento del océano representa más del 90% de la energía acumulada entre 1971 y 2010 (IPCC, 2013).

Las concentraciones atmosféricas de los gases de efecto invernadero dióxido de carbono ( $\text{CO}_2$ ), metano ( $\text{CH}_4$ ) y óxido nitroso ( $\text{N}_2\text{O}$ ) han aumentado desde 1750, debido a las actividades humanas, como la quema de combustibles fósiles y los cambios en el uso del suelo. En 2011 las concentraciones de estos gases superaron los niveles pre-industriales en un 40%, 150% y 20%, respectivamente (IPCC, 2013). De éstos, el  $\text{CO}_2$  es gas de efecto invernadero emitido principalmente debido a las actividades humanas y domina el forzamiento radiativo total causado por los gases de efecto invernadero (Hofmann *et al.*, 2011), siendo junto al  $\text{CH}_4$  los únicos que siguen aumentando a un ritmo regular (<http://www.esrl.noaa.gov/>). El registro de  $\text{CO}_2$  atmosférico de Manua Loa (Figura 1.2a) se inició en 1958 por Charles David Keeling. Este registro, que ha llamado «Curva de Keeling», se ha convertido en un ícono gráfico del cambio climático, siendo el primero en evidenciar el aumento claro de las concentraciones de  $\text{CO}_2$  en la atmósfera, cuyos promedios anuales han aumentado desde 277ppm en 1750 (Joos y Spahni, 2008) a 395.31 ppm en 2013 (Dlugokencky y Tans, 2013). La emisión continuada de gases de efecto invernadero provocará más calentamiento y cambios en todos los componentes del sistema climático, de acuerdo con proyecciones recientes basadas en distintos escenarios de concentraciones, que representan distintas trayectorias de concentraciones de gases de efecto invernadero (IPCC, 2013) (Figura 1.2b).

Las emisiones de  $\text{CO}_2$  antropogénico ( $\text{C}_{\text{ant}}$ ) se producen dentro del ciclo natural del carbono (Figura 1.3), que circula carbono entre la atmósfera, los océanos y la biosfera terrestre en una amplia gama de escalas de tiempo. Se pueden diferenciar dos dominios principales en el ciclo global del carbono (Zeebe, 2012; Ciais *et al.*, 2013):

- Un dominio rápido, que consta del carbono en la atmósfera, el océano, los sedimentos oceánicos superficiales y la vegetación terrestre, los suelos y las aguas dulces. Se caracteriza por flujos grandes de intercambio

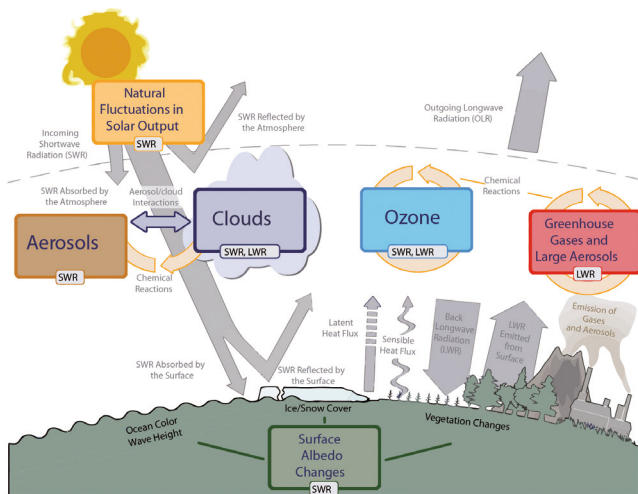


**Figura 1.1.** Causas principales del cambio climático. El balance radiativo entre la radiación solar de onda corta entrante (SWR) y la radiación de onda larga saliente (LWR) está influenciada por diferentes factores globales del clima. Las fluctuaciones naturales en la radiación solar (ciclos solares) pueden causar cambios en el balance de energía a través de las fluctuaciones en la cantidad de SWR entrante. La actividad humana cambia las emisiones de gases y, a su vez, la cantidad de aerosoles y ozono, que también influyen en el balance energético. Los cambios en las propiedades de las nubes por medio de los aerosoles también tienen importantes implicaciones para el balance radiativo. Los cambios antropogénicos en los gases de efecto invernadero y aerosoles modifican la cantidad de LWR saliente mediante la absorción de ésta y se reemisión a una temperatura más baja (por ejemplo, CO<sub>2</sub>, CH<sub>4</sub> y N<sub>2</sub>O explican un 80% del forzamiento radiativo total de los gases de efecto invernadero bien mezclados CO<sub>2</sub>, CH<sub>4</sub>, N<sub>2</sub>O, O<sub>3</sub> y CFC). El albedo superficial se modifica debido a los cambios en la vegetación o las propiedades de la superficie de la tierra, nieve o la cobertura de hielo y el color del océano. Estos cambios están impulsados por cambios naturales, así como por la influencia humana. Fuente: IPCC (2013).

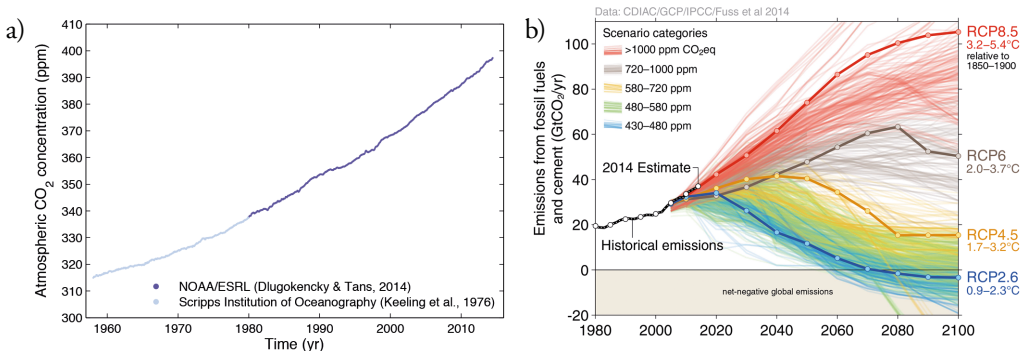


**Figura 1.2.** a) Concentraciones de CO<sub>2</sub> atmosférico superficiales medias, desestacionalizadas (ppm). Los datos mensuales para el período 1980-2014 son un promedio de medidas atmosféricas directas de estaciones múltiples en la capa límite oceánica de la NOAA / ESRL. Los datos para el período 1958-1979 son datos mensuales del Scripps Institution of Oceanography, en base a un promedio de mediciones directas de CO<sub>2</sub> atmosférico en la estación de Mauna Loa y del Polo Sur. Fuente: Le Quéré et al., (2015). b) Emisiones de CO<sub>2</sub> derivadas de los combustibles fósiles y el cemento asociadas a distintos escenarios de concentración representativos utilizados en modelos. El aumento de las temperaturas superficiales medias globales para 2081-2100 con respecto a 1986-2005 se prevé que sea probablemente en los rangos de 0.3°C a 1.7°C (RCP2.6), 1.1°C a 2.6°C (RCP4.5), 1.4°C a 3.1°C (RCP6.0), 2.6°C a 4.8°C (RCP8.5). Fuente: Global Carbon Project (<http://www.globalcarbonproject.org/>).

y tiempos de renovación relativamente rápidos que oscilan entre unos pocos años para la atmósfera a décadas o milenios para los principales reservorios de carbono de la vegetación, el suelo y el océano.

- Un dominio lento que consiste en el carbono almacenado en rocas y sedimentos, con tiempos de rotación de 10.000 años o más.

Los dos dominios intercambian carbono a través de las emisiones volcánicas de CO<sub>2</sub>, la erosión química, la erosión y la formación de sedimento en el fondo del mar. Antes de la era industrial el dominio rápido estaba cerca de un estado estacionario, pero la quema de combustibles fósiles ha resultado en la transferencia de una cantidad significativa de carbono fósil desde los sumideros geológicos al dominio rápido. Esto ha provocado una perturbación sin precedentes del ciclo del carbono debido a la actividad humana.

La necesidad conocer las emisiones C<sub>ant</sub> y su redistribución entre los principales sumideros ha llevado a los esfuerzos de colaboración internacionales para completar y actualizar continuamente el balance global de carbono (Le Quéré et al, 2013; Le Quéré et al, 2014; Le Quéré et al., 2015). Básicamente, el balance global se cuantifica en cinco componentes principales (Figura 1.4 y Tabla 1.1). Todos los componentes excepto los cambios del uso del suelo han crecido desde 1959, mostrando cierta variabilidad decenal (Tabla 1; de Le Quéré et al, (2015).). Aunque los sumideros de CO<sub>2</sub> han seguido creciendo con el aumento de las emisiones, el cambio climático afectará a los procesos del ciclo de carbono que intercambian carbono entre los principales reservorios de una manera que va a agravar el aumento de CO<sub>2</sub> en la atmósfera (IPCC, 2013).

El sumidero oceánico contiene ~ 45% de las emisiones de combustibles fósiles durante el período industrial, y ~ 30% de las emisiones totales de C<sub>ant</sub> desde la era preindustrial (Sabine et al., 2004; Khatiwala et al, 2013). La tasa de crecimiento de este sumidero ha aumentado de 1.1 ± 0.5 Gt año<sup>-1</sup> en los años 1960 a 2.6 ± 0.5 Gt año<sup>-1</sup> para el período 2004 a 2013 (Le Quéré et al., 2015), más o menos en línea con el incremento atmosférico cuando se promedia sobre grandes regiones durante las últimas décadas (Ciais et al., 2013). La captación y el almacenamiento de C<sub>ant</sub> por el océano depende de la ventilación, la formación y el transporte de masas de agua y muestran una variabilidad regional y temporal considerable (Gruber et al, 2009; Sabine y Tanhua, 2010; Khatiwala et al, 2013; DeVries, 2014). La absorción de CO<sub>2</sub> por el océano contribuye a mitigar el calentamiento global, pero el equilibrio químico del C<sub>ant</sub> en agua de mar deriva a una reducción progresiva en el pH del agua de mar y los estados de saturación de minerales de carbonato de calcio en un proceso conocido como acidificación oceánica (Doney et al. 2009; Feely et al, 2009). Este cambio sustancial en la química de los océanos ha provocado cambios en la fisiología de los organismos marinos (Riebesell et al., 2000; Fabry et al, 2008; Iglesias-Rodríguez et al, 2008; Ries et al., 2009; Sett et al, 2014; Bach, 2015; Meyer y Riebesell, 2015), repercutiendo de esta manera en la ecología del océano (Guinotte y Fabry, 2008; Doney et al, 2012;.. Andersson et al, 2015; Bach et al., 2015). Dado que es un fenómeno que afecta no sólo a la biología sino también a los procesos químicos y bioquímicos, la acidificación del océano se ha denominado «el otro problema del CO<sub>2</sub>» (Doney et al., 2009), para llevar la atención de la opinión pública a esta amenaza global tan importante como el calentamiento global (IPCC, 2013).

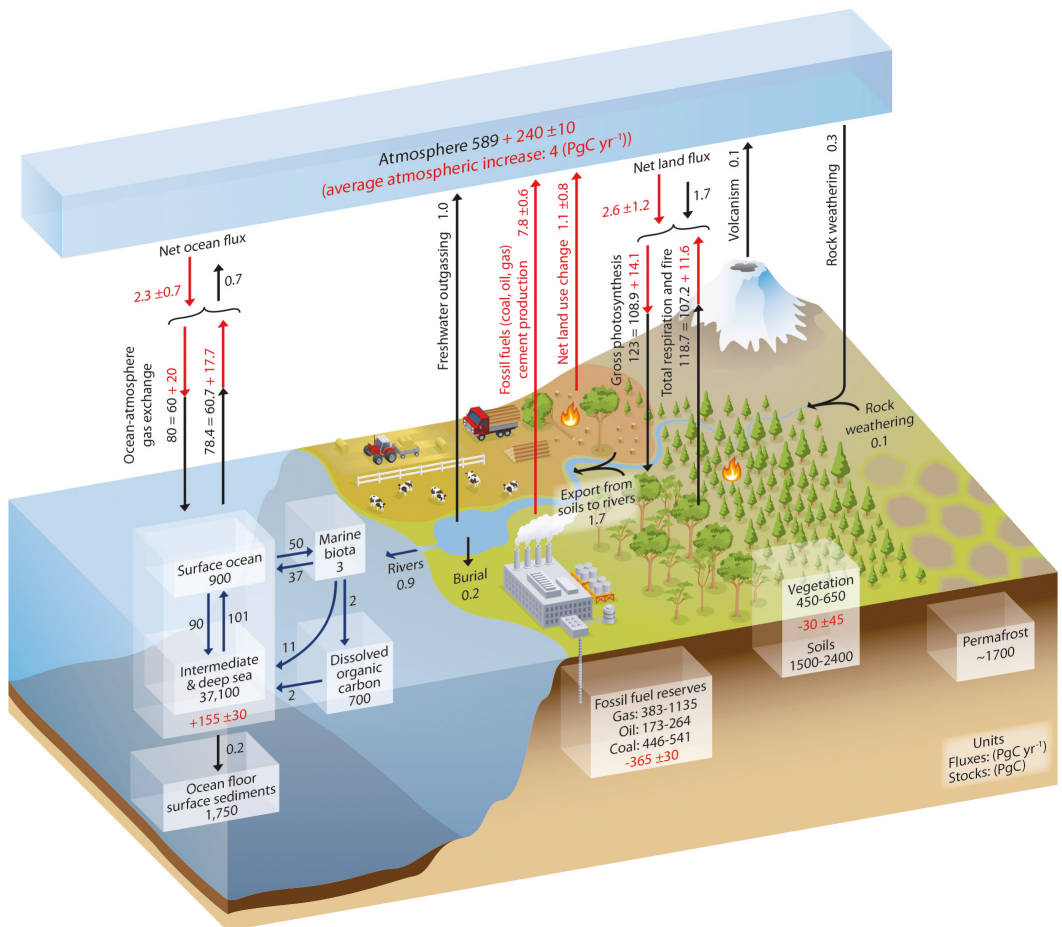


**Figura 1.3.** Esquema del ciclo global del carbono. Los números representan reservorios en PgC ( $1 \text{ PgC} = 10^{15} \text{ gC}$ ) y los flujos de intercambio de carbono anuales (en  $\text{PgC año}^{-1}$ ). Los números y flechas negras indican los reservorios y flujos de intercambio estimados para el tiempo antes de la era industrial (~ 1750). Las flechas y los números rojos indican los flujos medios antropogénicos anuales sobre el período 2000-2009. Estos flujos son una perturbación del ciclo del carbono durante la era industrial (post 1750). Las partes rojas de las flechas rojas del «flujo neto terrestre» y el «flujo neto oceánico» son la captación de  $\text{CO}_2$  antropogénico en el océano y los ecosistemas terrestres, respectivamente (sumideros de carbono). Los números rojos en los sumideros denotan cambios acumulativos de carbono antropogénico durante el período desde 1750 hasta 2011. Por convención, un cambio de acumulación positivo significa que un reservorio ha ganado carbono desde 1750. Las incertidumbres se presentan como los intervalos de confianza al 90%. Fuente: Ciais *et al.* (2013).

**Tabla I.1.** Promedio decenal en los cinco componentes del balance del CO<sub>2</sub> antropogénico para los períodos 1960 - 1969, 1970-1979, 1980-1989, 1990-1999, 2000-2009 y la última década (2004-2013). Todos los valores están en GtC año<sup>-1</sup>. Todas las incertidumbres se indican como  $\pm 1\sigma$ . La base de datos que contiene los datos de cada año durante 1959-2013 está disponible en <http://cdiac.ornl.gov/GCP/carbonbudget/2014/>. Fuente: modificado de Le Quéré et al. (2015).

	Mean (GtC yr <sup>-1</sup> )						
	1960–1969	1970–1979	1980–1989	1990–1999	2000–2009	2004–2013	2013
<i>Emissions</i>							
Fossil fuel combustion and cement production	3.1 $\pm$ 0.2	4.7 $\pm$ 0.2	5.5 $\pm$ 0.3	6.4 $\pm$ 0.3	7.8 $\pm$ 0.4	8.9 $\pm$ 0.4	9.9 $\pm$ 0.5
Land-use-change emissions	1.5 $\pm$ 0.5	1.3 $\pm$ 0.5	1.4 $\pm$ 0.5	1.6 $\pm$ 0.5	1.0 $\pm$ 0.5	0.9 $\pm$ 0.5	0.9 $\pm$ 0.5
<i>Partitioning</i>							
Atmospheric growth rate	1.7 $\pm$ 0.1	2.8 $\pm$ 0.1	3.4 $\pm$ 0.1	3.1 $\pm$ 0.1	4.0 $\pm$ 0.1	4.3 $\pm$ 0.1	5.4 $\pm$ 0.2
Ocean sink	1.1 $\pm$ 0.5	1.5 $\pm$ 0.5	1.9 $\pm$ 0.5	2.2 $\pm$ 0.5	2.4 $\pm$ 0.5	2.6 $\pm$ 0.5	2.9 $\pm$ 0.5
Residual terrestrial sink	1.8 $\pm$ 0.7	1.8 $\pm$ 0.8	1.6 $\pm$ 0.8	2.7 $\pm$ 0.8	2.4 $\pm$ 0.8	2.9 $\pm$ 0.8	2.5 $\pm$ 0.9

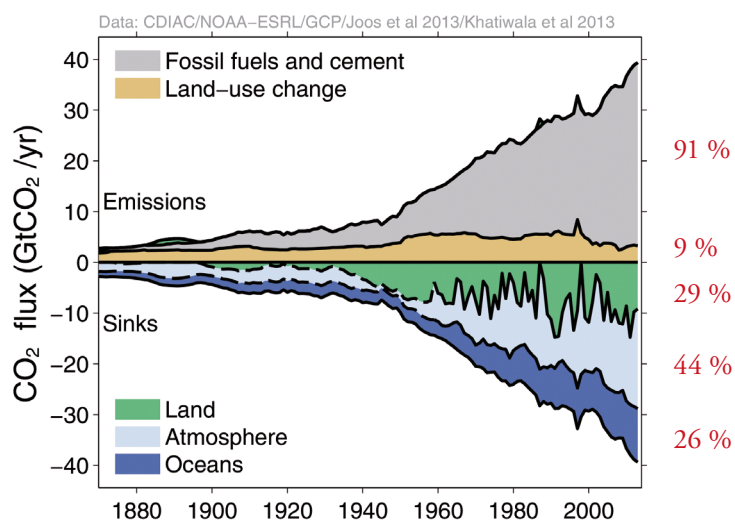


**Figura I.4.** Componentes del balance global de carbono en función del tiempo: emisiones de CO<sub>2</sub> antropogénico (C<sub>anth</sub>) anuales y su repartición entre los principales reservorios (GtC año<sup>-1</sup>) desde 1750 a 2013. Los valores rojos en % muestran la contribución media global de los cinco componentes descritos, en la década 2004 -2013: emisiones de combustibles fósiles y cemento (gris), las emisiones derivadas de cambios de uso del suelo (marrón), tasa de crecimiento del CO<sub>2</sub> atmosférico (azul claro), sumidero de CO<sub>2</sub> del océano (azul oscuro) y sumidero terrestre (verde). Fuente: adaptado del Global Carbon Budget 2014 (<http://www.globalcarbonproject.org/>); valores promedio en % de Le Quéré et al. (2015).

Existe la necesidad de entender mejor la perturbación antropogénica y la variabilidad intrínseca del ciclo natural del carbono en el océano, y establecer la velocidad a la que la acidificación del océano se está produciendo. Esto permitirá desentrañar la respuesta del océano como sumidero y los ecosistemas marinos a los cambios en el clima, que es información fundamental para establecer los límites de emisiones de CO<sub>2</sub> para lograr objetivos de estabilización de las concentraciones.

## EL SUMIDERO OCEÁNICO DE CO<sub>2</sub>

El océano desempeña un papel clave en la regulación del clima de la Tierra, ya que intercambia grandes cantidades de calor, agua, gases y partículas con la atmósfera. La continua interacción entre la atmósfera y el océano conduce a intercambio de CO<sub>2</sub> en forma de gas entre estos dos grandes reservorios que se traduce, en promedio, en una absorción de CO<sub>2</sub> antropogénico en las capas superficiales del océano. Teniendo en cuenta que la renovación del océano es del orden de un milenio (Holzer and Primeau, 2006), pequeños cambios en el gran reservorio oceánico pueden inducir cambios significativos en la concentración de CO<sub>2</sub> en la atmósfera y, a su vez, las perturbaciones en el CO<sub>2</sub> atmosférico pueden ser amortiguadas por el océano, lo que lleva, por ejemplo, a los ciclos típicos de CO<sub>2</sub> de los ciclos glacial-interglacial (Luthi *et al.*, 2008).

### Perspectiva general sobre el ciclo oceánico del carbono

Los océanos regulan el CO<sub>2</sub> atmosférico, principalmente a través de tres mecanismos (Volk y Hoffert, 1985) (Figura 1.5):

- Bomba de solubilidad. Se trata de procesos de absorción o liberación de CO<sub>2</sub> en la interfase atmósfera-océano, debido a los cambios en la solubilidad del CO<sub>2</sub> gaseoso. El secuestro de CO<sub>2</sub> atmosférico a través de este mecanismo comienza con la disolución de CO<sub>2</sub>, su hidratación en ácido carbónico y la disociación del ácido carbónico que conduce al sistema de carbonato en agua de mar, y continúa con el transporte y mezcla de las diferentes formas de CO<sub>2</sub> disuelto a través de su hundimiento a las profundidades del océano (bomba física).
- Bomba del carbono orgánico (tejido blando). Consiste en la absorción de CO<sub>2</sub> y su fijación en materia orgánica en las aguas superficiales por medio de la fotosíntesis, su exportación al océano profundo y la remineralización gradual de esta materia orgánica a CO<sub>2</sub> y nutrientes.
- Bomba de carbonato. Consiste en la formación de estructuras de carbonato de calcico (CaCO<sub>3</sub>) por organismos calcificadores en la superficie del océano, y su disolución en profundidad. Este proceso representa uno de los componentes de la bomba de carbono biológica, pero opera en contra de la bomba de carbono orgánico, que tiende a reducir el CO<sub>2</sub> atmosférico. Por el contrario, la precipitación de CaCO<sub>3</sub> implica un aumento en CO<sub>2</sub> porque este gas se libera durante la precipitación de CaCO<sub>3</sub> según la reacción:



Sin embargo, el aumento de CO<sub>2</sub> no es de un mol por mol de CaCO<sub>3</sub> precipitado, si no un poco menos

(hoy en día es de aproximadamente 0.6 moles por mol, (Frankignoulle *et al.*, 1994)) a causa del tamponamiento ya que la mayor parte del CO<sub>2</sub> recién formado se convertirá en bicarbonato. No obstante, el medio disminuye su pH con la precipitación de CaCO<sub>3</sub>. Por lo tanto, la producción de CaCO<sub>3</sub> en la superficie del océano tiende a aumentar el CO<sub>2</sub> atmosférico.

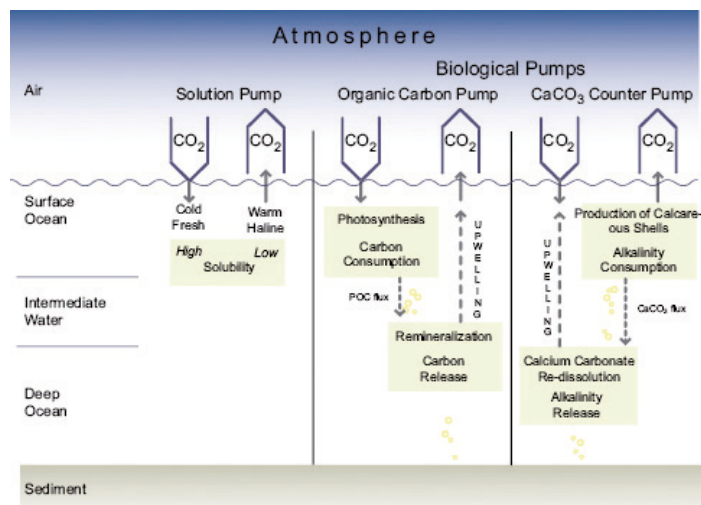
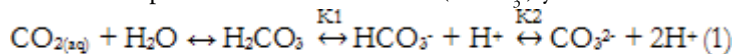


**Figura 1.5.** Bombas oceánicas de carbono principales, que controlan la regulación de los cambios naturales de CO<sub>2</sub> atmosférico por el océano: la bomba de solubilidad, la bomba de carbono orgánico y bomba de carbonato. Heinze *et al.* (1991).

### El sistema del carbónico en agua de mar

El aumento de CO<sub>2</sub> en agua de mar induce cambios en la química del sistema del carbónico en agua de mar (Zeebe y Wolf-Gladrow, 2001). El CO<sub>2</sub> disuelto (CO<sub>2(aq)</sub>) reacciona con agua de mar para formar ácido carbónico (H<sub>2</sub>CO<sub>3</sub>) que se disocia rápidamente en bicarbonato (HCO<sub>3</sub><sup>-</sup>) y iones de carbonato (CO<sub>3</sub><sup>2-</sup>):



donde K<sub>1</sub>\* y K<sub>2</sub>\* son las constantes de equilibrio estequiométricas que se denominan a menudo como la primera y segunda constantes de disociación del ácido carbónico. Estas reacciones producen protones que reducen el pH del agua de mar. Sin embargo, el CO<sub>2</sub> que se disuelve en el agua de mar no se disocia completamente en carbonato ya que también se neutraliza eficazmente al reaccionar con CO<sub>3</sub><sup>2-</sup> para producir HCO<sub>3</sub><sup>-</sup> debido a la capacidad de tamponamiento del agua de mar. El HCO<sub>3</sub><sup>-</sup> producido se disocia parcialmente, liberando protones y por lo tanto disminuyendo el pH. La disminución resultante del pH es, no obstante, mucho menor que para un sistema no tamponado. La suma de todas las especies de CO<sub>2</sub> disuelto se llama carbono inorgánico disuelto total (C<sub>T</sub>):

$$C_T = [\text{CO}_2] + [\text{HCO}_3^-] + [\text{CO}_3^{2-}] \quad (2)$$

Esta cantidad también puede ser nombrada como DIC, TIC, TCO<sub>2</sub> o ΣCO<sub>2</sub>. La distribución de C<sub>T</sub> entre

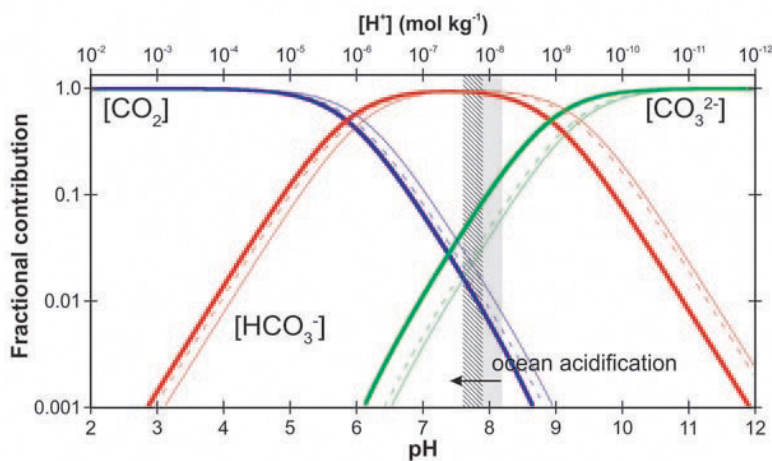


**Figura 1.6.** Gráfico de Bjerrum que muestra las proporciones relativas de  $[\text{HCO}_3^-]$ ,  $[\text{CO}_3^{2-}]$  y  $[\text{CO}_2]$  al carbono inorgánico disuelto total en el agua de mar a diferentes salinidades ( $S$ ), temperaturas ( $T$ ) y presiones ( $P$ ) (curvas sólidas gruesas a  $S = 35, T = 25^\circ\text{C}, P = 0 \text{ dbar}$ ; curvas sólidas finas a  $S = 35, T = 0^\circ\text{C}, P = 0 \text{ dbar}$ ; curvas a trazos a  $S = 35, T = 0^\circ\text{C}, P = 3000 \text{ dbar}$ ). La región sombreada refleja el rango del océano superficial moderno (promedio anual), donde la región tramada refleja el pH proyectado al año 2100. Adaptado de Barker y Ridgwell (2012).

las diferentes especies varía con el pH del agua de mar (Figura 1.6). La mayor parte del  $\text{CO}_2$  disuelto está en forma de  $\text{HCO}_3^-$  y no en forma de  $\text{CO}_2$ . Si el resto de propiedades se mantiene, a medida que se añade más  $\text{CO}_2$  al agua de mar, la proporción entre las tres especies del carbónico cambiará, provocando un incremento de  $[\text{CO}_{2(\text{aq})}]$  y  $[\text{HCO}_3^-]$  y la disminución de  $[\text{CO}_3^{2-}]$ , por lo que disminuye el pH. Esta es la huella de la acidificación antropogénica de los océanos.

El siguiente parámetro esencial para la descripción del sistema de carbónico es la alcalinidad total ( $A_T$ ). Esta cantidad está relacionada con el balance de cargas en agua de mar. Se puede definir como el exceso de bases (aceptores de protones) sobre ácidos (donantes de protones) en agua de mar, que refleja la capacidad de agua de mar para neutralizar los ácidos o aceptar protones. Por esta razón, no sólo el sistema del carbónico si no cualquier sistema ácido-base similar en solución contribuirán a la alcalinidad. Según Dickson (1981), la alcalinidad es «el número de moles de iones de hidrógeno ( $\text{H}^+$ ) equivalentes al exceso de aceptores de protones (bases formadas a partir de ácidos débiles con una constante de dissociación  $K \leq 10^{-4.5}$ , a  $25^\circ\text{C}$  y fuerza iónica cero) sobre donantes de protones (ácidos con  $K > 10^{-4.5}$ ) en un kilogramo de muestra». La expresión para la  $A_T$  derivada de esta definición es:

$$A_T = [\text{HCO}_3^-] + 2[\text{CO}_3^{2-}] + [\text{B(OH)}_4^-] + [\text{OH}^-] + [\text{HPO}_4^{2-}] + 2[\text{PO}_4^{3-}] + [\text{SiO(OH)}_3^-] + [\text{HS}^-] + 2[\text{S}_2^-] + [\text{NH}_3] - [\text{H}^+]F - [\text{HSO}_4^-] - [\text{HF}] - [\text{H}_3\text{PO}_4] \quad (3)$$

donde las especies del carbónico contribuyen en un 96% a la  $A_T$ . Además de ácido carbónico, los sistemas ácido-base más importantes que contribuyen a la  $A_T$  son el ácido bórico y el agua en sí misma, con los contribuyentes restantes actuando como micro-compuestos. El  $C_T$  y la  $A_T$  son cantidades conservativas, es decir,

sus concentraciones, medidas en mol·kg<sup>-1</sup> no se ven afectadas por los cambios de presión o temperatura, y obedecen la ley de mezcla lineal. Finalmente, el sistema del carbónico incluye el gua y sus productos de disociación H<sup>+</sup> y OH<sup>-</sup>. El pH se determina por la concentración de H<sup>+</sup> (-log10 [H<sup>+</sup>]) en solución y depende de la temperatura y la presión.

Todo el sistema del carbónico puede describirse si se conocen dos parámetros concretos (Zeebe y Wolf-Ga-drow, 2001). Para este propósito, los parámetros más usados son pH, C<sub>T</sub>, A<sub>T</sub> y presión parcial de CO<sub>2</sub> (pCO<sub>2</sub>), ya que estos se pueden determinar analíticamente con gran precisión (Dickson *et al.*, 2007).

El sistema del carbónico es un tampón natural del pH del agua de mar. La capacidad de amortiguación del agua de mar depende de la cantidad presente de CO<sub>3</sub><sup>2-</sup> para aceptar protones y su conversión a HCO<sub>3</sub><sup>-</sup>. A medida que se añade más CO<sub>2</sub> se consume progresivamente más CO<sub>3</sub><sup>2-</sup>, la capacidad de tamponamiento del agua de mar disminuye, lo que lleva a un aumento en la proporción de CO<sub>2</sub> que permanece como CO<sub>2(aq)</sub>. Este efecto se cuantifica por el factor Revelle (Revelle y Suess, 1957), que relaciona la ratio del cambio relativo de [CO<sub>2</sub>] respecto al cambio relativo de C<sub>T</sub>:

$$\text{Factor de Revelle} = (\Delta[\text{CO}_2] / [\text{CO}_2]) / (\Delta[\text{C}_T] / [\text{C}_T])$$

Es un indicador de la capacidad de tamponamiento del océano para absorber CO<sub>2</sub>. Cuanto menor sea el Factor Revelle mayor será la capacidad de tamponamiento del agua de mar. El aumento del CO<sub>2</sub> atmosférico aumenta el factor Revelle, provocando que el océano sea menos eficiente al absorber más CO<sub>2</sub>. Los factores Revelle actuales ya están cerca de una unidad más altos de lo que eran en el océano preindustrial (Sabine *et al.*, 2004).

### Química del carbónico, controles y acidificación oceánica

La reducción de iones de carbonato lleva a una disminución en los estados de saturación de CaCO<sub>3</sub>. El estado de saturación de minerales de CaCO<sub>3</sub> ( $\Omega$ ) se define como:

$$\Omega = [\text{Ca}^{2+}] [\text{CO}_3^{2-}] / K_{\text{sp}}$$

el producto iónico de las concentraciones de iones de calcio y de iones carbonato, dividido por el producto de solubilidad ( $K_{\text{ps}}$ ) para una determinada fase mineral de CaCO<sub>3</sub>. Principalmente, el CaCO<sub>3</sub> se produce ya sea como aragonita o como calcita. La aragonita es más soluble debido a su estructura cristalina que es menos estable que la de calcita. Como el [Ca<sup>2+</sup>] es estrechamente proporcional a la salinidad,  $\Omega$  está principalmente determinada por las variaciones en [CO<sub>3</sub><sup>2-</sup>]:

$$\Omega = [\text{CO}_3^{2-}]_{\text{in situ}} / [\text{CO}_3^{2-}]_{\text{saturación}}$$

Por lo tanto,  $\Omega$  refleja el punto de equilibrio entre la tendencia del [CO<sub>3</sub><sup>2-</sup>] disuelto para unirse a la superficie de un cristal (precipitación) o para desprenderse del cristal y entrar en disolución (disolución). De acuerdo con esto, la precipitación de CaCO<sub>3</sub> se produce en condiciones de sobresaturación ( $\Omega > 1$ ) y la disolución bajo condiciones de subsaturación ( $\Omega < 1$ ). El nivel de profundidad en el que  $\Omega = 1$  representa el nivel de saturación o el horizonte de saturación.

El sumidero oceánico contribuye a mitigar el calentamiento global. Sin embargo, la invasión oceánica de CO<sub>2</sub> antropogénico resultante afecta los equilibrios químicos del sistema del carbónico, aumentando la cantidad de C<sub>T</sub> en las capas superficiales, que se traduce en una disminución del pH superficial del océano. En promedio, las aguas superficiales del océano ya se han acidificado en 0.1 unidades de pH respecto a los niveles preindustriales (Raven *et al.*, 2005). Probablemente, el pH del océano superficial no ha estado por debajo de 8.1 durante los últimos 20 millones de años (Pelejero *et al.*, 2010) y las referencias en él) y, si continúan las emisiones de C<sub>ant</sub>, el pH superficial del océano podría disminuir en aproximadamente 0.7 unidades para el año 2300 (Zeebe *et al.*, 2008). Teniendo en cuenta los posibles impactos de la acidificación del océano en una serie de propiedades y procesos biogeoquímicos importantes, se ha denominado “el otro problema del CO<sub>2</sub>” (Doney *et al.*, 2009). Una implicación bien documentada es la disminución de los estados de saturación de CaCO<sub>3</sub>, que tiene efectos adversos para los organismos marinos, donde los calcificadores son los afectados de forma más clara (Bach, 2015; Bach *et al.*, 2015; Chan y Connolly, 2013). Establecer la tasa a la que el océano se está acidificando es importante no sólo para estudiar el posible destino de la mayoría de la biota marina ante este cambio global, sino también para comprender la capacidad cada vez menor de los océanos para absorber el CO<sub>2</sub> atmosférico en el futuro (Sabine y Tanhua, 2010).

#### CO<sub>2</sub> antropogénico oceánico. Metodología para su estimación.

El C<sub>ant</sub> en el océano se define como el exceso de CO<sub>2</sub> en relación con los niveles preindustriales (o naturales) de CO<sub>2</sub>. Se han desarrollado varios métodos para su estimación. Esencialmente, las concentraciones de C<sub>ant</sub> se pueden abordar por dos tipos principales de metodologías: los llamados métodos de retrocálculo o basados en medidas de CO<sub>2</sub> y los métodos basados en trazadores.

Los principios de los métodos basados en medidas de CO<sub>2</sub> fueron establecidos por Brewer (1978) y Chen y Millero (1979) y se basan en la separación de las contribuciones al C<sub>T</sub> de la remineralización de materia orgánica y la disolución de CaCO<sub>3</sub>, de acuerdo a las ecuaciones de Redfield. El método clásico ΔC\* (Gruber *et al.*, 1996) introdujo por primera vez el término de desequilibrio a las técnicas de retrocálculo. Los autores propusieron el desequilibrio como uno de los dos términos en que separaban el C<sub>T</sub> preformado, junto con un término de referencia de C<sub>ant</sub> cero que se puede estimar de acuerdo con el sistema del carbónico asumiendo condiciones preindustriales. El método φC<sub>T</sub><sup>0</sup> (Vázquez-Rodríguez *et al.*, 2009a) comparte principios con el método ΔC\*. Propone algunas mejoras a la determinaciones del desequilibrio y la A<sub>T</sub> preformada mediante el uso de los valores de la capa subsuperficial (100-200m) como referencia para la caracterización de propiedades de masa de agua en sus condiciones de formación. Un punto importante de este enfoque es que ninguna de las parametrizaciones de alcalinidad preformada o el desequilibrio se basan en datos de CFC sino exclusivamente en parámetros conservativos. El método TrOCA (Touratier y Goyet, 2004; Touratier *et al.*, 2007) comparte con los métodos anteriores las contribución biológica al C<sub>T</sub> a través de las ratios de Redfield, pero no tiene en cuenta la estimación de un C<sub>T</sub> preformado en su parametrización.

El método TTD (Waugh *et al.*, 2006), se basa en mediciones de CFCs y no de CO<sub>2</sub>. Al igual que todos los métodos basados en trazadores, tiene como objetivo describir matemáticamente las llamadas Distribuciones Tránsitorias (TTD) a partir de observaciones de CFCs para “calibrar” la forma en que la circulación del océano conecta condiciones de contorno de superficie con concentraciones en el océano interior. Para estimar C<sub>ant</sub> en cualquier punto del espacio y tiempo determinado en el interior del océano, la única información necesaria es el conocimiento sobre la evolución temporal de C<sub>anto</sub> en la capa de mezcla superficial y la velocidad a la que esta condición de superficie se transporta y se mezcla con el océano interior.

## EL OCÉANO ATLÁNTICO NORTE SUBTROPICAL

### Perspectiva física: características de la circulación

El Atlántico Norte es una cuenca oceánica que se divide en el Atlántico Norte y el Atlántico Sur a través del Ecuador. La región del Atlántico Norte (Figura 1.7) tiene un papel importante en la regulación del clima, debido principalmente a los intercambios de calor y de agua dulce con la atmósfera que tienen lugar durante el transporte de aguas cálidas de latitudes más bajas hacia el norte. El Atlántico Norte es también una región climática clave debido al proceso de formación de aguas profundas, cuando las aguas cálidas superficiales alcanzan latitudes subpolares y se enfrián y se hunden, dando lugar a lo que se considera el punto de partida principal de la circulación de retorno (MOC).

La circulación superficial del Atlántico Norte subtropical incluye un giro subtropical antíclínico (NASTG), mientras que la circulación tropical es fuertemente zonal. El NASTG está situado entre Europa y América en el rango de 15 a 45°N de latitud (Figura 1.7). Como todos los giros subtropicales, es asimétrico, con corrientes fuertes y estrechas occidentales y un amplio flujo hacia el sur a lo largo de las regiones subtropicales central y oriental. El sistema de corrientes occidental subtropical se compone de la Corriente del Golfo y la Corriente Noratlántica. La corriente del Golfo es la ruta principal de las aguas superficiales cálidas de latitudes bajas para alcanzar latitudes altas en el hemisferio norte. El sistema de corrientes oriental se compone de la Corriente de Canarias y la Corriente de Portugal Sistema (Figura 1.7). La corriente de Canarias fluye hacia el suroeste y se une a la Corriente NorEcuatorial.

Las corrientes superficiales juegan un papel importante en el transporte de calor desde la zona ecuatorial hacia latitudes polares. En este camino se producen cambios en su densidad que acaba favoreciendo su hundimiento en el interior del océano. El hundimiento de las aguas en las latitudes altas, un proceso conocido como la formación de masas de aguas profundas, se equilibra con el afloramiento y el retorno del agua desde la profundidad a la superficie. De esta manera, la circulación del océano profundo se impulsa por los cambios de densidad y el fujo de estas corrientes profundas se conoce como circulación termohalina o de retorno (MOC) (Figura 1.8), donde la palabra “retorno” implica una transformación vertical de la masa de agua.

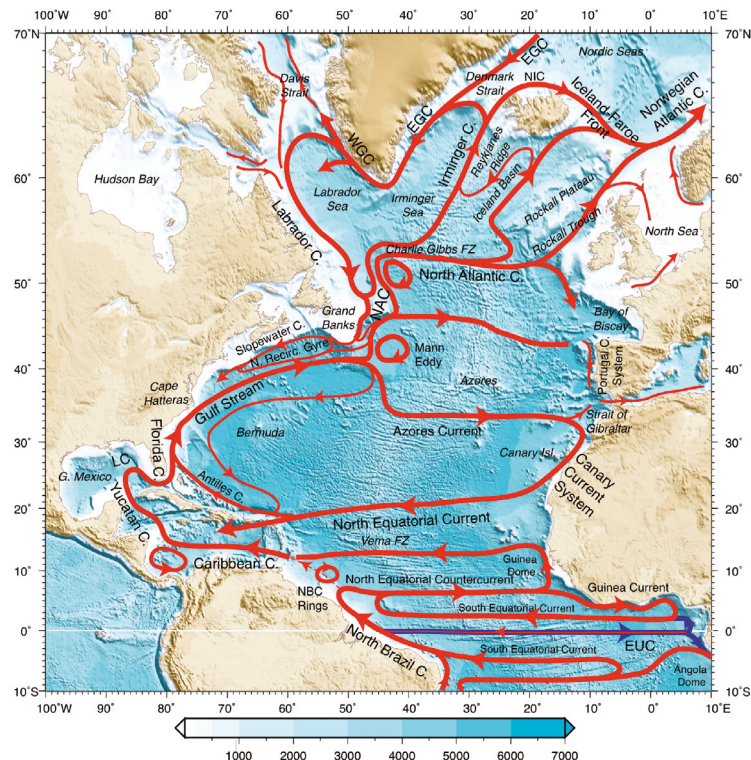


**Figura 1.7.** Atlántico Norte. Circulación superficial (rojo). Fuente: Talley et al., (2011).

La comprensión de la variabilidad de la MOC es un reto importante para la comunidad científica. Varias líneas de investigación sugieren que se ha estado produciendo una desaceleración de la MOC en las últimas décadas, lo que ha dado lugar a un enfriamiento en el Atlántico norte (Robson et al, 2014; Rahmstorf et al, 2015). Existe un efecto indirecto relacionado con la capacidad del Atlántico Norte para absorber y almacenar  $C_{ant}$ , ya que el proceso de formación de masas de agua profunda lleva asociada la transferencia de grandes cantidades de  $C_{ant}$  al océano profundo, lo que convierte al Atlántico Norte es uno de los mayores sumideros de  $C_{ant}$  del océano global (Sabine et al, 2004; Steinfeldt et al, 2009; Pérez et al., 2010).

#### Perspectiva química: la variabilidad espacio-temporal en el sistema del carbónico

Una motivación importante en la investigación biogeoquímica marina durante las últimas décadas ha sido intentar comprender mejor el papel del océano como sumidero de  $CO_2$  antropogénico. A su vez, la evaluación de la acidificación asociada también ha sido de gran interés.

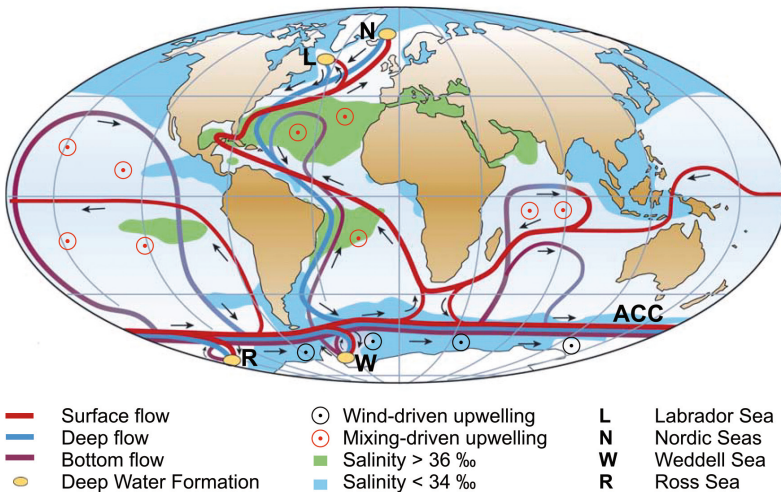


**Figura 1.8.** Esquema del sistema de circulación de retorno. En el Atlántico, aguas cálidas y salinas fluyen hacia el norte hasta el mar de Labrador y los mares nórdicos. En el Océano Austral las aguas se vuelven más densas y por lo tanto llegan a niveles más profundos que las del Atlántico Norte. Fuente.: Kuhlbrodt *et al.*, (2007).

Las variaciones interanuales a estacionales o a más largo plazo en los parámetros del sistema del carbónico en el giro subtropical han sido evaluadas en las dos series temporales BATS y ESTOC (Bates *et al.*, 1996; Bates, 2001; González-Dávila *et al.*, 2003; Bates, 2007; Santana-Casiano *et al.*, 2007; González-Dávila *et al.*, 2010; Bates *et al.*, 2012; Bates *et al.*, 2014) (Figura 1.9).

El Océano Atlántico Norte presenta la mayor tasa de almacenamiento de  $C_{ant}$  de todos los océanos ( $0.386 \pm 0.012$  Pg  $y^{-1}$ ) (Mikaloff Fletcher *et al.*, 2007). Más del 23% del inventario oceánico mundial de  $C_{ant}$  se encuentra en el Atlántico Norte a pesar de que la región sólo cubre aproximadamente el 15% de los océanos del mundo (Figura 1.10a) (Sabine *et al.*, 2004; Sabine y Tanhua, 2010). El mecanismo clave que contribuye a este valor tan alto es el transporte hacia el norte de las aguas cálidas subtropicales que contienen altas concentraciones de  $C_{ant}$  a las regiones de formación de aguas profundas, a través de la MOC, que sostiene hasta un  $65 \pm 13\%$  del almacenamiento de  $C_{ant}$  en el Atlántico Norte (Figura 1.10b) (Álvarez *et al.*, 2003; Macdonald *et al.*, 2003; Rosón *et al.*, 2003; Sabine *et al.*, 2004; Pérez *et al.*, 2013). A pesar de su alta tasa de almacenamiento de  $C_{ant}$ , la captación en la región subpolar no es predominantemente antropogénica porque, a medida que estas aguas cálidas se mueven hacia el norte, se enfrián, favoreciendo la absorción de  $CO_2$  natural sobre la perturbación antropogénica (Watson *et al.*, 1995; Pérez *et al.*, 2013). Por lo tanto, en el Atlántico Norte subpolar, la convección profunda de invierno contribuye tanto al almacenamiento de  $C_{ant}$  como de  $CO_2$  natural en profundidad, lo que contribuye de manera significativa a la eficiencia del sumidero del Atlántico

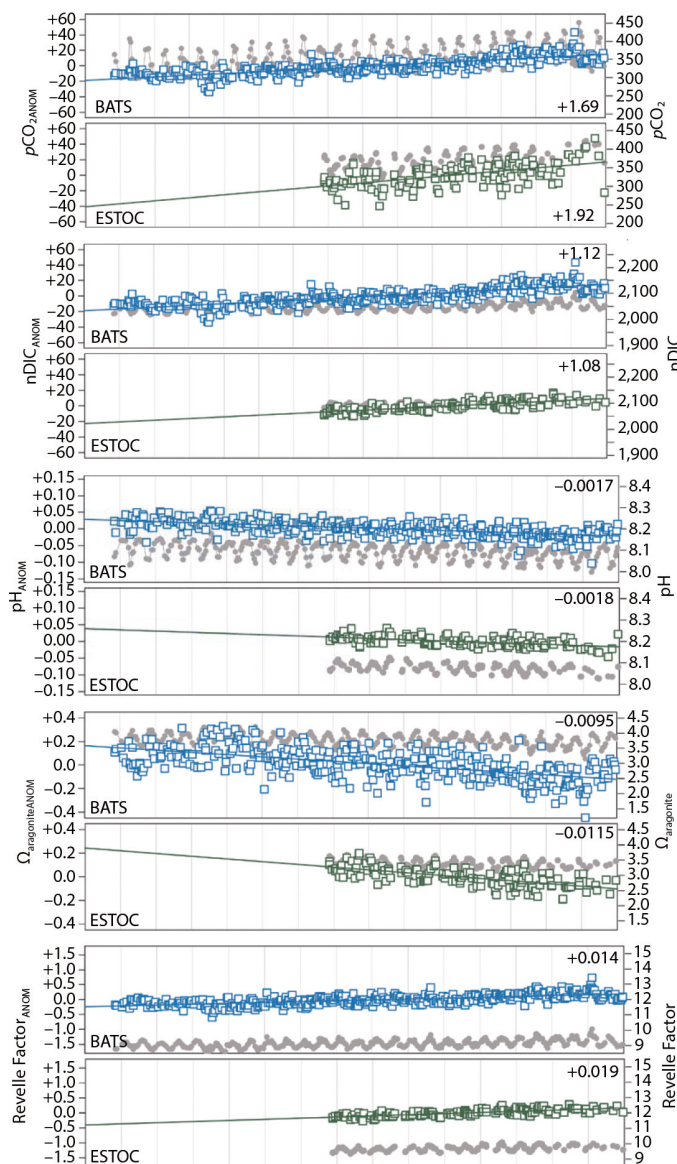


**Figura 1.9.** Series temporales de las anomalías superficiales (símbolos coloreados), observaciones (símbolos grises), con tendencias (líneas continuas) en la esquina superior derecha de cada panel, de los diferentes parámetros del sistema de carbónico en BATS y ESTOC: (a);  $p\text{CO}_2$  superficial del océano; b) DIC normalizado por la salinidad ( $n\text{DIC}$ , en  $\mu\text{mol kg}^{-1}$ ); c) pH; d) estado de saturación de aragonita ( $\Omega_{\text{aragonite}}$ ) y e) factor Revelle. Adaptado de Bates et al., (2014).

Norte. Estas aguas profundas vuelven hacia el sur en la corriente profunda de frontera oeste, que contiene niveles moderados aunque crecientes de  $C_{ant}$  (Pérez et al., 2008; Steinfeldt et al., 2009; Pérez et al., 2010). La advección de las señales físico-químicas del agua Noratlántica profunda formada (NADW) dentro de la corriente profunda de frontera oeste explica por qué el Atlántico Norte occidental es el principal contribuyente a los inventarios totales de  $C_{ant}$  (Kortzinger et al., 1998; Brown et al., 2010) y CFC (Kieke et al., 2007; Kieke et al., 2006; Steinfeldt et al., 2007) de la cuenca entera. La variabilidad del almacenamiento decenal de los inventarios de  $C_{ant}$  (Pérez et al., 2013) y CFC depende de y está modulada por la tasa de formación de esta masa de agua profunda y, más particularmente, por el componente del agua del mar de Labrador (LSW).

Al comparar “instantáneas” hidrográficas del océano, por medio de la comparación de la misma sección hidrográfica a través del tiempo, un problema clásico asociado a la interpretación de los cambios decenales es el posible solapamiento de los cambios en el estado del océano en escalas de tiempo más cortas (Atkinson et al., 2012), ya que los procesos que afectan el clima pueden presentar una considerable variabilidad natural en una amplia gama de escalas espaciales y temporales. En el Atlántico tropical, Zunino et al., (2015) observaron un aumento en el transporte de  $C_{ant}$  a través de 7.5°N y 24.5°N entre 1993 y 2010 y de 1992 a 2011, respectivamente, que se dio como resultado de los cambios en la circulación en las capas intermedias y profundas a través de estas secciones, así como al aumento del  $C_{ant}$  dentro de las aguas de la termoclinia. Los autores también describen el almacenamiento de  $C_{ant}$  sustancial en las aguas profundas del Atlántico tropical localizadas entre las dos secciones debido a la inyección de  $C_{ant}$  a través de 24.5°N dentro de la corriente profunda de frontera oeste y a la recirculación hacia el norte de la NADW a lo largo de 7.5°N. La NADW enriquecida en  $C_{ant}$  ha sido explicada como debida a la fuerte renovación de LSW a mediados de la década de 1990, coincidiendo con una fase positiva de la Oscilación del Atlántico Norte (NAO) durante ese período (Pérez et al., 2008). De hecho, gran parte de la variabilidad en el Atlántico Norte se asocia con el modo climático NAO (Walker y Bliss, 1932; Barnston y Livezey, 1987). Los modos de baja frecuencia como la NAO no pueden influir en sí mismos en los flujos de  $CO_2$  aire-mar, pero sí en parámetros físicos como la temperatura superficial del mar y la velocidad del viento que pueden, a su vez, influenciar la  $pCO_2$  del agua de mar y, por tanto, los flujos entre el aire y el mar (Bates, 2007). Los valores positivos (negativos) del índice NAO de invierno están asociados con un fuerte (débil) flujo zonal entre Azores e Islandia (Rogers, 1984). Como el índice NAO afecta el campo de viento, los cambios a gran escala en el forzamiento atmosférico relacionado con los cambios en la NAO mantenidos durante varios años afectan a la circulación en los giros subtropical y subpolar, que tienen respuestas contrastadas a las diferentes fases de la NAO. La intensificación de la convección de invierno en el giro subpolar durante los períodos de alto índice NAO aumenta la captación y almacenamiento de  $CO_2$  de esta región (Pérez et al., 2010). En cambio, en el giro subtropical, aumenta la absorción de  $CO_2$  durante los años de bajo índice NAO (Gruber et al., 2002; Bates, 2007). El cambio entre los estados climáticos puede ocurrir como resultado de la variabilidad natural, o debido a forzamiento externo. Por tanto, es necesario entender la relación entre la variabilidad climática natural, la posible existencia de forzamiento antropogénico y las respuestas derivadas para descifrar cómo el ciclo del carbono en el Atlántico Norte evolucionará en el futuro debido al cambio climático.

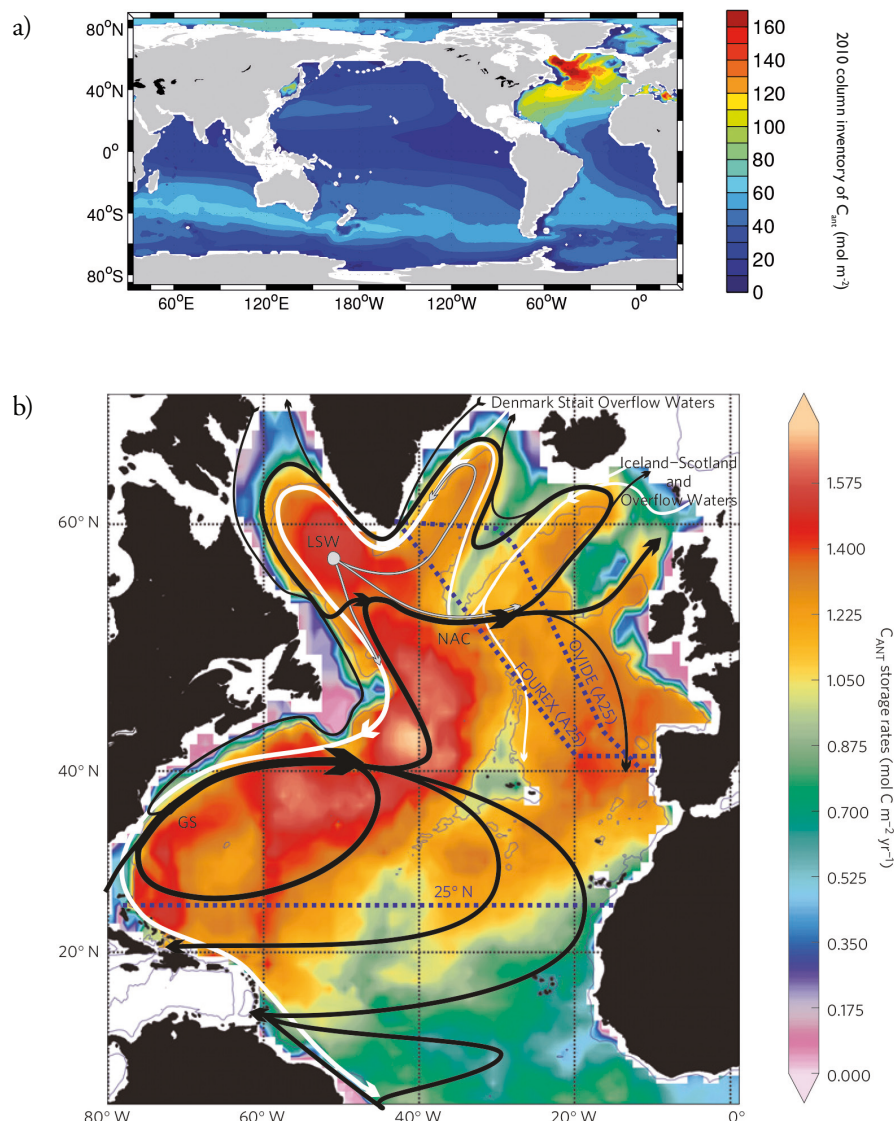


**Figura 1.10.** a) Inventario global de  $C_{ant}$  en 2010 en la columna de agua (mol m $^{-2}$ ) con exclusión de los mares marginales (Fuente: Modificado de Khatiwala et al (2013)). b) Circulación y Canto en el Atlántico Norte; Tasas de almacenamiento de  $C_{ant}$  (mol  $C_{ant}$  m $^{-2}$  año $^{-1}$ ) y principales masas de agua y corrientes implicadas en la AMOC (línea negra: Corriente del Atlántico Norte (NAC) y la Corriente del Golfo (GS); línea gris: agua de Labrador (LSW); líneas blancas: Aguas de desbordamiento del estrecho de Dinamarca e Islandia-Escocia (DSOW y ISOOW)). Se indica la derrota de las secciones A05 (25°N), FOUREX y Ovide (líneas de puntos azules). Fuente: Pérez et al. (2013).

## 2. OBJETIVO DEL ESTUDIO Y RECOPILACIÓN DE DATOS

### OBJETIVOS Y ESQUEMA DE LA TESIS

El objetivo principal de esta tesis es mejorar nuestro conocimiento sobre la variabilidad espacio-temporal del sistema de carbónico en la región (sub)tropical del Atlántico Norte. Este objetivo general se puede dividir en las siguientes preguntas principales, ya planteadas en la introducción general, que se corresponden con los capítulos de la tesis:

**¿Cuál es la distribución espacial y temporal del CO<sub>2</sub> antropogénico en la región (sub)tropical del Atlántico Norte?**

**Capítulo 3.1.** Tendencias en el CO<sub>2</sub> antropogénico en las masas de agua del Atlántico Norte Subtropical.

**Capítulo 3.2.** Cambios en el CO<sub>2</sub> antropogénico en el océano Atlántico Ecuatorial.

La recolección continuada de datos de campo referentes al sistema del carbónico en agua de mar, mediante la repetición de campañas oceanográficas a lo largo de dos secciones hidrográficas localizadas en la región (sub)tropical del Atlántico Norte entre las décadas de principios de 1990 y principios de 2010, nos llevó a evaluar los cambios en la distribución de C<sub>ant</sub> en esta región durante este período. Para ello, se usaron datos históricos y modernos, junto con la aplicación de diferentes técnicas de estimación de C<sub>ant</sub> con fines comparativos. Los datos históricos de referencia fueron revisados y actualizados para poder realizar las comparaciones temporales. Una vez revisados, y para favorecer su uso en la evaluación de cambios en las variables del sistema de carbónico, se informó de ellos a CDIAC para ponerlos a disposición de la comunidad científica.

**¿Cómo han afectado los cambios en la distribución del CO<sub>2</sub> antropogénico al pH de las masas de agua del Atlántico Norte subtropical y cuáles son las contribuciones antropogénicas y naturales relativas?**

**Capítulo 3.3.** Acidificación oceánica a lo largo de la sección 24.5°N en el Atlántico Norte Subtropical.

El estudio de los cambios en las distribuciones C<sub>ant</sub> nos llevó a investigar los cambios de pH asociados que han ocurrido en el Atlántico Norte subtropical entre 1992 y 2011. Para investigar tales cambios se utilizaron mediciones directas de pH. Por otra parte, también se evaluó en qué medida estos cambios de pH se explican debido a la acumulación de C<sub>ant</sub> y qué parte se debe a la contribución de la variabilidad natural. Con este propósito, la variabilidad de los cambios de pH naturales se estimó a partir de cambios en la concentración de oxígeno disuelto.

## CAMPAÑAS OCEANOGRÁFICAS EN EL ATLÁNTICO (SUB)TROPICAL

El registro hidrográfico de las secciones WOCE A05 (también llamada 24N o 25N) y A06 ha permitido el estudio de las fluctuaciones de las masas de agua que fluyen a través de éstas a escala decenal y cuál es su influencia en la circulación de retorno (Hernández-Guerra *et al.*, 2014) que, a su vez, regula el transporte de  $C_{ant}$  y hace del Atlántico Norte uno de los sus principales sumideros dentro del océano global. Respecto a nuestro objetivo en esta tesis, los registros de datos de las secciones A05 y A06 permitieron evaluar la variabilidad decenal y espacial del sistema de carbónico en el Atlántico Norte (sub)tropical a partir de observaciones, poniendo de manifiesto su idoneidad como secciones clave para el estudio del sumidero de  $C_{ant}$  del Atlántico Norte.

### Sección WOCE A05

La sección A05 se encuentra a la latitud de 24.5°N, extendiéndose a través del Giro Subtropical del Atlántico Norte. La sección ha sido ocupada en varias ocasiones desde 1957, pero fue en 1992 cuando se realizaron observaciones de las propiedades del sistema de carbónico a lo largo de ésta por primera vez, dentro del programa WOCE. Desde entonces ha habido cuatro ocupaciones más de interés, en 1998, 2004, 2010 y 2011 (Figura 2.1. y Tabla 2.1.), en referencia a la reevaluación de esas primeras observaciones. Los datos de las campañas de 1992 y 1998 están disponibles en la base de datos GLODAP (<http://cdiac.ornl.gov/oceans/glodap/>), que recopila datos históricos de la década de 1990. Los datos de 2004, 2010 y 2011 corresponden a repeticiones modernas de la derrota seguida en 1998, cuyos datos se pueden encontrar en la base de datos CARINA (<http://cdiac.ornl.gov/oceans/CARINA/>). Existen varios estudios sobre las distribuciones y flujos de parámetros del sistema del carbónico y el  $C_{ant}$  a lo largo de esta sección, realizados a partir de las mediciones de 1992 (Rosón *et al.*, 2003), 1998 (Macdonald *et al.*, 2003) y 2004 (Brown *et al.*, 2010). En esta memoria de tesis, las dos ocupaciones más recientes de la sección, realizadas en 2010 y 2011, se añaden al registro de datos de la A05 con el fin de hacer frente a una serie de preguntas acerca de la variabilidad espacio-temporal del sistema de carbónico entre 1992-2011, en el Atlántico Norte subtropical.

### Sección WOCE A06

La sección A06 se encuentra a 7.5°N de latitud, en la región tropical del Atlántico Norte. Fue ocupada por primera vez en 1957 durante el Año Geofísico Internacional y se incluyó dentro de la red de secciones a ser estudiadas dentro del programa WOCE en la década de 1990 (Figura 2.1.y Tabla 2.2). Fue en 1993 cuando se realizó la primera evaluación del sistema de carbónico a lo largo de esta sección. Estos datos no se incluyeron en la base de datos GLODAP (Wanninkhof *et al.*, 2003), pero están disponibles en otros repositorios de bases de datos (p. ej. en Clivar & Carbon Hydrographic Data Office, CCHDO). La sección volvió ser ocupada en 2010, siguiendo la misma derrota que en 1993. En esta memoria de tesis, los datos de la última ocupación de la A06 se usan para estudiar los cambios en el sistema del carboónico entre 1993-2010 en la región tropical del Atlántico Norte.

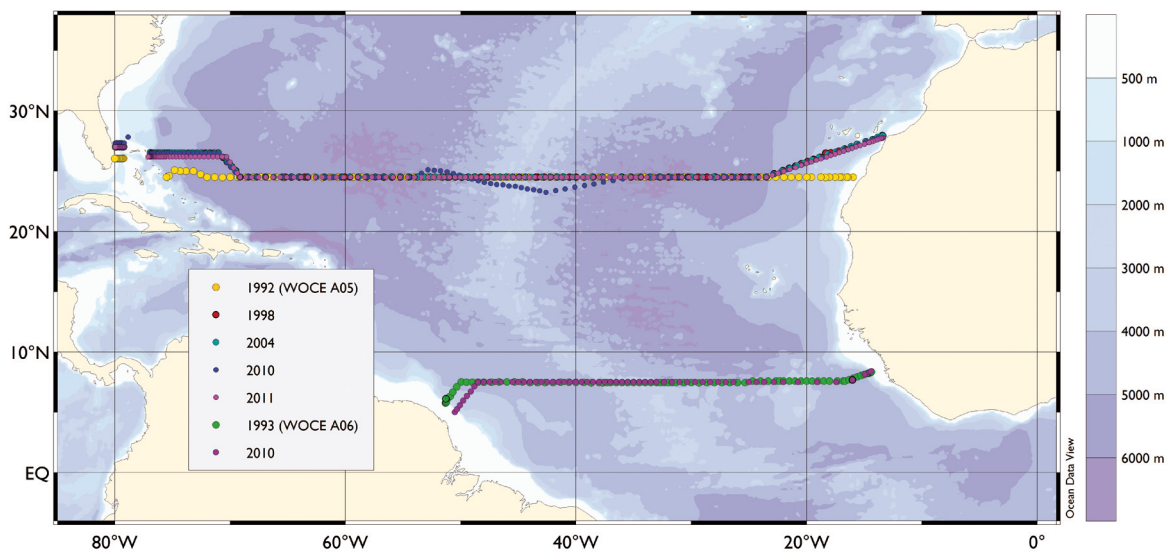


**Figura 2.1. a)** Derrota y ubicación de las estaciones de las distintas repeticiones de la sección A05, realizadas en 1992, 1998, 2004, 2010 y 2011, a lo largo de 24,5°N en el Atlántico Norte subtropical y de las dos repeticiones de la sección A06 de 1993 y 2010, a lo largo de 7,5°N en el Atlántico Norte tropical.

### Medidas analíticas

La última realización de la sección A06 se llevó a cabo en 2010, a bordo del BIO Hespérides, como parte del proyecto MOC<sup>2</sup> (Memoria Ocenánica del Clima: flujos de aguas intermedias en el Atlántico Austral y su transformación en aguas superficiales en el Atlántico Ecuatorial). La campaña ocupó 110 estaciones hidrográficas, desde el 5 de abril al 16 de mayo de 2010. En 2011 se realizó la ocupación más reciente de la sección A05, a bordo del BIO Sarmiento de Gamboa, como parte de la Expedición de Circunnavegación Malaspina 2010 (<http://www.expedicionmalaspina.es/>). Desde el 27 de enero al 15 de marzo de 2011, la campaña ocupó 167 estaciones. En ambas campañas se obtuvieron perfiles continuos de temperatura, salinidad y oxígeno disuelto, en cada estación, utilizando un instrumento de conductividad-temperatura-profundidad (CTD). El CTD se incorporó a una roseta equipada con 24 botellas Niskin que fue utilizada para recoger muestras de agua. Las muestras para el análisis químico de agua de mar se recogieron en el siguiente orden: O<sub>2</sub>, pH, carbono inorgánico disuelto total (C<sub>T</sub>), alcalinidad total (A<sub>T</sub>), nutrientes y salinidad, en las dos campañas (Tabla 2.3.).

### pH

Las muestras de agua de mar para medidas de pH se recogieron en todos los niveles de profundidad, directamente en cubetas de vidrio óptico de 28 ml, que se llenaban hasta rebasar para luego cerrarlas inmediatamente, impidiendo así la entrada de burbujas de aire. Las cubetas se metían en un baño termostático

**Tabla 2.1.** Información de las campañas referentes a la sección A05. Los datos de las distintas ocupaciones de la sección están disponibles en la web de CDIAC (Carbon Dioxide Information Analysis Center): <http://cdiac.ornl.gov/oceans/RepeatSections/>. a (m) = parámetro medido, (calc) = parámetro calculado.

Nombre (Expocode)	Base datos	Año	Fechas	Buque	Estaciones muestreadas	Parámetros $\text{CO}_2$	PI(s) datos carbónico
29HE06_1-3	GLODAP	1992	7/14 - 8/15	R/V <i>Bio Hespérides</i>	112	$\text{A}_T(\text{m})$ , $\text{pH}(\text{m})$ , $\text{C}_T(\text{calc})$	F. Millero /A.F. Ríos
33RO19980123	CARINA	1998	1/23-2/24	R/V <i>Ronald H. Brown</i>	130	$\text{A}_T(\text{m})$ , $\text{pH}(\text{m})$ , $\text{C}_T(\text{m})$	R. Wanninkhof/ R.Feely
74DI20040404	CARINA	2004	4/4-5/10	R/V <i>Discovery</i>	125	$\text{A}_T(\text{m})$ , $\text{C}_T(\text{m})$	U. Schuster
74DI20100106	CARINA	2010	1/6-2/18	R/V <i>Discovery</i>	135	$\text{A}_T(\text{m})$ , $\text{C}_T(\text{m})$	U. Schuster
29AH20110128	CARINA	2011	1/28-3/14	R/V <i>Sarmiento de Gamboa</i>	167	$\text{A}_T(\text{m})$ , $\text{pH}(\text{m})$ , $\text{C}_T(\text{calc})$	A.F. Ríos/F.F. Pérez

**Tabla 2.2.** Información de las campañas referentes a la sección A06. Los datos de las distintas ocupaciones de la sección están disponibles en la web de CDIAC (Carbon Dioxide Information Analysis Center): <http://cdiac.ornl.gov/oceans/RepeatSections/> y de CCHDO (Clivar & Carbon Hydrographic Data Office): <http://cchdo.ucsd.edu/> a (m) = parámetro medido, (calc) = parámetro calculado.

Nombre (Expocode)	Base datos	Año	Fechas	Buque	Estaciones muestreadas	Parámetros $\text{CO}_2$	PI(s) datos carbónico
WOCE A06	CCHDO	1993	4/5- 5/16	R/V <i>L'Atalante</i>	82	$\text{A}_T(\text{m})$ , $\text{pH}(\text{m})$ , $\text{C}_T(\text{m})$	Claude Oudot
29HE20100405	CARINA	2010	2/13- 3/19	R/V <i>Bio Hespérides</i>	57	$\text{A}_T(\text{m})$ , $\text{pH}(\text{m})$ , $\text{C}_T(\text{calc})$	A.F. Ríos/F.F. Pérez

**Tabla 2.3.** Número de estaciones muestreadas para diferentes parámetros químicos durante la realización de las secciones A05 en 2011 y A06 en 2010.

	$\text{O}_2$	$\text{C}_T$	pH	$\text{A}_T$	nutrientes	salinidad
A05	167	11	167	67	167	167
A06	72	16	70	43	104	85

para estabilizarlas a una temperatura de 25°C antes del análisis. El pH del agua de mar se midió siguiendo el método espectrofotométrico descrito por Clayton y Byrne (1993). Este método consiste en la adición de un volumen de solución indicadora a la muestra de agua de mar, de modo que la medición su absorbancia a diferentes longitudes de onda y la obtención de la relación entre dos absorbancias a dos longitudes de onda concretas es proporcional al pH de la muestra. El indicador es una solución de púrpura de m-cresol preparado en agua de mar, a una concentración de 2 mM. El pH se obtiene en la escala total siguiendo la fórmula de Clayton y Byrne (1993):

$pH_T = 1245,69 / T + 3,8275 + 2,11 \cdot 10^{-3} (35 - S) + \log ((R - 0,0069) / (2,222 - 0,133 R^*))$  donde R es la relación entre las absorbancias de las formas ácida y básica del indicador, en su longitud de onda de absorción máxima (es decir,  $R = A_{578}/A_{434}$ ), corregidas por la absorbancia de referencia, a la longitud de onda no absorbente de 730nm, T es la temperatura en la escala Kelvin y S es la salinidad. R se calcula según las ecuaciones descritas en Dickson *et al.*, (2007). Todas las mediciones de absorbancia se obtuvieron con un espectrofotómetro Perkin Elmer Lambda 800 UV-VIS (A05) y un espectrofotómetro Shimadzu UV-2041 PC (A06). Los datos de 2010 se corrigieron según del Valls y Dickson (1998). A los datos de 2011 se les aplicó una corrección con respecto a las impurezas del indicador (Yao *et al.*, 2007).

### Alcalinidad

Las muestras para las medidas de  $A_T$  se recogieron cada dos estaciones, aproximadamente. Las muestras de agua se tomaron directamente de las botellas Niskin en botellas de vidrio de borosilicato de 600 mL, evitando la formación de burbujas de aire. Las muestras no se filtraron, según Chanson y Millero (2007) y se almacenaron durante al menos 24 horas antes de su análisis. Las mediciones de  $A_T$  se realizaron utilizando un titulador potenciométrico automático (Titrande de Metrohm) conectado a un electrodo de vidrio y una sonda de temperatura (Pérez y Fraga, 1987). Se usó una pipeta Knudsen calibrada (~ 195 ml) para transferir un volumen determinado de muestra a un matraz Erlenmeyer abierto, en el que se llevó a cabo la valoración potenciométrica con ácido clorhídrico ( $[HCl] = 0,1\text{ M}$ ). El volumen final de la titulación se determinó por medio de dos puntos finales de pH muy cercanos uno del otro (i.e. 4.45 y 4.42) (Mintrop *et al.*, 2000). Cada muestra se analizó dos veces como control de calidad. Se usó material de referencia certificado (CRM, lote # 100 distribuido por AG Dickson del Scripps Institution of Oceanography) antes de cada sesión de análisis para calibrar las mediciones. Además, se usó una calibración adicional al principio y al final de cada lote de muestras que pertenecían a una misma sesión de análisis, a partir de mediciones de agua de mar subestándar. Este agua subestándar era agua de mar profunda y muy estable almacenada en la oscuridad, en un recipiente grande (50-75L), durante algunos días antes de su uso, que sirvió como agua de referencia con el fin de controlar la deriva en el tiempo de las determinaciones de  $A_T$ , durante la sesión de análisis.

### Carbono inorgánico disuelto

Los datos de la  $C_T$  se calcularon a partir  $A_T$  y pH, mediante el uso de las constantes de disociación de Mehrbach *et al.*, (1973) revisadas por Dickson y Millero (1987), utilizando el programa CO2SYS (Pierrot *et al.*,

2006). De todos modos, se tomaron muestras discretas de  $C_T$  a determinadas profundidades, en 11 estaciones, y se analizaron como control de calidad de los datos calculados. La consistencia interna entre el  $C_T$  calculado y medido se estimó en  $0.9 \pm 3.5 \text{ mmol}\cdot\text{kg}^{-1}$  ( $n = 22$ ) para los datos de la A05 y de  $2.8 \pm 3.9 \text{ mmol}\cdot\text{kg}^{-1}$  ( $n = 43$ ) para los datos de la A06. Las muestras de agua de mar para el análisis de  $C_T$  se tomaron directamente de las botellas Niskin en botellas de vidrio de borosilicato de 600 ml. El muestreo se hizo evitando la formación de burbujas de aire. Las muestras se prepararon para su almacenamiento descartando parte de la muestra, dejando un espacio libre de aproximadamente el 1% del volumen de la botella y añadiendo 0,3 ml de solución acuosa saturada de cloruro de mercurio para evitar la alteración biológica de la muestra. Las botellas se sellaron con tapones de vidrio cubiertos con grasa Apiezon-L y se almacenaron en la oscuridad a temperatura ambiente hasta su análisis una vez en tierra. Las mediciones de  $C_T$  se realizaron en el laboratorio del IIM-CSIC mediante una determinación coulombimétrico mediante el uso de un aparato SOMMA (Single-Operator Multiparameter Metabolic Analyzer) (Johnson *et al.*, 1998). Cada muestra fue analizada dos veces como control de calidad.

### Oxígeno

A fin de poder realizar estimaciones de  $C_{ant}$ , se determinó la concentración de  $O_2$  en muestras de agua en cada nivel de profundidad de cada estación. Las muestras se tomaron en botellas de vidrio calibradas (~ 120 ml). El muestreo se llevó a cabo evitando cuidadosamente la entrada de burbujas de aire. La temperatura de la muestra se midió con una sonda electrónica durante el llenado de las botellas. Después, las muestras se fijaban mediante una precipitación del  $O_2$  con 0.6 ml de cloruro de manganeso ( $MnCl_2 \cdot 4H_2O$ ) y 0.6 ml de solución alcalina de yoduro sódico ( $NaOH + NaI$ ) y se almacenaron en la oscuridad durante al menos 24 horas para que se estabilizaran a temperatura ambiente antes del análisis. La concentración de  $O_2$  se determinó mediante valoración potenciométrica según el método Winkler, siguiendo los estándares WOCE (Culberson, 1991). Las muestras se acidificaron antes de la titulación con 0.8 ml de ácido sulfúrico (5 M). La titulación se realizó con una solución de tiosulfato de sodio 0.02 N. La concentración de esta solución de tiosulfato se determinaba diariamente con una solución de yodato de potasio 0,020013 N. También se realizaba la medición de blancos al comienzo de cada sesión de análisis para tener en cuenta la introducción de  $O_2$  a través de los reactivos y para las impurezas en el  $MnCl_2$ .

### Nutrientes

Se recogieron muestras de agua para medir nutrientes, nitrato ( $NO_3^-$ ), fosfato ( $PO_4^{3-}$ ) y silicato ( $SiO_4^{4-}$ ), en todos los niveles de profundidad. Las muestras se tomaron directamente de las botellas Niskin en tubos de polipropileno de 125ml que eran congelados inmediatamente hasta su análisis en tierra (A05) o a bordo (A06). En las dos campañas, las concentraciones de nutrientes se determinaron con un autoanalizador Technicon siguiendo los métodos descritos por (Alvarez-Salgado *et al.*, 1992).

### Salinidad

Se tomaron muestras para medir salinidad con el fin de calibrar el sensor de conductividad. La medición de la salinidad en las diferentes profundidades de muestreo también es importante para las determinaciones de  $A_T$ . Las muestras se tomaron directamente de las botellas Niskin en botellas de vidrio cerradas selladas por una junta de goma. Las muestras se almacenaban en el laboratorio de análisis a una temperatura controlada durante más de 24 horas para que se estabilizaran. Las muestras se analizaron con un salinómetro Autosal en los dos cruceros, siguiendo las normas WOCE (Culberson, 1991).

### Recuperación de datos históricos de la sección A05

Como ha indicado con anterioridad, la sección A05 se incluyó en la red de secciones hidrográficas a estudiar en el marco del programa WOCE. La campaña oceanográfica se llevó a cabo entre el 14 de julio y el 15 de agosto de 1992, a lo largo de 24°N, a bordo del BIO Hespérides, desde Cádiz (España) a Miami (Florida, EE.UU.). Se muestrearon 112 estaciones hidrográficas, realizando los correspondientes perfiles verticales de CTD. En cada estación, se tomaron muestras de agua a diferentes profundidades para obtener una serie de medidas químicas del agua del mar. Se puede encontrar una descripción detallada de la campaña y los análisis realizados en Millero *et al.*, (2000): [Http://cdiac.ornl.gov/oceans/ndp\\_074/](http://cdiac.ornl.gov/oceans/ndp_074/). En cuanto a la caracterización del sistema de carbónico en agua de mar, se obtuvieron dos bases de datos distintas:

- Una más corta, que consiste en medidas de  $C_T$ ,  $A_T$  y pH obtenidas en 33 estaciones por el grupo de la Rosenstiel School of Marine and Atmospheric Science (RSMAS) de la Universidad de Miami, Florida. Este conjunto de datos se envió a CCHDO y CDIAC.
- Una base de datos más amplia, que consiste en medidas de pH y  $A_T$ , obtenidas en 107 de las estaciones, por el grupo del CO<sub>2</sub> del Instituto de Investigaciones Mariñas (CSIC) de Vigo. España.

La segunda base de datos no se envió a ningún repositorio de datos hidrográficos globales, a pesar de haber pasado un control de calidad durante la síntesis de medidas del carbónico de 1990 a 1998 en el Atlántico, de GLODAP (Wanninkhof *et al.*, 2003). Sin embargo, ésta fue la base de datos usada en todos los estudios sobre la distribución y transportes de los parámetros del sistema de carbónico en la sección A05 (Brown *et al.*, 2010;.. Macdonald *et al*, 2003; Rosón *et al.*, 2003). La razón principal para elegir este conjunto de datos fue que incluía cuatro veces más datos que el conjunto de datos disponibles en CCHDO o CDIAC y, aún más importante, ya que incluye también el muestreo del estrecho de Florida, que es crucial para evaluar correctamente los flujos a través de esta sección. La mejor cobertura espacial de la sección lograda en la obtención de la base de datos IIM permite una mejor descripción de las variables del sistema del carbónico con el tiempo a lo largo de la sección A05. Este hecho impulsó la notificación de estos datos a CDIAC (<http://cdiac.ornl.gov/oceans/>) para facilitar su disponibilidad para estudios posteriores. La revisión y el informe de esta base de datos ha sido una de las principales aportaciones de esta tesis, convirtiéndose así en el punto de referencia

de los estudios sobre la sección A05 presentados en esta tesis. Recientemente también ha sido utilizada en el último estudio sobre el transporte de Cant a través de esta sección (Zunino *et al.*, 2015).

El Apéndice I incluye el informe sobre la evaluación de este conjunto de dato, enviado a CDIAC: Guallart, E. F., F. F. Pérez, G. Roson, and A. F. Ríos. 2013. High spatial resolution alkalinity and pH measurements by IIM-CSIC group along 24.5°N during the R/V Hesperides WOCE Section A05 cruise. (July 14 - August 15, 1992). [http://cdiac.ornl.gov/ftp/ndp074IIIM\\_CSIC\\_data](http://cdiac.ornl.gov/ftp/ndp074IIIM_CSIC_data). Carbon Dioxide Information Analysis Center, Oak Ridge National Laboratory, US Department of Energy, Oak Ridge, Tennessee. doi: 10.3334/CDIAC/OTG.IIM\_CSIC\_WOCE\_A05.

En resumen, el conjunto de datos IIM se sometió a un control de calidad secundario (2ndQC) siguiendo los procedimientos de CARINA (CARBON IN the Atlantic) (Tanhua *et al.*, 2010), que básicamente consistió en la comparación de los datos de interés con los datos respectivos de otras campañas en localizaciones de intersección, en el océano profundo, con la intención de cuantificar los posibles sesgos sistemáticos existentes. El 2ndQC se realizó para los datos medidos de pH y  $A_T$  y los datos calculados de  $C_T$ . La comparación sección a sección se realizó entre los datos situados por debajo de 1500 dbar, para obtener una serie de sesgos que a continuación se utilizaron para calcular una corrección media final para cada parámetro. Los datos de pH fueron corregidos en -0.009 unidades, ya que el sesgo final encontrado casi duplicaba el umbral recomendado para un ajuste mínimo (0.005 unidades). Los datos de  $A_T$  también se ajustaron en  $-4 \text{ mol}\cdot\text{kg}^{-1}$ , a pesar de no superar el umbral recomendado ( $6 \text{ mol}\cdot\text{kg}^{-1}$ ), a fin de evitar un nuevo sesgo en los datos de  $C_T$  calculados debido a una reducción de los valores de pH sin cambiar los de  $A_T$ . Al hacer esto, los datos originales de  $C_T$ , que habían mostrado un sesgo muy bajo (de sólo  $1 \mu\text{mol}\cdot\text{kg}^{-1}$ ) después del 2ndQC, se mantuvieron invariables. Es importante remarcar que el 2ndQC realizado es el mejor indicador de la consistencia de los datos de pH,  $A_T$  y  $C_T$  con respecto a otros conjuntos de datos, y por tanto, de su exactitud. Se debería considerar que, en los últimos años, la investigación sobre el CO<sub>2</sub> en el océano ha evolucionado de los estudios clásicos centrados sólo en inventarios y transportes de  $C_T$  y  $C_{\text{ant}}$ , en los que la consideración más importante era obtener la medida de  $C_T$ , a una gama más amplia de temas de investigación que también se centran en el resto de variables del sistema de carbónico, tales como el pH o los estados de saturación de carbonato. En este sentido, y siguiendo el consejo CARINA, los datos de pH y  $A_T$  medidos en 1992 se ajustaron para permitir un uso más provechoso de éstos en este tipo de nuevos estudios.

### Comparación por capas y regiones

Con el fin de evaluar mejor los procesos detrás de los cambios observados en los parámetros del sistema del carbónico entre 1992 y 2011 (A05) y 1993-2010 (A06), la columna de agua a lo largo de ambas secciones se dividió en seis categorías de densidad, según Talley *et al.*, (2011) (Figura 2.2). De esta manera, se identificaron las masas de agua del Atlántico Norte presentes en cada sección. En el Atlántico subtropical se identificaron: capa superior (uNACW) e inferior (INACW) del agua central norAtlántica, agua intermedia antártica

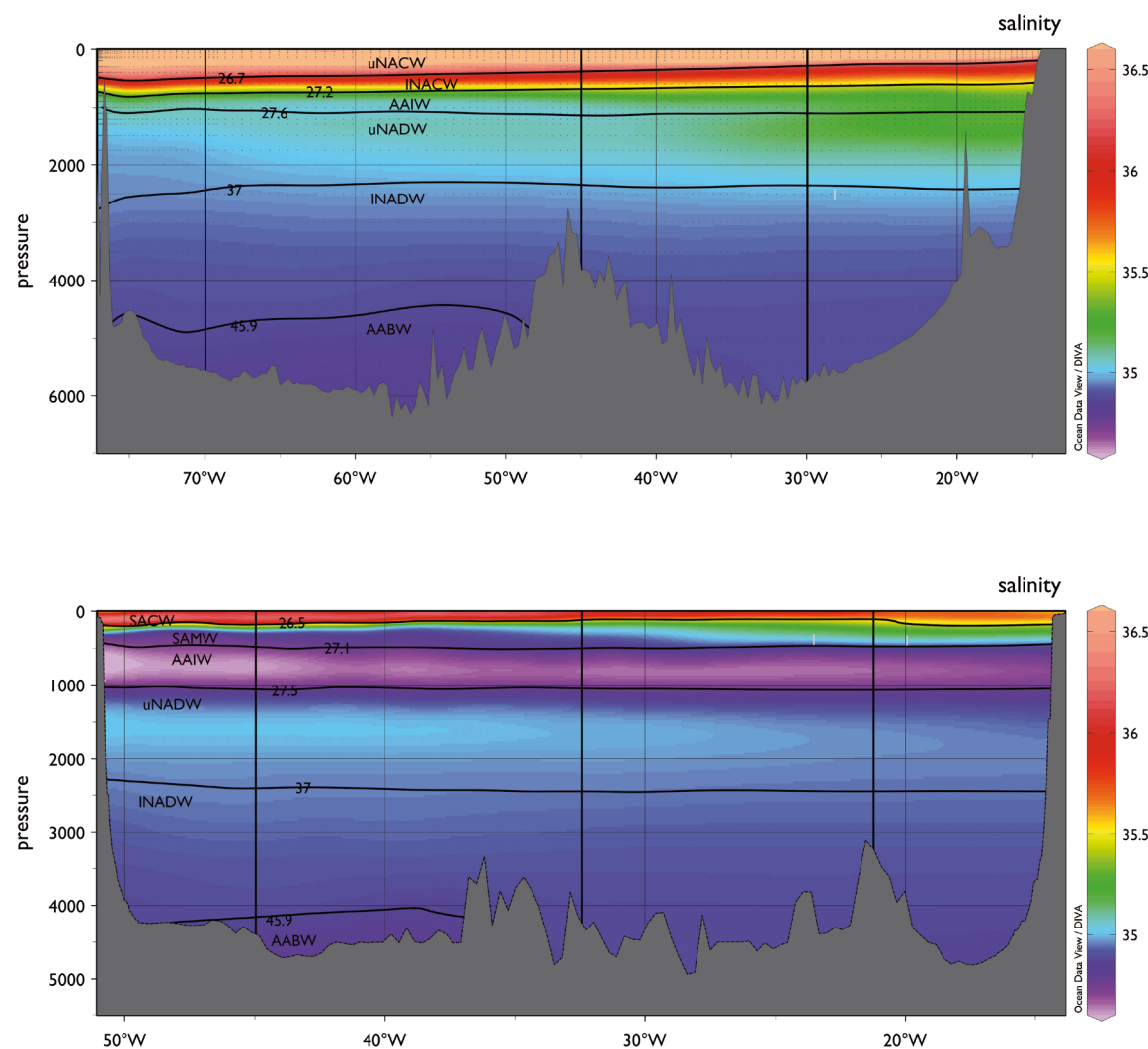


**Figura 2.2.** Regiones hidrográficas y masas de agua en las que se dividieron las secciones a) A05 y b) A06, sobre la distribución de salinidad de las campañas de 2011 (A05) y 2010 (A06). Los límites de las diferentes subdivisiones siguen detalles dados en la Tabla 2.4.

(AAIW), capa superior (uNADW) e inferior (INADW) del agua NorAtlántica profunda y agua de fondo antártica (AABW). En el Atlántico tropical se identificaron: agua central surAtlántica (SACW), agua modal subantártica (SAMW), agua intermedia antártica (AAIW), capa superior (uNADW) e inferior (INADW) del agua NorAtlántica profunda y agua de fondo antártica (AABW). Los conjuntos de datos también se separaron longitudinalmente en distintas regiones. Se tuvo en cuenta la separación de cada sección entre las cuencas principales (occidental y oriental). Esta división se refinó en cada caso de acuerdo a características oceanográficas, en cada sección. En la cuenca oeste de la sección A05 se aisló una primera región como la zona de ventilación de la corriente profunda de frontera oeste (R1), separándola de la zona donde la AABW ocupa un volumen considerable del fondo del océano (R2). La cuenca este se dividió más o menos por la mitad para aislar una tercera región interior (R3) de la zona de influencia del agua mediterránea (R4). El estrecho de Florida se mantuvo como una región aislada (R0) de la sección principal. La sección A06 se dividió en dos regiones distintas en la cuenca oeste, aislando la región de mayor influencia del DWBC (R1) de la de mayor influencia de AABW (R2). La cuenca este se dividió también en dos regiones, separando la llanura abisal de Gambia (R3) de la cuenca de Sierra Leona (R4). La tabla 2.4. resume las isopicnas y coordenadas geográficas que se tuvieron en cuenta para dividir las secciones A05 y A06 en diferentes subdivisiones.

**Tabla 2.4.** Isopicna y coordenadas geográficas consideradas para dividir las secciones A05 y A06 en diferentes subdivisiones según criterios hidrográficos.

	Masa de Agua	capa de densidad	REGIÓN	Longitud
A05	<i>uNACW</i>	$\sigma_0 < 26.7$	<b>R0</b>	Florida
	<i>INACW</i>	$26.7 < \sigma_0 < 27.2$	<b>R1</b>	$80^{\circ}\text{W}$ to $70^{\circ}\text{W}$
	<i>AAIW</i>	$27.2 < \sigma_0 < 27.6$	<b>R2</b>	$70^{\circ}\text{W}$ to $45^{\circ}\text{W}$
	<i>uNADW</i>	$\sigma_0 > 27.6$ and $\sigma_2 < 37$	<b>R3</b>	$45^{\circ}\text{W}$ to $30^{\circ}\text{W}$
	<i>INADW</i>	$\sigma_2 > 37$ and $\sigma_4 < 45.9$	<b>R4</b>	$30^{\circ}\text{W}$ to $10^{\circ}\text{W}$
	<i>AABW</i>	$\sigma_4 < 45.9$		
A06	<i>uNACW</i>	$\sigma_0 < 26.5$	<b>R1</b>	$50.5^{\circ}\text{W}$ to $45^{\circ}\text{W}$
	<i>INACW</i>	$26.5 < \sigma_0 < 27.1$	<b>R2</b>	$45^{\circ}\text{W}$ to $32.5^{\circ}\text{W}$
	<i>AAIW</i>	$27.1 < \sigma_0 < 27.5$	<b>R3</b>	$32.5^{\circ}\text{W}$ to $21^{\circ}\text{W}$
	<i>uNADW</i>	$\sigma_0 > 27.6$ and $\sigma_2 < 37$	<b>R4</b>	$21^{\circ}\text{W}$ to $14.5^{\circ}\text{W}$
	<i>INADW</i>	$\sigma_2 > 37$ and $\sigma_4 < 45.9$		
	<i>AABW</i>	$\sigma_4 < 45.9$		

### 3. RESULTADOS

#### 3.1. Tendencias en el CO<sub>2</sub> antropogénico en las masas de agua del Atlántico Norte Subtropical

Se estudió la variabilidad en el almacenamiento de CO<sub>2</sub> antropogénico ( $C_{ant}$ ) a escala de tiempo decenal, en las masas de agua del Atlántico Norte Subtropical, a lo largo de 24.5°N. Para ello, las mediciones del sistema del carbónico de las ocupaciones más recientes de la sección WOCE A05, de 2010 y 2011, se compararon con los datos disponibles de las tres campañas anteriores. Por lo tanto, se usaron un total de cinco campañas para evaluar los cambios en las distribuciones de  $C_{ant}$  entre 1992 y 2011 (Figura 3.1.). Para evaluar mejor la acumulación de  $C_{ant}$ , éstas concentraciones se obtuvieron mediante el uso de cuatro métodos de estimación diferentes, que incluyen tanto métodos basados en trazadores (TTD) como en mediciones de CO<sub>2</sub> ( $\Delta C^*$ , TrOCA,  $\phi C_T^0$ ). Los cambios temporales en las concentraciones medias  $C_{ant}$  ( $[C_{ant}^{OCT}]$ ,  $[C_{ant}^{TrOCA}]$ ,  $[C_{ant}^{\Delta C^*}]$ ,  $[C_{ant}^{TTD}]$ ) para el período 1992-2011 se estudió mediante dos aproximaciones diferentes. La primera consistió en la realización de regresiones lineales entre los cinco años en que se obtuvieron las diferentes bases de datos y sus correspondientes concentraciones medias para estimar la tendencia decenal (DT, en  $\mu\text{mol}\cdot\text{kg}^{-1}\cdot\text{año}^{-1}$ ). El segundo enfoque consistió en la estimación de las respectivas tasas de almacenamiento  $C_{ant}$  ( $\mu\text{mol}\cdot\text{kg}^{-1}\cdot\text{año}^{-1}$ ) suponiendo un estado estacionario constante de la distribución oceánica de  $C_{ant}$ , considerando una tasa de porcentaje anual específica de  $[C_{ant}]$ , de acuerdo con la literatura. La tabla 3.1. resúme los resultados obtenidos.

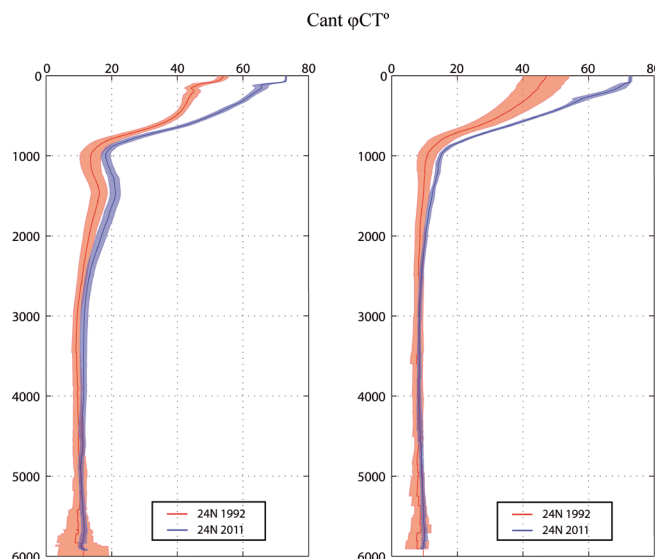


**Figura 3.1.** Distribuciones medias de  $C_{ant}^{OCT}$  ( $\mu\text{mol}\cdot\text{kg}^{-1}$ ) a lo largo de la sección A05 en las cuencas oriental (panel derecho) y occidental (panel izquierdo) del Atlántico Norte subtropical, en 1992 (línea roja) y 2011 (línea azul). Las respectivas áreas sombreadas de esos mismos colores corresponden a la desviación estándar de la estima promedio de  $C_{ant}^{OCT}$ .

Se encontró una buena concordancia tanto en los resultados de distribución como de acumulación de  $C_{ant}$  obtenidos utilizando clorofluorocarbonos o mediciones de  $CO_2$ , en los perfiles vertical y horizontal. La distribución general de  $C_{ant}$  mostró mayores concentraciones cerca de la superficie y su progresiva disminución a valores cada vez más bajos con el aumento de la profundidad. Se observaron mayores tasas de acumulación en las aguas centrales (Figura 3.2.). La uNACW mostró una acumulación media anual de alrededor de  $\sim 1 \mu\text{mol}\cdot\text{kg}^{-1}\cdot\text{año}^{-1}$  mientras que el valore fue de aproximadamente  $\sim 0.5 \mu\text{mol}\cdot\text{kg}^{-1}\cdot\text{año}^{-1}$  para la INACW. Los resultados para la uNACW son consistentes con las tasas de acumulación de  $C_{ant}$  y  $C_T$  normalizado descritas es las series temporales del Giro Subtropical del Atlántico Norte, BATS (Bates, 2012) y ESTOC (González-Dávila *et al.*, 2010). Por debajo de las capas centrales, las masas de agua intermedias y profundas mostraron tasas de almacenamiento promedio para toda la sección mucho más bajas ( $<0.25 \mu\text{mol}\cdot\text{kg}^{-1}\cdot\text{año}^{-1}$ ). Se detectaron gradientes horizontales en la acumulación de  $C_{ant}$ . Este hallazgo fue muy consistente entre métodos para las masas de agua intermedia y profunda, cuando se estudiaron las tasas de acumulación en regiones longitudinalmente diferenciadas a lo largo de la sección. Los cuatro métodos dieron evidencia de mayores tasas de almacenamiento de  $C_{ant}$  cerca del talud continental oeste, debido al papel transportador de la corriente profunda de frontera oeste (Deep Western Boundary Current, DWBC), en comparación con las tasas más bajas de almacenamiento de  $C_{ant}$  descritas para las regiones del océano interior. En particular, al oeste de  $70^\circ\text{W}$  la contribución del agua de Labrador recientemente ventilada explicó una tasa de acumulación notable, de hasta  $\sim 0.5 \text{ mol}\cdot\text{kg}^{-1}\cdot\text{año}^{-1}$ , entre 1000 y 2500 dbar. La detección de gradientes horizontales en la acumulación de  $C_{ant}$  en las aguas del océano superficial fue menos clara, debido a una mayor variabilidad entre los métodos de estimación. De todos modos, los resultados observados sugieren que, al menos durante el período de estudio, el  $C_{ant}$  podría haber sido absorbido con mayor intensidad en el lado occidental del Giro subtropical, aunque se necesitan más evidencias para confirmar esto. Cuando se consideró un estado estacionario transitorio de las distribuciones de  $C_{ant}$ , las tendencias bi-decanales en el almacenamiento de  $C_{ant}$  en las aguas profundas aguas del Atlántico Norte resultaban significativas, de acuerdo con estimaciones recientes.

En general, los cuatro métodos de estimación de  $C_{ant}$  dieron tasas de almacenamiento consistentes, lo cual sugiere una buena concordancia entre resultados obtenidos a través de trazadores y los basados en medidas de  $CO_2$ . Sin embargo, se observaron algunas diferencias particulares en las distintas tasas de almacenamiento obtenidas: el método TTD podría haber subestimado los almacenamientos en las dos capas superiores (aguas modales). El método  $\Delta C^*$  dio valores de almacenamiento ligeramente más altos que los otros tres métodos en la cuenca oriental, en las capas intermedias y profundas, lo que probablemente es resultado de la estimación de sus desequilibrios. La acumulación de  $C_{ant}$  calculada utilizando el método TrOCA generalmente recae en medio de los resultados  $\Delta C^*$  y los resultados  $\phi C_T^0$ , y este último método sugiere tasas de almacenamiento más cercanas al método de TTD.

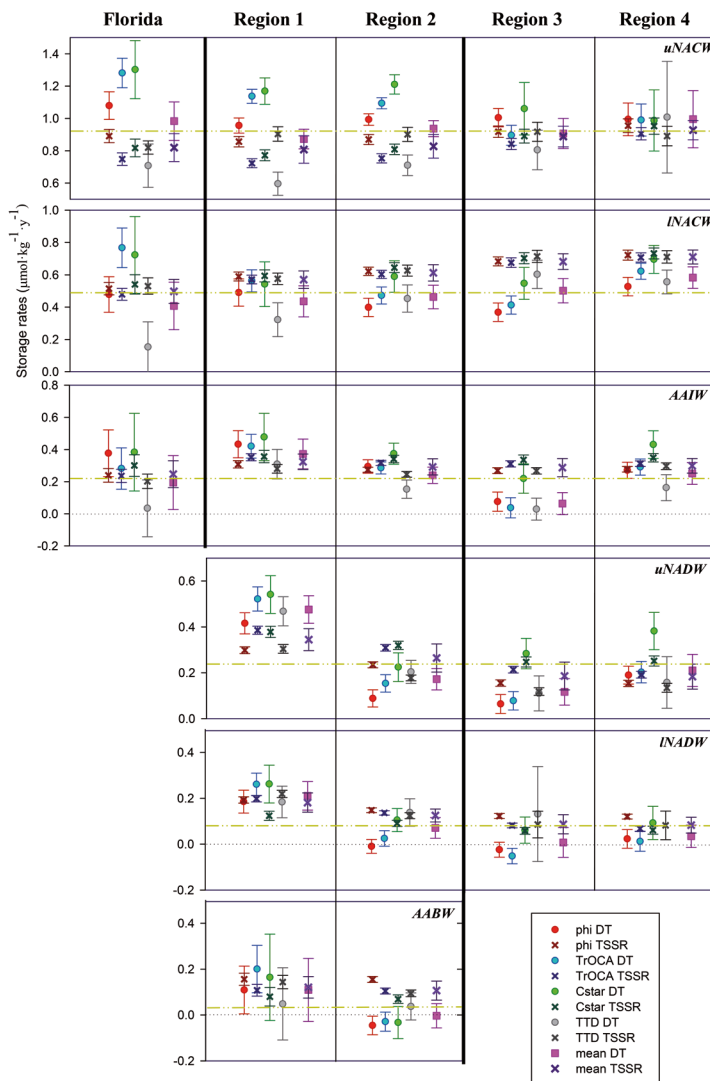


**Figura 3.2.** Tasas de almacenamiento de  $C_{\text{ant}}$  ( $\mu\text{mol} \cdot \text{kg}^{-1} \cdot \text{año}^{-1}$ ), con su incertidumbre. Se muestran las tasas de almacenamiento calculadas a través de dos aproximaciones o enfoques: Tendencia Decadal, DT (círculos de colores) o Tasa Estado Estacionario Transitorio, TSSR (cruces de colores), mediante el uso de cada método de estimación:  $\Delta C^*$  (verde),  $\phi C_T^0$  (rojo), TrOCA (azul) y TTD (gris). Los valores promedio, teniendo en cuenta los cuatro métodos, a través de la aproximación DT (rosa) y TSSR (púrpura) también se muestran. Cada panel horizontal corresponde a cada capa o masa de agua, que a su vez se dividen en subpaneles que identifican las regiones horizontalmente. La línea de puntos discontinuos amarilla indica el DT promedio a lo largo de cada capa en conjunto, sin considerar las regiones. Las líneas más gruesas verticales destacan el límite entre el estrecho de Florida y la sección principal y entre las cuencas oeste y este a lo largo de la dorsal oceánica. Los valores correspondientes se presentan en la Tabla 3.1. Téngase en cuenta que la escala en el eje y es diferente dependiendo de la capa, con el fin de ayudar a distinguir los valores de las tasas de almacenamiento entre los métodos. El rango total del eje y se extiende en  $1 \mu\text{mol} \cdot \text{kg}^{-1} \cdot \text{año}^{-1}$ , para los paneles uNACW, INACW y AAIW, y en  $0.7 \mu\text{mol} \cdot \text{kg}^{-1} \cdot \text{año}^{-1}$  para los paneles uNADW, INADW y AABW.

**Tabla 3.1.** Tendencia decenal (DT) ( $\mu\text{mol kg}^{-1} \text{a}\text{\~n}^{-1}$ ) y Tasa Estado Estacionario Transitorio (TSSR) ( $\mu\text{mol kg}^{-1} \text{a}\text{\~n}^{-1}$ ) mediante el uso de cada m\'etodo de estimaci\'on de  $C_{\text{ant}}$  ( $\Delta C^*$ , TrOCA,  $\varphi C_T^0$  y TTD), para cada subdivisi\'on de la secci\'on A05. El DT ponderado y el TSSR promedio de los cuatro m\'etodos se muestran en negrita. Las estimaciones promedio normalizadas al a\'no 2000 ( $C_{\text{ant}}^{2000}$ ,  $\mu\text{mol kg}^{-1} \text{a}\text{\~n}^{-1}$ ) tambi\'en se muestran en negrita.

Capa Regi\'on	Tendencia Decenal (DT)				ponderado	Tasa Estado Estacionario Transitorio (TSSR)				$C_{\text{anth}}^{2000}$
	$\varphi C_T^0$	TrOCA	$\Delta C^*$	TTD		$\varphi C_T^0$	TrOCA	$\Delta C^*$	TTD	
<b>uNACW</b>										
Florida	1.08±0.09	1.28±0.09	1.30±0.18	0.71±0.13	<b>0.98±0.12</b>	0.89±0.04	0.75±0.04	0.82±0.05	0.82±0.04	<b>0.82±0.09</b>
R1	0.96±0.05	1.14±0.04	1.17±0.08	0.60±0.07	<b>0.87±0.06</b>	0.86±0.03	0.72±0.03	0.77±0.03	0.90±0.04	<b>0.81±0.08</b>
R2	0.99±0.04	1.09±0.03	1.21±0.06	0.71±0.06	<b>0.94±0.05</b>	0.87±0.03	0.75±0.03	0.81±0.03	0.90±0.04	<b>0.83±0.07</b>
R3	1.00±0.06	0.90±0.06	1.06±0.16	0.80±0.12	<b>0.91±0.09</b>	0.92±0.04	0.84±0.03	0.89±0.04	0.92±0.06	<b>0.89±0.06</b>
R4	0.99±0.10	0.99±0.10	0.99±0.19	1.01±0.35	<b>1.00±0.18</b>	0.96±0.04	0.91±0.04	0.95±0.05	0.89±0.06	<b>0.93±0.06</b>
<b>INACW</b>										
Florida	0.48±0.11	0.77±0.12	0.72±0.24	0.15±0.16	<b>0.41±0.15</b>	0.51±0.04	0.48±0.04	0.54±0.06	0.53±0.05	<b>0.50±0.07</b>
R1	0.49±0.08	0.56±0.07	0.54±0.14	0.32±0.10	<b>0.44±0.10</b>	0.59±0.03	0.57±0.03	0.59±0.04	0.58±0.04	<b>0.57±0.05</b>
R2	0.40±0.06	0.47±0.05	0.59±0.10	0.45±0.08	<b>0.46±0.07</b>	0.62±0.03	0.60±0.03	0.64±0.03	0.63±0.03	<b>0.61±0.05</b>
R3	0.37±0.06	0.41±0.06	0.55±0.10	0.60±0.09	<b>0.50±0.08</b>	0.68±0.03	0.68±0.03	0.70±0.03	0.71±0.04	<b>0.68±0.05</b>
R4	0.53±0.06	0.62±0.05	0.70±0.09	0.56±0.07	<b>0.58±0.07</b>	0.72±0.03	0.71±0.03	0.73±0.03	0.71±0.04	<b>0.71±0.04</b>
<b>AAIW</b>										
Florida	0.38±0.15	0.28±0.13	0.38±0.24	0.03±0.18	<b>0.19±0.17</b>	0.24±0.04	0.24±0.04	0.30±0.07	0.20±0.04	<b>0.25±0.08</b>
R1	0.43±0.08	0.42±0.07	0.48±0.15	0.31±0.09	<b>0.37±0.09</b>	0.31±0.02	0.35±0.02	0.36±0.04	0.28±0.03	<b>0.32±0.05</b>
R2	0.29±0.04	0.29±0.04	0.37±0.07	0.15±0.06	<b>0.24±0.05</b>	0.27±0.02	0.32±0.02	0.34±0.02	0.25±0.02	<b>0.29±0.05</b>
R3	0.08±0.06	0.04±0.06	0.22±0.09	0.03±0.07	<b>0.06±0.07</b>	0.27±0.02	0.31±0.02	0.34±0.03	0.27±0.02	<b>0.29±0.06</b>
R4	0.27±0.05	0.29±0.05	0.43±0.09	0.16±0.08	<b>0.25±0.07</b>	0.28±0.02	0.31±0.02	0.35±0.03	0.30±0.02	<b>0.30±0.05</b>
<b>uNADW</b>										
R1	0.42±0.05	0.52±0.05	0.54±0.08	0.47±0.06	<b>0.48±0.06</b>	0.30±0.01	0.39±0.02	0.38±0.02	0.30±0.02	<b>0.34±0.05</b>
R2	0.09±0.04	0.15±0.04	0.22±0.06	0.20±0.05	<b>0.17±0.05</b>	0.23±0.01	0.31±0.01	0.32±0.02	0.18±0.01	<b>0.26±0.06</b>
R3	0.06±0.04	0.08±0.04	0.28±0.07	0.11±0.08	<b>0.12±0.06</b>	0.16±0.01	0.21±0.01	0.25±0.02	0.12±0.02	<b>0.19±0.06</b>
R4	0.19±0.04	0.20±0.05	0.38±0.08	0.16±0.11	<b>0.21±0.07</b>	0.15±0.01	0.19±0.01	0.25±0.02	0.13±0.02	<b>0.18±0.05</b>
<b>INADW</b>										
R1	0.19±0.05	0.26±0.05	0.26±0.08	0.18±0.07	<b>0.21±0.06</b>	0.19±0.01	0.20±0.01	0.12±0.02	0.22±0.02	<b>0.18±0.04</b>
R2	-0.01±0.03	0.02±0.03	0.10±0.05	0.14±0.06	<b>0.07±0.05</b>	0.15±0.01	0.14±0.01	0.09±0.01	0.12±0.01	<b>0.12±0.03</b>
R3	-0.02±0.03	-0.05±0.03	0.06±0.06	0.13±0.21	<b>0.01±0.06</b>	0.12±0.01	0.08±0.01	0.06±0.01	0.09±0.06	<b>0.09±0.04</b>
R4	0.02±0.04	0.01±0.04	0.09±0.07	--	<b>0.03±0.05</b>	0.12±0.01	0.07±0.01	0.06±0.02	0.08±0.06	<b>0.08±0.03</b>
<b>AABW</b>										
R1	0.11±0.10	0.20±0.10	0.16±0.19	0.05±0.16	<b>0.11±0.14</b>	0.16±0.03	0.11±0.03	0.08±0.04	0.14±0.03	<b>0.12±0.05</b>
R2	-0.05±0.04	-0.03±0.04	-0.03±0.07	0.04±0.06	<b>0.00±0.05</b>	0.15±0.01	0.10±0.01	0.07±0.02	0.09±0.01	<b>0.11±0.04</b>

### 3.2. Cambios en el CO<sub>2</sub> antropogénico en el océano Atlántico Ecuatorial

Se estudió la variabilidad en el almacenamiento de CO<sub>2</sub> antropogénico (C<sub>ant</sub>) en el océano Atlántico Ecuatorial, a lo largo de 7.5°N. Para ello, se usaron los datos del sistema del carbónico correspondientes a dos campañas oceanográficas realizadas a lo largo de esta latitud, en 1993 y 2010. Las concentraciones de C<sub>ant</sub> se describieron de acuerdo a dos métodos de estimación diferentes, uno basado en trazadores (TTD) y el otro en medidas de CO<sub>2</sub> ( $\phi C_T^0$ ). Una vez obtenidas, se evaluó el cambio en las concentraciones en el período 1993-2010, se obtuvo los inventarios específicos para cada año y las tasas de almacenamiento de C<sub>ant</sub>, a lo largo de la sección.

En ambas campañas, y según ambos métodos, la distribución general de C<sub>ant</sub> mostró mayores concentraciones cerca de la superficie y su progresiva disminución a valores cada vez más bajos hacia capas más profundas (Figura 3.3). En general, las concentraciones aumentaron de 1993 a 2010, con una penetración muy clara de la señal antropogénica en las aguas centrales. Este incremento dio lugar a tasas de acumulación de entre ~0.65 a ~1 μmol·kg<sup>-1</sup>·año<sup>-1</sup> para las distintas regiones descritas longitudinalmente a lo largo de la sección. En las aguas profundas es muy clara la señal de C<sub>ant</sub> del agua de Labrador en la capa uNADW. En particular para esta capa, la diferencia en la concentración de C<sub>ant</sub> entre 1993 y 2010 sugiere una tasa de acumulación de  $-0.18 \pm 0.03$  ( $\phi C_T^0$ ) o  $0.17 \pm 0.03$  (TTD) μmol·kg<sup>-1</sup>·año<sup>-1</sup> en la región con mayor almacenamiento.

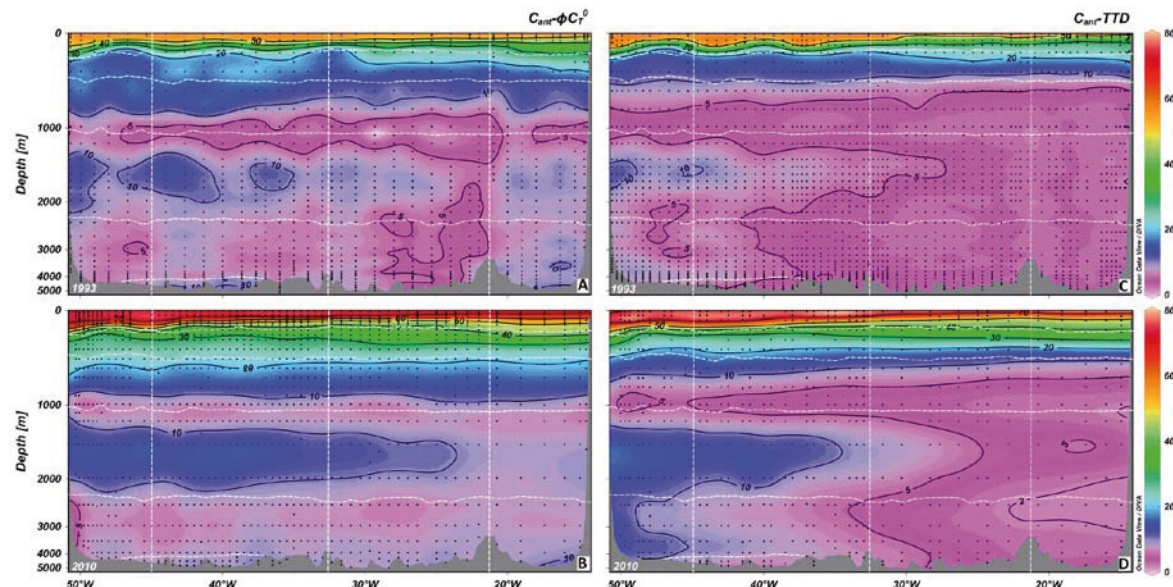


**Figura 3.3.** Distribución de C<sub>ant</sub>- $\phi C_T^0$  y C<sub>ant</sub>-TTD (mol·kg<sup>-1</sup>) a lo largo de la sección 7.5°N en 1993 (A, C) y 2010 (B, D). Los paneles (A) y (B) muestran los perfiles de C<sub>ant</sub>- $\phi C_T^0$  mientras que los paneles (C) y (D) muestran los perfiles de C<sub>ant</sub>-TTD. Las líneas blancas discontinuas horizontales marcan los límites entre capas y las verticales los límites entre regiones.

En 2010, el inventario de  $C_{\text{ant}}$  para toda la sección asciende a  $58.9 \pm 2.2$  y  $45.1 \pm 2.0 \text{ mol} \cdot \text{m}^{-2}$ , según los métodos  $\phi C_T^0$  y TTD, respectivamente (Tabla 3.2.). Los inventarios específicos obtenidos según el método TTD fueron en general más bajos que los obtenidos con el método  $\phi C_T^0$ . Según el método TTD el inventario de la cuenca occidental era mayor que en la oriental, aunque esto no se observaba con el método  $\phi C_T^0$ .

**Tabla 3.2.** Inventarios específicos de  $C_{\text{ant}}\text{-}\phi C_T^0$  y  $C_{\text{ant}}\text{-TTD}$ , en  $\text{mol} \cdot \text{m}^{-2}$ , para cada campaña oceanográfica y cada cuenca a lo largo de  $7.5^\circ\text{N}$ .

Año	$iC_{\text{ant}}\text{-}\phi C_T^0 (\text{mol} \cdot \text{m}^{-2})$				$iC_{\text{ant}}\text{-TTD} (\text{mol} \cdot \text{m}^{-2})$			
	OESTE		ESTE		OESTE		ESTE	
	R1	R2	R3	R4	R1	R2	R3	R4
1993	40.1±3.4	42.8±4.4	40.0±4.7	44.1±3.7	41.3±3.7	37.3±4.0	27.3±4.3	23.6±4.2
2010	56.1±3.5	62.2±4.0	58.2±4.5	56.7±4.0	57.4±3.7	53.3±4.2	37.0±4.3	32.9±4.1
1993	41.9±3.2		41.5±3.3		38.6±2.9		26.0±3.2	
2010	60.2±3.0		57.7±3.2		54.7±3.2		35.5±3.0	
1993	41.7±2.3				32.3±2.3			
2010	58.9±2.2				45.1±2.0			

La tasa de almacenamiento para toda la sección fue de  $1.01 \pm 0.18 \text{ mol} \cdot \text{m}^{-2} \cdot \text{año}^{-1}$  ( $\phi C_T^0$ ) y  $0.75 \pm 0.17 \text{ mol} \cdot \text{m}^{-2} \cdot \text{año}^{-1}$  (TTD) (Tabla 3.3.). A parte, las tasas de acumulación se obtuvieron también suponiendo un estado estacionario (SS) de la distribución oceánica de  $C_{\text{ant}}$ , considerando una tasa de porcentaje anual específica de acuerdo con la literatura, para compararlas con los resultados observados. La comparación de las tasas de acumulación observadas con las esperadas de acuerdo a un estado estacionario de las concentraciones reveló que el Cant se había acumulado al ritmo estacionario esperado en las masas de agua por debajo de  $\sim 1000 \text{ m}$ . Por encima de esta profundidad la acumulación de  $C_{\text{ant}}$  había sido más rápida de lo esperado. Este resultado se explica debido a un debilitamiento de la advección hacia el norte de agua intermedia antártica, que favoreció la mayor influencia de las aguas circundantes, más cargadas de  $C_{\text{ant}}$ , en las concentraciones descritas en el rango de densidad de aguas intermedias.

**Tabla 3.3.** Tasas de acumulación de  $C_{\text{ant}}$  y tasas asumiendo un estado estacionario ( $SS\_C_{\text{ant}}$ ) ( $\text{mol} \cdot \text{m}^{-2} \cdot \text{año}^{-1}$ ) para las cuencas occidental y oriental y para toda la sección  $7.5^\circ\text{N}$ , obtenidos con los métodos  $\phi C_T^0$  y TTD. Las tasas de almacenamiento también se muestran para las capas del océano superior (fuente regular) y profundo (fuente cursiva).

Tasa almacenamiento $C_{\text{ant}}$ ( $\text{mol} \cdot \text{m}^{-2} \cdot \text{año}^{-1}$ )	Cuenca oeste		Cuenca este		7.5°N Toda
	Toda	Superior/Profundo	Toda	Superior/Profundo	
$C_{\text{ant}}\text{-}\phi C_T^0$	$1.07 \pm 0.23$	$0.67 \pm 0.07$ $0.40 \pm 0.21$	$0.95 \pm 0.27$	$0.76 \pm 0.08$ $0.19 \pm 0.26$	$1.01 \pm 0.18$
$SS\_C_{\text{ant}}\text{-}\phi C_T^0$	$0.86 \pm 0.04$	$0.41 \pm 0.01$ $0.45 \pm 0.04$	$0.84 \pm 0.04$	$0.41 \pm 0.01$ $0.43 \pm 0.04$	$0.85 \pm 0.03$
$C_{\text{ant}}\text{-TTD}$	$0.95 \pm 0.24$	$0.44 \pm 0.09$ $0.50 \pm 0.22$	$0.56 \pm 0.25$	$0.46 \pm 0.08$ $0.10 \pm 0.24$	$0.75 \pm 0.17$
$SS\_C_{\text{ant}}\text{-TTD}$	$0.79 \pm 0.04$	$0.36 \pm 0.01$ $0.42 \pm 0.04$	$0.52 \pm 0.04$	$0.33 \pm 0.01$ $0.19 \pm 0.04$	$0.65 \pm 0.03$

### 3.3. Acidificación oceánica a lo largo de la sección 24.5°N en el Atlántico Norte Subtropical

La acidificación del océano está directamente relacionada con el aumento de los niveles de CO<sub>2</sub> en la atmósfera debido a las actividades humanas y el papel activo del océano en la absorción de parte de este CO<sub>2</sub> antropogénico. Aquí se estudiaron los cambios de pH producidos a lo largo de 24.5°N, en el Atlántico Norte subtropical, mediante la comparación de las observaciones de pH realizadas en las ocupaciones de la sección A05 de 1992 y 2011 (Figura 3.4. y Tabla 3.3.). Esta comparación puso de manifiesto una disminución general de los valores de pH en los primeros 1000 dbar de la columna de agua. Curiosamente, las tasas de mayor acidificación se encontraron por debajo de la termoclina estacional. El patrón de cambios de pH encontrado era causado por una combinación de componentes antropogénica y no antropogénica, de magnitudes similares pero diferentes representaciones con la profundidad y la longitud a lo largo de la sección. El componente antropogénico fue, como se esperaba, más importante hacia la superficie. El componente no antropogénico, básicamente debido a variabilidad natural, mostró un patrón mucho más heterogéneo, con tasas de pH decrecientes altas en regiones específicas, como por ejemplo la zona por debajo de la termoclina estacional al este de 35°W y entre 500 y 800 dbar en la cuenca oeste, por encima de la zona del mínimo de oxígeno. El componente natural, sobre todo debido a cambios en los niveles de oxígeno en regiones particulares de la sección, también condujo a la basificación de regiones específicas. En las aguas profundas, por debajo de 1000 dbar, se observó una clara evidencia de acidificación debida al componente antropogénico dentro de las aguas que se dirigen al sur dentro de la corriente profunda de frontera oeste (DWBC).

Dado que se el componente natural explicaba en algunos casos hasta un 50% de los cambios de pH observados, la detección de las tendencias a largo plazo en el oxígeno disuelto cobran bastante importancia para realizar proyecciones de las condiciones futuras de pH en la región de estudio, ya que los cambios en el oxígeno modulan la acidificación de origen antropogénico.

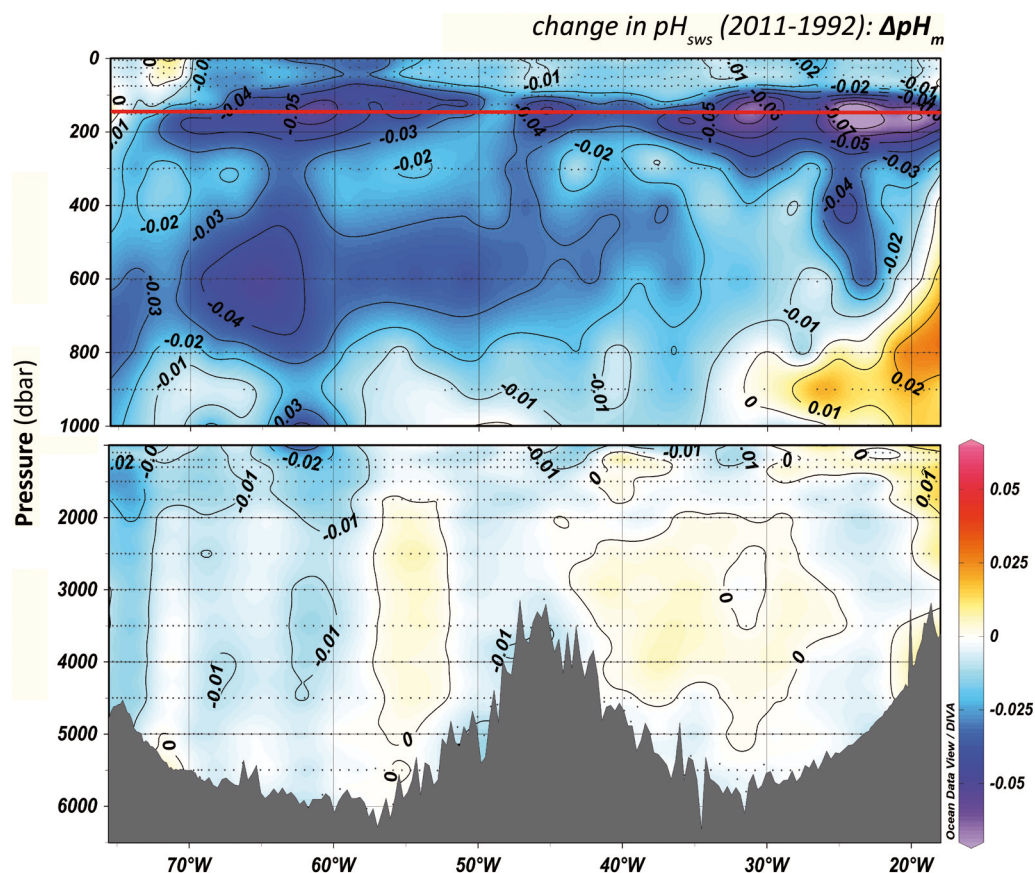


**Figura 3.4.** Cambio en el pH del agua de mar,  $\Delta\text{pH}$ , a lo largo de la sección A05 entre 1992 y 2011. La línea roja muestra la ubicación de la termoclina estacional en estas latitudes (González-Dávila et al., 2010; Bates et al., 2012).

**Tabla 3.4.** Valores medios ± desviación estándar ( $X \pm SD$ ) para pH medido ( $pH_{sws25}$ ) en 2011 y 1992, el cambio en el pH medido ( $\Delta pH_m$ ), las contribuciones antropogénica ( $\Delta pH_{ant}$ ) y no antropogénica ( $\Delta pH_{var}$ ) a  $\Delta pH_m$ , cambio en la utilización de oxígeno Aparente ( $\Delta AOU$ ) en  $\mu\text{mol} \cdot \text{kg}^{-1}$ , cambio de  $C_{ant}$  con el método  $\varphi C_T^0$  ( $\Delta \varphi C_T^0$ ) en  $\mu\text{mol} \cdot \text{kg}^{-1}$ , dentro de cada subdivisión por capas y regiones. Al dividir el  $\Delta pH_{ant}$  por el tiempo de estudio, en las regiones 1 y 4 en uNACW, región 4 en AAIW y uNADW y la región 1 en uNADW, se obtienen las siguientes tendencias en el pH (unidades de  $\text{pH} \cdot \text{año}^{-1}$ ): respectivamente:  $-0,0014 \pm 0,0004$ ,  $-0,0018 \pm 0,0004$ ,  $0,0004 - 0,0008 \pm 0,0006 \pm 0,0005$  y  $-0,0008 \pm 0,0005$ . La columna N indica el número de valores dentro de cada subdivisión.

		$pH_{sws25}$ 2011	$pH_{sws25}$ 1992	N	$\Delta pH_m$ (2011-1992)	p- valor	$\Delta pH_{ant}$ (2011-1992)	p- valor	$\Delta pH_{var}$ (2011-1992)	p- valor	$\Delta AOU$ (2011-1992)	$\Delta \varphi C_T^0$ (2011-1992)	$\Delta TTD$ (2011-1992)
uNACW	1	7.972±0.036	7.992±0.033	48	<b>-0.020±0.015</b>	0.000	<b>-0.028±0.008</b>	0.000	<b>0.008±0.012</b>	0.000	<b>-3.4±9.8</b>	<b>16.2±4.8</b>	<b>20.9±1.6</b>
	2	7.950±0.034	7.980±0.040	139	<b>-0.030±0.014</b>	0.000	<b>-0.032±0.008</b>	0.000	<b>0.002±0.009</b>	0.048	<b>2.5±8.2</b>	<b>18.4±5.4</b>	<b>21.3±1.7</b>
	3	7.953±0.038	7.984±0.046	67	<b>-0.031±0.023</b>	0.000	<b>-0.025±0.015</b>	0.000	<b>-0.006±0.012</b>	0.000	<b>8.6±10.4</b>	<b>14.5±9.0</b>	<b>21.7±1.7</b>
	4	7.922±0.030	7.984±0.025	29	<b>-0.062±0.028</b>	0.000	<b>-0.034±0.008</b>	0.000	<b>-0.028±0.027</b>	0.000	<b>28.1±18.7</b>	<b>19.3±4.6</b>	<b>21.9±0.8</b>
INACW	1	7.794±0.050	7.824±0.051	21	<b>-0.029±0.007</b>	0.000	<b>-0.027±0.010</b>	0.000	<b>-0.003±0.007</b>	0.080	<b>3.7±4.7</b>	<b>12.4±4.2</b>	<b>13.3±2.4</b>
	2	7.792±0.039	7.830±0.038	56	<b>-0.038±0.010</b>	0.000	<b>-0.018±0.009</b>	0.000	<b>-0.019±0.010</b>	0.000	<b>14.2±6.0</b>	<b>8.5±4.3</b>	<b>14.3±2.0</b>
	3	7.812±0.055	7.837±0.057	67	<b>-0.025±0.011</b>	0.000	<b>-0.018±0.008</b>	0.000	<b>-0.006±0.011</b>	0.000	<b>8.0±7.6</b>	<b>8.9±4.1</b>	<b>15.4±2.7</b>
	4	7.797±0.065	7.816±0.068	63	<b>-0.019±0.024</b>	0.000	<b>-0.020±0.012</b>	0.000	<b>0.001±0.026</b>	0.764	<b>2.8±18.1</b>	<b>9.5±5.7</b>	<b>15.9±2.5</b>
AAIW	1	7.674±0.011	7.691±0.013	42	<b>-0.017±0.009</b>	0.000	<b>-0.018±0.007</b>	0.000	<b>0.000±0.008</b>	0.201	<b>0.7±4.8</b>	<b>7.1±3.0</b>	<b>6.8±0.9</b>
	2	7.666±0.017	7.681±0.017	118	<b>-0.015±0.015</b>	0.000	<b>-0.008±0.011</b>	0.000	<b>-0.006±0.015</b>	0.000	<b>2.4±6.9</b>	<b>3.4±4.4</b>	<b>5.3±1.2</b>
	3	7.664±0.012	7.676±0.013	93	<b>-0.012±0.009</b>	0.000	<b>-0.010±0.006</b>	0.000	<b>-0.002±0.011</b>	0.187	<b>1.4±5.2</b>	<b>4.1±2.3</b>	<b>4.5±1.3</b>
	4	7.646±0.019	7.638±0.019	66	<b>0.008±0.021</b>	0.000	<b>-0.014±0.008</b>	0.000	<b>0.025±0.018</b>	0.000	<b>-8.7±8.5</b>	<b>5.7±3.2</b>	<b>4.8±1.9</b>
uNADW	1	7.718±0.011	7.732±0.013	99	<b>-0.015±0.008</b>	0.000	<b>-0.016±0.009</b>	0.000	<b>0.001±0.003</b>	0.000	<b>-0.5±1.6</b>	<b>6.6±3.6</b>	<b>7.8±1.4</b>
	2	7.716±0.015	7.725±0.015	238	<b>-0.008±0.007</b>	0.000	<b>-0.008±0.007</b>	0.000	<b>-0.001±0.005</b>	0.089	<b>-1.1±2.9</b>	<b>3.2±3.0</b>	<b>4.8±1.6</b>
	3	7.704±0.019	7.706±0.019	160	<b>-0.003±0.007</b>	0.000	<b>-0.007±0.007</b>	0.000	<b>0.004±0.006</b>	0.000	<b>-0.3±2.9</b>	<b>2.9±2.7</b>	<b>2.7±0.4</b>
	4	7.698±0.016	7.697±0.018	121	<b>0.001±0.008</b>	0.143	<b>-0.012±0.009</b>	0.000	<b>0.013±0.011</b>	0.000	<b>-2.8±3.7</b>	<b>5.1±3.7</b>	<b>2.8±1.0</b>
INADW	1	7.730±0.004	7.738±0.006	74	<b>-0.008±0.007</b>	0.000	<b>-0.008±0.009</b>	0.000	<b>0.000±0.004</b>	0.605	<b>1.0±2.2</b>	<b>3.2±3.9</b>	<b>4.8±0.6</b>
	2	7.729±0.004	7.735±0.006	209	<b>-0.005±0.006</b>	0.000	<b>-0.002±0.006</b>	0.000	<b>-0.003±0.003</b>	0.000	<b>1.1±2.4</b>	<b>0.7±2.7</b>	<b>2.6±0.8</b>
	3	7.724±0.004	7.724±0.006	203	<b>0.000±0.006</b>	0.542	<b>-0.001±0.006</b>	0.032	<b>0.001±0.003</b>	0.011	<b>2.1±1.9</b>	<b>0.4±2.4</b>	<b>1.6±0.3</b>
	4	7.723±0.005	7.726±0.006	117	<b>-0.002±0.006</b>	0.000	<b>-0.006±0.006</b>	0.000	<b>0.003±0.003</b>	0.000	<b>-0.5±3.0</b>	<b>2.4±2.7</b>	<b>1.5±0.2</b>
AABW	1	7.719±0.006	7.725±0.010	18	<b>-0.004±0.008</b>	0.061	<b>-0.001±0.012</b>	0.614	<b>-0.003±0.006</b>	0.082	<b>1.0±2.8</b>	<b>0.7±5.0</b>	<b>3.0±0.8</b>
	2	7.711±0.007	7.715±0.008	112	<b>-0.004±0.007</b>	0.000	<b>0.000±0.006</b>	0.506	<b>-0.005±0.004</b>	0.000	<b>2.4±2.1</b>	<b>-0.2±2.7</b>	<b>2.6±1.4</b>

## 4. DISCUSIÓN Y CONCLUSIONES

### SÍNTESIS DE LOS RESULTADOS Y DISCUSIÓN GENERAL

En las tres secciones anteriores hemos detallado algunos aspectos cruciales con respecto a la penetración de  $C_{\text{ant}}$  en el Océano Atlántico y la acidificación oceánica asociada. Cada una de estas secciones, que ya han sido publicadas como artículos de investigación científica independientes, se ha centrado de forma independiente en una de las dos secciones estudiadas, ya sea la WOCE A05 a 24.5°N o la WOCE A06 a 7.5°N. En esta sección de síntesis y discusión, se hace un resumen de los principales resultados obtenidos y se discuten todos los datos de una manera integrada, mediante la comparación de los cambios ocurridos a lo largo de ambas secciones oceanográficas para ponerlos en un contexto más amplio. Esta comparación se hizo en primer lugar para estudiar más en profundidad la magnitud y las regiones principales de acumulación y transporte de  $C_{\text{ant}}$  en el Atlántico Norte y, en segundo lugar, para profundizar sobre la acidificación de la columna de agua y los cambios en el estado de saturación del carbonato de calcio con respecto a la aragonita asociados. A este respecto, se estudian las tendencias en la disminución esperada de los estados de saturación de aragonita, evaluándolas para las dos secciones y se realizan predicciones sobre el número de años pendientes para alcanzar del nivel de saturación en las masas de agua del océano superior en la región subtropical y tropical del Atlántico Norte.

#### $\text{CO}_2$ antropogénico

La variabilidad del  $C_{\text{ant}}$  está relacionada con la circulación de las masas de agua. Como el  $C_{\text{ant}}$  se absorbe en las aguas superficiales durante los eventos de convección en la mezcla invernal, las masas de agua centrales de las dos secciones estudiadas (A05 a 24.5°N y A06 a 7.5°N) muestran los valores más altos de  $C_{\text{ant}}$ . Esto es así debido a que estas masas de agua se forman en los alrededores de ambas secciones y por lo tanto son las que han experimentado el contacto más reciente con la atmósfera, en comparación con las masas de agua que hay por debajo de ellas. En general, los gradientes verticales muestran concentraciones superficiales altas que disminuyen hacia el fondo, a lo largo de las dos secciones. Este descenso es rápido en el océano superficial, mientras que, por debajo de 1000 dbar, las concentraciones de  $C_{\text{ant}}$  son bajas en general ya que las masas de agua profundas y de fondo se formaron hace mucho tiempo, y reflejan la concentración de una atmósfera anterior con menos  $C_{\text{ant}}$ . El patrón general de concentraciones dentro de las capas intermedias y profundas a lo largo de las dos secciones está determinado por su advección desde sus respectivas regiones de formación. Cada una de las capas intermedias y profundas, que corresponden aproximadamente a las diferentes masas de agua intermedias, profundas y de fondo, muestran un contenido particular de  $C_{\text{ant}}$  dependiendo de su ventilación específica (es decir, en el tiempo específico transcurrido para cada capa hasta alcanzar las latitudes de 24.5°N y 7.5°N desde sus regiones de formación, donde estuvieron por última vez en contacto con la atmósfera). Dado que estas capas se originan ya sea en el Atlántico Norte subpolar o en el Océano Austral, su organización vertical de acuerdo con la densidad que adquieren en el momento de su formación conduce a un perfil vertical que intercala máximos y mínimos relativos de  $C_{\text{ant}}$ , respectivamente en función de su origen norte o

sur. La AAIW y la AABW se forman en el lejano Océano Austral y por tanto muestran niveles más bajos que  $C_{ant}$  que la LSW (uNADW) y, en menor medida, que la LNADW, que se forman en la región del Atlántico Norte subpolar. En este sentido, las aguas antárticas intermedias y de fondo muestran una influencia menor de la mezcla con aguas más profundas y más enriquecidas en  $C_{ant}$  del Atlántico Norte a 7.5°N que a 24.5 ° N.

En las dos secciones se detectó una señal de  $C_{ant}$  notable, situada entre 1200-1800 dbar, debido a la advección hacia el sur de LSW (Steinfeldt *et al.*, 2009), como parte del núcleo superior de la corriente profunda de frontera oeste. La LSW es una masa de agua de reciente formación en comparación con el resto de masas de agua profunda que fluyen a través de las dos secciones. Esta masa de agua muestra una ventilación de alrededor de una década a 24.5°N (van Sebille *et al.*, 2011) y de cerca de tres décadas en el ecuador a 7.5°N (Rhein *et al.*, 2015). Durante su viaje hacia el sur, la LSW también se mezcla con aguas menos cargadas de  $C_{ant}$  a esas densidades (Steinfeldt *et al.*, 2007; van Sebille *et al.*, 2011). Como se muestra en las secciones 3.1 y 3.2. de esta tesis, este hecho fue identificado como una señal de  $C_{ant}$  de niveles moderados ( $20 - 25 \mu\text{mol}\cdot\text{kg}^{-1}$ ) a 24.5°N, que entraba en la sección por el oeste, que influía en las concentraciones hacia el este y dentro del núcleo inferior de la corriente de profunda de frontera. La huella de  $C_{ant}$  de la LSW se diluía más al sur a 7.5°N, debido a la existencia de vías secundarias alternativas secundarias para el transporte más allá de la corriente de frontera (van Sebille *et al.*, 2011), pero que aún así era detectable mostrando niveles de  $C_{ant}$  inferiores ( $10 \mu\text{mol}\cdot\text{kg}^{-1}$ ) que llegaban a la cuenca oriental debido a la recirculación hacia el este de la NADW (Arhan *et al.*, 1998; Mémery *et al.*, 2000).

El perfil general de la distribución de  $C_{ant}$  a lo largo de las dos secciones se confirmó mediante todos los métodos de estimación de  $C_{ant}$  utilizados, en los capítulos 3.1. y 3.2 de esta tesis. Cuando las dos secciones se comparan en términos de los cambios decenales observados en sus distribuciones de  $C_{ant}$  (es decir, sus tasas decenales respectivas de almacenamiento de  $C_{ant}$ , Figura 4.1.), aparecen algunas similitudes y diferencias entre ellas. Las dos secciones muestran mayores tasas de almacenamiento a lo largo de las capas centrales. Esta observación es consistente con el hecho de que estas son las capas más ventiladas a lo largo del perfil vertical y por lo tanto en ellas se acumula  $C_{ant}$  más rápidamente. A su vez, las tasas de almacenamiento de  $C_{ant}$  dentro de las capas centrales son mayores a 24.5°N que a 7.5°N. Este es un resultado esperable, ya que la sección 24.5°N está más cerca de la región de formación (es decir, el mar de los Sargazos) de los diferentes componentes de masas de agua dentro de la NACW, de lo que lo está la sección 7.5°N de sus respectivas regiones de formación de SACW (es decir, el Atlántico Sur). Además, la proximidad relativa de cada sección a las regiones de formación de agua profunda (NADW) explica las mayores tasas de almacenamiento de  $C_{ant}$  observadas dentro de la corriente profunda de frontera oeste a 24.5°N que a 7.5°N (Figura 4.1.), lo cual también es un resultado esperado, debido a la ubicación más al norte de la primera sección. Sin embargo, esto está en desacuerdo con un resultado inesperado, en que se observan tasas de almacenamiento más altas en las capas de la NADW a 7.5°N, en las dos regiones interiores, en comparación con las observadas a 24.5°N. Una posible explicación es que la ventilación de la corriente profunda de frontera oeste a 24.5°N se limita al oeste de 70°W y las regiones

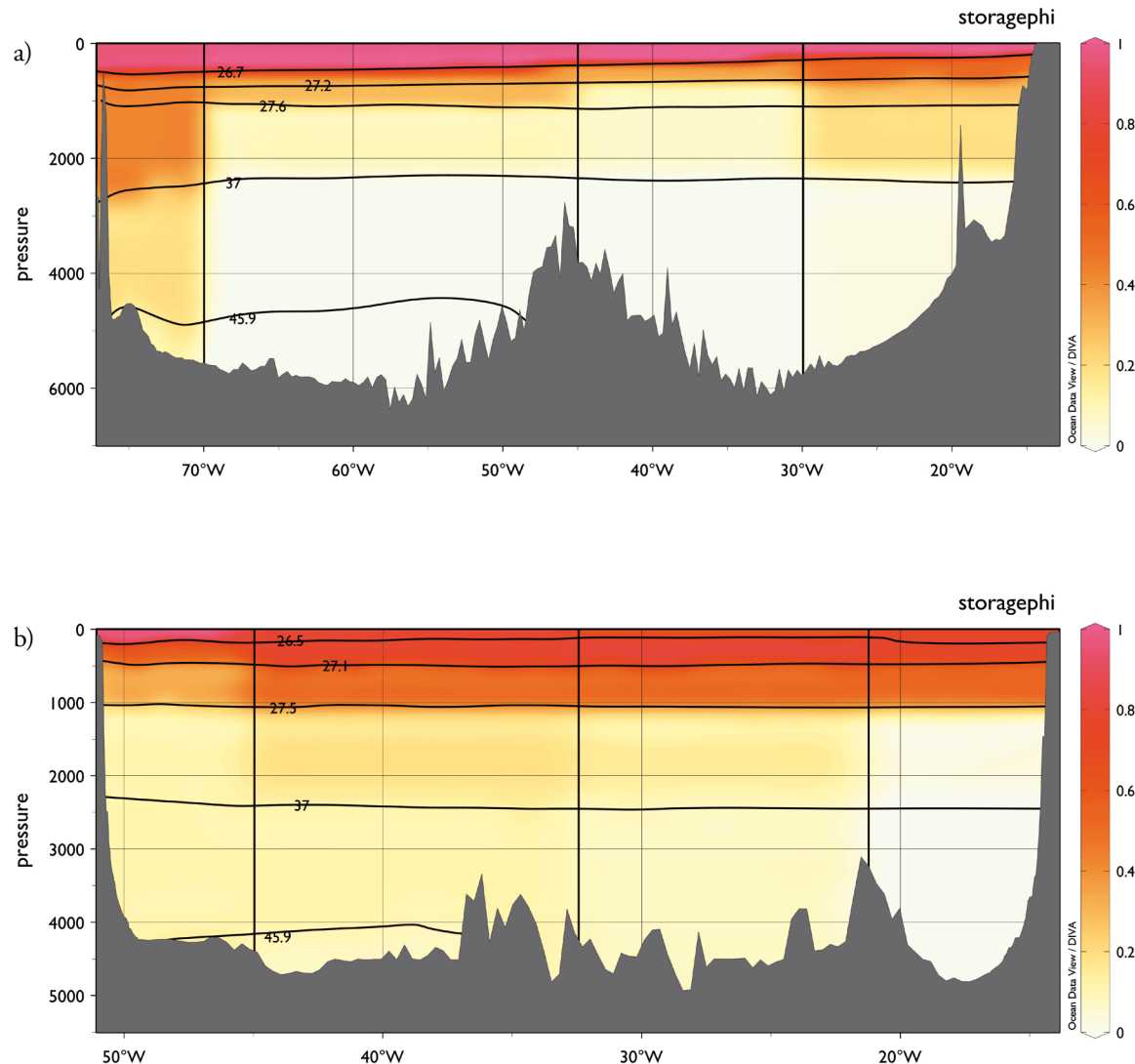


**Figura 4.1.** Tasas de almacenamiento de  $C_{ant}$  ( $\text{mol kg}^{-1} \cdot \text{año}^{-1}$ ) según el método de estimación  $\varphi C_T^0$ , en escala de colores. a) tasas de almacenamiento de  $C_{ant}$  entre 1992 y 2011, a  $24.5^\circ\text{N}$ , a lo largo de la sección A05. b) Tasas de almacenamiento de  $C_{ant}$  entre 1993 y 2010, a  $7.5^\circ\text{N}$ , a lo largo de la sección A06.

del interior del océano a lo largo de esta sección sólo reciben aportes de  $C_{ant}$  a través de procesos de mezcla, debido a la inexistencia de vías de transporte importantes en estas regiones interiores. Por el contrario, a 7.5°N la vía de advección de NADW se separa del margen continental occidental haciendo que esta masa de agua recircule y penetre hacia el este. Dado que en 1993 sólo había niveles detectables de  $C_{ant}$  en la NADW en la región más próxima al margen occidental, los mayores incrementos de  $C_{ant}$  observados para esta masa de agua a lo largo de 7.5°N entre 1993 y 2010 se produjeron en las dos regiones del interior, que no mostraban niveles detectables de  $C_{ant}$  en 1993. Como se explicó en el capítulo 3.2. de esta tesis, esta acumulación de  $C_{ant}$  ocurrió a unas tasas consistentes con una circulación estacionaria, a medida que la NADW rica en  $C_{ant}$  fue llegando a latitudes ecuatoriales. En este sentido, nuestros resultados también sugieren que la recirculación de NADW todavía no ha llegado a la región más próxima del margen oriental.

En cambio, a 24.5°N, las dos regiones del interior del océano muestran tasas de almacenamiento inferiores a lo que se esperaría bajo una circulación estacionaria, posiblemente debido a que las vías de propagación de las masas de agua que transportan la señal de  $C_{ant}$  dentro de las capas profundas a esta latitud están confinadas a las regiones limítrofes oriental (MW) y occidental (LSW). Debido a que la transferencia de  $C_{ant}$  hacia las regiones del océano interior depende de la mezcla de MW y LSW, ya que estas dos regiones no son zonas para su tránsito directo, esto puede explicar por qué el  $C_{ant}$  en estas regiones ha ido aumentando a un ritmo más lento de lo que se habría esperado de acuerdo a una circulación estacionaria. Además, dentro de la corriente profunda de frontera oeste, las tasas de almacenamiento de  $C_{ant}$  son mayores que las esperadas de acuerdo con una acumulación estacionaria, seguramente debido a la llegada del pulso importante de LSW enriquecida en  $C_{ant}$  que se formó durante la década de 1990. Por lo tanto, los cambios recientes en la circulación también explican la desviación del estado estacionario en las tasas de almacenamiento en algunas regiones y capas. Los cambios decenales en circulación pueden ser la causa del crecimiento inesperado en los niveles  $C_{ant}$ , por encima y por debajo de una acumulación estacionaria, en la AAIW a 7.5°N y a 24.5°N, respectivamente. Sin embargo, también debe tenerse en cuenta que los cambios a lo largo de 7.5°N se calcularon a partir de sólo dos campañas y por lo tanto las tasas de almacenamiento resultantes pueden reflejar de forma más parcial la variabilidad decenal existente en comparación con las tasas de almacenamiento a 24.5°N, que se calcularon mediante el uso de cinco campañas que supervisan de manera más regular los cambios ocurridos durante el período estudiado.

En resumen, los cambios decenales observados en las distribuciones de  $C_{ant}$  a lo largo de las dos secciones (Figura 4.1) apuntan a dos conclusiones principales:

- 1) El perfil vertical en la acumulación de  $C_{ant}$  se corresponde con el perfil de concentraciones de  $C_{ant}$ , mostrando mayores tasas de almacenamiento a lo largo de las aguas centrales y las tasas más bajas de almacenamiento en capas más profundas del océano.
- 2) Existen gradientes zonales claros en las tasas de almacenamiento de  $C_{ant}$  a lo largo de las masas de agua intermedias y profundas.

La figura 4.1. muestra un tercer factor que no se había considerado todavía, que tiene repercusiones importantes para el estudio del almacenamiento de  $C_{ant}$  integrado en la columna de agua, a lo largo de las dos secciones, que es el espesor de las diferentes masas de agua consideradas. Las aguas centrales muestran las tasas de almacenamiento más altas y, por tanto, acumulan  $C_{ant}$  relativamente rápido ( $\sim 0,5$  a  $1 \mu\text{mol}\cdot\text{kg}^{-1}\cdot\text{año}^{-1}$ ), pero tienen un espesor relativamente pequeño, de unos pocos cientos de metros. Por el contrario, las capas intermedias y profundas muestran tasas de almacenamiento mucho más bajas (en su mayoría por debajo de  $\sim 0,20 \mu\text{mol}\cdot\text{kg}^{-1}\cdot\text{año}^{-1}$ ), pero abarcan grandes volúmenes de agua, de miles de metros de profundidad que, a lo largo de estas secciones, representan alrededor del 80% de la columna de agua. Por lo tanto, contribuyen de manera significativa al almacenamiento integrado de  $C_{ant}$  a lo largo de la columna de agua. Además, el espesor de las diferentes masas de agua gana importancia cuando el almacenamiento se evalúa mediante el fraccionamiento de las secciones en diferentes regiones. A pesar de que las capas intermedias, profundas y de fondo muestran tasas de almacenamiento bajas en general, las pequeñas diferencias zonales en las tasas de almacenamiento entre regiones ganan importancia, ya que pueden tener un impacto significativo en el almacenamiento integrado de  $C_{ant}$  a lo largo de las secciones.

En la tabla 4 del capítulo 3.2 de esta tesis se informó de las tasas de almacenamiento de  $C_{ant}$  integradas a  $7.5^\circ\text{N}$ , para el período de 1993 a 2010, separadamente para las cuencas occidental y oriental, según los métodos  $\varphi C_T^0$  y TTD. Las tasas de almacenamiento de  $C_{ant}$  obtenidas mediante el método  $\varphi C_T^0$  indicaron que las dos cuencas habían ido acumulando  $C_{ant}$  aproximadamente la misma tasa ( $a 1,07 \pm 0,23 \text{ mol}\cdot\text{m}^{-2}\cdot\text{año}^{-1}$  en el oeste y a  $0,95 \pm 0,27 \text{ mol}\cdot\text{m}^{-2}\cdot\text{año}^{-1}$  en el este). Sin embargo, las tasas de almacenamiento correspondientes obtenidas mediante el método TTD sugirieron una acumulación más rápida en el oeste ( $0,95 \pm 0,24 \text{ mol}\cdot\text{m}^{-2}\cdot\text{año}^{-1}$ ) que en la cuenca oriental ( $0,56 \pm 0,25 \text{ mol}\cdot\text{m}^{-2}\cdot\text{año}^{-1}$ ). Esta inconsistencia se debió al hecho de que a pesar de que los dos métodos sugerían un mayor almacenamiento de  $C_{ant}$  en el océano profundo occidental que en la cuenca profunda oriental (en las masas de agua por debajo de  $\sim 1.000 \text{ dbar}$ ), los dos métodos de estimación mostraron resultados diferentes con respecto a los almacenamientos integrados entre las dos cuencas, en el océano superior (que comprendía las aguas intermedias y centrales). Mientras el método TTD sugirió que el  $C_{ant}$  se había ido acumulando al mismo ritmo en las dos cuencas, el método  $\varphi C_T^0$  sugirió una mayor tasa de acumulación de la parte oriental que resultó en el balance de los almacenamientos integrados entre las dos cuencas.

La tabla 4.1 recoge las tasas de almacenamiento integrado de  $C_{ant}$  a  $24.5^\circ\text{N}$  para el período 1992-2011, separadamente para cada una de las cuatro regiones en las que se dividió la sección y para el estrecho de Florida, calculados utilizando los métodos  $\varphi C_T^0$  y TTD. Inicialmente, las regiones de la sección principal no se fusionaron en las cuencas occidental y oriental y se estudiaron por separado debido a la alta heterogeneidad observada en el gradiente horizontal de las tasas de almacenamiento dentro de las capas intermedias y profundas (Figura 4.1). Tanto el método  $\varphi C_T^0$  como el TTD sugieren un mayor almacenamiento integrado de  $C_{ant}$  en la región 1, la cual coincide con la zona de propagación de la corriente profunda de frontera oeste, que en

**Tabla 4.1.** Tasas de almacenamiento de  $C_{ant}$  ( $\text{mol m}^2 \text{y}^{-1}$ ) integradas para toda la columna de agua, en cada una de las cuatro regiones de la sección principal y el estrecho de Florida. Estas se calcularon teniendo en cuenta las tasas de almacenamiento decenales de  $C_{ant}$  descritas en cada caja y el espesor medio de cada capa. El valor de almacenamiento para R4 según el método TTD falta debido a la ausencia de datos  $C_{ant}$ -TTD para la NADW.

Almacenamiento $\text{mol m}^2 \text{y}^{-1}$	R0 Florida	R1 80°W a 70°W	R2 70°W a 45°W	R3 45°W a 30°W	R4 30°W a 10°W
$\varphi C_T^0$	0.49±0.06	1.83±0.31	0.66±0.23	0.49±0.22	0.84±0.23
TTD	0.27±0.09	1.62±0.44	1.12±0.36	1.03±0.86	-

las demás regiones del océano interior. La diferencia entre el almacenamiento en R1 y el de R2 a R4 muestra un gradiente horizontal muy contrastado mediante el método  $\varphi C_T^0$ , mientras que las diferencias son menos pronunciadas según el método TTD. La explicación para esto podría ser que la metodología para estimar  $C_{ant}$  TTD se basa en la resolución de una ecuación de advección-difusión con la velocidad y la difusividad constante bajo el supuesto de una circulación en estado estacionario (Waugh *et al.*, 2006) que conllevaría a un comportamiento más parecido entre regiones. Además, otra explicación para el diferente comportamiento entre los métodos es que, como se observó en los capítulos 3.1. y 3.2. de esta tesis, el método de  $\varphi C_T^0$  parece ser particularmente sensible a los cambios en las masas de agua en relación con los procesos naturales en los que el oxígeno disuelto está implicado, a través de las relaciones de Redfield. Por ejemplo, este hecho parece ser causa de las bajas tasas de almacenamiento encontradas para AAIW y uNADW en R3 y, de una manera más general, podría ser una explicación para los almacenamientos más bajos observados en el interior del océano mediante el uso de este método. En cualquier caso, e independientemente de cuál la relación más ajustada entre el almacenamiento que se produce en la región de la corriente de frontera oeste y las regiones restantes, los dos métodos muestran que esta diferencia se incrementa significativamente cuando las capas profundas se incluyen en los cálculos. Esto significa que el almacenamiento más rápido de  $C_{ant}$  descrito en la región 1 se explica principalmente por la capa de NADW y por lo tanto, debido principalmente a la advección de LSW enriquecida en  $C_{ant}$  dentro de la corriente profunda de frontera oeste (capítulos 3.1. y 3.2. de esta tesis). La NADW, incluyendo sus capas superior e inferior, muestra un espesor muy similar a lo largo de toda la sección (aproximadamente 70% de la columna de agua en promedio, en cada región definida) pero contribuye aproximadamente en un 60% a 70% al almacenamiento integrado descrito en R1, según los métodos  $\varphi C_T^0$  y TTD, respectivamente. Las capas de la NADW explican una parte mucho menor del almacenamiento observado en las tres regiones restantes, ya que contribuye en un 15% a un 40% en promedio, al almacenamiento de  $C_{ant}$  en el océano interior y la región limítrofes oriental, según los métodos  $\varphi C_T^0$  y TTD, respectivamente.

En resumen, el estudio de las tasas de almacenamiento integrado de  $C_{ant}$  a lo largo de 7.5°N y 24.5°N separadamente en regiones o cuencas destaca que, en una escala de tiempo de décadas, la variabilidad espacial en el almacenamiento de  $C_{ant}$  a lo largo del Atlántico Norte subtropical y tropical está fuertemente relacionado con la señal profunda de  $C_{ant}$  transportada por la corriente principal en la circulación (es decir la corriente

profunda de frontera oeste) que se propaga a través de las dos secciones. Como se explicó en los capítulos 3.1. y 3.2. de esta tesis, es ampliamente conocido que esta advección profunda de  $C_{ant}$  está relacionada con un periodo excepcional de convección intensa en el giro subpolar del Atlántico Norte que dio lugar a un pulso mayor de LSW a principios de 1990, durante un período de fase positiva de la NAO (Lazier *et al.*, 2002). El gran pulso de LSW resultante también se ha relacionado con las mayores tasas de almacenamiento de  $C_{ant}$  en el Atlántico Norte subpolar que se produjeron durante ese período (Pérez *et al.*, 2008; Pérez *et al.*, 2010), que, a su vez, se han correlacionado con la intensidad de la corriente de retorno, mediante los cambios en el  $C_{ant}$  transportado desde latitudes bajas del giro subtropical en cada una de las fases de la NAO (Pérez *et al.*, 2013).

El almacenamiento contrastado de  $C_{ant}$  a lo largo de 24.5°N, al oeste de 70°W respecto a las tres regiones restantes, también es de gran importancia si se tiene en cuenta que existe una covarianza entre este gradiente de almacenamiento y el transporte de agua a cada lado de 70°W. Se sabe que la circulación ciclónica de las aguas profundas a lo largo de la sección A05 consta de un transporte de agua intenso hacia el sur dentro de la corriente de frontera oeste, al oeste de 70°W y una recirculación de menor intensidad hacia el norte, a través del océano interior (Atkinson *et al.*, 2012. Hernández-Guerra *et al.*, 2014). La recirculación de agua a través del interior del océano es de aproximadamente la mitad de la intensidad dentro de la corriente de frontera (Macdonald *et al.*, 2003; Zunino *et al.*, 2015). Por lo tanto, el  $C_{ant}$  dentro de la corriente de frontera (R1) es transportado hacia el sur de forma más intensa que el que se mueve hacia el norte dentro del océano interior (R2 a R4).

### Acidificación y estados de saturación de $\text{CaCO}_3$

La comparación de las observaciones de pH realizadas en 1992 y 2011, a lo largo de 24.5°N en el Atlántico Norte Subtropical, evidenció una disminución general de los valores de pH en los primeros 1000 dbar de la columna de agua (Capítulo 3.3.). Los cambios de pH descritos se tradujeron en tendencias de acidificación considerables a lo largo de las aguas centrales en toda su extensión y también en tendencias decrecientes en los valores de pH significativas en zonas más concretas en las masas de agua intermedia y profunda. La acidificación del océano se caracteriza por un aumento en la concentración de protones ( $\text{H}^+$ ) que causa una disminución del pH y una disminución concomitante de la concentración de iones de carbonato ( $\text{CO}_3^{2-}$ ). Esto, a su vez, provoca cambios en los estados de saturación de  $\text{CaCO}_3$  del agua de mar con respecto a la calcita y la aragonita. En esta sección nos centramos en estos últimos parámetros, que limitan los procesos de calcificación y disolución en la columna de agua, y por lo tanto son importantes al evaluar los posibles efectos de la acidificación del océano sobre los organismos marinos. Mediante la comparación de los datos obtenidos durante las diferentes campañas a través del tiempo, se presenta un primer intento para evaluar los cambios decenales en los estados de saturación de carbonato con el tiempo. Nos centramos en la aragonita, porque es una forma mineral de  $\text{CaCO}_3$  más soluble que la calcita, para la cual se alcanzará mucho antes la subsaturación, a medida que el pH del océano siga bajando (p. ej. Feely *et al.*, 2009; Turley *et al.*, 2010). Al evaluar los cambios en la distribución del estado de saturación de aragonita ( $\Omega_{\text{arg}}$ ) a lo largo de 24.5°N (A05) y

7.5°N (A06), se observa que los patrones generales de distribución en 2011 y 2010 son, respectivamente, prácticamente el mismo que los determinados a partir del uso de los datos recogidos en 1992 y 1993 (Figura 4.2.).

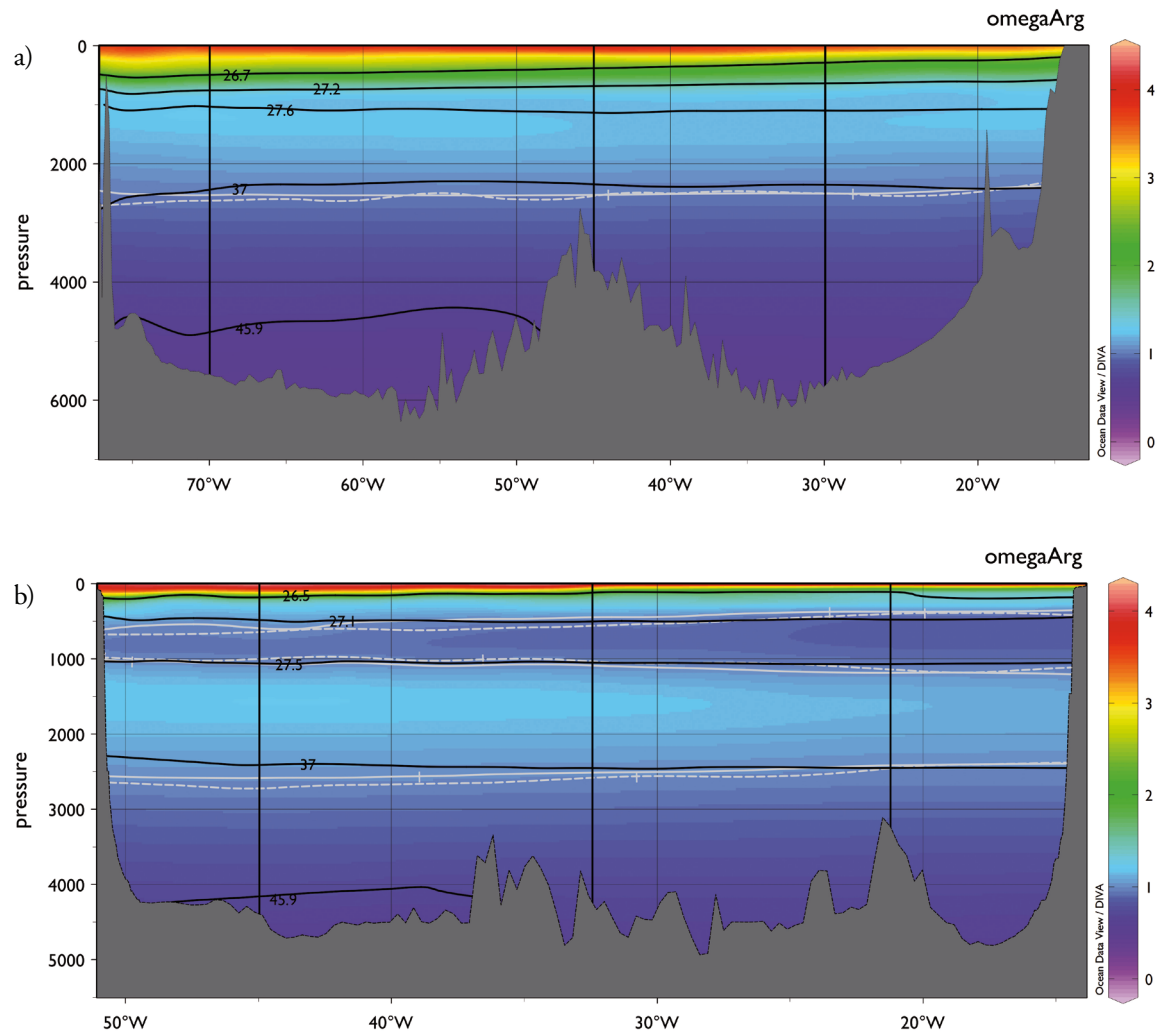


**Figura 4.2.** Distribución de  $\Omega_{\text{arg}}$  a a) 24.5°N en 2011 y a b) 7.5°N en 2010. Los horizontes de saturación ( $\Omega_{\text{arg}} = 1$ ) están representados como líneas grises discontinuas (años 1992 y 1993 para 24.5°N y 7.5°N, respectivamente) y líneas continuas grises (años 2011 y 2010 para 24.5°N y 7.5°N, respectivamente). Las líneas sólidas negras horizontales indican las isopicnas ( $\text{kg m}^{-3}$ ) que acotan los límites de densidad considerados para dividir la sección en diferentes masas de agua. Líneas sólidas negras verticales indican los límites horizontales que delimitan las diferentes regiones a lo largo de cada sección.

A 24.5°N, el agua de mar en el océano superficial está sobresaturada ( $\Omega_{\text{arg}} > 1$ ), y los valores disminuyen progresivamente con el aumento de la presión hasta que se alcanza el nivel de saturación ( $\Omega_{\text{arg}} = 1$ ) alrededor de 2500 dbar, coincidiendo aproximadamente con la isopicna que delimita la INADW a lo largo de su límite superior. Por debajo de este rango de presión los niveles de subsaturación ( $\Omega_{\text{arg}} < 1$ ) se incrementan hacia el fondo. A 7.5°N, el perfil vertical muestra valores de  $\Omega_{\text{arg}}$  en general más bajos que los que están a 24.5°N. El océano superficial también está sobresaturado con respecto a la aragonita pero la disminución de los valores de  $\Omega_{\text{arg}}$  con la profundidad es más pronunciado, ya que éstos alcanzan un primer nivel de saturación a aproximadamente 500 dbar, coincidiendo aproximadamente con la isopicna que delimita el límite superior de la AAIW. La capa entera de AAIW está subsaturada respecto a la aragonita. Por debajo de esta masa de agua, los valores de  $\Omega_{\text{arg}}$  aumentan de nuevo por encima de la saturación, a lo largo de la uNADW, y un segundo horizonte de la saturación se alcanza de nuevo a alrededor de 2500 dbar, coincidiendo aproximadamente con el isopicna del límite superior de la INADW, de manera similar a lo que ocurre a 24.5°N. Debajo de este rango de presión la subsaturación aumenta hacia el fondo marino.

Teniendo en cuenta que los respectivos niveles de saturación profundos (-2500 dbar) no cambiaron significativamente con el tiempo a lo largo de las dos secciones, en adelante nos centramos en los cambios en el estado de saturación de aragonita en el océano superior (<1200 dbar). A 24.5°N, los cambios en las distribuciones de  $\Omega_{\text{arg}}$  entre 1992 y 2011 en la parte superior del océano mostraron una disminución evidente que dio lugar a la ascensión de los diferentes niveles de sobresaturación por encima del valor de  $\Omega_{\text{arg}} = 1.5$ . A 7.5 ° N, a pesar de que los valores de  $\Omega_{\text{arg}}$  eran generalmente más bajos en comparación con los descritos a 24.5°N, los respectivos cambios observados entre 1993 y 2010 parecían ser más pequeños en magnitud. En 2010 la mayor parte de las masas de agua centrales mostraban valores de sobresaturación muy cercanos a los observados en 1993.

Se calculó la sobresaturación de ión  $\text{CO}_3^{2-}$  con respecto a la concentración de saturación de aragonita en los primeros 1200 dbar de la columna de agua, a lo largo de las dos secciones, como:

$$\delta_{\text{Arg}} = [\text{CO}_3^{2-}] - [\text{CO}_3^{2-}]_{\text{SatArg}}$$

donde  $[\text{CO}_3^{2-}]$  es la concentración de iones carbonato in situ y  $[\text{CO}_3^{2-}]_{\text{SatArg}}$  la concentración de saturación de aragonita (es decir, la concentración de carbonato a la que precipita la aragonita), en  $\mu\text{kg}\cdot\text{mol}^{-1}$ . Los valores de  $\delta_{\text{Arg}}$  se obtuvieron para cuatro de las campañas de la sección A05, realizadas en 1992, 1998, 2004 y 2011 y para las dos campañas de la A06, realizadas en 1993 y 2010. Los correspondientes valores de  $\delta_{\text{Arg}}$  calculados para cada año se promediaron dentro de las diferentes masas de agua presentes en los primeros 1200 dbar de la columna de agua, de forma separada para las cuencas occidental y oriental. Por último, los promedios de  $\delta_{\text{Arg}}$  obtenidos se estudiaron en términos del exceso ( $\Delta[\text{CO}_2]$ ) de  $\text{CO}_2$  en la atmósfera en cada año de realización de cada campaña con respecto a los niveles preindustriales de  $\text{CO}_2$  en la atmósfera:

$$\Delta[\text{CO}_2] = [\text{CO}_2]_y - 280$$

donde  $[\text{CO}_2]_y$  equivale a los niveles atmosféricos de  $\text{CO}_2$  en el año de cada campaña y 280 es igual a los niveles atmosféricos de  $\text{CO}_2$  preindustriales, en ppm. La Figura 4.3. muestra la relación entre la sobresaturación

media de  $\text{CO}_3^{2-}$  con respecto a la concentración de saturación de aragonita ( $\delta_{\text{Arg}}$ ) en relación con el aumento de  $\text{CO}_2$  atmosférico desde la era preindustrial ( $\Delta[\text{CO}_2]$ ), para las cuatro repeticiones de la A05 consideradas. Esta relación se muestra por separado para las cuencas occidental y oriental.

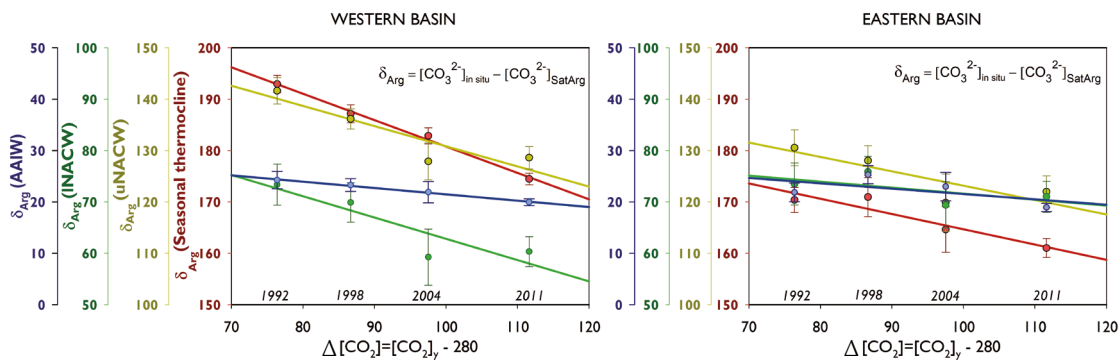


**Figura 4.3.** Valores medios de  $\delta_{\text{Arg}}$   $\pm$  error estándar de la media, con respecto al aumento de  $\text{CO}_2$  en la atmósfera desde la era preindustrial, para las campañas de 1992, 1998, 2004 y 2011 de la sección A05. Las líneas de color asociadas son las respectivas tendencias en el promedio de  $\delta_{\text{Arg}}$  entre 1992 y 2011. Los resultados dentro de la termoclina estacional (primeros 150 dbar, rojo), uNACW (amarillo), INACV (verde) y AAIW (azul) se presentan, por separado las cuencas oeste (panel izquierdo) y este (panel derecho). Se debe tener en cuenta que la escala en el eje y es diferente dependiendo de la masa de agua, sin embargo, el rango total del eje y se extiende en 50  $\mu\text{mol kg}^{-1}$ , con el fin de ayudar a distinguir el cambio en  $\delta_{\text{Arg}}$  entre las capas y cuencas. Los datos de  $\text{CO}_2$  utilizados están disponibles en: <http://www.esrl.noaa.gov/gmd/obop/mlo/>.

Como se evidencia en la Figura 4.3, el cambio decenal en la media de  $\delta_{\text{Arg}}$  se corresponde de forma bastante lineal con el correspondiente exceso de  $\text{CO}_2$  atmosférico en la atmósfera respecto a la era preindustrial. Esto significa que las tendencias decenales en la media de  $\delta_{\text{Arg}}$  están en conformidad con una absorción oceánica relativamente constante del  $\text{CO}_2$  acumulado en la atmósfera. Sin embargo, las pendientes resultantes de estas tendencias lineales dependen de la masa de agua y también difieren entre cuencas. Los valores respectivos de estas pendientes (mostrados en la Tabla 4.2.) sugieren mayores tasas de desaturación en la termoclina estacional y la existencia de tasas progresivamente más bajas a medida que aumenta la presión. Por otra parte, las tasas de desaturación parecen ser más rápidas en el oeste en comparación con la cuenca este. Teniendo en cuenta las incertidumbres, algunas de las tendencias en la cuenca este no son significativamente diferentes de cero, lo que indica una ausencia de cambio en  $\delta_{\text{Arg}}$ . La estadística de regresión del ajuste lineal (Tabla 4.2.) permite el cálculo de algunos parámetros de interés, bajo el supuesto de que la relación encontrada entre  $\delta_{\text{Arg}}$  y  $\Delta[\text{CO}_2]$  es representativa de su variabilidad más allá de la escala de tiempo decenal. El término de intersección ( $b$ ) indica el valor de  $\delta_{\text{Arg}}$  en la era pre-industrial (es decir, cuando  $\Delta[\text{CO}_2]=0$  o  $[\text{CO}_2]_y=280$ ). La relación entre la intersección y la pendiente de cada ajuste lineal indica el valor de  $\Delta[\text{CO}_2]$  al que se alcanzará el nivel de saturación ( $[\text{CO}_3^{2-}]_{\text{in situ}} = [\text{CO}_3^{2-}]_{\text{SatArg}}$ ) dentro de cada capa y en cada cuenca estudiada. Si se considera un  $\Delta[\text{CO}_2]$  de  $\sim 120$  ppm en 2014 (Tabla 4.2.), quedarían alrededor de 132 a 154 ppm por acumularse en la

atmósfera hasta alcanzar la saturación dentro de la INACW y la AAIW, respectivamente. Teniendo en cuenta la tasa de crecimiento anual de  $\text{pCO}_2$  actual, de  $\sim 2 \text{ ppm año}^{-1}$  (Tabla 4.2.), esto indicaría que la saturación dentro de estas dos masas de agua se alcanzará en unos 66 y 77 años, respectivamente, en la cuenca occidental de la sección, a pesar de que estas masas de agua no muestran las mayores tasas de desaturación a lo largo de la sección. Por el contrario, se tardará más de 150 años para alcanzar la saturación a lo largo de la uNACW y dentro de la termoclinia aunque muestren mayores tasas de desaturación. Esto se debe a la menor temperatura, mayor concentración de  $C_T$  y menor alcalinidad de la INACW y la AAIW. La Tabla 4.2. también muestra la misma información a lo largo de  $7.5^\circ\text{N}$ . Sin embargo, debe tenerse en cuenta que ya que existen sólo dos repeticiones de esta sección, la estadística de regresión del ajuste lineal entre dos pares de datos pierde gran parte de su sentido, teniendo en cuenta que las diferencias entre los dos años no son capaces de informar sobre tendencias si no sólo sobre los cambios en un período de tiempo determinado. Teniendo en cuenta que estos resultados deben ser interpretados con más cautela, la comparación de los valores promedio de  $\delta_{\text{Arg}}$  entre 1993 y 2010 sugiere que no se han producido cambios significativos a lo largo del Atlántico tropical durante el período estudiado, con la excepción de una disminución notable de  $\delta_{\text{Arg}}$  en la SACW en la cuenca oriental.

Otro importante hallazgo en el capítulo 3.3. fue que la acidificación observada a lo largo del océano superficial a  $24.5^\circ\text{N}$  también se explica por cambios particulares en los niveles de oxígeno y no sólo debido a la acumulación de  $C_{\text{ant}}$ . A pesar de que mostraban una distribución más confinada en comparación con  $C_{\text{ant}}$ , los cambios en oxígeno eran responsables de una parte importante de los cambios en el pH en regiones específicas de la sección. Por ejemplo, los procesos relacionados con la expansión de la zona del mínimo de oxígeno explicaban casi la mitad de la disminución en el pH observada entre 1992 y 2011. Por lo tanto, además del  $C_{\text{ant}}$ , los posibles cambios en oxígeno surgen como un factor importante en la modulación de las tendencias de pH y los estados de saturación a largo plazo en la región estudiada. En cuanto al sistema del carbónico y al oxígeno, gran parte de la variabilidad decenal se asocia con los diferentes estados de la NAO, en el Atlántico Norte, que se manifiesta en la superficie del mar y en última instancia, induce cambios en la circulación y en las tasas de formación de masas de agua y sus propiedades. De todos modos, el cambio entre estados puede ocurrir como resultado de la variabilidad natural, o en respuesta a un forzamiento externo. Por lo tanto, la relación aún desconocida entre la variabilidad, el forzamiento y las respuestas derivadas a escala decenal revela la complejidad saber cuál será la dinámica del sistema del carbónico en el futuro.

**Tabla 4.2.** Datos en relación con los cambios temporales en el  $\delta_{\text{Arg}}$  promedio dentro de las masas de agua de la del océano superficial, por separado para las cuencas oeste y este, a lo largo de las secciones A05 y A06. Los valores promedio  $\pm$  incertidumbre de  $\delta_{\text{Arg}}$  inicial ( $\delta_{\text{Arg}}$  inicial) y final ( $\delta_{\text{Arg}}$  finales) de los períodos estudiados, y para el período entero ( $\delta_{\text{Arg}}$  promedio), en  $\mu\text{mol kg}^{-1}$ . Estadística de la regresión entre  $\delta_{\text{Arg}}$  y  $\Delta[\text{CO}_2]$ : pendiente (m, es decir, tendencia en  $\delta_{\text{Arg}}$ ) en  $\mu\text{mol kg}^{-1} \text{ ppm}^{-1}$ , término de intersección (b, es decir  $\delta_{\text{Arg}}$  en la era preindustrial) en  $\mu\text{mol kg}^{-1}$  y coeficiente de determinación ( $r^2$ ) del ajuste lineal. La última columna informa del tiempo que queda hasta llegar a la saturación (años SatArg) en años. Este último parámetro se calcula a partir de los datos de  $\text{CO}_2$  del Observatorio de Mauna Loa (MLO, disponibles en: <http://www.esrl.noaa.gov/gmd/obop/mlo/>) que se indican en el pie de la tabla, mediante la eliminación de  $\Delta[\text{CO}_2]$  en 2014 de la  $\Delta[\text{CO}_2]$  en la que se alcanza la saturación (b/m) y dividiendo  $\Delta[\text{CO}_2]$  resultante por la tasa de crecimiento de  $\text{pCO}_2$  actual.

		$\delta_{\text{Arg}}$ inicial $\mu\text{mol kg}^{-1}$	$\delta_{\text{Arg}}$ final $\mu\text{mol kg}^{-1}$	$\delta_{\text{Arg}}$ promedio $\mu\text{mol kg}^{-1}$	pendiente (m) $\delta_{\text{Arg}}$ Trend $\mu\text{mol kg}^{-1} \text{ ppm}^{-1}$	intersección (b) $\delta_{\text{Arg}}$ Prein $\mu\text{mol kg}^{-1}$	$r^2$	años SatArg yr
<b>A05</b> <b>(24.5°N)</b> 1992- 2011	Western Basin							
	Thermocline	193 $\pm$ 2	174 $\pm$ 1	184 $\pm$ 8	-0.51 $\pm$ 0.03	232 $\pm$ 3	0.99	166
	uNACW	142 $\pm$ 3	129 $\pm$ 2	134 $\pm$ 7	-0.39 $\pm$ 0.13	170 $\pm$ 12	0.82	157
	INACW	73 $\pm$ 4	60 $\pm$ 3	66 $\pm$ 7	-0.41 $\pm$ 0.15	104 $\pm$ 14	0.80	66
	AAIW	24 $\pm$ 2	20 $\pm$ 1	22 $\pm$ 2	-0.12 $\pm$ 0.01	34 $\pm$ 1	0.99	77
	Eastern Basin							
	Thermocline	170 $\pm$ 2	161 $\pm$ 2	167 $\pm$ 5	-0.30 $\pm$ 0.07	194 $\pm$ 7	0.89	267
	uNACW	131 $\pm$ 3	122 $\pm$ 3	125 $\pm$ 5	-0.28 $\pm$ 0.13	151 $\pm$ 12	0.71	210
<b>A06</b> <b>(7.5°N)</b> 1993 - 2010	INACW	74 $\pm$ 4	71 $\pm$ 3	72 $\pm$ 3	-0.12 $\pm$ 0.10	83 $\pm$ 10	0.38	297
	AAIW	22 $\pm$ 2	19 $\pm$ 1	22 $\pm$ 3	-0.10 $\pm$ 0.10	32 $\pm$ 9	0.35	93
	Western Basin							
	SACW	167 $\pm$ 8	161 $\pm$ 6	164 $\pm$ 4	-0.17	180	-	463
	SAMW	29 $\pm$ 5	24 $\pm$ 3	27 $\pm$ 4	-0.15	41	-	74
	AAIW	0 $\pm$ 1	-4 $\pm$ 1	-2 $\pm$ 3	-0.12	9	-	-21
	Eastern Basin							
	SACW	122 $\pm$ 15	108 $\pm$ 12	115 $\pm$ 10	-0.43	155	-	121
	SAMW	21 $\pm$ 5	20 $\pm$ 3	21 $\pm$ 1	n.s	24	-	278
	AAIW	-6 $\pm$ 1	-9 $\pm$ 1	-7 $\pm$ 2	-0.08	0	-	-59

MLO – promedio anual  $\text{CO}_2$  2014 = 399 ppm;  $\Delta[\text{CO}_2]$  = 398.55-280 = 119 ppm ;  $\Delta[\text{CO}_2]$ =~120 ppm

MLO - tasa promedio crecimiento anual  $\text{CO}_2$  2014 = 2.13 ppm año $^{-1}$ ; tasa crecimiento  $\text{CO}_2$  = ~ 2 ppm año $^{-1}$

## CONCLUSIONES PRINCIPALES por capítulos

**Capítulo 3.1.** Se utilizaron cinco años de datos del sistema del carbónico en agua de mar, que cubren un período de estudio entre 1992 y 2011, para investigar la variabilidad decenal en el almacenamiento de  $C_{ant}$  a lo largo del Atlántico Norte subtropical. Hemos observado que la distribución general de concentraciones mostró valores altos y mayores tasas de almacenamiento decenales cerca de la superficie. Ambos valores decrecían en profundidad. Esto se confirmó mediante los cuatro métodos de estimación utilizados. Detectamos gradientes horizontales en el almacenamiento de  $C_{ant}$  en toda la columna de agua, lo cual se explica por las características de la circulación. Este resultado fue más robusto para las masas de agua intermedias y profundas, que mostraron tasas de almacenamiento notablemente más altas cerca del margen continental occidental debido al papel transportador de la corriente profunda de frontera oeste, con una contribución especial del agua de Labrador más recientemente ventilada. También encontramos tendencias significativas en las tasas de almacenamiento de  $C_{ant}$  en las masas de agua más profundas, donde los límites de detección de  $C_{ant}$  ganan importancia, asumiendo un estado transitorio estacionario de las distribuciones de  $C_{ant}$  (es decir, suponiendo que la acumulación de  $C_{ant}$  no se vio afectada por los cambios recientes en circulación).

**Capítulo 3.2.** Se investigaron los cambios decenales en las distribuciones de  $C_{ant}$  a lo largo del Atlántico Norte tropical, a través de la comparación de datos del sistema del carbónico recogidos en 1993 y 2010. Esta comparación mostró concentraciones de  $C_{ant}$  y tasas de almacenamiento más altas en las capas superiores, con ambos valores disminuyendo con la profundidad. Las aguas intermedias mostraron concentraciones relativas mínimas con respecto a las aguas circundantes. Esto fue confirmado mediante el uso de dos métodos de estimación  $C_{ant}$ . La región tropical occidental mostró un inventario más alto de  $C_{ant}$ . Observamos gradientes horizontales claros en el almacenamiento de  $C_{ant}$  dentro de las aguas profundas, de acuerdo con el camino de propagación de la corriente profunda de frontera oeste, que recircula hacia el este y redistribuye el  $C_{ant}$  hacia la cuenca oriental. Los cambios en la distribución de las concentraciones de  $C_{ant}$  en las capas del océano superficial parecieron estar afectadas por los cambios estacionales en la circulación y la retracción de las aguas intermedias.

**Capítulo 3.3.** La comparación de las observaciones de pH realizadas en 1992 y 2011 mostró una disminución general de los valores de pH en los primeros 1000 dbar de la columna de agua, en el Atlántico Norte subtropical. La separación de las diferencias temporales de pH en los componentes antropogénico y no antropogénico (natural) mostró que éstos son de magnitudes similares, pero tienen diferentes representaciones con la profundidad y la longitud en la sección estudiada: los cambios de pH de origen antropogénico dominaron en aguas superficiales y profundas, mientras que tanto el componente antropogénico como el naturales afectaron a las aguas modales (centrales) y intermedias. La variabilidad natural se explicó como debida principalmente a los cambios en los niveles de oxígeno, que mostraban un patrón bastante heterogéneos y podían atribuirse a diferentes procesos con una variabilidad temporal de un rango de escalas temporales amplio. Hemos observado que los cambios en los niveles de oxígeno modulan la acidificación antropogénica. Estos

resultados ponen en relieve la necesidad de distinguir si las tendencias a largo plazo en el oxígeno disuelto obedecen a diferentes estados del modo climático de la Oscilación del Atlántico Norte o deben atribuirse a un forzamiento del clima inducido por el hombre, ya que afectan a las tendencias de acidificación.

## Conclusiones generales

La hidrografía repetida del sistema del carbónico de las secciones A05 y A06 permitió la cuantificación del almacenamiento de  $C_{\text{ant}}$  a lo largo del Atlántico Norte subtropical y tropical en escalas de tiempo decenales. También se evaluaron las interacciones entre la circulación oceánica y el sistema del carbónico, en particular con respecto a los procesos que controlan y modulan las tasas de almacenamiento observadas. Esto se logró mediante la división de las masas de agua presentes en cada una de las dos secciones en regiones horizontalmente separadas, que fueron definidas siguiendo criterios oceanográficos, con el fin de estudiar la acumulación de  $C_{\text{ant}}$  dentro de ellos. Este enfoque metodológico mostró que la variabilidad espacio-temporal en el almacenamiento de  $C_{\text{ant}}$  a lo largo de las dos secciones está fuertemente relacionada con la señal profunda de  $C_{\text{ant}}$  transportada por la corriente principal de la circulación (es decir, la corriente profunda de frontera oeste) que se propaga a través de las dos secciones. Además, los cambios en la circulación en el Agua Intermedia Antártica parecen explicar el almacenamiento de  $C_{\text{ant}}$  observado en el océano superficial.

Se evaluaron los cambios decenales y tendencias en algunos de los parámetros del sistema del carbónico, tales como  $C_{\text{ant}}$  y pH, con una primera evaluación de los estados de saturación de  $\text{CaCO}_3$  con respecto a la aragonita. La proyección de las tasas de cambio descritas hacia el futuro debe hacerse con precaución, bajo el supuesto de que la variabilidad descrita es representativa de períodos de tiempo más allá de la escala de tiempo decenal. En este sentido, es necesaria una mayor comprensión de la variabilidad de los procesos detrás de las tasas observadas, para distinguir entre la variabilidad natural y el forzamiento antropogénico del sistema climático.

## PERSPECTIVAS FUTURAS Y PREGUNTAS ABIERTAS

La inclusión de medidas sistemáticas dentro de una red de secciones hidrográficas repetidamente ha permitido a los científicos describir tendencias en los diferentes parámetros del agua de mar alrededor del mundo. Pese al reto que supone conseguir este tipo de observaciones de campo, esta información proporciona herramientas y conocimientos valiosos para la evaluación directa de los modelos numéricos del ciclo del carbono en el océano que se utilizan para la identificación de los procesos responsables de la variabilidad del clima. Como resultado, la recopilación y el análisis de estas observaciones y en el desarrollo y aplicación de modelos del sistema climático hace posible supervisar, simular y proyectar el clima global con gran precisión. Las estimaciones de  $C_{\text{ant}}$  basadas en observaciones y los modelos de circulación oceánica se han combinado en esquemas inversos para estimar flujos de  $C_{\text{ant}}$  aire-oceáno, tasas de acumulación de  $C_{\text{ant}}$ , y transportes de  $C_{\text{ant}}$  en el interior del océano (Mikaloff Fletcher *et al.*, 2006; Gruber *et al.*, 2009; DeVries, 2014). De todos modos, es necesario evaluar el rendimiento de estos modelos del ciclo del carbono respecto a las estimaciones basadas en observaciones de la absorción oceánica de  $C_{\text{ant}}$  (Khatriwala *et al.*, 2009). Este tipo de comprobaciones se necesitan para ganar confianza en las predicciones de los modelos, pero éstas están limitadas por la disponibilidad de datos que reflejen la variabilidad del sistema climático en una amplia gama tanto de las escalas espaciales como temporales.

Uno de los principales retos para hacer predicciones del futuro del sistema del carbónico y los impactos relacionados sobre el clima en escalas de tiempo de años a décadas es la capacidad de obtener una alta calidad de observaciones del sistema del carbónico de suficiente resolución espacial y temporal, con el fin de acoplarlos con la gran cantidad de datos ya disponibles que se han utilizado para describir la variabilidad en la circulación en escalas de tiempo desde subanuales a plurianuales. Por lo tanto, el desarrollo de métodos de observación del sistema de carbonato mediante el uso de plataformas autónomas y la transmisión de esos datos serán crucial. Ya se han hecho algunos avances en este sentido, con el fin de estimar con precisión el pH y los estados de saturación de  $\text{CaCO}_3$  a partir de perfiladores Argo (Juranek *et al.*, 2011). El desarrollo de sensores autónomos precisos de los diferentes parámetros del sistema de carbonato y la combinación de las mediciones obtenidas a partir de anclajes, drifters o mediante teledetección arrojará información referente al océano superficial. Obtener este tipo de datos en el interior del océano será más difícil. En este sentido, el uso de técnicas basadas en redes neuronales con el fin de reconstruir las relaciones no lineales entre los parámetros biogeoquímicos también será una prioridad (Telszewski *et al.*, 2009; Velo *et al.*, 2013).





## References

- Álvarez-Salgado, X.A., Fraga, F., Pérez, F.F., 1992. Determination of nutrient salts by automatic methods both in seawater and brackish water: the phosphate blank. *Marine Chemistry*, 39, 311-319.
- Álvarez, M., Ríos, A.F., Pérez, F.F., Bryden, H.L., Rosón, G., 2003. Transports and budgets of total inorganic carbon in the subpolar and temperate North Atlantic. *Global Biogeochem. Cycles*, 17, 1002.
- Anderson, L.A., Sarmiento, J.L., 1994. Redfield ratios of remineralization determined by nutrient data analysis. *Global Biogeochemical Cycles*, 8, 65-80.
- Andersson, A.J., Kline, D.I., Edmunds, P.J., Archer, S.D., Bednářek, N., Carpenter, R.C., Chadsey, M., Goldstein, P., Grottoli, A.G., Hurst, T.P., King, A.L., Kübler, J.E., Kuffner, I.B., Mackey, K.R.M., Menge, B.A., Paytan, A., Riebesell, U., Schnetzer, A., Warner, M.E., R.C., Z., 2015. Understanding ocean acidification impacts on organismal to ecological scales. . *Oceanography*, 28, 16-27.
- Archer, D., 2005. Fate of fossil fuel CO<sub>2</sub> in geologic time. *Journal of Geophysical Research: Oceans*, 110.
- Archer, D., Winguth, A., Lea, D., Mahowald, N., 2000. What caused the glacial/interglacial atmospheric pCO<sub>2</sub> cycles? *Reviews of Geophysics*, 38, 159-189.
- Arhan, M., Mercier, H., Bourlès, B., Gouriou, Y., 1998. Hydrographic sections across the Atlantic at 7°30N and 4°30S. *Deep Sea Research Part I: Oceanographic Research Papers*, 45, 829-872.
- Astor, Y.M., Lorenzoni, L., Thunell, R., Varela, R., Muller-Karger, F., Troccoli, L., Taylor, G.T., Scranton, M.I., Tappa, E., Rueda, D., 2013. Interannual variability in sea surface temperature and fCO<sub>2</sub> changes in the Cariaco Basin. *Deep Sea Research Part II: Topical Studies in Oceanography*, 93, 33-43.
- Astor, Y.M., Scranton, M.I., Muller-Karger, F., Bohrer, R., García, J., 2005. fCO<sub>2</sub> variability at the CARIACO tropical coastal upwelling time series station. *Marine Chemistry*, 97, 245-261.
- Atkinson, C.P., Bryden, H.L., Cunningham, S.A., King, B.A., 2012. Atlantic transport variability at 25° N in six hydrographic sections. *Ocean Sci.*, 8, 497-523.
- Atkinson, C.P., Bryden, H.L., Hirschi, J.J.M., Kanzow, T., 2010. On the seasonal cycles and variability of Florida Straits, Ekman and Sverdrup transports at 26° N in the Atlantic Ocean. *Ocean Sci.*, 6, 837-859.
- Bach, L.T., 2015. Reconsidering the role of carbonate ion concentration in calcification by marine organisms. *Biogeosciences*, 12, 4939-4951.
- Bach, L.T., Riebesell, U., Gutowska, M.A., Federwisch, L., Schulz, K.G., 2015. A unifying concept of coccolithophore sensitivity to changing carbonate chemistry embedded in an ecological framework. *Progress In Oceanography*, 135, 125-138.
- Baringer, M.O.N., Larsen, J.C., 2001. Sixteen years of Florida Current Transport at 27° N. *Geophysical Research Letters*, 28, 3179-3182.
- Barker, S., Ridgwell, A.J., 2012. Ocean Acidification. *Nature Education Knowledge*, 3, 21.
- Barnston, A.G., Livezey, R.E., 1987. Classification, Seasonality and Persistence of Low-Frequency Atmospheric Circulation Patterns. *Monthly Weather Review*, 115, 1083-1126.
- Barrett, P.M., Resing, J.A., Buck, N.J., Feely, R.A., Bullister, J.L., Buck, C.S., Landing, W.M., 2014. Calcium carbonate dissolution in the upper 1000 m of the eastern North Atlantic. *Global Biogeochemical Cycles*, 28, 386-397.
- Bates, N.R., 2001. Interannual variability of oceanic CO<sub>2</sub> and biogeochemical properties in the Western North Atlantic subtropical gyre. *Deep Sea Research Part II: Topical Studies in Oceanography*, 48, 1507-1528.
- Bates, N.R., 2007. Interannual variability of the oceanic CO<sub>2</sub> sink in the subtropical gyre of the North Atlantic Ocean over the last 2 decades. *Journal of Geophysical Research: Oceans*, 112, C09013.

- Bates, N.R., 2012. Multi-decadal uptake of carbon dioxide into subtropical mode water of the North Atlantic Ocean. *Biogeosciences*, 9, 2649-2659.
- Bates, N.R., Astor, Y.M., Church, M.J., Currie, K., Dore, J.E., González-Dávila, M., Lorenzoni, L., Muller-Karger, F., Olafsson, J., Santana-Casiano, J.M., 2014. A time-series view of changing ocean chemistry due to ocean uptake of anthropogenic CO<sub>2</sub> and ocean acidification. *Oceanography*, 27, 26-141.
- Bates, N.R., Best, M.H.P., Neely, K., Garley, R., Dickson, A.G., Johnson, R.J., 2012. Detecting anthropogenic carbon dioxide uptake and ocean acidification in the North Atlantic Ocean. *Biogeosciences*, 9, 2509-2522.
- Bates, N.R., Michaels, A.F., Knap, A.H., 1996. Seasonal and interannual variability of oceanic carbon dioxide species at the U.S. JGOFS Bermuda Atlantic Time-series Study (BATS) site. Deep Sea Research Part II: Topical Studies in Oceanography, 43, 347-383.
- Brewer, P.G., 1978. Direct observation of the oceanic CO<sub>2</sub> increase. *Geophysical Research Letters*, 5, 997-1000.
- Broecker, W.S., 1974. "NO" a conservative water mass tracer. *Earth and Planetary Science Letters*, 23, 8761-8776.
- Broecker, W.S., Peng, T.H., 1974. Gas exchange rates between air and sea. *Tellus*, 26, 21-35.
- Broecker, W.S., 1987. The biggest chill.
- Brown, P.J., Bakker, D.C.E., Schuster, U., Watson, A.J., 2010. Anthropogenic carbon accumulation in the subtropical North Atlantic. *Journal of Geophysical Research-Oceans*, 115, 4016.
- Bryden, H.L., King, B.A., McCarthy, G.D., McDonagh, E.L., 2014. Impact of a 30% reduction in Atlantic meridional overturning during 2009-2010. *Ocean Sci.*, 10, 683-691.
- Bryden, H.L., Longworth, H.R., Cunningham, S.A., 2005. Slowing of the Atlantic meridional overturning circulation at 25°N. *Nature*, 438, 655-657.
- Calvo, E., Pelejero, C., Logan, G.A., De Deckker, P., 2004. Dust-induced changes in phytoplankton composition in the Tasman Sea during the last four glacial cycles. *Paleoceanography*, 19.
- Calvo, E., Pelejero, C., Pena, L.D., Cacho, I., Logan, G.A., 2011. Eastern Equatorial Pacific productivity and related CO<sub>2</sub> changes since the last glacial period. *Proceedings of the National Academy of Sciences*, 108, 5537-5541.
- Castaño-Carrera, M., Pardo, P.C., Álvarez, M., Lavín, A., Rodríguez, C., Carballo, R., Ríos, A.F., Pérez, F.F., 2012. Anthropogenic carbon and water masses in the bay of Biscay. *Ciencias Marinas*, 38, 191-207.
- Chan, N.C.S., Connolly, S.R., 2013. Sensitivity of coral calcification to ocean acidification: a meta-analysis. *Global Change Biology*, 19, 282-290.
- Chanson, M., Millero, F.J., 2007. Effect of filtration on the total alkalinity of open-ocean seawater. *Limnology and Oceanography: Methods*, 5, 293-295.
- Chen, G.T., Millero, F.J., 1979. Gradual increase of oceanic CO<sub>2</sub>. *Nature*, 277, 205-206.
- Chung, S.N., Lee, K., Feely, R.A., Sabine, C.L., Millero, F.J., Wanninkhof, R., Bullister, J.L., Key, R.M., Peng, T.H., 2003. Calcium carbonate budget in the Atlantic Ocean based on water column inorganic carbon chemistry. *Global Biogeochemical Cycles*, 17, doi:10.1029/2002GB002001.
- Chung, S.N., Park, G.H., Lee, K., Key, R.M., Millero, F.J., Feely, R.A., Sabine, C.L., Falkowski, P.G., 2004. Postindustrial enhancement of aragonite undersaturation in the upper tropical and subtropical Atlantic Ocean: The role of fossil fuel CO<sub>2</sub>. *Limnology & Oceanography*, 49, 315-321.
- Caias, P., Sabine, C., Bala, G., Bopp, L., Brovkin, V., Canadell, J., Chhabra, A., DeFries, R., Galloway, J., Heimann, M., Jones, C., Le Quéré, C., Myneni, R.B., Piao, S., Thornton, P., 2013. Carbon and Other Biogeochemical Cycles. In Stocker, T.F., Qin, D., Plattner, G.-K., Tignor, M., Allen, S.K., Boschung, J., Nauels, A., Xia, Y., Bex, V., Midgley, P.M. (Eds.), *Climate Change 2013: The Physical Science Basis. Contribution of Working Group I to*

- the Fifth Assessment Report of the Intergovernmental Panel on Climate Change (pp. 465–570). Cambridge, United Kingdom and New York, NY, USA: Cambridge University Press.
- Clayton, T.D., Byrne, R.H., 1993. Spectrophotometric seawater pH measurements: total hydrogen ion concentration scale calibration of m-cresol purple and at-sea results. Deep Sea Research Part I: Oceanographic Research Papers, 40, 2115-2129.
- Culberson, C.H., 1991. WOCE Operations Manual (WHP Operations and Methods), WHPO 91/1. Woods Hole Oceanogr. Inst., Woods Hole, Mass.
- Cunningham, S.A., Kanzow, T., Rayner, D., Baringer, M.O., Johns, W.E., Marotzke, J., Longworth, H.R., Grant, E.M., Hirschi, J.J.-M., Beal, L.M., Meinen, C.S., Bryden, H.L., 2007. Temporal Variability of the Atlantic Meridional Overturning Circulation at 26.5°N. *Science*, 317, 935-938.
- Currie, K., Reid, M., Hunter, K., 2011. Interannual variability of carbon dioxide drawdown by subantarctic surface water near New Zealand. *Biogeochemistry*, 104, 23-34.
- Dassié, E.P., Lemley, G.M., Linsley, B.K., 2013. The Suess effect in Fiji coral  $\delta^{13}\text{C}$  and its potential as a tracer of anthropogenic  $\text{CO}_2$  uptake. *Palaeogeography, Palaeoclimatology, Palaeoecology*, 370, 30-40.
- DeValls, T.A., Dickson, A.G., 1998. The pH of buffers based on 2-amino-2-hydroxymethyl-1,3-propanediol ('tris') in synthetic sea water. Deep Sea Research Part I: Oceanographic Research Papers, 45, 1541-1554.
- DeVries, T., 2014. The oceanic anthropogenic  $\text{CO}_2$  sink: Storage, air-sea fluxes, and transports over the industrial era. *Global Biogeochemical Cycles*, 28, 631-647.
- Dickson, A.G., 1981. An exact definition of total alkalinity and a procedure for the estimation of alkalinity and total inorganic carbon from titration data. Deep Sea Research Part A. Oceanographic Research Papers, 28, 609-623.
- Dickson, A.G., Millero, F.J., 1987. A comparison of the equilibrium constants for the dissociation of carbonic acid in seawater media. Deep Sea Research Part A. Oceanographic Research Papers, 34, 1733-1743.
- Dickson, A.G., Sabine, C.L., Christian, J.R., 2007. Guide to best practices for ocean  $\text{CO}_2$  measurements.
- DLugokenky, E., Tans, P., 2013. Trends in atmospheric carbon dioxide. Earth System Research Laboratory, National Oceanic and Atmospheric Administration, USA: <http://www.esrl.noaa.gov/gmd/ccgg/trends/global.html>.
- Doney, S.C., Fabry, V.J., Feely, R.A., Kleypas, J.A., 2009. Ocean Acidification: The other  $\text{CO}_2$  problem. *Annual Review of Marine Science*, 1, doi:10.1146/annurev.marine.010908.163834.
- Doney, S.C., Ruckelshaus, M., Duffy, J.E., Barry, J.P., Chan, F., English, C.A., Galindo, H.M., Grebmeier, J.M., Hollowed, A.B., Knowlton, N., Polovina, J., Rabalais, N.N., Sydeman, W.J., Talley, L.D., 2012. Climate Change Impacts on Marine Ecosystems. *Annual Review of Marine Science*, 4, 11-37.
- Dore, J.E., Lukas, R., Sadler, D.W., Church, M.J., Karl, D.M., 2009. Physical and biogeochemical modulation of ocean acidification in the central North Pacific. *Proceedings of the National Academy of Sciences*, 106, 12235-12240.
- Fabry, V.J., Seibel, B.A., Feely, R.A., Orr, J.C., 2008. Impacts of ocean acidification on marine fauna and ecosystem processes. *ICES J. Mar. Sci.*, 65, 414-432.
- Fajar, N.M., Pardo, P.C., Carracedo, L., Vázquez-Rodríguez, M., Ríos, A.F., Pérez, F.F., 2012. Trends of anthropogenic  $\text{CO}_2$  along 20°W in the Iberian Basin. *Ciencias Marinas*, 38, 287-306.
- Feely, R.A., Doney, S.C., Cooley, S.R., 2009. Ocean acidification: Present conditions and future changes in a high- $\text{CO}_2$  world. *Oceanography*, 22(4):36-47, 36-47.
- Feely, R.A., Sabine, C.L., Lee, K., Berelson, W., Kleypas, J., Fabry, V.J., Millero, F.J., 2004. Impact of Anthropogenic  $\text{CO}_2$  on the  $\text{CaCO}_3$  system in the oceans. *Science*, 305, 362-366.
- Flecha, S., Pérez, F.F., Navarro, G., Ruiz, J., Olivé, I., Rodríguez-Gálvez, S., Costas, E., Huertas, I.E., 2012. Anthropogenic carbon inventory in the Gulf of Cádiz. *Journal of Marine Systems*, 92, 67-75.

- Frankignoulle, M., Canon, C., Gattuso, J.-P., 1994. Marine calcification as a source of carbon dioxide: Positive feedback of increasing atmospheric CO<sub>2</sub>. *Limnology and Oceanography*, 39, 458-462.
- Friis, K., Körtzinger, A., Pätsch, J., Wallace, D.W.R., 2005. On the temporal increase of anthropogenic CO<sub>2</sub> in the sub-polar North Atlantic. *Deep Sea Research Part I: Oceanographic Research Papers*, 52, 681-698.
- Gammon, R.H., Cline, J., Wisegarver, D., 1982. Chlorofluoromethanes in the northeast Pacific Ocean: Measured vertical distributions and application as transient tracers of upper ocean mixing. *Journal of Geophysical Research: Oceans*, 87, 9441-9454.
- González-Dávila, M., Santana-Casiano, J.M., Rueda, M.-J., Llinás, O., González-Dávila, E.-F., 2003. Seasonal and inter-annual variability of sea-surface carbon dioxide species at the European Station for Time Series in the Ocean at the Canary Islands (ESTOC) between 1996 and 2000. *Global Biogeochemical Cycles*, 17, 1076.
- González-Dávila, M., Santana-Casiano, J.M., Rueda, M.J., Llinás, O., 2010. The water column distribution of carbonate system variables at the ESTOC site from 1995 to 2004. *Biogeosciences*, 7, 3067-3081.
- Goodkin, N.F., Levine, N.M., Doney, S.C., Wanninkhof, R., 2011. Impacts of temporal CO<sub>2</sub> and climate trends on the detection of ocean anthropogenic CO<sub>2</sub> accumulation. *Global Biogeochemical Cycles*, 25.
- Goyet, C., Coatanoan, C., Eischeid, G., Amaoka, T., Okuda, K., Healy, R., Tsunogai, S., 1999. Spatial variation of total CO<sub>2</sub> and total alkalinity in the northern Indian Ocean: A novel approach for the quantification of anthropogenic CO<sub>2</sub> in seawater. *Journal of Marine Research*, 57, 135-163.
- Gruber, N., Gloo, M., Mikaloff Fletcher, S.E., Doney, S.C., Dutkiewicz, S., Follows, M.J., Gerber, M., Jacobson, A.R., Joos, F., Lindsay, K., Menemenlis, D., Mouchet, A., Müller, S.A., Sarmiento, J.L., Takahashi, T., 2009. Oceanic sources, sinks, and transport of atmospheric CO<sub>2</sub>. *Global Biogeochemical Cycles*, 23, GB1005.
- Gruber, N., Keeling, C.D., Bates, N.R., 2002. Interannual Variability in the North Atlantic Ocean Carbon Sink. *Science*, 298, 2374-2378.
- Gruber, N., Sarmiento, J.L., Stocker, T.F., 1996. An improved method for detecting anthropogenic CO<sub>2</sub> in the oceans. *Global Biogeochemical Cycles*, 10, 809-837.
- Guinotte, J.M., Fabry, V.J., 2008. Ocean Acidification and Its Potential Effects on Marine Ecosystems. *Annals of the New York Academy of Sciences*, 1134, 320-342.
- Haine, T.W.N., Hall, T.M., 2002. A Generalized Transport Theory: Water-Mass Composition and Age. *Journal of Physical Oceanography*, 32, 1932.
- Häkkinen, S., 1999. Variability of the simulated meridional heat transport in the North Atlantic for the period 1951–1993. *Journal of Geophysical Research: Oceans*, 104, 10991-11007.
- Hall, T.M., Haine, T.W.N., Waugh, D.W., 2002. Inferring the concentration of anthropogenic carbon in the ocean from tracers. *Global Biogeochemical Cycles*, 16, 78-71-78-15.
- Haywood, A.M., Ridgwell, A., Lunt, D.J., Hill, D.J., Pound, M.J., Dowsett, H.J., Dolan, A.M., Francis, J.E., Williams, M., 2011. Are there pre-Quaternary geological analogues for a future greenhouse warming? *Philosophical Transactions of the Royal Society of London A: Mathematical, Physical and Engineering Sciences*, 369, 933-956.
- Heinze, C., 2004. Simulating oceanic CaCO<sub>3</sub> export production in the greenhouse. *Geophysical Research Letters*, 31, L16308.
- Heinze, C., Maier-Reimer, E., Winn, K., 1991. Glacial pCO<sub>2</sub> Reduction by the World Ocean: Experiments With the Hamburg Carbon Cycle Model. *Paleoceanography*, 6, 395-430.
- Heinze, C., Meyer, S., Goris, N., Anderson, L., Steinfeldt, R., Chang, N., Le Quéré, C., Bakker, D.C.E., 2015. The ocean carbon sink – impacts, vulnerabilities and challenges. *Earth Syst. Dynam.*, 6, 327-358.

- Hernández-Guerra, A., Pelegrí, J.L., Fraile-Nuez, E., Benítez-Barrios, V., Emelianov, M., Pérez-Hernández, M.D., Vélez-Belchí, P., 2014. Meridional overturning transports at 7.5N and 24.5N in the Atlantic Ocean during 1992–93 and 2010–11. *Progress In Oceanography*, 128, 98-114.
- Hofmann, D.J., Butler, J.H., Dlugokencky, E.J., Elkins, J.W., Masarie, K., Montzka, S.A., Tans, P., 2011. The role of carbon dioxide in climate forcing from 1979 to 2004: introduction of the Annual Greenhouse Gas Index. *Tellus B*, 58.
- Hofmann, M., Schellnhuber, H.-J., 2009. Oceanic acidification affects marine carbon pump and triggers extended marine oxygen holes. *Proceedings of the National Academy of Sciences*, 106, 3017-3022.
- Holzer, M., Primeau, F.W., 2006. The diffusive ocean conveyor. *Geophysical Research Letters*, 33, L14618, doi:14610.11029/12006gl026232.
- Hönisch, B., Ridgwell, A., Schmidt, D.N., Thomas, E., Gibbs, S.J., Sluijs, A., Zeebe, R., Kump, L., Martindale, R.C., Greene, S.E., Kiessling, W., Ries, J., Zachos, J.C., Royer, D.L., Barker, S., Marchitto, T.M., Moyer, R., Pelejero, C., Ziveri, P., Foster, G.L., Williams, B., 2012. The Geological Record of Ocean Acidification. *Science*, 335, 1058-1063.
- Iglesias-Rodriguez, M.D., Halloran, P.R., Rickaby, R.E.M., Hall, I.R., Colmenero-Hidalgo, E., Gittins, J.R., Green, D.R.H., Tyrrell, T., Gibbs, S.J., von Dassow, P., Rehm, E., Armbrust, E.V., Boessenkool, K.P., 2008. Phytoplankton calcification in a high-CO<sub>2</sub> world. *Science*, 320, 336-340.
- Ilyina, T., Zeebe, R.E., 2012. Detection and projection of carbonate dissolution in the water column and deep-sea sediments due to ocean acidification. *Geophysical Research Letters*, 39.
- Ilyina, T., Zeebe, R.E., Maier-Reimer, E., Heinze, C., 2009. Early detection of ocean acidification effects on marine calcification. *Global Biogeochemical Cycles*, 23.
- IPCC, 2013. Climate Change 2013: The Physical Science Basis. Contribution of Working Group I to the Fifth Assessment Report of the Intergovernmental Panel on Climate Change. Cambridge, United Kingdom and New York, NY, USA: Cambridge University Press.
- Johnson, K.M., Dickson, A.G., Eischeid, G., Goyet, C., Guenther, P., Key, R.M., Millero, F.J., Purkerson, D., Sabine, C.L., Schortle, R.G., Wallace, D.W.R., Wilke, R.J., Winn, C.D., 1998. Coulometric total carbon dioxide analysis for marine studies: Assessment of the quality of total inorganic carbon measurements made during the US Indian Ocean CO<sub>2</sub> survey 1994-1996. *Marine Chemistry*, 63, 21-37.
- Joos, F., Spahni, R., 2008. Rates of change in natural and anthropogenic radiative forcing over the past 20,000 years. *Proceedings of the National Academy of Sciences*, 105, 1425-1430.
- Juranek, L.W., Feely, R.A., Gilbert, D., Freeland, H., Miller, L.A., 2011. Real-time estimation of pH and aragonite saturation state from Argo profiling floats: Prospects for an autonomous carbon observing strategy. *Geophysical Research Letters*, 38.
- Kanzow, T., Cunningham, S.A., Johns, W.E., Hirschi, J.J.M., Marotzke, J., Baringer, M.O., Meinen, C.S., Chidichimo, M.P., Atkinson, C., Beal, L.M., Bryden, H.L., Collins, J., 2010. Seasonal Variability of the Atlantic Meridional Overturning Circulation at 26.5°N. *Journal of Climate*, 23, 5678-5698.
- Khatiwala, S., Primeau, F., Hall, T., 2009. Reconstruction of the history of anthropogenic CO<sub>2</sub> concentrations in the ocean. *Nature*, 462, 346-349.
- Khatiwala, S., Tanhua, T., Mikaloff Fletcher, S., Gerber, M., Doney, S.C., Graven, H.D., Gruber, N., McKinley, G.A., Murata, A., Ríos, A.F., Sabine, C.L., Sarmiento, J.L., 2013. Global ocean storage of anthropogenic carbon. *Biogeosciences*, 10, 2169-2191.
- Khatiwala, S., Visbeck, M., Schlosser, P., 2001. Age tracers in an ocean GCM. *Deep Sea Research Part I: Oceanographic Research Papers*, 48, 1423-1441.

- Körtzinger, A., Mintrop, L., Duinker, J.C., 1998. On the penetration of anthropogenic CO<sub>2</sub> into the North Atlantic Ocean. *Journal of Geophysical Research C: Oceans*, 103, 18681-18689.
- Körtzinger, A., Mintrop, L., Duinker, J.C., 1998. On the penetration of anthropogenic CO<sub>2</sub> into the North Atlantic Ocean. *Journal of Geophysical Research: Oceans*, 103, 18681-18689.
- Kuhlbrodt, T., Griesel, A., Montoya, M., Levermann, A., Hofmann, M., Rahmstorf, S., 2007. On the driving processes of the Atlantic meridional overturning circulation. *Reviews of Geophysics*, 45.
- Lazier, J., Hendry, R., Clarke, A., Yashayaev, I., Rhines, P., 2002. Convection and restratification in the Labrador Sea, 1990–2000. *Deep Sea Research Part I: Oceanographic Research Papers*, 49, 1819-1835.
- Le Quéré, C., Andres, R.J., Boden, T., Conway, T., Houghton, R.A., House, J.I., Marland, G., Peters, G.P., van der Werf, G.R., Ahlström, A., Andrew, R.M., Bopp, L., Canadell, J.G., Ciais, P., Doney, S.C., Enright, C., Friedlingstein, P., Huntingford, C., Jain, A.K., Jourdain, C., Kato, E., Keeling, R.F., Klein Goldewijk, K., Levis, S., Levy, P., Lomas, M., Poulter, B., Raupach, M.R., Schwinger, J., Sitch, S., Stocker, B.D., Viovy, N., Zaehle, S., Zeng, N., 2013. The global carbon budget 1959–2011. *Earth Syst. Sci. Data*, 5, 165-185.
- Le Quéré, C., Moriarty, R., Andrew, R.M., Peters, G.P., Ciais, P., Friedlingstein, P., Jones, S.D., Sitch, S., Tans, P., Arneth, A., Boden, T.A., Bopp, L., Bozec, Y., Canadell, J.G., Chini, L.P., Chevallier, F., Cosca, C.E., Harris, I., Hoppe- ma, M., Houghton, R.A., House, J.I., Jain, A.K., Johannessen, T., Kato, E., Keeling, R.F., Kitidis, V., Klein Goldewijk, K., Koven, C., Landa, C.S., Landschützer, P., Lenton, A., Lima, I.D., Marland, G., Mathis, J.T., Metzl, N., Nojiri, Y., Olsen, A., Ono, T., Peng, S., Peters, W., Pfeil, B., Poulter, B., Raupach, M.R., Regnier, P., Rödenbeck, C., Saito, S., Salisbury, J.E., Schuster, U., Schwinger, J., Séférian, R., Segschneider, J., Steinhoff, T., Stocker, B.D., Sutton, A.J., Takahashi, T., Tilbrook, B., van der Werf, G.R., Viovy, N., Wang, Y.P., Wanninkhof, R., Wiltshire, A., Zeng, N., 2015. Global carbon budget 2014. *Earth Syst. Sci. Data*, 7, 47-85.
- Le Quéré, C., Peters, G.P., Andres, R.J., Andrew, R.M., Boden, T.A., Ciais, P., Friedlingstein, P., Houghton, R.A., Marland, G., Moriarty, R., Sitch, S., Tans, P., Arneth, A., Arvanitis, A., Bakker, D.C.E., Bopp, L., Canadell, J.G., Chini, L.P., Doney, S.C., Harper, A., Harris, I., House, J.I., Jain, A.K., Jones, S.D., Kato, E., Keeling, R.F., Klein Goldewijk, K., Körtzinger, A., Koven, C., Lefèvre, N., Maignan, F., Omar, A., Ono, T., Park, G.H., Pfeil, B., Poulter, B., Raupach, M.R., Regnier, P., Rödenbeck, C., Saito, S., Schwinger, J., Segschneider, J., Stocker, B.D., Takahashi, T., Tilbrook, B., van Heuven, S., Viovy, N., Wanninkhof, R., Wiltshire, A., Zaehle, S., 2014. Global carbon budget 2013. *Earth Syst. Sci. Data*, 6, 235-263.
- Levine, N.M., Doney, S.C., Wanninkhof, R., Lindsay, K., Fung, I.Y., 2008. Impact of ocean carbon system variability on the detection of temporal increases in anthropogenic CO<sub>2</sub>. *Journal of Geophysical Research: Oceans*, 113, C03019.
- Lo Monaco, C., Goyet, C., Metzl, N., Poisson, A., Touratier, F., 2005. Distribution and inventory of anthropogenic CO<sub>2</sub> in the Southern Ocean: Comparison of three data-based methods. *Journal of Geophysical Research C: Oceans*, 110, 1-12.
- Luthi, D., Le Floch, M., Bereiter, B., Blunier, T., Barnola, J.-M., Siegenthaler, U., Raynaud, D., Jouzel, J., Fischer, H., Kawamura, K., Stocker, T.F., 2008. High-resolution carbon dioxide concentration record 650,000–800,000 years before present. *Nature*, 453, 379-382.
- Macdonald, A.M., Baringer, M.O., Wanninkhof, R., Lee, K., Wallace, D.W.R., 2003. A 1998–1992 comparison of inorganic carbon and its transport across 24.5°N in the Atlantic. *Deep Sea Research Part II: Topical Studies in Oceanography*, 50, 3041-3064.
- Machín, F., Hernández-Guerra, A., Pelegrí, J.L., 2006. Mass fluxes in the Canary Basin. *Progress In Oceanography*, 70, 416-447.
- Matsumoto, K., Gruber, N., 2005. How accurate is the estimation of anthropogenic carbon in the ocean? An evaluation of the ΔC\* method. *Global Biogeochemical Cycles*, 19, GB3014.
- McCarthy, G., Frajka-Williams, E., Johns, W.E., Baringer, M.O., Meinen, C.S., Bryden, H.L., Rayner, D., Duchez, A.,

- Roberts, C., Cunningham, S.A., 2012. Observed interannual variability of the Atlantic meridional overturning circulation at 26.5°N. *Geophysical Research Letters*, 39, L19609.
- McCarthy, G.D., Smeed, D.A., Johns, W.E., Frajka-Williams, E., Moat, B.I., Rayner, D., Baringer, M.O., Meinen, C.S., Collins, J., Bryden, H.L., 2015. Measuring the Atlantic Meridional Overturning Circulation at 26°N. *Progress In Oceanography*, 130, 91-111.
- Mehrbach, C., Culberson, C.H., Hawley, J.E., Pytkowicz, R.M., 1973. Measurement of the Apparent Dissociation Constants of Carbonic Acid in Seawater at Atmospheric Pressure. *Limnology and Oceanography*, 18, 897-907.
- Mémery, L., Arhan, M., Alvarez-Salgado, X.A., Messias, M.J., Mercier, H., Castro, C.G., Rios, A.F., 2000. The water masses along the western boundary of the south and equatorial Atlantic. *Progress In Oceanography*, 47, 69-98.
- Meyer, J., Riebesell, U., 2015. Reviews and Syntheses: Responses of coccolithophores to ocean acidification: a meta-analysis. *Biogeosciences*, 12, 1671-1682.
- Mikaloff Fletcher, S.E., Gruber, N., Jacobson, A.R., Doney, S.C., Dutkiewicz, S., Gerber, M., Follows, M., Joos, F., Lindsay, K., Menemenlis, D., Mouchet, A., Müller, S.A., Sarmiento, J.L., 2006. Inverse estimates of anthropogenic CO<sub>2</sub> uptake, transport, and storage by the ocean. *Global Biogeochemical Cycles*, 20, GB2002.
- Mikaloff Fletcher, S.E., Gruber, N., Jacobson, A.R., Gloor, M., Doney, S.C., Dutkiewicz, S., Gerber, M., Follows, M., Joos, F., Lindsay, K., Menemenlis, D., Mouchet, A., Müller, S.A., Sarmiento, J.L., 2007. Inverse estimates of the oceanic sources and sinks of natural CO<sub>2</sub> and the implied oceanic carbon transport. *Global Biogeochemical Cycles*, 21, GB1010.
- Millero, F., 2006. *Chemical Oceanography*, Third Edition.
- Millero, F.J., Fiol, S., Campbell, D.M., Parrilla, G., 2000. Carbon Dioxide, Hydrographic, and Chemical Data Obtained During the R/V *Hespérides* Cruise in the Atlantic Ocean (WOCE Section A5, July 14 - August 15, 1992).
- Milliman, J., Droxler, A., 1996. Neritic and pelagic carbonate sedimentation in the marine environment: ignorance is not bliss. *Geologische Rundschau*, 85, 496-504.
- Milliman, J.D., Troy, P.J., Balch, W.M., Adams, A.K., Li, Y.H., Mackenzie, F.T., 1999. Biologically mediated dissolution of calcium carbonate above the chemical lysocline? Deep Sea Research Part I: Oceanographic Research Papers, 46, 1653-1669.
- Mintrop, L., Pérez, F.F., González-Dávila, M., Santana-Casiano, J.M., Kötzinger, A., 2000. Alkalinity determination by potentiometry: Intercalibration using three different methods. *Ciencias Marinas*, 26, 23-27. <http://hdl.handle.net/10261/25136>.
- Olafsson, J., Olafsdottir, S.R., Benoit-Cattin, A., Danielsen, M., Arnarson, T.S., Takahashi, T., 2009. Rate of Iceland Sea acidification from time series measurements. *Biogeosciences*, 6, 2661-2668.
- Olafsson, J., Olafsdottir, S.R., Benoit-Cattin, A., Takahashi, T., 2010. The Irminger Sea and the Iceland Sea time series measurements of sea water carbon and nutrient chemistry 1983–2008. *Earth Syst. Sci. Data*, 2, 99-104.
- Oudot, C., Montel, Y., 1988. A high-sensitivity method for the determination of nanomolar concentrations of nitrate and nitrite in seawater with a technicon autoanalyzer-II. *Marine Chemistry*, 24, 239–252.
- Pelejero, C., Calvo, E., Hoegh-Guldberg, O., 2010. Paleo-perspectives on ocean acidification. *Trends in Ecology & Evolution*, 25, 332-344.
- Perez, F.F., Fraga, F., 1987. A precise and rapid analytical procedure for alkalinity determination. *Marine Chemistry*, 21, 169-182.
- Pérez, F.F., Mercier, H., Vázquez-Rodríguez, M., Lherminier, P., Velo, A., Pardo, P.C., Rosón, G., Ríos, A.F., 2013. Atlantic Ocean CO<sub>2</sub> uptake reduced by weakening of the meridional overturning circulation. *Nature Geoscience*, 6, 146-152.

- Pérez, F.F., Vázquez-Rodríguez, M., Louarn, E., Padín, X.A., Mercier, H., Ríos, A.F., 2008. Temporal variability of the anthropogenic CO<sub>2</sub> storage in the Irminger Sea. *Biogeosciences*, 5, 1669-1679.
- Pérez, F.F., Vázquez-Rodríguez, M., Mercier, H., Velo, A., Lherminier, P., Ríos, A.F., 2010. Trends of anthropogenic CO<sub>2</sub> storage in North Atlantic water masses. *Biogeosciences*, 7, 1789-1807.
- Pierrot, D., Lewis, E., Wallace, D., 2006. MS Excel Program Developed for CO<sub>2</sub> System Calculations, ORNL/CDIAC-105a. Carbon Dioxide Information Analysis Center, Oak Ridge National Laboratory, US Department of Energy, Oak Ridge, Tennessee.
- Rae, J.W.B., Sarnthein, M., Foster, G.L., Ridgwell, A., Grootes, P.M., Elliott, T., 2014. Deep water formation in the North Pacific and deglacial CO<sub>2</sub> rise. *Paleoceanography*, 29, 645-667.
- Rahmstorf, S., Box, J.E., Feulner, G., Mann, M.E., Robinson, A., Rutherford, S., Schaffernicht, E.J., 2015. Exceptional twentieth-century slowdown in Atlantic Ocean overturning circulation. *Nature Clim. Change*, 5, 475-480.
- Raven, J., Caldeira, K., Elderfield, H., Hoegh-Guldberg, O., Liss, P., Riebesell, U., Shepherd, J., Turley, C., Watson, A., 2005. Ocean acidification due to increasing atmospheric carbon dioxide: The Royal Society.
- Revelle, R., Suess, H.E., 1957. Carbon Dioxide Exchange Between Atmosphere and Ocean and the Question of an Increase of Atmospheric CO<sub>2</sub> during the Past Decades. *Tellus*, 9, 18-27.
- Rhein, M., Kieke, D., Steinfeldt, R., 2015. Advection of North Atlantic Deep Water from the Labrador Sea to the southern hemisphere. *Journal of Geophysical Research: Oceans*, 120, 2471-2487.
- Riebesell, U., Zondervan, I., Rost, B., Tortell, P.D., Zeebe, R.E., Morel, F.M.M., 2000. Reduced calcification of marine plankton in response to increased atmospheric CO<sub>2</sub>. *Nature*, 407, 364-367.
- Ries, J.B., Cohen, A.L., McCorkle, D.C., 2009. Marine calcifiers exhibit mixed responses to CO<sub>2</sub>-induced ocean acidification. *Geology*, 37, 1131-1134.
- Ríos, A.F., Fraga, F., Pérez, F.F., 1989. Estimation of coefficients for the calculation of "NO", "PO" and "CO", starting from the elemental composition of natural phytoplankton. *Scientia Marina*, 53, 779-784.
- Ríos, A.F., Velo, A., Pardo, P.C., Hoppema, M., Pérez, F.F., 2012. An update of anthropogenic CO<sub>2</sub> storage rates in the western South Atlantic basin and the role of Antarctic Bottom Water. *Journal of Marine Systems*, 94, 197-203.
- Robson, J., Hodson, D., Hawkins, E., Sutton, R., 2014. Atlantic overturning in decline? *Nature Geosci*, 7, 2-3.
- Rogers, J.C., 1984. The Association between the North Atlantic Oscillation and the Southern Oscillation in the Northern Hemisphere. *Monthly Weather Review*, 112, 1999-2015.
- Rosón, G., Ríos, A.F., Pérez, F.F., Lavín, A., Bryden, H.L., 2003. Carbon distribution, fluxes, and budgets in the subtropical North Atlantic Ocean (24.5°N). *Journal of Geophysical Research: Oceans*, 108.
- Sabine, C.L., Feely, R.A., Gruber, N., Key, R.M., Lee, K., Bullister, J.L., Wanninkhof, R., Wong, C.S., Wallace, D.W.R., Tilbrook, B., Millero, F.J., Peng, T.-H., Kozyr, A., Ono, T., Ríos, A.F., 2004. The oceanic sink for anthropogenic CO<sub>2</sub>. *Science*, 305, 367-371.
- Sabine, C.L., Tanhua, T., 2010. Estimation of Anthropogenic CO<sub>2</sub> Inventories in the Ocean. *Annual Review of Marine Science*, 2, 175-198.
- Santana-Casiano, J.M., González-Dávila, M., Rueda, M.-J., Llinás, O., González-Dávila, E.-F., 2007. The interannual variability of oceanic CO<sub>2</sub> parameters in the northeast Atlantic subtropical gyre at the ESTOC site. *Global Biogeochemical Cycles*, 21, GB1015.
- Sarmiento, J.L., Orr, J.C., Siegenthaler, U., 1992. A perturbation simulation of CO<sub>2</sub> uptake in an ocean general circulation model. *Journal of Geophysical Research: Oceans*, 97, 3621-3645.

- Schmitz Jr, W.J., 1996. On the World Ocean Circulation. Volume 1. Some Global Features/North Atlantic Circulation. DTIC Document.
- Sett, S., Bach, L.T., Schulz, K.G., Koch-Klavsen, S., Lebrato, M., Riebesell, U., 2014. Temperature Modulates Cocco-lithophorid Sensitivity of Growth, Photosynthesis and Calcification to Increasing Seawater CO<sub>2</sub>. PLoS ONE, 9, e88308.
- Sigman, D.M., McCorkle, D.C., Martin, W.R., 1998. The calcite lysocline as a constraint on glacial/interglacial low-latitude production changes. *Global Biogeochemical Cycles*, 12, 409-427.
- Skjelvan, I., Falck, E., Rey, F., Kringstad, S.B., 2008. Inorganic carbon time series at Ocean Weather Station M in the Norwegian Sea. *Biogeosciences*, 5, 549-560.
- Smeed, D.A., McCarthy, G.D., Cunningham, S.A., Frajka-Williams, E., Rayner, D., Johns, W.E., Meinen, C.S., Baringer, M.O., Moat, B.I., Duce, A., Bryden, H.L., 2014. Observed decline of the Atlantic meridional overturning circulation 2004–2012. *Ocean Sci.*, 10, 29-38.
- Srokosz, M., Baringer, M., Bryden, H., Cunningham, S., Delworth, T., Lozier, S., Marotzke, J., Sutton, R., 2012. Past, Present, and Future Changes in the Atlantic Meridional Overturning Circulation. *Bulletin of the American Meteorological Society*, 93, 1663-1676.
- Srokosz, M.A., Bryden, H.L., 2015. Observing the Atlantic Meridional Overturning Circulation yields a decade of inevitable surprises. *Science*, 348.
- Steinacher, M., Joos, F., Frölicher, T.L., Plattner, G.K., Doney, S.C., 2009. Imminent ocean acidification in the Arctic projected with the NCAR global coupled carbon cycle-climate model. *Biogeosciences*, 6, 515-533.
- Steinberg, D.K., Carlson, C.A., Bates, N.R., Johnson, R.J., Michaels, A.F., Knap, A.H., 2001. Overview of the US JGOFS Bermuda Atlantic Time-series Study (BATS): a decade-scale look at ocean biology and biogeochemistry. *Deep Sea Research Part II: Topical Studies in Oceanography*, 48, 1405-1447.
- Steinfeldt, R., Rhein, M., Bullister, J.L., Tanhua, T., 2009. Inventory changes in anthropogenic carbon from 1997–2003 in the Atlantic Ocean between 20°S and 65°N. *Global Biogeochemical Cycles*, 23, GB3010.
- Steinfeldt, R., Rhein, M., Walter, M., 2007. NADW transformation at the western boundary between and. *Deep Sea Research Part I: Oceanographic Research Papers*, 54, 835-855.
- Stramma, L., Johnson, G.C., Sprintall, J., Mohrholz, V., 2008. Expanding Oxygen-Minimum Zones in the Tropical Oceans. *Science*, 320, 655-658.
- Takahashi, T., Sutherland, S.C., Sweeney, C., Poisson, A., Metzl, N., Tilbrook, B., Bates, N., Wanninkhof, R., Feely, R.A., Sabine, C., Olafsson, J., Nojiri, Y., 2002. Global sea-air CO<sub>2</sub> flux based on climatological surface ocean pCO<sub>2</sub>, and seasonal biological and temperature effects. *Deep Sea Research Part II: Topical Studies in Oceanography*, 49, 1601-1622.
- Takahashi, T., Sutherland, S.C., Wanninkhof, R., Sweeney, C., Feely, R.A., Chipman, D.W., Hales, B., Friederich, G., Chavez, F., Sabine, C., Watson, A., Bakker, D.C.E., Schuster, U., Metzl, N., Yoshikawa-Inoue, H., Ishii, M., Midorikawa, T., Nojiri, Y., Körtzinger, A., Steinhoff, T., Hoppema, M., Olafsson, J., Arnarson, T.S., Tilbrook, B., Johannessen, T., Olsen, A., Bellerby, R., Wong, C.S., Délie, B., Bates, N.R., de Baar, H.J.W., 2009. Climatological mean and decadal change in surface ocean pCO<sub>2</sub>, and net sea-air CO<sub>2</sub> flux over the global oceans. *Deep Sea Research Part II: Topical Studies in Oceanography*, 56, 554-577.
- Talley, L.D., Pickard, G.L., Emery, W.J., Swift, J.H., 2011. Chapter 9 - Atlantic Ocean. Descriptive Physical Oceanography (Sixth Edition) (pp. 245-301). Boston: Academic Press.
- Tanhua, T., Biastoch, A., Körtzinger, A., Lüger, H., Böning, C., Wallace, D.W.R., 2006. Changes of anthropogenic CO<sub>2</sub> and CFCs in the North Atlantic between 1981 and 2004. *Global Biogeochemical Cycles*, 20, GB4017.

- Tanhua, T., Körtzinger, A., Friis, K., Waugh, D.W., Wallace, D.W.R., 2007. An estimate of anthropogenic CO<sub>2</sub> inventory from decadal changes in oceanic carbon content. *Proceedings of the National Academy of Sciences*, 104, 3037-3042.
- Tanhua, T., van Heuven, S., Key, R.M., Velo, A., Olsen, A., Schirnick, C., 2010. Quality control procedures and methods of the CARINA database. *Earth system science data*, 2, 35-49.
- Tanhua, T., Waugh, D.W., Wallace, D.W.R., 2008. Use of SF6 to estimate anthropogenic CO<sub>2</sub> in the upper ocean. *Journal of Geophysical Research C: Oceans*, 113.
- Taylor, G.T., Muller-Karger, F.E., Thunell, R.C., Scranton, M.I., Astor, Y., Varela, R., Ghinaglia, L.T., Lorenzoni, L., Fanning, K.A., Hameed, S., Doherty, O., 2012. Ecosystem responses in the southern Caribbean Sea to global climate change. *Proceedings of the National Academy of Sciences*, 109, 19315-19320.
- Telszewski, M., Chazottes, A., Schuster, U., Watson, A.J., Moulin, C., Bakker, D.C.E., González-Dávila, M., Johannessen, T., Körtzinger, A., Lüger, H., Olsen, A., Omar, A., Padin, X.A., Ríos, A.F., Steinhoff, T., Santana-Casiano, M., Wallace, D.W.R., Wanninkhof, R., 2009. Estimating the monthly pCO<sub>2</sub> distribution in the North Atlantic using a self-organizing neural network. *Biogeosciences*, 6, 1405-1421.
- Thomas, H., Ittekkot, V., 2001. Determination of anthropogenic CO<sub>2</sub> in the North Atlantic Ocean using water mass ages and CO<sub>2</sub> equilibrium chemistry. *Journal of Marine Systems*, 27, 325-336.
- Touratier, F., Azouzi, L., Goyet, C., 2007. CFC-11, Δ14C and 3H tracers as a means to assess anthropogenic CO<sub>2</sub> concentrations in the ocean. *Tellus, Series B: Chemical and Physical Meteorology*, 59, 318-325.
- Touratier, F., Goyet, C., 2004. Definition, properties, and Atlantic Ocean distribution of the new tracer TrOCA. *Journal of Marine Systems*, 46, 169-179.
- Treguer, P., Le Corre, P., 1975. Manuel d'Analyse des Sels Nutritifs dans l'Eau de Mer. Utilisation de l'Autoanalyzer II Technicon (R). Laboratoire d'Oceanologie Chimique, Université de Bretagne Occidentale, Brest.
- Tsurushima, N., Nojiri, Y., Imai, K., Watanabe, S., 2002. Seasonal variations of carbon dioxide system and nutrients in the surface mixed layer at station KNOT (44°N, 155°E) in the subarctic western North Pacific. *Deep Sea Research Part II: Topical Studies in Oceanography*, 49, 5377-5394.
- Turley, C., Eby, M., Ridgwell, A.J., Schmidt, D.N., Findlay, H.S., Brownlee, C., Riebesell, U., Fabry, V.J., Feely, R.A., Gattuso, J.P., 2010. The societal challenge of ocean acidification. *Marine Pollution Bulletin*, 60, 787-792.
- van Sebille, E., Baringer, M.O., Johns, W.E., Meinen, C.S., Beal, L.M., de Jong, M.F., van Aken, H.M., 2011. Propagation pathways of classical Labrador Sea water from its source region to 26°N. *Journal of Geophysical Research: Oceans*, 116, C12027.
- Vázquez-Rodríguez, M., Padin, X.A., Pardo, P.C., Ríos, A.F., Pérez, F.F., 2012. The subsurface layer reference to calculate preformed alkalinity and air-sea CO<sub>2</sub> disequilibrium in the Atlantic Ocean. *Journal of Marine Systems*, 94, 52-63.
- Vázquez-Rodríguez, M., Padin, X.A., Ríos, A.F., Bellerby, R.G.J., Pérez, F.F., 2009a. An upgraded carbon-based method to estimate the anthropogenic fraction of dissolved CO<sub>2</sub> in the Atlantic Ocean. *Biogeosciences Discuss.*, 6, 4527.
- Vázquez-Rodríguez, M., Touratier, F., Lo Monaco, C., Waugh, D.W., Padin, X.A., Bellerby, R.G.J., Goyet, C., Metzl, N., Ríos, A.F., Pérez, F.F., 2009b. Anthropogenic carbon distributions in the Atlantic Ocean: data-based estimates from the Arctic to the Antarctic. *Biogeosciences*, 6, 439-451.
- Velo, A., Pérez, F.F., Tanhua, T., Gilcoto, M., Ríos, A.F., Key, R.M., 2013. Total alkalinity estimation using MLR and neural network techniques. *Journal of Marine Systems*, 111-112, 11-18.
- Volk, T., Hoffert, M.I., 1985. Ocean Carbon Pumps: Analysis of Relative Strengths and Efficiencies in Ocean-Driven

- Atmospheric CO<sub>2</sub> Changes. The Carbon Cycle and Atmospheric CO<sub>2</sub>: Natural Variations Archean to Present (pp. 99-110): American Geophysical Union.
- Wakita, M., Watanabe, S., Murata, A., Tsurushima, N., Honda, M., 2010. Decadal change of dissolved inorganic carbon in the subarctic western North Pacific Ocean. *Tellus B*, 62, 608-620.
- Wakita, M., Watanabe, S., Watanabe, Y., Ono, T., Tsurushima, N., Tsunogai, S., 2005. Temporal Change of Dissolved Inorganic Carbon in the Subsurface Water at Station KNOT (44°N, 155°E) in the Western North Pacific Sub-polar Region. *Journal of Oceanography*, 61, 129-139.
- Walker, G.T., Bliss, E.W., 1932. World weather. V. *Mem. Roy. Meteor. Soc.*, 4, 53-84.
- Wallace, D.W., 1995. Monitoring global ocean carbon inventories: Ocean Observing System Development Panel.
- Wanninkhof, R., Peng, T.-H., Huss, B., Sabine, C.L., Lee, K., 2003. Comparison of Inorganic Carbon System Parameters Measured in the Atlantic Ocean from 1990 to 1998 and Recommended Adjustments. Oak ridge, Tennessee: Carbon Dioxide Information Analysis Center, Oak Ridge National Laboratory, US Department of Energy.
- Watson, A.J., Nightingale, P.D., Cooper, D.J., 1995. Modelling atmosphere-ocean CO<sub>2</sub> transfer. *Philosophical Transactions - Royal Society of London*, B, 348, 125-132.
- Watson, A.J., Schuster, U., Bakker, D.C.E., Bates, N.R., Corbière, A., González-Dávila, M., Friedrich, T., Hauck, J., Heinze, C., Johannessen, T., Kötzinger, A., Metzl, N., Olafsson, J., Olsen, A., Oschlies, A., Padin, X.A., Pfeil, B., Santana-Casiano, J.M., Steinhoff, T., Telszewski, M., Rios, A.F., Wallace, D.W.R., Wanninkhof, R., 2009. Tracking the Variable North Atlantic Sink for Atmospheric CO<sub>2</sub>. *Science*, 326, 1391-1393.
- Waugh, D.W., Haine, T.W.N., Hall, T.M., 2004. Transport times and anthropogenic carbon in the subpolar North Atlantic Ocean. *Deep-Sea Research Part I: Oceanographic Research Papers*, 51, 1475-1491.
- Waugh, D.W., Hall, T.M., McNeil, B.I., Key, R., Matear, R.J., 2006. Anthropogenic CO<sub>2</sub> in the oceans estimated using transit time distributions. *Tellus, Series B: Chemical and Physical Meteorology*, 58, 376-389.
- Weaver, A.J., Sedláček, J., Eby, M., Alexander, K., Crespin, E., Fichefet, T., Philippon-Berthier, G., Joos, F., Kawamiya, M., Matsumoto, K., Steinacher, M., Tachiiri, K., Tokos, K., Yoshimori, M., Zickfeld, K., 2012. Stability of the Atlantic meridional overturning circulation: A model intercomparison. *Geophysical Research Letters*, 39.
- Yao, W., Liu, X., Byrne, R.H., 2007. Impurities in indicators used for spectrophotometric seawater pH measurements: Assessment and remedies. *Marine Chemistry*, 107, 167-172.
- Yool, A., Oschlies, A., Nurser, A.J.G., Gruber, N., 2010. A model-based assessment of the TrOCA approach for estimating anthropogenic carbon in the ocean. *Biogeosciences*, 7, 723-751.
- Zachos, J.C., Röhl, U., Schellenberg, S.A., Sluijs, A., Hodell, D.A., Kelly, D.C., Thomas, E., Nicolo, M., Raffi, I., Lourens, L.J., McCaren, H., Kroon, D., 2005. Rapid Acidification of the Ocean During the Paleocene-Eocene Thermal Maximum. *Science*, 308, 1611-1615.
- Zeebe, R.E., 2012. History of Seawater Carbonate Chemistry, Atmospheric CO<sub>2</sub>, and Ocean Acidification. *Annual Review of Earth and Planetary Sciences*, 40, 141-165.
- Zeebe, R.E., Wolf-Gladrow, (Eds.), 2001. CO<sub>2</sub> in Seawater: Equilibrium, Kinetics, Isotopes. Amsterdam: Elsevier Science, B.V.
- Zeebe, R.E., Zachos, J.C., Caldeira, K., Tyrrell, T., 2008. Carbon Emissions and Acidification. *Science*, 321, 51-52.
- Zeebe, R.E., Zachos, J.C., Dickens, G.R., 2009. Carbon dioxide forcing alone insufficient to explain Palaeocene-Eocene Thermal Maximum warming. *Nature Geosci*, 2, 576-580.
- Zunino, P., Pérez, F.F., Fajar, N.M., Guallart, E.F., Ríos, A.F., Pelegrí, J.L., Hernández-Guerra, A., 2015. Transports and budgets of anthropogenic CO<sub>2</sub> in the tropical North Atlantic in 1992–1993 and 2010–2011. *Global Biogeochemical Cycles*, 29, 1075-1091.



# Appendix I

Guallart, E. F., F. F. Pérez, G. Rosón, and A. F. Ríos. 2013. High spatial resolution alkalinity and pH measurements by IIM-CSIC group along 24.5°N during the R/V Hespérides WOCE Section A05 cruise (July 14 - August 15, 1992).  
[http://cdiac.ornl.gov/ftp/ndp074/IIM\\_CSIC\\_data](http://cdiac.ornl.gov/ftp/ndp074/IIM_CSIC_data). Carbon Dioxide Information Analysis Center, Oak Ridge National Laboratory, US Department of Energy, Oak Ridge, Tennessee.  
doi: 10.3334/CDIAC/OTG.IIM\_CSIC\_WOCE\_A05



## CONTENTS

LIST OF FIGURES	248
LIST OF TABLES	249
ABREVIATIONS AND ACRONYMS	250
ABSTRACT	251
1. BACKGROUND INFORMATION	252
2. DESCRIPTION OF THE EXPEDITION	254
3. DESCRIPTION OF METHODS FOR CARBON PARAMETERS	254
3.1. <i>CO<sub>2</sub> parameters measurements</i>	254
4. DATA EVALUATION	257
4.1. <i>Linear correlations between RSMAS and IIM carbon datasets</i>	257
4.2. <i>Crossover analysis</i>	257
5. RESULTS	262
5.1. <i>Carbon species distribution along A05 section</i>	262
5.2. <i>CO<sub>2</sub> variables along the Florida Strait</i>	266
6. REFERENCES	268

## LIST OF FIGURES

1. *Fig 1.* Cruise track of the WOCE A05 section on board the R/V BIO Hespérides. 253
2. *Fig 2.* Sampling stations and depths for CO<sub>2</sub> measurements along WOCE section A05. 2a) Sampling stations performed by IIM CO<sub>2</sub> group for pH<sub>NBS15</sub> and total alkalinity (A<sub>T</sub>) concentration determinations. 2b) Sampling stations performed by RSMAS CO<sub>2</sub> group 255
3. *Fig 3.* C<sub>T</sub> (upper panel), A<sub>T</sub> (middle panel) and pH<sub>SWS25</sub> (lower panel) linear correlations between final RSMAS and IIM datasets for values obtained along the A05 section in 1992. Linear regression, coefficient of determination ( $r^2$ ) for each parameter and the averaged difference  $\pm$  standard deviation (IIM-RSMAS) found are shown in red. 258
4. *Fig 4.* C<sub>T</sub> (upper panel), A<sub>T</sub> (middle panel) and pH<sub>SWS25</sub> (lower panel) crossover analysis results for the IIM CO<sub>2</sub> database. Mean and standard deviation of the offset between cruises (black) and corrective adjustment found for each parameter studied using least square models (red line). 260
5. *Fig 5.* Dissolved inorganic carbon (C<sub>T</sub>) concentration along A05 section in 1992: IIM (upper panel) and IIM<sub>QCed</sub> (lower panel) data. 263
6. *Fig 6.* Total alkalinity (A<sub>T</sub>) concentration along A05 section in 1992: IIM (upper panel) and IIM<sub>QCed</sub> (lower panel) fields. 264
7. *Fig 7.* Fields of pH distributions in the seawater scale and referred to 25°C (pH<sub>SWS25</sub>) along A05 section in 1992: IIM (upper panel) and IIM<sub>QCed</sub> (lower panel) data. 265
8. *Fig 8.* Dissolved inorganic carbon (C<sub>T</sub>, left panel), total alkalinity (A<sub>T</sub>, middle panel) and pH (pH<sub>SWS25</sub>, right panel) distributions of the IIM<sub>QCed</sub> data along the Florida Strait. 267

## LIST OF TABLES

1. *Table 1.* Summary of CO<sub>2</sub> system stations sampled by IIM group during the cruise. (\*) Sampled parameter, (-) No sampled parameter. 256
2. *Table 2.* Selected cruises to perform the crossover analysis in 1992 WOCE A05 carbon datasets, following CARINA secondary Quality Control (2nQC) procedures. 259
3. *Table 3.* Corrective adjustments found following CARINA second quality control procedures for C<sub>T</sub>, A<sub>T</sub> and pH in each (RSMAS, IIM) carbon dataset studied. 259

## ABBREVIATIONS AND ACRONYMS

2ndQC	Secondary Quality Control
AAIW	Antarctic Intermediate Water
AABW	Antarctic Bottom Water
AMOC	Atlantic Meridional Overturning Circulation
$A_T$	Total Alkalinity
$^{14}\text{C}$	Radiocarbon
$\text{CaCO}_3$	Calcium carbonate
$C_{\text{ANT}}$	Anthropogenic $\text{CO}_2$
CFCs	Chlorofluorocarbons
CARINA	CARbon IN the Atlantic
CCHDO	Carbon Hydrographic Data Office
CDIAC	Carbon Dioxide Information Analysis Center
CLIVAR	The Climate Variability and Predictability
$\text{CO}_2$	Carbon dioxide
$\text{CO}_3^{2-}$	Carbonate ion
CRM	Certified Reference Material
CSIC	Consejo Superior de Investigaciones Científicas
$C_T$	Dissolved Inorganic Carbon
GLODAP	Global Ocean Data Analysis
IIM	Instituto de Investigaciones Marinas
LSW	Labrador Sea Water
NADW	North Atlantic Deep Water
NBS	National Bureau of Standards
$\text{pH}_{\text{NBS15}}$	pH on the NBS scale and referred to 15°C
$\text{pH}_{\text{SWS25}}$	pH on the SWS and referred to 25°C
QCed	Quality controlled
RSMAS	Rosenstiel School of Marine and Atmospheric Science
SWS	Sea Water Scale
U.S.A.	United States of America
WAVES	Web Accessible Visualization and Extraction System
WCRP	World Climate Research Programme
WOCE	World Ocean Circulation Experiment

## ABSTRACT

Guallart, E. F., F. F. Pérez, G. Rosón, and A. F. Ríos. 2013. High spatial resolution alkalinity and pH measurements by IIM-CSIC group along 24.5°N during the R/V Hespérides WOCE Section A05 cruise (July 14 - August 15, 1992). [http://cdiac.ornl.gov/ftp/ndp074/IIM\\_CSIC\\_data](http://cdiac.ornl.gov/ftp/ndp074/IIM_CSIC_data). Carbon Dioxide Information Analysis Center, Oak Ridge National Laboratory, US Department of Energy, Oak Ridge, Tennessee. doi: 10.3334/CDIAC/OTG.IIM\_CSIC\_WOCE\_A05

This report presents the carbon dataset collected during the R/V BIO Hespérides oceanographic cruise along 24.5°N latitude (WOCE A05 section) in 1992, by the Instituto de Investigaciones Marinas (IIM) CO<sub>2</sub> group. The IIM CO<sub>2</sub> dataset has never been reported in public databases though has already been used in three works on carbon transports and distributions across the 24.5°N section in the North Atlantic (Brown *et al.*, 2010; Macdonald *et al.*, 2003; Rosón *et al.*, 2003). It consists in dissolved inorganic carbon (C<sub>T</sub>) calculated from total alkalinity (A<sub>T</sub>) and pH direct potentiometric measurements performed in 107 stations of the section that include the sampling of the Florida Strait for CO<sub>2</sub> measurements. The current CO<sub>2</sub> dataset reported for the WOCE A05 in the CLIVAR & Carbon Hydrographic Data Office (CCHDO) and the Carbon Dioxide Information Analysis Center (CDIAC) was collected at 33 stations of the same cruise, by the Rosenstiel School of Marine and Atmospheric Science (RSMAS) and consists in C<sub>T</sub>, A<sub>T</sub> and pH direct measurements from titrations of seawater. Due to the better spatial coverage achieved in the IIM dataset in relation to the available one on CDIAC and CCHDO sites, this work aims to provide these CO<sub>2</sub> data together with a quality control analysis. With this purpose, the IIM dataset was subjected to a secondary quality control (2ndQC) following the procedures used in CARINA (CARbon IN the Atlantic), which basically consisted in crossovers analysis to quantify possible systematic biases. After the crossover analysis the data were bias-adjusted by -4.μmol kg<sup>-1</sup> for A<sub>T</sub> and -0.009 units for pH. The IIM quality controlled dataset measurements allows to obtain high spatial resolution C<sub>T</sub>, A<sub>T</sub>, and pH distributions along the WOCE A05 section.

Keywords: Carbon dioxide, pH, alkalinity, carbon cycle, World Ocean Circulation Experiment, hydrographic measurements, quality control, North Atlantic Ocean.

## I. BACKGROUND INFORMATION

The ocean plays an important role as a sink for carbon dioxide ( $\text{CO}_2$ ) released to the atmosphere. At least, oceans have absorbed about one third of all anthropogenic  $\text{CO}_2$  emissions produced in the last three centuries (Sabine *et al.*, 2004) and, in this context, the North Atlantic Ocean plays an important part in absorbing, and especially accumulating, emitted  $\text{CO}_2$  (Vázquez-Rodríguez *et al.*, 2009). This basin is considered to contain 23% of the global oceanic anthropogenic  $\text{CO}_2$  (Sabine *et al.*, 2004) so it is crucial in its penetration and balancing in the whole ocean. Once  $\text{CO}_2$  is in solution, dissolved inorganic carbon ( $\text{C}_\text{T}$ ) levels rise and chemical balances of the  $\text{CO}_2$  system in seawater are affected leading to the formation of hydrogen ions that lower seawater pH while consuming carbonate ( $\text{CO}_3^{2-}$ ) ions. These ions control the rate of calcium carbonate ( $\text{CaCO}_3$ ) precipitation and dissolution in the ocean, which in turn constrain the amount of carbon that is buried in the sediments during extended periods of time. Overall, the atmospheric  $\text{CO}_2$  removing capacity of the ocean will decrease in the future as a consequence of the continuous oceanic entrance of atmospheric  $\text{CO}_2$  (Feely *et al.*, 2004). But, how marine carbon cycle will evolve in the future is still one of the main issues in Ocean Sciences (Sabine and Tanhua, 2009).

In the nineties, the World Ocean Circulation Experiment (WOCE), as a part of the World Climate Research Programme (WCRP), was the first attempt to study physical processes that affect oceanic circulation globally and, together with the inclusion of systematic chemical measurements and the repetition of some of these sections through time, allow describing trends of different seawater variables. Regarding  $\text{CO}_2$  system dynamics in seawater, large amounts of direct  $\text{C}_\text{T}$  and total alkalinity ( $\text{A}_\text{T}$ ) measurements have been collected since a few decades ago.

Included in the WOCE project, the WOCE A05 section, across 24.5°N in the North Atlantic subtropical gyre (Fig. 1), has been occupied several times since 1957, allowing multi-decadal-scale variability studies which were specially focused in the meridional transport of mass and heat. In 1992, the section was included in the net of selected hydrographic cruises to be studied within the frame of the WOCE Project and high spatial resolution in situ carbon system measurements were taken for the first time. Since then, five occupations have been conducted, in 1992, 1998, 2004, 2010 and 2011, providing a great opportunity to analyze and quantify changes in pH, carbon budget, and natural and anthropogenic carbon in the North Atlantic. In 1992, two different carbon system datasets were obtained: a shorter one, of  $\text{C}_\text{T}$  and  $\text{A}_\text{T}$  measurements, taken by the group of the Rosenstiel School of Marine and Atmospheric Science (RSMAS) University of Miami, Florida, which was reported in the CLIVAR & Carbon Hydrographic Data Office (CCHDO) and the Carbon Dioxide Information Analysis Center (CDIAC) databases after an accurate quality control (Millero *et al.*, 2000); and a larger dataset, consisting in pH and  $\text{A}_\text{T}$  measurements, obtained by the  $\text{CO}_2$  group of the Instituto de Investigaciones Marinas (IIM-CSIC) of Vigo, Spain. This last dataset has never been reported in global hydrographic data centers despite having been quality controlled, also, in the first Atlantic synthesis

on carbon measurements from 1990 to 1998 (Wanninkhof *et al.*, 2003) that supposed a big effort to assess the consistency of large-scale inorganic carbon data among the different cruises performed during this time period. In addition, the IIM dataset has been used in three studies (Brown *et al.*, 2010; Macdonald *et al.*, 2003; Rosón *et al.*, 2003) where  $C_T$ ,  $A_T$  and anthropogenic  $\text{CO}_2$  meridional fluxes in the North Atlantic were analyzed. Since this dataset includes four times more data than the available in CCHDO or CDIAC, it allows to reduce uncertainties in the estimations of  $C_T$  fluxes and inventories, and enables a better description of the carbon system variables over time along the A05 section.

Due to the better spatial coverage of the section in the IIM  $\text{CO}_2$  dataset, our main goal with this report is to review and refine these  $\text{CO}_2$  system measurements to enlarge the available North Atlantic  $\text{CO}_2$  information for future carbon studies.

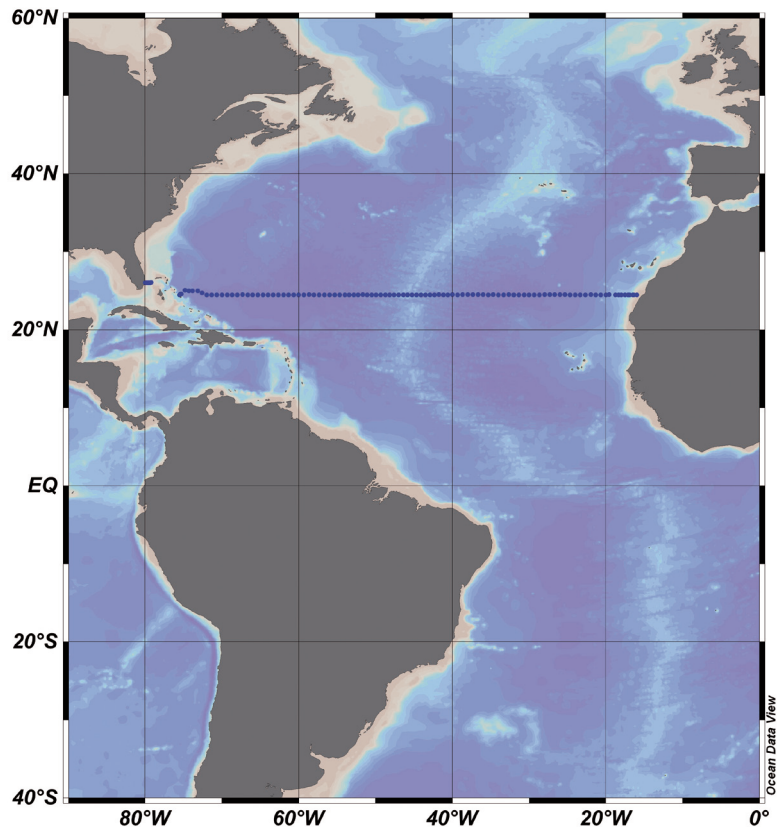


**Fig I.** Cruise track of the WOCE A05 section on board the R/V BIO Hespérides.

## 2. DESCRIPTION OF THE EXPEDITION

The cruise HE06 (WOCE A05 section) was carried out between 14 July and 15 August 1992 along 24°N on board the R/V Hespérides from Cadiz (Spain) to Miami (Florida, U.S.A.). Full-depth CTD profiles were performed at 112 hydrographic stations. At each station, water samples were taken at different depths for different chemical analyses including salinity, oxygen, nutrients, chlorofluorocarbons (CFCs), pH,  $A_T$ ,  $C_T$ , primary production, aluminium and radiocarbon ( $^{14}\text{C}$ ). The cruise track and station locations are shown in Fig. 1. A detailed description of the cruise can be found in (Millero *et al.*, 2000): [http://cdiac.ornl.gov/oceans/ndp\\_074/](http://cdiac.ornl.gov/oceans/ndp_074/).

## 3. DESCRIPTION OF METHODS FOR CARBON PARAMETERS

### 3.1. $\text{CO}_2$ parameters measurements

The IIM group took inorganic  $\text{CO}_2$  measurements of seawater in almost each station of the section (Fig. 2a), by sampling 107 full depth profiles for  $A_T$  and pH analysis. All the sampled stations are summarized in Table 1 and procedures for chemical analysis are described in (Rosón *et al.*, 2003). The pH was measured potentiometrically in the NBS scale with a combined glass electrode associated to a thermo-compensator and referred to 15°C (Perez and Fraga, 1987a). The method had a shipboard precision of 0.005 units, based on 184 replicate analysis corresponding to two different oceanographic bottles fired at the same depth at each station (Ríos and Rosón, 1996).  $A_T$  measurements were made by titration of seawater with potentiometric endpoint detection (Perez and Fraga, 1987b), reaching a precision of  $\pm 1 \mu\text{mol kg}^{-1}$ . Total dissolved inorganic carbon was calculated from measured  $\text{pH}_{\text{NBS15}}$  and  $A_T$  using equilibrium constants of (Mehrbach *et al.*, 1973) and the boric acid constants reported by (Lyman, 1956). The calculations were checked for accuracy three times during the cruise against Dickson standards of seawater, comparing estimated  $C_T$  from pH and  $A_T$  measurements done in a number of samples of the Certified Reference Materials (CRMs, Batch#12) with the certified  $C_T$  concentration given for that batch ( $1984 \mu\text{mol kg}^{-1}$ ). Following this methodology, both analytical errors of pH ( $\pm 0.005$ ) (Perez and Fraga, 1987a) and  $A_T$  ( $\pm 2 \mu\text{mol kg}^{-1}$ ) (Perez and Fraga, 1987b) produce together an error of  $\pm 4 \mu\text{mol kg}^{-1}$  in  $C_T$  calculations (Zirino, 1985).

In the RSMAS dataset,  $C_T$ ,  $A_T$ , and pH were determined from titrations of seawater samples collected at 33 stations of the whole section (Fig. 2b). The titration systems were calibrated with CRMs. Procedures followed for sample analysis are described in (Millero *et al.*, 2000). They basically consisted in the use of three titration systems to determine  $A_T$  and  $C_T$ . The pH values were determined in the seawater scale, from the initial titrations voltage reading relative to TRIS buffers. The accuracy/precision of the measured parameters was estimated to be  $\pm 7 \mu\text{mol kg}^{-1}/\pm 2 \mu\text{mol kg}^{-1}$  for  $A_T$ ,  $\pm 7 \mu\text{mol kg}^{-1}/\pm 5 \mu\text{mol kg}^{-1}$  for  $C_T$ , and  $\pm 0.02/\pm 0.005$  for pH. This carbon dataset followed the corresponding quality review at the Carbon Dioxide Information Analysis Center (CDIAC) ensuring proper data examination to supply accurate carbon information for researchers.

The full dataset is available at the CDIAC website ([http://cdiac.ornl.gov/oceans/ndp\\_074/](http://cdiac.ornl.gov/oceans/ndp_074/)) or at the CCHDO website ([http://cchdo.ucsd.edu/cruise/29HE06\\_1](http://cchdo.ucsd.edu/cruise/29HE06_1)). The quality controlled version of the dataset, without questionable or bad measurements, is available on the Global Ocean Data Analysis (GLODAP) bottle database search tool: Web Accessible Visualization and Extraction System (WAVES, <http://cdiac3.ornl.gov/waves/discrete/>) through the OUTPUT option.

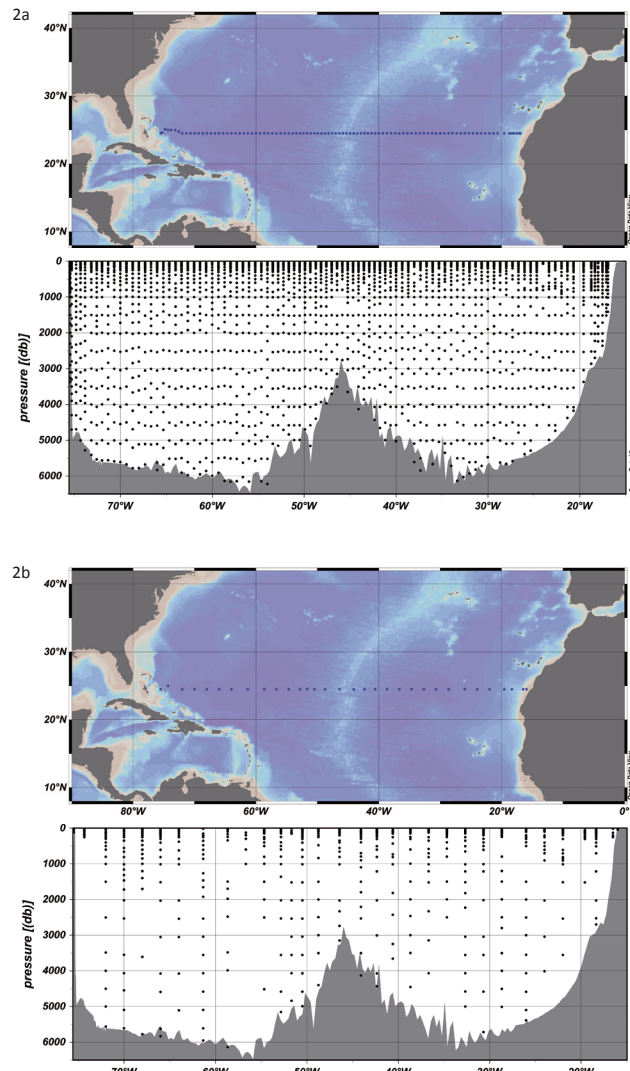


**Fig 2.** Sampling stations and depths for  $\text{CO}_2$  measurements along WOCE section A05. 2a) Sampling stations performed by IIM  $\text{CO}_2$  group for  $\text{pH}_{\text{NBSIS}}$  and total alkalinity ( $A_T$ ) concentration determinations. 2b) Sampling stations performed by RSMAS  $\text{CO}_2$  group for alkalinity ( $A_T$ ) and dissolved inorganic carbon ( $C_T$ ) determinations.

Station	Longitude [°E]	Latitude [°N]	Bottom Depth [m]	Absolutinity	PHMSL5	Date	Station	Longitude [°E]	Latitude [°N]	Bottom Depth [m]	Absolutinity	PHMSL5	Date	Station	Longitude [°E]	Latitude [°N]	Bottom Depth [m]	Absolutinity	PHMSL5	Date
1	-15.97	24.50	53	*	-	20/7/2012	39	-38.01	24.51	5066	*	*	30/7/2012	77	-61.33	24.49	5965	*	*	8/8/2012
2	-16.41	24.50	117	*	-	20/7/2012	40	-38.66	24.51	4580	*	*	30/7/2012	78	-61.99	24.49	5227	*	*	8/8/2012
3	-16.50	24.50	575	*	-	20/7/2012	41	-59.33	24.49	4194	*	*	31/7/2012	79	-62.66	24.50	5988	*	*	9/8/2012
4	-16.93	24.50	1545	*	-	21/7/2012	42	-40.00	24.51	5139	*	*	31/7/2012	80	-63.34	24.50	5928	*	*	9/8/2012
5	-17.09	24.50	1936	*	-	21/7/2012	43	-40.58	24.50	4551	*	*	31/7/2012	81	-64.00	24.50	5858	*	*	9/8/2012
6	-17.51	24.49	2407	*	*	21/7/2012	44	-41.16	24.50	5195	*	*	31/7/2012	82	-64.67	24.50	5791	*	*	10/8/2012
7	-18.00	24.50	2224	*	*	21/7/2012	45	-41.75	24.51	4640	*	*	18/8/2012	83	-65.33	24.49	5769	*	*	10/8/2012
8	-18.34	24.49	2736	*	*	21/7/2012	46	-42.33	24.50	4410	*	*	18/8/2012	84	-66.00	24.50	5832	*	*	10/8/2012
9	-18.75	24.50	2948	*	*	21/7/2012	47	-42.91	24.50	3605	*	*	18/8/2012	85	-66.66	24.51	5705	*	*	11/8/2012
10	-	-	-	-	-	22/7/2012	48	-43.50	24.50	3867	*	*	18/8/2012	86	-67.32	24.52	5734	*	*	11/8/2012
11	-19.58	24.51	3393	*	*	22/7/2012	49	-44.08	24.50	4182	*	*	18/8/2012	87	-68.00	24.50	5805	*	*	11/8/2012
12	-20.00	24.50	3755	*	*	23/7/2012	50	-44.67	24.50	2999	*	*	28/8/2012	88	-68.66	24.50	5784	*	*	11/8/2012
13	-20.67	24.50	4186	*	*	23/7/2012	51	-45.25	24.51	3658	*	*	28/8/2012	89	-69.33	24.50	5685	*	*	12/8/2012
14	-21.33	24.50	4379	*	*	23/7/2012	52	-45.83	24.50	2777	*	*	28/8/2012	90	-70.00	24.50	5626	*	*	12/8/2012
15	-21.98	24.51	4705	*	*	24/7/2012	53	-46.41	24.49	3518	*	*	28/8/2012	91	-70.66	24.49	5694	*	*	12/8/2012
16	-22.67	24.50	4663	*	*	24/7/2012	54	-47.00	24.50	3727	*	*	28/8/2012	92	-71.33	24.50	5582	*	*	12/8/2012
17	-23.34	24.50	4914	*	*	24/7/2012	55	-47.58	24.50	4021	*	*	3/9/2012	93	-72.00	24.50	5571	*	*	12/8/2012
18	-24.00	24.50	5149	*	*	24/7/2012	56	-48.16	24.49	3930	*	*	3/9/2012	94	-72.57	24.75	5559	*	*	13/8/2012
19	-24.67	24.50	5120	*	*	25/7/2012	57	-48.73	24.50	4541	*	*	3/8/2012	95	-73.17	24.99	5401	*	*	13/8/2012
20	-25.34	24.51	5339	*	*	25/7/2012	58	-49.33	24.50	5159	*	*	3/8/2012	96	-73.84	25.00	5288	*	*	13/8/2012
21	-26.00	24.51	5297	*	*	25/7/2012	59	-49.91	24.50	4758	*	*	3/8/2012	97	-74.33	25.01	4994	*	*	13/8/2012
22	-26.67	24.51	4715	*	*	26/7/2012	60	-50.49	24.50	4975	*	*	4/8/2012	98	-74.82	25.10	4730	*	*	14/8/2012
23	-27.32	24.51	5595	*	*	26/7/2012	61	-51.08	24.50	5040	*	*	4/8/2012	99	-75.46	24.55	3341	*	*	14/8/2012
24	-28.00	24.52	5669	*	*	26/7/2012	62	-51.66	24.51	4888	*	*	4/8/2012	100	-76.30	24.61	4831	*	*	14/8/2012
25	-28.65	24.50	5723	*	*	26/7/2012	63	-52.25	24.50	4789	*	*	4/8/2012	101	-75.52	24.50	1040	*	*	14/8/2012
26	-29.33	24.50	4862	*	*	27/7/2012	64	-52.83	24.50	5231	*	*	5/8/2012	102	-79.23	26.07	362	*	*	15/8/2012
27	-30.01	24.50	5479	*	*	27/7/2012	65	-53.41	24.50	5638	*	*	5/8/2012	103	-79.31	26.05	496	*	*	15/8/2012
28	-30.67	24.50	5617	*	*	27/7/2012	66	-54.00	24.50	6226	*	*	5/8/2012	104	-79.40	26.06	601	*	*	15/8/2012
29	-31.34	24.50	5717	*	*	28/7/2012	67	-54.67	24.50	6275	*	*	5/8/2012	105	-79.48	26.06	685	*	*	15/8/2012
30	-32.00	24.50	5817	*	*	28/7/2012	68	-55.33	24.50	5614	*	*	6/8/2012	106	-79.57	26.06	772	*	*	15/8/2012
31	-32.67	24.51	6426	*	*	28/7/2012	69	-56.00	24.50	6566	*	*	6/8/2012	107	-79.67	26.06	708	*	*	15/8/2012
32	-33.34	24.51	6191	*	*	28/7/2012	70	-56.67	24.50	6024	*	*	6/8/2012	108	-79.77	26.06	397	*	*	15/8/2012
33	-34.00	24.50	5737	*	*	29/7/2012	71	-57.34	24.49	6116	*	*	6/8/2012	109	-79.85	26.03	321	*	*	15/8/2012
34	-34.68	24.51	5354	*	*	29/7/2012	72	-58.01	24.49	6209	*	*	7/8/2012	110	-79.93	26.05	262	*	*	15/8/2012
35	-35.33	24.50	4966	*	*	29/7/2012	73	-58.67	24.51	6145	*	*	7/8/2012	111	-80.00	26.05	256	*	*	15/8/2012
36	-36.01	24.51	5747	*	*	29/7/2012	74	-59.33	24.50	5903	*	*	7/8/2012	112	-80.07	26.05	128	*	*	16/8/2012
37	-36.66	24.51	5008	*	*	30/7/2012	75	-60.00	24.50	6095	*	*	8/8/2012							
38	-37.33	24.51	5872	*	*	30/7/2012	76	-60.67	24.50	5867	*	*	8/8/2012							

Table 1. Summary of CO<sub>2</sub> system stations sampled by IIM group during the cruise. (\*) No sampled parameter, (-) No sampled parameter.

## 4. DATA EVALUATION

The quality of the CO<sub>2</sub> data was rechecked in both CO<sub>2</sub> datasets and the consistency between them was also evaluated. To this end, final CO<sub>2</sub> data from the RSMAS group was obtained through the OUTPUT option of the WAVES search system and compared to the also final IIM CO<sub>2</sub> data in terms of C<sub>T</sub>, A<sub>T</sub> and pH. In the case of pH some calculations had to be done in order to work with comparable data: measured pH<sub>NBS15</sub> from the IIM dataset was converted to the Sea Water Scale (SWS) and referred to 25°C, obtaining the variable pH<sub>SWS25</sub>. This last parameter was calculated for the RSMAS dataset from C<sub>T</sub> and A<sub>T</sub> measurements with dissociation constants of (Mehrbach *et al.*, 1973) refitted by (Dickson and Millero, 1987) and boric acid constants from (Dickson, 1990) using CO2sys program (Pierrot *et al.*, 2006) because no measured pH data was available in the final version of the RSMAS dataset obtained from GLODAP. Measured A<sub>T</sub> values, for both cases, could be compared directly. For C<sub>T</sub>, comparisons were performed directly, too, despite being a calculated parameter in the IIM dataset, as the change in scale was performed keeping invariable C<sub>T</sub>. Thus, values did not need to be recalculated.

### 4.1. Linear correlations between RSMAS and IIM carbon datasets

As a first step, linear correlations were performed between C<sub>T</sub>, A<sub>T</sub> and pH from each dataset. Results are shown in Figure 3. The three carbon parameters showed good agreement. Regression coefficients and the coefficient of determination found were 0.99 ( $r^2=0.96$ ) for C<sub>T</sub>, 0.96 ( $r^2=0.98$ ) for A<sub>T</sub> and 0.99 ( $r^2=0.98$ ) for pH<sub>SWS25</sub>. All p-values were smaller than 2.2e-16. Averaged differences ± Standard deviation (IIM-RSMAS) were 1±11.5 µmol kg<sup>-1</sup> for C<sub>T</sub>, -2.3±6 µmol kg<sup>-1</sup> for A<sub>T</sub>, and 0.007±0.021 units for pH<sub>SWS25</sub>.

### 4.2. Crossover analysis

Both datasets were gone through secondary quality control (2ndQC) procedures used in CARINA (CARbon IN the Atlantic) which involve crossovers analysis to quantify possible systematic biases (Key *et al.*, 2010; Tanhua *et al.*, 2010). Thus, both datasets were compared with different historical cruises that have taken place intersecting the 24.5°N section somewhere along its defined transect. Table 2 summarizes the list of selected cruises to carry out the 2ndQC.

Crossover analyses between both WOCE A05 carbon datasets (RSMAS and IIM) and each one of the other considered sections were carried comparing data values below 1500 dbar for stations that were located within two degrees of latitude. The following parameters were checked: A<sub>T</sub>, C<sub>T</sub>, and pH<sub>SWS25</sub>. As a result of this analysis, a mean and standard deviation of the offset, defined as the difference between two cruises, was quantified in each comparison, for each of the given carbon parameters. Then, the offsets derived were used to calculate an additive adjustment for C<sub>T</sub>, A<sub>T</sub>, and pH data in both datasets using least square models. The corrections obtained are summarized in Table 3. Figure 4 shows the cruise to cruise offsets found for the IIM dataset and the final adjustment obtained, for each carbon parameter.

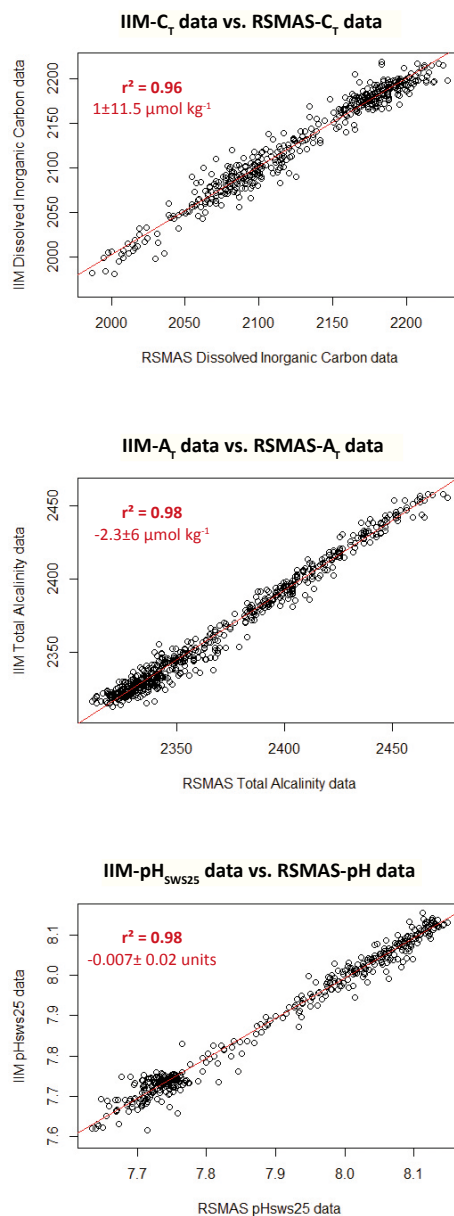


**Fig 3.** C<sub>T</sub> (upper panel), A<sub>T</sub> (middle panel) and pH<sub>SWS25</sub> (lower panel) linear correlations between final RSMAS and IIM datasets for values obtained along the A05 section in 1992. Linear regression, coefficient of determination ( $r^2$ ) for each parameter and the averaged difference  $\pm$  standard deviation (IIM-RSMAS) found are shown in red.

**Table 2.** Selected cruises to perform the crossover analysis in 1992 WOCE A05 carbon datasets, following CARINA secondary Quality Control (2nQC) procedures.

CARINA Cruise ID	New Expocode	Synonyms (includes old expocode)	Ship	Cruise Name	Chief Scientist	Carbon P.I.
32	06MT20040311	06MT20040311	Meteor	M60-5	D.Wallace	D.Wallace
63	29HE20030408	29HE091; FICA-RAM VI	Hesperides	FICARAM VI	A.F.Rios	A.F.Rios, R.Wanninkhof
68	316N20030922	316N20030922	Knorr	North Atlantic	J. Swift	-
69	316N20031023	316N20031023	Knorr	North Atlantic	J. Swift	-
85	33RO19980123	33RO19980123	-	-	-	-
86	33RO20030604	33RO2003060	Ronald H. Brown	Atlantic Ocean	-	-
172	74DI19980423	74DI233	Discovery	-	Smythe-Wright	M.Alvarez, I.S.Aristegui
173	74DI20040404	74DI20040404	Discovery	Atlantic zonal section at 24.5N	S. Cunningham	U. Schuster

<http://carina.geomar.de/cruises/list>

GLODAP Cruise ID	New Expocode	Synonyms (includes old expocode)	Ship	Cruise Name	Chief Scientist	Carbon P.I.
9	29HE06_1-3	29HE06_1-3 (A05)	BIO Hesperides		G. Parrilla	F.Millero, A.F.Rios
25	316N151_3	316N151_3 (A20)	RV Knorr		R.Pickart	F.Millero, C.Sabine, D.Wallace
26	316N151_4	316N151_4 (A22)	RV Knorr		T.Joyce	F.Millero, C.Sabine, D.Wallace
23	OACES93, 3175MB93	OACES93 (A16Na, AR21),NATL-93	Baldridge	OACES 93	R.Wanninkhof	F.Millero, R.Feely
45	TTO-NAS	316N19810401(L1), 316N19810416(L2), 316N19810516(L3), 316N19810721(L4), 316N19810619(L5), 316N19810821(L6), 316N19810923(L7)	RV Knorr	ANAS	P.Brewer(L1), J.Sarmiento(L2), L.Armi(L3), W.Broecker(L4), T.Takahashi(L5), W.Jenkins(L6), P.Brewer(L7)	P.Brewer, T.Takahashi
46	TTO-TAS	316N198212_1(L1), 316N198212_2(L2), 316N198301(L3)	RV Knorr	ATAS	J.Sarmiento(L1), C.Rooth(L2), T.Takahashi(L3)	T.Takahashi

<http://cdiac.ornl.gov/oceans/glodap/AtTable1.html>

**Table 3.** Corrective adjustments found following CARINA second quality control procedures for  $C_T$ ,  $A_T$  and pH in each (RSMAS, IIM) carbon dataset studied.

Adjustments			
	$A_T$	$C_T$	pH <sub>sws25</sub>
RSMAS	2.6	0.4	0.011
IIM	4.0	1.0	0.009

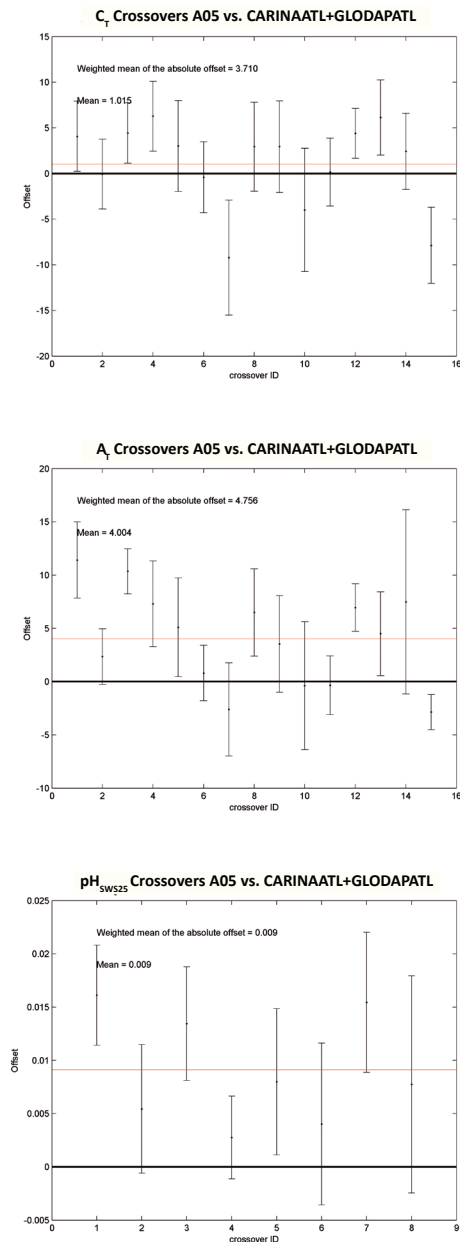


**Fig. 4.**  $C_T$  (upper panel),  $A_T$  (middle panel) and  $pH_{SW525}$  (lower panel) crossover analysis results for the IIM  $\text{CO}_2$  database. Mean and standard deviation of the offset between cruises (black) and corrective adjustment found for each parameter studied using least square models (red line).

In the first work where the IIM dataset was gone under quality control, no adjustments were proposed for any of the parameters studied (Wanninkhof *et al.*, 2003). GLODAP procedures recommended an offset of 4  $\mu\text{mol kg}^{-1}$  for  $C_T$  and 6  $\mu\text{mol kg}^{-1}$  for  $A_T$  to take into consideration a change in measured data and no tips or bias thresholds were proposed in the case of pH. Thus, the dataset was considered to be inside quality requirements of GLODAP and no adjustments were proposed. Following CARINA procedures, offsets of 4  $\mu\text{mol kg}^{-1}$  for  $C_T$ , 6  $\mu\text{mol kg}^{-1}$  for  $A_T$  and 0.005 units for  $\text{pH}_{\text{SWS25}}$  are suggested to be apply as the best adjustment (Key *et al.*, 2010). In the case of the IIM dataset, the measured data were biased by 4.0  $\mu\text{mol kg}^{-1}$  for  $A_T$  and by 0.009 units for  $\text{pH}_{\text{SWS25}}$ . The  $C_T$  calculated from the two previous parameters with dissociation constants of (Mehrbach *et al.*, 1973) refitted by (Dickson and Millero, 1987) and boric acid constants from (Dickson, 1990) had an offset of 1.0  $\mu\text{mol kg}^{-1}$ . From these results, it can be concluded that both quality control procedures were consistent for IIM  $C_T$  and  $A_T$ . Nevertheless, taking into account the recommended minimum offsets to adjust carbon data in CARINA,  $\text{pH}_{\text{SWS25}}$  measurements should be improved.

In this context, it should be taken into consideration that, over the last few years ocean  $\text{CO}_2$  research, this has evolved from classical studies based only on  $\text{CO}_2$  inventories and transports estimations, where the amount of  $C_T$  data and its accuracy were the most critical considerations, to a wider range of research topics that are focused in other  $\text{CO}_2$  variables, such as pH or carbonate saturation levels. In this sense, following the CARINA advice, the IIM measured pH should be adjusted to reduce the offset of 0.009 units that almost doubles the recommended threshold and could lead to errors if data are used in works where pH changes are evaluated. Furthermore, as not all  $A_T$  titrations performed during the cruise were calibrated with CRMs (Rosón *et al.*, 2003), we have considered better to apply also the adjustment to  $A_T$  data in order to reduce the bias and avoid new bias in the original calculated  $C_T$ , that showed to have accurate levels according to crossovers, due to a reduction of pH values without changing alkalinity. Consequently,  $A_T$  and  $\text{pH}_{\text{SWS25}}$  data were bias-adjusted and  $C_T$  was calculated again with the same dissociation constants used previously, obtaining a 2ndQC IIM dataset (IIMQCed). The offsets of the new dataset were reduced to zero for the three  $\text{CO}_2$  parameters. Adjustments found for RSMAS dataset ( $A_T \approx 2.7 \mu\text{mol kg}^{-1}$ ,  $C_T \approx 0.4 \mu\text{mol kg}^{-1}$  and  $\text{pH}_{\text{SWS25}} = 0.011$  units) were inside the limits permitted in CARINA for  $A_T$  and  $C_T$  although not for pH.

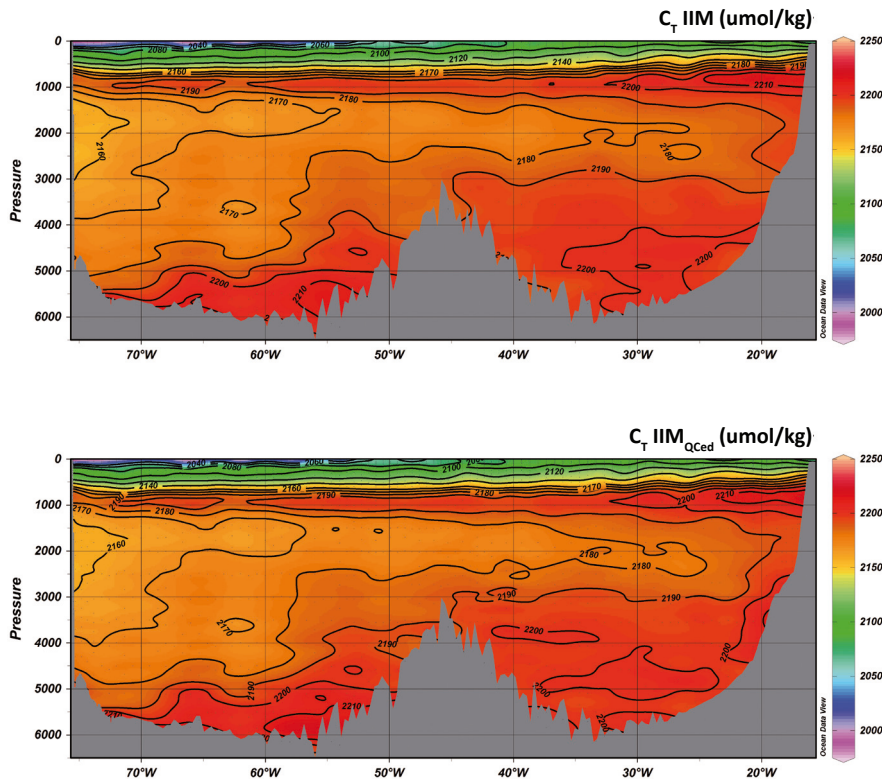
## 5. RESULTS

### 5.1. Carbon species distribution along A05 section

In figures 5, 6, 7 and 8, IIM and IIM<sub>QCed</sub> distributions of C<sub>T</sub>, A<sub>T</sub> and pH<sub>SWS25</sub> fields along the WOCE A05 section at 24.5°N in 1992 are presented.

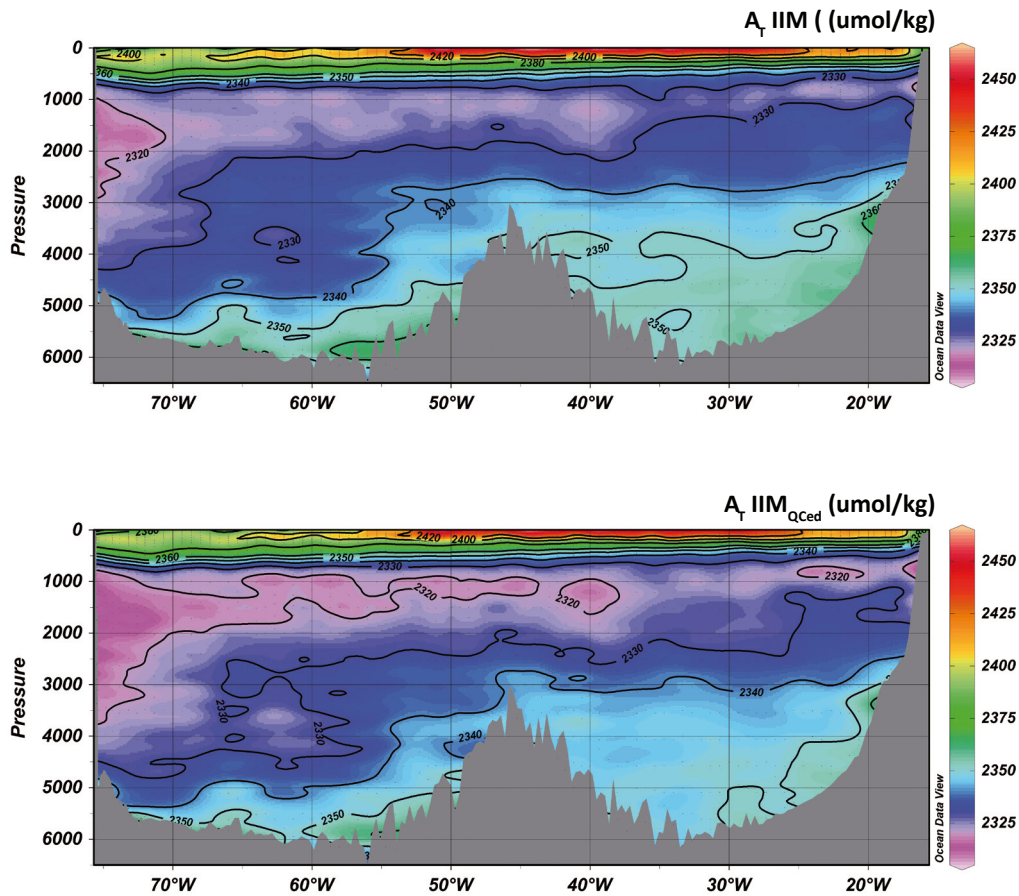
Figure 5 shows the distribution of C<sub>T</sub> ( $\mu\text{mol kg}^{-1}$ ) along the WOCE A05 section of the IIM (original and QCed) data. In general, the C<sub>T</sub> concentrations are greater in the east than in the west and increase from the surface towards the bottom. There is a strong vertical gradient in the upper layers, from the surface (2010-2090  $\mu\text{mol}\cdot\text{kg}^{-1}$ ) to 1000 dbar (2180-2210  $\mu\text{mol}\cdot\text{kg}^{-1}$ ), where a first relative maximum across the entire section is appreciated, because of the presence of Antarctic Intermediate Water (AAIW), that is more intensified in the eastern basin due to a signal associated with the Mediterranean outflow. Below that level, values turn back to 2170-2190  $\mu\text{mol}\cdot\text{kg}^{-1}$  and increase slowly with depth, reaching the same values than in the shallower maximum near the bottom. This deep smoother gradient is due to Upper and Lower North Atlantic Deep Water (NADW) presence, which while spreading to the south occupy largely the section almost until the bottom, crossing amid Antarctic waters. Included within them, Labrador Sea Water (LSW) signal is easily identified around ~1200-2300 dbar, which has greater presence on the western boundary and arrives until half of the eastern basin getting mixed on its way with Antarctic water and so increasing its carbon concentration gradually. LSW pattern can be described accurately, showing how different vertical boundaries appear going down until ~5000 dbar, about each ten degrees of latitude along the entire western basin, clearly lagged below the main core while it moves on and changes its carbon concentration. The limit of the lower NADW is situated just on the top of the Mid Atlantic Ridge and from there on, a more homogeneous water in concentration (2190-2200  $\mu\text{mol}\cdot\text{kg}^{-1}$ ) fills the rest of the eastern basin. Near the bottom the C<sub>T</sub> exhibits the highest concentrations, more intensified in the west (>2200  $\mu\text{mol}\cdot\text{kg}^{-1}$ ) associated with Antarctic Bottom Water (AABW).

Figure 6 shows the distribution of A<sub>T</sub> concentrations ( $\mu\text{mol}\cdot\text{kg}^{-1}$ ) along WOCE A05 section of IIM (original and QCed) data. Opposite to the C<sub>T</sub> field, the highest concentrations are found at the surface (2420-2450  $\mu\text{mol}\cdot\text{kg}^{-1}$ ) and decrease rapidly down to ~800-1000 dbar increasing then again in deep waters. A<sub>T</sub> concentrations are higher in the east than in the west and the lowest values (2310-2320  $\mu\text{mol}\cdot\text{kg}^{-1}$ ) are distributed in good agreement with the C<sub>T</sub> relative minimum that denotes LSW presence. A<sub>T</sub> minimum starts at the western boundary ranging in depth between ~1000 and 4000 dbar for about five degrees of latitude to the right, then narrows forming an horizontal band that extends from ~1000 to 2000 dbar and continues far away almost to the first half of the eastern basin. This low concentration (2320  $\mu\text{mol}\cdot\text{kg}^{-1}$ ) band seems to be coated with a second continuous (2330  $\mu\text{mol}\cdot\text{kg}^{-1}$ ) that narrows too, and spreads to the other margin, finally connecting to a low concentration signal coming from the east. The lower limit of NADW (2340  $\mu\text{mol}\cdot\text{kg}^{-1}$ ) crossing the entire section is deeper in the western basin and swallows afterward the Mid Atlantic Ridge. In the western basin high values (> 2340  $\mu\text{mol}\cdot\text{kg}^{-1}$ ) are found close to the bottom, where AABW extends. In the eastern basin those A<sub>T</sub> concentrations have a wider distribution between 3000 dbar and the bottom.



**Fig 5.** Dissolved inorganic carbon ( $C_T$ ) concentration along A05 section in 1992: IIM (upper panel) and IIM<sub>QCed</sub> (lower panel) data.

Figure 7 shows the distribution of  $pH_{SWS25}$  along WOCE A05 section of the IIM (original and QCed) data. Large-scale pH distribution is well described, where higher values (8-8.1 pH units) are found at the surface and decrease quickly with depth, according to the previously described increasing  $C_T$  and decreasing  $A_T$  strong gradients from the upper layers, until a pH minimum zone. Then, rises a little and decreases again until the bottom. The pH minimum zone (7.65-7.7 pH units), associated to the presence of AAIW, is situated around ~1000 dbar where is enhanced its presence in the eastern margin. Within the NADW, the LSW pH signal is less evident than in the  $C_T$  or  $A_T$  fields because the non-saline dependence of pH. The full distribution of deep waters shows a relatively low pH signal that appears to decrease gradually by the mixing of water masses from west to east. Near the bottom, AABW, with a clear relative pH minimum, is well identified.



**Fig 6.** Total alkalinity ( $A_t$ ) concentration along A05 section in 1992: IIM (upper panel) and IIM<sub>QCed</sub> (lower panel) fields.

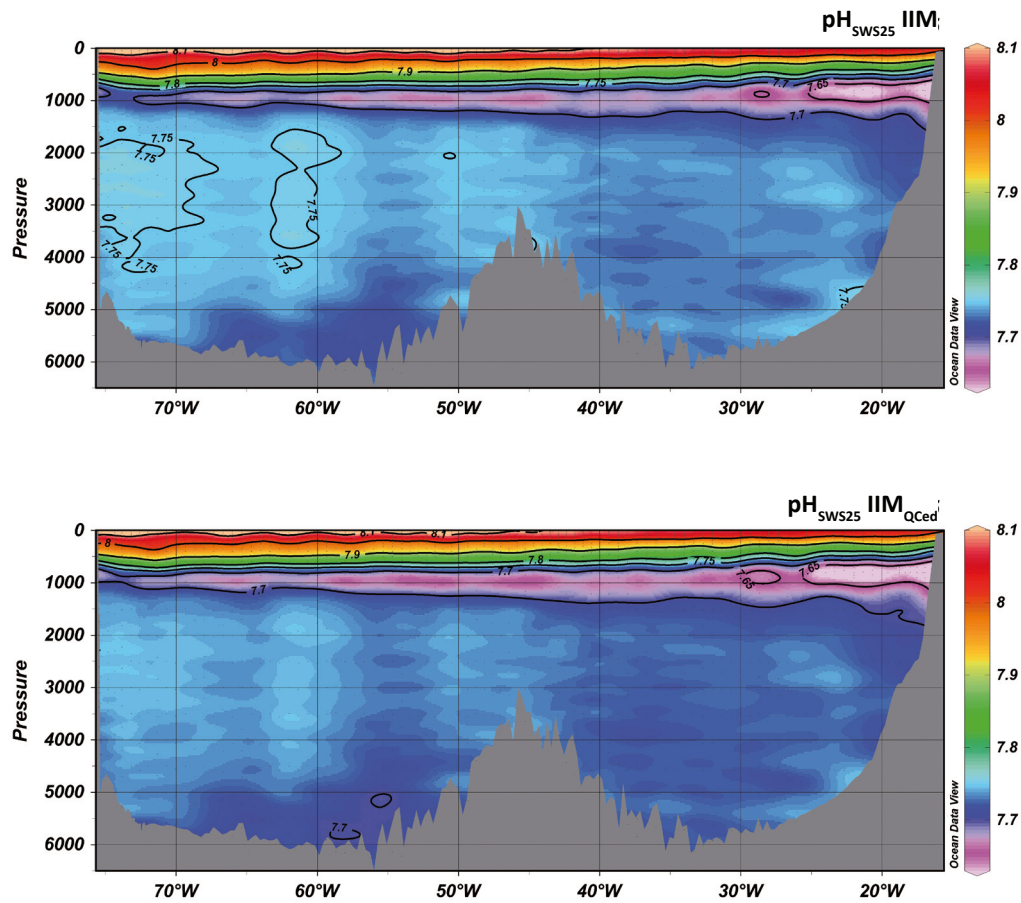


**Fig 7 .** Fields of pH distributions in the seawater scale and referred to 25°C ( $\text{pHSWS25}$ ) along A05 section in 1992: IIM (upper panel) and IIM<sub>QCed</sub> (lower panel) data.

## 5.2. CO<sub>2</sub> variables along the Florida Strait

The IIM dataset and its quality controlled version also include the sampling of ten stations in the Florida Strait, as an exclusive feature. They are enumerated in Table 1 and located in a narrow track between -79.23°W and -80.07°W at 26°N, northernmost than the main section. The region was not covered in the RSMAS dataset and no public carbon data are available in the zone for the 1992 occupation. The Florida Current is composed of wind-driven circulation and the upper layer of the Atlantic Meridional Overturning Circulation (AMOC) that plays an important role in the heat budget of the North Atlantic region. The AMOC supplies the warm waters of the Gulf Stream system, that at this latitude is confined to this shallow (<800m) and narrow (<100km) channel. So, transports measurements in the Florida Strait, in terms of heat and mass, are supposed to be important for understanding global climate and a number of observational programs have been developed during extended periods of time to record its high frequency variability (Baringer and Larsen, 2001). Likewise, carbon transport measurements in Florida Strait are of major importance to correctly understand how the North Atlantic works in its CO<sub>2</sub> sink role. As first described in (Rosón *et al.*, 2003), the C<sub>ANT</sub> transport at 24.5°N is northward and mainly takes place in the first 1000m (94%), dominated by the flux of the Florida Current.

Figure 8 shows the C<sub>T</sub>, A<sub>T</sub>, and pH<sub>SWS25</sub> IIM<sub>QCed</sub> profiles in Florida Strait. The most significant feature is that there exists a very strong horizontal gradient in the three carbon species fields below the first 100m, due to the tilting down of the values isolines of all the parameters towards the east. As described in Rosón *et al.* (2003), the jet of maximum geostrophic velocity is located near the surface very close to the western margin, resulting in the shallowing of the isopycnals towards the west, bringing older waters near the surface and giving rise to a very strong horizontal gradient in all physical and chemical properties. Furthermore, observed ranges in C<sub>T</sub> and A<sub>T</sub> concentrations and pH<sub>SWS25</sub> values are wide and, from the surface to the bottom, are distributed in a relatively short depth compared to the main section. So, the vertical chemical gradient is also very strong in the Florida Strait. All together, these two pronounced spatial gradients make the zone to be highly heterogeneous in terms of the CO<sub>2</sub> system properties. Then, accurate and well distributed measurements are important to correctly describe the Florida Strait inorganic carbon dynamics. The distribution of some CO<sub>2</sub> variables and C<sub>ANT</sub> estimates in the region were presented in Rosón *et al.*, (2003). As showed in figure 8, C<sub>T</sub> and pH<sub>SWS25</sub> present very similar distribution fields but with opposite trends: while C<sub>T</sub> concentration is the lowest at the surface and increases progressively towards the bottom, pH reaches its lowest values there and shows the highest levels at the surface. A<sub>T</sub> field shows a similar pattern to the ones of C<sub>T</sub> and pH<sub>SWS25</sub>, decreasing towards the bottom and influenced by a salinity maximum around ~200 dbar (data not shown) that interrupts the A<sub>T</sub> gradient.

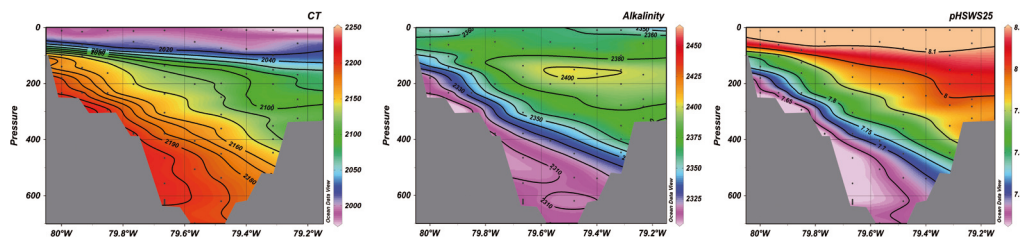


**Fig 8.** Dissolved inorganic carbon ( $C_T$ , left panel), total alkalinity ( $A_T$ , middle panel) and pH ( $pH_{SWS25}$ , right panel) distributions of the  $IIM_{QCed}$  data along the Florida Strait.

## 6. REFERENCES

- Baringer, M.O.N., Larsen, J.C., 2001. Sixteen years of Florida Current Transport at 27° N. *Geophysical Research Letters* 28 (16), 3179-3182.
- Brown, P.J., Bakker, D.C.E., Schuster, U., Watson, A.J., 2010. Anthropogenic carbon accumulation in the subtropical North Atlantic. *Journal of Geophysical Research-Oceans* 115, 4016.
- Dickson, A.G., 1990. Thermodynamics of the dissociation of boric acid in synthetic seawater from 273.15 to 318.15 K. *Deep Sea Research Part A: Oceanographic Research Papers* 37 (5), 755-766.
- Dickson, A.G., Millero, F.J., 1987. A comparison of the equilibrium constants for the dissociation of carbonic acid in seawater media. *Deep Sea Research Part A: Oceanographic Research Papers* 34 (10), 1733-1743.
- Feely, R.A., Sabine, C.L., Lee, K., Berelson, W., Kleypas, J., Fabry, V.J., Millero, F.J., 2004. Impact of Anthropogenic CO<sub>2</sub> on the CaCO<sub>3</sub> system in the oceans. *Science* 305 (5682), 362-366.
- Key, R.M., Tanhua, T., Olsen, A., Hoppema, M., Jutterström, S., Schirnick, C., Van Heuven, S., Kozyr, A., Lin, X., Velo, A., Wallace, D.W.R., Mintrop, L., 2010. The CARINA data synthesis project: introduction and overview. *Earth system science data* 2, 105-121.
- Lyman, J., 1956. Buffer mechanisms of seawater. Ph.D. thesis, University of California, Los Angeles.
- Macdonald, A.M., Baringer, M.O., Wanninkhof, R., Lee, K., Wallace, D.W.R., 2003. A 1998–1992 comparison of inorganic carbon and its transport across 24.5°N in the Atlantic. *Deep Sea Research Part II: Topical Studies in Oceanography* 50 (22–26), 3041-3064.
- Mehrbach, C., Culberson, C.H., Hawley, J.E., Pytkowicz, R.M., 1973. Measurement of the Apparent Dissociation Constants of Carbonic Acid in Seawater at Atmospheric Pressure. *Limnology and Oceanography* 18 (6), 897-907.
- Millero, F.J., Fiol, S., Campbell, D.M., Parrilla, G., 2000. Carbon Dioxide, Hydrographic, and Chemical Data Obtained During the R/V *Hespérides* Cruise in the Atlantic Ocean (WOCE Section A5, July 14 - August 15, 1992).
- Perez, F.F., Fraga, F., 1987a. The pH measurements in seawater on the NBS scale. *Marine Chemistry* 21 (4), 315-327.
- Perez, F.F., Fraga, F., 1987b. A precise and rapid analytical procedure for alkalinity determination. *Marine Chemistry* 21 (2), 169-182.
- Pierrot, D., Lewis, E., Wallace, D., 2006. MS Excel Program Developed for CO<sub>2</sub> System Calculations, ORNL/CDIAC-105a. Carbon Dioxide Information Analysis Center, Oak Ridge National Laboratory, US Department of Energy, Oak Ridge, TN.
- Ríos, A.F., Rosón, G., 1996. pH and alkalinity measurements. Recueil de données par Le Groupe CITHER-2. Lab. de Phys. des Océans, Brest, pp. 64–73.
- Rosón, G., Ríos, A.F., Pérez, F.F., Lavín, A., Bryden, H.L., 2003. Carbon distribution, fluxes, and budgets in the subtropical North Atlantic Ocean (24.5°N). *Journal of Geophysical Research: Oceans* 108 (C5).
- Sabine, C.L., Feely, R.A., Gruber, N., Key, R.M., Lee, K., Bullister, J.L., Wanninkhof, R., Wong, C.S., Wallace, D.W.R., Tilbrook, B., Millero, F.J., Peng, T.-H., Kozyr, A., Ono, T., Rios, A.F., 2004. The oceanic sink for anthropogenic CO<sub>2</sub>. *Science* 305 (5682), 367-371.
- Sabine, C.L., Tanhua, T., 2009. Estimation of Anthropogenic CO<sub>2</sub> Inventories in the Ocean. *Annual Review of Marine Science* 2 (1), 175-198.

Tanhua, T., van Heuven, S., Key, R.M., Velo, A., Olsen, A., Schirnick, C., 2010. Quality control procedures and methods of the CARINA database. *Earth system science data* 2, 35-49.

Vázquez-Rodríguez, M., Touratier, F., Lo Monaco, C., Waugh, D.W., Padin, X.A., Bellerby, R.G.J., Goyet, C., Metzl, N., Ríos, A.F., Pérez, F.F., 2009. Anthropogenic carbon distributions in the Atlantic Ocean: data-based estimates from the Arctic to the Antarctic. *Biogeosciences* 6 (3), 439-451.

Wanninkhof, R., Peng, T.-H., Huss, B., Sabine, C.L., Lee, K., 2003. Comparison of Inorganic Carbon System Parameters Measured in the Atlantic Ocean from 1990 to 1998 and Recommended Adjustments.

Zirino, A., 1985. Mapping strategies in chemical oceanography, 2nd ed, 470 pp., Am. Chem. Soc., Washington, d.C.



## Abbreviations and acronyms

$\Delta C^*$	method for anthropogenic carbon estimation
$\Delta pH_{ant}$	anthropogenic contribution to changes in measured pH
$\Delta pH_m$	difference in measured pH
$\Delta pH_{var}$	natural (non-anthropogenic) contribution to changes in measured pH
$\Delta X$	difference or change in parameter X
$\delta_{Arg}$	oversaturation of carbonate ion with respect to the saturation concentration of aragonite
$\Theta$	potential temperature
$\lambda$	annual rate increase
$\sigma$	standard deviation
$\sigma_x$	potential density referenced to "x" dbar
$\phi C_T^0$	method for anthropogenic carbon estimation
$\Omega_x$	saturation state for calcium carbonate minerals, where x = calcite or aragonite
$^{\circ}C$	degree Celsius
$^{14}C$	radiocarbon
2ndQC	Secondary Quality Control
AABW	Antarctic Bottom Water
AAIW	Antarctic Intermediate Water
ACC	Antarctic Circumpolar Current
ALOHA	A Long-term Oligotrophic Habitat Assessment
AMOC	Atlantic Meridional Overturning Circulation
AOU	Apparent Oxygen Utilization
$A_T$	total alkalinity
$A_T^0$	preformed alkalinity
b	intercept
BATS	Bermuda Atlantic Time series Study
BIO	Buque de Investigación Oceanográfica
$Ca^{2+}$	calcium ion
$CaCO_3$	calcium carbonate
$C_{ant}$	anthropogenic carbon dioxide
$[C_{ant}^X]$	mean $C_{ant}$ values for method X, where X = $C_T^0$ , TrOCA, $\Delta C^*$ or TTD
$C_{ant}-X$	$C_{ant}$ values for method X
CARIACO	CARbon Retention In A Colored Ocean
CARINA	CARbon IN the Atlantic Ocean
$C_{bio}$	biological contribution to measured dissolved inorganic carbon

CCHDO	CLIVAR & Carbon Hydrographic Data Office
CCl <sub>4</sub>	carbon tetrachloride
CDIAC	Carbon Dioxide Information and Analysis Center
C <sub>dis</sub>	air-sea disequilibrium
C <sub>eq</sub>	air-sea equilibrium
CFCs	chlorofluorocarbons
CH <sub>4</sub>	methane
CLIVAR	Climate and Ocean Variability Predictability and Change
C <sub>m</sub>	measured dissolved inorganic carbon
CMIP-5	Coupled Model Intercomparison Project Phase 5
CO <sub>2</sub>	carbon dioxide
CO <sub>2(aq)</sub>	dissolved carbon dioxide
CO <sub>2(g)</sub>	gaseous carbon dioxide
CO <sub>3<sup>2-</sup></sub>	carbonate ion
[CO <sub>3<sup>2-</sup></sub> ] <sub>in situ</sub>	carbonate ion concentration
[CO <sub>3<sup>2-</sup></sub> ] <sub>SatArg</sub>	saturation concentration for aragonite
C <sub>phys</sub>	physical contribution to measured dissolved inorganic carbon
CRM	Certified Reference Material
CSIC	Consejo Superior de Investigaciones Científicas
C <sub>T</sub>	dissolved inorganic carbon. Also referred to as DIC, TIC, TCO <sub>2</sub> or ΣCO <sub>2</sub>
C <sub>T, 280</sub>	dissolved inorganic carbon in equilibrium with the preindustrial atmosphere
CTD	Conductivity-Temperature-Depth instrument
DT(X)	Decadal Trend ± uncertainty in C <sub>ant</sub> accumulation for method X, where X = φC <sub>T</sub> <sup>0</sup> , TrO CA, ΔC* or TTD
DWBC	Deep Western Boundary Current
EB	eastern boundary
eMLR	method for anthropogenic carbon estimation (extended Multiple Linear Regresion)
eOMP	extended Optimum MultiParameter
ER	eastern ridge
ESTOC	European Station for Time series in the Ocean
EUC	Equatorial Undercurrent
fCO <sub>2</sub>	fugacity of CO <sub>2</sub>
FS	Florida Strait
GD	Guinea dome
GEOSECS	Geochemical Ocean Sections Study
GF	method for anthropogenic carbon estimation (Green's function)

GHGs	green house gases
GLODAP	GLobal Ocean Data Analysis Project
GS	Gulf Stream
GtC	Gigatonnes of carbon (1GtC = 1 PgC = $10^{15}$ gC)
H <sup>+</sup>	hydrogen ion or proton
H <sub>2</sub> CO <sub>3</sub>	carbonic acid
HCO <sub>3</sub> <sup>-</sup>	bicarbonate ion
HOT	Hawaii Ocean Time series
iC <sub>ant</sub> y -X	C <sub>ant</sub> specific inventory for method X, and year y
IIM	Insituto de Investigacíons Mariñas
IPCC	Intergovernmental Panel on Climate Change
IS-ts	Iceland Sea time series
ITCZ	Intertropical Convergence Zone
JGOFS	Joint Global Ocean Flux Study
k <sub>0</sub>	solubility constant of carbon dioxide
K	dissociation constant
K <sub>1</sub>	first equilibrium constant of dissociation of carbonic acid
K <sub>2</sub>	second equilibrium constant of dissociation of carbonic acid
K <sub>sp</sub>	solubility constant of calcium carbonate
KNOT	Kyodo North Pacific Ocean Time series
LGMAC	Laboratory for Global Marine and Atmospheric Chemistry
INACW	lower North Atlantic Central Water
INADW	lower North Atlantic Deep Water
LSW	Labrador Sea Water
LWR	longwave radiation
MAR	Mid Atlantic Ridge
MOC	Meridional Overturning Circulation
MOC <sup>2</sup>	Ocean Climate Memory project
MW	Mediterranean Water
N <sub>2</sub> O	nitrous oxide
NAC	North Atlantic Current
NADW	North Atlantic Deep Water
NAO	North Atlantic Oscillation
NASPG	North Atlantic Subpolar gyre
NASTG	North Atlantic Subtropical Gyre
nA <sub>T</sub>	salinity normalized total alkalinity

NBC	North Brasil Current
NBS	National Bureau of Standards
nC <sub>T</sub>	salinity normalized dissolved inorganic carbon
NEC	North Equatorial Current
NECC	North Equatorial Countercurrent
NEUC	North Equatorial Undercurrent
NO <sub>3</sub> <sup>-</sup>	nitrate
NOAA	National Oceanic and Atmospheric Administration
O <sub>2</sub>	dissolved oxygen
OACES	Ocean-Atmosphere Carbon Exchange Study
OH <sup>-</sup>	hydroxide ion
OMZ	oxygen minimum zone
P	pressure
PA <sub>T</sub>	potential alkalinity
PgC	Petagrams of carbon (1PgC = 1 GtC = 10 <sup>15</sup> gC)
pCO <sub>2</sub>	partial pressure of carbon dioxide
PETM	Paleocene-Eocene Thermal Maximum
pH <sub>NBS15</sub>	pH on the NBS scale and referred to 15°C
pH <sub>sws25</sub>	pH on the seawater scale and referred to 25°C
pH <sub>SWSinsitu</sub>	pH on the seawater scale at in situ temperature
pH <sub>T25</sub>	pH on the total hydrogen scale and referred to 25°C
PO <sub>4</sub> <sup>3-</sup>	phosphate
ppm	parts per million
PW	10 <sup>3</sup> Watts
QC	quality control
QCed	quality controlled
r <sup>2</sup>	coefficient of determination
Rc	oxygen to carbon Redfield ratio
RCP	Representative Concentration Pathway
RSMAS	Rosenstiel School of Marine and Atmospheric Science
R/V	Research Vessel
S	salinity
SAC	South Atlantic Current
SACW	South Atlantic Central Water
SAMW	South Atlantic Mode Water
SAVE	South Atlantic Ventilation Experiment

<b>SEC</b>	South Equatorial Current
<b>SD</b>	standard deviation
<b>SF<sub>6</sub></b>	sulfur hexafluoride
<b>SiO<sub>2</sub></b>	silicate
<b>SOMMA</b>	Single-Operator Multiparameter Metabolic Analyzer
<b>SS</b>	steady state
<b>SS_C<sub>ant</sub> -X</b>	C <sub>ant</sub> storage rate assuming steady state for method X
<b>STMW</b>	Subtropical Mode Water
<b>Sv</b>	Sverdrups ( $1\text{Sv} = 10^6 \text{ m}^3 \cdot \text{s}^{-1}$ )
<b>SWR</b>	shortwave radiation
<b>SWS</b>	sea water scale
<b>T</b>	temperature
<b>TrOCA</b>	method for anthropogenic carbon estimation (Tracer combining Oxygen, C <sub>T</sub> and A <sub>T</sub> )
<b>TSSR(X)</b>	Transient Stationary State rate $\pm$ uncertainty in C <sub>ant</sub> accumulation for method X, where X = $\phi C_T^0$ , TrOCA, $\Delta C^*$ or TTD
<b>TTD</b>	method for anthropogenic carbon estimation (Transient Time Distributions)
<b>TTO</b>	Transient Tracers in the Ocean
<b>uNACW</b>	upper North Atlantic Central Water
<b>uNADW</b>	upper North Atlantic Deep Water
<b>WAVES</b>	Web Accessible Visualization and Extraction System
<b>WB</b>	western boundary
<b>WCRP</b>	World Climate Research Program
<b>WML</b>	winter mixed layer
<b>WOCE</b>	World Ocean Circulation Experiment
<b>WR</b>	western ridge





---

## Agradecimientos

*The intellect of a man is forced to choose  
Perfection of the life, or of the work,  
and if it takes the second, must refuse  
a heavenly mansion, raging in the dark.  
When all that story's finished, what's the news?  
In luck or out, the toil has left its mark:  
That old perplexity, an empty purse,  
or the day's vanity, the night's remorse \**

William Butler Yeats

Por alguna casualidad, o sincronicidad, cuando empecé el doctorado fue a parar a mis manos la autobiografía de Rita Levi-Montalcini. Ella dio a sus memorias el nombre de *Elogio de la imperfección*. En ellas, analiza y explica a través del relato de su vida las ventajas de haberse sentido siempre imperfecta en la vida y en la ciencia, para rendir así un tributo a la imperfección como motor para aspirar, si no a la perfección, sí a mejorar continuamente en ambos aspectos. Y lo resume de esta forma en el prólogo: “En mi vida he procurado, conciliar dos aspiraciones inconciliables: <<perfection of the life, or of the work>>, en palabras del poeta Yeats. Es decir, que he realizado lo que podríamos llamar, la <<imperfection of the life and of the work>>. Y el que una actividad desarrollada de manera tan imperfecta haya sido y siga siendo para mí una fuente inagotable de goce me lleva a creer que la imperfección de nuestras realizaciones se compadece mejor con la imperfecta naturaleza humana que la perfección”.

Supongo que porque me pilló sintiéndome yo un poco verde en muchos aspectos para meterme en esto de la ciencia, en aquél entonces pensaba que si fuera un poco más perfecta en la vida no sabía si eso me llevaría a alcanzar mayor perfección en el trabajo, que seguramente sí, pero al menos seguro que podría trabajar mucho más tranquila. Tranquila conmigo. Tranquila con mi entorno. Esa pequeña inquietud inicial me ha llevado a reencontrarme inevitablemente con las reflexiones de la científica Rita Levi-Montalcini respecto a la dualidad vida-trabajo en numerosas ocasiones, circunstancias y ejemplos, míos o ajenos, durante estos años, como si fueran un percutor que golpea en el cerebro periódicamente. Y digamos que fue mi deformación personal, más que profesional, la que me ha hecho prestar una atención particular a cómo todas las personas que me han acompañado en estos años se debaten también entre estos dos aspectos.

Recordando otro comentario sobre las memorias, se podría decir que los científicos sean personas bastante conscientes sobre el valor de la imperfección, porque ¿qué es la ciencia sino mejorar continuamente explicaciones imperfectas? En este empeño, considero que los científicos (y como científicos me refiero a estudiantes, doctorandos, postdocs, técnicos e investigadores consolidados) más “perfectos” que he podido conocer son aquellos que aun no dejando de lado las exigencias del trabajo, tenían sus inquietudes personales presentes y atendidas de igual modo. Agradezco haberme encontrado con personas tan competentes como entrañables a la vez, en este tiempo.

\* <<El intelecto del hombre ha de escoger/entre la perfección en la vida y la del trabajo/Y si elige la segunda, debe renunciar/a una mansión celestial, y rabiar en la oscuridad./ Cuando todo ha acabado , ¿qué queda? / Con suerte o sin ella, el trabajo ha marcado:/quedan la perplejidad, la bolsa vacía, /o por el día vanidad, por la noche remordimiento.>>

---

Mis “jefes” son inalcanzablemente competentes y particularmente entrañables. Les agradezco una serie de aspectos a los dos. Gracias por su confianza. Pero sobre todo por su tiempo, que nunca me han denegado. Por haber compartido su tiempo conmigo. Por atender a todas mis preguntas y dudas con buen tono, aunque a veces fueran poco concretas, descontextualizadas, redundantes o inoportunas. Por esperar que las tuviera. Por su paciencia. Por haber leído todo todo lo que he escrito y devolvérmelo más trabajado (bastante rápido, por cierto). Por compartir conmigo su sabiduría ancestral. Admiro sus mentes receptivas, despiertas, capaces de conectar con tanta rapidez todo lo que saben, todo lo que leen. Por sus pequeñas bromas, su sutil ironía y su sentido del humor. También por sus objeciones y deseares. Por haberme dejado expresar los míos. Gracias por haber compartido conmigo esos tiempos. Por haberme ayudado a mejorar.

Gracias a muchas más personas competentes y entrañables, que he conocido a lo largo de estos años. Siento por los más curiosos que no me sale escribir una lista de sus nombres, me dejaría muchas. Pero puedo resumir. Gracias a mis compañeros y amigos de Barcelona. Gracias al ritmo ajetreado, hacendoso y alegre, expansivo, casi tropical, de un edificio transparente frente al mar rodeado de palmeras y turistas. Por el trabajo entre risas, por los muestreos en equipo, por dejarme dormirme en la furgoneta o tener largas charlas transportando agua. Gracias por mi pequeña familia del despacho. Gracias por los Friday Beer en la Barceloneta, por los desayunos y todos los cafés. Gracias por haber estado aunque yo no estuviera. Gracias a mis compañeros y amigos de Galicia. Gracias al ritmo sereno, distendido, hogareño, constante, casi oriental, del interior de un edificio frío y mojado por fuera el invierno entero por la lluvia. Por todos los paraguas que se me han roto. Por el trabajo entre sonrisas, por dejarme estar al lado de la estufa, dejarme una manta o tener largas charlas frente al ordenador. Gracias a mi pequeña familia de “niñas CSIC” y a mi hermana mayor de minidespacho. Gracias por los magostos y las escapadas en fin de semana, por los desayunos con pincho o galletas (y los quilos que engordé así) y los cafés. Gracias por tenerme presente aun estando lejos.

Gracias a todos los famosos que conocí la primera vez que subí a un barco. Nunca hubiera empezado todo esto de no ser por aquella experiencia. Gracias a todas las personas que he conocido en alta mar.

Gracias al Consejo Superior de Investigaciones Científicas por mi beca (esto es importante).

Gracias a mis amigas y amigos, por quererme incondicionalmente. Gracias a mi familia, por estar conmigo.

Y como no sé cómo acabar sólo diré que está bien a veces acabar brindando...

... (con ratafia y licor café)...

¡Salud!

